

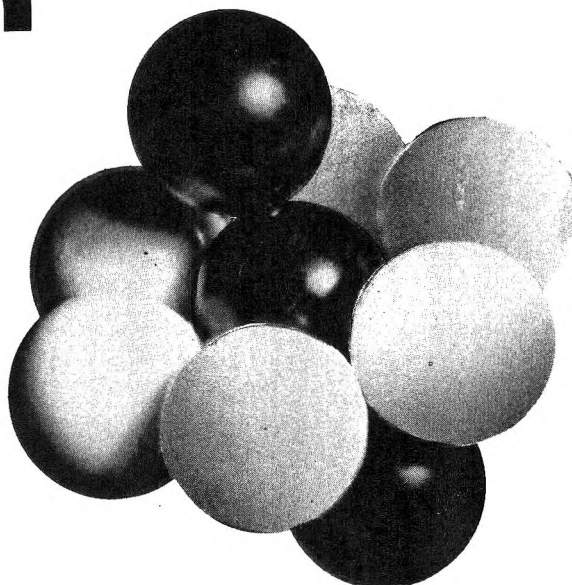
VOLUME 75 SEPTEMBER 2, 1971 NUMBER 18

JPCHA x

THE JOURNAL OF
PHYSICAL
CHEMISTRY

PUBLISHED BIWEEKLY BY THE AMERICAN CHEMICAL SOCIETY

Molecular Sieve Zeolites



ADVANCES IN CHEMISTRY SERIES No. 101 and 102

Seventy-seven papers from a symposium co-sponsored by the Divisions of Colloid and Surface Chemistry, Petroleum Chemistry, and Physical Chemistry of the American Chemical Society and Worcester Polytechnic Institute, Edith M. Flanigen and Leonard B. Sand, co-chairmen.

Do you need a group of substances that can remove radioactive isotopes from nuclear wastes, remove ammonia from secondary sewage effluents, remove sulfur dioxide from waste gases, foster formation of actinides, or disrupt bacterial cells? These and many other possibilities are available through research on molecular sieve zeolites. For example, they are used for

- separating hydrogen isotopes
- solubilizing enzymes
- carrying active catalysts in curing of plastics
- transporting soil nutrients in fertilizers
- filtering tars from cigarette smoke

"Molecular Sieve Zeolites" reports recent advances in this rapidly developing field. Volume I offers 41 papers devoted to the synthesis, structure, mineralogy, and modification of sieve zeolites. These are followed in Volume II by 36 papers discussing sorption and catalysts.

Volume I: 526 pages with index. Cloth bound (1971)
\$16.00

Volume II: 459 pages with index. Cloth bound (1971)
\$16.00

No. 101 and 102 ordered together \$30.00

Postpaid in U.S. and Canada; plus 35 cents elsewhere.

Set of L.C. cards with library orders upon request.

Other books in the ADVANCES IN CHEMISTRY SERIES of interest to colloid and surface, petroleum, and physical chemists include:

- | | | | | |
|---|-----------|-------------|--------|---------|
| No. 97 Refining Petroleum for Chemicals | 293 pages | Cloth bound | (1970) | \$11.50 |
| No. 89 Isotope Effects in Chemical Processes | 278 pages | Cloth bound | (1969) | \$13.00 |
| No. 87 Interaction of Liquids at Solid Substrates | 212 pages | Cloth bound | (1968) | \$9.50 |
| No. 86 Pesticidal Formulations Research. Physical and Colloidal Chemical Aspects | 212 pages | Cloth bound | (1969) | \$9.50 |
| No. 79 Adsorption from Aqueous Solution | 212 pages | Cloth bound | (1968) | \$10.00 |
| No. 43 Contact Angle, Wettability, and Adhesion | 389 pages | Cloth bound | (1964) | \$10.50 |
| No. 31 Critical Solution Temperatures | 246 pages | Cloth bound | (1961) | \$8.00 |
| No. 29 Physical Properties of Chemical Compounds—III | 489 pages | Cloth bound | (1961) | \$10.00 |
| No. 22 Physical Properties of Chemical Compounds—II | 491 pages | Cloth bound | (1959) | \$10.00 |
| No. 20 Literature of the Combustion of Petroleum | 295 pages | Paper bound | (1958) | \$8.00 |
| No. 15 Physical Properties of Chemical Compounds | 536 pages | Cloth bound | (1955) | \$10.00 |

Order from:

Special Issues Sales
American Chemical Society
1155 16th St., N.W.
Washington, D.C. 20036

THE JOURNAL OF
PHYSICAL
CHEMISTRY

Volume 75

SEPTEMBER—DECEMBER 1971

PAGES 2711—4068

INDEXES TO VOLUME 75

BRYCE CRAWFORD, JR., *Editor*

STEPHEN PRAGER, *Associate Editor*

ROBERT W. CARR, JR., FREDERIC A. VAN-CATLEDGE, *Assistant Editors*

EDITORIAL BOARD

A. O. ALLEN
R. BERSOHN
J. R. BOLTON
S. BRUNAUER
M. FIXMAN
H. S. FRANK
J. R. HUIZENGA

M. KASHA
W. J. KAUFMANN
W. R. KRIGBAUM
R. A. MARCUS
W. J. MOORE
J. A. POPLER
B. S. RABINOVITCH

H. REISS
S. A. RICE
R. E. RICHARDS
F. S. ROWLAND
R. L. SCOTT
R. SEIFERT

CHARLES R. BERTSCH, *Manager, Editorial Production*

AMERICAN CHEMICAL SOCIETY

FREDERICK T. WALL, *Executive Director*

BOOKS AND JOURNALS DIVISION

JOSEPH H. KUNNEY

Head, Business Operations Department

JOHN K. CRUM
Director (Acting)

RUTH REYNARD
Assistant to the Director

THE JOURNAL OF PHYSICAL CHEMISTRY

BRYCE CRAWFORD, Jr., *Editor*

STEPHEN PRAGER, *Associate Editor*

ROBERT W. CARR, Jr., FREDERIC A. VAN CATLEDGE, *Assistant Editors*

EDITORIAL BOARD: A. O. ALLEN (1970-1974), R. BERSOHN (1967-1971), J. R. BOLTON (1971-1975), S. BRUNAUER (1967-1971), M. FIXMAN (1970-1974), H. S. FRANK (1970-1974), J. R. HUIZENGA (1969-1973), M. KASHA (1967-1971), W. J. KAUZMANN (1969-1973), W. R. KRIGBAUM (1969-1973), R. A. MARCUS (1968-1972), W. J. MOORE (1969-1973), J. A. POPLE (1971-1975), B. S. RABINOVITCH (1971-1975), H. REISS (1970-1974), S. A. RICE (1969-1975), R. E. RICHARDS (1967-1971), F. S. ROWLAND (1968-1972), R. L. SCOTT (1968-1972), R. SEIFERT (1968-1972)

CHARLES R. BERTSCH, *Manager, Editorial Production*

AMERICAN CHEMICAL SOCIETY, 1155 Sixteenth St., N.W., Washington, D. C. 20036

FREDERICK T. WALL, *Executive Director*

Books and Journals Division

JOHN K CRUM, *Director (Acting)*

JOSEPH H. KUNEY, *Head, Business Operations Department*

RUTH REYNARD, *Assistant to the Director*

©Copyright, 1971, by the American Chemical Society. Published biweekly by the American Chemical Society at 20th and Northampton Sts., Easton, Pa. 18042. Second-class postage paid at Easton, Pa.

All manuscripts should be sent to *The Journal of Physical Chemistry*, Department of Chemistry, University of Minnesota, Minneapolis, Minn. 55455.

Additions and Corrections are published once yearly in the final issue. See Volume 74, Number 26 for the proper form.

Extensive or unusual alterations in an article after it has been set in type are made at the author's expense, and it is understood that by requesting such alterations the author agrees to defray the cost thereof.

The American Chemical Society and the Editor of *The Journal of Physical Chemistry* assume no responsibility for the statements and opinions advanced by contributors.

Correspondence regarding accepted copy, proofs, and reprints should be directed to Editorial Production Office, American Chemical Society, 20th and Northampton Sts., Easton, Pa. 18042. Manager: CHARLES R. BERTSCH. Assistant Editor: EDWARD A. BORGER. Editorial Assistant: EVELYN J. UHLER.

Advertising Office: Century Communications Corporation, 142 East Avenue, Norwalk, Conn. 06851.

Business and Subscription Information

Remittances and orders for subscriptions and for single copies,

notices of changes of address and new professional connections, and claims for missing numbers should be sent to the Subscription Service Department, American Chemical Society, 1155 Sixteenth St., N.W., Washington, D. C. 20036. Allow 4 weeks for changes of address. Please include an old address label with the notification.

Claims for missing numbers will not be allowed (1) if received more than sixty days from date of issue, (2) if loss was due to failure of notice of change of address to be received before the date specified in the preceding paragraph, or (3) if the reason for the claim is "missing from files."

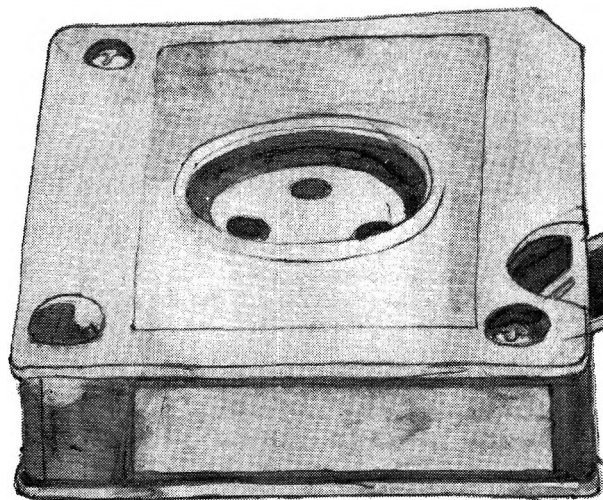
Subscription rates (1971): members of the American Chemical Society, \$20.00 for 1 year; to nonmembers, \$40.00 for 1 year. Those interested in becoming members should write to the Admissions Department, American Chemical Society, 1155 Sixteenth St., N.W., Washington, D. C. 20036. Postage to Canada and countries in the Pan-American Union, \$4.00; all other countries, \$5.00. Single copies for current year: \$2.00. Rates for back issues from Volume 56 to date are available from the Special Issues Sales Department, 1155 Sixteenth St., N.W., Washington, D. C. 20036.

This publication and the other ACS periodical publications are now available on microfilm. For information write to: MICROFILM, Special Issues Sales Department, 1155 Sixteenth St., N.W., Washington, D. C. 20036.

"Primary Publications on Microfilm"

Your Key to—

- Dramatic savings in archival space and dollars . . . over **1,000,000** pages of chemical literature contained in a carousel measuring only 17" x 17" x 39".
- Faster access to needed data. Slash costly search and retrieval time required of your scientists and librarians.
- Unlimited distribution of copyrighted scientific data. "ACS Primary Publications on Microfilm" are available under a unique licensing agreement permitting you to make as many enlarged photocopies per page as desired . . . for distribution throughout your company.



American Chemical Society Primary Publications included in this microfilm program:

JOURNAL OF THE AMERICAN CHEMICAL SOCIETY
INDUSTRIAL & ENGINEERING CHEMISTRY
CHEMICAL TECHNOLOGY
CHEMICAL & ENGINEERING NEWS
CHEMICAL & ENGINEERING NEWS ANNUAL INDEXES
ANALYTICAL CHEMISTRY
JOURNAL OF PHYSICAL CHEMISTRY
JOURNAL OF AGRICULTURAL AND FOOD CHEMISTRY
JOURNAL OF ORGANIC CHEMISTRY
JOURNAL OF CHEMICAL AND ENGINEERING DATA
CHEMICAL REVIEWS
JOURNAL OF CHEMICAL DOCUMENTATION
I&EC FUNDAMENTALS
I&EC PROCESS DESIGN AND DEVELOPMENT
I&EC PRODUCT RESEARCH AND DEVELOPMENT
BIOCHEMISTRY
INORGANIC CHEMISTRY
JOURNAL OF MEDICINAL CHEMISTRY
CHEMISTRY
ENVIRONMENTAL SCIENCE & TECHNOLOGY
ACCOUNTS OF CHEMICAL RESEARCH
MACROMOLECULES

For information on "ACS Primary Publications on Microfilm", write or call:
Mr. George Virvan
Special Issues Sales
American Chemical Society
1155 16th Street, N.W.
Washington, D.C. 20036
(202-737-3337)

THE JOURNAL OF PHYSICAL CHEMISTRY

Volume 75, Number 18 September 2, 1971

Reactions of Borane (BH_3). III. Absolute Rates of Formation of the Donor-Acceptor Adducts BH_3PF_3 and $\text{BH}_3\text{N}(\text{CH}_3)_3$	S. A. Fridmann and T. P. Fehlner	2711
The Dynamic Adsorption of Water Vapor by a Fiber Drawn from a Melt of Vycor	Victor R. Deitz and Noel H. Turner	2718
Concentration Quenching of Proflavine Hydrochloride in Dry Films of Sodium Deoxyribonucleate and Poly(vinyl alcohol)	G. Strauss, S. B. Brojde, and T. Kurucsev	2727
The Photodecomposition of γ -Butyrolactone in the Vapor Phase	R. Simonaitis and J. N. Pitts, Jr.	2733
The Photochemical Oxidation of Some Substituted Aromatic Amines in Chloroform	E. A. Fitzgerald, Jr., P. Wuelfing, Jr., and H. H. Richtol	2737
The Photochemistry of the Xylenes. A Discussion of Method	W. Albert Noyes, Jr., and D. A. Harter	2741
An Investigation of Radicals Produced in the Photolysis of Thiosulfate Solutions by Electron Spin Resonance	D. Behar and Richard W. Fessenden	2752
γ Radiolysis of Liquid Ethanol. Yields of Hydrogen and Free Ions. Solvated Electron Rate Constants	S. M. S. Akhtar and G. R. Freeman	2756
Mechanism of the Radiation-Induced Dechlorination of 1,1,1-Trichloro-2,2-bis(<i>p</i> -chlorophenyl)ethane in Alcoholic Solution	Rudolph Evans, Edwin Nesyto, Cecilia Radlowski, and Warren V. Sherman	2762
An Electron Spin Resonance and Electron Nuclear Double Resonance Study of the 4-Formyl-2,6-di- <i>tert</i> -butylphenoxy Radical	Robert D. Allendoerfer and Daniel J. Eustace	2765
An Electron Spin Resonance Line-Shape Analysis for Determination of Unresolved Metal Hyperfine Splittings in Ion Pairs. Its Application to the Benzene Anion Radical	M. T. Jones, M. Komarynsky, and R. D. Rataiczak	2769
An Infrared Study of Surface Properties of α -Chromia. I. Preparation and Adsorption of Water, Heavy Water, and Carbon Monoxide	A. Zecchina, S. Coluccia, E. Guglielminotti, and G. Ghiotti	2774
An Infrared Study of Surface Properties of α -Chromia. II. Oxygen Chemisorption	A. Zecchina, S. Coluccia, L. Cerruti, and E. Borello	2783
An Infrared Study of Surface Properties of α -Chromia. III. Adsorption of Carbon Dioxide	A. Zecchina, S. Coluccia, E. Guglielminotti, and G. Ghiotti	2790
The Absorption Spectrum of e_{aq}^- in the Temperature Range -4 to 390°	B. D. Michael, Edwin J. Hart, and Klaus H. Schmidt	2793
Vibrational Spectra of <i>tert</i> -Butyl Cyanide	G. A. Crowder	2806
Ionic Radii from Scaled Particle Theory of the Salt Effect	W. L. Masterton, David Bolocofsky, and Tei Pei Lee	2809
Investigations on the Ion-Exchange and Ionic Transport Properties of Glass Membranes in Molten Salts by an Electrolytic Transport Technique	T. J. van Reenen, Marie van Niekerk, and W. J. de Wet	2815
Ellipsometric Investigations of Anodic Film Growth on Iron in Neutral Solution. The Prepassive Film	H. Wroblowa, V. Brusica, and J. O'M. Bockris	2823
The Effect of Magnetic Fields on the pH of Water	T. I. Quickenden, D. M. Betts, B. Cole, and M. Noble	2830
Solubility of Helium and Argon in Liquid Sodium	Ewald Veleckis, Sanat K. Dhar, Fred A. Cafasso, and Harold M. Feder	2832
Transitions in Mesophase Forming Systems. I. Transformation Kinetics and Pretransition Effects in Cholesteryl Myristate	Fraser P. Price and Joachim H. Wendorff	2839
Transitions in Mesophase Forming Systems. II. Transformation Kinetics and Properties of Cholesteryl Acetate	Fraser P. Price and Joachim H. Wendorff	2849

The Radiolysis of Liquid <i>n</i> -Butane	Noboru Fujisaki, Shoji Shida, Yoshihiko Hatano, and Kuniyasu Tanno	2854
The Radical Anions of Vitamin A Aldehyde and Related Schiff Bases	C. M. Lang, J. Harbour, and A. V. Guzzo	2861
¹²⁹ I Mössbauer Studies of the Chemical Effects of Nuclear Transformations in Compounds of Tellurium	J. L. Warren, C. H. W. Jones, and P. Vasudev	2867

NOTES

Freezing Point Depression Measurements in <i>N</i> -Methylacetamide as a Solvent	O. D. Bonner and G. B. Woolsey	2879
Relations of Iodine with Olefins. II. Radiative Neutron Capture Induced Reactions of Iodine-128 with Various C ₃ Isomers: Evidence for a Mechanism Other Than Autoradiolysis in the Condensed State	R. L. Ayres, O. C. Gadeken, and E. P. Rack	2880

AUTHOR INDEX

Akhtar, S. M. S., 2756	Deitz, V. R., 2718	Guzzo, A. V., 2861	Nesyto, E., 2762	Strauss, G., 2727
Allendoerfer, R. D., 2765	de Wet, W. J., 2815	Harbour, J., 2861	Noble, M., 2830	Tanno, K., 2854
Ayres, R. L., 2880	Dhar, S. K., 2832	Hart, E. J., 2798	Noyes, W. A., Jr., 2741	Turner, N. H., 2718
Behar, D., 2752	Eustace, D. J., 2765	Harter, D. A., 2741	Pitts, J. N., Jr., 2733	van Niekerk, M., 2815
Betts, D. M., 2830	Evans, R., 2762	Hatano, Y., 2854	Price, F. P., 2839, 2849	van Reenen, T. J., 2815
Bockris, J. O'M., 2823	Feder, H. M., 2832	Jones, C. H. W., 2867	Quickenden, T. I., 2830	Vasudev, P., 2867
Bolocofsky, D., 2809	Fehlner, T. P., 2711	Jones, M. T., 2769	Rack, E. P., 2880	Veleckis, E., 2832
Bonner, O. D., 2879	Fessenden, R. W., 2752	Komarynsky, M., 2769	Radlowski, C., 2762	Warren, J. L., 2867
Borello, E., 2783	Fitzgerald, E. A., Jr., 2737	Kurucsev, T., 2727	Rataiczak, R. D., 2769	Wendorff, J. H., 2839, 2849
Broyde, S. B., 2727	Freeman, G. R., 2756	Lang, C. M., 2861	Richtol, H. H., 2737	Woolsey, G. B., 2879
Brusic, V., 2823	Fridmann, S. A., 2711	Lee, T. P., 2809	Schmidt, K. H., 2798	Wroblowa, H., 2823
Cafasso, F. A., 2832	Fujisaki, N., 2854	Masterton, W. L., 2809	Sherman, W. V., 2762	Wuelfing, P., Jr., 2737
Cerruti, L., 2783	Gadeken, O. C., 2880	Michael, B. D., 2798	Shida, S., 2854	Zecchina, A., 2774, 2783, 2790
Cole, B., 2830	Ghiotti, G., 2774, 2790		Simonaitis, R., 2733	
Coluccia, S., 2774, 2783, 2790	Guglielminotti, E., 2774, 2790			
Crowder, G. A., 2806				

In papers with more than one author the name of the author to whom inquiries about the paper should be addressed is marked with an asterisk in the by-line.

THE JOURNAL OF PHYSICAL CHEMISTRY

Registered in U. S. Patent Office © Copyright, 1971, by the American Chemical Society

VOLUME 75, NUMBER 18 SEPTEMBER 2, 1971

Reactions of Borane (BH₃). III. Absolute Rates of Formation of the Donor-Acceptor Adducts BH₃PF₃ and BH₃N(CH₃)₃¹

by S. A. Fridmann and T. P. Fehlner*

Department of Chemistry and Radiation Laboratory,² University of Notre Dame, Notre Dame, Indiana 46556
(Received February 22, 1971)

Publication costs assisted by the National Science Foundation

Absolute rate constants for the reactions of free borane, BH₃, with phosphorus trifluoride, PF₃, and trimethylamine, N(CH₃)₃, have been directly measured by observing the formation of the two donor-acceptor adducts BH₃PF₃ and BH₃N(CH₃)₃, respectively. At 500°K and at a total pressure of 6 Torr (ca. 98% helium) the rate constant for the formation of BH₃PF₃ is 1.5×10^8 l./mol sec while the rate constant for the formation of BH₃N(CH₃)₃ is 1.1×10^9 l./mol sec. The former may not be the high-pressure limiting value while the latter is probably close to the high-pressure limiting rate constant. These results are briefly discussed in terms of presently held concepts of donor-acceptor reactions.

The process in which an electron-pair donor molecule interacts with a tricoordinate boron atom to form a stable adduct is not well understood³ despite qualitative correlations with some structural properties of both donor and acceptor.³⁻⁷ Among the factors considered to be important for promoting donor-acceptor reactions are electron withdrawing and donating substituents on the acceptor and donor, the ability of the planar tricoordinate acceptor molecule to distort to a pyramidal geometry, and the absence of highly bulky substituents on either species which would interfere with their close approach. Thermochemical studies of the reactions of boron trihalides with the donor molecule pyridine⁴ have demonstrated that acceptor strength parallels the ease of distortion of the acceptor molecule:^{4,8} BBr₃ > BCl₃ > BF₃. BF₃ was found to be the weakest acceptor among the boron trihalides which is consistent with its high planar rigidity resulting from substantial π bonding.^{8,9} Several kinetic studies of the reactions of BF₃ with the methylamines and ammonia have been carried out.^{7,10} The following order of rate constants was obtained for the reactions of BF₃ with (a) ammonia, (m) mono-, (d) di-, and (t) trimethylamine; $k_a < k_m <$

$k_t < k_d$. More recently, however, the variation of k_m/k_t with pressure has been reported and at high pressures it is apparent that $k_m > k_t$.¹¹ The last result is attributed to a steric effect.

(1) Supported in major part by the National Science Foundation under Grant No. GP 10199.

(2) The Radiation Laboratory is operated by the University of Notre Dame under contract with the Atomic Energy Commission. This is AEC Document No. COO-38-773.

(3) E. L. Muetterties, "The Chemistry of Boron and Its Compounds," Wiley, New York, N. Y., 1967, Chapter 1.

(4) H. C. Brown and R. R. Holmes, *J. Amer. Chem. Soc.*, **78**, 2173 (1956).

(5) J. M. Miller and M. Onyszczuk, *Can. J. Chem.*, **42**, 1518 (1964).

(6) C. M. Bax, A. R. Katritzky, and L. E. Sutton, *J. Chem. Soc.*, 1254, 1258 (1958).

(7) S. H. Bauer, *Advan. Chem. Ser.*, No. 32, 88 (1961); No. 42, 35 (1964).

(8) F. A. Cotton and J. R. Leto, *J. Chem. Phys.*, **30**, 993 (1959).

(9) M. E. Schwartz and L. C. Allen, *J. Amer. Chem. Soc.*, **92**, 730 (1970).

(10) See the following leading reference and other papers cited therein, F. T. Smith and G. B. Kistiakowsky, *J. Chem. Phys.*, **31**, 621 (1959).

(11) S. Glicker and R. A. Marcus, *J. Amer. Chem. Soc.*, **91**, 7607 (1969).

The significance of steric effects on donor-acceptor reactions is part of a more fundamental question, namely, the intermolecular distance at which attractive interaction sets in and its dependence on relative orientation. Mulliken's charge-transfer theory for such reactions¹² provides a basis for qualitatively discussing this problem in terms of structural properties. The effective range of attractive interaction is the intermolecular distance at which electron transfer from donor to acceptor occurs. This is inversely proportional to the difference between ionization potential of the donor and electron affinity of the acceptor. Long-range interactions would minimize steric effects and, with a given acceptor, one would expect a correlation with the ionization potential of the donor. With shorter range interactions steric effects would play a role.

Knowledge of the acceptor behavior of the reactive species BH_3 with a somewhat smaller and supposedly more flexible structure than BF_3 ^{8,9} would be distinctly useful in furthering our understanding of these reactions. Consequently, we have compared the reactivity of BH_3 and BF_3 toward both the same donor and different donors.

Experimental Section

Technique. The apparatus consists of a fast-flow gas-phase reactor coupled to a mass spectrometer utilizing a modulated molecular beam sampling technique. Detailed descriptions appear elsewhere¹³⁻¹⁷ and here only one major modification will be described. The original solid rod on which the thermocouple was mounted and scanned along the reactor was replaced by a quartz tube through which gases are directly introduced into the reactor. This dual-purpose inlet tube and thermocouple probe can be scanned along the axis of the main flow tube as before. Its approximate size and geometry are shown schematically in relation to the main flow tube in Figure 1. The 2 mm i.d. and 3 mm o.d. tubing is drawn to a capillary tip on which the thermocouple is mounted. Several millimeters above the tip are located the three exit holes (*ca.* 1 mm diameter) through which gas enters the main flow stream. Full details appear elsewhere.¹⁶

In making kinetic measurements, partial pressures of BH_3CO or BH_3PF_3 , up to 100 mTorr with the reactor unheated, are introduced into the main helium flow-stream. The pyrolysis of the BH_3 source gas in the decomposition zone (D) produces BH_3 which reacts in the reaction zone (R). Here, along with recombination to form diborane, association with suitable substrate species takes place. As they are not mutually too reactive, BH_3CO source gas and PF_3 substrate gas are metered through separate leaks and are mixed with the helium carrier gas before entering the decomposition zone. However, trimethylamine is known to react readily with both BH_3CO ^{18,19} and BH_3PF_3 ²⁰ and therefore was injected directly into the reaction zone through

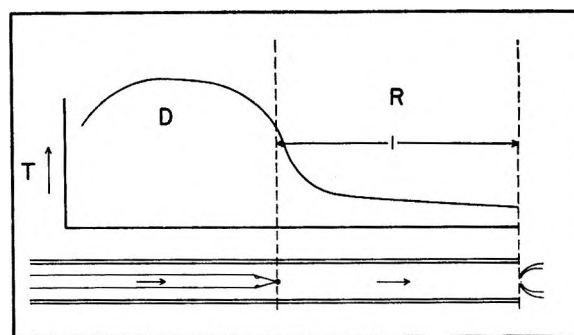


Figure 1. Schematic diagram of the inlet probe. T is the temperature of the gas along the axis of the flow tube, D is the decomposition zone used to prepare BH_3 from BH_3PF_3 or BH_3CO , R is the reaction zone, and l is the distance between probe tip and the end of the flow tube.

the inlet probe, as shown in Figure 1. This allowed the study of the formation of BH_3NMe_3 from BH_3 and NMe_3 without major complications from side reactions. In addition, use of the probe enables one to vary the residence time of the amine in the reaction zone by varying distance l between the probe tip and the end of the flow tube. This feature is essential to the difference method discussed below.

A typical kinetic run consists of making three sets of measurements apart from the initial sensitivity calibrations. Initial pressures (P)₀ of source and substrate gases introduced at several assigned leak settings are measured with the reactor unheated, by means of their appropriate ion intensities. Two additional sets of measurements using the same leak settings are made alternately at the short (S) and long (L) profiles to yield sample partial pressures at the beginning (P)_S and end (P)_L of the reaction zone, respectively.¹⁷ At the end of the long profile shown in Figure 1 products from the recombination zone are sampled and consist of borane adducts, diborane and unreacted BH_3 . Sample pressures at the beginning of this zone are measured at the short profile, which is set up by reproducing zone D close to the sampling leak. Pressures of amine or PF_3 substrate are those measured initially and do not change when the reactor is heated.

- (12) R. S. Mulliken, *J. Amer. Chem. Soc.*, **74**, 811 (1952).
- (13) G. W. Mappes, Ph.D. Thesis, University of Notre Dame, 1969.
- (14) G. W. Mappes and T. P. Fehlner, *J. Amer. Chem. Soc.*, **92**, 1562 (1970).
- (15) T. P. Fehlner, *ibid.*, **90**, 4817 (1968).
- (16) S. A. Fridmann, Ph.D. Thesis, University of Notre Dame, 1971.
- (17) G. W. Mappes, S. A. Fridmann, and T. P. Fehlner, *J. Phys. Chem.*, **74**, 3307 (1970).
- (18) A. B. Burg and H. I. Schlesinger, *J. Amer. Chem. Soc.*, **59**, 780 (1937).
- (19) J. Grotewold, E. A. Lissi, and A. E. Villa, *J. Chem. Soc.*, **A**, 1034, 1038 (1966).
- (20) R. W. Parry and T. C. Bissot, *J. Amer. Chem. Soc.*, **78**, 1524 (1956).

The technique of injecting gaseous reactants into a flow stream through a fixed or movable inlet probe is one which has been described in conjunction with several kinetic studies.²¹⁻²⁴ Depending on the geometry of the probe and the mass flow of gas issuing from it, more or less severe concentration gradients occur at the tip of the probe and persist downstream for some distance before complete mixing occurs. It has been noted²⁴ that two opposing errors are introduced into observed rate measurements as a result of delayed mixing, one due to the reduced extent of reaction in regions where mixing has not occurred, the other to enhanced reaction along boundaries where high local concentrations of reactants exist. Since these effects do not in general cancel, precise analysis of the kinetic data requires prior careful analysis of the flow.²²⁻²⁴ An exception is the case where a difference technique (*e.g.* use of a movable probe) can be used to approximately cancel the effects of anomalous reaction in the vicinity of the tip.²¹ This was the type of method which was adopted in these studies.

A preliminary experiment was designed to examine the degree of mixing between probe gas and helium carrier gas as a function of distance downstream from the tip of the probe. PF₃ was introduced through the probe to give a pressure of *ca.* 300 mTorr in the reactor, corresponding to a flow of 0.79 Torr l./sec. The intensity of the *m/e* 69 ion peak from PF₃, which is a measure of the axial PF₃ concentration, was measured at various probe positions with respect to the end of the flow tube. Figure 2 is a plot of the log of the *m/e* 69 ion intensity at any probe position minus the position independent intensity achieved at large distances from the leak. The mixing is approximately exponential with a half-life of *ca.* 1 cm. The results were the same for lower flows of PF₃ (0.20 and 0.40 Torr l./sec).

Methods of calibration under various conditions of flow and temperature and the determination of the relative sensitivity of BH₃ have been described previously.

Materials. BH₃PF₃ was prepared according to the method of Parry and Bissot.²⁰ The material was distilled in the same manner as BH₃CO, the preparation of which is described elsewhere.²⁵ The maximum impurities after distillation were 5% of B₂H₆ or of PF₃.

BH₃NMe₃ was prepared by reaction between diborane and trimethylamine. The 1.2 mmol of B₂H₆ and 3.5 mmol of Me₃N were condensed at -196° into a U trap on a vacuum line and warmed slowly to -60°. Excess amine and other volatiles were distilled by several freeze-pump-thaw cycles between -60° and room temperature. The final vapor pressure of *ca.* 0.8 Torr at room temperature corresponds to that reported for the adduct.²⁶ A partial mass spectrum of this material was obtained and found to correspond within experimental precision to that of the product observed in the trimethylamine experiments. The relative intensities

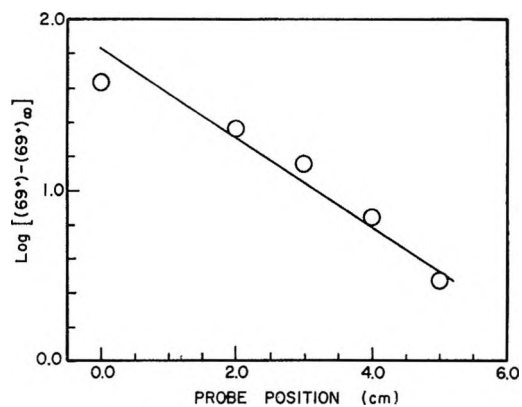


Figure 2. Plot of the log of the *m/e* 69 ion signal from PF₃ at any probe position minus the intensity at long mixing times at 298°K, 4.6 Torr total pressure, and a partial pressure of PF₃ of 300 mTorr.

of ion peaks *m/e* 73:72:71 were as follows: prepared adduct, 5.3:100:31; observed product, 2.9:100:30.

PF₃ of unspecified purity was obtained from Peninsular ChemResearch and trimethylamine of stated purity 99.0% from Matheson Co.

Results

$BH_3 + PF_3 \xrightarrow{k_2} BH_3PF_3$. The main kinetic data on this reaction are given in Table I. T_R is the mean temperature along the recombination zone and T_D the maximum temperature in the decomposition zone. t is the reaction time defined by l/v , where l is the length of, and v the temperature corrected²⁷ linear flow rate through, the recombination zone. p is the pressure read at the bottom of the flow tube after steady flow is established. The mass spectrometer sensitivity S is expressed in the same arbitrary units used previously.¹⁷ The measured pressures (P)₀, (P)_S, and (P)_L are defined above. BH₃ pressures were measured with PF₃ present in the flow stream at the corresponding pressures (PF₃)₀. An exception to this procedure occurs in experiment 27 where all but one of the values for (BH₃)_S were measured without PF₃ present and are indicated by parentheses. Adding PF₃ to the flow stream does not measurably change the BH₃ level, as indicated by the remaining value not in parentheses. However, a similar check at the long profile shows a decrease in BH₃

(21) A. A. Westenberg and N. de Haas, *J. Chem. Phys.*, **46**, 490 (1967).

(22) G. C. Frazier, Jr., and W. J. Kooyman, *Chem. Eng. Sci.*, **23**, 353 (1968).

(23) V. L. Talrose, V. P. Strunin, A. F. Dodonov, and G. K. Lavroskaya, *Advan. Mass Spectrom.*, **3**, 993 (1966).

(24) E. E. Ferguson, T. C. Fehsenfeld, and A. L. Schmeltekopf, *Advan. At. Mol. Phys.*, **5**, 1 (1969).

(25) T. P. Fehlner and G. W. Mappes, *J. Phys. Chem.*, **73**, 873 (1969).

(26) E. R. Alton, R. D. Brown, J. C. Carter, and R. C. Taylor, *J. Amer. Chem. Soc.*, **81**, 3550 (1959).

(27) The correction to the flow rate measured at room temperature is $T_R/298$. See ref 24.

Table I: Partial Pressures of the Adduct from the Reaction of BH_3 and PF_3 in mTorr at 500°K and a Total Pressure of 5.7 Torr

Conditions	Expt	$(\text{PF}_3)_0$	$(\text{BH}_3\text{CO})_0$	$(\text{BH}_3\text{CO})_S$	$(\text{BH}_3)_S$	$(\text{BH}_3)_L$	$(\overline{\text{BH}_3})$	$(\text{BH}_2\text{PF}_3)_S$	$(\text{BH}_2\text{PF}_3)_L$	$10^{-4} k_2$, l./mol sec
$T_R = 500^\circ\text{K}$ $T_D = 650^\circ\text{K}$ $t = 0.537$ msec $10^{-3}v = 7.45$ cm/sec $P = 5.74$ Torr $S = 13.6$	24	10.0	47.9	15.1	10.2	1.0	5.6		0.22	2.2
		20.2	29.3		7.1	2.2	4.9		0.26	1.5
		45.0	18.6		3.3	0.87	2.1		0.25	1.5
		45.0	47.9	15.1	10.2	0.66	5.4	<0.02	0.70	1.7
$T_R = 507^\circ\text{K}$ $T_D = 649^\circ\text{K}$ $t = 0.513$ msec $10^{-3}v = 7.80$ cm/sec $P = 5.79$ Torr $S = 18.2$	30	52.5	14.7	5.0	2.1	1.8	2.0		0.18	1.1
		52.5	33.2	11.2	7.6	3.2	5.4		0.37	0.80
		52.5	60.2	22.0	8.5	6.0	7.2		0.49	0.79
		126.2	14.7	5.0	1.7	1.5	1.6		0.31	0.92
		126.2	33.2	11.2	6.5	2.6	4.6		0.41	0.43
$T_R = 494^\circ\text{K}$ $T_D = 652^\circ\text{K}$ $t = 0.611$ msec $10^{-3}v = 6.58$ cm/sec $P = 5.62$ Torr $S = 17.8$	27	12.7	11.0		(0.91)	0.00	0.45		0.086	7.5
		12.7	19.5	6.9	(1.8)	1.4	1.6		0.059	1.5
		12.7	36.0	11.6	(4.3)	2.2	3.3		0.096	1.2
		50.3	11.0		(0.91)	0.0	0.45		0.20	4.6
		50.3	19.5	6.9	(1.8)	1.2	1.5		0.35	2.4
		50.3	36.0	11.6	(4.3)	2.2	3.2		0.40	1.2
		136	11.0		(0.91)	0.04	0.48		0.43	3.3
136	19.5	6.9	1.8	0.74	1.3		0.83	2.4		
136	36.0	11.6	(4.3)	1.7	3.0	<0.11	1.07	1.3		

from 1.3 to 0.74 mTorr upon adding 136 mTorr of PF_3 . This corresponds to a second-order rate constant of 1.7×10^8 l./mol sec based on BH_3 loss.

$(\overline{\text{BH}_3})$ is the arithmetic mean of $(\text{BH}_3)_S$ and $(\text{BH}_3)_L$. No measurable BH_3PF_3 was observed for the short profile within the indicated limits of detectability. The precision in measuring (BH_3) is low and stems from the fact that it is calculated from m/e 13 ion intensities corrected for large contributions from BH_3CO and smaller ones from B_2H_6 and BH_3PF_3 . The total correction varies between 40 and 80% of the observed (13^+) intensity. The contributions to m/e 13 from these species are determined from the intensities of major ions (n^+) and the following ratios ($13^+/n^+$): ($13^+/40^+$)- $\text{BH}_3\text{CO} = 0.28$, ($13^+/26^+$)- $\text{B}_2\text{H}_6 = 0.12$ and ($13^+/100^+$)- $\text{BH}_3\text{PF}_3 = 0.31$. The intensities of these major ions and of m/e 88 from PF_3 were used without correction to calculate the other pressures in Table I. The rate constants appearing in Table I were calculated from the approximate expression

$$k_2 = \frac{(\text{BH}_3\text{PF}_3)_L}{(\text{PF}_3)_0(\overline{\text{BH}_3})t}$$

The average value for k_2 , weighted in a manner which is appropriate for data in which there is large scatter,²⁸ is 1.51×10^8 l./mol sec with an error factor (corresponding to one standard deviation) of 2.1. This value is the same as that calculated above on the basis of BH_3 loss.

A separate experiment was done to determine the extent of BH_3PF_3 decomposition in the reaction zone under the conditions used in the measurements of the

association reaction. The decomposition was followed by observing the m/e 100 ion signal from BH_3PF_3 for various leak settings and reaction times at a uniform temperature of 494°K . This was accomplished by using three flat temperature profiles of lengths in the ratio 1:2:3 extending up to the sampling orifice. The two reaction times, 0.324 and 0.648 msec, were established by the displacements between the short profile and each of the two longer ones. Data obtained for two mass flows of BH_3PF_3 are plotted against reaction time in Figure 3. The first-order rate constant obtained from the averaged slopes is *ca.* 300 sec^{-1} at 494°K and 6.0 Torr of helium pressure. Calculations based on this value indicate a correction of no more than 10% to k_2 to account for decomposition of product. This correction was judged small enough to be negligible. The facts that the measurements of k_2 were made at the lowest possible reaction zone temperature and BH_3PF_3 appears partially decomposed at this temperature rule out the measurement of an activation energy for k_2 .

An additional set of experiments was designed to test whether the following reactions were contributing significantly to the formation of adduct observed.



Procedures similar to those discussed above yielded the following upper limits to the respective bimolecular rate constants: $k_a \leq 4 \times 10^6$ l./mol sec and $k_b \leq 1.1 \times 10^7$

(28) T. P. Kohman, *J. Chem. Educ.*, **47**, 657 (1970).

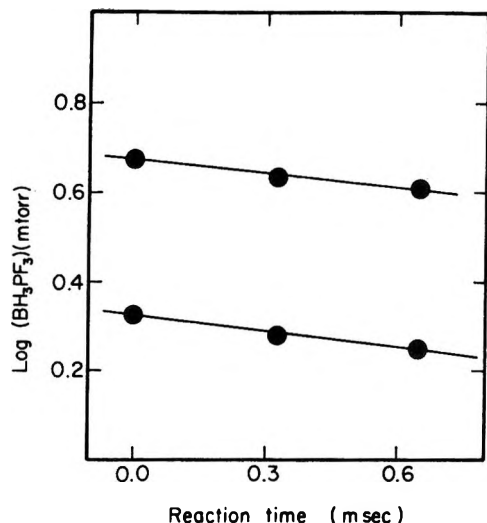


Figure 3. First-order plots for the loss of BH₃PF₃ as a function of time for two initial values of (BH₃PF₃)₀ at 500°K and a total pressure of 6 Torr (ca. 98% helium).

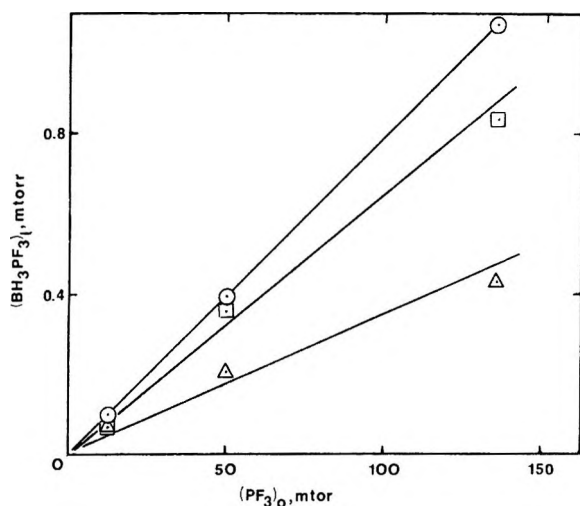


Figure 4. Borane adduct observed as a function of initial PF₃ partial pressure from Table I. Triangles, squares, and circles refer to (BH₃)₀ = 0.91, 1.8, and 4.3 mTorr, respectively.

l./mol sec, both at 500°K and 6 Torr of helium pressure. Calculations based on these values indicate that as much as 10% of the adduct may be formed by reaction a and 1% by reaction b.

It has been assumed thus far that formation of BH₃PF₃ from BH₃ and PF₃ is first order in both reactants. First-order dependence on PF₃ is demonstrated in Figure 4, where product observed is plotted against PF₃ pressure at several fixed levels of BH₃. Whereas these plots show good linearity, similar plots of product vs. BH₃ pressure show positive curvature and more scatter. The curvature arises from the approximate expression used to calculate the rate constant and the fact that this expression ignores the loss of BH₃ by the competitive recombination reaction to form diborane. Thus, the

approximation of the average (BH₃) as the mean of the initial and final values overestimates the true average (BH₃) and the error increases for increasing initial (BH₃) and decreasing PF₃ pressures. The resulting negative error in the rate constant is not readily corrected. However, the error is small compared with the precision in measuring k_2 . As far as can be judged, the association reaction is first order in BH₃ as well as PF₃.

$BH_3 + NMe_3 \xrightarrow{k_t} BH_3NMe_3$. The kinetics of this process were studied using BH₃PF₃ as the source of BH₃. Trimethylamine was injected directly into the reaction zone through the inlet probe and the formation of BH₃NMe₃ was observed as a function of probe position and mass flows. BH₃PF₃ decomposes completely in the decomposition zone to yield PF₃ and BH₃. The identification of the amine adduct by the mass spectrum of authentic material was discussed above. The data of kinetic value are given in Table II, where the reaction parameters have the same meaning as in Table I. The reaction time t , however, is now proportional to the distance, l , between tip of probe and end of flow-tube. A long profile permitting a maximum reaction zone length of 4.20 cm was used to obtain all data except the BH₃ pressure. The latter was measured at the midpoint of the reaction zone by reproducing the same temperature profile 2.15 cm closer to the leak. This midpoint value, (BH₃)_m, was used to calculate the BH₃ level along the entire recombination zone, in the absence of amine, using the previously reported decay of BH₃.¹⁷ These calculated values of the BH₃ level at each probe position are listed in Table II. They are denoted as (BH₃)₀ as they are the initial partial pressures of BH₃ at the indicated probe positions.

Adduct pressures observed for various times and reactant pressures are also listed in Table II. The

Table II: Partial Pressures of the Adduct from the Reaction of BH₃ and N(CH₃)₃ in mTorr at 500°K and a Total Pressure of 5.5 Torr

Conditions	(Me ₃ N) ₀	l , cm	(BH ₃ -NMe ₃)	(BH ₃) ₀
$T_R = 501^\circ K$ $T_D = 655^\circ K$	6.25	0.00	0.34	2.78
		1.05	0.49	3.00
		2.05	0.70	3.24
		3.20	0.69	3.67
		4.20	0.81	4.27
$10^{-3}v = 7.92$ cm/sec $P = 5.52$ Torr	16.4	0.00	0.65	2.78
		1.05	0.89	3.00
		2.05	1.15	3.24
		3.20	1.38	3.67
		4.20	1.58	4.27
$S = 1.75$ (BH ₃ PF ₃) ₀ = 27.8 mTorr (BH ₃) _m = 3.2 mTorr	51.4	0.00	0.99	2.78
		1.05	1.50	3.00
		2.05	1.80	3.24
		3.20	2.59	3.67
		4.20	2.82	4.27

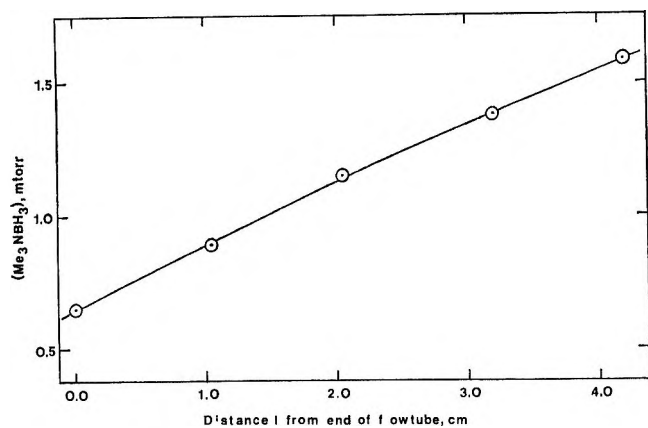


Figure 5. Trimethylamine borane adduct as a function of probe position for $(\text{Me}_3\text{N})_0 = 16.4$ mTorr at 500°K and a total pressure of 5.5 Torr.

data for $(\text{NMe}_3)_0 = 16.4$ mTorr are illustrated graphically in Figure 5. A sizeable amount of adduct is observed even at the shortest probe position ($l = 0.0$ cm), indicating that considerable reaction occurs in the vicinity of the probe tip. (The sampling leak is situated about 4 mm past the end of the flow tube.) Mixing effects are therefore significant and a simple calculation of the rate constant analogous to that used for the PF_3 studies is not applicable. A differential method was therefore used, employing the variation of adduct observed *vs.* probe position to extract the rate constant.

The differential rate equation for formation of adduct (A) can be written as

$$\frac{d(A)}{dt} = -\frac{d(\text{BH}_3)}{dt} = k_t(\text{Me}_3\text{N})(\text{BH}_3) \quad (1)$$

since in the presence of excess amine, adduct formation is the major pathway for loss of BH_3 . The integrated rate expression is

$$\log \frac{(\text{BH}_3)_0}{(\text{BH}_3)} = \log \frac{(\text{BH}_3)_0}{(\text{BH}_3)_0 - (\text{BH}_3\text{NMe}_3)} = \frac{(\overline{\text{Me}_3\text{N}})k_t t}{2.303} \quad (2)$$

if 1:1 stoichiometry between BH_3 lost and adduct formed and near constancy of the amine pressure are assumed. The error in neglecting BH_3 loss by dimerization is greatest at the lowest amine pressure. Here, for example, the error in $\log (\text{BH}_3)_0/(\text{BH}_3)$ is about 30% at $l = 2.0$ cm and $(\text{Me}_3\text{N})_0 = 6.25$ mTorr. A typical plot of $\log (\text{BH}_3)_0/(\text{BH}_3)$ (as defined above) *vs.* probe position is shown in Figure 6 with the open circles. The pronounced curvature at longer reaction times (larger l) is partly attributable to the approximation discussed above, since the BH_3 concentration increases with distance from the end of the flow tube. It may also be due to a systematic error in the relative sensitivity of BH_3NMe_3 with respect to BH_3 that puts

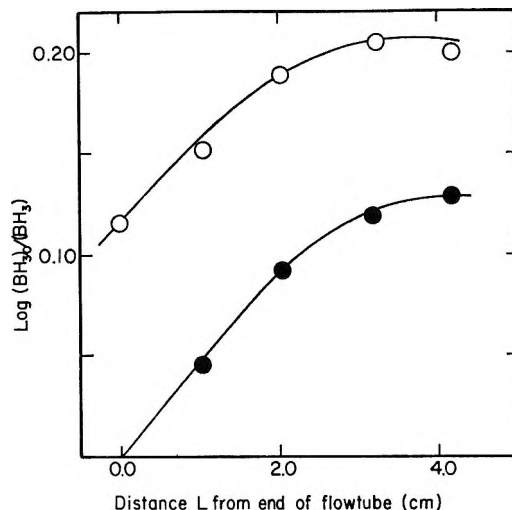


Figure 6. Plot of $\log (\text{BH}_3)_0/(\text{BH}_3)$ *vs.* probe position for $(\text{Me}_3\text{N}) = 15.6$ mTorr where $(\text{BH}_3) = (\text{BH}_2)_0 - (\text{BH}_3\text{NMe}_3)$. The data is from Table II. The open and closed circles refer to unnormalized and normalized functions, respectively (see text).

an apparent upper limit on the fraction of BH_3 which reacts to give adduct. The nonzero intercept is largely due to excess reaction occurring in the vicinity of the probe tip, which inflates the ordinate function at shorter probe positions. To approximately correct for excess reaction at the tip, the data were replotted using the following modified rate equation

$$\log \frac{(\text{BH}_3)_0 - (\text{BH}_3\text{NMe}_3)_0}{(\text{BH}_3)} = \frac{(\overline{\text{NMe}_3})k_t t}{2.303} \quad (3)$$

where $(\text{BH}_3\text{NMe}_3)_0$ is the adduct pressure observed at $l = 0.0$ cm. This modification normalizes $\log (\text{BH}_3)_0/(\text{BH}_3)$ to zero at zero probe position. The normalized plot is shown by the solid circles in Figure 6. The slightly greater slope of the linear portion of this curve is a better measure of the second-order rate constant k_2 than that of the original curve. According to eq 2 the slope of a plot such as that shown in Figure 6 divided by the average amine pressure yields k_t directly. The average amine pressure is approximately $(\overline{\text{Me}_3\text{N}}) = (\text{Me}_3\text{N})_0 - 1/2(\text{BH}_3\text{NMe}_3)$, where the 1:1 stoichiometry between amine lost and adduct formed is used to account for the small depletion of amine during reaction. The best estimate of k_t , using all the data, is obtained by taking the slope of the plot shown in Figure 7, where the initial slopes of three curves such as that shown in Figure 6 are plotted against amine pressure. The second-order rate constant obtained from the normalized data is $k_t = 1.3 \times 10^9$ l./mol sec at 500°K and 5.5 Torr helium pressure.

It remains to examine possible corrections for alternate pathways for the formation or loss of adduct. At these temperatures and reaction times the decomposition of adduct is not likely to be significant. Although

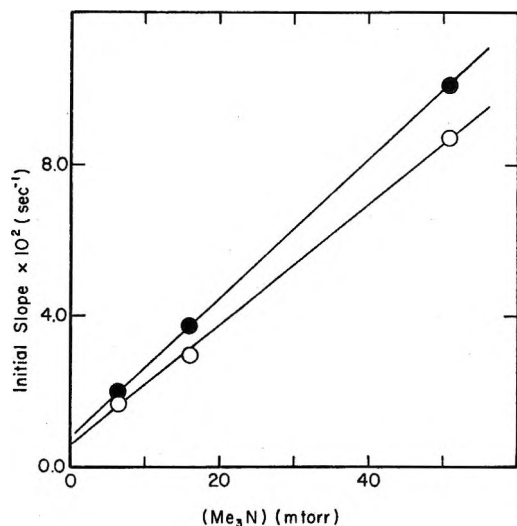


Figure 7. Initial slope of $\log(BH_3)_0/(BH_3)$ vs. time plotted against amine pressure. Closed and open circles represent slopes of normalized and unnormalized curves, respectively (see Figure 6 and text).

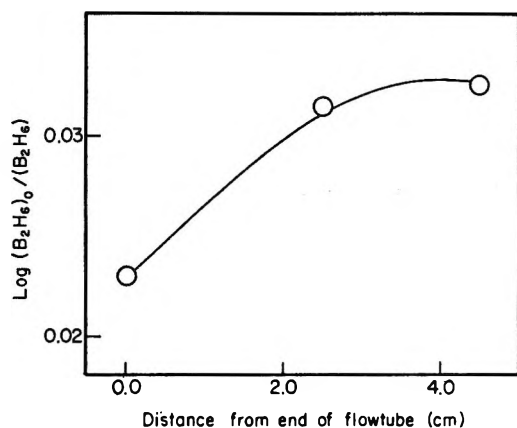
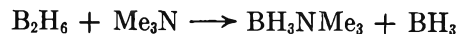


Figure 8. Plot of $\log(B_2H_6)_0/(B_2H_6)$ vs. probe position for $(Me_3N)_0 = 13.7$ mTorr where $(B_2H_6) = (B_2H_6)_0 - (BH_3NMe_3)$.

the decomposition of BH_3PF_3 was found to be appreciable, its dissociation enthalpy (*ca.* 23 kcal)²⁹ is considerably less than that estimated for BH_3NMe_3 (32 kcal).³⁰ The direct reaction between amine and BH_3PF_3 is excluded by the experimental method, but the following reaction can occur



since diborane is present in the reaction zone from the recombination of BH_3 (typically 3 mTorr at the midpoint of the reaction zone in the absence of amine). A control experiment to assess the importance of this process was performed. Diborane and amine were introduced into the reactor under conditions similar to the experiments with BH_3 . An example of a plot of $\log(B_2H_6)_0/[(B_2H_6)_0 - (BH_3NMe_3)]$ vs. probe position is given in Figure 8. The measured rate constant is 2.9×10^8 l./mol sec and probably refers to the reaction



although the mechanisms suggested by Bauer⁷ cannot be ruled out. It is not necessary to know the actual reaction, however, to correct k_t . Under the conditions used to measure the reaction of BH_3 with amine, the reaction of amine with diborane accounts for 15% of the total adduct observed and the final corrected value is $k_t = 1.1 \times 10^9$ l./mol sec with an estimated error factor of 2 to 3.

Discussion

The rate constants measured in this work are compared with measurements on the reaction of BF_3 with $(CH_3)_3N$ in Table III. The reaction of BF_3 with PF_3 to form an adduct has not been observed. Although the rate constants for the reaction of BF_3 were measured at lower temperatures, the temperature dependence of this reaction is probably insignificant.¹⁰ As the species involved in these reactions are fairly small, one must consider the possibility that the rate constants measured are not the high-pressure limiting values. Unfortunately, the technique used in our study is poorly suited for total pressure variation and consequently we have no direct information on this point.

Table III: Rate Constants for the Formation of Donor-Acceptor Complexes

A + B $\xrightarrow{k_{AB}}$ AB		k_{AB} , l./mol sec	E_a , kcal	Pressure, Torr	Ref
BH ₃	PF ₃	1.5×10^8 ^a		6	This work
BH ₃	(CH ₃) ₃ N	1.1×10^9		6	This work
BF ₃	(CH ₃) ₃ N	2.8×10^9	<3	0.1	10
BF ₃	(CH ₃) ₃ N	$\geq 5 \times 10^9$		Variable	11

^a May not be the high-pressure limiting value.

As was mentioned above, however, the ratio of rate constants for the reaction of monomethylamine and trimethylamine with BF_3 has been measured as a function of total pressure.¹¹ It appears clear from this work that the reaction of monomethylamine with BF_3 would be in the falloff region under our conditions. For this reason, it is quite possible that the reaction of BH_3 with PF_3 is also in the falloff region under our conditions. Because of this uncertainty, 1.5×10^8 l./mol sec must be taken as a lower limit for the rate constant. On the other hand, the rate constant for the reaction of trimethylamine with BF_3 under our conditions would probably be within a factor of 2 or 3 of the high-pressure limiting value. Therefore, our value for the reaction of

(29) A. B. Burg and Y. Fu, *J. Amer. Chem. Soc.*, **88**, 1147 (1966).

(30) R. E. McCoy and S. H. Bauer, *ibid.*, **78**, 2061 (1956).

BH_3 with trimethylamine is probably equal, within experimental error, to the high-pressure limiting value.

The comparison of the rates for the association of trimethylamine with BF_3 and with BH_3 is informative about the role of boranes as electron pair acceptors. Any ordering of so-called "acceptor strength" based on simple structural correlations is apt to be misleading. Although BH_3 is estimated to be much less stabilized in its planar geometry than BF_3 ,^{8,9} it is clearly an even less efficient acceptor toward trimethylamine than BF_3 . A similar conclusion can be made with respect to the reference base pyridine on the basis of thermochemical results.^{4,31} It is evident that the efficiency of BH_3 as an acceptor species in the presence of a typical amine donors is not enhanced by virtue of its more flexible structure compared with BF_3 . Apparently, in the reaction of BF_3 with amine donors, even as highly substituted as trimethylamine, any additional energy required to overcome planar stabilization in BF_3 is readily supplied by the reaction mechanism. This observation complies qualitatively with Mulliken's charge-transfer model if it is also postulated that a change from planar to pyramidal geometry is energetically favored during the ap-

proach of an electron to either BF_3 or BH_3 . Apparently this gain in energy is also sufficient to effect charge transfer at donor-acceptor separations large enough to make any difference in the relative sizes of BF_3 and BH_3 an unimportant factor in the reaction rates. Finally, as the intermolecular distance at which electron transfer takes place is reflected to some extent in the collision efficiency with which these reactions take place, our results indicate that the interaction distance for BF_3 is larger than for BH_3 . This in turn suggests a larger electron affinity for BF_3 than for BH_3 , which is quite reasonable.

Under our conditions, BH_3 reacts less efficiently with PF_3 than with $(\text{CH}_3)_3\text{N}$. However, if one were able to take into account the falloff behavior of the PF_3 system, the rate constants might well turn out to be comparable at the high-pressure limit.

Acknowledgments. The assistance of G. W. Mappes in setting up the apparatus is gratefully acknowledged.

(31) H. C. Brown and L. Domash, *J. Amer. Chem. Soc.*, **78**, 5384 (1956).

The Dynamic Adsorption of Water Vapor by a Fiber Drawn from a Melt of Vycor

by Victor R. Deitz* and Noel H. Turner

Naval Research Laboratory, Washington, D. C. 20390 (Received December 31, 1970)

Publication costs assisted by the Naval Research Laboratory

The adsorption of water vapor was measured volumetrically on pristine nonporous fiber drawn from a melt of Vycor rods at 2050°. The fiber was pristine in that it had never been in contact with aqueous media or high relative humidities prior to the adsorption measurements. The krypton surface area of the fiber was 0.073 m²/g. One sample of fiber was used for all reported measurements, and it was heated under vacuum to either 300, 500, or 800° before each exposure to water vapor. The water vapor adsorption was then followed at either 60, 80, 100, or 120° at p/p_0 of 0.04 and below, where p is pressure and p_0 is the vapor pressure of water at the temperature of adsorption. The amount of water vapor adsorbed increased with time, up to contact times of 4000 min. The hydration of a silica network, containing 3% boric oxide, was a dynamic process with a positive temperature coefficient over the experimental range employed. The data were fitted by an isochronal adsorption model where each isochrone followed a linear behavior $N_{i,T} = k_{i,T}p + i_{i,T}$, where $N_{i,T}$ is the amount adsorbed, $k_{i,T}$ the slope, and $i_{i,T}$ the intercept on the $N_{i,T}$ axis; the subscripts i and T designate the time and temperature, respectively. The significance of the constants $k_{i,T}$ and $i_{i,T}$ are discussed. Desorption measurements indicated that the water vapor was adsorbed tightly. The similarity of the results after fiber pretreatment at 300, 500, or 800° indicated that the interior of the fiber could be dehydrated with relatively little change in the surface sites. This was indicated by a similar magnitude in the interaction with water vapor measured at 120°. The first stage of the surface hydration process was the dissociative adsorption of a water molecule and the hydration of a siloxane bond. The second stage, in rapid succession, was the further adsorption of water molecules through hydrogen bonding to the surface products formed.

Introduction

The boundary of a glass fiber at the gas-solid interface can gain or lose water by (a) adsorption or desorption process *via* the gas phase and (b) migration from and to

the bulk glass by some solid transport mechanism. At sufficiently high temperatures and partial pressures of water vapor, both processes can contribute and the overall gain or loss may be written



where S_{glass} and V_{glass} represent the surface and volume, respectively. Although, as indicated, these overall reactions can be reversed, it has been very difficult to establish the extent to which a steady state might have been approached. At temperatures below 200°, the water vapor flux at the glass surface appears to be dominated by a gas-adsorption process. Previous studies of the water vapor-silica reaction have been concerned with the amount of initial surface water and the nature of the surface bonds.

This study is concerned with the interaction of water vapor with a fiber drawn from a melt of nonporous Vycor.¹ Many previous investigations have been concerned with a large variety of silica solids formed by precipitation^{2,3} or as a product of gas reactions,^{4,5} for example, Cabosil. The dehydration of these materials by heat treatments *in vacuo* form the adsorption sites for water vapor in the boundary surface. The present study uses a pristine silica surface, *i.e.*, one which had never been in contact with a high relative humidity or with aqueous media. The latter are known to modify silica surfaces to varying extents⁶ since contact with aqueous systems expedites the removal and/or deposition of hydrolysis products.

In the present study the adsorption process has been followed at rather low partial pressures in order to avoid any appeal to a capillary condensation model. The highest relative pressures employed at the temperatures studied were 0.04 at 60°, 0.02 at 80°, 0.008 at 100°, and 0.004 at 120°. A low surface coverage should result at these relative pressures if a physical adsorption process alone were present, and, accordingly, attention could be focused on the first step of the hydration process. Actually, the observations have shown that the hydration of a silica network is a dynamic process with a positive temperature coefficient over the experimental range employed.

Experimental Section

Formation of Fiber. The fiber was drawn from a melt of Vycor rod (Corning No. 7913) in a single-bushing tungsten crucible at 2050° with the kind cooperation of the Whittaker Corp.⁷ The operations were conducted in purified argon. The fiber, accumulated on a rotating drum also mounted within the argon atmosphere, was transferred to the reaction vessel A of fused quartz shown in Figure 1. The evacuated tube D was inserted to diminish the dead space, and the closure was made using ConFlat flanges with a copper gasket. The upper Pyrex tubulation, equipped with a seal-off bubble E, was attached to the vacuum system.

Both the Vycor rod and the resulting fiber have been analyzed and the B_2O_3 contents were 3.02 and 2.96%, respectively.⁸ This result agrees closely with the analyses published by Nordberg in 1944.⁹ The sample

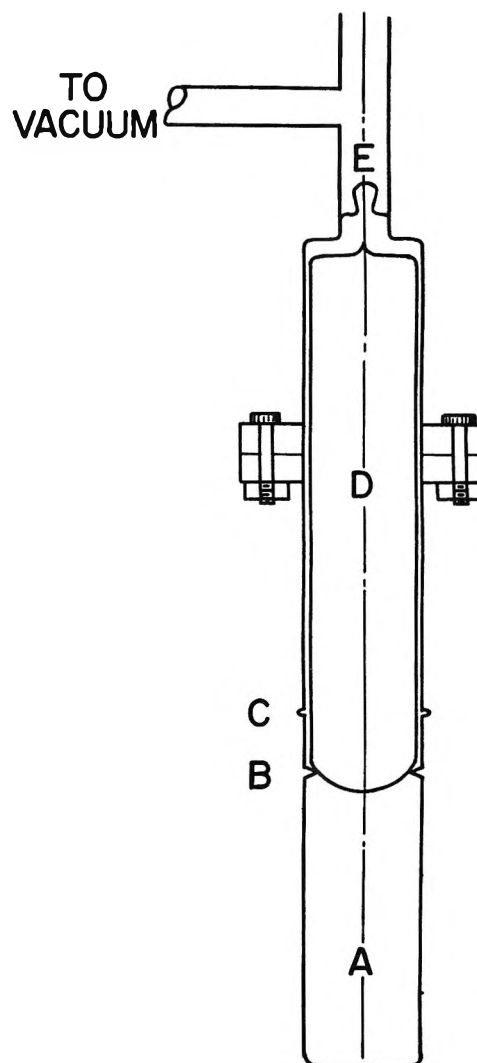


Figure 1. Diagrammatic sketch of reaction vessel.

of fiber (58.731 g) had a BET krypton area of 4.3 m² per sample, using 20.4 Å² per adsorbed Kr atom.¹⁰ The geometrical area calculated from the weight, length, and density of the fiber was 4.2 m². Hence, the fiber

- (1) V. R. Deitz and N. H. Turner, *J. Phys. Chem.*, **74**, 3832 (1970).
- (2) R. K. Iler, "The Colloid Chemistry of Silica and Silicates," Cornell University Press, Ithaca, N. Y., 1955.
- (3) W. H. Wade, R. L. Every, and N. Hackerman, *J. Phys. Chem.*, **64**, 355 (1960).
- (4) R. S. McDonald, *ibid.*, **62**, 1168 (1958).
- (5) J. J. Fripiat and J. Uytterhoven, *ibid.*, **66**, 800 (1962).
- (6) L. Holland, "The Properties of Glass Surfaces," Chapman and Hall, London, 1964, p 546.
- (7) One of the authors (V. R. D.) wishes to acknowledge Mr. Stanley Freske of the Narmco Research and Development Division for his complete cooperation in overcoming the problems in drawing the fiber.
- (8) The authors are indebted to O. R. Gates and S. H. Cress of the Analytical Chemistry Branch of this Laboratory for these analyses.
- (9) M. E. Nordberg, *J. Amer. Ceram. Soc.*, **27**, 299 (1944).
- (10) V. R. Deitz and N. H. Turner, "Cross-Sectional Area of Adsorbed Gases on Pristine E-Glass Fibre of Known Area," Surface Area Determination (Supplement to Pure and Applied Chemistry), International Symposium on Surface Area Determination, Butterworths, London, 1970, pp 43-54.

was essentially nonporous and smooth. The distribution of the boria in the sample is unknown; it is conceivable that a selective surface adsorption may have taken place in drawing the fiber. However, the high viscosity of the melt and the rapid cooling of the fiber make appreciable migration unlikely. All of the experimental work was carried out on the above sample of fiber weighing 58.731 g.

The adsorption measurements were made by a volumetric procedure already described.¹¹ A capacitance manometer was used with readout *via* an integrating digital voltmeter. The calibration was made against a precision McLeod gauge and checked at frequent intervals. The capacitance manometer readings C and the pressures P were correlated by a series of relationships of the type

$$P = \frac{C}{k_1 + k_2 C}$$

A computer program was written to facilitate the calculations.

The water vapor was quantitatively introduced in known amounts from a special device¹¹ in multiple doses of 9.769 μmol . It was stored in a cold finger cooled with liquid nitrogen. Time zero of the water reaction was counted from the moment when the liquid nitrogen was removed and the finger heated rapidly to ambient temperature with a small hot air source.

The importance of the correction for the adsorption of water vapor by the walls of the apparatus has already been discussed.¹¹ It was necessary to make a series of measurements using an empty sample container with the temperature gradients of the experimental procedure. In this manner, the corrections for wall adsorption can be made to include those for thermal transpiration which become significant when the absolute pressures are below 1 Torr. The temperature gradient between the sample space and the controlled rack temperature (26.9°) is located in the annular region defined by two concentric cylinders C and D. The corrections for thermal transpiration^{12,13} have not been calculated for this geometry, which makes calibration necessary.

The reaction vessel and the sample were outgassed at temperatures of 300, 500, or 800°. A furnace with the necessary temperature control was raised into position for this purpose. For the water vapor adsorption measurements the reaction vessel was surrounded by a jacket through which a stream of thermostated oil ($\pm 0.10^\circ$) was circulated.

The outgassing process of a solid is a very important operation. According to the mechanism of outgassing mentioned at the beginning of this paper, the first heating may release the molecular species held on the surface and the additional heatings to higher temperatures can then evolve species that diffuse from the interior. It appeared feasible with the pristine fiber from Vycor to remove the adsorbed gases preferentially

by heating in a vacuum at 300° for periods of 1–3 days. The outgassing was interrupted at regular intervals by isolating the reaction vessel and measuring the pressure buildup during 30 or 60 min. This procedure was repeated until the final pressure change decreased to a rate corresponding to 1 nmol/hr m² of the sample; the rate included the outgassing of the walls of the adsorption system. The behavior upon dehydrating the sample at 500 and 800° will be discussed in the Results section following the presentation of the adsorption data for the 300°-treated sample.

Results

Frequent measurements of krypton adsorption at 77.4°K were made during the investigation. The surface area during the series with 300° outgassing averaged 4.3 ± 0.2 m² per sample, or 0.073 m²/g. After the several pretreatments at 500° the average area was 4.9 ± 0.1 m² and after the 800° treatment 4.7 ± 0.1 m².

When the evacuated and dehydrated fiber was exposed to water vapor, the pressure decreased continuously and the changes were measurable over a 3–4-day period. Figure 2 shows the behavior when 78.15 μmol of water vapor was introduced at 100°. Since the pressure decrease was in part due to a small adsorption on the walls of the system, the kinetic interpretation to be given will be based on the corrected adsorption by the sample. Figure 2 also gives the amount of water vapor adsorbed by the fiber alone, *i.e.*, after correcting for the wall adsorption

The sequence in the magnitudes of water introduced to the outgassed sample was varied without influence on the good reproducibility that was realized in all cases. All together, four different additions of water vapor were studied at each of four temperatures (60, 80, 100, and 120°).

The above data were based on the outgassing at 300°; these were followed by two groups of measurements made on the sample after outgassing at 500° and at 800°, respectively. After outgassing the sample at 300°, the system was isolated from the pumps and the heating continued at 500° with liquid nitrogen on the cold finger. The residual gas at 77.4°K, a small fraction of the total, was determined. Periodically, the cold finger was isolated from the sample and the condensable gases determined from the total pressure after warming. Figure 3 is concerned with the summation of the total gas evolved upon heating at 500°. The interval designated A (72 hr) in Figure 3 covers the initial outgassing in this range. At that point the sample was cooled to 120° and water vapor (97.69 μmol) was introduced for an adsorption experiment.

(11) V. R. Deitz and N. H. Turner, *J. Vac. Sci. Tech.*, **7**, 577 (1970).

(12) F. C. Tompkins and D. E. Wheeler, *Trans. Faraday Soc.*, **29**, 1248 (1933).

(13) T. Takaishi and Y. Sensui, *ibid.*, **59**, 2503 (1963).

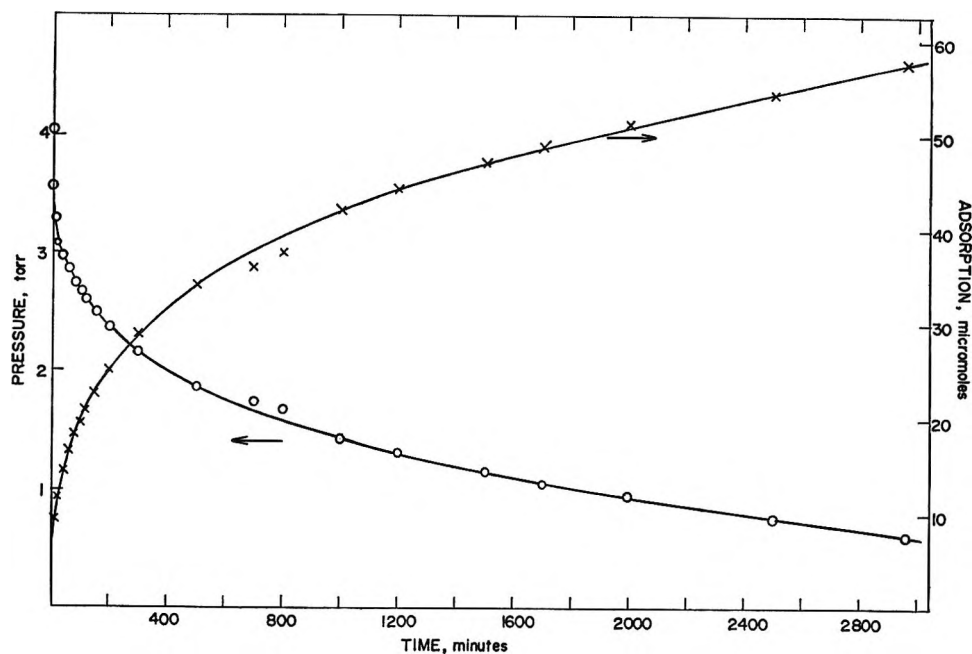


Figure 2. Time dependence of pressure decrease and of the adsorption of water vapor ($78.15 \mu\text{mol}$ introduced) at 100° by the fiber alone corrected for wall adsorption.

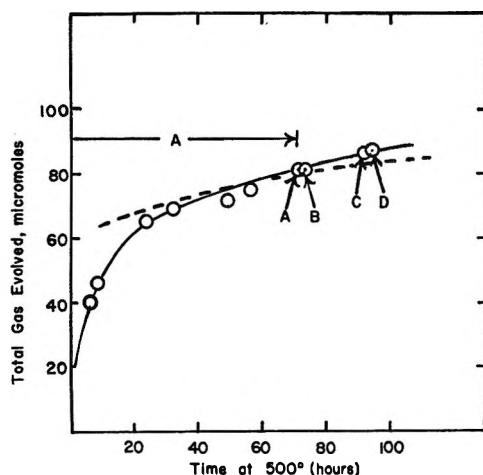


Figure 3. Outgassing at 500° after evacuation at 300° : A, initial heating at 500° ; B, after $97.69 \mu\text{mol}$ of H_2O introduced at 120° ; C, after $48.8 \mu\text{mol}$ of H_2O introduced at 120° ; D, after $78.1 \mu\text{mol}$ of H_2O introduced at 120° .

Thereafter, the sample was heated again at 500° and the difference between that introduced and that evolved was plotted as point B. Subsequent additions behaved as shown in Figure 3. Two conclusions seem warranted from these data. First, both time and temperature are important factors in outgassing the fiber at 500° , and the persistent evolution of gas is direct evidence of a diffusion of products from the interior of the fiber. This technique shows that the fiber exhibited a memory of the time spent at 500° . Todd¹⁴ reported in 1955 the temperature dependence in the outgassing of a number of glasses including Vycor brand 96% silica glass, No. 7910. The dotted line in

Figure 3 was calculated from his results for behavior at 500° . Todd interpreted his results in terms of diffusion from a semiinfinite body which gave linear plots of the amount evolved *vs.* \sqrt{t} . The present results for Vycor fiber show distinct curvature in such a plot.

The second conclusion derived from Figure 3 is based on the fact that the adsorption of water vapor at 120° was not influenced by the previous outgassing at 500° ; this indicates that during the adsorption process there was no appreciable diffusion of the water vapor below the surface boundary. The adsorption is not to be interpreted as the invasion of water vapor into the silica structure below the boundary of the fiber; instead, it will be ascribed to the piling up of water molecules by hydrogen bonding to the silanol groups formed on the boundary.

Table I is a summary of the outgassing products expressed as the residual gas at 77.4°K and the condensable gas determined after warming the cold finger. Using short heating times (60 min) at 500° , an amount of condensable gas evolved approximately equivalent to the water vapor introduced, but for long heating times (1000 and 4300 min) at the same temperature of 500° , additional quantities of gas, both condensable and noncondensable at 77.4°K , were obtained. At 800° condensable and noncondensable gas at 77.4°K was obtained in excess to the water vapor introduced.

One important question to be raised is the possible influence of the more extensive dehydration of the whole fiber on the subsequent hydration of the surface. The water vapor adsorption at 120° after an initial

(14) B. J. Todd, *J. Appl. Phys.*, **26**, 1238 (1955).

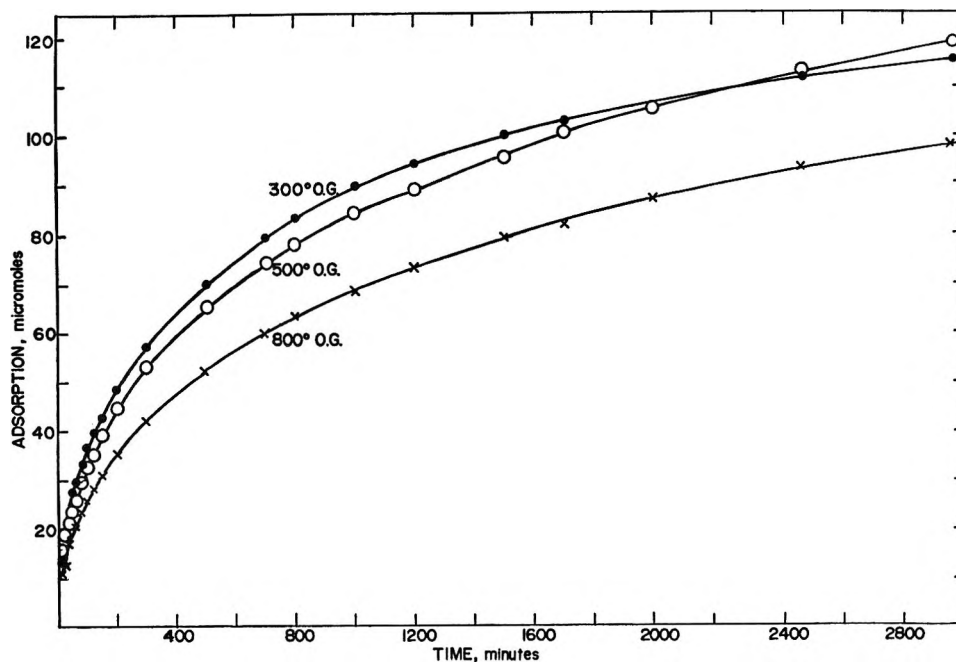


Figure 4. The adsorption of water vapor at 120° per sample (58.731 g) and for an initial dose of 156.3 μmol when the fiber was pretreated at 300, 500, and 800°.

Table I: Dehydration of Fiber When Heated above 300°

Previous dose of water vapor, μmol	Dehydration		Gas evolved, μmol per sample	
	Temp, °C	Time, min	Condensable at 77.4°K	Residual at 77.4°K
...	500	4300	72	3
97.7	500	60	94	3
48.8	500	1000		
78.1	500	60	78	
...	500	120	27	4.8
...	800	40	115	23.0
156.3	800	40	129	22.0
78.1	800	30	116	2.0

^a After evacuation at 300°. ^b After evacuation at 500°.

addition of 156.3 μmol is given in Figure 4 for samples outgassed at 300, 500, or 800°. The main conclusion to be drawn from these results is that the water vapor adsorption is essentially the same at the temperature of 120° after either 300 or 500° pretreatments of the fiber. After the 800° pretreatment the water vapor adsorption is reduced by approximately $1/3$ after comparable contact times, despite the more extensive dehydration of the fiber. However, it is important to note that it is possible to select a longer contact time after the 800° pretreatment when the adsorption at 120° equals that observed after either the 300 or 500° treatments at the shorter contact time.

Isochronal Adsorption

The strong dependence of water vapor adsorption on contact time, observed up to 4000 min, suggested that

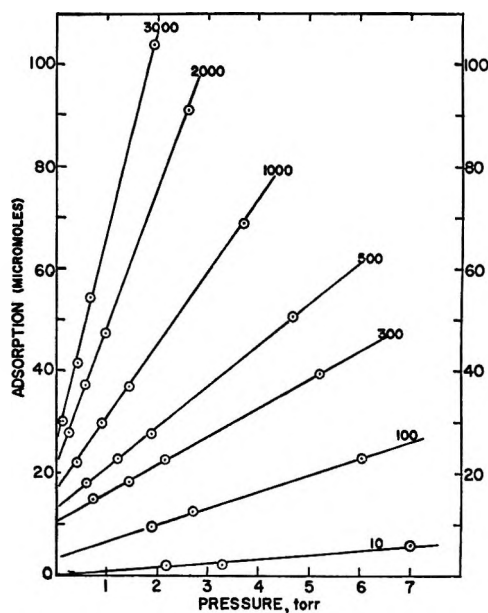


Figure 5. The isochronal adsorption isotherms of water vapor for the sample of fiber (58.731 g) at 100° after a common pretreatment at 300°.

the adsorption could be presented as a series of isochrones. The data of Figure 2 and those for other doses at the same temperature permit the determination of pressure and amount adsorbed at a specified time interval. The resulting isochronal adsorption isotherms (10, 100, 300, 500, 1000, 2000, and 3000 min) at 100° are given in Figure 5. Each isochronal isotherm follows a linear behavior

$$N_{t,T} = k_{t,T} p + i_{t,T} \quad (1)$$

Table II: Values of the Slopes (k) and Intercepts (i) for the Adsorption Isochrones (Cf. Eq 1) per Sample of Fiber (58.731 g)

Time, min	60°		80°		100°		120°	
	k	i	k	i	k	i	k	i
100	2.90	9.3	3.53	9.1	3.74	9.5	4.19	12.0
300	5.19	11.3	6.84	11.2	6.00	14.1	8.33	17.7
500	7.06	12.1	9.10	13.2	9.32	16.1	12.17	20.6
1000	11.09	13.6	15.56	14.9	15.71	19.1	21.77	25.5
2000	17.18	16.8	24.83	20.6	29.38	22.3	36.83	32.0

where $N_{i,T}$ is the amount adsorbed, p the pressure, $k_{i,T}$ the slope, and $i_{i,T}$ the intercept on the vertical axis; the subscripts i and T designate the time and temperature, respectively.

Similar behavior has been found at 60, 80, 100, and 120°, and Table II summarizes the values of the slopes and intercepts for five isochrones at each temperature. The correlation indices for the linearity of the 20 isochrones were in the range 0.97–0.999.

It is proposed that the above interaction consists of two consecutive reactions (designated by subscripts 1 and 2) and that the rate-controlling factors in the formation of the two adsorption complexes follow Langmuir kinetics

$$N_{i,T} = \frac{N_{1(i,T)}K_{1(i,T)}p}{1 + K_{1(i,T)}p} + \frac{N_{2(i,T)}K_{2(i,T)}p}{1 + K_{2(i,T)}p} \quad (2)$$

Should

$$K_{1(i,T)}p \gg 1 \text{ and } K_{2(i,T)}p \ll 1 \quad (3)$$

then

$$N_{(i,T)} \cong N_{1(i,T)} + N_{2(i,T)}K_{2(i,T)}p \quad (4)$$

Equation 4 is of the same form as eq 1.

The first pressure term of eq 2 would correspond to a chemisorption process with no evident pressure dependence in the measured range. The second term is the subsequent adsorption process in which additional water vapor interacts with the localized products of chemisorption. The driving force of the second step is probably the formation of hydrogen bonds to the silanol groups.

When the proposed chemisorption step is examined in detail, it is obvious that the mechanism is quite complex. The activation process must supply sufficient energy to dissociate the water molecule into H and OH (119 kcal) and to dissociate a –Si–O–Si– bond (77 kcal). The activation energy may well be smaller than either of these quantities since the reaction path on a real surface may follow that of lower energy.

On the other hand, the second process of eq 2 will entail the adsorption of $H_2O(g)$ to new silanol bonds formed and is thus concerned with the energy of the hydrogen bond (3–5 kcal). Hence, the ratio $K_{1(i,T)}/K_{2(i,T)}$, estimated from $e^{E_1/RT}/e^{E_2/RT}$, will have a very

large value. This is one requirement of the proposed model (*i.e.*, eq 3).

The summation of the energy requirements to break and to form the required bonds is not large. The enthalpy of formation of known hydrated silicas has been calculated from thermochemical data¹⁵ and the results given in Table III are in the range 7–10 kcal/mol of H_2O . Thermodynamically, the hydrolysis reaction is possible.

Table III: Enthalpy of Formations of Hydrated Silicas (Calculated from Thermochemical Data¹⁵)

Reaction	Mole ratio H_2O/SiO_2	Enthalpy per H_2O , kcal
$H_2O(g) + 2SiO_2(c) \rightarrow H_2Si_2O_5(c)$	0.5	–7.0
$H_2O(g) + SiO_2(c) \rightarrow H_2SiO_3(c)$	1.0	–9.0
$3H_2O(g) + 2SiO_2(c) \rightarrow H_6Si_2O_7(c)$	1.5	–10.2
$2H_2O(g) + SiO_2(c) \rightarrow H_4SiO_4(c)$	2.0	–10.7

The intercepts on the vertical axis of the isochrones of Figure 5 are a measure of $N_{1(i,T)}$. Using these values, tests were made for the order of the reaction with respect to the amount of water vapor chemisorbed, but no indication was found that it was either first, second, $1/2$, or $3/2$ order. A number of perturbing factors contribute to the complexity of the reactions. First, the siloxane bonds when broken would probably expose other silicon atoms of the strained network. A contributing factor would be rotation of the silanol bond to a position that exposed more silicon atoms in the lower level. Thus, a multiplicity of surface sites are generated. Second, boria is present to about 3% by weight, or 2.5 mol %, and the boroxane is a competitor for the water vapor. While the gross amount is small, there may be a higher concentration at the interface compared with bulk concentration. Such an excess would appear to be unlikely in view of the volatility of boria at 2050°, the temperature of the tungsten bushing during fiber formation.

(15) D. D. Wagman, W. H. Evans, I. Halow, V. B. Parker, S. M. Bailey, and R. H. Schumm, *Nat. Bur. Stand. (U. S.) Tech. Note*, 270–273 (1968).

(16) A. Glassner, "The Thermodynamic Properties of the Oxides, Fluorides and Chlorides at 2500°K," U. S. Atomic Energy Report ANL-5750.

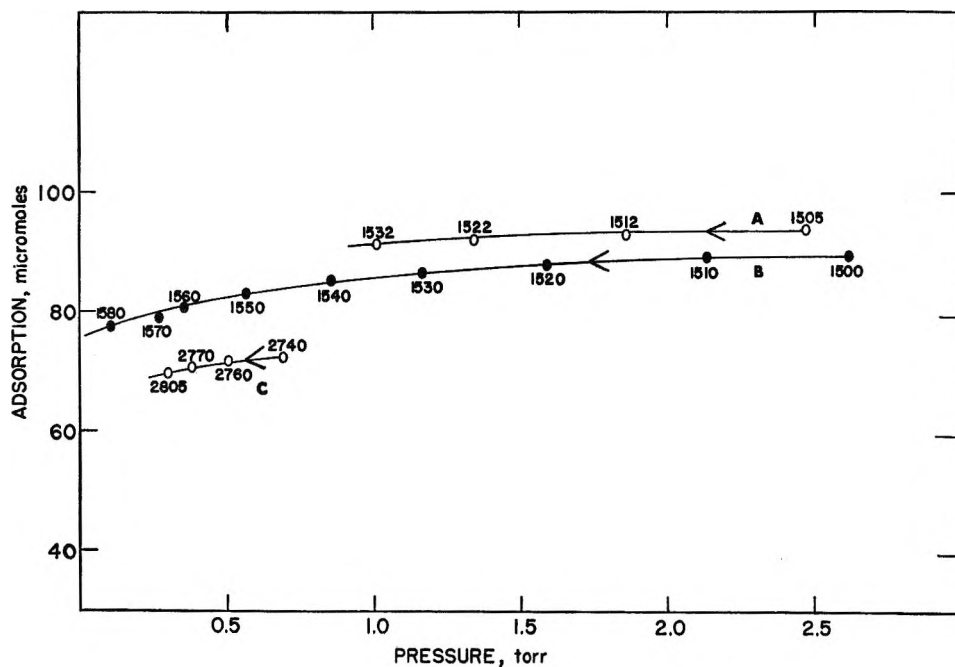


Figure 6. Desorption studies by rapid removal of water vapor at 120° in small quantities from the sample of fiber (58.731 g): A, after 16 doses at 120° (300° outgassing); B, after 16 doses at 120° (500° outgassing); C, after 10 doses at 120° (300° outgassing).

Desorption. In view of the indicated strong adsorption of water vapor, a study was made of a rapid desorption applied after the adsorption had been followed for a specified time. Some of the results of this procedure are given in Figure 6. The two curves, A and B, differ only in the fact that the temperatures of the outgassing pretreatments had been 300° and 500°, respectively. The points were determined in intervals of about 10 min; 2 min was required to remove a known decrement of water vapor from the dosing space and then to reconnect the system to the sample space. The pressure was followed for 8 min and found to change little, tending to increase somewhat as the wall adsorption adjusted to the lower residual pressure. The amount of desorption at 120° was quite small despite the reduction in pressure to about 0.1 Torr. The water vapor adsorbed at 120° is obviously strongly held and simple physical adsorption is definitely not an important factor.

The hydrolysis of the exposed siloxane network to form silanol groups can continue and in the limit form the geminal configuration, *i.e.*, =Si(OH)₂. If it is assumed that the surface structure has the atomic separation of the rhombohedral model of silica and that this network extends over the measured krypton area, then the formation of the geminal grouping would lead to the adsorption of 35 μmol of water vapor per sample. The desorption curves B and C of Figure 6, observed to water vapor pressures of about 0.2 Torr, appear to be headed for a limiting value at low pressures greater than the geminal configuration. This is compatible with an adsorbate consisting of both silanol groups and adsorbed water vapor.

Isochronal Temperature Coefficient. In conventional Henry's law behavior, the amount adsorbed, N_a , is given by the following: $N_a = k_{T_1} p_{T_1}$, and the pressure ratio is $p_{T_1}/p_{T_2} = k_{T_2}/k_{T_1}$; therefore, the calculated isosteric heat of adsorption is constant. The pressure ratio for the isochronal behavior expressed in eq 1 is given by

$$p_{T_1, t} / p_{T_2, t} = \frac{k_{T_2, t}}{k_{T_1, t}} \left[\frac{N_{t, T_1} - i_{T_1, t}}{N_{t, T_2} - i_{T_2, t}} \right]$$

and therefore, a quantity calculated from the slope of $\ln p$ vs. $1/T$ for given isochrones depends on the amount adsorbed. However, for time-dependent reactions, one is not justified thermodynamically in using the Clapyron equation. One can, nevertheless, view such a quantity in terms of an estimated temperature coefficient of the process. With increasing adsorption, the temperature coefficient $[\Delta \ln p_{T, t} / \Delta(1/T)]$ should approach a constant value. Such a constant value is indicated in Figure 7 where the least-squares calculated temperature coefficients, based on the constants of Table II for 60, 80, 100, and 120°, are given as a function of the total amount adsorbed. The magnitude is small for the shorter times where some calorimeter measurement might be made. Nevertheless, it appears feasible and, in fact, highly desirable that some attempt should be made to measure this quantity calorimetrically.

Discussion

The dual-site model for interpreting the isochronal adsorption of water vapor by a silica network appears to be a minimal elaboration on what must be a complex

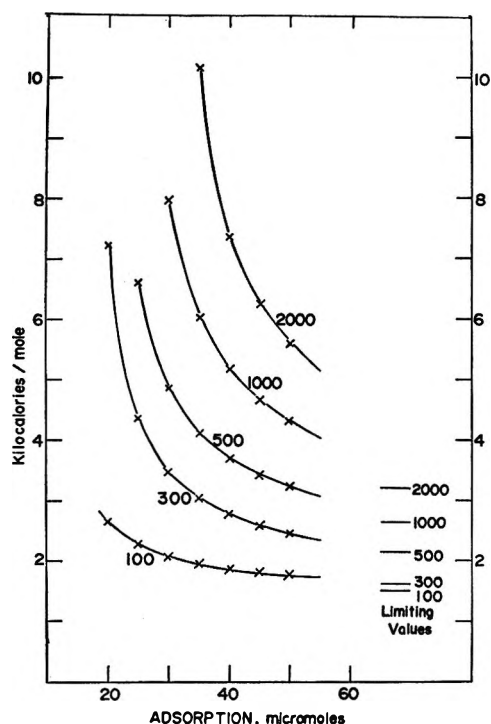


Figure 7. A possible temperature coefficient for the isochronal adsorption of water vapor.

reaction mechanism. The kinetic interpretation of the interaction must take into account the fact that the silica network itself is a reactant. The processes of adsorption or desorption are usually the slow steps in gas-solid reactions and the common procedure is to express the surface concentrations of reactants in accordance with some adsorption model.

The results shown in Figure 2 can also be presented as a function of $\log t$ (see Figure 8). This transformation magnifies the lack of approach to steady-state values. In addition, one may observe the validity of the integrated form of the Elovich equation,^{17,18} namely

$$N_{a,t} = \frac{1}{b} [\ln(t + t_0) - \ln t_0]$$

where $N_{a,t}$ is the quantity adsorbed in time t , a and b are constants, and $t_0 = 1/ab$. It is possible to linearize the plot as shown in Figure 7 by the choice of $t_0 = 70$ min for the data at 100° for eight doses of water vapor. The Elovich plot is linear over the three decades of time within the experimental error. Winter¹⁷ concluded, from models of surfaces having as few as three to five sets of energy sites, each of equal number, that the Elovich equations may adequately describe the chemisorption of a gas. From an analysis of the data by the method of McLintock,¹⁹ it appears that the fiber surface consists of a number of water vapor adsorbing sites having different energies and that these may be distributed in some nonuniform manner on the surface.

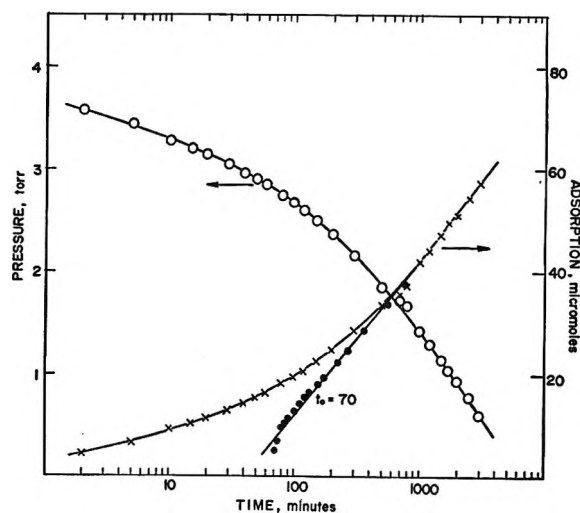


Figure 8. The adsorption of water vapor by the sample (58.731 g) at 100° vs. $\log t$. The linear plot corresponds to the Elovich constant $t_0 = 70$.

They are close enough energetically to overlap and thus may operate in sequence or in parallel.

Attempts were also made at finding the kinetic order of the rate of disappearance of water vapor. Swinbourne's modification²⁰ of Guggenheim's method²¹ for determining first-order rate constants was used with a time interval of 200 min and a typical plot of $N_{a,t+200}$ vs. $N_{a,t}$ is shown in Figure 9. The necessary straight lines required of the method were obtained for 23 separate experiments with correlation indexes ranging from 0.995 to 0.999. However, when the resultant value for $N_{a,\infty}$, the value of $N_{a,t}$ at $t = \infty$, was substituted into a standard first-order expression, the resulting plot of $\ln [N_{a,\infty}/(N_{a,\infty} - N_{a,t})]$ vs. t was not a straight line for times less than 100 min. This is a most critical region since the straight line generated by points above $t = 100$ did not pass through the origin as required for a first-order reaction. The Guggenheim method was selected for the test of kinetic order because the procedure could be followed after the wall adsorption correction had been made. In all cases the calculated values of $N_{a,\infty}$ were less than the corresponding amounts of water vapor introduced and the differences were reasonable values for the wall adsorption in the temperature region of the measurements. Also, $N_{a,\infty}$ at 120° changed only slightly after each of the three pretreatment temperatures for a given dose of water vapor. These values are given in Table IV for three doses of water.

The method of initial slopes²² was also tried to find

- (17) E. R. S. Winter, *J. Catal.*, **4**, 134 (1965).
- (18) M. J. D. Low, *Chem. Rev.*, **60**, 267 (1960).
- (19) I. S. McLintock, *Nature*, **216**, 1204 (1967).
- (20) E. S. Swinbourne, *J. Chem. Soc.*, 2371 (1960).
- (21) E. A. Guggenheim, *Phil. Mag.*, **2**, 538 (1926).
- (22) K. J. Laidler, "Chemical Kinetics," 2nd ed, McGraw-Hill, New York, N. Y., 1965, p 15 ff.

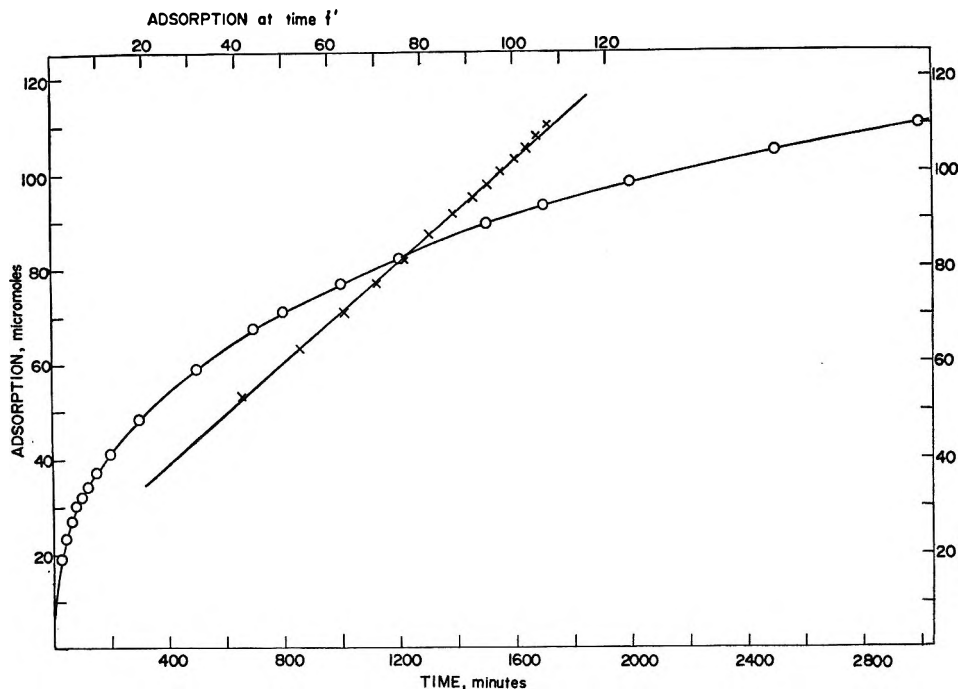


Figure 9. Guggenheim test plot for a first-order reaction with respect to the water vapor adsorbed. A constant time interval of 200 min was used.

Table IV: Influence of Dehydration Temperature on the Subsequent Water Vapor Adsorption at 120°

Vacuum pretreatment	$N_{a,\infty}$, $\mu\text{mol}/\text{m}^2$		
	Dose	Dose	Dose
	156.3	78.15	48.84
300°	27.4	14	8.8
500°	29	15	8.8
800°	24	13	7.9

the order of the disappearance of water vapor. The results indicated an order of about 0.8, but the scatter due to wall adsorption in the early stages of the reaction and to the system geometry makes this value quite uncertain.

The value of knowing the order of a reaction between a gas and a surface is questionable when the latter is a participating component. The evaluation of the order of the activity of the surface requires highly detailed information which is not available for polycrystalline solids. At best, therefore, a knowledge of the order based on the appearance or disappearance of a gas can only give a limited account of the gas-surface reaction.

A deeper insight into the dynamic aspects of the water vapor-silica interaction could be obtained by using infrared absorption. A considerable knowledge of the structure of silica surfaces has come from infrared studies²³ of high area samples (200 to 800 m^2/g) formed into thin wafers. The source has been precipitated amorphous silica, high-temperature products from silicon tetrachloride and steam, and porous silica from leaching borosilicate glass. These high area

materials are prone to contain varying adsorbed impurities. Although it is well known²³ that the relative intensities of the absorption bands depend on the origin of the sample and the evacuation program (time and temperature), very little has been done to study the hydration process directly. The measurements reported in this paper show that the actual adsorption of water vapor depends on temperature, partial pressure of water vapor, and the contact time; samples prepared for infrared absorption should show this variability. Hockey and Pethica²⁴ reported a difference in the water adsorption with contact times of 15 min and 1 hr, but their infrared absorption studies were concerned only with conventional dehydration behavior under vacuum. Perhaps the large scatter of the infrared results among various investigators²³ might be decreased should comparable contact times and water vapor pressures be used.

The sample of fiber used in the present study may not be the best for infrared studies. Low, Ramasubramanian, and Ramamurthy²⁵ have identified a band in Cabosil at 3702 cm^{-1} which they ascribe to $-\text{BOH}$ groups brought about by heating the silica at 800° in a Vycor vessel with subsequent hydration. The possible influence of boria on the present measurements has

(23) A. V. Kiselev and V. I. Lygin, "Surface Hydroxyl Groups and Their Perturbance by Adsorbed Molecules," "Infrared Spectra of Adsorbed Species," L. H. Little, Ed., Academic Press, New York, N. Y., 1966, pp 274-295.

(24) N. A. Hockey and B. A. Pethica, *Trans. Faraday Soc.*, **57**, 2247 (1961).

(25) M. J. D. Low, N. Ramasubramanian, and P. Ramamurthy, *J. Vac. Sci. Tech.*, **4**, 111 (1967).

already been discussed. Vycor (Corning 7910) shows a sharp infrared absorption band at 3560 cm^{-1} ,²⁶ not at the position reported for Cabosil, *i.e.* 3750 cm^{-1} .

Asher, Goodman, and Gregg²⁷ reported that silica which had been calcined at 900° became "hydrophobic," but it then became "hydrophilic" after a lengthy exposure to water vapor during the determination. This behavior is in agreement with the dynamic aspects of the present observations. Our results show quantitatively a high degree of reversibility after surface dehydration at 300 , 500 , and 800° and hydration taking place at 60 , 80 , 100 , or 120° . After the 800° outgassing the silica networks need only more contact time to hydrate at 120° to the same extent as for a 300° outgassing. Presumably, there are fewer nucleation sites present after the 800° treatment to initiate the reactions and this would require a greater energy of activation.

The majority of adsorption isotherms of water vapor on silica have been measured at ambient temperatures. The present investigation demonstrates that the conditions for the chemisorption of water vapor are also the conditions for adsorption as the water molecule. The question had been raised—can a silica network be hydroxylated without also adsorbing water vapor as H_2O ? The present measurements and the isochrone model suggest that both occur in rapid succession during the adsorption process. On the other hand, a desorp-

tion process at a controlled higher temperature may fractionate the adsorbate and perhaps leave only silanol groups as suggested by many investigators using infrared absorption.

The coverage of a silica network by water molecules can be calculated in one of several ways. If the rhombohedral structure of silica extends into the surface, and if only vicinal silanol groups are present where the silicon atoms are exposed, then complete coverage corresponds to a cross-sectional area of 20.7 \AA^2 per water molecule. For the geminal structure monolayer coverage corresponds to 10.3 \AA^2 per molecule. Using the density of liquid water at 25° , the molecular area is 10.5 \AA^2 .²⁸ Thus, any calculation of surface coverage by water molecules is seen to depend on the model adopted for the water-solid interaction. It is interesting, however, that one cannot distinguish between packing that corresponds to either liquid-like packing or interactions to form geminal bonds with the silica network.

Acknowledgment. This work was supported, in part, by Naval Air Systems Command.

(26) W. Espe, "Materials of High Vacuum Technology," Vol. 2, Pergamon Press, New York, N. Y., 1968, p 426.

(27) R. C. Asher, J. F. Goodman, S. J. Gregg, *Proc. Brit. Ceram. Soc.*, **5**, 125 (1965).

(28) A. L. McClellan and H. F. Harnsberger, *J. Colloid Interface Sci.*, **23**, 577 (1967).

Concentration Quenching of Proflavine Hydrochloride in Dry Films of Sodium Deoxyribonucleate and Poly(vinyl alcohol)¹

by G. Strauss,* S. B. Broyde, and T. Kurucsev²

School of Chemistry, Rutgers University, The State University of New Jersey, New Brunswick, New Jersey 08903 (Received April 5, 1971)

Publication costs assisted by University College, Rutgers University

Concentration quenching of proflavine hydrochloride was studied in dry films of sodium deoxyribonucleate (DNA) and poly(vinyl alcohol) (PVA) by measuring the decline of flash-induced triplet formation with increasing dye concentration. The quencher was identified as the dimeric species of proflavine. The quenching of the excited singlet state may be interpreted in terms of long-range Förster-type energy-transfer mechanism. Critical donor-acceptor distances were found to be 33.5 and 46.3 \AA in DNA and PVA, respectively; these differences may be explained by consideration of the polymer-dye interactions.

Introduction

The well established biological activity of acridine dyes and other polycyclic hydrocarbons structurally related to these dyes has provided the motivation for numerous studies in recent years concerned particularly

with the structural aspects of the interaction of these materials with DNA and other polymers.³⁻⁵ The

(1) This work was supported by a grant from the Rutgers Research Council to G. Strauss and by a grant (65/15799) from the Australian Research Grants Committee to T. Kurucsev.

(2) On study leave from the University of Adelaide, South Australia.

study of electronic energy transfer between acridine dyes bound to DNA and other polymers must be considered as complementary to such structural studies from this point of view since it is probable that the biochemical behavior of these molecules is related to their photophysical properties. Furthermore, since energy transfer between dye molecules is sensitive to their environment, such studies may provide alternative avenues for the elucidation of dye-polymer interactions.

Energy-transfer studies confined to systems where the energy donor and the energy acceptor are different chemical species are relatively easy to interpret unambiguously since deactivation of the donor and/or excitation of the acceptor are easily recognized and differentiated from each other. However, in polymer-dye systems the simultaneous use of two dye species may lead to difficulties due to the possibility of competitive binding or to the formation of several types of polymer-dye complexes. For these reasons our studies were restricted to a single cationic acridine dye, 3,6-diaminoacridine or proflavine hydrochloride (PF) dispersed in dry solid films of sodium deoxyribonucleate (DNA) and of poly(vinyl alcohol) (PVA). In comparison with DNA, PVA lacks ionic groups and has a more flexible chain structure of much smaller diameter. Thus comparison of the results in the two media may provide information about the effect of these polymer characteristics on energy transfer. Energy transfer from dye donors under these conditions may be ascertained from the study of concentration quenching or self-quenching, terms used to describe the decrease in fluorescence, triplet formation, or phosphorescence with increasing concentration of a solute. We used a microbeam flash photolysis technique to measure triplet yields and triplet lifetimes of proflavine over a range of dye molarity, C , of $10^{-3} < C < 4 \times 10^{-2}$. It is to be emphasized that in these experiments only the proflavine was excited and energy transfer from DNA to PF^{6,7} could not take place.

Theoretical Model

Quenching Processes. Proflavine is known to form nonfluorescent dimers in dilute solutions.⁸ In the systems studied in this work the absorber or energy donor is the fluorescent proflavine monomer; thus concentration quenching, a decrease in triplet yield and/or triplet lifetime, may be the result of one or more of the following concentration-dependent processes: (i) kinetic encounters between excited and ground-state molecules; (ii) static quenching due to the formation of nonfluorescent dye dimers that simply decrease the fraction of fluorescent dye molecules; (iii) dynamic quenching due to energy transfer from excited monomers to dimers acting as energy sinks; and (iv) energy transfer to impurities introduced into the system with the dye.

In the solid solutions studied here process (i) may be excluded from consideration. Process (ii) may be allowed for by calculating the triplet yield on the basis

of light absorbed by the monomer (donor) only rather than on the basis of the total light absorbed. Furthermore, as we shall show, chance impurities may be eliminated as the dominant energy sinks and accordingly the concentration-dependent decrease in the monomer-based triplet yield must be ascribed to process (iii). This model implies the existence of a material balance between donor (monomer) concentration, C_D , acceptor (dimer) concentration, C_A , and the total dye concentration, C

$$C = C_D + 2C_A \quad (1)$$

Equation 1 renders the interpretation of self-quenching data in terms of energy transfer relatively straightforward, since it enables the calculation of acceptor concentrations with fair precision even in the presence of a large excess of the donor substances. It is noteworthy that for these purposes there is no need to postulate the existence of an equilibrium between donor and acceptor species.

Energy-Transfer Mechanism. The concentrations used in this work correspond to average solute distances of between 75 and 20 Å. The predominant energy-transfer mechanism under these conditions is expected to be dipole-dipole inductive resonance.⁹ Central in the theory of this particular transfer mechanism is the parameter R_0 , referred to as the critical donor-acceptor distance and defined as the distance at which the rate of the bimolecular energy-transfer process equals the rate of the decay of the donor excitation by all other (unimolecular) processes. As an alternative to R_0 one may use the parameter C_A^0 , referred to as the critical acceptor concentration and related to R_0 by

$$C_A^0 = 1500/(\pi^{3/2}N_A R_0^3) \quad (2)$$

where N_A is the Avogadro number.

The values for the critical parameters may be obtained from experimental determinations of the yield, ϕ , of any unimolecular process originating from the excited state such as, for example, triplet formation or fluorescence. If one defines a reduced acceptor concentration, γ by

$$\gamma = C_A/C_A^0 \quad (3)$$

then theoretically the relative lowering of the yield due to the presence of the energy acceptor may be expressed as a function of γ ^{10,11}

- (3) A. Blake and A. R. Peacocke, *Biopolymers*, **6**, 1225 (1968).
- (4) H. J. Li and D. M. Crothers, *J. Mol. Biol.*, **39**, 461 (1969).
- (5) R. W. Armstrong, T. Kurucsev, and U. P. Strauss, *J. Amer. Chem. Soc.*, **92**, 3174 (1970).
- (6) G. Weill and M. Calvin, *Biopolymers*, **1**, 401 (1963).
- (7) W. C. Galley, *ibid.*, **6**, 1279 (1968).
- (8) R. C. Haugen and N. H. Melhuish, *Trans. Faraday Soc.*, **60**, 386 (1964).
- (9) For a general discussion of this energy-transfer mechanism, see T. Förster, *Discuss. Faraday Soc.*, **27**, 7 (1959). *N.b.*: Sensitizer fluorescence should read sensitized fluorescence in the legend of Figure 3 there.

$$\left(\frac{\phi}{\phi^0}\right)_D = 1 - F(\gamma) \quad (4)$$

In this equation ϕ^0 refers to the yield in the absence of an acceptor (at infinite dilution) and the subscript D is a reminder that the yields must be based on light absorbed by the donor only. The form of the function $F(\gamma)$ applicable to the systems studied here which contain molecules with fixed orientations is given graphically in Figure 3 of ref 9.

R_0 is also related to experimental quantities through the equation⁹

$$R_0^6 = 8.79 \times 10^{-25} \kappa^2 \phi_D^0 \Omega / n^4 \quad (5)$$

where n is the index of refraction of the matrix, κ^2 an orientation factor to be discussed below, ϕ_D^0 is the donor fluorescence efficiency in the absence of transfer (at infinite dilution), and Ω is an overlap integral given by

$$\Omega = \int_0^\infty f_D(\bar{\nu}) \epsilon_A(\bar{\nu}) d\bar{\nu} / \bar{\nu}^4 \Big/ \int_0^\infty f_D(\bar{\nu}) d\bar{\nu} \quad (6)$$

In this equation $f_D(\bar{\nu})$ is the fluorescence intensity of the donor and $\epsilon_A(\bar{\nu})$ is the molar extinction coefficient of the acceptor, both as functions of the wave number $\bar{\nu}$.

The molecular orientation factor, κ^2 , is taken generally to be $2/3$ in dilute liquid solutions for freely rotating randomly oriented molecular transition dipoles. For stationary molecules at random orientation its value is 0.475; it is 0.594 for parallel transition dipoles and 4.0 for dipoles that are both parallel and coaxial.¹² Thus calculation of κ^2 using eq 5 with the values of R_0 derived via eq 4 provides information about the extent of order within the systems studied.

Experimental Section

Materials. Proflavine monohydrochloride was purified by a method described elsewhere.⁵ The purified sample contained no divalent metal ion impurities in detectable amounts. Concentrations of PF in aqueous solutions were calculated on the basis of a molar extinction coefficient of 4.1×10^4 l. mol⁻¹ cm⁻¹ at the 444-nm maximum. The stock solutions were made up in Teflon bottles using 0.002 M tetramethylammonium cacodylate buffer of pH 6.50 as the solvent. The stock solutions were about 0.0025 M in dye.

Salmon sperm DNA (Worthington Biochemical Corp.; Lot 6HA) was purified as described elsewhere.⁵ The molar extinction coefficient of the sample at 259 nm in aqueous solutions was 6550 l. (g-atom of P)⁻¹ cm⁻¹. Stock solutions contained about 0.025 g-atom of P l.⁻¹.

Poly(vinyl alcohol) (J. T. Baker, fully hydrolyzed; Lot 2-838) was used without further purification. Stock solutions were 10% by weight of PVA dissolved in 1:3 (by volume) ethanol-water.

Preparation of Films. Appropriate volumes of dye and polymer stock solutions delivered by means of glass

syringes were mixed in small Teflon beakers with magnetic stirring. The dye solutions were diluted with 10–20 volumes of water prior to addition to the DNA stock; by this method local high dye concentrations that led to precipitation were avoided. The mixed solutions were poured into cylindrical holes cut into a Lucite block, the block was floated on mercury, and the solutions were allowed to dry slowly at room temperature protected from light. The resulting films were of uniform thickness and absorbance except at the edges; these were trimmed off. Film thicknesses ranged from 10 to 50 μ m; they were measured with a vernier micrometer caliper with a precision of ± 2 μ m. Film densities were determined by finding the density of the acetone-chloroform mixture in which the films remained suspended. At 25° the densities of dry DNA and PVA films were 0.98 and 1.32, respectively.

Apparatus. The microbeam flash apparatus used was similar in design to one described previously.¹³ The flash tube (FX-1; Xenon Corp.) used with a 5- μ F low-inductance capacitor at 5.5 kV gave an energy dissipation of 75 J and a flash duration (half-peak) of 10 μ sec. The samples to be flashed were enclosed in an evacuated quartz tube and placed into the 10 \times 2 mm rectangular cross section of the tube that fitted onto the stage of a microscope. The excitation flash reached the sample in the tube obliquely from above the microscope stage. As the monitoring light we used a slide projector with a 500-W tungsten lamp powered by a variable dc power supply. The monitoring light passed in succession through the substage condenser, the sample, the microscope objective, and the monochromator before reaching the photomultiplier cathode (EMI 9558). The excitation flash triggered an oscilloscope which then displayed the output of the photomultiplier. The oscilloscope traces were photographed and used to calculate triplet yields and decay rates.

Spectra. Absorption spectra of the films were recorded on a Cary Model 14 spectrophotometer using films without dye as reference to allow for scattering. Absorbances at specific wavelengths were also measured in the microbeam apparatus. Fluorescence spectra were obtained by the use of a Fluorospec recording spectrofluorimeter (Baird-Atomic, Model ST-1S). Relative emission intensities were corrected for variation in phototube sensitivity with wavelength.

Results

Determination of Donor and Acceptor Concentrations. If the dye is present in the films either as the monomer (donor) species or as the dimer (acceptor) species, then

(10) T. Förster, *Ann. Phys. (Leipzig)*, **2**, 55 (1948).

(11) R. G. Bennett and R. E. Kellogg, *Progr. React. Kinet.*, **4**, 217 (1967); *Photochem. Photobiol.*, **7**, 571 (1968).

(12) M. Z. Maksimov and I. M. Rozman, *Opt. Spectrosc. (USSR)*, **12**, 337 (1962).

(13) G. Porter and G. Strauss, *Proc. Roy. Soc., Ser. A*, **295**, 1 (1966).

at any fixed wavelength the following identity holds relating the total measured absorbance, A , to the monomer and dimer absorptivities, ϵ_D and ϵ_A , to their respective molarities, C_D and C_A and to the thickness, t , of the films

$$A = t(\epsilon_D C_D + \epsilon_A C_A) \quad (7)$$

Combining eq 7 with eq 1 there result formulas suitable for determining species concentrations provided that C , ϵ_D , and ϵ_A are known.

$$\begin{aligned} C_D &= [(2A/t) - \epsilon_A C]/(2\epsilon_D - \epsilon_A) \\ C_A &= [\epsilon_D C - (A/t)]/(2\epsilon_D - \epsilon_A) \end{aligned} \quad (8)$$

Total dye concentrations, C , were calculated from the dye-polymer weight ratios used in preparing the sample and the experimentally determined densities of the films.

We choose A , ϵ_D , and ϵ_A in eq 8 to refer to the visible maximum of the dye-polymer systems since absorbances are determined with greatest precision at maxima and since the largest changes in intensity with concentration were found to occur at the maximum. The value of ϵ_D was obtained by plotting $\epsilon = A/Ct$ against the total concentration and extrapolating to $C = 0$. Similarly, ϵ_A was determined by the extrapolation of ϵ vs. $1/C$ plots to zero. This latter extrapolation is consistent with the assumption that the solutions contained no aggregates higher than dimers. The two plots are shown in Figure 1 and the values of ϵ_D and ϵ_A derived and used in subsequent calculations are listed in Table I.

Table I: Physical Data and Derived Parameters for the Systems PF-DNA and PF-PVA in the Absence of Water

	PF-DNA	PF-PVA
Film density	0.98	1.32
Refractive index, n	1.46	1.51
Molar extinction coefficient at absorption maximum		
Monomer, ϵ_D		4.0×10^4 l. mol ⁻¹ cm ⁻¹
Dimer, ϵ_A		1.2×10^4 l. mol ⁻¹ cm ⁻¹
Overlap integral, Ω	1.79×10^{-14}	5.19×10^{-14}
Critical parameters		
Molarity, C_A^0	0.012	0.0064
Distance, R_0	33.5 Å	46.3 Å
Orientation factor, κ^2	1.1	2.6

It should be pointed out that in the solid films complete equilibration between monomer and dimer is prevented by the restriction on diffusion during the drying process. Accordingly, C_D and C_A cannot be obtained by the use of a unique dimerization constant, as is possible in liquid solutions.

Triplet Yields. These may be determined directly by

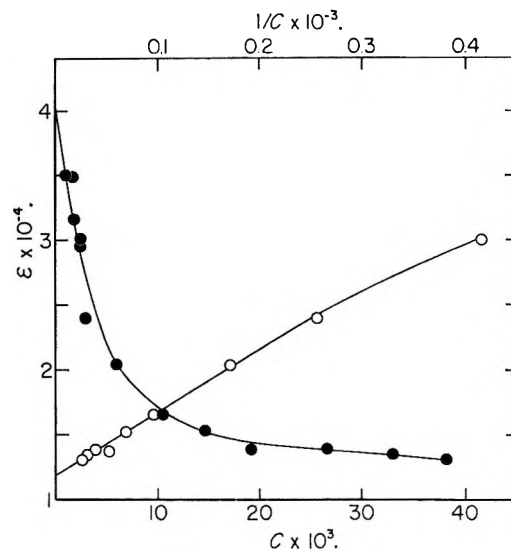


Figure 1. Determination of monomer and dimer absorptivities for PF in DNA films by plotting total absorptivity, ϵ , vs. total dye molarity, C , (●) and vs. reciprocal total dye molarity, $1/C$, (○).

absorption measurements at the proflavine triplet-triplet absorption peaks at 280 or 1100 nm.¹⁴ However, both these wavelengths were outside the range of our instrument and therefore the concentration of the flash-induced triplets was obtained by the measurement of the ground-state depletion at 465 nm (PF in DNA) and at 470 nm (PF in PVA). The conditions of the experiments are shown in Table II.

The decrease in absorbance, ΔA , is proportional to the number of triplets formed, while the fraction of light absorbed from the flash is proportional to I_a/I_0 , the ratio of absorbed to incident light intensity at the wavelength of the measurement. Thus the quantum yield of triplet formation, ϕ , referred to total light absorbed is given in arbitrary units by

$$\phi f = \Delta A/[1 - \text{antilog}(-A)] \quad (9)$$

where f is a proportionality constant. Triplet yields referred to total light absorbed are given as relative values in Table II, $(\phi/\phi^0)_T$, where $\phi^0 f$ is obtained by extrapolating the ϕf values to $C = 0$.

Since triplets are produced by the donors only the theoretically significant relative triplet yields are those in terms of light absorbed by the proflavine monomer only, $(I_a/I_0)_D$. This quantity may be calculated from

$$(I_a/I_0)_D = 1 - \text{antilog}(-\epsilon_D C_D t) \quad (10)$$

and the corresponding relative triplet yields referred to light absorbed by the donor only, $(\phi/\phi^0)_D$, are listed as the last column in Table II.

The set of data shown in Table III refers to films prepared from a common PF-PVA stock solution; however, the temperature at which they were dried was

(14) V. Zanker and E. Miethke, *Z. Naturforsch. A*, **12**, 385 (1957).

Table II: Experimental Triplet Yield Data for Proflavine in DNA and PVA Films Prepared by Evaporation at Room Temperature

Absorbance, A	Thickness, $t, \mu\text{m}$	Total C , $C \times 10^3$	Monomer, $C_D \times 10^3$	Dimer, $C_A \times 10^3$	ΔA , (flash)	$\left(\frac{\phi}{\phi^0}\right)_T$	$\left(\frac{\phi}{\phi^0}\right)_D$
PF-DNA							
0.252	41.5	1.92	1.45	0.24	0.044	0.95	0.97
0.216	29.7	2.41	1.72	0.35	0.038	0.91	0.95
0.473	50.5	3.90	2.09	0.91	0.065	0.86	0.92
0.460	38.1	5.90	2.52	1.69	0.049	0.71	0.78
0.528	30.5	10.4	3.25	3.57	0.047	0.61	0.73
0.776	35.0	14.5	3.95	5.27	0.041	0.56	0.63
0.400	15.2	19.1	4.37	7.40	0.026	0.40	0.54
0.850	22.9	26.6	6.22	10.2	0.036	0.39	0.46
0.451	10.2	32.8	7.18	12.7	0.017	0.24	0.33
0.892	17.8	38.2	7.98	15.1	0.021	0.23	0.27
PF-PVA							
0.161	86	0.50	0.46	0.02	0.038	0.93	0.94
0.362	84	1.45	1.01	0.22	0.069	0.92	0.97
0.531	84	2.40	1.44	0.48	0.078	0.84	0.88
1.078	66	8.50	3.30	2.60	0.059	0.49	0.60
0.906	55	9.15	3.22	2.96	0.066	0.57	0.63
0.278	11	15.1	4.78	5.18	0.023	0.37	0.45
1.805	58	20.0	5.62	7.20	0.039	0.30	0.31
0.825	25	23.9	5.48	8.97	0.024	0.21	0.25
0.995	27	27.3	6.02	10.62	0.019	0.16	0.18

Table III: Effect of the Temperature of Drying on Species Concentrations and Triplet Yield in PF-PVA Films (Total Dye Molarity, $C = 6.36 \times 10^{-3}$)

Drying temp., $^{\circ}\text{C}$	Absorbance, A	Thickness, t , μm	Monomer, $C_D \times 10^3$	Dimer, $C_A \times 10^3$	$\left(\frac{\phi}{\phi^0}\right)_T$	$\left(\frac{\phi}{\phi^0}\right)_D$
25	0.396	30.0	2.75	1.80	0.62	0.70
50	0.475	30.5	3.46	1.45	0.71	0.76
75	0.396	21.7	4.25	1.05	0.80	0.84
90	0.305	15.8	4.55	0.90	0.83	0.86

varied, in order to produce different dimer concentrations while holding the total dye concentration constant.

Triplet Decay. Analysis of the oscilloscope transients showed that the decay was of first order in all cases studied. The decay rate was only poorly reproducible. For PF in DNA the decay rate constant was approximately 18 sec^{-1} and independent of the dye concentration; in PVA the decay rate constant decreased from 18 sec^{-1} to 7 sec^{-1} as the molarity rose from 0.001 to 0.005 and remained constant at higher concentrations.

Spectra. Visible absorption spectra of the films were measured at various dye concentrations and the spectra of the monomeric species were obtained by extrapolation to $C = 0$. The shapes of the monomer spectra in PVA and in DNA were found to be similar; however, the maximum is slightly red-shifted in PVA relative to that in DNA (465 nm and 470 nm). The spectrum of the dimer was found as the difference between total and monomer spectra using values of C_D and C_A obtained

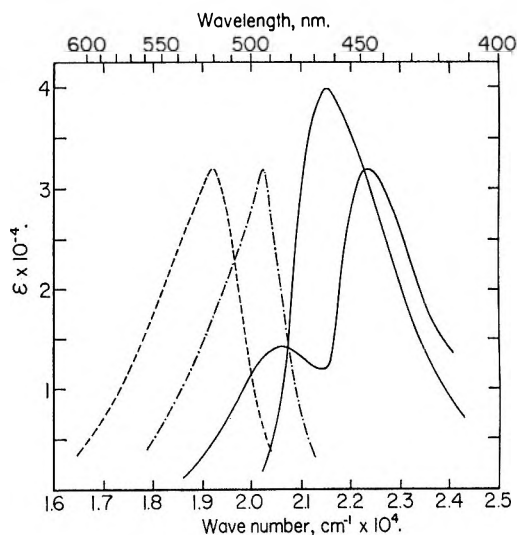


Figure 2. Absorption spectra of PF monomer in DNA and of PF dimer in either DNA or PVA (—). Fluorescence emission spectra of PF in DNA (---) and in PVA (— · —) in arbitrary units.

through the use of eq 8. The dimer spectrum of proflavine derived from the two types of films studied was the same and is shown in Figure 2. Except for a red shift the dimer spectrum in the film agrees substantially with that derived from aqueous solution studies^{8,15} and from the study of wet PF-DNA films.¹⁶

(15) The dimer spectrum derived is only approximate since concentrated samples were too dense optically for accurate instrumental response while in dilute samples the proportion of the dimer is small.

(16) D. M. Neville and D. R. Davis, *J. Mol. Biol.*, **17**, 57 (1966).

The fluorescence spectra of proflavine in DNA and in PVA films are shown in Figure 2; they differ considerably with respect to the position of their maxima which lie at 521 nm in DNA and at 494 nm in PVA. The fluorescence intensities are plotted in arbitrary units and the two curves are normalized relative to each other. Overlap integrals, Ω , calculated according to eq 6 for the two systems studied are included in Table I.

Discussion

Energy Acceptor Species. The results listed in Table III may be regarded as compelling evidence that the acceptor species is the dimer of proflavine under the conditions of the experiments. If impurities introduced with the dye were the dominant energy sinks, films having the same total dye concentration would show no variation in the triplet yield since the concentration of any impurity in these films must be identical. The fact that the monomer-based triplet yields when plotted against the dimer concentration (Figure 3) fall on the same curve, regardless of the temperature of evaporation, is further proof that the yields are independent of the total dye concentration and are a function of the dimer concentration only.

Nature of the Quenching Process. The pronounced change in triplet yield accompanied with little or no change in triplet lifetime with increasing concentration of the dye indicates that no concentration-dependent quenching of the triplet state occurred. Variations in triplet lifetime were observed in PVA films at low concentrations only and accordingly these were more likely the result of changes in the local rigidity of the matrix, than due to triplet-triplet energy transfer. Thus the drop in triplet yield with increasing dye concentration is to be assigned to the quenching of the excited singlet state.

In Figure 3 the two curves drawn correspond to theoretical quenching curves based on eq 4 with critical parameters C_A^0 and R_0 given in Table I. A random distribution of donors and acceptors was assumed in the calculation of these parameters which thus represent average values and do not reflect any local fluctuations of donor-acceptor distances. The good fit of these theoretical curves to the experimental points over a wide range of acceptor concentrations indicates that the concentration quenching observed may be described as energy transfer from proflavine monomers to proflavine dimers acting as energy sinks predominantly *via* dipole-dipole inductive resonance.

Effect of Polymer on Energy Transfer. In general, the efficiency of energy transfer is connected closely with the extent of overlap between the fluorescence spectrum of the donor and the absorption spectrum of the acceptor. The relatively lower transfer rates observed in DNA as compared with PVA apparent from Figure 3 are consistent with the above general principle (see Figure 2 and the values of Ω in Table I); the fluorescence peak of

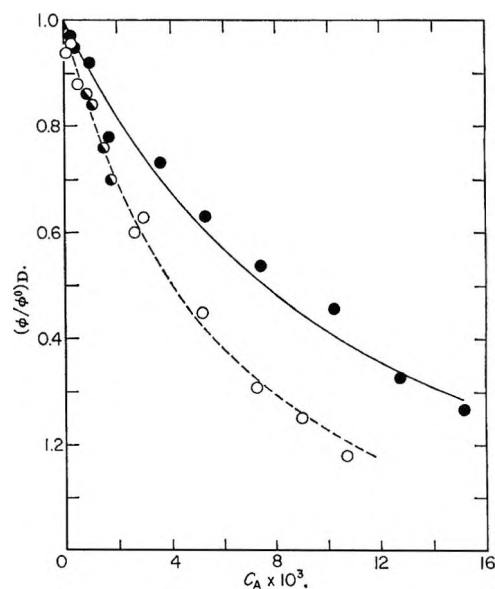


Figure 3. Relative triplet yields based on light absorbed by donor only, $(\phi/\phi^0)_D$, as function of dimer concentration: points, experimental values in DNA (●); in PVA (○); and in PVA at constant total dye concentration (●); curves, calculated from eq 4 with critical parameters listed in Table I: in DNA (—); in PVA (---).

proflavine monomer in DNA suffers a larger bathochromic shift than that in PVA and as a consequence the overlaps with the absorption spectrum of the dimer in the two media differ considerably. The relative positions of absorption and fluorescence maxima are governed by the nature and the relative magnitudes of solute-solvent interactions.¹⁷ Thus the stronger, perhaps predominantly ionic interaction between proflavine monomer and DNA compared with the interaction between proflavine and nonionic PVA is directly responsible for the reduction in the value of the overlap integral and in the transfer rate, as a result.

A second factor related to the nature of the polymer that may influence transfer efficiency is the extent of deviation from completely random orientation of the donor and acceptor transition dipoles. A measure of this orientation factor, κ^2 , may be estimated by the use of eq 5. The values of Ω and R_0 needed for this purpose are listed in Table I. We measured and found the refractive index, n , of DNA films to be 1.46 and that of PVA films to be 1.51. Finally, we found that the fluorescence quantum yield of proflavine in DNA and in PVA films was 1.4 ± 0.1 relative to that of proflavine in aqueous solution at pH 6.5. Given the absolute value of the fluorescence quantum yield in aqueous solutions to be 0.34,⁸ one arrives at the value of 0.5 for proflavine in the polymer films. Using the above values κ^2 was calculated for the two types of system and the results are included in Table I. It may be seen that κ^2 is well in excess of its value representing random orienta-

(17) For example, E. Lippert, *Angew. Chem.*, **73**, 695 (1961).

tions for both the systems studied. This result is readily explained since DNA, by virtue of its highly ordered conformation, is expected to produce some order in the dye molecules associated with it and PVA is well known to crystallize readily thereby affecting the relative orientations of the dye molecules dissolved in the crystalline regions. However, the relative efficiency of the two media in introducing nonrandom orientation of the dye molecules would have been difficult to predict *a priori*.

Dimer-Monomer Ratio. The monomer-dimer concentration ratio in the dry films was found to fall with increasing dye concentration (Table II), a situation superficially similar to liquid solutions of the dye. However, the quantity C_A/C_D^2 shows wide variations especially at low concentrations demonstrating the lack of equilibration in the films. This discrepancy may be accounted for by considering the sequence of events during film formation. At the initial stages of evaporation continual adjustment of the equilibrium is possible resulting in a steady increase in C_A as the total concen-

tration, C , increases. However, as the liquid solvent evaporates diffusion of the dye becomes increasingly more difficult and results in the eventual cessation in the establishment of the equilibrium between monomeric and dimeric dye species. It is of interest that the maximum value of C_A/C_D^2 of 240 l. mol⁻¹ found in PVA films is only about 1/2 of the dimerization constant of proflavine in aqueous solutions.⁸ However, the corresponding maximum ratio of 390 l. mol⁻¹ found in DNA films differs by several orders of magnitude from the formation constant of PF dimer bound to DNA in aqueous solution.⁵ The above result is consistent with the strong binding of PF to DNA, already inferred from consideration of the spectra; dye diffusion is restricted by strong PF-DNA interactions to a greater extent than by the relatively weak dye-PVA interactions.

Acknowledgments. We thank Professor U. P. Strauss for many helpful discussions and for enabling T. Kurucsev to spend his study leave at the School of Chemistry, Rutgers University.

The Photodecomposition of γ -Butyrolactone in the Vapor Phase

by R. Simonaitis*¹ and J. N. Pitts, Jr.

Department of Chemistry, University of California, Riverside, California 92502 (Received July 25, 1970)

Publication costs assisted by the University of California, Riverside

When γ -butyrolactone is irradiated in the vapor phase at 125° with radiation in the region 2100–2600 Å, it (1) isomerizes to succinaldehyde, (2) undergoes a fragmentation reaction to give ethylene, carbon monoxide, and formaldehyde, and (3) undergoes a fragmentation reaction to give propylene or cyclopropane and carbon dioxide. Hg sensitization favors the formation of the C₃ products. It is concluded that succinaldehyde and ethylene are probably singlet-state products, whereas cyclopropane and propylene are probably triplet-state products. Pressure-quenching experiments indicate that the propylene and cyclopropane do not have a common intermediate.

Introduction

The liquid-phase photochemistry of γ -butyrolactone has been the subject of earlier publications in this series.² The irradiation of γ -butyrolactone in the liquid phase leads to isomerization to succinaldehyde and allyl formate and to decarboxylation to give cyclopropane. In the liquid state the formation of allyl formate and cyclopropane proceeds *via* the triplet state, whereas the formation of succinaldehyde proceeds *via* the singlet state.

In this paper we report on the direct and Hg-sensitized photodecomposition of γ -butyrolactone in the vapor phase.³

Experimental Section

The purification of γ -butyrolactone has been described in an earlier publication.² Matheson "Spectro Quality" *n*-hexane was found to be free of impurities by glc and did not absorb above 2000 Å.

The cell was a 5 × 10 cm quartz cylinder enclosed in

(1) College of Engineering, The Pennsylvania State University, University Park, Pa. 16802.

(2) R. Simonaitis and J. N. Pitts, Jr., *J. Amer. Chem. Soc.*, **90**, 1389 (1968); **91**, 108 (1969).

(3) A brief report on the Hg-sensitized decomposition of γ -butyrolactone in a low-pressure flow system has appeared since this work was completed; I. S. Krull and D. R. Arnold, *Tetrahedron Lett.*, 1247 (1969).

an aluminum block. Provision was made to introduce the lactone or lactone-hexane mixtures into the cell from a glass bulb. The whole assembly including the pressure transducer (Statham Co.) was enclosed in a well insulated box, the temperature of which was controlled to $\pm 1^\circ$.

Irradiation was from a Hanovia 500-W medium-pressure lamp. In all experiments, radiation above 2600 Å was removed with a Cl_2 filter (5 cm) to prevent decomposition of the aldehyde product. When only the Cl_2 filter was used the effective radiation was between 2100 and 2600 Å. In some experiments radiation below 2500 Å was removed with a red-purple Corex filter used in combination with the Cl_2 filter.

For the Hg-sensitized runs a Hanovia (SH) low-pressure mercury resonance lamp, emitting mainly 2537-Å radiation, was employed. Radiation below 2500 Å was removed with a red-purple Corex filter.

After irradiation the contents of the cell were condensed (-196°) in a side arm and the noncondensables were collected with a Toepler pump. Their volume and pressure were measured in a calibrated tube, and the gasses were analyzed by mass spectrometry. The noncondensable fraction did not contain any C_2 - C_3 products. The temperature of the side arm was then raised to -127° (CS_2 slush) and the C_2 - C_3 products collected. In order to collect all the C_2 - C_3 products, the contents of the side arm were warmed to room temperature and refrozen at -127° several times. Analysis of the residual fraction showed that even in the presence of large amounts of hexane, all the C_2 - C_3 products were recovered. The C_2 - C_3 products were analyzed with flame ionization gas chromatography using a hexadecane column (30 ft \times $1/8$ in.; 25°). The remaining fraction was analyzed directly for higher boiling products using a Carbowax 20M column (20 ft \times $1/8$ in.).

An estimate of the formaldehyde yield relative to the ethylene yield was made in separate experiments in the absence of hexane. The noncondensable gases were removed at -196° and the fraction volatile at -76° was analyzed by mass spectrometry. From the intensity of the $m/e = 30$ and $m/e = 28$ peaks of the unknown mixture compared with a known mixture of formaldehyde and ethylene an estimate of the relative yields was obtained. The contribution to the intensity of these two peaks from the cyclo- C_3H_6 and C_3H_6 was negligible.

Results

The following products were obtained when γ -butyrolactone was irradiated with a medium-pressure lamp (effective wavelengths 2100-2600 Å) at 125° : ethylene, carbon monoxide, formaldehyde, succinaldehyde, cyclopropane, propylene, and carbon dioxide. The effect of added n -hexane on the rate of product formation is shown in Figure 1. Most of the data in Figure 1 are for a lactone pressure of 20.0 Torr and for irradiation times of 20.0 min, corresponding to conversions of

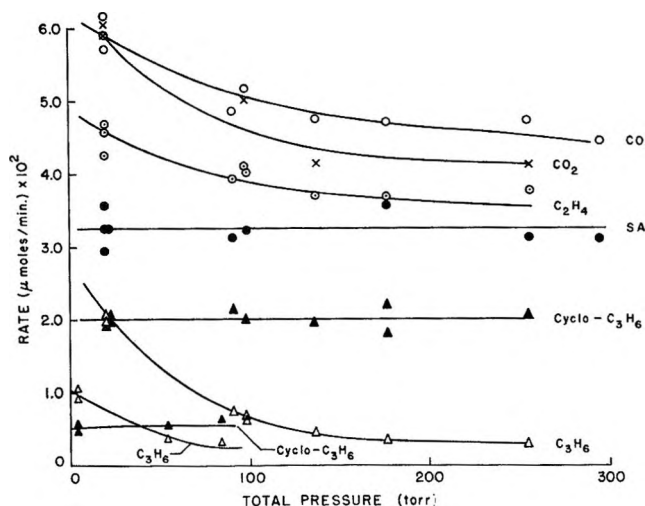


Figure 1. The rate of product formation vs. total pressure. Pressure of γ -butyrolactone is 20.0 Torr for the upper curves and 5.0 Torr for the two curves in the lower left-hand corner, temperature 125° : O, CO; ●, succinaldehyde; ○, ethylene; ▲, cyclopropane; Δ, propylene; pressurizing gas, n -hexane.

$<0.1\%$. A few runs were done at lower conversions (2.0-min runs) with no effect upon the results. The effect of n -hexane on the rates of cyclopropane and propylene formation at a lactone pressure of 5.0 Torr is also presented in Figure 1. The rate of formaldehyde formation relative to the rate of ethylene formation was determined only in the absence of n -hexane by mass spectrometric analysis. The relative rate was found to be approximately 1 ± 0.3 .

Figure 1 shows that the rates of succinaldehyde and cyclopropane formation are independent of the total pressure. The rate of propylene formation, and to a lesser extent the rate of formation of the other products, decreases with increasing pressure. From Figure 1 it is also apparent that the rate of CO_2 formation is greater than the rate of C_3 formation and the rate of CO formation is somewhat greater than the rate of ethylene formation. This lack of a complete material balance may be due to a small amount of polymer formation which would have escaped detection, because of the small conversions employed. Krull and Arnold found that polymer formation occurs in the Hg-sensitized decomposition of γ -butyrolactone.³

Some experiments were also done at longer wavelengths and the Hg($^3\text{P}_1$)-photosensitized decomposition of γ -butyrolactone was also briefly examined. The products at longer wavelengths and in the Hg-sensitized experiments are the same as before, but their relative yields are different. Table I presents the relative product quantum yields for the two different wavelength regions and for the Hg-sensitized experiments at the same conditions of temperature and pressure.

Table I shows that the most important trends are that the longer wavelengths favor the formation of cyclopropane and propylene and that in the Hg-sen-

Table I: Relative Quantum Yields for the Direct and Sensitized Irradiation of γ -Butyrolactone at 125° and 20 Torr

	$\Phi_{\text{cyclo-C}_3\text{H}_6}/\Phi_{\text{SA}}^a$	$\Phi_{\text{cyclo-C}_3\text{H}_6}/\Phi_{\text{C}_2\text{H}_4}$	$\Phi_{\text{cyclo-C}_3\text{H}_6}/\Phi_{\text{C}_3\text{H}_6}$
Direct 2537 Å ^b	1.1	1.2	3.7
Direct 2100–2600 Å ^c	0.62	0.43	1.0
Hg(³ P ₁)-sensitized	4.4	3.0 ^d	4.0 ^d

^a SA-succinaldehyde. ^b Average of two experiments. ^c Average of data presented in Figure 1. ^d Extrapolated to zero time.

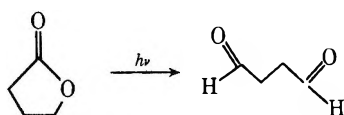
sitized photodecomposition when compared with the direct irradiation at 2537 Å, the formation of ethylene and succinaldehyde is much less important than the formation of cyclopropane and propylene. In the Hg-sensitized experiments $\Phi_{\text{cyclo-C}_3\text{H}_6}/\Phi_{\text{C}_3\text{H}_6}$ and $\Phi_{\text{cyclo-C}_3\text{H}_6}/\Phi_{\text{C}_2\text{H}_4}$ were found to be strongly dependent on the time of irradiation (Table II). Presumably this effect is due to scavenging of the olefin products by radicals produced in secondary reactions. A similar effect has been observed by Norrish and Wayne⁴ in their study of the Hg-sensitized decomposition of carbonyl compounds. For this reason the values for $\Phi_{\text{cyclo-C}_3\text{H}_6}/\Phi_{\text{C}_3\text{H}_6}$ and $\Phi_{\text{cyclo-C}_3\text{H}_6}/\Phi_{\text{C}_2\text{H}_4}$ were extrapolated to zero time for comparison to the unsensitized experiments. Within experimental error $\Phi_{\text{cyclo-C}_3\text{H}_6}/\Phi_{\text{C}_3\text{H}_6}$ is the same in the Hg-sensitized and in the unsensitized experiments at 2537 Å.

Table II: Effect of Time in the Hg(³P₁)-Sensitized Decomposition of γ -Butyrolactone at 20.0 Torr and 125°

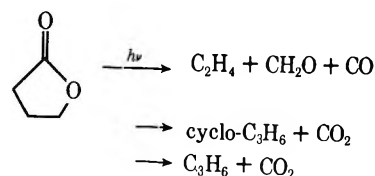
Time, sec	$\Phi_{\text{cyclo-C}_3\text{H}_6}/\Phi_{\text{C}_3\text{H}_6}$	$\Phi_{\text{cyclo-C}_3\text{H}_6}/\Phi_{\text{C}_2\text{H}_4}$
600.0	12.6	
60.0	15.0	18
28.0	12.6	
16.0	10.5	
8.0	7.2	4.2
2.0	4.3	3.2

Discussion

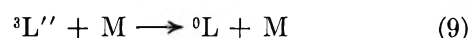
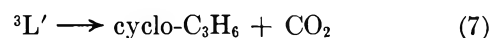
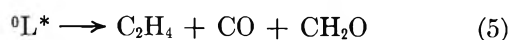
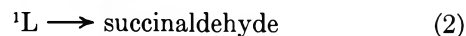
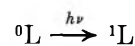
The formation of succinaldehyde can be rationalized by an α cleavage of the C–O bond and a transfer of a γ -hydrogen to the carbonyl carbon in stepwise or concerted fashion.



One fragmentation mode of the lactone gives rise to ethylene, CO, and formaldehyde, and another fragmentation mode gives the C₃ products and CO₂.



The following set of reactions is proposed to explain the data



In this scheme L stands for γ -butyrolactone and M stands for lactone or hexane. The superscripts 0, 1, and 3 refer to ground, singlet, and triplet lactone, respectively.

The absorption spectrum of γ -butyrolactone exhibits a weak $n-\pi^*$ transition commencing at about 2600 Å and a maximum at about 2100 Å.⁵ Below about 2000 Å a second very intense band begins to appear which may to some extent overlap with the $n-\pi^*$ band below ~ 2200 –2300 Å. The species ${}^1\text{L}^*$ produced when the exciting light is in the region 2100–2600 Å is probably predominantly the ${}^1(n,\pi^*)$ state, because the effective radiation is mostly above 2300 Å. When the exciting radiation is 2537 Å, ${}^1\text{L}$ is probably exclusively the ${}^1(n,\pi^*)$ state.

The proposal that succinaldehyde and ethylene originate from the singlet manifold and that propylene and cyclopropane originate from the triplet manifold of γ -butyrolactone is based on the fact that the formation of the latter products are favored over the former in the Hg-sensitized experiments, because sensitization by Hg(³P₁) is expected to give triplet lactone due to spin conservation. Since some succinaldehyde and ethylene are formed, this indicates that either the singlet manifold is populated to some extent or that these products may also be formed from the triplet lactone. The former case appears to be more likely, because in the Hg(³P₁)-sensitized decomposition of cyclobutanone about 10% of the products are formed

(4) R. G. W. Norrish and R. P. Wayne, *Proc. Roy. Soc., Ser. A*, **284**, 1 (1965).

(5) W. D. Closson and P. Haug, *J. Amer. Chem. Soc.*, **86**, 2384 (1964).

through a singlet pathway.⁶ The possibility that some direct photolysis is also occurring can be excluded, because the absorption coefficients for Hg and γ -butyrolactone are $\sim 10^7$ and < 1 l./mol-cm, respectively, and the ratio $[\text{Hg}]/[\gamma\text{-butyrolactone}]$ is $\sim 10^{-4}$. The suggestion that succinaldehyde is a singlet-state product is consistent with our study of γ -butyrolactone photochemistry in the liquid phase.²

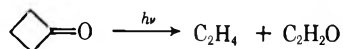
The events in the singlet manifold can be delineated in more detail. Since the formation of succinaldehyde is not pressure quenched, while the formation of ethylene is quenched, this indicates that these two products arise from different intermediates. Although the data could probably be accommodated by two electronically excited singlet states, we favor one of these intermediates to be vibrationally excited ground-state lactone produced by internal conversion, because of our observation that the thermal decomposition of γ -butyrolactone apparently gives rise to ethylene as one of the major products.⁷

From the mechanism the following relationship can be derived

$$R_{\text{C}_2\text{H}_4}^{-1} = R_{\text{CO}}^{-1} = \frac{\alpha}{k_1 I_a} + \frac{k_6 \alpha M}{k_5 k_1 I_a} \quad (\text{a})$$

where $\alpha = k_1 + k_2 + k_3 + k_4$ and M stands for any molecule in the system. From Figure 1 we see that R_{CO} is slightly greater than $R_{\text{C}_2\text{H}_4}$, indicating a small additional source of CO, possibly due to some polymer formation. A plot of R_{CO}^{-1} and $R_{\text{C}_2\text{H}_4}^{-1}$ vs. M is linear within the very limited extent of quenching, and the half-quenching pressure is 660 Torr for C_2H_4 and CO.

The photolysis of cyclobutanone also gives rise to ethylene.⁸ Lee has shown that the ethylene and ketene



arise from a "hot" ground state of cyclobutanone. The half-quenching pressure for ethylene is 5×10^3 Torr when propylene is the added gas and when the excitation energy is 112 kcal/mol. This is about a factor of 8 greater than the value for γ -butyrolactone using n -hexane as the pressurizing gas in spite of the greater average excitation energy. The lower half-quenching pressure for the lactone no doubt reflects the greater number of oscillators possessed by it and by the pressurizing gas.

The photolysis of cyclobutanone also gives rise to cyclopropane and propylene. The propylene is believed to be formed exclusively by the isomerization of the "hot" cyclopropane intermediate.⁸ This mechanism requires that there be a concomitant increase in $\Phi_{\text{cyclo-C}_3\text{H}_6}$ with a decrease in $\Phi_{\text{C}_3\text{H}_6}$ vs. pressure, such that $\Phi_{\text{cyclo-C}_3\text{H}_6} + \Phi_{\text{C}_3\text{H}_6} = \text{constant}$. In the present system propylene formation is strongly quenched with increasing pressure, but cyclopropane formation is unaffected. This result requires that the two C_3 products be produced from different precursors, designated as

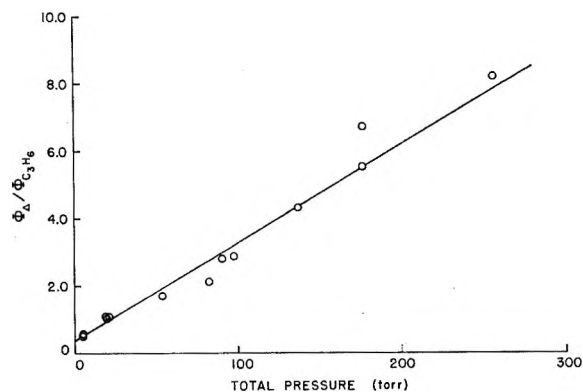
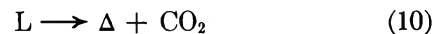


Figure 2. $\Phi_{\text{cyclo-C}_3\text{H}_6}/\Phi_{\text{C}_3\text{H}_6}$ vs. total pressure for the direct irradiation of γ -butyrolactone at 125°.

$^3\text{L}'$ and $^3\text{L}''$ in the mechanistic scheme (reactions 7 and 8).

Initially the cyclopropane must be produced with an energy content of less than 65 kcal/mol, for otherwise it would isomerize to propylene.⁹ Reaction 10 is en-



dothemic by about 7 kcal/mol at 125°.¹⁰ Since the excitation energy is at least 112 kcal/mol, the energy to be distributed among the products can be greater than about 105 kcal/mol. Therefore, the CO_2 must take up a considerable portion of the energy either as vibrational energy or perhaps as electronic energy. There appears to be sufficient energy to form triplet CO_2 , since the triplet state energy of CO_2 is only about 85 kcal/mol.¹¹

To explain the decrease in the rate of propylene formation with increasing pressure, it is necessary to assume that the state responsible for its production is quenched to starting material (reaction 9). Reaction 9 requires that the rate of CO_2 formation must decrease with increasing pressure; this is observed.

From the mechanism the following relation can be derived

$$\frac{R_{\text{cyclo-C}_3\text{H}_6}}{R_{\text{C}_3\text{H}_6}} = \frac{k_3}{k_4} + \frac{k_3 k_9}{k_4 k_8} M \quad (\text{b})$$

(6) D. C. Montague and F. S. Rowland, *J. Amer. Chem. Soc.*, **91**, 7230 (1969).

(7) We did not study the thermal decomposition of γ -butyrolactone in detail, except to see if ethylene is a major product. Ethylene was found to be the major product; no C_3 products or succinaldehyde were detected.

(8) N. E. Lee and E. K. C. Lee, *J. Chem. Phys.*, **50**, 2094 (1965).

(9) S. W. Benson, "The Foundations of Chemical Kinetics," McGraw-Hill, New York, N. Y., 1960.

(10) A reasonable estimate for the heat of formation of γ -butyrolactone can be made as follows: ΔH_f (4 carbon straight chain esters) + e (ring strain) + ΔH_f (n -hexane) - ΔH_f (cyclohexane) = $-106 + 6 + 10 = -90$ kcal/mol.

(11) M. A. A. Clyne and B. A. Thrush, *Proc. Roy. Soc., Ser. A*, **269**, 404 (1962).

A plot of $R_{\text{cyclo-C}_3\text{H}_8}/R_{\text{C}_3\text{H}_6}$ vs. pressure is presented in Figure 2. The intercept gives $k_3/k_4 = 0.40$ and from the slope and intercept we get $k_9/k_8 = 0.078 \text{ Torr}^{-1}$.

Acknowledgment. This research was supported by Grant AP 00109, Research Grants Branch, National

Air Pollution Control Administration, Consumer Protection and Environmental Health Service, U. S. Health Service. R. S. also wishes to thank the Public Health Service, Division of Air Pollution, for a Post-doctoral Fellowship.

The Photochemical Oxidation of Some Substituted Aromatic

Amines in Chloroform

by E. A. Fitzgerald, Jr., P. Wuelfing, Jr., and H. H. Richtol*

Department of Chemistry, Rensselaer Polytechnic Institute, Troy, New York 12181 (Received October 26, 1970)

Publication costs borne completely by The Journal of Physical Chemistry

The solution phase photochemistry of *N,N'*-diphenyl-*p*-phenylenediamine (DPPD), *N,N'*-dimethyl-*N,N'*-diphenyl-*p*-phenylenediamine (DMDPPD), *N,N,N',N'*-tetraphenyl-*p*-phenylenediamine (TPPD), and *p*-hydroxydiphenylamine (HDPDA) has been studied. Absorption of ultraviolet radiation by these compounds in chloroform or carbon tetrachloride yields permanent photooxidation. The products are the colored radical cations of the amines which are also produced by chemical and electrochemical oxidation with bromine. Irradiation of the amines in nonhalogenated solvents (*e.g.*, ethanol, benzene) yields fluorescence emission only and no permanent oxidation. Oxidation quantum yields are greater than one for several of the amines, indicating that the oxidation can occur by a thermal mechanism after the primary photoprocess. The presence of dissolved oxygen increases the quantum yields significantly and identification of products resulting from the reaction of solvent radicals with oxygen suggests the thermal mechanism. Finally, the triplet states of the amines have been observed by flash photolysis experiments in degassed nonhalogenated solvents in which oxidation does not occur.

The purpose of this work is to investigate the mechanism of photooxidation of certain aromatic amines in fluid solution. Photooxidation of many similar compounds had been studied previously either in rigid solution where the radical cation product is isolated or by flash photolytic techniques in inert fluid solvents in which the reaction is not permanent and the radical cation decomposes very rapidly. Lewis and coworkers^{1,2} were first to investigate photooxidation in rigid medium. They found that photooxidation occurred for aromatic compounds containing the amino, hydroxy, and mercapto substituents and the product was identical with the radical-cation produced by chemical oxidation. Other workers have made quantitative studies of photooxidation of aromatic amines in rigid solutions.^{3,4} Cadogan and Albrecht^{5,6} found evidence that the photooxidation of *N,N,N',N'*-tetramethyl-*p*-phenylenediamine (TMPD) in rigid solution occurred by a two-photon process *via* a triplet-state intermediate. Radical cations of similar amines have been observed^{7,8} as transient species after flash photolysis in fluid solution. Recently, Meyer⁹ has investigated the photooxi-

dation of TMPD in several halogenated solvents, including chloroform. The radical cations of the amines studied in this work, with the exception of tetraphenyl-*p*-phenylenediamine (TPPD), are sufficiently stable in chloroform to allow the product formation to be analyzed by conventional spectrophotometry at room temperature. The radical cation of TPPD decomposes after it is formed photochemically but the rate of de-

(1) G. N. Lewis and D. Lipkin, *J. Amer. Chem. Soc.*, **64**, 2801 (1942).

(2) G. N. Lewis and J. Bigeleisen, *ibid.*, **65**, 2424 (1943).

(3) H. Linschitz, J. Rennert, and T. M. Korn, *ibid.*, **76**, 5839 (1954).

(4) W. E. Meyer and A. C. Albrecht, *J. Phys. Chem.*, **66**, 1168 (1962).

(5) K. D. Cadogan and A. C. Albrecht, *J. Chem. Phys.*, **43**, 2550 (1965).

(6) K. D. Cadogan and A. C. Albrecht, *J. Phys. Chem.*, **72**, 929 (1969).

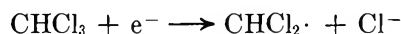
(7) O. D. Dmitrievskii, *Opt. Spektrosk.*, **19**, 828 (1965).

(8) H. Linschitz, M. Ottolenghi, and R. Bensasson, *J. Amer. Chem. Soc.*, **89**, 4592 (1967).

(9) W. C. Meyer, *J. Phys. Chem.*, **74**, 2118 (1970).

composition is sufficiently slow at 0° to allow its absorbance to be measured.

The energy of ultraviolet light necessary to cause oxidation (*ca.* 3.5 eV) has been found to be significantly less than ionization potentials of similar amines (*ca.* 6 to 7 eV). The additional necessary energy in these systems is apparently provided by secondary thermal reactions. The key to the energetics of the photooxidation reaction is the dissociative electron attachment reaction which occurs with chloroform and other halogenated compounds.



This reaction is exothermic by 16 kcal/mol for chloroform.¹⁰ It is believed that the energy supplied by this reaction and the solvation energy of the ionic products in chloroform are sufficient to make the process energetically feasible. Meyer⁹ has found evidence for a charge-transfer complex in the photooxidation of TM-PPD in chloroform. The presence of chloroform does not alter the absorption spectra of the amines studied in this work and no evidence for charge-transfer complexes has been found. The dissociative electron attachment reactions of chloroform, carbon tetrachloride, and other halogenated compounds have been studied by Hamill and coworkers,^{11,12} who found evidence for the halomethane free radical and halide ion after electron attachment by γ radiolysis. The quantum yield studies and identification of coproducts of the radical cations in this work suggest a mechanism of photooxidation by a primary photoprocess and secondary thermal mechanism which includes dissociative electron attachment of the solvent.

Experimental Section

General. Dimethyldiphenyl-*p*-phenylenediamine (DMDPPD) was prepared from diphenyl-*p*-phenylenediamine (DPPD) (Eastman) by the methylation procedure of Picard.¹³ Tetraphenyl-*p*-phenylenediamine (TPPD) was prepared from DPPD by the method of Fox.¹⁴ Hydroxydiphenylamine (HDP A) was Eastman technical grade. The amines were purified by several recrystallizations from ethanol, except for HDP A which was recrystallized twice from ligroin and twice from water. The chloroform used was Fisher Reagent grade purified by the method of Gillo¹⁵ and distilled. All other solvents were Fisher Spectranalyzed grade and were used without further purification.

The absorptivities of the radical cations were determined by oxidation of successive amounts of amine with coulometrically generated bromine and measurement of the absorbance at each increment of bromine generated.¹⁶ This procedure yielded reproducible Beer's law plots at the wavelength of maximum absorbance. The absorptivities thus determined, the quantum yields of oxidation were then determined by spectrophotometric analysis of the radical cations generated.

Degassed solutions were prepared by seven freeze-pump-thaw cycles on the vacuum rack.

Actinometry and Light Sources. The incident light intensity was determined by potassium ferrioxalate actinometry.¹⁷

The quantum yield studies were conducted at 366 $m\mu$ by irradiation with a 1000-W Hanovia high-pressure mercury-xenon lamp. The 366- $m\mu$ line was isolated with a Corning No. 5970 glass filter (half bandwidth of approximately 25 $m\mu$). The light source employed for the study of quantum yield variation with exciting wavelength was an Osram SBO 150-W xenon lamp. The exciting wavelength was selected by focusing the beam through a Bausch and Lomb 250-mm grating monochromator with slits set at 1 mm (half bandwidth 7 $m\mu$). The spectral cells containing the solutions to be photolyzed were contained in a thermostated cell holder and the temperature was maintained within $\pm 2^\circ$.

The quantum yields determined in this work were calculated as the integral quantum yields as defined by Albrecht and Meyer.¹⁸ The products absorb in the region of exciting wavelength and a correction for product absorbance is included in the above treatment. Simplifying assumptions were made to the mathematical treatment and include the assumption that reactant absorbance is essentially constant and does not vary with time and the assumption that the rate of product formation is linear with time over the initial short time period of the exposure. Experimentally, the conversion of the reactant was limited to 5% or less and solutions were irradiated for a fixed time period in all experiments. The rate of product formation was found to be linear in the irradiation time period employed experimentally. The above assumptions and experimental error in the quantum yield determinations lead to an error of $\pm 7\%$ for the quantum yields reported.

Luminescence and Flash Photolysis Studies. The luminescence studies were performed on a modified Beckman DU quartz spectrophotometer¹⁹ equipped for recording emission spectra. Fluorescence quantum yields were determined by comparison to 0.1 ppm quinine sulfate standard solution.

(10) L. J. Forrestal and W. H. Hamill, *J. Amer. Chem. Soc.*, **83**, 1535 (1961).

(11) M. R. Ronayne, J. P. Guarino, and W. H. Hamill, *ibid.*, **84**, 4230 (1962).

(12) J. B. Gallivan and W. H. Hamill, *Trans. Faraday Soc.*, **61**, 1 (1965).

(13) J. Picard, *J. Amer. Chem. Soc.*, **48**, 2355 (1926).

(14) C. J. Fox, *Chem. Abstr.*, **60**, 14051g (1964).

(15) J. Gillo, *Ann. Chim. (Paris)*, **12**, 281 (1939).

(16) E. A. Fitzgerald, P. Wuefing, Jr., and H. H. Richtol, *Anal. Chem.*, **42**, 229 (1970).

(17) C. G. Hatchard and C. A. Parker, *Proc. Roy. Soc.*, **235**, 518 (1950).

(18) W. E. Meyer and A. C. Albrecht, *J. Phys. Chem.*, **66**, 1168 (1962).

(19) H. H. Richtol and F. H. Klappmeier, *J. Chem. Phys.*, **44**, 1519 (1966).

The flash photolysis experiments were conducted with an apparatus described by Strong, *et al.*²⁰

Results and Discussion

Absorption and Fluorescence Spectra. Irradiation of the amines in chloroform in the wavelength range of 290 to 370 m μ produces colored solutions. The visible spectra obtained matched the previously reported radical cation spectrum of DPPD³ which was generated photochemically. The other radical cations have not been reported previously by photochemical generation but match those obtained electrochemically.¹⁶ The spectral data for the radical cations studied in this work are summarized in Table I.

Table I: Spectral Data for the Amine Radical Cations in Chloroform

Compd	Wavelength maximum, m μ	Absorptivity at maximum, $\times 10^{-3}$	Fluorescence maximum of parent amine, m μ
DPPD	700	10.8	380
DMDPPD	675	9.4	400
TPPD	725	6.0	405
HDP A	450	1.45	380

Irradiation of the amines in the nonhalogenated solvents ethanol, benzene, acetone, or hexane produces no visible color and the ultraviolet spectra of the amines do not change after irradiation. There is apparently no efficient photochemical reaction in these solvents. Fluorescence is found in all these solvents and the fluorescence wavelength maximum is also given in Table I.

Quantum Yield Studies. The quantum yields of oxidation of the amines in chloroform were studied as a function of amine concentration and the results are shown in Table II.

The oxidation quantum yields are greater than unity for DMDPPD, DPPD, and HDP A and are virtually independent of amine concentration. The 25% decrease in quantum yield as concentration is increased tenfold for DMDPPD is not large compared with the experimental error of $\pm 7\%$ and there appears to be no large concentration dependence in this case. TPPD exhibits a definite increase in quantum yield as concentration is increased. The magnitudes of the quantum yields of DMDPPD, DPPD, and HDP A indicate that oxidized product is formed in secondary thermal reactions. The concentration dependence for TPPD suggests that the amine is being oxidized in a secondary thermal step but also the fading of the TPPD radical cation color at room temperature is an indication of thermal instability of this species. All the other radical cations studied are stable and do not bleach.

Table II: Oxidation Quantum Yields as a Function of Amine Concentration in Air-Saturated Chloroform^a

Compd	Concn, $M \times 10^4$	Quantum yield
DMDPPD	3.0	2.0 ± 0.5
	7.0	1.6 ± 0.4
	30	1.4 ± 0.2
HDP A	3.0	1.9 ± 0.2
	7.0	1.7 ± 0.2
	20	1.7 ± 0.2
TPPD ^b	1.0	0.15 ± 0.02
	2.0	0.24 ± 0.02
	3.0	0.37 ± 0.04
	5.0	0.55 ± 0.06
DPPD	3.9	1.2 ± 0.2
	5.8	1.3 ± 0.2
	8.9	1.3 ± 0.2

^a $T = 25^\circ$, $\lambda_{ex} 366 \text{ m}\mu$. ^b Irradiated at 0° .

The magnitudes of the oxidation quantum yields in chloroform have also been found to be dependent on oxygen concentration. Table III is a comparison of quantum yields in degassed and air-saturated chloroform solutions for TPPD and HDP A, where this effect has been carefully studied.

Table III: Oxidation Quantum Yield as a Function of the Presence of Oxygen^a

Compd	Concn, M	Oxygen concentration	Quantum yield
TPPD ^b	3×10^{-4}	Degassed	0.115 ± 0.02
		Degassed	0.12 ± 0.02
	3×10^{-4}	Air-saturated	0.30 ± 0.03
		Air-saturated	0.32 ± 0.03
	HDP A	2×10^{-3}	Degassed
2×10^{-3}		Degassed	0.8 ± 0.1
2×10^{-3}		Air-saturated	1.7 ± 0.2
	2×10^{-3}	Air-saturated	1.5 ± 0.2

^a $T = 25^\circ$, $\lambda_{ex} 366 \text{ m}\mu$. ^b $T = 0^\circ$.

It can be seen from the data in Table III that an approximately twofold increase in oxidation quantum yields is found in the presence of oxygen. This indicates that oxygen is entering into secondary thermal reactions that produce amine radical cations. Somewhat similar results are obtained in CCl_4 solvent, but due to the radical cation salt being insoluble, this system was not investigated very thoroughly.

Irradiation of solutions of the amines in ethanol containing low concentrations of added chloroform produces both fluorescence and oxidation. Figure 1 shows that, as the concentration of added chloroform is in-

(20) R. L. Strong and J. Perano, *J. Amer. Chem. Soc.*, **89**, 2535 (1967).

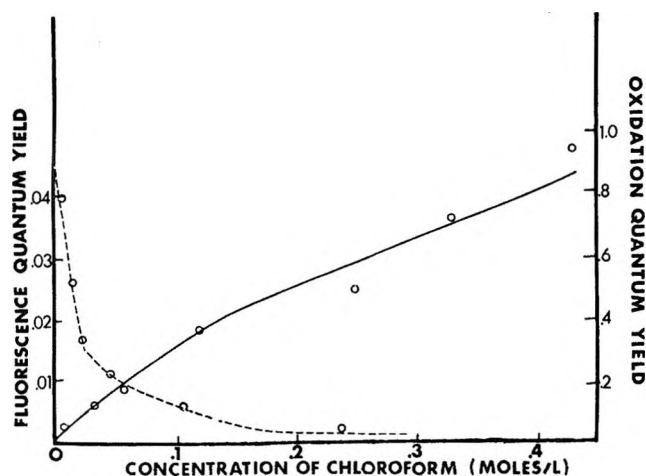


Figure 1. The effect of added chloroform on the fluorescence and quantum yields of DMDPPD in air-saturated ethanol: [DMDPPD] = 10^{-3} M; λ_{ex} 366 m μ ; —, oxidation quantum yield; - - -, fluorescence quantum yield.

creased, the quantum yield of oxidation increases and the quantum yield of fluorescence decreases. These data suggest that the two processes are occurring from the same excited state. Thus, the excited state from which oxidation occurs is most probably the first excited singlet state. The participation of the singlet state in the oxidation mechanism is also suggested by the oxygen effect. If the triplet state were involved in the oxidation, one would expect a marked decrease or complete quenching of reaction in the presence of oxygen.

Identification of Coproducts of the Radical Cations. Several other products have been found after irradiation of air-saturated solutions of the amines in chloroform. Hydrogen ion is produced after irradiation. Table IV shows the results of titration of the chloroform solutions with sodium ethoxide after irradiation.

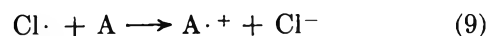
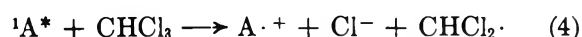
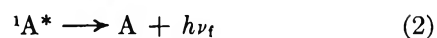
Table IV: Results of Sodium Ethoxide Titration after Irradiation

Compd	Mequiv of amine oxidized	Mequiv of H ⁺ found
DMDPPD	0.09 ± 0.01	0.065 ± 0.01
	0.09 ± 0.01	0.065 ± 0.01
TPPD	0.026 ± 0.03	0.033 ± 0.006
	0.026 ± 0.03	0.030 ± 0.006
HDPA	0.11 ± 0.01	0.073 ± 0.015
	0.11 ± 0.01	0.075 ± 0.015

The data of Table IV indicate that approximately 1 mol of H⁺ is formed for each mole of amine oxidized. Phosgene has also been found after photooxidation by its characteristic condensation reaction with benzidine. Chloride ion was detected by precipitation with silver nitrate. Also, ethyl formate was identified by gas chromatographic and infrared analysis after 1% ethanol

was added to the chloroform solution of amine and irradiation was conducted. It is believed that the ethyl formate found results from the "trapping" of formyl chloride intermediate by its esterification with ethanol.

Mechanism of the Photooxidation. The following mechanism is proposed on the basis of the above results



where A = amine, ${}^1A^*$ = excited singlet state of amine, $A\cdot^+$ = amine radical cation, and $h\nu_f$ = quantum of fluorescent light. Steps 1–3 are standard and need no further elaboration. Step 4 is the oxidation of the excited singlet state of the amine accompanied by dissociative electron attachment of the solvent. Similarly, Bowen and Rhoatgi²¹ found that photooxidation of anthracene in the presence of oxygen in chloroform solution appeared to proceed *via* the singlet state. The decomposition of the dichloromethyl radical *via* a peroxy radical intermediate in steps 5–8 includes steps which have been found to be operative in similar systems.^{22–26} The ethyl formate produced in the presence of ethanol suggests these intermediate steps. The oxidation of amine by chlorine radical in step 9 accounts for the quantum yields of DPPD, DMDPPD, and HDPA which are greater than one and also for the oxidation quantum yield being approximately twice as great in the presence of oxygen (steps 5–9).

According to the mechanism, the presence of oxygen should double the oxidation quantum yield and 1 mol of HCl should be found for every mole of amine oxidized to the radical cation. This is reflected in the experimental results.

Other mechanisms have been proposed for the oxidation of DPPD⁸ and TMPD^{5,6} but these have not been

(21) E. J. Bowen and K. K. Rhoatgi, *Discuss. Faraday Soc.*, **14**, 146 (1953).

(22) H. A. Staab, *Angew. Chem.*, **75**, 1203 (1963).

(23) W. Brenschede and H. J. Schumacher, *Z. Phys. Chem., Abt. A*, **177**, 245 (1936).

(24) H. J. Schumacher and K. Wolff, *ibid.*, *Abt. B*, **26**, 453 (1934).

(25) K. B. Krauskopf and G. K. Rollefson, *J. Amer. Chem. Soc.*, **56**, 2542 (1934).

(26) J. W. T. Spinks, *Chem. Rev.*, **26**, 129 (1940).

performed in the presence of CHCl_3 . In the presence of CHCl_3 , the above proposed mechanism is so efficient that all other mechanisms are unimportant.

Flash Photolysis Studies. Flash photolysis of degassed solutions of the amines in nonhalogenated solvents yielded transient species which had absorption maxima between 590 and 660 $\text{m}\mu$. The absorbance of the transients decayed by first-order kinetics. No transient spectra were observed when air was allowed to enter the photolysis cell before flashing. Table V shows

Table V: Flash Photolytic Data for the Amines in Degassed Solvents

Amine	Solvent	λ_{max} of transient, $\text{m}\mu$	k_1 , $\text{sec}^{-1} \times 10^{-3}$
HDP A	Benzene	590	1.0 ± 0.1
TPPD	Benzene	660	4.8 ± 0.5
DMDPPD	Ethanol	640	11.0 ± 1.0

the absorption maxima and first-order decay constants for the three transients studied.

The above data indicate that the transient species observed is the triplet state. Phosphorescence emission of the amines in rigid solution has been observed with the emission maxima at approximately 500 $\text{m}\mu$ in all cases. Linschitz³ and coworkers have observed a similar transient absorption after flash photolysis of DPPD in rigid solvent and attributed this to the triplet state. They obtained an intermediate with an absorption maximum at 610 $\text{m}\mu$ and a first-order rate constant of decay in the range of 10 sec^{-1} at -160° in rigid EPA. The triplet state apparently is not involved in the photooxidation in chloroform.

Acknowledgment. E. A. F. gratefully acknowledges the support of a National Aeronautics and Space Administration Fellowship. This work was supported by the National Science Foundation under Grant No. GP5268.

The Photochemistry of the Xylenes. A Discussion of Method¹

by W. Albert Noyes, Jr.,* and D. A. Harter

Chemistry Division, Argonne National Laboratory, Argonne, Illinois 60439 (Received March 22, 1971)

Publication costs assisted by the Argonne National Laboratory

Quantum yields of isomerization of the three xylenes increase with decrease in incident wavelength to about 240 nm. These quantum yields are not identical with formation yields for intermediates such as dimethyl benzvalenes and dimethyl prismanes. The latter are destroyed by a variety of processes and their primary yields may be severalfold greater than the yields of ultimate isomers. Yields generally increase with temperature and decrease with increase in total pressure. Yields at long wavelengths and high total pressures approximate those in the liquid phase. Toward the long wave limit of the absorption region (260–270 nm) the sums of fluorescent and of triplet-state yields approximate unity. The latter have been determined by the Cundall method. A critical survey of triplet-state methods is made. Valid objections may be raised to all of them. The use of biacetyl is not in general to be recommended. In all probability the emitter in the case of biacetyl-aromatic mixtures is a complex and apparent yields are often unacceptably high. Oxygen quenches the fluorescences of the three xylenes effectively. Both fluorescence and crossover to the triplet state diminish as incident wavelengths decrease, thus indicating that other processes become of increasing importance at high vibrational levels of the excited singlet state. A fairly consistent picture of the photochemical behaviors of the xylenes can be given. *p*-Xylene appears to have considerably greater photochemical stability than the other xylenes and has the highest fluorescent yields.

The photochemistry of simple aromatic compounds has received so much attention during recent years that no attempt will be made to cite references to more than those papers of immediate interest to the problems at hand.

It is now recognized that benzene and simple benzene derivatives isomerize under the influence of ultraviolet light in the region 240–270 nm.² The isomers so far

identified are: benzvalene, prismane, Dewar benzene, and fulvene. Of these, Dewar benzene seems not to be

(1) Work performed under the auspices of the U. S. Atomic Energy Commission.

(2) (a) K. E. Wilzbach and L. Kaplan, *J. Amer. Chem. Soc.*, **86**, 2307 (1964); (b) L. Kaplan, K. E. Wilzbach, W. Brown, and S. S. Yang, *ibid.*, **87**, 675 (1965); (c) K. E. Wilzbach and L. Kaplan, *ibid.*, **87**, 4004 (1965); (d) I. E. Den Besten, I. Kaplan, and K. E. Wilzbach, *ibid.*, **90**, 5868 (1968).

formed directly upon irradiation of benzene although this isomer may apparently be formed by irradiation of certain halogenated benzenes.³

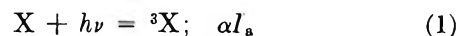
Further facts about these compounds may be stated briefly. (1) Yields of isomers in the gas phase depend on the initially formed vibrational level of the excited state and in a general way the higher the vibrational level the greater the isomerization. (2) Fluorescence is observed from all aromatic compounds which are not heterocyclic but yields of fluorescence are wavelength dependent and decrease with decrease in incident wavelength. (3) Toward the long wavelength end of the absorption region (wavelengths greater than about 259 nm) it is probable that the sum of fluorescent yield and triplet-state yield is unity, but this is not true at shorter wavelengths.⁴ (4) It is recognized that available methods for determining triplet-state yields are not sound except under restricted conditions and that, therefore, conclusions such as those stated are subject to uncertainty.⁵ (5) Quite probably both fluorescence and crossover to the triplet state have optimum yields from low lying vibrational levels of the first excited singlet state.⁶ (6) Since yields of fluorescence, of isomerization, and of other known processes do not add to unity at short wavelengths it is evident that one or more processes take place which have not been identified completely at the present time.

One may therefore conclude that the complete histories of many excited singlet-state aromatic molecules may be given if they are formed in low vibrational levels in the gas phase.⁵ The detailed descriptions of the behaviors of triplet-state molecules may not be given. Such molecules do not emit light in the gaseous phase and do so only in glassy matrices at low temperatures. There is no evidence that they isomerize although the formation of isomers which revert quantitatively to the parent molecules may not be excluded. It is unlikely that unidentified products are being formed so that one must conclude that as the wavelength of the incident light decreases a larger and larger fraction of the absorbing molecules by some process or other have their energy degraded to heat without formation either of identifiable intermediates or of final products. Excimer formation is of undoubted importance in liquid-phase systems involving aromatic molecules, but evidence for such products in the gas phase is meager.⁷

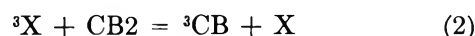
It is, therefore, impossible to give in the gas phase complete histories of absorbing molecules beginning with the act of absorption and ending either with identifiable products or with inactive parent molecules. The situation in the gas phase is, nevertheless, somewhat better than in the liquid phase. The present work was undertaken with a view of trying to make this story as complete as possible for the three xylenes. The situation still leaves much to be desired.

Critique of Triplet-State Methods

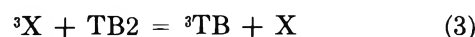
*The Cundall Method.*⁸ If X is the absorbing molecule and α is the fraction of the absorbing molecules which reach the triplet state, one may write



where I_a is the number of photons absorbed per milliliter per second. By the method of Cundall either *cis*- or *trans*-butene-2 is added to the system and one may write either



or



where CB2 and TB2 are *cis*- and *trans*-butene-2, respectively. The transfer of energy by (2) and (3) should produce triplet butene-2 molecules with single bonds between the two central carbon atoms. At this point an assumption is made, *viz.* the mean lifetimes of ${}^3\text{CB}$ and of ${}^3\text{TB}$ are such that they are in effect during their lifetimes equivalent to each other. If this assumption is made one may write



Thus if the added butene is CB2 the yield of TB2 is

$$\Phi_{\text{TB2}} = \alpha [k_6 / (k_4 + k_5)] \quad (8)$$

and if it is TB-2 the yield of CB-2 is

$$\Phi_{\text{CB2}} = \alpha [k_6 / (k_6 + k_7)] \quad (9)$$

Since the quantum yield of the triplet is stated to be α

$$\Phi_{\text{trip}} = \alpha = \Phi_{\text{TB2}} + \Phi_{\text{CB2}} \quad (10)$$

where Φ_{TB2} and Φ_{CB2} are obtained from two different experiments with *cis*- and with *trans*-butene-2, respectively.

(3) (a) I. Haller, *J. Amer. Chem. Soc.*, **88**, 2070 (1966); (b) D. Phillips, *J. Chem. Phys.*, **46**, 4679 (1967); (c) I. Haller, *ibid.*, **47**, 1117 (1967); (d) G. Camaggi, F. Gozzo, and G. Cevidalli, *Chem. Commun.*, 313 (1966).

(4) (a) H. Ishikawa and W. A. Noyes, Jr., *J. Chem. Phys.*, **37**, 583 (1962); (b) D. Phillips, *J. Phys. Chem.*, **71**, 1839 (1967); (c) C. S. Burton and W. A. Noyes, Jr., *J. Chem. Phys.*, **49**, 1705 (1968); (d) K. Nakamura, *ibid.*, **53**, 998 (1970).

(5) (a) W. A. Noyes, Jr., and C. S. Burton, *Z. Elektrochem.*, **72**, 146 (1968); (b) W. A. Noyes, Jr., D. Anderson, and D. A. Harter, *J. Chim. Phys. Physicochim. Biol.*, **204** (1970) (20th Reunion of Societe de Chemie Physique, held May 1969); (c) V. L. Ermolaev, *Izv. Akad. Nauk SSSR, Ser. Fiz.*, **32** (8), 1287 (1968).

(6) R. Bensasson, R. Bonneau, J. Joussot-Dubien, and J. Faure, ref 5b, p 133.

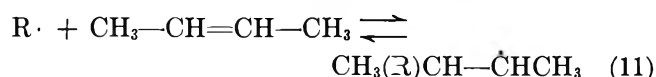
(7) J. B. Birks, *Progr. React. Kinet.*, **5**, 181 (1970).

(8) (a) R. B. Cundall and T. F. Palmer, *Trans. Faraday Soc.*, **56**, 1211 (1960); (b) R. B. Cundall, F. J. Fletcher, and D. G. Milne, *ibid.*, **60**, 1146 (1964).

It should be noted that (10) is valid even if the branching ratio is not unity provided ${}^3\text{CB}$ and ${}^3\text{TB}$ are in fact the same state. The best evidence that this is true at least under certain experimental conditions is found in the work of Haninger and Lee,⁹ who showed that the branching ratio is unity. However, all authors who have worked with this method show fairly large scatters in their results, mainly due to difficulties in the determination of a small amount of one isomer in the presence of a large amount of the other.

The rates of (4)–(7) are not known although to a first approximation they are all equal. It is conceivable that under some conditions this equality may not exist and the triplet states of the butenes may have “memories.”

Four other factors must be kept in mind with this method. (a) In the liquid phase an adduct between benzene (benzvalene) and the butene-2's¹⁰ has been reported by Wilzbach and Kaplan. There is even evidence that trace amounts are formed also in the gas phase.¹¹ The effect of this on triplet-state determinations is probably slight but is at present unknown. (b) Certain radicals may induce a chain isomerization of the butene-2's¹² presumably by the reversible reaction



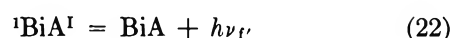
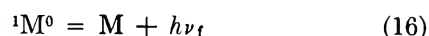
The radical on the right would have free rotation around the central carbon-carbon bond so that the reaction right to left may lead to either CB2 or TB2. On the other hand, the activation energy for (11) is such that chain reactions would probably not be important at 25°. However, some triplet-state molecules might act as free radicals. (c) It has been shown that the butene-2's are effective in producing vibrational relaxation.^{8,14} It has been shown also by Lee¹² that for certain molecules the effectiveness per collision in producing vibrational relaxation is much greater than leading to electronic energy transfer by (2) and (3). Thus, the Cundall method can never provide a measure of crossover from singlet to triplet state from the vibrational level initially formed by absorption but only from lower vibrational levels. (d) The effective cross sections for (2) and (3) are not accurately known although it is generally assumed that complete quenching is not achieved by pressures of butene less than 30–40 Torr.⁸ The value of the necessary pressure will vary with the mean life of the triplet state.

Triplet-state yields may not be obtained either by the Cundall method or by any other strictly chemical method at single vibrational levels initially formed by the absorption of radiation. Since crossover to the triplet state and fluorescence are not the only processes which can occur from excited singlet states of polyatomic molecules, the data at present leave much to be desired.

The Biacetyl Method. Upon absorption of radiation at 435.8 and at 404.7 nm as well as at 366 nm (if the total pressure is high enough to cause vibrational relaxation) biacetyl fluoresces weakly in the blue and phosphoresces much more strongly in the green.^{15,16} The ratio of green to blue emission, which is independent of incident wavelength, is 58 ± 8 .¹⁷ According to Bäckström and Sandros,¹⁵ all absorbing molecules which do not fluoresce cross over to the triplet state.

Ishikawa⁴ used biacetyl emission to estimate the triplet yield of benzene since energy transfer from triplet benzene should preferentially excite the triplet state of biacetyl.

To discuss the use of the biacetyl method for the xylenes it is best first to present a simplified mechanism which ignores the details of vibrational relaxation. This is given in reactions 12–28 inclusive which follow.



(9) G. A. Haninger and E. K. C. Lee, *J. Phys. Chem.*, **71**, 3104 (1967).

(10) K. E. Wilzbach and L. Kaplan, *J. Amer. Chem. Soc.*, **88**, 2066 (1966).

(11) (a) W. A. Noyes, Jr., and D. A. Harter, *J. Chem. Phys.*, **46**, 674 (1967); (b) A. Morikawa, S. Brownstein, and R. N. Cvetanovic, *J. Amer. Chem. Soc.*, **92**, 1471 (1970).

(12) (a) M. W. Schmidt and E. K. C. Lee, *J. Chem. Phys.*, **51**, 2024 (1969); (b) E. Anderson and G. B. Kistiakowsky, *ibid.*, **48**, 4787 (1968).

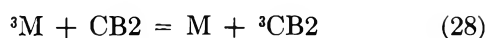
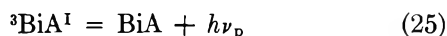
(13) S. W. Benson, "The Foundations of Chemical Kinetics," McGraw-Hill, New York, N. Y., 1960, p 296.

(14) (a) M. W. Schmidt and E. K. C. Lee, *J. Amer. Chem. Soc.*, **90**, 5919 (1968); (b) M. W. Schmidt and E. K. C. Lee, *ibid.*, **92**, 3579 (1970).

(15) H. J. L. Bäckström and K. Sandros, *Acta Chem. Scand.*, **14**, 48 (1960).

(16) G. M. Almy and P. R. Gillette, *J. Chem. Phys.*, **11**, 188 (1943), place the yield at 0.145 ± 0.03 for green emission. S. S. Collier, D. H. Slater, and J. G. Calvert, *Photochem. Photobiol.*, **7**, 737 (1968), give 0.149 ± 0.009 . A. Horowitz and J. G. Calvert, *J. Amer. Chem. Soc.*, (in press), give 0.15 ± 0.01 as the value to use.

(17) H. Okabe and W. A. Noyes, Jr., *J. Amer. Chem. Soc.*, **79**, 801 (1957).



M is the absorbing molecule, BiA is a biacetyl molecule, and CB2 is a molecule of *cis*-2-butene. The presubscripts indicate the multiplicities: super v or 0 indicates the vibrational level, the latter indicating molecules with vibrational energy equilibrated with the surroundings. Sub f and sub p indicate emission from singlet and from triplet states, respectively, and super I and II denote the first excited and the second excited states, respectively.

Collisions between ${}^1\text{M}^{\text{v}}$ and BiA are not included although there is some evidence that the ratio of (19) and (21) increases with the amount of vibrational energy in ${}^1\text{M}^{\text{v}}$.

By assumption of the steady state one can derive expressions for emission efficiencies. Let

Q_{f}^0 = emission efficiency from the singlet state of M when biacetyl = 0

Q_{f} = emission efficiency from the singlet state of M when biacetyl is present

Q_{p} = emission efficiency from the lowest excited triplet state of biacetyl (reaction 25)

The quantity desired by a triplet-state method is $\alpha = \Phi_{\text{trip}}^0$ (eq 1) and this is given by

$$\Phi_{18}^0 = k_{18}/(k_{16} + k_{17} + k_{18}) \quad (29)$$

also

$$Q_{\text{f}}^0 = k_{16}/(k_{16} + k_{17} + k_{18}) \quad (30)$$

The fluorescent yield of M in the presence of biacetyl and the triplet state yield of M in the presence of biacetyl are given, respectively, by

$$Q_{\text{f}} = k_{16}/[k_{16} + k_{17} + k_{18} + (k_{19} + k_{21})(\text{BiA})] \quad (31)$$

where (BiA) is the concentration of biacetyl and

$$\Phi_{18} = k_{18}/[k_{16} + k_{17} + k_{18} + (k_{19} + k_{21})(\text{BiA})] \quad (32)$$

Hence

$$\Phi_{18}^0/Q_{\text{f}}^0 = \frac{k_{18}}{k_{16}} = \Phi_{18}/Q_{\text{f}} \quad (33)$$

Equation 33 would be generally applicable to any triplet-state method which involves addition of a substance which destroys the singlet state from which the triplet state is formed.

With (33) in mind and with assumption of the steady state one finds

$$\Phi_{18}^0 = \left[\frac{Q_{\text{f}}^0(Q_{\text{p}})}{Q_{\text{f}}(\beta)} - \gamma\delta \left(\frac{Q_{\text{f}}^0}{Q_{\text{f}}} - 1 \right) \right] \quad (34)$$

where β is $k_{25}/(k_{25} + k_{26})$, *i.e.*, the fraction of ${}^3\text{BiA}^{\text{I}}$ molecules which emit (eq 25); $\delta = k_{23}/(k_{22} + k_{23})$, *i.e.*, the fraction of the ${}^1\text{BiA}^{\text{I}}$ molecules which cross over to ${}^3\text{BiA}^{\text{I}}$, and $\gamma = k_{21}/(k_{19} + k_{21})$.

The value of β is given by Almy and Gillette¹⁶ as 0.145 ± 0.030 . The value of δ may be determined from the work of Bäckström and Sandros,¹⁵ who state that all ${}^1\text{BiA}^{\text{I}}$ molecules which do not fluoresce in the blue (eq 22) cross over to the triplet state (eq 23) and the ratio of green to blue emission from biacetyl excited at 435.8 nm which is given by Okabe¹⁷ as 58 ± 8 . Thus, one may write

$$58 = \frac{\delta(0.145)}{1 - \delta}; \quad \delta = 0.9975 \quad (35)$$

The uncertainty in δ is hard to estimate but if one takes the limits given by the various authors for the quantities which enter into (35) the spread for δ would be 0.9965–0.9981. This uncertainty would be very minor in the second term in the brackets in (34).

The main uncertainty in (34) (aside from errors in the determination of Q_{f}^0 , Q_{f} , and Q_{p}) arises from β in the first term in the brackets and from γ unless $Q_{\text{f}}^0/Q_{\text{f}}$ is near unity.

If $\delta = 0.9975$ and reference is made to data for benzene and its quenching by biacetyl (Table I) $\delta[(Q_{\text{f}}^0/Q_{\text{f}}) - 1] = 0.0614$ when $P_{\text{BiA}} = 0.1$ Torr at 253 nm. $Q_{\text{p}}/Q_{\text{f}} = 0.61$. Therefore, $\Phi_{18}^0 = (0.18 \times 0.61/0.145 - 0.0619\gamma)$ where $Q_{\text{f}}^0 = 0.18$ at 20 Torr.¹⁸ This value in fact agrees with 0.20 given by Birks¹⁹ at 10 Torr since there is some decrease in Q_{f}^0 with increase in pressure between 10 and 20 Torr. Hence

$$\Phi_{18}^0 = 0.757 - 0.0619\gamma \quad (36)$$

Since the possible limits of γ are zero and unity, Φ_{18}^0 could be written 0.73 ± 0.03 at 253 nm. To do better than this would require an independent and unambiguous determination of γ . If reference is made to Table II and $0.73 = \Phi_{18}^0$ is accepted from the Cundall method, $\gamma = 0.44$. This figure has no real significance and the best that can be said is that it is not far from the figure found for fluorobenzene by Nakamura²⁰ by another method.

The same calculation may be made for benzene at 259 nm: $Q_{\text{p}}/Q_{\text{f}} = 0.552$, $[(Q_{\text{f}}^0/Q_{\text{f}}) - 1] = 0.0845$, $Q_{\text{f}}^0 = 0.20$, and $\Phi_{18}^0 = 0.72 \pm 0.04$, nearly the same as at 253 nm. However, a calculation of γ gives 0.37. This figure again probably has no real significance although it agrees satisfactorily with the value obtained at 253 nm.

One may draw one of two conclusions with regard to triplet yields in benzene vapor at a pressure of about

(18) W. A. Noyes, Jr., W. A. Mulac, and D. A. Harter, *J. Chem. Phys.*, **44**, 2100 (1966).

(19) J. B. Birks, "The Photophysics of Aromatic Molecules," Wiley-Interscience, New York, N. Y., 1970, p 241.

(20) K. Nakamura, *J. Chem. Phys.*, **54**, 4160 (1971).

Table I: Triplet-State Yields by the Cundall Method, $t = 25^\circ$

Substance	λ , nm	Φ_{18}^0 (Cundall)	Q_f^0	$\Phi_{18}^0 + Q_f^0$	Pressure, Torr
Benzene	253	0.73	0.18	0.91	15-20
	259	0.73	0.20	0.93	15-20
<i>o</i> -Xylene	253		0.26		
	259	0.60	0.34	0.94	5
<i>m</i> -Xylene	271	0.53	0.42	0.95	5
	248	0.47	0.04	0.51	5
	272.5	0.40	0.34	0.74	5
<i>p</i> -Xylene	248	0.43	0.22	0.65	5
	253		0.36		5
	266	0.50	0.46	0.96	5
	274	0.54	0.48	1.02	5

^a In most instances data were obtained both with *cis*-2-butene and with *trans*-2-butene and the average is used. Butene pressures were 40-50 Torr and hence caused extensive vibrational relaxation.

Table II: Quenching of Fluorescence by Biacetyl, $t = 25^\circ$

Wavelength, nm			Effective cross section, $\text{cm}^2 \times 10^{18}$
	A	B	
a. Benzene			
253	5.56	3.44	21
259	5.00	3.44	25
			Av 23
b. <i>o</i> -Xylene			
253	3.45	2.43	43
259	2.63	2.03	35
271	2.40	2.72	46
			Av 41
c. <i>m</i> -Xylene			
253	6.67	2.75	43
259	3.33	2.13	33
272.5	2.94	2.45	38
			Av 38
d. <i>p</i> -Xylene			
253	2.78	1.30	37
259	2.28	1.39	39
274	2.00	1.68	48
			Av 41

^a Radiative lifetimes² in nsec: C_6H_6 , 407; *o*-xylene, 153; *m*-xylene, 167; *p*-xylenes, 93. A and B are the constants in the equation $1/Q_f = A + BP_{\text{BIA}}$ where P_{BIA} is biacetyl pressure in Torr (see eq 31).

20 Torr at 25° . (a) Within the uncertainty in the second term in the brackets of (34) the biacetyl and the Cundall methods agree at 253 and at 259 nm if the biacetyl pressure is 0.1 Torr, that is, where a plot of Q_p vs. P_{BIA} shows a maximum.^{4a} (b) If the Cundall value

for Φ_{18}^0 is accepted, 30-40% of the collisions between $^1\text{B}_{2u}$ benzene molecules and biacetyl lead to $^1\text{BIA}^I$ and the rest to $^1\text{BIA}^{II}$. The latter do not either emit or cross over to a state which emits.

Thus there is no obvious reason to reject the biacetyl method for determination of triplet yields of benzene vapor provided it is used with a sufficiently low biacetyl pressure (*i.e.*, at the maximum of the Q_p vs. P_{BIA} plot).

It has now been shown, however, that the biacetyl method gives unacceptably high triplet-state yields for several molecules. As we indicate in a latter section, this is true of the xylenes.

Experimental Section

The data on the gas-phase fluorescences of the three xylenes have been published recently²¹ as have the isomerization yields in the liquid phase.²² The remaining data which can be obtained with presently available methods are: (1) yields of isomerization in the gas phase; (2) possibly triplet-state yields; and (3) attempts to ascertain whether isomerization comes from the singlet or from the triplet state.

A grease-free line fitted with metal valves either from Autoclave Engineering or from Hoke, Inc. was used.

Table III: Sensitized Biacetyl Emission, $P_{\text{BIA}} = 0.1$ Torr

Wavelength	Q_p	Pressure	Q_f^0
a. Benzene			
253 (25°)	0.117	15-20	0.18
259	0.121	15-20	0.20
b. <i>o</i> -Xylene			
253 (25°)	0.105	5	0.26
259	0.110	5	0.34
266		5	
271	0.127	5	0.42
266 (114°)		5	
271 (114°)		5	0.29
c. <i>m</i> -Xylene			
248 (25°)		5	0.04
253 (25°)	0.0769	5	0.15
259	0.102	5	0.30
272.5	0.115	5	0.34
d. <i>p</i> -Xylene			
248 (25°)		5	0.22
253	0.111	5	0.36
259	0.118	5	0.44
266		5	0.46
266 (114°)		5	
274 (25°)	0.132	5	0.48
274 (114°)		5	0.42

(21) W. A. Noyes, Jr., and D. A. Harter, *J. Amer. Chem. Soc.*, **91**, 7585 (1969).

(22) D. Anderson, *J. Phys. Chem.*, **74**, 1686 (1970).

Table IV: Effect of *cis*-2-Butene on Sensitized Biacetyl Emission $t = 25^\circ$ (Pressures are in Torr)

a. Benzene (19.65 Torr)					c. <i>m</i> -Xylene (7.0 Torr)							
$(P_{\text{BiA}} = 0.1; \lambda = 259 \text{ nm})$					$(P_{\text{BiA}} = 5.0; \lambda = 259 \text{ nm})$							
P_{CB2}	0	3.0	11.3	45.0	P_{CB2}	0		103.0				
Q_{p}	0.121	0.024	0.006	0.001	Q_{p}	0.032		0.025				
$(P_{\text{BiA}} = 3.00; \lambda = 259 \text{ nm})$					$(P_{\text{BiA}} = 0.1; \lambda = 272.5 \text{ nm})$							
P_{CB2}	0	1.0	10.0	50.0	P_{CB2}	0	2.0	12.0	49.0			
Q_{p}	0.045	0.049	0.026	0.011	Q_{p}	0.115	0.064	0.011	0.003			
$(P_{\text{BiA}} = 5.00; \lambda = 259 \text{ nm})$					$(P_{\text{BiA}} = 3.0; \lambda = 272.5 \text{ nm})$							
P_{CB2}	0	4.0	11.0	45.0	100.0	P_{CB2}	0	11.0	105.0			
Q_{p}	0.033	0.033	0.024	0.014	0.009	Q_{p}	0.040	0.037	0.027			
b. <i>o</i> -Xylene (5.0 Torr)					d. <i>p</i> -Xylene (6.0 Torr)							
$(P_{\text{BiA}} = 0.1; \lambda = 259 \text{ nm})$					$(P_{\text{BiA}} = 5.0; \lambda = 272.5 \text{ nm})$							
P_{CB2}	0	3.0	12.0	52.0	P_{CB2}	0		97.0				
Q_{p}	0.110	0.042	0.012	0.003	Q_{p}	0.026		0.022				
$(P_{\text{BiA}} = 3.0; \lambda = 259 \text{ nm})$					$(P_{\text{BiA}} = 0.1; \lambda = 259 \text{ nm})$							
P_{CB2}	0	11.0	52.0	98.0	P_{CB2}	0	2.0	12.0	50.0			
Q_{p}	0.053	0.047	0.028	0.028	Q_{p}	0.118	0.071	0.023	0.004			
$(P_{\text{BiA}} = 5.0; \lambda = 259 \text{ nm})$					$(P_{\text{BiA}} = 1.0; \lambda = 259 \text{ nm})$							
P_{CB2}	0			100.0	P_{CB2}	0	2.0	11.0	52.0			
Q_{p}	0.031			0.027	Q_{p}	0.090	0.085	0.063	0.034			
$(P_{\text{BiA}} = 0.1; \lambda = 271 \text{ nm})$					$(P_{\text{BiA}} = 3.0; \lambda = 259 \text{ nm})$							
P_{CB2}	0	2.0	11.0	51.0	P_{CB2}	0	2.0	11.0	51.0			
Q_{p}	0.127	0.055	0.010	0.006	Q_{p}	0.054	0.057	0.048	0.033			
$(P_{\text{BiA}} = 3.0; \lambda = 271 \text{ nm})$					$(P_{\text{BiA}} = 5.0; \lambda = 259 \text{ nm})$							
P_{CB2}	0	11.0	100.0		P_{CB2}	0	3.0	10.0	50.0			
Q_{p}	0.032	0.035	0.022		Q_{p}	0.035	0.038	0.032	0.032			
$(P_{\text{BiA}} = 5.0; \lambda = 271 \text{ nm})$					$(P_{\text{BiA}} = 0.1; \lambda = 274 \text{ nm})$							
P_{CB2}	0		99.0		P_{CB2}	0	2.0	11.0	53.0			
Q_{p}	0.025		0.026		Q_{p}	0.132	0.074	0.018	0.004			
c. <i>m</i> -Xylene (7.0 Torr)					$(P_{\text{BiA}} = 3.0; \lambda = 274 \text{ nm})$							
$(P_{\text{BiA}} = 0.1; \lambda = 259 \text{ nm})$					P_{CB2}					0	11.0	101.0
P_{CB2}	0	11.0	49		Q_{p}	0.045	0.042	0.032				
Q_{p}	0.102	0.009	0.003		$(P_{\text{BiA}} = 5.0; \lambda = 274 \text{ nm})$							
$(P_{\text{BiA}} = 3.0; \lambda = 259 \text{ nm})$					P_{CB2}					0	98.0	
P_{CB2}	0	11.0	96.0		Q_{p}	0.029		0.032				
Q_{p}	0.043	0.037	0.024									

The line was evacuated with an Eck and Krebs diffusion pump operated with silicone oil.

Light transmitted by the cell was measured by a ferrioxalate actinometer.²³ Corrections were made for absorption both by the actinometer window and by the rear window of the cell. A 935 phototube behind the cell was used to monitor the transmitted radiation and to determine the fraction of the radiation absorbed.

Since sufficient details of experimental methods have already been described^{4,21} they will not be repeated here. It should be noted that use of aliquot portions either for determination of triplet-state yields or of isomerization yields proved not to be reliable. Presumably some fractionation occurred in taking these portions so that checks were not good. The final results reported here were obtained after all precautions had been taken.

The determination of triplet state yields has been the object of much discussion^{4,5} and it is safe to conclude

that no presently available method is entirely free from criticism except, possibly, under those conditions where the methods of flash photolysis can be used.²⁴ That method is not applicable to benzene in the gas phase and probably would be of little use for most simple aromatic compounds.

Results

Triplet-State Yields. Triplet-state yields for the xylenes in the gas phase are shown in Table I. Data were obtained by using both *cis*-2-butene and *trans*-2-butene as starting materials and averaging the two results. Further details need not be given at this time.

Tables II–V present results pertinent to the application of the biacetyl method to the xylenes. Some data

(23) J. H. Baxendale and N. K. Bridge, *J. Phys. Chem.*, **59**, 783 (1955).

(24) (a) G. Porter and F. J. Wright, *Trans. Faraday Soc.*, **51**, 1205 (1955); (b) G. Porter and M. W. Windsor, *Proc. Roy. Soc., Ser. A*, **245**, 238 (1958).

Table V: Calculated and Found Values of $Q_p(P_{CB_2} > 50 \text{ Torr})$

Molecule	P_{BiA}	Wave-length, nm	P_{CB_2}	Q_p	
				Calcd	Found
Benzene	0.1	259	45	0.0003	0.001
	0.1		52	0.003	0.003
<i>o</i> -Xylene	3.0	271	98	0.030	0.028
	5.0		100	0.035	0.027
	0.1		51	0.004	0.006
	3.0		98	0.037	0.022
	5.0		100	0.037	0.026
<i>m</i> -Xylene	0.1	272.5	49	0.003	0.003
	3.0		96	0.029	0.024
	5.0		97	0.035	0.025
	0.1		49	0.003	0.003
	3.0		105	0.031	0.027
<i>p</i> -Xylene	5.0	274	97	0.035	0.022
	0.1		50	0.003	0.004
	3.0		97	0.030	0.032
	5.0		97	0.033	0.037
	0.1		53	0.004	0.004
	3.0	101	0.032	0.032	
	5.0	98	0.035	0.032	

for benzene are included for comparison. The use of these data will be given in some detail because the general usefulness of the method must be seriously questioned. The mechanism embodied in (12)–(28) will serve as the basis for presenting the results.

When P_{BiA} is 3–5 Torr or more the change in Q_p by addition of *cis*-2-butene seems to be negligible and indeed does not exceed experimental error (Table IV). This leads to the conclusion that at low (BiA) the $^3BiA^I$ arises from (24) but that at high (BiA) it arises from (21) allowed by (23). Benzene apparently is an exception.

The value of k_{24} is not known but should be about the same as ($k_{19} + k_{21}$) which can be calculated from the data in Table I since at 259 nm $1/(k_{16} + k_{17} + k_{18}) = 0.2 (407 \times 10^{-9}) \text{ sec}$ where $407 \times 10^{-9} \text{ sec}$ is the value of $1/k_{16}$.²⁵ The value of k_{27} has recently been questioned²⁶ but is certainly less than $5 \times 10^4 \text{ sec}^{-1}$.²⁷

Since k_{24} (BiA) when P_{BiA} is 0.1 Torr is about 10^6 sec^{-1} , k_{27} may be neglected. Thus, one calculates the effective cross section for (28) to be roughly $1.2 \times 10^{-16} \text{ cm}^2$ and *cis*-2-butene is about $1/20$ as effective as biacetyl in destroying the triplet state of benzene. Lee²⁸ has arrived at a somewhat similar conclusion.

A rough estimate may be made of k_{27} from data at high butene pressures. The value is not very accurate but k_{27} must be very small and can be neglected compared with k_{24} (BiA) even when $P_{BiA} = 0.1 \text{ Torr}$.

For benzene and for certain other simple aromatic molecules^{20,29} the biacetyl method for triplet yields agrees well with the Cundall method and sums of $\Phi_{trip}^0 + Q_f^0$ are acceptably less than unity. The situation is not the same for the xylenes as the following brief summary based on data in Tables I, III, and IV

will show: (a) *o*-xylene, 253 nm $\Phi_{18}^0 = 0.74 \pm 0.04$; $Q_f^0 + \Phi_{18}^0 = 1.00$, 259 nm $\Phi_{18}^0 = 0.77 \pm 0.03$; $Q_f^0 + \Phi_{18}^0 = 1.11$, 271 nm $\Phi_{18}^0 = 0.92 \pm 0.06$; $Q_f^0 + \Phi_{18}^0 = 1.34$; (b) *m*-xylene, 253 nm $\Phi_{18}^0 = 0.55 \pm 0.04$; $\Phi_{18}^0 + Q_f^0 = 0.70$, 259 nm $\Phi_{18}^0 = 0.72 \pm 0.03$; $\Phi_{18}^0 + Q_f^0 = 1.02$, 272.5 nm $\Phi_{18}^0 = 0.86$; $\Phi_{18}^0 + Q_f^0 = 1.20$; (c) *p*-xylene, 253 nm, $\Phi_{18}^0 = 0.78 \pm 0.02$; $\Phi_{18}^0 + Q_f^0 = 1.14$, 259 nm, $\Phi_{18}^0 = 0.86 \pm 0.03$; $\Phi_{18}^0 + Q_f^0 = 1.30$, 274 nm, $\Phi_{18}^0 = 0.99 \pm 0.04$; $\Phi_{18}^0 + Q_f^0 = 1.47$.

Reference to the data in Table IV permits certain conclusions to be drawn. The second term in the brackets of (34) is due to (21), (23), and (25) and may be estimated if γ and δ are known. The values of γ may be estimated in several ways including from the data in Tables II, III, and IV. A value of 0.30 is used as approximately correct for the xylenes. The value of δ has been discussed and may be taken as 0.9975 with a small uncertainty.

The following assumptions are made: (a) reaction 28 removes 3M completely if P_{CB_2} is 50 Torr or greater; (b) at such pressures of CB_2 the value of Q_p (Table IV) is based on $^3BiA^I$ arising from (21) followed by (23) and (25), *i.e.*

$$Q_p(P_{CB_2} > 50) = \left(1 - \frac{Q_f}{Q_f^0}\right)(\gamma)(\beta)(\delta) \quad (37)$$

$$= \left(1 - \frac{Q_f}{Q_f^0}\right)(0.3)(0.145)(0.9975) \quad (38)$$

$[1 - (Q_f/Q_f^0)]$ can be calculated from the data in Table I and $Q_p(P_{CB_2} > 50)$ is compared with the data in Table V.

The value of $\beta = 0.145$ satisfies the calculations just made and the upper limit of 0.175 given by Almy and Gillette would be barely acceptable. Thus, (21) seems to lead to $^3BiA^I$ analogous to that formed by direct absorption of photons by biacetyl. The triplet molecules formed from biacetyl in this way are normal. Since we are dealing with a second-order correction in (24), results are not very sensitive to small variations in β , γ , and δ .

Since corrections based on Table V never exceed 0.24 and since values of Φ_{18}^0 must in some instances be as much as 0.40 to 0.50 too high, the major difficulty must lie with the first term in the brackets in (34).

Ishikawa^{4a} found emission spectra in the green of biacetyl excited by direct absorption at 435.8 nm and excited by energy transfer from benzene to agree both as to relative peak height and as to wavelengths.

(25) I. B. Berlan, "Handbook of Fluorescence Spectra of Aromatic Molecules," Academic Press, New York, N. Y., 1965, p 42.

(26) C. S. Burton and H. E. Hunziker, Fifth International Conference on Photochemistry, Yorktown Heights, N. Y., Sept 1969.

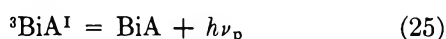
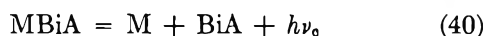
(27) C. S. Parmenter and M. W. Schuyler, ref 5b, p 92.

(28) E. K. C. Lee, H. O. Denschlag, and G. A. Haninger, Jr., *J. Chem. Phys.*, **48**, 4547 (1968).

(29) See M. Magat, N. Ivanoff, F. Lahmani, and M. P. Pileni, ref 5b, p 212.

Similar data for xylene-biacetyl mixtures have been obtained with generally similar results.

One is forced to one of the following conclusions. (a) The emissivity of ${}^3\text{BiA}^1$ depends on its method of formation. If (24) is merely triplet-state energy transfer there is no obvious reason for accepting this suggestion. (b) The emitter may be an aromatic-biacetyl complex and the following steps may be suggested



If ΔH for (39) is about -26 kcal, radiation from (40) could resemble closely that from (25).

If Q_p of (34) is $Q_{40} + Q_{25}$

$$\Phi_{18}^0 = \left(\frac{Q_f^0}{Q_f} \right) \left(\frac{Q_p - \left(1 - \frac{Q_f}{Q_f^0} \right) (0.145)(0.3)}{\epsilon(\beta - 1) + 1} \right) \quad (42)$$

where $\epsilon = k_{41}/(k_{40} + k_{41})$, $\gamma = 0.3$ and $\delta \sim 1$.

Excimer formation has been extensively discussed³⁰ and so has exciplex formation. Emission may in fact be either by (40) or by (25) and the wavelength of the emission may correspond closely to that of (25).

With the xylenes, the high triplet-state yields obtained by (34) could not be explained by exciplex formation from the singlet state ${}^1\text{M}^0$ followed by crossover to the triplet state.

From the data in Table III and the Cundall method yields in Table II one may calculate ϵ as well as $\epsilon(\beta - 1) + 1$. The latter replaces $\beta = 0.145$ in (34). The results are as follows: (a) *o*-xylene, $\epsilon = 0.89$, denominator = 0.24; (b) *m*-xylene, $\epsilon = 0.81$, denominator = 0.30; (c) *p*-xylene, $\epsilon = 0.81$, denominator = 0.27. These results are all for absorption at the long wave peaks of 271, 272.5, and 274 nm, respectively.

Thus, the modified mechanism may be used somewhat empirically to explain the results but further work must be done.

Vibrational Relaxation. It has long been recognized that collisional processes by removing vibrational energy may inhibit reactions such as dissociation and isomerization.^{31,32} Vapors of the xylenes exposed to radiation at wavelengths shorter than the O-O bands show this behavior in several different ways: (a) isomerization quantum yields diminish as pressure is increased; (b) isomerization yields in the liquid phase are always very low;²² (c) quantum yields of fluorescence increase with increase in pressure at short wavelengths.

The preceding paragraphs have ignored (13)-(15) in the mechanism. The reactions which involve biacetyl

and *cis*-2-butene will now be omitted: (19) to (26) inclusive and (28). Singlet emission is assumed to come solely from (16). Presumably this is not true at low pressures^{4d} as shown by Parmenter, *et al.*,^{5b} at least for benzene. Down to the pressures used in the present study (minimum about 1 Torr) no significant change with pressure of the intensity *vs.* wavelength plot could be observed. A more complete study of this matter should be made.

With restrictions listed, the following relationships are obtained

$$Q_f = \left(\frac{k_{15} + k_{14}(P)}{k_{13} + k_{14}(P) + k_{15}} \right) \left(\frac{k_{16}}{k_{16} + k_{17} + k_{18}} \right) \quad (43)$$

$$\frac{Q_f^0}{Q_f} = 1 + \frac{1}{\frac{k_{15}}{k_{13}} + \frac{k_{14}(P)}{k_{13}}} \quad (44)$$

Thus, by extrapolation to $(P) = 0$ it is possible to estimate k_{15}/k_{13} although the accuracy will be low and the treatment is somewhat empirical.

It may be noted in passing that benzene does not show a marked variation of Q_f with total pressure as do the xylenes and toluene. As Kistakowsky and Parmenter³³ first showed, Q_f decreases with increase in pressure up to perhaps 10 to 15 Torr and then changes very little with further increase in pressure.

By use of the values of Table VI, it is possible to estimate the pressures at which first-order vibrational relaxation and second-order vibrational relaxation by butane become equal. The accuracy of these calculations is poor but there is some tendency for this pressure to increase with increase in incident wavelength. Very rough figures are as follows: (a) *o*-xylene, 25 Torr (240 nm) to 50 Torr (259 nm); (b) *m*-xylene, 20 Torr (240 nm) to 50 Torr (253 nm); (c) *p*-xylene, 25 Torr (240 nm) to 50 Torr (259 nm). Thus, there is little variation with wavelength and not surprisingly more

Table VI: Values of k_{15}/k_{13} ^a

	Wavelength, nm			
	240	248	253	259
<i>o</i> -Xylene	0.04	0.65	3	18
<i>m</i> -Xylene	0.03	0.15	1	
<i>p</i> -Xylene	0.14	0.8	3	7

^a Based on data from W. A. Noyes, Jr., and D. A. Harter, *J. Amer. Chem. Soc.*, **91**, 7586 (1969).

(30) J. B. Birks, "The Photophysics of Aromatic Molecules," Wiley-Interscience, New York, N. Y., 1970, pp 343 and 436.

(31) F. C. Henriques and W. A. Noyes, Jr., *J. Amer. Chem. Soc.*, **62**, 1038 (1940).

(32) G. M. Almy, H. Q. Fuller, and G. D. Kinzer, *J. Chem. Phys.*, **8**, 37 (1940).

(33) G. B. Kistakowsky and C. S. Parmenter, *ibid.*, **42**, 2942 (1965).

collisions are required to attain vibrational equilibrium as equilibrium is approached.

Another interesting point arises from these calculations. Reaction 13 includes all first-order processes which destroy vibrationally rich excited singlet-state molecules except vibrational relaxation. These processes may include (a) dissociation; (b) isomerization; (c) radiation; and (d) crossover to the triplet state.

One concludes from these calculations that the processes included under (13) are very rapid at high vibrational levels of 1M but that they are very slow at low vibrational levels.

Dissociation of xylenes has not been observed at the wavelengths used. Isomerization will be discussed later but it has a low quantum yield. There are no adequate data on the forms of intensity of fluorescence *vs.* wavelength plots but resonance radiation is not obvious. More work needs to be done on this point.

Isomerization. Isomerization of substituted aromatic compounds by photochemical means has been observed by many investigators but most extensively by Wilzbach and Kaplan and their coworkers.² Much of this work has been performed in the liquid phase where yields are low and where variations of yields with wavelength have not been reported.⁹ Such data as are available for gas-phase photolyses tend to show that yields generally increase as wavelengths of incident radiation decrease, increase with increase in temperature, and at short wavelengths decrease with increase in pressure.

By reference to the discussion of Table VII one can estimate the mean lives of excited singlet molecules produced at various wavelengths. At 240 nm the lives are of the order of magnitude of a few tenths of a nanosecond and at 248 nm they are a few nanoseconds. Radiative lifetimes²⁶ vary from 93 nsec for *p*-xylene to 153 for ortho and 176 for meta. Thus, other processes have become so much more rapid than radiation below 248 nm that fluorescent efficiencies should be nearly zero as they are.

Several processes may increase in importance at short wavelengths and isomerization must be included in the

list. Benzvalene has been isolated by Wilzbach and Kaplan² and the Dewar forms of benzene³⁴ and of hexafluorobenzene have been obtained.^{3a, 35}

The isomers of benzene have been listed. Indirect evidence for such molecules made from substituted benzenes exists but the pure compounds have rarely if ever been isolated. In addition, Migirdicyan³⁶ has shown that hexatriene derivatives may be formed by exposing benzene in glassy matrices to radiation in the presence of certain molecules.

The predominant intermediates for isomerization of the xylenes are almost certainly dimethyl benzvalenes² and perhaps dimethyl prismanes.²⁴ Dewar benzene should not lead to isomerization. Dimethyl prismane might be the intermediate for the conversion of *o*-xylene to either *m*-xylene or *p*-xylene but dimethyl benzvalene would only lead to *m*-xylene.

Table VIII shows isomerization quantum yields for the xylenes in the gas phase at several wavelengths and pressures. It must be emphasized that these yields are not the primary isomer yields which must be used for (13), (17), and possibly (27) to obtain energy balances. This point has been discussed by several authors^{5b} and will be mentioned only briefly. Probably the most complete discussion of this point is in the papers of Kaplan, Wilzbach, *et al.*^{2b}

Exact heats of formation of these various isomers are not known but rough estimates may be made from bond energies, etc.³⁷ Formation of any of these isomers would be endothermic from the parent compounds to the extent of about 60 kcal/mol or more but all of them could be formed exothermally from either excited singlet or excited triplet states. They are, therefore, thermodynamically unstable with respect to the aromatic compounds from which they are derived.³⁸

These unstable isomers, from which the original and new xylenes may be formed, may resume their aromatic characters by one or more of the following methods: (a) thermal rearrangements either in the gas phase or on the walls; (b) photochemical reaction following direct absorption of photons since they all absorb in the same general region as aromatic compounds; (c) photochemical reactions sensitized by the parent aromatic compounds. Any of these processes would make the net isomer yields lower than the primary yield of formation of the intermediates. Photochemical processes might mean that the intermediate yield could be as much as four times the net yield. This assumes that

Table VII: Pressures Required for Rates of (13) and (14) to Be Approximately Equal^a

	Wavelength, nm			
	240	248	253	259
<i>o</i> -Xylene	300 Torr	35 Torr	3 Torr	0?
<i>m</i> -Xylene	450	150	58	?
<i>p</i> -Xylene	160	70	2	?

^a At 271–275 nm increase in pressure causes some decrease in Q_f as though vibrational relaxation causes some "warming" rather than "cooling" of excited molecules. At 259 nm enhancement of Q_f with increase in pressure is very small and the 3 Torr pressure calculated in the fourth column could also mean some "warming" of excited singlet molecules by relaxation.

(34) E. E. van Tamelen and S. P. Pappas, *J. Amer. Chem. Soc.*, **84**, 3789 (1962).

(35) G. P. Semeluk and R. D. S. Stevens, *Chem. Commun.*, **24**, 1720 (1970).

(36) E. Migirdicyan, *J. Chim. Phys. Physicochim. Biol.*, **63**, 520 (1966).

(37) S. W. Benson, "The Foundations of Chemical Kinetics," McGraw-Hill, New York, N. Y., 1960, p 662 ff.

(38) D. Roscher, private communication.

Table VIII: Isomerization Yields of the Xylenesⁱ

A. <i>o</i> -Xylene → <i>m</i> -Xylene				
Wavelength, nm	26° (1 Torr)	26° (5 Torr)	114° (1 Torr)	114° (5 Torr)
230		0.011		0.012
240	0.019	0.012	0.019	0.012
244	0.025		0.018	
248	0.025	0.011	0.018	0.015
248	0.010 ^h		0.019 ^h	
248	0.012 ^a	0.002 ^b	0.019 ^e	0.016 ^o
248	0.009 ^c	0.006 ^d	0.018 ^f	
248	0.010 ^e			
252		0.009		
253	0.017			
254			0.020	0.017
258	0.015	0.004		
259			0.010	
260				0.009
263	0.002	0.003	0.004	
265		0.003		0.005
271	0.000	0.002	0.002	0.004

B. <i>m</i> -Xylene → <i>p</i> -Xylene and <i>m</i> -Xylene → <i>o</i> -Xylene								
Wavelength, nm	26° (1 Torr)		26° (7 Torr)		114° (1 Torr)		114° (7 Torr)	
	Φ _(ortho)	Φ _(para)	Φ _(ortho)	Φ _(para)	Φ _(ortho)	Φ _(para)	Φ _(ortho)	Φ _(para)
240	0.002	0.039	0.000	0.042	0.006	0.032	0.001	0.038
244		0.035			0.007	0.038		
248	0.002	0.030	0.003	0.031	0.013	0.041	0.004	0.033
248	0.000 ^j	0.033 ^j	0.002 ^m	0.021 ^m	0.007 ⁿ	0.051 ⁿ	0.005 ^o	0.039 ^o
248		0.037 ^p			0.015 ^p	0.044 ^p		
248	0.002 ^k	0.031 ^k						
248	0.002 ^q	0.049 ^q						
254	0.002	0.043			0.007	0.036		
259	0.000	0.017	0.000	0.016				
259	0.000 ^l	0.000 ^l						
265	0.002	0.003	0.004	0.003	0.002	0.009	0.001	0.019
272.5	0.003	0.006	0.000	0.004	0.004	0.003	0.000	0.013

C. <i>p</i> -Xylene → <i>m</i> -Xylene				
Wavelength, nm	26° (1 Torr)	26° (7 Torr)	114° (1 Torr)	114° (7 Torr)
240	0.001		0.004	
248	0.002	0.002	0.007	0.003
248	0.000 ^r		0.001 ^t	
248	0.002 ^s		0.005 ^u	
248			0.008 ^v	
266	0.000		0.001	0.000
274	0.000	0.000	0.000	0.000

^a + 47 Torr *n*-C₄H₁₀. ^b + 50 Torr *cis*-butene-2. ^c + 283 Torr *n*-C₄H₁₀. ^d + 332 Torr *n*-C₄H₁₀. ^e + 50 Torr *n*-C₄H₁₀. ^f + 351 Torr *n*-C₄H₁₀. ^g + 270 Torr *n*-C₄H₁₀. ^h + 9 Torr C₆H₁₂. ⁱ Φ_(para) = 0 under all conditions. ^j + 238 Torr *n*-C₄H₁₀. ^k + 120 Torr xenon. ^l + 296 Torr *n*-C₄H₁₀. ^m + 310 Torr *n*-C₄H₁₀. ⁿ + 348 Torr *n*-C₄H₁₀. ^o + 250 Torr *n*-C₄H₁₀. ^p + 9 Torr C₆H₁₂. ^q + 70 Torr C₆H₆. ^r + 300 Torr *n*-C₄H₁₀. ^s + 90 Torr xenon. ^t + 240 Torr *n*-C₄H₁₀. ^u + 92 Torr xenon. ^v + 9 Torr C₆H₁₂. Φ_(ortho) = 0 under all conditions.

return to the original aromatic compound has an equal probability to formation of an isomer.

The highest isomer yields in Table VIII are generally found at 248 nm and they never exceed about 0.05. Thus, after reasonable allowance for reverse reactions the primary isomerization yields probably never exceed 0.2–0.3. Since yields of fluorescence at 248 nm are 0.3–0.5 at pressures of several hundred Torr and vary

from 0.04 to 0.22 at low pressures, $Q_f + \Phi_{\text{isom}}$ is well below unity at 240 and at 248 nm. Triplet yields by the Cundall method are accompanied by vibrational relaxation so that a complete accounting of the absorbed energy is impossible at these short wavelengths.

It is perhaps of interest that isomerization yields for *m*-xylene are higher than for the other xylenes and fluorescent yields are lowest. Conversely, *p*-xylene

shows the lowest isomerization yields and the highest fluorescent yields. Indeed isomerization yields for *p*-xylene differ from zero by little more than the experimental error.

As shown by Anderson,²² the reactions which produce isomerization show only a small temperature variation, *i.e.*, activation energies of 4–5 kcal/mol.

Fluorescence Quenching by Oxygen. It has already been shown by Ishikawa^{4a} that the effectiveness of oxygen in quenching the fluorescence of benzene vapor is comparable to that of biacetyl. Nevertheless the processes must in general be different since biacetyl undergoes some sensitized dissociation as well as some excitation to a state which can emit radiation. Dissociation of oxygen by benzene sensitization is energetically impossible but some peroxide formation is indicated¹⁸ and the possibility of formation of mucic aldehyde exists.³⁹ The main quenching reaction must result in ¹Δ oxygen molecules.⁴⁰

Reactions 45–46 may be added to the mechanism



Both reactions appear to be necessary since the effective cross sections for quenching vary with incident wavelength and with pressure of inert gas (butane).

Table IX summarizes the data obtained on quenching of xylene fluorescence by oxygen. $Q_r^0 = 0.18$ for benzene at 253 nm at a pressure of about 20 Torr was used as a standard.

Table IX: Quenching of Xylene Fluorescences by Oxygen (25°), $P_{O_2} \sim 3$ Torr

Xylene	Wave-length, nm	$k_{16} \times 10^{10}$	Effective cross section, ^a $cm^2 \times 10^{16}$
Ortho	248	5.9	37 ± 5
	253	4.1	26 ± 3
	259	2.4	15 ± 2
	271	2.1	13 ± 2
Meta	248 ^b		
	253	3.0	19 ± 3
	259	2.1	13 ± 4
	272.5	1.6	9 ± 3
Para	248	4.9	31 ± 3
	253	4.1	26 ± 4
	259	2.2	14 ± 3
	274	1.9	12 ± 1

^a The effective cross sections are calculated from $k_{16} = \sigma^2 (1.59 \times 10^6)$. ^b The fluorescence of *m*-xylene is so weak at 248 nm that the results would have no significance. Oxygen seems to be a somewhat less efficient quencher than does biacetyl.

σ^2 with decrease in wavelength is interpreted to mean that excited singlet molecules at high vibrational levels interact more strongly with oxygen than do those at low vibrational levels, the addition of butane should markedly lower the effective cross section for quenching of xylene fluorescence by oxygen. This is, in fact, the case as the following summary shows: pressure of butane about 80 Torr, pressure of oxygen about 2 Torr, pressure of xylene about 4 Torr. Effective cross sections for quenching by oxygen are: (a) *o*-xylene 18 (248); 15 (253); 12 (259); 18 (271); (b) *m*-xylene 19 (248); 9 (253); 9 (259); 8 (272.5); (c) *p*-xylene 15 (248); 23 (253); 15 (259); 15 (274).

Butane addition has the expected effect and it must be concluded that vibrationally excited singlet xylene molecules react more rapidly with oxygen than do those with vibrational energy equilibrated with the surroundings.

Discussion

A fairly satisfactory mechanism for describing the photochemistry of the xylenes has been given. There are several points not susceptible of proof with presently available data and some of the most needed data will be very difficult to obtain. Some points may be emphasized.

(a) *Primary Yields of Isomers.* Since these isomers are not stable, the amounts formed are difficult to determine. These yields are necessary if one wishes to account for the fates of absorbing molecules.

(b) *Yields of Triplet States, Preferably Following Absorption to Give Single Vibrational Levels of Excited States.* All methods presently available require addition of monitoring molecules which cause vibrational relaxation and other changes in the absorbing system.

(c) *Details of Energy Transfer, for Example, from Excited Singlet and Triplet Molecules to Molecules Such as Biacetyl.* Emission spectra must be analyzed carefully to ascertain whether the emitting species are the same as those produced by direct absorption by the biacetyl.

(d) *Fluorescent Yields from Single Vibrational Levels of Absorbing Molecules.* Much progress has been made along these lines by Parmenter²⁷ and by Ware.⁴¹ Difficulties are much greater for substituted aromatics.

It is significant that vibrational relaxation by collision does not compete successfully with first-order processes for destruction of excited singlet molecules at short incident wavelengths. Singlet molecules formed at these wavelengths must have very short mean lifetimes.

Since the data show triplet-state yields to be highest at low vibrational levels, the process or processes responsible for these short mean lives at high vibrational

It has already been shown¹¹ that addition of butane at short wavelengths enhances fluorescence by causing vibrational relaxation. If the apparent increase in

(39) G. Stein, private communication.

(40) K. Gollnick, *Advan. Photochem.*, **6**, 1 (1968).

(41) W. R. Ware, *Chem. Phys. Lett.*, **2**, 256 (1968).

levels must be mainly isomerization or possibly dissociation. One is forced to conclude that primary yields of isomers must be manifold greater than the yields shown in Table VIII. Even simple assumptions account easily for factors of 3 to 5 but these are not adequate in cases where fluorescent and presumably also triplet-state yields approach zero.

One of the most interesting questions raised by the present work relates to the ratio of rates of (19) and (21). In the case of benzene, Ishikawa^{4a} showed that excitation at 253.7 nm gave biacetyl decomposition corresponding to somewhat longer wavelengths but that no evidence for formation of ¹BiA^I could be found. Recent work by Nakamura²⁰ and this research indicate that perhaps 30–40% of the collisions of ¹M⁰ with biacetyl lead to ¹BiA^I and the rest to ¹BiA^{II}. The theory of this phenomenon is not evident.

Since emission resulting from collisions between triplet xylene molecules and biacetyl is too intense to give reasonable triplet-state yields at some incident wavelengths, it is necessary to conclude either that the

emitter is a complex or that for some reason the triplet biacetyl is formed in a state of higher emissivity than is produced by crossover from ¹BiA^I. This interesting phenomenon needs a careful study.

Finally the quenching of singlet xylene emission by oxygen proceeds with a relatively high cross section, a phenomenon observed previously for benzene.^{9,42} This matter is under investigation in other laboratories and will not be discussed in detail here. Presumably, singlet oxygen molecules are formed by collision between excited singlet aromatics and ground-state triplet oxygen.⁴²

Acknowledgment. The authors wish to thank Drs. K. F. Wilzbach and L. Kaplan for helpful discussions as well as Dr. K. Salisbury and T. Brewer of the University of Texas at Austin. Much related work mentioned in this article was performed at that university under a grant from the Robert A. Welch Foundation and is referred to often in the article.

(42) R. J. Cvetanovic, *J. Chem. Phys.*, **52**, 3237 (1970).

An Investigation of Radicals Produced in the Photolysis of Thiosulfate Solutions by Electron Spin Resonance¹

by D. Behar* and Richard W. Fessenden

Radiation Research Laboratories and Department of Chemistry, Mellon Institute of Science, Carnegie-Mellon University, Pittsburgh, Pennsylvania 15213 (Received April 5, 1971)

Publication costs assisted by Carnegie-Mellon University and the U. S. Atomic Energy Commission

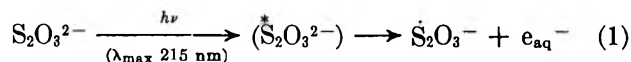
The photochemistry of alkaline, aqueous thiosulfate solutions has been studied in a flow system. The primary radicals produced were trapped with nitromethane and the resulting adducts were detected by esr. Three different intermediates were identified as a result of two different photolytic processes. The radicals \dot{S}^- and $\dot{S}O_3^-$ are produced as a result of excitation of the $n-\pi^*$ band involving the electrons on the sulfur atom: $S_2O_3^{2-} \xrightarrow{h\nu} \dot{S}^- + \dot{S}O_3^-$ (λ_{max} 240 nm) and the solvated electron is produced by excitation of the charge transfer to solvent band: $S_2O_3^{2-} \xrightarrow{h\nu} \dot{S}O_3^- + e_{aq}^-$ (λ_{max} 215 nm).

The ultraviolet absorption spectrum of thiosulfate in solution has been extensively studied by Sperling and Treinin.² In the region 190–300 nm the spectrum was found to consist of three bands labeled A, B, and C.² Band A, peaking at about 240 nm, was assigned to an $n \rightarrow \pi^*$ transition involving the nonbonding electrons on the sulfur atom. Band B, peaking at about 215 nm, was assigned to a charge transfer to solvent transition (ctts) and band C, peaking in the vacuum uv, was assigned to another $n \rightarrow \pi^*$ transition involving the non-

bonding electrons on the oxygen atoms. Less attention was paid to the photochemistry of the thiosulfate anion and to the correlation between the electron absorption spectra and the photochemical products. Sperling and Treinin measured a quantum yield of 0.08 for the solvated electron produced by the decomposition of the ctts state

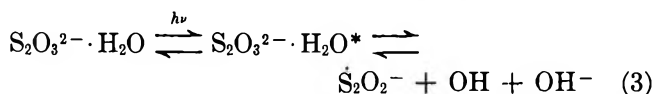
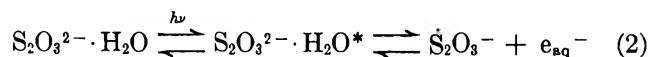
(1) Supported in part by the U. S. Atomic Energy Commission.

(2) R. Sperling and A. Treinin, *J. Phys. Chem.*, **68**, 897 (1964).



In addition, sulfur, sulfite, and H_2S were identified² but no explanation was given for the origin of these products.

In a recent paper of Dogliotti and Hayon³ the photochemistry of the thiosulfate anion was studied using the flash photolysis technique. To account for their results they proposed two sulfur-containing transients resulting from two different photolytic processes



Reaction 2 (the same as 1 above) was assumed to occur at wavelengths greater than 210 nm where band B, the cts band, is excited while reaction 3 was assumed to occur at wavelengths below 215 resulting from the excitation of band C (the $n \rightarrow \pi^*$ transition involving the electrons on the oxygen atom). The two absorption transients found by them have maxima at 280 and 380 nm and were assigned to the proposed $\dot{\text{S}}_2\text{O}_2^-$ radical and the $\dot{\text{S}}_2\text{O}_3^-$ radical, respectively. No mention was made of the results of excitation of band A peaking at 240 nm. Since these authors did not use filters to cut off the light above 240 nm we believe that they must have excited band A, and as a result should have produced some additional radicals from this excitation. The work reported here resulted from a further study of the photochemistry of thiosulfate using nitromethane as a trap for the primary radicals and esr for detection of the adduct radicals produced.

Experimental Section

The photolysis was performed under flow conditions with a flow rate of about 30 ml/min. The esr spectra were measured with an X-band spectrometer constructed in these laboratories, the details of which have been described elsewhere.⁴ The irradiation cell of fused silica (0.5 mm light path, 1 cm width, and 4 cm length) was mounted in a Varian V-4531 multipurpose cavity. A Hanovia 1-kW high-pressure mercury-xenon lamp (977-B1) was used for photolysis. The light output of concern here consists mainly of the pressure-broadened 254-nm mercury line.

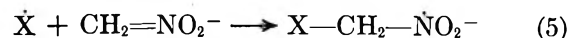
Fisher certified grade sodium thiosulfate and Fisher spectrograde nitromethane were used without further purification. The pH was adjusted with Baker potassium hydroxide; no buffers were used. Solutions were bubbled before and during irradiation with Airco nitrogen or Baker nitrous oxide without purification. Solutions were prepared with doubly distilled water.

Results and Discussion

Nitromethane exists in aqueous solution in equilibrium with the aci-anion form ($\text{p}K = 10.7$)⁵

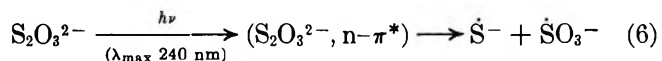


In the course of *in situ* radiolysis experiments⁶ it was found that this basic form is a good scavenger for many inorganic radicals because in most cases an addition reaction to the double bond takes place.

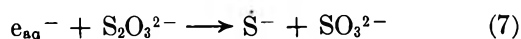


The resulting $\text{X}-\text{CH}_2-\dot{\text{N}}\text{O}_2^-$ radicals are generally long-lived and their magnetic parameters are governed to some extent by the radical $\dot{\text{X}}$. The variation in parameters is sufficient that a large number of different adducts can be distinguished.^{6,7} The radicals found in the present work were identified by comparison of their spectral parameters with those found for radiolytically produced radicals in related chemical systems.⁶

On photolyzing N_2 -saturated $10^{-2} M$ thiosulfate solutions to which $5 \times 10^{-4} M$ nitromethane had been added (pH ~ 13) two radical adducts to the nitromethane were detected. The spectrum of each was composed of nine lines with an intensity distribution of 1:2:1:1:2:1:1:2:1 as would be expected for the radical $\text{XCH}_2\dot{\text{N}}\text{O}_2^-$ produced in reaction 5 if the nuclei in X did not produce further hyperfine splitting. (The nine lines result from splitting by one ^{14}N nucleus and two equivalent protons.) Each spectrum can be described by two coupling constants: $a_{\text{N}} = 22.21 \text{ G}$, $a_{\text{H}} = 7.51 \text{ G}$ for the first and $a_{\text{N}} = 24.34 \text{ G}$, $a_{\text{H}} = 6.64 \text{ G}$ for the second. Spectra with the same coupling constants and g factors (within the experimental accuracy) were also produced in experiments involving electron irradiation of, respectively, Na_2SO_3 and Na_2S in alkaline nitromethane solutions saturated with N_2O .⁶ In these latter experiments the OH radical reacts with SO_3^{2-} or S^{2-} to produce the radicals $\dot{\text{S}}\text{O}_3^-$ or $\dot{\text{S}}^-$ which then react with $\text{CH}_2=\text{NO}_2^-$ according to reaction 5 to form the anion radicals $-\text{O}_3\text{SCH}_2\dot{\text{N}}\text{O}_2^-$ or $-\text{SCH}_2\dot{\text{N}}\text{O}_2^-$. The formation of these two radicals in the photolysis of solutions of $\text{Na}_2\text{S}_2\text{O}_3$ containing nitromethane implies the initial formation of the radicals $\dot{\text{S}}\text{O}_3^-$ and $\dot{\text{S}}^-$. The most obvious way of forming the radicals $\dot{\text{S}}^-$ and $\dot{\text{S}}\text{O}_3^-$ is by the direct split



However, because e_{aq}^- is also being formed by excitation in the cts band B, see below, it is necessary to eliminate the reaction



as the source of $\dot{\text{S}}^-$. Experiments were performed

(3) L. Dogliotti and E. Hayon, *J. Phys. Chem.*, **72**, 1800 (1968).

(4) R. W. Fessenden, *J. Chem. Phys.*, **48**, 3725 (1968).

(5) D. Turnbull and S. H. Aaron, *J. Amer. Chem. Soc.*, **65**, 212 (1943); G. W. Wheland in "Advanced Organic Chemistry," 2nd ed, Wiley, New York, N. Y., 1954, p 629.

(6) D. Behar and R. W. Fessenden, to be published.

(7) K. Eiben and R. W. Fessenden, *J. Phys. Chem.*, **72**, 3387 (1968).

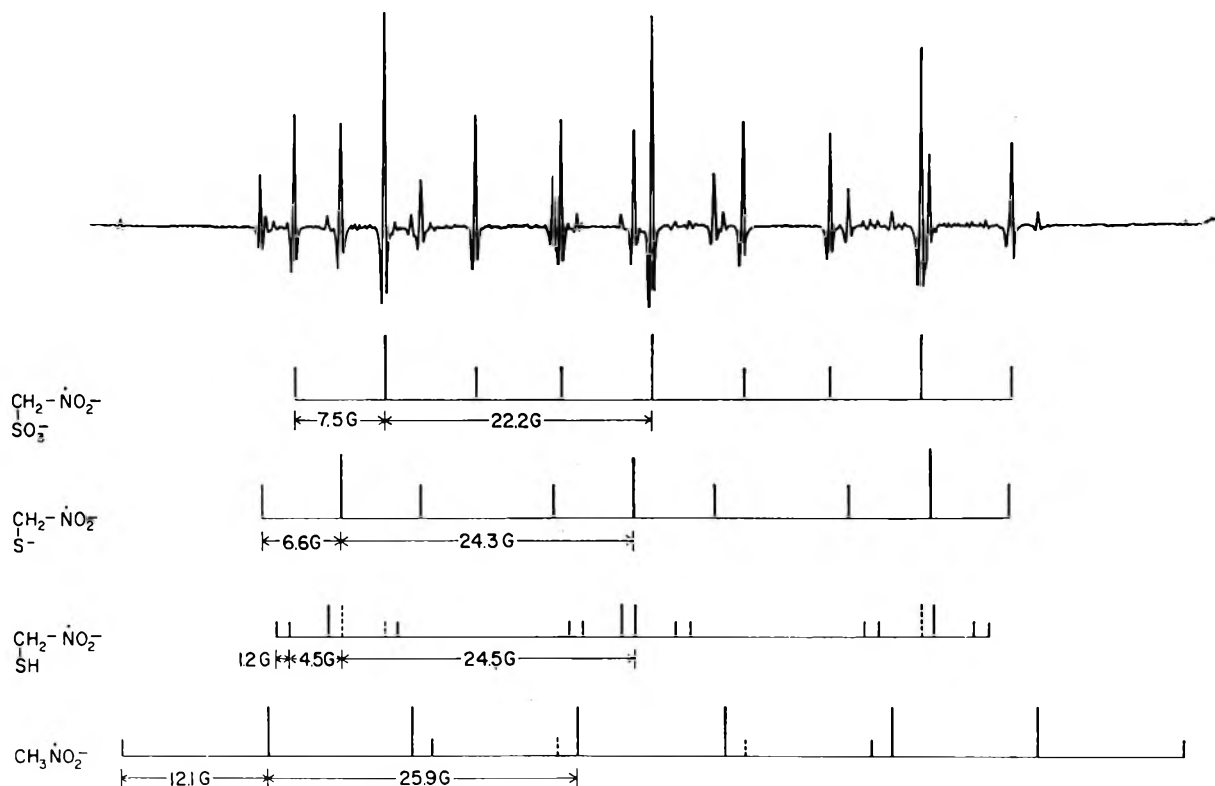
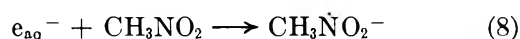


Figure 1. Second derivative esr spectrum obtained during photolysis of N_2 -saturated $10^{-2} M$ thiosulfate solution containing $2 \times 10^{-3} M$ nitromethane at pH 9.5. Spectra of four radicals are indicated. Two lines of the $CH_3\dot{N}O_2^-$ spectrum and three lines of the $HS-CH_2-\dot{N}O_2^-$ spectrum are masked by other lines. These were drawn as broken lines in the stick diagram.

with N_2O present and no effect on the intensity of the two spectra was found. (Any e_{aq}^- formed would be scavenged and converted to OH by $e_{aq}^- + N_2O \xrightarrow{H_2O} OH + N_2 + OH^-$.) Therefore, reaction 7 cannot be the source of \dot{S}^- . Accordingly, we believe that both \dot{S}^- and $\dot{S}O_3^-$ arise in reaction 6 and assign the excitation, as shown, to band A involving the $n \rightarrow \pi^*$ transition of the nonbonding electrons of the sulfur atom. Reaction 6 may explain the results of Sperling and Treinin where sulfur, H_2S , and sulfite were found in the photolysis of thiosulfate.²

Since the cttS band B of the thiosulfate overlaps the $n-\pi^*$ band A² an attempt was made to find conditions where some excitation of band B also can take place which would result in the formation of e_{aq}^- and $\dot{S}_2O_3^-$. From the radiolysis experiments with thiosulfate⁶ it was known that only low steady-state concentrations of the $\dot{S}_2O_3^-$ adduct to nitromethane could be produced (either the rate of formation is low or the rate of disappearance is high) and that consequently this adduct would not be detected in the photolytic system because its stationary concentration would be too small. The other radical of this pair, e_{aq}^- , should, however, be detectable as the nitromethane anion radical $CH_3\dot{N}O_2^-$ ⁷ if electrons are formed



Since both OH^- and the basic form of nitromethane ab-

sorb strongly in the uv^{8-10} a significant portion of the short wavelength light was absorbed by them at pH 13. Under these conditions excitation of the cttS band is very weak and no $CH_3\dot{N}O_2^-$ could be observed.

Upon decreasing the alkalinity to pH 9.5 the concentration of nitromethane could be raised up to $2 \times 10^{-3} M$ (the absorption of the neutral form of CH_3NO_2 is much lower than that of $CH_2=NO_2^-$ ⁹) and with $10^{-2} M S_2O_3^{2-}$ the uv light is absorbed mainly by the thiosulfate. An increase of the nitromethane concentration is essential in order to compete effectively with the thiosulfate for the electrons. Under these conditions, taking the values $k_8 = 2 \times 10^{10} M^{-1} sec^{-1}$,⁹ and $k_7 = 6 \times 10^8 M^{-1} sec^{-1}$,³ about 80% of the electrons will react with the nitromethane rather than with the thiosulfate. Figure 1 shows the esr spectrum resulting from the photolysis of this solution. Both bands A and B are excited yielding the radicals \dot{S}^- , $\dot{S}O_3^-$, e_{aq}^- , and $\dot{S}_2O_3^-$. Although in this experiment the pH was 9.5, enough of the nitromethane is in the basic form (about 10%) to scavenge the \dot{S}^- and $\dot{S}O_3^-$ radicals. Electrons, however, react directly with the nitromethane. The spectra of the three radicals $-O_3S-CH_2\dot{N}O_2^-$, $-S-CH_2\dot{N}O_2^-$, and $CH_3\dot{N}O_2^-$ are given in Figure 1 and the hyperfine

(8) H. Leg and B. Arends, *Z. Phys. Chem., Abt. B*, **6**, 240 (1930).

(9) K.-D. Asmus, A. Henglein, and G. Beck, *Ber. Bunsenges. Phys. Chem.*, **70**, 459 (1966).

(10) W. Karmann and A. Henglein, *ibid.*, **71**, 421 (1967).

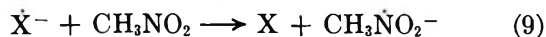
constants in Table I. The spectrum of a fourth radical is also present in Figure 1 and shows a 24.50-G triplet of 4.47-G triplets where each line is further split into a 1.18-G doublet. This spectrum, which was not observed at pH 13, is attributed to $\text{HS-CH}_2\dot{\text{N}}\text{O}_2^-$ where the 1.18-G splitting originates from the proton on the SH group. (The esr spectrum of $\text{HSCH}_2\dot{\text{N}}\text{O}_2^-$ was also observed when H_2S at pH ~ 9 was electron irradiated in the presence of nitromethane.) The coexistence of both spectra of the $\dot{\text{S}}^-$ and $\dot{\text{S}}\text{H}$ adducts to the nitromethane will be discussed elsewhere.⁶ It should be mentioned here that the relative intensities of the esr lines of the various adducts (see Figure 1) do not necessarily reflect radical production rates because the steady-state concentrations are also affected by the efficiency of trapping and the disappearance rates as well as by the esr line widths.

Table I: Hyperfine Constants of Nitromethane Adduct Radicals in the Photolysis of Thiosulfate Solution at pH 9.5

Radical	a^{N}	a_{α}^{H}	a_{β}^{H}	g factor ^a
$-\text{O}_3\text{SCH}_2\dot{\text{N}}\text{O}_2^-$	22.21	7.51		2.00493
$-\text{SCH}_2\dot{\text{N}}\text{O}_2^-$	24.34	6.64		2.00579
$\text{HSCH}_2\dot{\text{N}}\text{O}_2^-$	24.50	4.47	1.18	2.00603
$\text{CH}_3\dot{\text{N}}\text{O}_2^-$ ^b	25.95	12.13		2.00495

^a The hyperfine constants are given in gauss and are accurate to ± 0.05 G. The g factors are accurate to ± 0.00005 . Second-order corrections have been made when calculating the centers.
^b These values are slightly different from those reported previously.⁷ The earlier values for this radical seem to have been in error.

Some doubts could arise about the origin of the $\text{CH}_3\dot{\text{N}}\text{O}_2^-$ radical since one might expect an electron transfer from some other radical to nitromethane according to



Such a reaction was ruled out by an experiment in which N_2O was added. Under these conditions the electron adduct signals disappeared while the others were not influenced. The OH radicals produced from $e_{\text{aq}}^- + \text{N}_2\text{O} \xrightarrow{\text{H}_2\text{O}} \text{OH} + \text{N}_2 + \text{OH}^-$ will react mainly with $\text{S}_2\text{O}_3^{2-}$ producing $\dot{\text{S}}_2\text{O}_3^-$ (and as mentioned above detection of the $\dot{\text{S}}_2\text{O}_3^-$ radical is difficult under our conditions). As a blank an N_2 saturated solution of 2×10^{-3} M nitromethane (pH 9.5) was photolyzed, without other additives; no esr signals were detected.

An attempt was made to change the relative excitation in bands A and B by selective absorption of the

short wavelengths. Using acetic acid filters at different acid concentrations caused the reduction of the intensity of all lines, but none of the filters eliminated the electron adduct spectrum completely. The ratio between the $-\text{O}_3\text{SCH}_2\dot{\text{N}}\text{O}_2^-$ and the $\text{CH}_3\dot{\text{N}}\text{O}_2^-$ signals with the different filters is given in Table II. Because only a small change in this ratio occurred on changing the filter we conclude that most of the ctt's excitation occurred through the tail of band B which strongly overlaps band A. (Excitation near the maximum of band B (215 nm) is unlikely because of the low lamp output in this region.)

Table II: The Decrease in Signal Intensity of $-\text{O}_3\text{S-CH}_2\dot{\text{N}}\text{O}_2^-$ and $\text{CH}_3\dot{\text{N}}\text{O}_2^-$ Using Acetic Acid Filters

Acetic acid, %	$I_{\dot{\text{S}}\text{O}_3^-}$ ^a	I_{e^-} ^a	$I_{\dot{\text{S}}\text{O}_3^-}/I_{e_{\text{aq}}^-}$
0	37	6	6.2 ± 0.5
20	10.2	1.4	7.3 ± 0.5
50	9.4	1.2	7.8 ± 0.5
100	8.1	0.9	9.0 ± 3.5

^a $I_{\dot{\text{S}}\text{O}_3^-}$ and I_{e^-} stands for the esr signal intensity of the $-\text{O}_3\text{S-CH}_2\dot{\text{N}}\text{O}_2^-$ and $\text{CH}_3\dot{\text{N}}\text{O}_2^-$ lines, respectively.

From these esr results it seems clear that photolysis of thiosulfate produces $\dot{\text{S}}^-$, $\dot{\text{S}}\text{O}_3^-$ and e_{aq}^- as a result of excitation of bands A and B. Unfortunately, the very low intensity of the photolyzing light in the far-uv prevented study of the radicals produced by the excitation of band C. At this point it is appropriate to compare these esr results with the results reported by Dogliotti and Hayon.³ Those authors found absorption maxima at 280 and 380 nm and ascribed the two bands to $\dot{\text{S}}_2\text{O}_2^-$ and $\dot{\text{S}}_2\text{O}_3^-$, respectively. The latter product is quite consistent with the esr results in that its partner, e_{aq}^- , was detected. The esr experiments, however, also demonstrate formation of $\dot{\text{S}}^-$ and $\dot{\text{S}}\text{O}_3^-$. It is known that $\dot{\text{S}}\text{O}_3^-$ has an absorption maximum at 275 nm³ so that some portion of the absorption ascribed³ to $\dot{\text{S}}_2\text{O}_2^-$ must therefore belong to $\dot{\text{S}}\text{O}_3^-$ formed in reaction 6. In addition, $\dot{\text{S}}\text{H}$ has been found^{11,12} to have an absorption maximum at 384 nm near that ascribed to $\dot{\text{S}}_2\text{O}_3^-$. These overlapping spectra are potential complications in the kinetic analysis of the spectrophotometric results.

(11) J. Wendenburg, *Proc. Tihany Symp. Radiat. Chem.*, 2nd, 1966.

(12) J. Wendenburg, M. Möckel, A. Granzov, and A. Henglein, *Z. Naturforsch. B*, 21, 632 (1966).

γ Radiolysis of Liquid Ethanol. Yields of Hydrogen and Free Ions.Solvated Electron Rate Constants¹

by S. M. S. Akhtar and G. R. Freeman*

Department of Chemistry, University of Alberta, Edmonton 7, Alberta, Canada (Received April 19, 1971)

Publication costs borne completely by The Journal of Physical Chemistry

The initial hydrogen yield from pure ethanol at 20° is $G(\text{H}_2)_0 = 5.9$; the free ion yield is $G(e^-_{\text{solv}})_{\text{fi}} = 1.7$. Most of the values reported earlier were lower than these and seem to have been affected by impurities in the alcohol. The dose dependence of the hydrogen yields and the yields of hydrogen and nitrogen from nitrous oxide solutions agree with calculations based on $G(\text{H}_2)_0 = 5.9$, $G(e^-_{\text{solv}})_{\text{fi}} = G(\text{H}_2)_{\text{fi}}^{\text{max}} = G(\text{N}_2)_{\text{fi}}^{\text{max}} = 1.7$, using independently measured values of the rate constants. For the free ion reaction, 1.0 nitrogen molecule is formed for each solvated electron scavenged by nitrous oxide in ethanol. Rate constant ratios for reactions of solvated electrons were determined by competition kinetics. Using the previously reported² value $k(e^-_{\text{solv}} + \text{CH}_3\text{CHO}) = 4 \times 10^9 \text{ M}^{-1} \text{ sec}^{-1}$, the following values of k for other solutes were obtained at 20°, in units of $10^9 \text{ M}^{-1} \text{ sec}^{-1}$: N_2O , 7; $\text{C}_2\text{H}_5\text{OH}_2^+$, 29; $\text{C}(\text{NO}_2)_4$, 19; CCl_4 , <9; $n\text{-C}_2\text{H}_7\text{Br}$, ≤ 1.3 . Pulse-spectroscopic measurements gave higher values for the last three compounds: $\text{C}(\text{NO}_2)_4$, 35; CCl_4 , 11; $n\text{-C}_2\text{H}_7\text{Br}$, 3.0.

Introduction

Development of the theory of radiation chemistry requires accurate knowledge of the yields of intermediates and final products in irradiated systems. To this end several systems have been, and continue to be, intensively studied. One such system is liquid ethanol.²⁻¹³

For a number of years the initial yield of hydrogen from the γ radiolysis of liquid ethanol at room temperature has been thought to be $G(\text{H}_2)_0 = 5.0 \pm 0.1$,^{2,6,8-11} and the most widely accepted free ion yield has been $G(e^-_{\text{solv}})_{\text{fi}} = 1.0 \pm 0.1$.^{8-10,12,13} However, higher values of the hydrogen⁵ and free ion^{2,6,11} yields have been reported and the hydrogen yield has been found to increase in the presence of a trace of acid.^{11,14} The acid-sensitive intermediate has a G value of 0.8 in ethanol that gives an "initial" $G(\text{H}_2) = 5.1$.¹¹ Two possible interpretations of the results seem to be: (a) the ethanol contains a trace of electron-scavenging impurity, and absolutely pure ethanol would give $G(\text{H}_2)_0 = 5.9$ and $G(e^-_{\text{solv}})_{\text{fi}} = 1.7$ or (b) $G(\text{H}_2)_0 = 5.0$, $G(e^-_{\text{solv}})_{\text{fi}} \approx 1.0$ and the unidentified acid-sensitive species X has a yield $G(X) \approx 0.8$.¹⁵ The present work was undertaken to try to choose between these alternatives. At the same time the unexpectedly low rate constant reported for the reaction between electrons and carbon tetrachloride in ethanol⁸ has been investigated as a possibly related problem.

Since this project was begun articles have appeared which support $G(e^-_{\text{solv}})_{\text{fi}} = 1.7$,² and 1.0.^{12,13} The continuing large magnitude of the discrepancy makes it seem progressively more serious.

Experimental Section

Materials and Sample Preparation. Absolute ethanol from the Reliance Chemical Co. was subjected to the

purification method described earlier.¹⁶ However, a subsequent uv spectroanalysis of this alcohol using a 10-cm cell indicated trace amounts of carbonyl compounds. Therefore, absolute ethanol from the U. S. Industrial Chemical Co. was used. Analysis of this alcohol by the above method established an upper limit of impurities such as carbonyl compound and benzene at 10^{-5} M . Analysis provided by the U. S. Industrial Chemical Co. indicated the impurity levels as follows: water 50 ppm, benzene <1 ppm, methanol 2.5 ppm, acetaldehyde <1 ppm, and halogen compounds <1 ppm.

The ethanol was treated with KOH under vacuum and condensed in a trap at -196° while being evacua-

(1) Supported by the National Research Council of Canada.

(2) J. W. Fletcher, P. J. Richards, and W. A. Seddon, *Can. J. Chem.*, **48**, 1645 (1970).(3) W. R. McConell and A. S. Newton, *J. Amer. Chem. Soc.*, **76**, 4651 (1954).(4) G. E. Adams, J. H. Baxendale, and R. D. Sedgwick, *J. Phys. Chem.*, **63**, 854 (1959).(5) R. H. Johnsen, *ibid.*, **65**, 2144 (1961).(6) E. Hayon and J. J. Weiss, *J. Chem. Soc.*, 3962 (1961).(7) I. A. Taub, D. A. Harter, M. C. Sauer, Jr., and L. M. Dorfman, *J. Chem. Phys.*, **41**, 979 (1964).(8) G. E. Adams and R. D. Sedgwick, *Trans. Faraday Soc.*, **60**, 865 (1964).(9) J. J. J. Myron and G. R. Freeman, *Can. J. Chem.*, **43**, 381 (1965).(10) R. A. Basson, *J. Chem. Soc., A*, 1989 (1968).(11) J. C. Russell and G. R. Freeman, *J. Phys. Chem.*, **72**, 816 (1968).(12) S. J. Rzed and J. H. Fendler, *J. Chem. Phys.*, **52**, 5395 (1970).(13) E. Hayon, *ibid.*, **53**, 2353 (1970).

(14) J. W. Fletcher, Ph.D. Thesis, University of Alberta, 1966.

(15) G. R. Freeman, *Actions Chim. Biol. Radiat.*, **14**, 73 (1970).(16) J. C. Russell and G. R. Freeman, *J. Phys. Chem.*, **71**, 755 (1967).

ted. After thorough degassing the ethanol was finally recondensed in a storage bulb. The system handling ethanol contained greaseless Hoke valves.

Nitrous oxide was purified by passing it through a concentrated aqueous solution of KOH and subsequently passing it through a column packed with silica gel. Finally the gas was passed through KOH pellets, thoroughly degassed, and stored in a reservoir. Acetaldehyde was purified by fractional distillation using a 70-cm column packed with glass helices. The middle fraction was introduced into a storage bulb and degassed by pumping initially at -78° and finally at room temperature. The storage bulb was ultimately maintained at -78° .

Carbon tetrachloride and *n*-propyl bromide were purified by treatment with KHCO_3 followed by thorough washing with triply distilled water. They were degassed by repeated freeze-pump-thaw cycles. Tetranitromethane was also purified by the above method; however, in this case solutions of $\text{C}(\text{NO}_2)_4$ in ethanol were prepared immediately after purification and used as soon as possible.

Hydrogen chloride was passed over copper foil, thoroughly degassed, and stored in a Pyrex bulb. Hydrogen chloride, carbon tetrachloride, and *n*-propyl bromide were always recondensed and pumped on at -196° before use. The storage bulbs for ethanol and all other reagents were protected from light by aluminum foil.

Most samples were prepared by standard vacuum techniques. For acetaldehyde solutions the acetaldehyde was introduced into the sample cell by condensation at -78° , followed by the ethanol. The sample cell was gently vibrated to allow thorough mixing, cooled to -196° , and then sealed off under vacuum. This procedure was adopted to avoid freezing the pure acetaldehyde, which causes it to polymerize.

Tetranitromethane, potassium hydroxide, and sulfuric acid were added by introducing their solutions in ethanol into sample cells provided with a side arm, which was then sealed off. The volume of solutions thus introduced was generally 0.05–0.5 ml. The solution was degassed by freeze-pump-thaw cycles and then the required extra ethanol was distilled into the sample cell. The 5-ml samples were contained in 7-ml cells.

Irradiations. Irradiations were done at 20° in a ^{60}Co Gammacell 220 (Atomic Energy of Canada Ltd). The dose rate was 4×10^{17} eV/g min.

The yields of gaseous products were determined by refluxing the sample in a vacuum line and passing the gases so obtained through two cold traps kept at -196° . The pressure and volume of the products were measured in a Toepler-McLeod gauge, and the gases were then analyzed by gas chromatography. A 2-m molecular sieve column, helium carrier gas, and a thermal conductivity detector were used. The yield of each gas

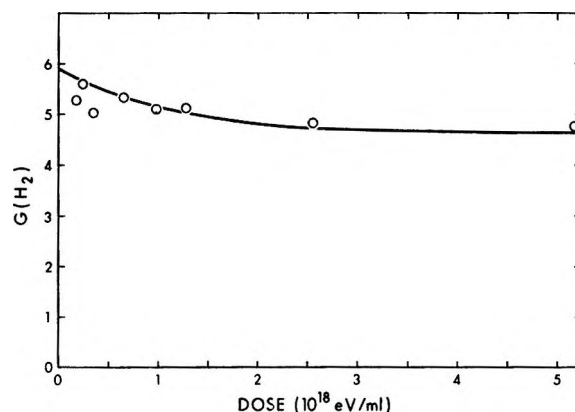


Figure 1. Hydrogen yield as a function of dose. The solid curve was calculated using eq II.

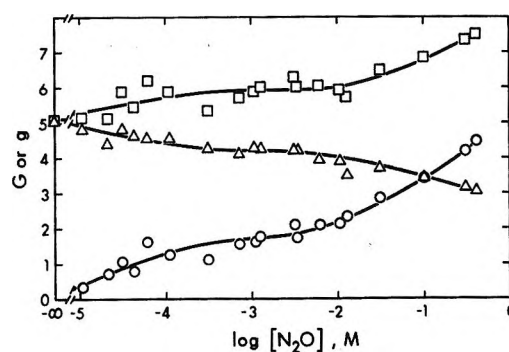


Figure 2. Hydrogen and nitrogen yields from nitrous oxide solutions in ethanol: \circ , $G(\text{N}_2)$; Δ , $g(\text{H}_2)$; \square , $G(\text{N}_2) + g(\text{H}_2)$. The solid curves at $N_{\text{N}_2\text{O}} < 10^{-3}$ were calculated using eq III and IV.

was calculated from the chromatogram, with calibrations for each gas.

Pulse Radiolysis. For pulse-radiolysis experiments the solutions of carbon tetrachloride were prepared by vacuum technique. The pure ethanol and solutions containing propyl bromide and tetranitromethane were deoxygenated by bubbling argon through them. The 1.0- μsec pulses of 1.7-MeV electrons imparted 5×10^{16} eV/ml to the samples. The temperature was 20° .

Results

The hydrogen yield from ethanol decreases with increasing dose (Figure 1). The initial yield deduced from mechanistic considerations (see Discussion) is $g(\text{H}_2) = 5.9$. For the rest of the experiments the dose used was 1×10^{18} eV/ml, unless otherwise stated.

The yields of hydrogen and nitrogen from nitrous oxide solutions in ethanol are shown in Figure 2. The reported nitrogen yields are based on the total energy absorbed by the solution and are designated by $G(\text{N}_2)$. The hydrogen yields from the solutions are calculated on the basis of the energy absorbed by the solvent only and are designated by $g(\text{H}_2)$. The hydrogen yield decreases and the nitrogen yield increases with increasing nitrous oxide concentration. The sum of the nitrogen

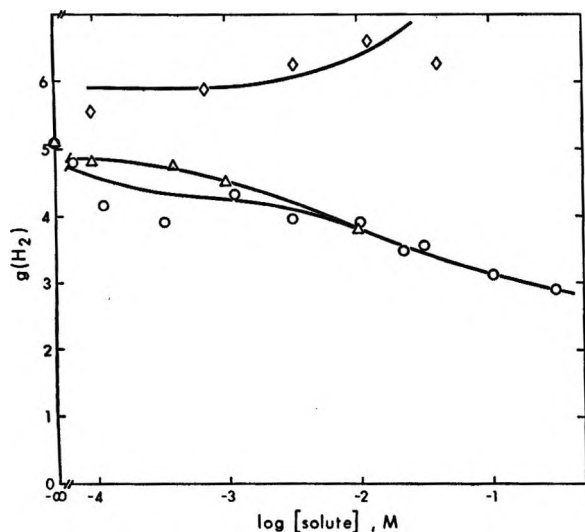


Figure 3. Hydrogen yields from solutions containing acetaldehyde, \circ , tetranitromethane, Δ , and $\text{C}_2\text{H}_5\text{OH}_2^+$ from sulfuric acid, \diamond . The line through the acetaldehyde points was calculated from eq II. The concentrations of the oxonium ions $\text{C}_2\text{H}_5\text{OH}_2^+$ were calculated on the basis of $k_{\text{diss}}(\text{H}_2\text{SO}_4) = 1.7 \times 10^{-3}$ in ethanol.

and hydrogen yields increases with increasing solute concentration.

Figure 3 represents the effects of sulfuric acid, acetaldehyde, and tetranitromethane on the yield of hydrogen. Acetaldehyde is itself a product of radiolysis of ethanol and it was estimated that after a dose of 1×10^{18} eV/ml had been absorbed the accumulated concentration of acetaldehyde in the sample was 5.2×10^{-5} M. The aldehyde is an electron scavenger and it interferes with reactions of other added solutes. In the case of acetaldehyde as solute, the time-averaged concentration of acetaldehyde would be 2.6×10^{-5} M higher than that initially added. The curve for the effect of the concentrations of acetaldehyde on the yield of hydrogen in Figure 3 was calculated using a method described later.

The yield of hydrogen decreases with the increase in the concentration of aldehyde or tetranitromethane (Figure 3). The yield of hydrogen from solutions of sulfuric acid in ethanol increases with acid concentration. Similar experiments with hydrochloric acid gave lower hydrogen yields presumably due to the formation of ethyl chloride.¹¹

The concentrations of $\text{C}_2\text{H}_5\text{OH}_2^+$ in the acid solutions in Figure 3 were computed on the basis that the dissociation constant of sulfuric acid in ethanol was $k_{\text{diss}} = 1.7 \times 10^{-3}$. This value of the dissociation constant was extrapolated from reported values of dissociation constants in methanol, $k_{\text{diss}}(\text{HCl}) = 0.25$,¹⁷ and $k_{\text{diss}}(\text{H}_2\text{SO}_4) = 0.028$,¹⁸ and the value for HCl in ethanol, $k_{\text{diss}}(\text{HCl}) = 0.015$.¹⁹

The effects of carbon tetrachloride and *n*-propyl bromide on the yield of hydrogen, both in the absence

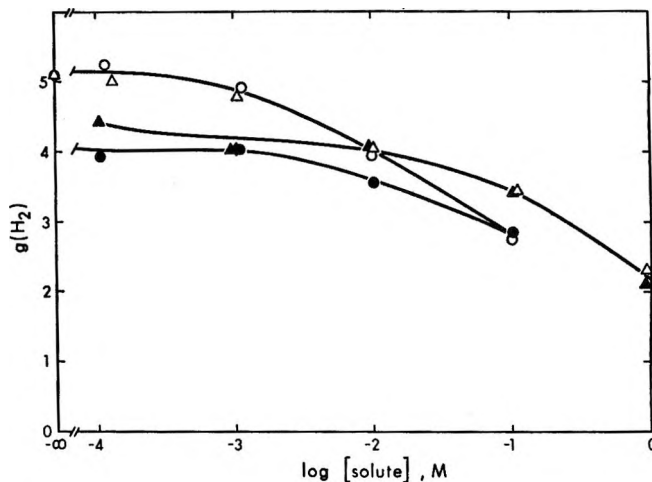


Figure 4. Hydrogen yields from solutions containing halides. Open points, no KOH added; closed points, KOH added (8 mM in CCl_4 and 0.8 mM in $n\text{-C}_3\text{H}_7\text{Br}$ solutions): carbon tetrachloride, \circ , 9×10^{17} eV/ml; \bullet , 3×10^{17} eV/ml; \bullet , 9×10^{17} eV/ml; *n*-propyl bromide, Δ , 9×10^{17} eV/ml.

and presence of potassium hydroxide, are represented in Figure 4. The yield of hydrogen in basic solutions of the halides decreases with the halide concentration. In the absence of alkali, however, the hydrogen yield remains practically unchanged at solute concentrations less than 5×10^{-4} M.

Figure 5 represents the effects of aldehyde and tetranitromethane on the yields of nitrogen and hydrogen from solutions of nitrous oxide in ethanol. At a fixed concentration of nitrous oxide, the yields of nitrogen and hydrogen decrease with the increasing concentration of acetaldehyde or tetranitromethane.

Figure 6 represents the effects of carbon tetrachloride and *n*-propyl bromide on the yields of nitrogen and hydrogen from nitrous oxide solution in ethanol, both in the absence and the presence of dilute potassium hydroxide. Figure 6 also shows the effect of dose on the yields from the ternary solutions. The nitrogen and hydrogen yields decrease with increase in the concentration of the halide. For a given concentration of nitrous oxide and carbon tetrachloride, $G(\text{N}_2)$ decreases and $g(\text{H}_2)$ increases with increasing dose in the absence of alkali (Figure 6A). In the presence of alkali there is no dose effect, and $g(\text{H}_2)$ decreases steadily with increasing carbon tetrachloride concentration. At a fixed concentration of nitrous oxide and *n*-propyl bromide, $G(\text{N}_2)$ decreases with increasing dose in the absence of alkali; however, there is practically no change in $g(\text{H}_2)$ with dose (Figure 6B). For a given concentration of *n*-propyl bromide and nitrous oxide in the presence of alkali the corresponding values of

(17) K. N. Jha and G. R. Freeman, *J. Chem. Phys.*, **48**, 5480 (1968).

(18) E. W. Kanning, E. G. Bobaleck, and J. B. Byrne, *J. Amer. Chem. Soc.*, **65**, 1111 (1943).

(19) I. I. Benzman and F. H. Nerhock, *ibid.*, **67**, 1330 (1945).

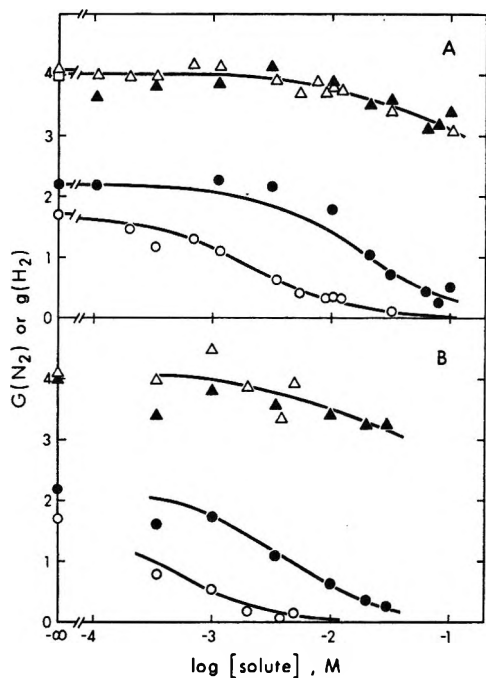


Figure 5. Competition of nitrous oxide with acetaldehyde (A) and tetranitromethane (B). Open points, $1.2 \times 10^{-3} M N_2O$; closed points $1.0 \times 10^{-2} M N_2O$: O, $G(N_2)$; Δ, $g(H_2)$. The curves for $G(N_2)$ were calculated using the competition rate constants listed in Table I.

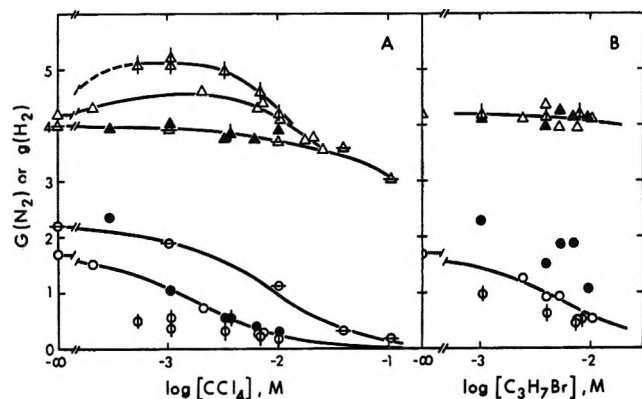


Figure 6. Competition of nitrous oxide with carbon tetrachloride (A) and *n*-propyl bromide (B). Open points, no KOH added; closed points, KOH added (8 mM in CCl_4 and 0.8 mM in *n*- C_3H_7Br solutions). The curves for $G(N_2)$ were calculated using $k(e^-_{solv} + N_2O) = 7 \times 10^9 M^{-1} sec^{-1}$, $k(e^-_{solv} + CCl_4) = 9 \times 10^9 M^{-1} sec^{-1}$ and $k(e^-_{solv} + n-C_3H_7Br) = 1.3 \times 10^9 M^{-1} sec^{-1}$; $[N_2O] = 2.2 \times 10^{-3}$ and $1.0 \times 10^{-2} M$ for the CCl_4 solutions and $[N_2O] = 1.0 \times 10^{-3} M$ for the *n*- C_3H_7Br solutions: O $G(N_2)$; Δ $g(H_2)$; (A) at $9 \times 10^{17} eV/ml$ O, Δ, $2.2 \times 10^{-3} M N_2O$; ●, ▲, $1.0 \times 10^{-2} M N_2O$; ●, ▲, $1.0 \times 10^{-3} M N_2O$; at $33 \times 10^{17} eV/ml$ ○, △, $1.0 \times 10^{-3} M N_2O$; (B) $1.0 \times 10^{-3} M N_2O$ ○, △, $9 \times 10^{17} eV/ml$; ○, △, $33 \times 10^{17} eV/ml$.

$G(N_2)$ are higher than those obtained in the absence of alkali, whereas $g(H_2)$ does not change.

The yield of nitrogen increases and that of hydrogen decreases with increase in concentration of nitrous oxide in solutions of sulfuric acid in ethanol (Figure 7A).

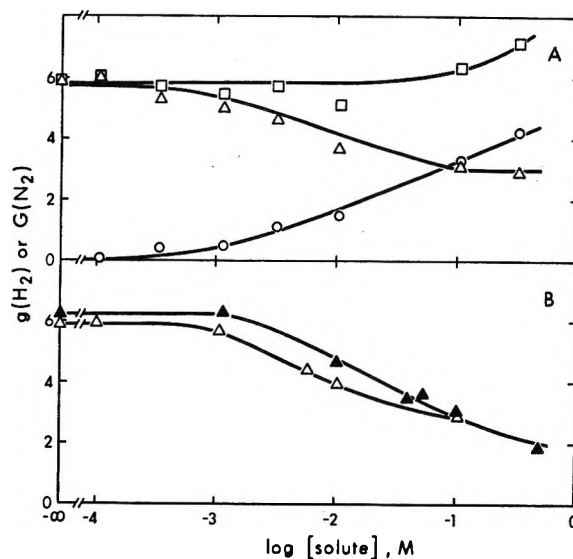


Figure 7. Competition of sulfuric acid with nitrous oxide (A) and carbon tetrachloride (B): O, $G(N_2)$; Δ, $g(H_2)$; □, $G(N_2) + g(H_2)$; open points $[C_2H_5OH_2^+] = 0.7 \times 10^{-3} M$; closed points $[C_2H_5OH_2^+] = 3.3 \times 10^{-3} M$. The curve for $G(N_2)$ was calculated using the competition rate constants listed in Table I.

The total yield of $(N_2 + H_2)$ remains unchanged up to $1 \times 10^{-2} M N_2O$ and then increases. The yield of hydrogen from 1 mM and 10 mM sulfuric acid solutions remains practically unchanged with the addition of up to $10^{-3} M$ carbon tetrachloride and then decreases as the halide concentration is increased.

Typical oscilloscope traces of the decay of the solvated electron absorption are represented in Figure 8. Figure 8A refers to pure ethanol, whereas B and C refer to $1.1 \times 10^{-4} M$ *n*-propyl bromide and $1.0 \times 10^{-4} M$ *n*-propyl bromide plus $8 \times 10^{-3} M$ KOH, respectively. The half-lives of the solvated electrons in these solutions were 3.8, 1.4, and 1.6 μsec, respectively. The half-life of solvated electrons in pure ethanol containing $8 \times 10^{-3} M$ KOH was 6.2 μsec. The value of the rate constant $k(e^-_{solv} + S)$ is calculated from eq I.

$$k(e^-_{solv} + S) = \frac{0.69}{[S]} \left(\frac{1}{t_{1/2}^s} - \frac{1}{t_{1/2}^0} \right) \quad (I)$$

where $t_{1/2}^s$ is the electron half-life in the presence of solute S at concentration [S] and $t_{1/2}^0$ is the half-life in the neutral or basic solvent, as appropriate. The above results give $k(e^-_{solv} + n-C_3H_7Br) = 2.8 \times 10^9 M^{-1} sec^{-1}$ in the neutral sample and $3.2 \times 10^9 M^{-1} sec^{-1}$ in the basic sample. The values in the presence and absence of base are essentially the same, with an average of $3.0 \times 10^9 M^{-1} sec^{-1}$.

Rate constants were similarly determined for the reactions of solvated electrons with tetranitromethane and carbon tetrachloride. The values are listed in Table I.

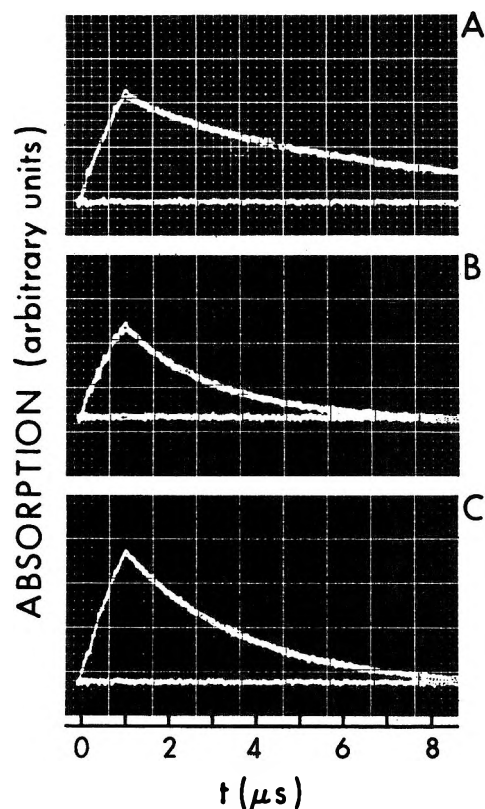


Figure 8. Typical oscilloscope traces of the decay of the solvated electron absorption, pulse dose $\approx 5 \times 10^{16}$ eV/g, sweep speed 1 $\mu\text{sec}/\text{cm}$: A, pure ethanol; B, 1.1×10^{-4} M $n\text{-C}_3\text{H}_7\text{Br}$; C, 1.1×10^{-4} M $n\text{-C}_3\text{H}_7\text{Br}$ + 8×10^{-3} M KOH.

Table I: Rate Constants for Reactions of e^-_{soln} in Ethanol

Solute	$k(e^-_{\text{soln}} + \text{S}), 10^9 M^{-1} \text{sec}^{-1}$		
	N_2O competition ^a	Pulse	Aqueous pulse ^e
CH_3CHO	(Assume 4)	4 ^f	3.5
N_2O	7		6.6
$\text{C}_2\text{H}_5\text{OH}_2^+$	29 (>20) ^b	$\geq 20^{b,d}$	22
$\text{C}(\text{NO}_2)_4$	19	35	46
CCl_4	<9	11 ^c	30
$n\text{-C}_3\text{H}_7\text{Br}$	≤ 1.3	3.0 ^c	8.5
Napthalene		4.5 ^g	5.4

^a Based on the assumed value for CH_3CHO . ^b The value $k(e^-_{\text{soln}} + \text{acid}) = 2.0 \times 10^{10} M^{-1} \text{sec}^{-1}$ would be obtained from the competition if the gross concentration of added sulfuric acid were used in the calculation. We used $k_{\text{diss}}(\text{H}_2\text{SO}_4) = 1.7 \times 10^{-3}$ in ethanol at 20°. The value $k(e^-_{\text{soln}} + \text{H}^+) = 2.0 \times 10^{10} M^{-1} \text{sec}^{-1}$ reported from a pulse study^d was obtained by assuming the dissociation to H^+ and HSO_4^- to be complete. The HCl solutions might have been contaminated by $\text{C}_2\text{H}_5\text{Cl}$ (see ref 11). ^c In neutral or basic solution. ^d I. A. Taub, D. A. Harter, M. C. Sauer, Jr., and L. M. Dorfman, *J. Chem. Phys.*, **41**, 979 (1964). ^e See ref 20. ^f See ref 2. ^g G. L. Bolton, private communication.

Discussion

Pure Ethanol. The present work combined with that of Fletcher and coworkers² demonstrates that $G(\text{H}_2)_0 =$

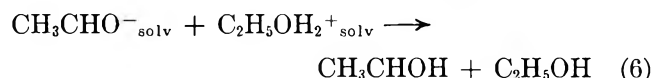
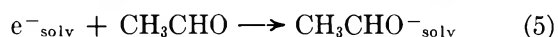
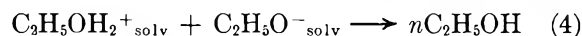
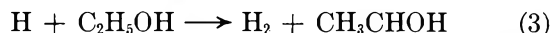
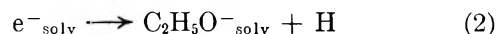
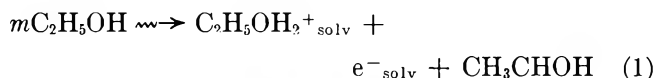
5.9 and $G(e^-_{\text{soln}})_{\text{fi}} = 1.7$. The effects previously attributed to an acid-sensitive species X,¹⁵ and the earlier reported "initial" hydrogen yield of 5.0 ± 0.1 ^{6,8-11} and free ion yield ≈ 1.0 were apparently caused by traces of impurities that react with solvated electrons. The ethanol used in the present experiments was of the highest purity that we have obtained thus far (see Experimental Section). The elimination of greased stopcocks from the vacuum system may also have reduced the possibilities of contamination.

The curve drawn through the hydrogen yields in Figure 1 was calculated from the expression

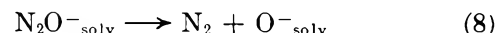
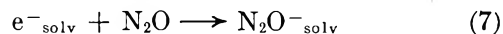
$$GH(\text{H}_2) = 5.9 - 1.7 \left(\frac{k_5[\text{CH}_3\text{CHO}]}{k_2 + k_5[\text{CH}_3\text{CHO}]} \right) \quad (\text{II})$$

where $5.9 = G(\text{H}_2)_0$, $1.7 = G(\text{H}_2)_{\text{fi}}$, $k_2 = 1.2 \times 10^9 \text{ sec}^{-1}$,² $k_5 = 4 \times 10^9 M^{-1} \text{sec}^{-1}$,² and $[\text{CH}_3\text{CHO}]$ is the average acetaldehyde concentration present during the radiolysis. The aldehyde is a radiolysis product and its yield is $G(\text{CH}_3\text{CHO}) = G(\text{H}_2) - 2.3$.⁹

Since we are concerned here with trace quantities of scavengers, only the free ions are involved in the competitions. This portion of the mechanism can be represented as follows.



Nitrous Oxide Solutions. At the dose used to study these solutions, 1×10^{18} eV/ml, in the absence of solute the hydrogen yield was 5.1 and the average acetaldehyde concentration during the irradiation was 2.6×10^{-5} M. Upon addition of nitrous oxide reaction 7 competes with (2) and (5).



The curves through the nitrogen and hydrogen yields in Figure 2 at nitrous oxide concentrations $\leq 10^{-3}$ M were calculated from eq III and IV, respectively. At these concentrations only the free ions participate in the scavenging kinetics.

$$G(\text{N}_2) = 1.7 \left(\frac{k_7[\text{N}_2\text{O}]}{k_2 + k_5[\text{CH}_3\text{CHO}] + k_7[\text{N}_2\text{O}]} \right) \quad (\text{III})$$

$$g(\text{H}_2) = 5.9 - 1.7 \times \left(\frac{k_5[\text{CH}_3\text{CHO}] + k_7[\text{N}_2\text{O}]}{k_2 + k_5[\text{CH}_3\text{CHO}] + k_7[\text{N}_2\text{O}]} \right) \quad (\text{IV})$$

The value of k_7 is $7 \times 10^9 M^{-1} \text{sec}^{-1}$ (see later). The curve through the $[G(\text{N}_2) + g(\text{H}_2)]$ points over this concentration region in Figure 2 represents the sum of eq III and IV.

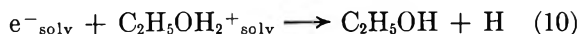
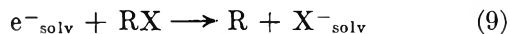
The agreement between the experimental and the calculated yields is satisfactory.

At solute concentrations $> 10^{-3} M$ scavenging occurs in the spurs. The kinetics of spur reactions has been treated earlier¹¹ and does not require discussion here.

Other Binary Solutions. The hydrogen yields from the acetaldehyde solutions (Figure 3) were similar to those from the nitrous oxide solutions (Figure 2), and those from the acid solutions (Figure 3) were similar to the combined $(\text{H}_2 + \text{N}_2)$ yields from the nitrous oxide solutions (Figure 2). The curves drawn for the acid and acetaldehyde results are simply the nitrous oxide curves shifted horizontally by factors equal to $k(e^-_{\text{soliv}} + \text{N}_2\text{O})/k(e^-_{\text{soliv}} + \text{S})$ that were determined from the competition studies discussed later.

The tetranitromethane and carbon tetrachloride solutions gave hydrogen yields greater than those from the acetaldehyde solutions (Figures 3 and 4). These results are contrary to what would be expected from the relative values of the rate constants shown in Table I; values for aqueous solutions²⁰ are given for comparison. Carbon tetrachloride in ethanol forms hydrochloric acid in a radiation-sensitized chain reaction.²¹ Although the chain length would be short in the present dilute solutions [$G(\text{HCl}) \approx 100$ in $4 M \text{CCl}_4$]²¹ and the concentrations shown in Figure 4 are 10^{-4} to $10^{-1} M$, sufficient hydrochloric acid was formed to increase the hydrogen yields. This was confirmed by the fact that $g(\text{H}_2)$ decreased when the solutions were made alkaline (Figure 4).

The formation of hydrobromic acid from *n*-propyl bromide²² and of nitrous acid from tetranitromethane explains the high hydrogen yields from those solutions in the absence of alkali (Figures 4 and 3, respectively). The electron scavenging efficiency of the acid formed is greater than that of the added organic solute (Table I). Acid formation in the tetranitromethane solutions was less serious than that in the halide systems.



The formation of acid explains the abnormally low efficiency of electron scavenging reported for carbon tetrachloride by Adams and Sedgwick.⁸

Electron Scavenging Competitions. Rate Constants. Competitions were run between nitrous oxide and other solutes to determine relative values of $k(e^-_{\text{soliv}} + \text{S})$. Results were plotted according to the expression

$$\frac{G(\text{N}_2)_0}{G(\text{N}_2)} = 1 + \frac{k_s[\text{S}]}{k_{\text{N}_2\text{O}}[\text{N}_2\text{O}]} \quad (\text{V})$$

where $G(\text{N}_2)_0$ is the yield in the absence of a second

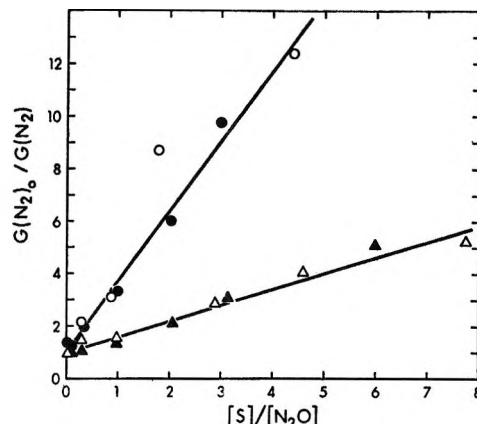


Figure 9. Kinetic analysis of competition of nitrous oxide with acetaldehyde and tetranitromethane for electrons: open points, $1.2 \times 10^{-3} M \text{N}_2\text{O}$; filled points, $1.0 \times 10^{-2} M \text{N}_2\text{O}$. Competitor S: Δ, \blacktriangle , acetaldehyde; \circ, \bullet , tetranitromethane.

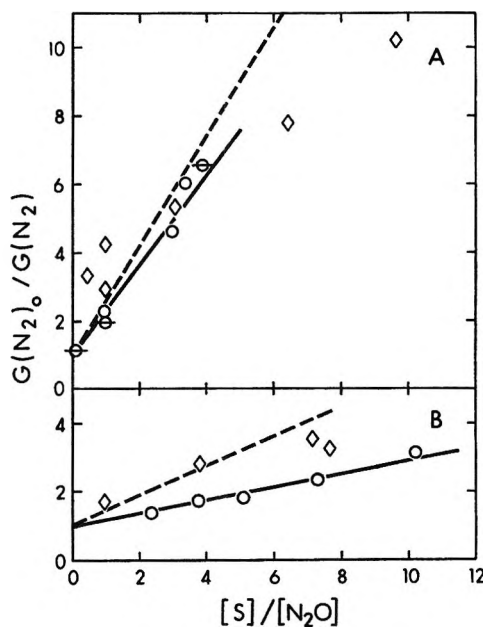


Figure 10. Kinetic analysis of competition between nitrous oxide and the halides: CCl_4 (A), $9 \times 10^{17} \text{eV/ml}$: \circ , $[\text{N}_2\text{O}] = 2.2 \times 10^{-3} M$; \ominus , $[\text{N}_2\text{O}] = 1.0 \times 10^{-2} M$; $33 \times 10^{17} \text{eV/ml}$: \diamond , $[\text{N}_2\text{O}] = 1.1 \times 10^{-3} M$; $\text{C}_2\text{H}_5\text{Br}$ (B), $[\text{N}_2\text{O}] = 1.0 \times 10^{-3} M$: \circ , $9 \times 10^{17} \text{eV/ml}$; \diamond , $33 \times 10^{17} \text{eV/ml}$. The dashed lines represent the rate constants obtained by the pulse-spectroscopic technique.

solute and $G(\text{N}_2)$ is the yield in the presence of concentration $[\text{S}]$ of the second solute. Plots for acetaldehyde and tetranitromethane are shown in Figure 9. The value $k(e^-_{\text{soliv}} + \text{CH}_3\text{CHO}) = 4 \times 10^9 M^{-1} \text{sec}^{-1}$ obtained from pulse measurements by Fletcher and co-workers² was then used to obtain the absolute values of the rate constants listed in Table I.

(20) E. J. Hart, *Actions Chim. Biol. Radiat.*, **10**, 1 (1966).

(21) G. L. Clark and P. E. Bierstedt, Jr., *Radiat. Res.*, **2**, 190, 295 (1955).

(22) W. V. Sherman, *J. Phys. Chem.*, **72**, 2287 (1968).

The competitions of nitrous oxide with acetaldehyde, tetranitromethane, and sulfuric acid were well behaved and they were described by eq V. However, the halide systems were complicated by the formation of acid. This was demonstrated by the effects of dose and the addition of base (Figures 6 and 10). The addition of base complicates the system further, because nitrous oxide can also form nitrogen by a chain process in irradiated alkaline solutions.²³ The rate constants given for CCl₄ and *n*-C₃H₇Br in the competition column of Table I were obtained from the solutions in which no base was added and which were given a dose of 9×10^{17} eV/ml; the values are upper limits because no correction was made for the acid formed. That an appreciable amount of acid was formed in the carbon tetrachloride solutions is indicated by the high hydrogen yields (Figure 6A). The acid effect in the *n*-propyl bromide competition was almost negligible, as indicated by the similar hydrogen yields in the presence and absence of base (Figure 6B).

Rate Constant Values. Pulse Radiolysis and Competition Kinetics. The values of $k(e^-_{\text{solv}} + S)$ obtained for tetranitromethane, carbon tetrachloride, and *n*-propyl bromide by the pulse-spectroscopic technique were significantly larger than those obtained from the competition with nitrous oxide (Table I). This type of difference has been noted for halides before²⁴ and might be due to an electron exchange reaction such as²⁵



The effect is not due to the production of acid in the pulse experiments because the same value of the rate constant was obtained in the presence and absence of an excess of alkali ($k = 11.5 \pm 1.5$ for CCl₄ and 3.0 ± 0.2 for *n*-C₃H₇Br, in units of $10^9 M^{-1} \text{sec}^{-1}$). The comparison of the two techniques merits further investigation.

(23) W. V. Sherman, *J. Phys Chem.*, **71**, 4245 (1967).

(24) S. R. Logan and P. B. Wilmot, *Chem. Commun.*, 558 (1966).

(25) G. R. Freeman and W. J. Holtzlander, *ibid.*, 205 (1967).

Mechanism of the Radiation-Induced Dechlorination of

1,1,1-Trichloro-2,2-bis(*p*-chlorophenyl)ethane in Alcoholic Solution

by Rudolph Evans,¹ Edwin Nesyto,¹ Cecilia Radlowski,¹ and Warren V. Sherman*

Department of Physical Sciences, Chicago State University, Chicago, Illinois 60621 (Received March 25, 1971)

Publication costs assisted by the Petroleum Research Fund

1,1,1-Trichloro-2,2-bis(*p*-chlorophenyl)ethane (DDT) undergoes dechlorination to 1,1-dichloro-2,2-bis(*p*-chlorophenyl)ethane (DDD) in γ -irradiated 2-propanol solution. The large *G* yields obtained indicate a chain mechanism for the process. Reduction in yield in the presence of small concentrations of free-radical scavengers shows the participation of free radicals as chain carriers, while the dependence of yield on dose rate is consistent with chain termination *via* bimolecular reaction of these radicals. A detailed mechanism is proposed for the reaction.

In the presence of aliphatic alcohols containing a carbinol hydrogen, carbon tetrachloride undergoes radiolytic dechlorination to chloroform and hydrochloric acid with high *G* yields,² indicating a chemical chain reaction. Since carbon tetrachloride may be considered a structural model for DDT it was of interest to extend the study of chlorinated hydrocarbons to solutions of DDT. In preliminary experiments³ it was in fact found that DDT underwent radiolytic chain dechlorination in 2-propanol solution similar to that of carbon tetrachloride. In the present communication details of the reaction mechanism are examined.

Experimental Section

Materials. DDT (City Chemical Corp. and Matheson Coleman and Bell, *p,p*-DDT) was recrystallized twice from petroleum ether (mp 107.5–109°). 2-Propanol (Baker spectroscopic grade) was used as received. The only detectable impurity was acetone

(1) Taken, in part, from theses in partial fulfillment for the degree of B.S. (C. R., E. N.) and M.S. (R. E.) at Chicago State University.

(2) C. Radlowski and W. V. Sherman, *J. Phys. Chem.*, **74**, 3043 (1970).

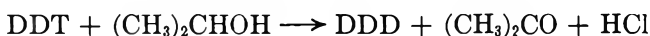
(3) W. V. Sherman, R. Evans, E. Nesyto, and C. Radlowski, *Nature*, **232**, 118 (1971).

($10^{-4} M$). All other materials were of reagent grade and were used as received.

Procedure. Solutions of DDT were placed in 15-mm o.d. Pyrex tubes, deaerated by flushing with argon which had been presaturated with solvent, sealed, and irradiated with ^{60}Co γ -rays. Irradiation was carried out in the Argonne A-063 cobalt chamber in which samples may be arranged radially around a vertical rod of cobalt. The radiation dose rate received by samples is thus varied by change in distance from the source. Doses were calculated using Fricke dosimetry in the reaction tubes and correcting for the lower electron densities of the DDT solutions. After irradiation the tubes were opened and HCl was estimated by acid-base titration. As a cross-check, total chloride ion was estimated by the Mohr method.⁴ Liquid and solid products were analyzed by gas chromatography using a Hewlett-Packard 5750 with flame-ionization detector. Acetone was analyzed on 10% Carbowax 20M on Chromosorb G, while pesticide residues DDE, DDD, and DDT were separated in an all-glass column system packed with 3.8% SE-30 on Chromosorb W(DMCS). The relative retention times were 0.57, 0.75, and 1.0, respectively. Benzhydrol (relative retention time 0.080), added to the solution after irradiation, was used as an internal standard.

Results and Discussion

The products identified in the radiolysis of deaerated 2-propanol solutions of DDT were hydrochloric acid, acetone, 1,1-dichloro-2,2-bis(*p*-chlorophenyl)ethane (DDD), and residual DDT. No 1,1-dichloro-2,2-bis(*p*-chlorophenyl)ethylene (DDE) could be identified. At all five radiation dose rates used in this study (13.6, 7.5, 4.6, 2.1, and 0.49×10^{17} eV ml⁻¹ min⁻¹) yields of all products and the consumption of DDT exhibited a linear dependence on total dose up to almost 100% consumption of DDT. The *G* values, obtained from these linear yield-dose plots (Table I), show that at the lower dose rates the reaction conforms to the stoichiometry



At the two higher dose rates there was a significant disparity between DDT consumed and DDD produced.

Table I: Product Yields in the Radiolysis of Deaerated Solutions of DDT in 2-Propanol^a

Dose rate, 10 ¹⁷ eV ml ⁻¹ min ⁻¹	<i>G</i> (HCl)	<i>G</i> (acetone)	<i>G</i> (DDD)	<i>G</i> (-DDT)
13.6	25	24	16	24
7.5	29	29	24	28
4.6	34	34	33	34
2.1	43	42	42	42
0.49	81	75	78	81

^a Initial concentration of DDT = 20 mM.

Table II: Effect of Free Radical Scavengers in the Radiolysis of Deaerated Solutions of DDT in 2-Propanol^{a,b}

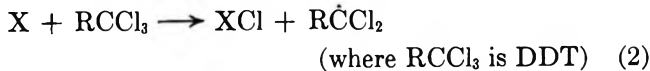
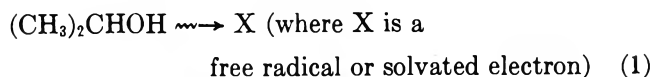
Scavenger	Scavenger concentration, mM	<i>G</i> (dechlorination) ^d
None		29
DPPH	10	7.9
I ₂	10	3
Nitrobenzene	10	2.4
Phenyl disulfide	10	2.0
O ₂	<i>c</i>	10

^a Initial DDT concentration, 20 mM. ^b Dose rate, 7.5×10^{17} eV ml⁻¹ min⁻¹. ^c Air saturated, [O₂] $\approx 10^{-3}$ M. ^d Measured by *G*(HCl), except in the case of I₂ where *G*(DDD) was used.

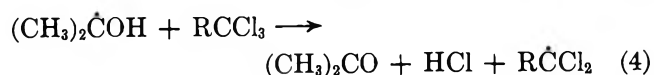
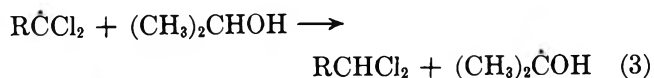
To verify whether dechlorination of DDT involves free-radical intermediates, solutions were irradiated in the presence of small concentrations ($\sim 10^{-2}$ M) of free-radical scavengers (DPPH, I₂, nitrobenzene, phenyl disulfide, and O₂) (Table II). In all cases dechlorination yields were significantly reduced. Assuming that the yield of radiolytic free radicals which are amenable for reaction with a solute is 6.7 radicals/100 eV in 2-propanol,⁵ then at all the dose rates used in the present study, *G*(dechlorination) in the absence of added scavenger significantly exceeds the radiolytic yield of free radicals, and hence a chain process is indicated. If one assumes that all these radicals are successful in initiating dechlorination, then at the lowest dose rate the chain length is 12. (If the initiating step occurs with less than 100% efficiency then this estimate of the chain length is only a lower limit.)

The data for DDT in 2-propanol are consistent with the same free-radical mechanism postulated for the carbon tetrachloride-2-propanol system² (reactions 1-4)

initiation



propagation



(4) D. A. Skoog and D. M. West, "Fundamentals of Analytical Chemistry," 2nd ed, Holt, Rinehart and Winston, New York, N. Y., 1969, p 232.

(5) (a) G. E. Adams, J. H. Baxendale, and R. D. Sedgwick, *J. Phys. Chem.*, **63**, 854 (1959); (b) W. V. Sherman, *Advan. Free-Radical Chem.*, **3** (1969).

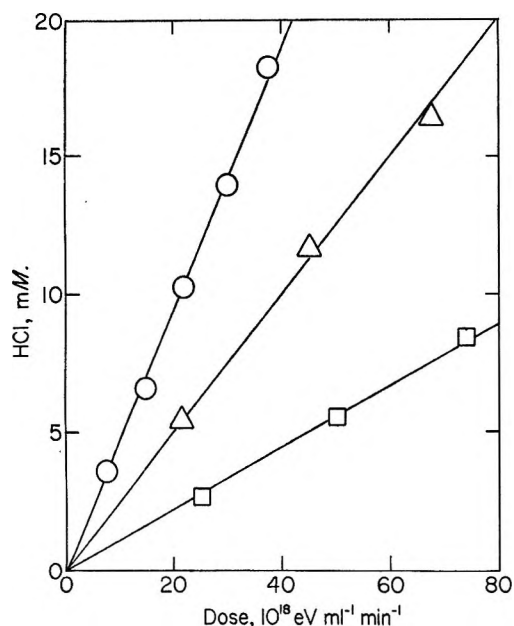


Figure 1. Effect of solvent on the dechlorination of DDT: 2-propanol, -O-; 1-propanol, - Δ -; *tert*-butyl alcohol, - \square -.

The lack of dependence of $G(\text{dechlorination})$ upon DDT concentration (differential G values at the beginning of irradiation, where the DDT concentration was 20 mM, and after radiation times where almost all the DDT had been consumed were essentially identical) indicates that reaction 4 is not the rate-determining step in the chain. Confirmation that reaction 3 is the slow step is found in the data for the radiolysis of DDT in alcohols containing C-H bonds with strengths different to that of the weakest bond in 2-propanol (Figure 1). Hence, at a dose rate where $G(\text{dechlorination})$ in 2-propanol was 29, in 1-propanol and *tert*-butyl alcohol $G(\text{dechlorination})$ was 15 and 6.8, respectively. The order of decreasing yield parallels the order of increasing bond strength.

If termination of the chain involves reaction between two DDT radicals (reaction 5), then assuming homogeneous kinetics

$G(\text{dechlorination}) =$

$$G(\text{X}) + 10k_3[(\text{CH}_3)_2\text{CHOH}] \left[\frac{G(\text{X})}{k_5 D} \right]^{1/2} \quad (\text{I})$$

where k_5 is the rate constant for reaction between two DDT radicals, and D is the radiation dose rate. The good straight line plots obtained when (a) $G(\text{dechlorination})$ data from Table I are plotted *vs.* $D^{-1/2}$ (Figure 2), and (b) $G(\text{dechlorination})$ is plotted *vs.* 2-propanol concentration for solutions diluted with *tert*-butyl alcohol (Figure 3), are both consistent with eq I. Assuming that $G(\text{X}) = 6.7$, then the values obtained for $dG(\text{dechlorination})/dD^{-1/2}$ (Figure 2), and $dG(\text{dechlorination})/d[2\text{-propanol}]$ (Figure 3) are consistent with k_3 , having the value $2.5 \times 10^{-5} (k_5)^{1/2} M^{-1/2}$

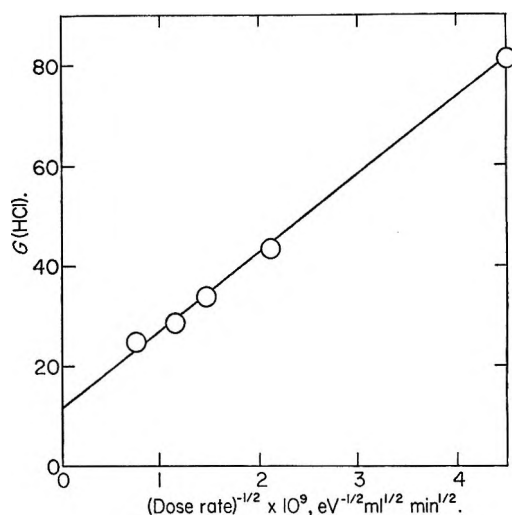


Figure 2. Effect of dose rate on the dechlorination of DDT in 2-propanol.

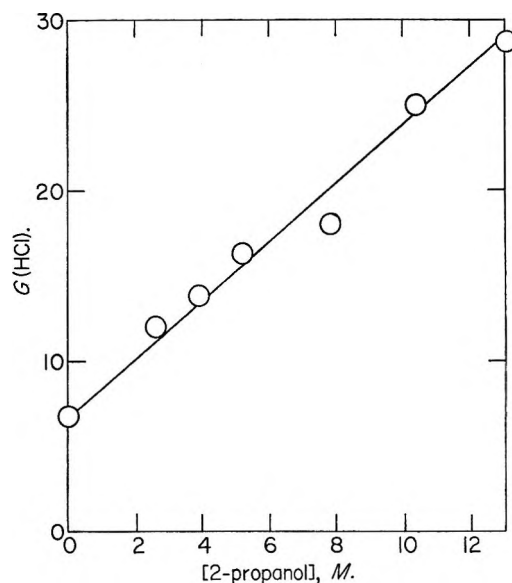


Figure 3. Dechlorination yield as a function of 2-propanol concentration in the mixed solvent 2-propanol-*tert*-butyl alcohol. Dose rate, $7.5 \times 10^{17} \text{ eV ml}^{-1} \text{ min}^{-1}$. (Note that pure 2-propanol is 13 M.)

$\text{sec}^{-1/2}$. The upper limit for reaction of two DDT radicals is a diffusion-controlled process ($k_5 = 3 \times 10^9 M^{-1} \text{ sec}^{-1}$),⁶ hence $k_3 \leq 1 M^{-1} \text{ sec}^{-1}$.

It is interesting to note that the value for k_3/k_5 is an order of magnitude lower than the analogous rate-constant ratio obtained for carbon tetrachloride in 2-propanol.² The lower propensity for DDT radicals to undergo hydrogen abstraction (in competition to dimerization/disproportionation) compared with trichloromethyl radicals is reflected in the results obtained in our laboratory on the radiolysis of DDT in cyclohexane.

(6) Calculated using the simplified Debye expression [P. Debye, *Trans. Electrochem. Soc.*, **82**, 265 (1942)].

Dechlorination yields were typical of those obtained from cyclohexane solutions of a halogenated hydrocarbon which does not undergo chain dechlorination.⁷ Carbon tetrachloride under the same conditions undergoes chain dechlorination principally to chloroform.⁷ Mosier, Guenzi, and Miller have found that when subjected to 2537-Å photolysis in *n*-hexane, DDT undergoes dechlorination with quantum yield of less than unity.⁸ While they conclude that the low quantum yield indicates a nonchain free-radical process must be responsible for the observed dechlorination, it may be argued that the observed low quantum yield could be a consequence of an inefficient initiation step in a chain mechanism (recombination of primary chlorine atom and DDT radical). In the radiolytic reaction, chain initiation occurs not principally *via* radicals formed in pairs, but rather singly *via* a dissociative electron capture process.^{5b} Hence our results on the radiolysis of DDT in cyclohexane are more substantial evidence that

DDT radicals do not enter into a chain process in alkane solvents.

Chain dechlorination of DDT in 2-propanol solution has also been observed in preliminary experiments in our laboratory in which chain-initiating free radicals were generated photochemically either by direct photolysis of DDT at 2537 Å or long wavelength (>3000 Å) photolysis of dissolved di-*tert*-butyl peroxide. The results seem to be compatible with the mechanism proposed for the radiolytic reaction.

Acknowledgments. This work was supported in part by grants from the Petroleum Research fund administered by the American Chemical Society and the Committee on Organized Research of Chicago State University. We are grateful to the Chemistry Division, Argonne National Laboratory, for use of the cobalt facility.

(7) J. A. Stone and P. J. Dyne, *Can. J. Chem.*, **42**, 669 (1964).

(8) A. R. Mosier, W. D. Guenzi, and L. L. Miller, *Science*, **164**, 1083 (1969).

An Electron Spin Resonance and Electron Nuclear Double Resonance Study of the 4-Formyl-2,6-di-*tert*-butylphenoxy Radical

by Robert D. Allendoerfer* and Daniel J. Eustace

Department of Chemistry, State University of New York at Buffalo, Buffalo, New York 14214
(Received January 21, 1971)

Publication costs assisted by the Petroleum Research Fund

The electron nuclear double resonance (ENDOR) and esr spectra of the 4-formyl-2,6-di-*tert*-butylphenoxy radical are interpreted as a function of temperature and the strong temperature dependence of the formyl proton coupling ascribed to torsional oscillations of the formyl group. An empirical correlation between ENDOR intensity and proton type is also presented.

Introduction

There have been several reports in the past of the observations of the 4-formyl-2,6-di-*tert*-butylphenoxy radical by esr,¹⁻⁴ but with widely varying values of the hyperfine couplings reported. The hyperfine coupling of the 4-formyl proton is of particular interest because it is expected to be very sensitive to the conformation of the molecule. As the simplest member of the series of substituted phenoxy radicals studied by Kreilick,⁴ the temperature dependence of this coupling should serve as a model for that observed in other members of the series. However, because of the complex nature of the esr spectra previously obtained, this effect has not been studied. Using the inherently simpler ENDOR spectra,

we have been able to follow this coupling over an extensive temperature range and to correlate the observed variations with conformational changes through Hückel molecular orbital theory.

One difficulty in using ENDOR spectra to interpret esr data is that the ENDOR transitions are not predicted to have the same intensity per proton unless the magnetic

(1) J. K. Becconsall, S. Clough, and G. Scott, *Proc. Chem. Soc.*, 308 (1959).

(2) J. K. Becconsall, S. Clough, and G. Scott, *Trans. Faraday Soc.*, **56**, 459 (1960).

(3) E. Müller, K. Ley, K. Scheffler, and R. Mayer, *Chem. Ber.*, **91**, 2682 (1958).

(4) R. W. Kreilick, *J. Amer. Chem. Soc.*, **88**, 5284 (1966).

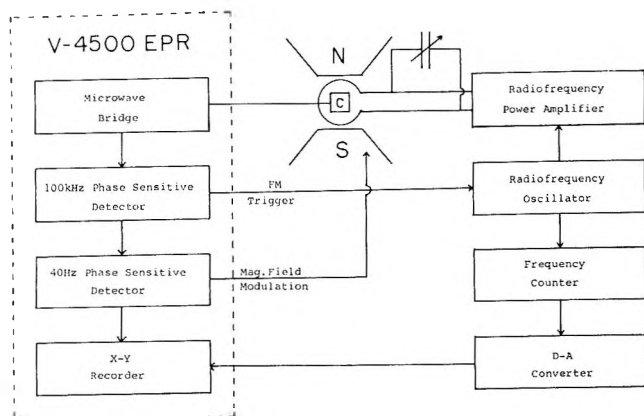


Figure 1. Block diagram of the endor spectrometer.

environments found by the nuclei are identical.^{5,6} We have collected relative intensity data for proton endor spectra from the literature and this experiment to look for trends related to the magnetic environment which might form useful criteria for assigning endor transitions to particular types of protons.

Experimental Section

The high-power cw endor spectrometer used in our experiments is similar to that described previously⁷ in principle; however, it differs from that previously described in that it may be viewed as an accessory to a popular commercial epr spectrometer. A block diagram of the spectrometer is given in Figure 1. No hard wired modifications of the Varian V-4502 epr spectrometer are necessary. The components on the right-hand side of the diagram are all commercially available and used without modification. The radio-frequency power amplifier is an Instrument for Industry Model 404A from which we obtain up to 500 W of power over the frequency range 1–200 MHz without switching or tuning. In the configuration shown, the RF coil is matched over the range 5–30 MHz. The experiments are normally run at 300 W output and a VSWR slightly less than 4 corresponding to 2–3 G radio-frequency magnetic fields at the microwave cavity. The oscillator, counter, and D-A converter are Hewlett-Packard Models 202H and 207H, 5245L, and 581A. Under normal operating conditions, the frequency modulated radiofrequency is swept through the resonance point and its effect on the esr signal is detected first by the 100-kHz phase sensitive detector which causes first derivative presentation of the enhancement signal and then at 40 Hz, the magnetic field modulation frequency, to remove any spurious radio-frequency signals. The peak-to-peak line widths of the first derivative spectra obtained on other spectrometers⁶ are generally in the range 50–100 kHz and thus great care must be taken when recording spectra to avoid distorting the lines if accurate first derivative presentation is desired. To choose the best FM

deviation and detection phase, we have followed the following procedure. With the FM deviation adjusted to a modulation index of about 1, distortion due to modulation side bands is readily apparent if the phase of the 100-kHz phase sensitive detector is not exactly in phase with the modulation so the detector phase is adjusted to remove this distortion. If the FM deviation is greater than the line width, the derivative peak remains split in the center with barely observable side bands on each side and this distortion is removed by decreasing the deviation until it is less than 25% of the peak-to-peak line width. In no case can modulation indices much greater than 2 be used because too much power is lost to higher order side bands and they severely distort the spectrum at all detector phase angles.

The mechanism of and the reaction products obtained on oxidation of 3,5-di-*tert*-butyl-4-hydroxybenzaldehyde and 3,5-di-*tert*-butyl-4-hydroxytoluene have been the subject of considerable discussion.⁸ We originally attempted to prepare the formyl-phenoxy radical by oxidation with PbO₂ following Becconsall, *et al.*,^{1,2} and obtained time-dependent spectra substantially in agreement with those they reported.² Careful examination of the spectrum of the first stable radical obtained, a simple 1:2:1 triplet, by esr and endor gave no hint of a hyperfine splitting due to the single formyl proton; in fact, no couplings less than the 1.86-G triplet could ever be resolved by esr. Careful drying of the solvent, cyclohexane, and the use of freshly prepared PbO₂ changed the results substantially. Under these conditions, oxidation of 3,5-di-*tert*-butyl-4-hydroxybenzaldehyde gave a triplet esr spectrum with a splitting of 2.1 G and each line was further split by a single proton, coupling about 0.4 G. This radical is green, stable indefinitely in frozen solution where it exists as a diamagnetic dimer, and has a half-life of about 1 day at room temperature in hexane solution. On further standing, it changes to the yellow radical whose 1.86-G triplet spectrum has been described above. These coupling constants are in complete agreement with those obtained by Kreilick,⁴ who also resolved the 19 *tert*-butyl lines. Thus we believe that the radical observed is indeed the 4-formyl-2,6-di-*tert*-butylphenoxy radical. The radical reported by Becconsall, *et al.*,² is apparently a secondary radical formed by further reaction at the carbon position para to the phenoxy oxygen. Since within the limits of resolution of endor spectroscopy we observe no proton couplings from groups attached to

(5) J. H. Freed, *J. Chem. Phys.*, **43**, 2312 (1965).

(6) R. D. Allendoerfer and A. H. Maki, *J. Magn. Resonance*, **3**, 396 (1970).

(7) A. H. Maki, R. D. Allendoerfer, J. C. Danner, and R. T. Keys, *J. Amer. Chem. Soc.*, **90**, 4225 (1968).

(8) A. R. Forrester, J. M. Hay, and R. H. Thomson, "Organic Chemistry of Stable Free Radicals," Academic Press, New York, N. Y., 1968, Chapter 7.

this carbon, we assume the radical is of the quinol ether-type dimer discussed by Forrester, *et al.*⁸ Becconsall, *et al.*,² also observed the same radical as a secondary product from oxidation of 3,5-di-*tert*-butyl-4-hydroxytoluene and we have confirmed this result. However, it should be noted that this radical with the 1.86-G triplet splitting is not the 4-formyl radical and the implications about the oxidation mechanism of 3,5-di-*tert*-butyl-4-hydroxytoluene (BHT) drawn from this work by many succeeding authors are thus incorrect.

Results

The difficulty in interpreting endor spectra when intensities must be relied on for the assignment of couplings to molecular positions is strikingly apparent from the endor spectrum of the 4-formyl-2,6-di-*tert*-butylphenoxy radical. Figure 2 shows the spectrum obtained from a 10^{-3} M solution in mineral oil taken at room temperature. By comparison with Kreilick's⁴ esr data, the pair of lines at 12 and 18 MHz come from the two meta-ring protons, the outer pair of the central quartet from the formyl proton, and the innermost pair from the 18 *o*-*tert*-butyl protons. Thus one might have expected intensity ratios of 2:1:18 rather than the 2:0.37:0.35 obtained. For hyperfine couplings greater than about 1 G, the RF enhancement effect⁹ makes the high-frequency line of an endor pair more intense than the low one so we have used the average intensity of each pair in our comparisons. This averaging also tends to reduce the effects of varying RF field intensity caused by the varying impedance match of the RF amplifier to the RF coil. Allendoerfer and Maki⁶ have suggested that endor intensities ought to be corrected for overlap of the esr transitions involved by

$$I = I_0 \frac{(T_2 \Delta \omega)^2}{(T_2 \Delta \omega)^2 + 2.5} \quad (1)$$

where T_2 is the spin-spin relaxation time and $\Delta \omega$ the hyperfine coupling constant. This requires knowledge of T_2 which is not directly available from the esr spectrum since in mineral oil, $1/T_2$ is greater than the *tert*-butyl group coupling constant (0.075 G); however, $1-3 \times 10^{-7}$ sec appears to be a reasonable estimate for T_2 in this solvent.⁶ An arbitrary choice of 1.7×10^{-7} sec for T_2 gives intensity ratios of 2:0.34:0.36 in remarkable agreement with those observed.

Measurement of the temperature dependence of the hyperfine couplings in this radical is complicated by the reversible dimerization which occurs on cooling and by increasingly rapid radical decay on heating. ESR spectroscopy is sufficiently sensitive to observe the radical in equilibrium with its dimer down to -90° in hexane; however, the spectrum is not fully resolved unless the formyl proton coupling is an integral multiple of the *tert*-butyl coupling. This resolution point is strongly temperature and solvent dependent,

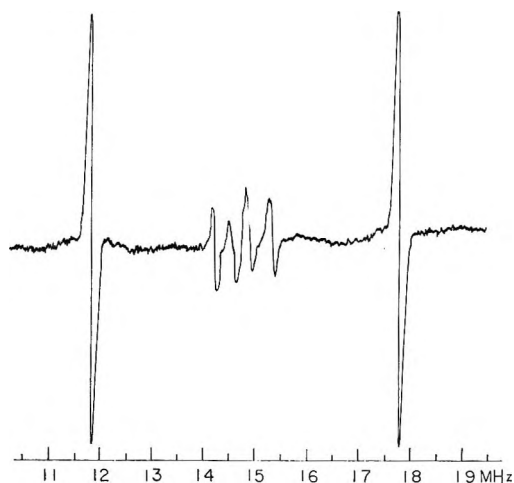


Figure 2. The endor spectrum of the 4-formyl-2,6-di-*tert*-butylphenoxy radical.

occurring with $a^{\text{H}}_{\text{formyl}} = 5 \times a^{\text{H}}_{\text{tert-butyl}}$ at 10° in hexane but at room temperature in cyclohexane, for example. We believe this behavior explains the widely varying spectral resolutions reported in the past and that because of this effect, this type of radical is a poor choice for resolution comparisons between spectrometers.

Using a combination of esr and endor we have been able to follow the temperature dependence of the couplings in the 4-formyl-2,6-di-*tert*-butylphenoxy radical over a range of 110° . The actual measurements are from calibrated esr spectra using approximate endor obtained values to interpret the spectra. The meta ring protons and *o*-*tert*-butyl groups behave similarly to those previously reported for the 2,4,6-tri-*tert*-butylphenoxy radical⁶ and thus we believe reflect only changes in the σ - π interactions responsible for the splittings and do not indicate any conformational change in the molecule. On the other hand, the temperature dependence of the formyl group is much stronger than predicted by this type of consideration. Figure 3 shows this effect for a 10^{-3} M solution in hexane.

Discussion

Becconsall, *et al.*,² speculated that their inability to resolve the 4-formyl proton was due to its lying parallel to the plane of the benzene ring and therefore at a node in the π -molecular orbital containing the unpaired electron while Kreilick⁴ felt that the small splitting observed could only be accounted for by a substantial twist of the formyl group with respect to the plane of the benzene ring. An INDO calculation¹⁰ of this splitting gave a result an order of magnitude too large, so we have

(9) S. Geschwind, "Hyperfine Interactions," A. J. Freeman and R. B. Frankel, Ed., Academic Press, New York, N. Y., 1967.

(10) D. J. Eustace, Senior Thesis, State University of New York at Buffalo, 1970.

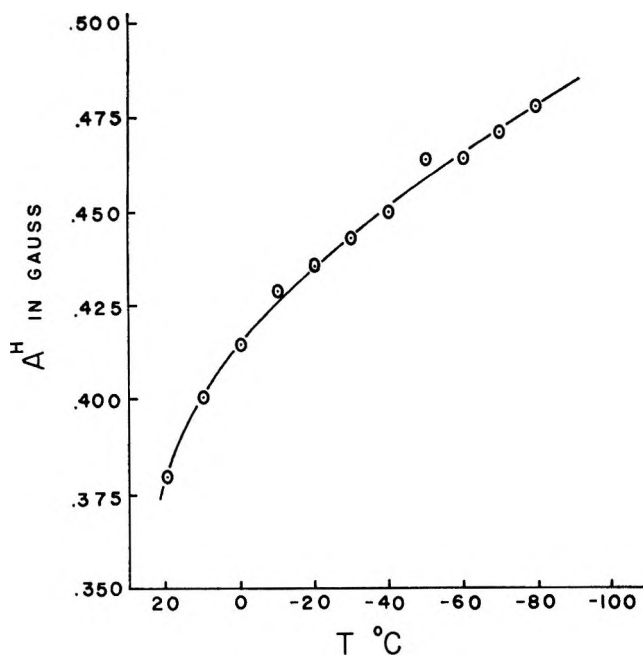


Figure 3. Temperature dependence of the formyl proton coupling constant.

attempted to calculate this splitting using McLachlan's modification of HMO theory.¹¹ The values of Q , λ , and the MO parameters for the phenoxy oxygen were chosen to fit the hyperfine couplings of the phenoxy radical¹² exactly. This problem is overdetermined so the actual values used are of little interest since many sets give the same result. Next, parameters describing the *tert*-butyl groups were taken from Trapp, *et al.*,¹³ and those for the formyl group from a standard text.¹⁴ Using the value of the resonance integral (β) for the formyl carbon to four-ring carbon as our only undetermined variable we can match the observed hyperfine splitting for the formyl proton over the whole range of temperature studied, assuming the coupling is positive, by varying this β from 0.75 to 1.00. We interpret this decrease in β with increasing temperature as indicating torsional oscillations of the formal group of increasing amplitude with increasing temperature. Stone and Carrington¹⁵ have proposed a similar explanation for the temperature dependence of the 4-amino-2,6-di-*tert*-butylphenoxy radical spectrum. Assuming $\beta = \beta_0 \cos \theta$,¹⁴ we find a mean deviation from planarity of about 40° at room temperature and no measurable oscillation at -90°.

Our observation that once the overlap correction⁶ has been made all the protons in the 4-formyl-2,6-di-*tert*-butylphenoxy radical have the same endor intensity per proton deserves some further comment since this also appears to be the case for many other radicals as well. Freed's theory of the endor enhancement⁵ predicts a very complicated dependence of the relative endor intensities on the magnetic environment and it is thus somewhat surprising that none is found. Apparently

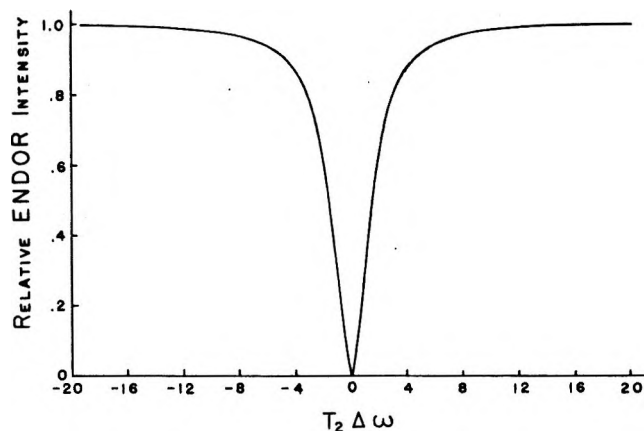
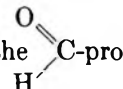


Figure 4. Relative endor intensities as a function of $T_2\Delta\omega$.

the effects he describes fortuitously cancel each other in our particular case. In collecting other data from the literature that bear on this point, we have found it necessary to employ Allendoerfer and Maki's overlap correction⁶ on some of the smaller splittings. The effect of this correction is illustrated in Figure 4. It can be readily seen that unless the coupling constant is greater than about four times the line width, a substantial error is made by neglecting it.

Correcting the intensity data as suggested above, we find that the CH_3 protons in the *p*-tolyl-diphenylmethyl radical and many related radicals^{16,17} have the same intensity per proton as the aromatic ones. This same result is obtained for the CH_3O protons in bis(*p*-methoxyphenyl) nitroxide,¹⁸ the $(\text{CH}_3)_3\text{C}$ protons in the tri-

tert-butylphenoxy radical⁶, and herein for the 

ton in the 4-formyl-2,6-di-*tert*-butylphenoxy radical. Thus we have found no deviations in the intensity per proton for the endor signals relating to the class of proton or type of radical. Endor signals are inherently noisy and in some instances the relative intensities cannot be measured to better than 25%. The value of T_2 used in eq 1 and eq 1 itself are only approximations which might well be in error by 50% so the agreement found above should not be taken as confirming or disagreeing with the theories put forward by Freed, *et al.*⁵

(11) A. D. McLachlan, *Mol. Phys.*, **3**, 233 (1960).

(12) P. B. Sogo, M. Nakazaki, and M. Calvin, *J. Chem. Phys.*, **26**, 1343 (1957).

(13) C. Trapp, C. A. Tyson, and G. Giacometti, *J. Amer. Chem. Soc.*, **90**, 1394 (1968).

(14) A. Streitwieser, "Molecular Orbital Theory for Organic Chemists," Wiley, New York, N. Y., 1961.

(15) A. J. Stone and A. Carrington, *Trans. Faraday Soc.*, **61**, 2593 (1965).

(16) R. D. Allendoerfer and A. H. Maki, *J. Amer. Chem. Soc.*, **91**, 1088 (1969).

(17) L. D. Kispert, J. S. Hyde, C. deBoer, D. LaFollette, and R. Breslow, *J. Phys. Chem.*, **72**, 4276 (1968).

(18) R. D. Allendoerfer and J. H. Engelmann, *Mol. Phys.*, **20**, 569 (1971).

The usefulness of the correlation suggested above is, we feel, best illustrated by reference to the 4-formyl-2,6-di-*tert*-butylphenoxy radical. At first glance the relative intensities of the formyl and *tert*-butyl endors appear to be different by 1800% and the overlap correction has reduced this to 12%. Similar use of this equation, we feel, will greatly simplify the interpretation of other endor spectra.

In rigid media¹⁹ and in hydrocarbon solvents cooled near their freezing points²⁰ methyl groups have been observed to give stronger endor signals than aromatic protons and this has been interpreted as being caused by differences in the electron-nuclear dipolar interaction for these two types of protons. Thus the above simpli-

fied method of interpreting endor spectra must be restricted to the free tumbling region where the dipolar coupling of the rigidly fixed protons is also rapidly averaged.

Acknowledgments. Acknowledgment is made to the donors of the Petroleum Research Fund, administered by the American Chemical Society, and to the Research Foundation of the State University of New York for support of this work.

(19) J. S. Hyde, G. H. Rist, and L. E. G. Eriksson, *J. Phys. Chem.*, **72**, 4269 (1968).

(20) K. Mobius, H. van Willigen, and A. H. Maki, *Mol. Phys.*, **20**, 289 (1971).

An Electron Spin Resonance Line-Shape Analysis for Determination of Unresolved Metal Hyperfine Splittings in Ion Pairs. Its Application to the Benzene Anion Radical¹

by M. T. Jones,* M. Komarynsky, and R. D. Rataiczak

Department of Chemistry, University of Missouri—St. Louis, St. Louis, Missouri 63121 (Received February 18, 1971)

Publication costs assisted by the National Science Foundation

A line-shape analysis is presented which allows the extension of the study of ion pairing into the spectral region where the metal hyperfine splitting (hfs) can no longer be resolved. The analysis allows one to quantitatively evaluate the metal hfs and the component line widths from experimentally measured line shapes and line widths. The utility of the analysis procedure is demonstrated by its application to the benzene anion radical. The unresolved metal hfs in the benzene anion radical ranges from -75 mG at -120° to $+150$ mG at -30° . The component line widths are found to range from ~ 200 mG at -120° to ~ 650 mG at -30° .

Introduction

There has been considerable interest in the use of esr techniques to study ion-pairing effects.² To date, it has been necessary to explicitly resolve the metal hyperfine splitting (hfs) in order to study such effects. Although, very recently certain changes in g values have also been associated with ion pairing.³ A line-shape analysis is presented which will allow the extension of the study of ion pairing into the spectral region where the metal hfs can no longer be resolved. The analysis allows one to quantitatively evaluate the metal hfs and the component line width (hence to obtain the "true" T_2) from experimentally measured line shapes and line widths. The utility of the analysis procedure will be demonstrated by its application to the benzene anion radical.⁴

The underlying basis of the analysis procedure is the fact that esr spectral line shapes are strongly dependent upon the metal hfs even when the individual components are not resolved. The analysis consists of determining precisely what the line shape looks like as the metal hfs increases from zero to the point where the individual

(1) Presented at the Second Symposium on Electron Spin Resonance held at the University of Georgia, Athens, Georgia, Dec 1970.

(2) (a) See for example E. de Boer, *Recl. Trav. Chim. Pays-Bas*, **84**, 609 (1965); (b) N. M. Atherton and S. I. Weissman, *J. Amer. Chem. Soc.*, **82**, 2537 (1960); (c) N. Hirota, *ibid.*, **90**, 3603 (1968); (d) M. T. Jones and D. E. Zeller, *J. Chem. Phys.*, **48**, 334 (1968); (e) N. Hirota in "Radical Ions," E. T. Kaiser and L. Kevan, Ed., Interscience, New York, N. Y., 1968, Chapter 2; (f) I. B. Goldberg and J. R. Bolton, *J. Phys. Chem.*, **74**, 1965 (1970).

(3) (a) C. L. Dodson and A. H. Reddock, *J. Chem. Phys.*, **48**, 3226 (1968); (b) W. G. Williams, R. J. Pritchett, and G. K. Fraenkel, *ibid.*, **52**, 5584 (1970).

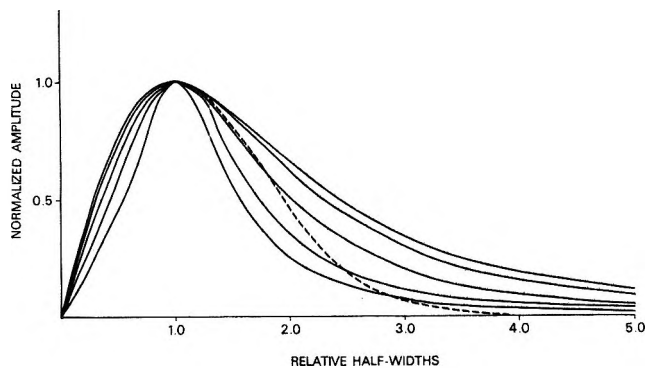


Figure 1. Normalized plot of half of the derivative of the resonance line shape for various ratios of hfs to ΔH_C . The individual components consisted of four equally intense Lorentzian shaped lines. The values of the ratio $hfs/\Delta H_C$ shown are 0, 0.17, 0.34, 0.52, and 0.69 in order of decreasing amplitude in the wings. The dotted line represents a pure Gaussian line shape.

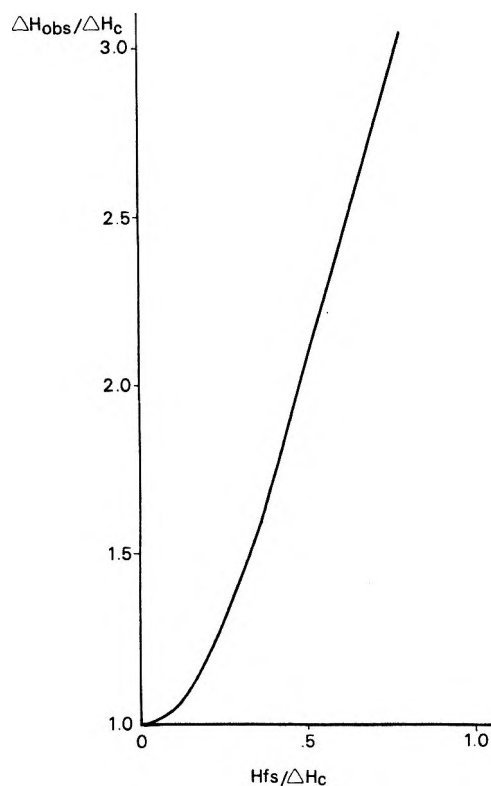


Figure 2. Plot of the ratio of the calculated line width (ΔH_{obsd}) to the individual component line width (ΔH_C) vs. the ratio of $hfs/\Delta H_C$. The individual components consisted of four equally intense Lorentzian shaped lines. When the ratio $hfs/\Delta H_C \geq 0.86$ the individual component lines just begin to be resolved.

components just begin to become resolved. For the calculations described here, it is assumed that the lifetime of the cation-anion pair is long compared with the inverse of the metal hfs .

Experimental Details and Results

The spectral line shapes were simulated for an esr

line which consists of n closely spaced individual component lines. For example, in the case of ion-pair formation with a single sodium ion, four equally intense component lines are used. The simulation calculations were performed in such a manner that errors due to truncation of the individual component lines fell outside of the region of interest. The density of points calculated was such that the percentage of error associated with picking the correct half-width at extreme slope ranged from $\pm 1\%$ when $(hfs/\Delta H_C) = 0$ to $\pm 0.25\%$ when $(hfs/\Delta H_C) = 1.0$ and $\pm 0.5\%$ when $(hfs/\Delta H_C) = 0$ to $\pm 0.3\%$ when $(hfs/\Delta H_C) = 1.6$ for Lorentzian and Gaussian component line shapes, respectively. The component line width is given by ΔH_C . Figure 1 shows normalized plots of half of the derivative of the resonance line shape for various ratios of hfs to ΔH_C starting with four equally intense Lorentzian-shaped components. The data in Figure 1 show that as the hfs increases from zero relative to ΔH_C the line shape becomes less and less Lorentzian. It falls off in the wings much more rapidly than a Lorentzian. For $hfs/\Delta H_C$ ratios > 0.6 the line shape falls off even more rapidly than a single Gaussian component. Similar behavior is observed when Gaussian components are used except that their limiting line shape is a Gaussian and they fall off more rapidly than a Gaussian in the wings as the ratio of $hfs/\Delta H_C$ is increased.

Figure 2 shows a plot of the ratio of the calculated line width (ΔH_{obsd}) to the individual component line width (ΔH_C) vs. the ratio of $hfs/\Delta H_C$. One notes that as the ratio of $hfs/\Delta H_C$ is increased so too is ΔH_{obsd} . A similar result is observed when Gaussian components are used. The results shown in Figures 1 and 2 are changed by an insignificant amount if one chooses instead of four equally intense lines, two sets of four equally intense lines with relative intensity and relative hfs appropriate to the case of ion-pair formation with potassium ions instead of sodium.

The question immediately arises: are there ex-

(4) The suggestion that the benzene anion radical might be ion-paired is not original with the work reported here. However, the evidence presented leaves no doubt that the benzene anion radical in solution is ion-paired. Malinoski and Bruning⁶ first suggested that the benzene anion radical might be ion-paired on the basis of their studies of the rate of electron transfer between the benzene anion radical and neutral benzene and their attempts to simulate the electron transfer broadened esr spectra. Their suggestion was criticized by Kooser, Volland, and Freed⁶ (see their footnote 52a), who argued among other things that published simulated spectra (*cf.* Y. S. Ledev, *et al.*, "Atlas of Electron Spin Resonance Spectra," Consultants Bureau, New York, N. Y., 1963) decayed more slowly in the wings than did a pure Lorentzian line shape which was contrary to experiment. Subsequently, Das, Wagner, and Freed⁷ on the basis of more experimental evidence revised their criticism of Malinoski and Bruning's suggestion. Apparently, their revision includes a reinterpretation of the simulated spectra of Lebedev, *et al.*, which now agrees qualitatively with experiment and with the results reported in this paper.

(5) G. L. Malinoski and W. H. Bruning, *Angew. Chem., Int. Ed. Engl.*, **7**, 953 (1968); *J. Chem. Phys.*, **50**, 3637 (1969).

(6) R. G. Kooser, W. V. Volland, and J. H. Freed, *ibid.*, **50**, 5243 (1969).

(7) M. R. Das, S. B. Wagner, and J. H. Freed, *ibid.*, **52**, 5404 (1970).

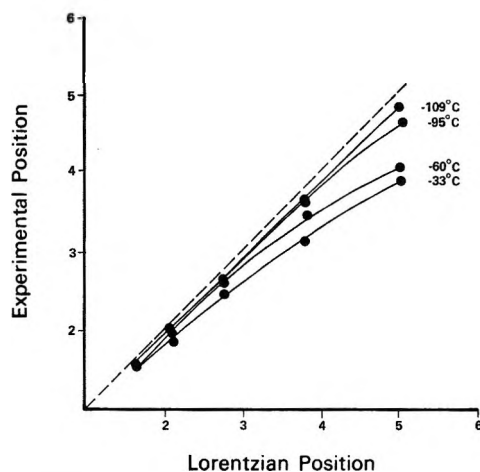


Figure 3. Line shape of the $M_H = 0$ component in the first derivative esr spectrum of the benzene anion radical in 2:1 (THF-DME) solvent (0.3 M benzene) at different temperatures. The dashed line traces the locus of the Lorentzian line. See text for details of measurement.

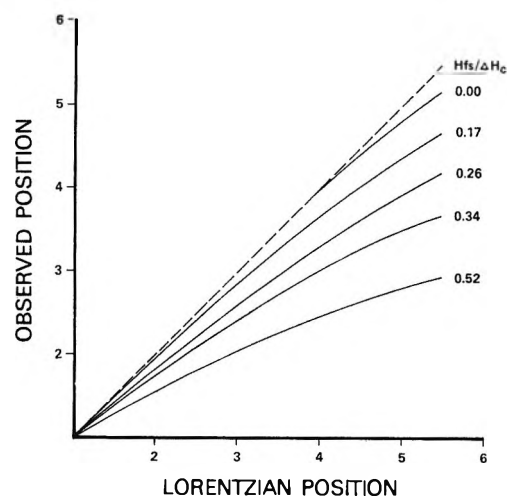


Figure 5. Plot of the "observed" or "calculated" resonance line position vs. the "theoretical" Lorentzian position for a series of increasing values of the metal $hfs/\Delta H_C$ ratio. The ^{13}C $hfs/\Delta H_C$ ratio for the calculations shown here is 8.

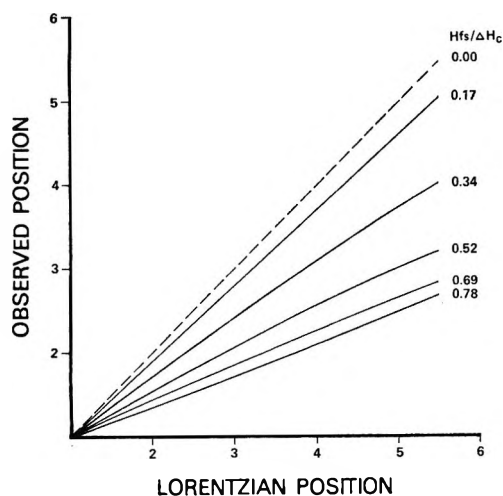


Figure 4. Plot of the "observed" or "calculated" resonance line position vs. the "theoretical" Lorentzian position for a series of increasing values of the metal $hfs/\Delta H_C$ ratio. The effect of ^{13}C hfs is not included.

amples of the behavior of line shapes as described above? The answer, of course, is yes. Past studies on very dilute water solutions ($9.5 \times 10^{-5} M$) of peroxyamine disulfonate anion radical have shown that the line shape is non-Lorentzian with a more rapid falloff in the wings.⁸ Figure 4 of ref 8 shows a normalized plot of the derivative of the resonance absorption curve of peroxyamine disulfonate anion radical in comparison with pure Lorentzian and Gaussian line shapes.⁹

Careful studies of the line shape of the benzene anion radical in solution show that (a) it is dependent upon the benzene concentration, (b) it is temperature dependent, and (c) it falls off more rapidly in the wings than does a Lorentzian line.^{6,7,10} This behavior is demonstrated in Figure 3 for a solution of the benzene anion radical in a 2:1 mixture of tetrahydrofuran and 1,2-dimethoxyethane which is 0.3 M in benzene.

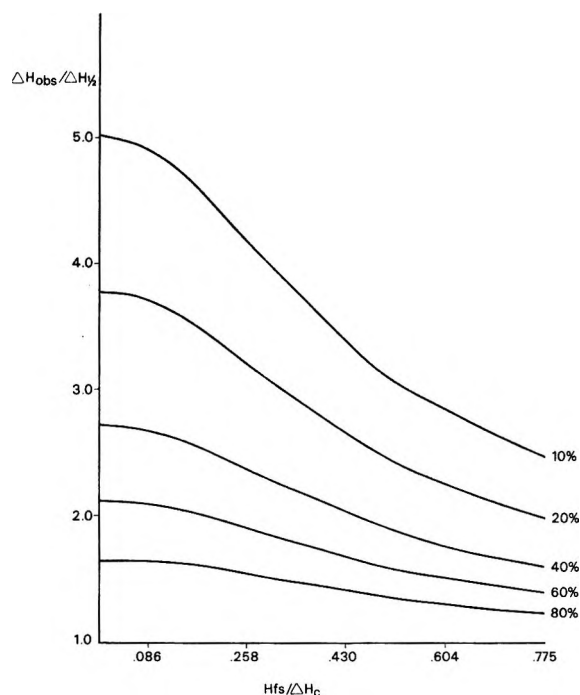


Figure 6. Plot of line positions in units of peak-to-peak half width vs. the metal $hfs/\Delta H_C$ ratio for various different relative heights. The effect of ^{13}C hfs is not included in this plot.

Figure 3 shows another way of looking at the information shown in Figure 1. On the ordinate is plotted the "observed" line position vs. that of a pure Lorentzian line for fixed percentages of the height. The analysis

(8) M. T. Jones, *J. Chem. Phys.*, **38**, 2892 (1963).

(9) While the analysis of the peroxyamine disulfonate spectra line shapes will not be considered further here, it is of interest and studies in our laboratory are underway.

(10) (a) R. D. Rataiczak, Ph.D. Thesis, St. Louis University, 1970; (b) R. D. Rataiczak and M. T. Jones, submitted for publication in *J. Chem. Phys.*

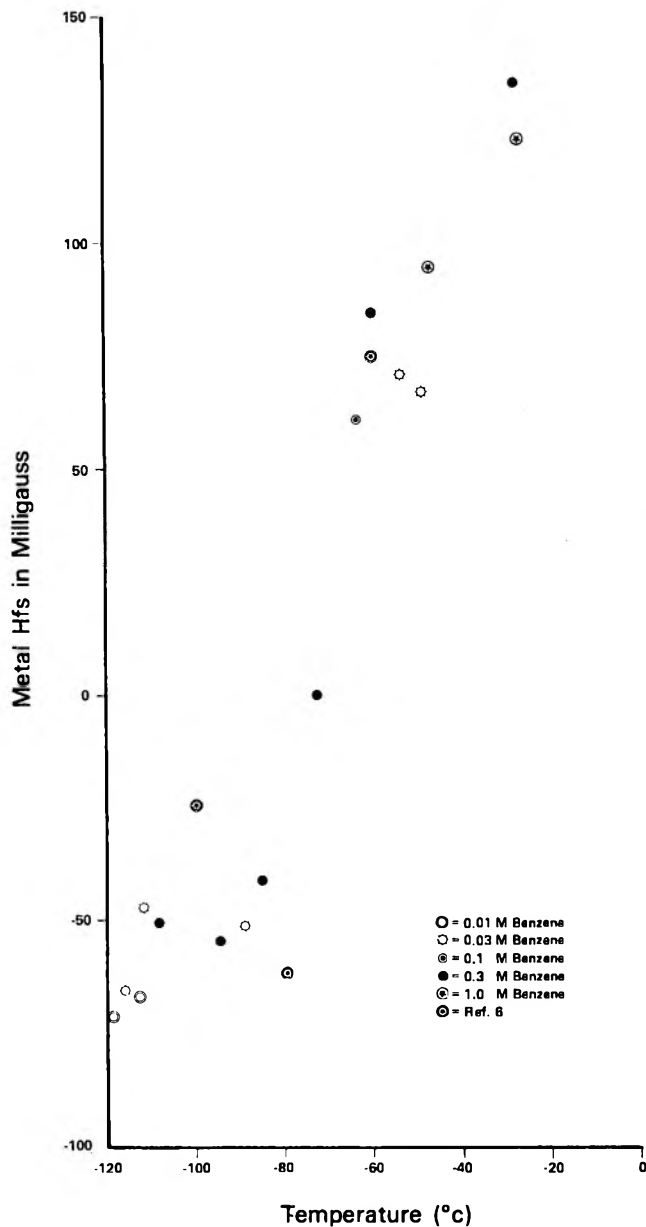


Figure 7. Plot of the metal hfs vs. temperature for a series of different benzene concentrations.

procedure consists of marking off the base line in units of $1/2$ the peak-to-peak width. The height of the curve is marked off in percentage of the maximum height (which occurs at $\pm 1/2$ the peak-to-peak width) from the base line. The distance (normalized with respect to $1/2$ the peak-to-peak width) from the center of the resonance line to the decaying wing at a given percentage of the height is measured and plotted as shown in Figure 3 against the corresponding value for a pure Lorentzian line. A pure Lorentzian line shape yields points which fall along the dashed line.

Whereas the data plotted in Figure 3 are "experimental," the data shown in Figures 4 and 5 are obtained from calculations of the expected line shape of the central line in the benzene anion radical excluding and including the effect of the hfs arising from the natural

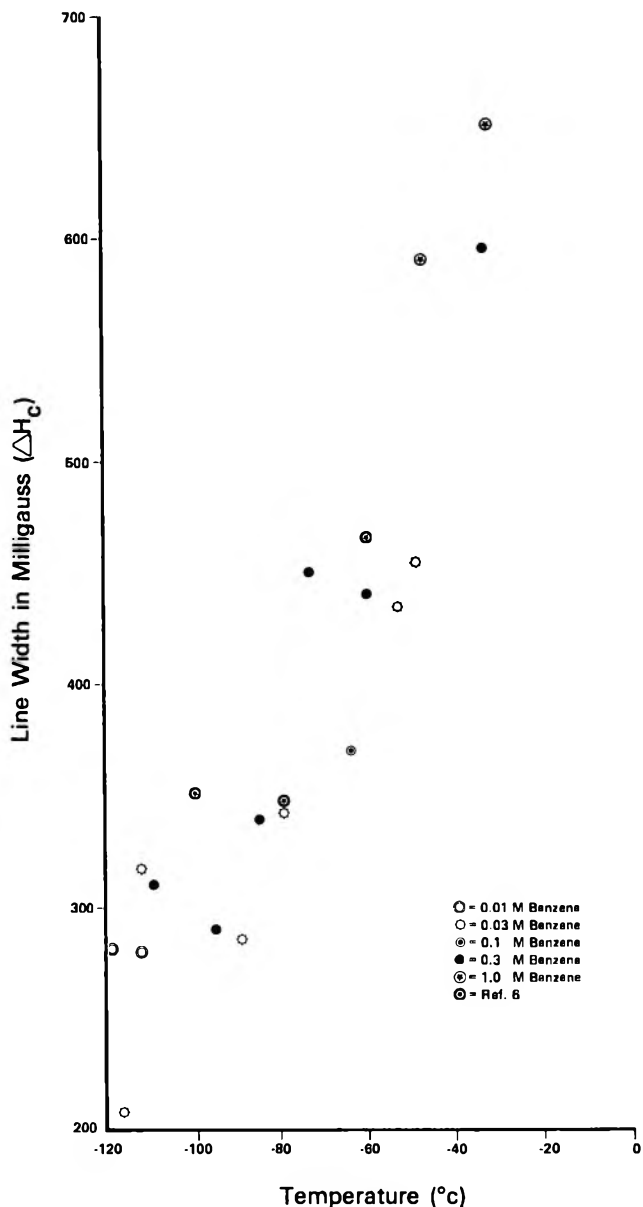


Figure 8. Plot of component line width (ΔH_C) vs. temperature for a series of different benzene concentrations.

abundance of ^{13}C , respectively.¹¹ Note that in Figure 4 there are a series of straight lines coming out of the origin. The larger the ratio metal hfs/ ΔH_C the lower the slope. The inclusion of the effect of the ^{13}C hfs leaves a portion of the data in Figure 4 unchanged, namely that portion along the abscissa from 1 to approximately 3. For distances greater than 3 half-widths, the individual curves are pulled down toward the abscissa as shown in Figure 5. Note the good agree-

(11) J. R. Bolton, *Mol. Phys.*, **6**, 219 (1963), reports that the value of the ^{13}C hfs is $2.8 (\pm 0.1)$ G at -100° . Additional work in our laboratory shows that it is temperature dependent and that it increases with increasing temperature. This latter observation agrees with that of Danner and Maki¹² for the hexakis(trifluoromethyl)benzene anion radical. Our values are 2.70 G at -100° , 2.79 G at -80° , and 2.85 G at -62° .

(12) J. C. Danner and A. H. Maki, *J. Amer. Chem. Soc.*, **88**, 4297 (1966).

ment between the data shown in Figure 3 and those in Figure 5.

In Figure 6 is shown a plot of the data obtained from our calculations which allows a rather easy comparison of the calculations with experimental results. Line positions in units of half-widths are plotted *vs.* the ratio $\text{hfs}/\Delta H_C$ for a series or family of curves taken at different relative heights. Our calculations show that the positions associated with points at 80, 60, and 40% of the maximum height are not significantly perturbed by the presence of the ^{13}C hfs.¹³ Thus, we may safely compare "experimental" positions at 80, 60, and 40% of the maximum height with the curves shown in Figure 6. One obtains in this way the "best" fit of the experimental data and the value of the ratio $\text{hfs}/\Delta H_C$ at which it occurs. Using Figure 2, one can convert this ratio into a number which gives the ratio of the "observed" line width to the component line width. These two ratios plus the experimentally measured line width yield the information we are seeking, namely, the metal hfs and the component line width.

Figure 7 shows the results of such an analysis for the metal hfs for a large range of benzene anion radical concentrations and temperatures. Of course, the analysis is not capable of determining the sign of the hfs, although we have plotted the data through the origin. There is no incontrovertible proof that the metal hfs does in fact change sign. However, one can argue in analogy with a number of other ion-paired radicals where the hfs values are known to go through zero.^{2a, 2c, 2f} It is significant that the metal hfs values are relatively independent of the benzene concentration and hence the benzene anion radical concentration.

This fact taken together with the fact that the method of analysis appears to work over such a large range of benzene and benzene anion concentrations suggests that the assumption, that the lifetime of the benzene anion radical-metal ion pair is long compared with the inverse of the metal hfs, is justified.¹⁴

Figure 8 shows a plot of the component line width *vs.* temperature for the same range of concentration as shown in Figure 7. The line widths are dependent upon concentration, although the scatter is larger than one might like to see. In addition, the temperature dependence appears to level off at about -80° . This is to be contrasted with the inhomogeneously broadened line which displays a minimum at -100° .¹⁰

Acknowledgment. The partial support of this research by the National Science Foundation through Grant GP-15619 is acknowledged. The support of the University of Missouri—St. Louis Computer Center is also acknowledged as is the support of R. D. R. by NASA through Grant No. Nsg(T)-74.

(13) Our calculations show that for ^{13}C $\text{hfs}/\Delta H_C$ ratios greater than 5 and metal $\text{hfs}/\Delta H_C$ ratios less than approximately 0.36 (as the former becomes larger so does the latter ratio) the presence of the ^{13}C hfs can be ignored in the analysis procedure. Very few spectra have been observed to date which do not fall into the above category.

(14) This observation is consistent with the low electron transfer rate between the benzene and the benzene anion radical observed by Malinoski and Bruning (ref 5) and suggests that the electron transfer takes place with the simultaneous transfer of the metal ion (see ref 10b for an extended discussion of this point). We plan further computer simulations which will include the effects of metal ion exchange and electron transfer. However, we are, at present, quite impressed with the success we have had to date by neglecting such effects and the lack of evidence that they need to be included for adequate spectra simulation.

An Infrared Study of Surface Properties of α -Chromia. I. Preparation and Adsorption of Water, Heavy Water, and Carbon Monoxide¹

by A. Zecchina, S. Coluccia, E. Guglielminotti, and G. Ghiotti

Istituto di Chimica Fisica dell'Università di Torino, Turin, Italy (Received October 19, 1970)

Publication costs assisted by the Consiglio Italiano delle Ricerche (C.N.R.)

Samples of α -chromia of high surface area and suitable for spectroscopic work have been prepared in a controlled manner. Crystals mainly expose the (001) face on which the adsorption of H₂O, D₂O, and CO has been studied. At low coverages, water adsorption at room temperature is dissociative and hydroxyl groups are formed. At higher coverages a nondissociative chemisorption is observed and discussed. Carbon monoxide is adsorbed onto surface Cr³⁺ ions to form σ adducts, and the adsorbed amount solely depends on surface dehydration.

Introduction

Ir studies have been reported of CO and CO₂ adsorbed on chromium oxide supported on silica and alumina,²⁻⁵ but no spectroscopic data are available concerning unsupported chromium oxide, both in the amorphous and in the crystalline form.

We chose to study the adsorptive properties of this oxide, because another study has been done in this laboratory dealing with chromium oxide supported on silica and also because this material should be very convenient for checking the application limits of Burwell's "surface coordinative unsaturation" theory.

Ir technique is particularly useful in this field, for in the spectroscopic assignment of adsorbed species the enormous amount of work done with coordination compounds can be used as a reference.

Unless otherwise stated, our experiments dealt with a microcrystalline form of α -Cr₂O₃, obtained from the thermal decomposition of ammonium dichromate. It is well known⁶ that in this way either an amorphous, nonstoichiometric modification or mixtures of that and a crystalline phase (α) can be obtained.

For this reason, special care has been spent in the preparation and characterization of the material, to get an oxide that is fully crystalline and reproducible. Both the sample preparation and the ir measurement technique will be carefully described.

Experimental Section

Sample Preparation and Characterization. Ammonium dichromate was decomposed *in vacuo*, as described by Harbard, *et al.*,⁶ yielding a dark, bulky powder of chromium oxide with a large excess of oxygen and exhibiting no X-ray diffraction lines due to crystalline phases.

This amorphous oxide was compressed, under a pressure of 100–120 kg/cm², into pellets of good mechanical resistance, that were about 0.2 mm thick and

contained approximately 10 mg of chromium oxide per square centimeter.

Since our aim was to check the surface properties of α -chromia, the amorphous samples were placed in an ir cell, described elsewhere,⁷ and underwent a thermal treatment in three steps whose final result was a reproducible crystalline modification. After each step, the state of the sample and its reproducibility were controlled by determining ir spectrum, BET surface area, X-ray diffraction spectrum, and electron micrographs.

The three steps of the thermal treatment are as follows: phase 1, 16 hr of sample activation at 400°, *in vacuo* (all vacuum treatments were carried out at a residual pressure $\leq 10^{-5}$ Torr); phase 2, 6 hr of sample crystallization at 400° under a 5×10^{-2} Torr pressure of oxygen, water vapor being condensed in a liquid nitrogen cold trap; phase 3, 4 hr of sample reduction at 400° with an excess of CO.

Physical characteristics of the material in the various phases can be summarized. Phase I: The amorphous starting material exhibits a very poor transparency in the infrared (see Figures 1 and 2, curve 1). At the end of this phase I, the spectrum is as reported in Figures 1 and 2, curve 6. Curves 2 to 5 refer to intermediate activation temperatures. The sample is brown in color and still completely amorphous. The BET surface area now ranges between 120 and 130 m²/g.

(1) All correspondence should be sent to E. Borello, Istituto di Chimica Fisica dell'Università di Torino, Turin, Italy.

(2) (a) E. Borello, A. Zecchina, C. Morterra, and G. Ghiotti, *J. Phys. Chem.*, **73**, 1286 (1969); (b) A. Zecchina, C. Morterra, G. Ghiotti, and E. Borello, *ibid.*, **73**, 1292 (1969).

(3) A. Zecchina, G. Ghiotti, C. Morterra, and E. Borello, *ibid.*, **73**, 1295 (1969).

(4) A. Zecchina, E. Guglielminotti, S. Coluccia, and E. Borello, *J. Chem. Soc. A*, 2196 (1969).

(5) L. H. Little and C. H. Amberg, *Can. J. Chem.*, **40**, 1997 (1962).

(6) E. H. Harbard and A. King, *J. Chem. Soc.*, 955 (1938).

(7) E. Borello, A. Zecchina, and M. Castelli, *Ann. Chim. (Rome)*, **53**, 690 (1963).

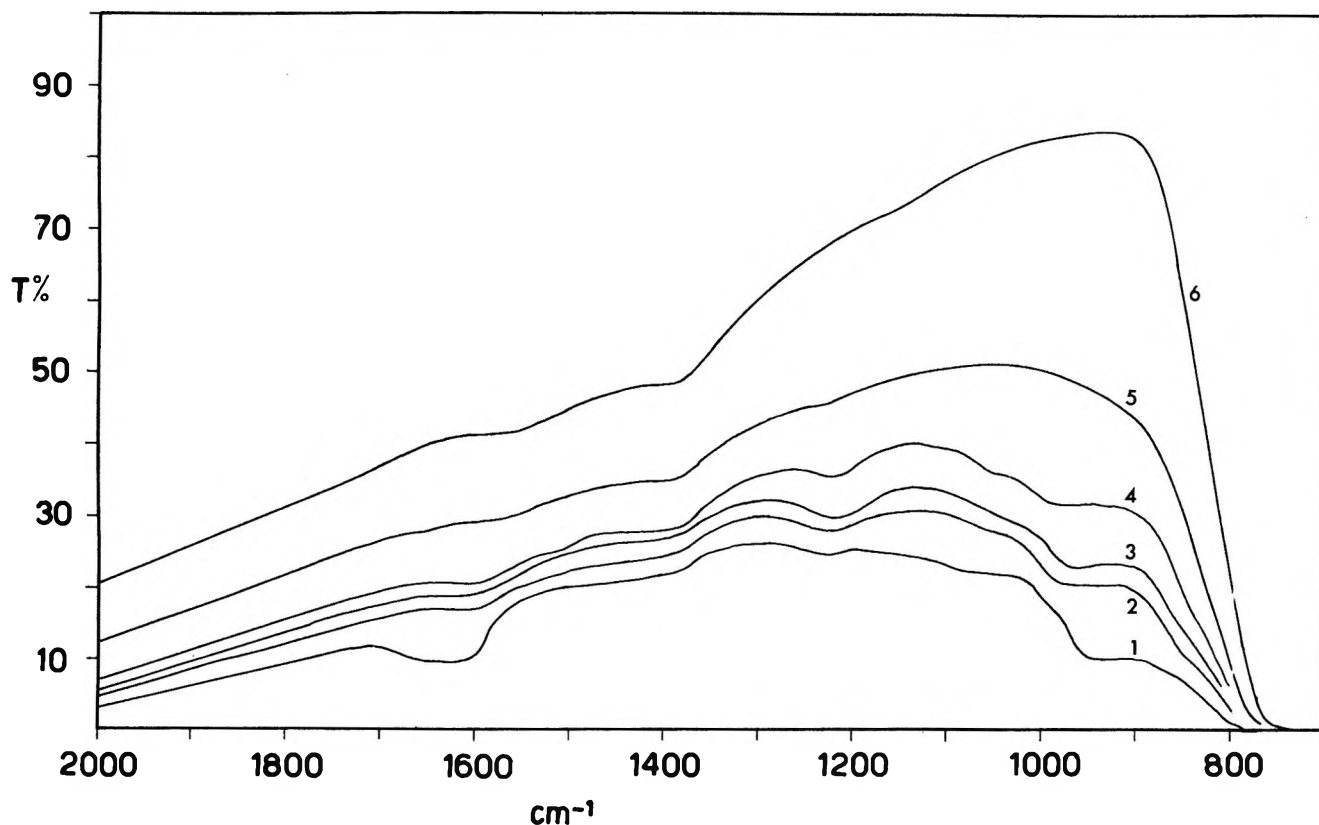


Figure 1. Infrared spectra of amorphous Cr_2O_3 (% transmission vs. wavelength in cm^{-1}): curve 1, before evacuation; curve 2, after evacuation at room temperature; curves 3-6, after degassing, times and temperatures being 1 hr at 100° , 1 hr at 200° , 1 hr at 300° , and 16 hr at 400° .

Light scattering phenomena still predominate in the high frequency range, so that spectra of Figure 2, obtained with wide slits and heavy reference beam screenings, are much poorer than spectra of Figure 1. Phase II: The infrared spectrum is now as reported in Figure 3, dotted line. Strong absorptions in the $1040\text{--}750\text{-cm}^{-1}$ range are due to chemisorbed oxygen and will be discussed elsewhere (part II). Oxygen contact at 400° has also caused the sample crystallization, as revealed by the presence of X-ray diffraction lines typical of α -chromia, just a little broader than usual, due to small crystal size. The color is now green; BET surface area is $60\text{--}70\text{ m}^2/\text{g}$ and the t-plot method⁸ does not reveal the presence of micropores. Electron microscopy shows crystals whose linear dimensions are in the $300\text{--}600\text{-\AA}$ range. The form is of very thin laminae of hexagonal or octagonal contour and (001) face is definitely predominant.⁹ Crystallization can be also promoted with higher oxygen pressures. The process is then faster and sometimes violent, but surface area of the final product falls in a wider range and in an unpredictable fashion. All these phenomena are quite well known¹⁰ and will not be discussed further. Phase III: Chemisorbed oxygen (bands in the $1040\text{--}750\text{-cm}^{-1}$ range) cannot be removed by degassing alone at 400° . Since we are interested in the adsorptive characteristics of pure chromia, the material is reduced at 400° with

CO (the gaseous phase is renewed several times), and then degassed at 400° to get rid of CO and CO_2 possibly chemisorbed. The final spectrum is reported in Figure 3, solid line. BET surface area has not changed during phase III.

The spectrum of microcrystalline chromia (Figure 3, solid line) exhibits a few bands, weak but well defined, in the $1300\text{--}750\text{-cm}^{-1}$ range, that are not present in the spectrum of amorphous chromia (Figure 1, curve 6). There is a general disagreement on the origin of these bands. Therefore, we have compared several samples that are quite different in surface area, crystallinity, nonstoichiometry, and degree of oxidation. Figure 4 shows the spectrum of an amorphous sample (BET surface area $130\text{ m}^2/\text{g}$), a microcrystalline sample free from chemisorbed oxygen (BET surface area $68\text{ m}^2/\text{g}$), a crystallized sample, obtained by sintering the microcrystalline one in air at about 900° , and a microcrystalline sample reduced with hydrogen and degassed at 800° (BET surface area $35\text{ m}^2/\text{g}$). This comparison led us

(8) G. A. Nicolaon, *J. Chim. Phys.*, **66**, 1783 (1969), and references therein.

(9) P. Groth, "Chemische Krystallographie," Wilhelm Engelmann, Leipzig, 1906.

(10) R. L. Burwell, Jr., G. L. Haller, K. C. Taylor, and J. F. Read, *Advan. Catal.*, **19**, 62 (1969).

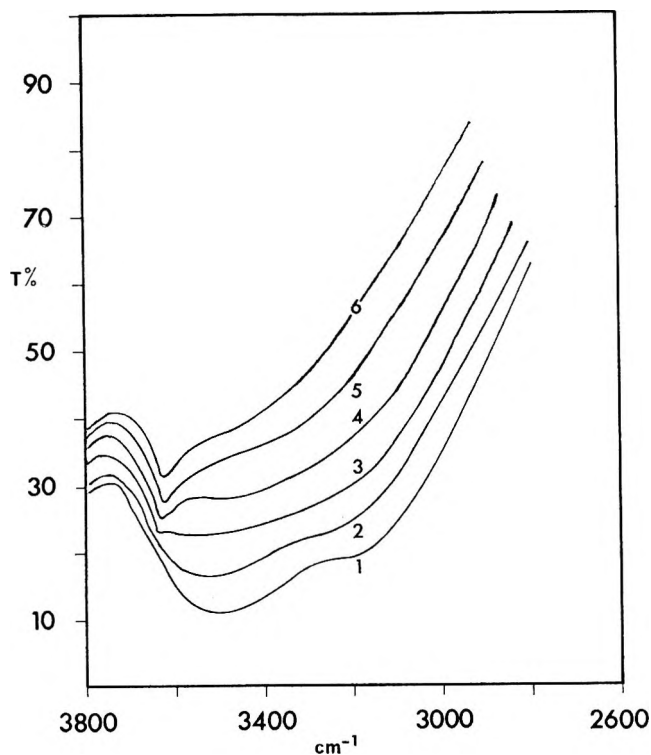


Figure 2. Infrared spectra of amorphous Cr_2O_3 (% transmission vs. wavelength in cm^{-1}): curve 1, before evacuation; curve 2, after evacuation at room temperature; curves 3-6, after degassing, times and temperatures being 1 hr at 100° , 1 hr at 200° , 1 hr at 300° , and 16 hr at 400° .

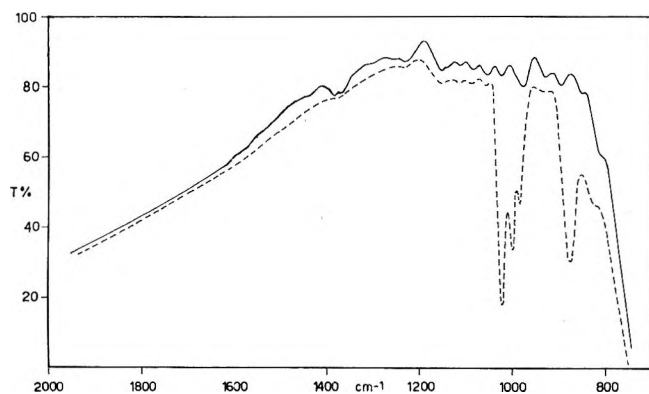


Figure 3. Infrared spectra of $\alpha\text{-Cr}_2\text{O}_3$ (% transmission vs. wavelength in cm^{-1}): -----, after phase II; —, after phase III (see text for definitions of phases II and III).

to a complete assignment of the bands in the $1300\text{--}750\text{-cm}^{-1}$ region.

Few adsorption experiments have been run at temperatures higher than 25° . So we thought it was useful to test the stability of the material, prepared by means of the three phases described, towards various gases at temperatures higher than room temperature. On repeating phase II and phase III four times, the surface area loss was lower than 5%. H_2O , D_2O , and CO_2 contacted with the material at temperatures up to

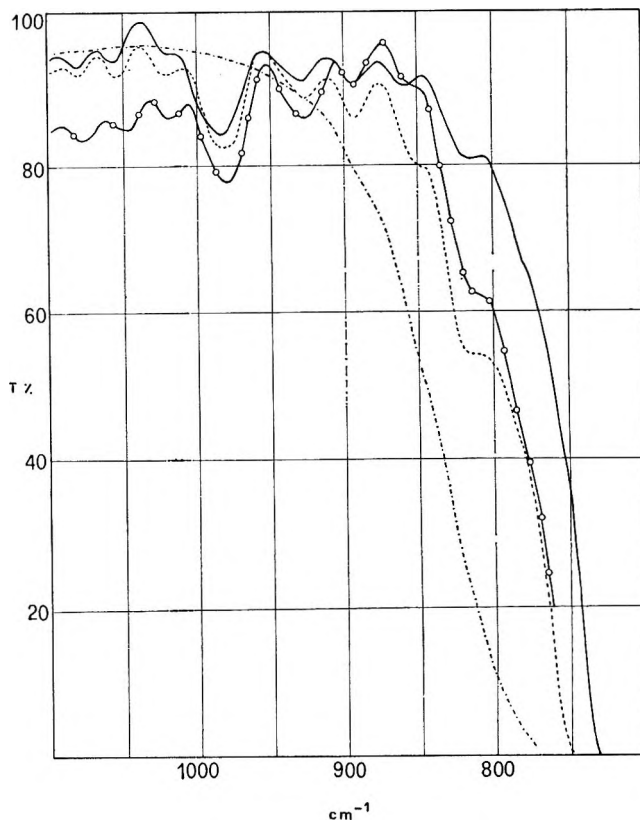


Figure 4. Infrared spectra of various Cr_2O_3 samples (% transmission vs. wavelength in cm^{-1}): —, sample sintered in air at 900° ; -O-O-, crystalline sample reduced in hydrogen at 800° (surface area: $35\text{ m}^2/\text{g}$); ·····, crystalline sample after phases I-III (surface area $68\text{ m}^2/\text{g}$); -·-·-, amorphous sample after phase I (surface area $130\text{ m}^2/\text{g}$).

400° had no effect on the surface area. A pressure of ~ 40 Torr of oxygen does not alter the microcrystalline material, provided the temperature is equal to or lower than 400° .

Spectroscopic Technique in the Study of Adsorption Phenomena. All the ir spectra have been recorded on a Beckman IR7 double beam spectrophotometer. Arbitrary 100% transmission lines have been obtained, range by range, by screening the reference beam. Spectral slit widths were $3\text{--}6\text{ cm}^{-1}$ in the $700\text{--}1800\text{-cm}^{-1}$ region, $6\text{--}10\text{ cm}^{-1}$ in the $1800\text{--}2000\text{-cm}^{-1}$ region, and $10\text{--}20\text{ cm}^{-1}$ in the $2000\text{--}3800\text{-cm}^{-1}$ region.

Water and CO Adsorption. Water vapor adsorption onto a microcrystalline sample (after phase III of the thermal treatments) gives rise to absorption in the following ranges: $3800\text{--}3000\text{ cm}^{-1}$, $1630\text{--}1580\text{ cm}^{-1}$, $1100\text{--}750\text{ cm}^{-1}$. Spectral determinations in the first range are very poor due to heavy light scattering. Therefore parallel experiments have been run with water and heavy water: in the latter case the first range is shifted to $2700\text{--}2000\text{ cm}^{-1}$, where better optical conditions allow reasonably good spectra to be recorded.

Figure 5a shows the spectra of α -chromia, on which adsorption of D_2O at room temperature (at different

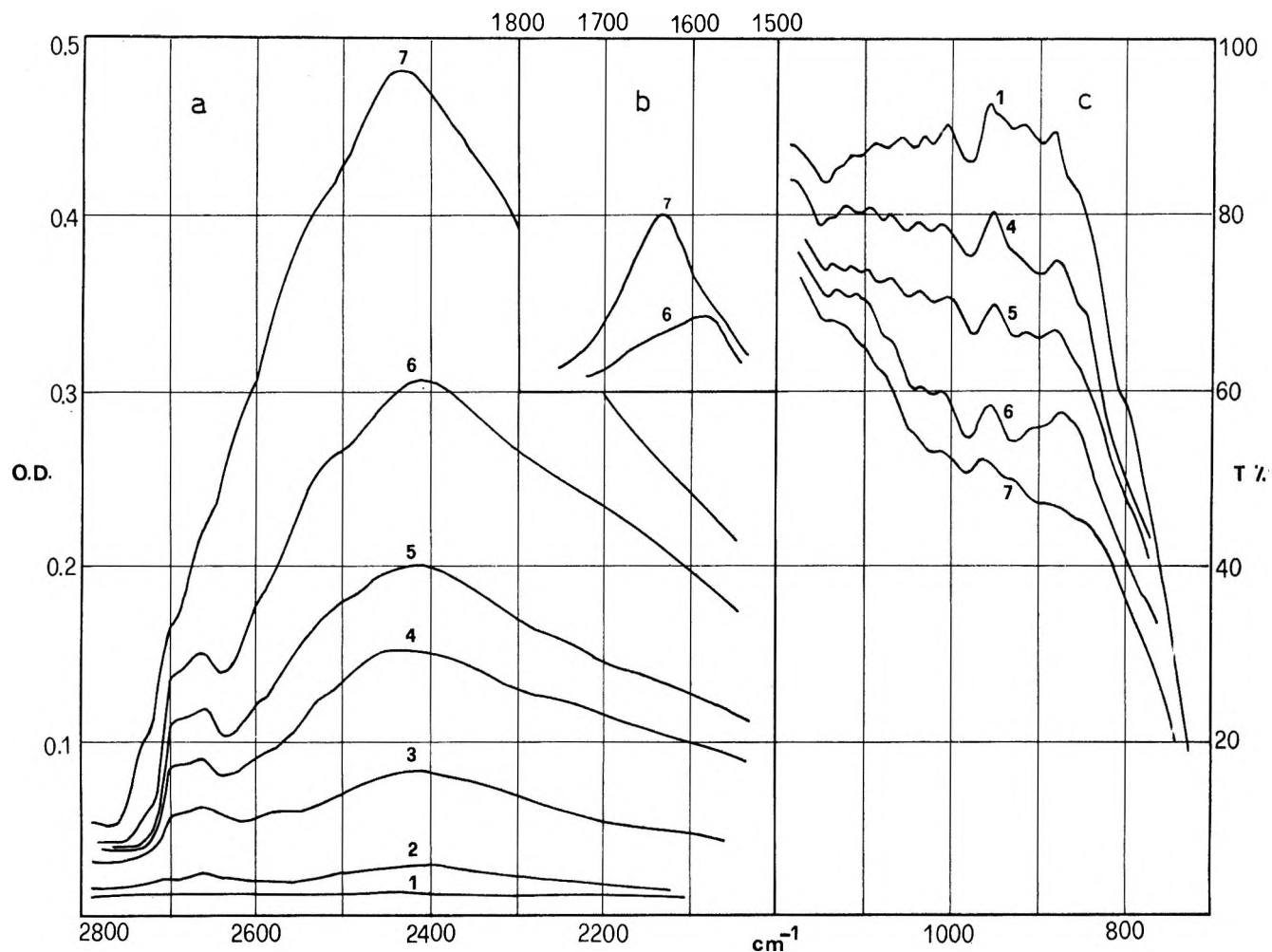


Figure 5. (a) Infrared spectra of α -Cr₂O₃ (optical density vs. wavelength in cm⁻¹): curve 1, background after phase III; curves 2-7, at increasing D₂O coverages at room temperature (D₂O equilibrium pressures are $< 10^{-3}$ Torr for curves 2-5, 0.15 Torr for curve 6, and 4 Torr for curve 7). (b) Infrared spectra of α -Cr₂O₃ (optical density vs. wavelength in cm⁻¹): curve 6, 7, H₂O adsorption (equilibrium pressures are 0.15 Torr and 4 Torr, respectively). (c) Infrared spectra of α -Cr₂O₃ (% transmission vs. wavelength in cm⁻¹): curve 1, background after phase III; curves 2-7, increasing H₂O coverages at room temperature (equilibrium pressures are as reported in Figure 5a).

coverages) is taking place. Figures 5b and c refer to the adsorption of H₂O. Spectra of Figures 5a and b have been run with a reference sample on the reference beam so as to balance scattering phenomena. Spectra of Figure 5c were obtained with the usual screening technique, owing to the presence of weak background absorptions in the 1300-700-cm⁻¹ range, that might cause ambiguous results, especially at very low water coverages. Numbers marked on spectra of Figure 5 refer to equal or almost equal coverages in the three adsorption series. Notice that in Figure 5c, spectra 2 and 3 are missing due to the very weak intensity, hardly distinguishable from the background.

Figure 6a, dotted line, shows the spectrum of a microcrystalline sample, oxygen free, on which carbon monoxide¹¹ is chemisorbed at room temperature. Figure 6b shows the effect of carbon monoxide on an amorphous sample, desorption times and all conditions being the same as Figure 6a. Preadsorption of H₂O (or D₂O) on

Cr₂O₃ completely inhibits the activity towards CO, activity that is recovered upon degassing at gradually higher temperatures. The experiment (Figure 7) has been run as follows. The sample that underwent the three phases of thermal treatment was contacted with 8 Torr of D₂O, and the adsorption was assumed to be over when no further change was observed in the ir spectrum (this end point was attained in 30 min at 400° and in few hours at room temperature, but the final spectrum was the same). No CO adsorption was exhibited by the sample that was degassed at room temperature, nor at 100°, but higher and higher adsorptive capacity toward CO was developed by the hydrate oxide upon degassing at temperatures up to 400°. Meanwhile, a decrease is observed (Figure 7a) in the intensity of absorptions in the 2700-2000-cm⁻¹ region, where stretching surface OD groups absorb.

(11) CO was 5N grade, from SIO, Milano.

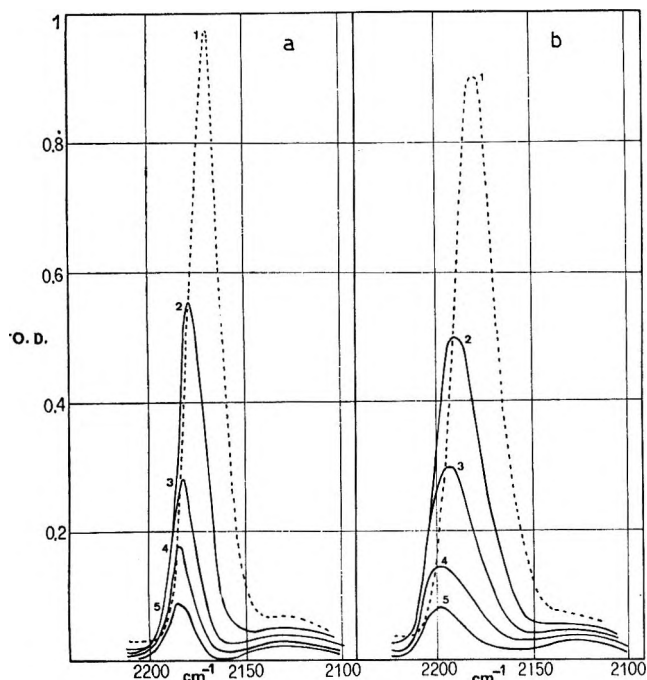


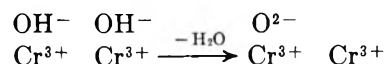
Figure 6. (a) Infrared spectra of α - Cr_2O_3 (optical density vs. wavelength in cm^{-1}): curve 1, CO adsorption at room temperature (equilibrium pressure 40 Torr); curves 2-5, at decreasing CO coverages (final pressure for curve 5 $< 10^{-4}$ Torr). (b) Infrared spectra of amorphous Cr_2O_3 (optical density vs. wavelength in cm^{-1}): curve 1, CO adsorption at room temperature (equilibrium pressure 40 Torr); curves 2-5, decreasing CO coverages (conditions are as reported in Figure 6a).

A 13-hr degassing produced no further change of CO activity that was lower than the initial activity of the nonhydrated sample and that could only be reproduced by repeating phases II and III of the thermal treatment. Notice that on repeating the two phases the spectrum in the 2700 – 2000 - cm^{-1} region is also modified (Figure 7a, dotted line).

Discussion

Ir Spectrum of Amorphous Cr_2O_3 . Water adsorption on various oxides usually brings about absorptions in three spectral regions. The 3800 – 3000 - cm^{-1} region is due to the stretching of surface hydroxyls originated by a dissociative water chemisorption and to the OH stretching of nondissociated water molecules. These absorptions are shifted to 2700 – 2000 cm^{-1} in the case of heavy water. The 1630 – 1580 - cm^{-1} region is due to bending modes of nondissociated water. Corresponding absorptions of heavy water are at 1200 – 1180 cm^{-1} . The 1000 – 700 - cm^{-1} region is due to bending modes of surface hydroxyls, originated by dissociative water chemisorption. No OD bending modes are observable on chromia, whose cut off is at 700 cm^{-1} .^{12,13} Amorphous chromium oxide originated by decomposition of ammonium dichromate (Figure 1, curve 6) has a good transparency around 1000 cm^{-1} , while at higher wavenumbers heavy light scattering predominates. The

spectrum is quite similar to that of chromium oxide gels and is typical of amorphous Cr_2O_3 phase, no matter what the preparation method has been. Freshly prepared samples are very opaque in the whole ir range. Evacuation at room temperature eliminates a broad band at ~ 1630 cm^{-1} , probably due to physically adsorbed water. At higher evacuation temperatures, another broad band gradually decreases at 1000 – 900 cm^{-1} (surface hydroxyls bending) together with a complex band system at 3800 – 3000 cm^{-1} , due to the stretching of both free and hydrogen-bonded hydroxyls. The activation process of phase I has likely caused a dehydration reaction that, according to that proposed¹⁰⁻¹⁴ for Cr_2O_3 gel, could be



Cr^{3+} ions are thought to be coordinatively unsaturated (c.u.s.) and to represent adsorption centers for CO and O_2 .

Ir Spectrum of α -Chromia. The major feature in the spectrum of α -chromia is a series of weak, characteristic bands in the 1300 – 750 - cm^{-1} region (Figure 3, solid line). Roev, *et al.*,¹⁵ assigned these absorptions to surface hydroxyls typical of high surface area oxides. Such an assignment contradicts what is observed in the case of amorphous chromia (samples after phase I) and of chromia gel,¹⁶ where bands in the 1300 – 750 - cm^{-1} range are entirely missing. Shopov, *et al.*,¹⁶ observed weak bands in the 1300 – 750 - cm^{-1} region only on samples that chemisorbed oxygen and were degassed at 340° , and they thought that the bands were due to nondesorbed oxygen. On the other hand, amorphous chromium oxide easily crystallizes in the presence of oxygen so that it is quite difficult to decide whether oxygen is still present on the surface or the observed bands are typical of crystalline chromia. To answer the question and to distinguish between background bands and oxygen bands in the 1300 – 750 - cm^{-1} range special care has been used in the assignment, and many experiments have been made to confirm or reject the following hypotheses. (a) If some of the bands were due to surface hydroxyls, they should not be observed on low area samples and should be shifted by isotopic exchange. (b) If they were due to chemisorbed oxygen, still present also after the reduction treatment of phase III, they should be decreased in intensity by further reduction with hydrogen at 800° and should not be visible on low-area samples. (c) If they were due

(12) J. E. Evans and T. L. Whateley, *Trans. Faraday Soc.*, **63**, 2769 (1967).

(13) H. A. Benesi and A. C. Jones, *J. Phys. Chem.*, **63**, 179 (1959).

(14) R. L. Burwell, Jr., J. F. Read, K. C. Taylor, and G. L. Haller, *Z. Phys. Chem.*, **64**, 18 (1969).

(15) L. M. Roev and A. N. Terenin, *Dokl. Akad. Nauk SSSR*, **124**, 373 (1969).

(16) D. M. Shopov and A. N. Palazov, *Kinet. Katal.*, **6**, 864 (1965).

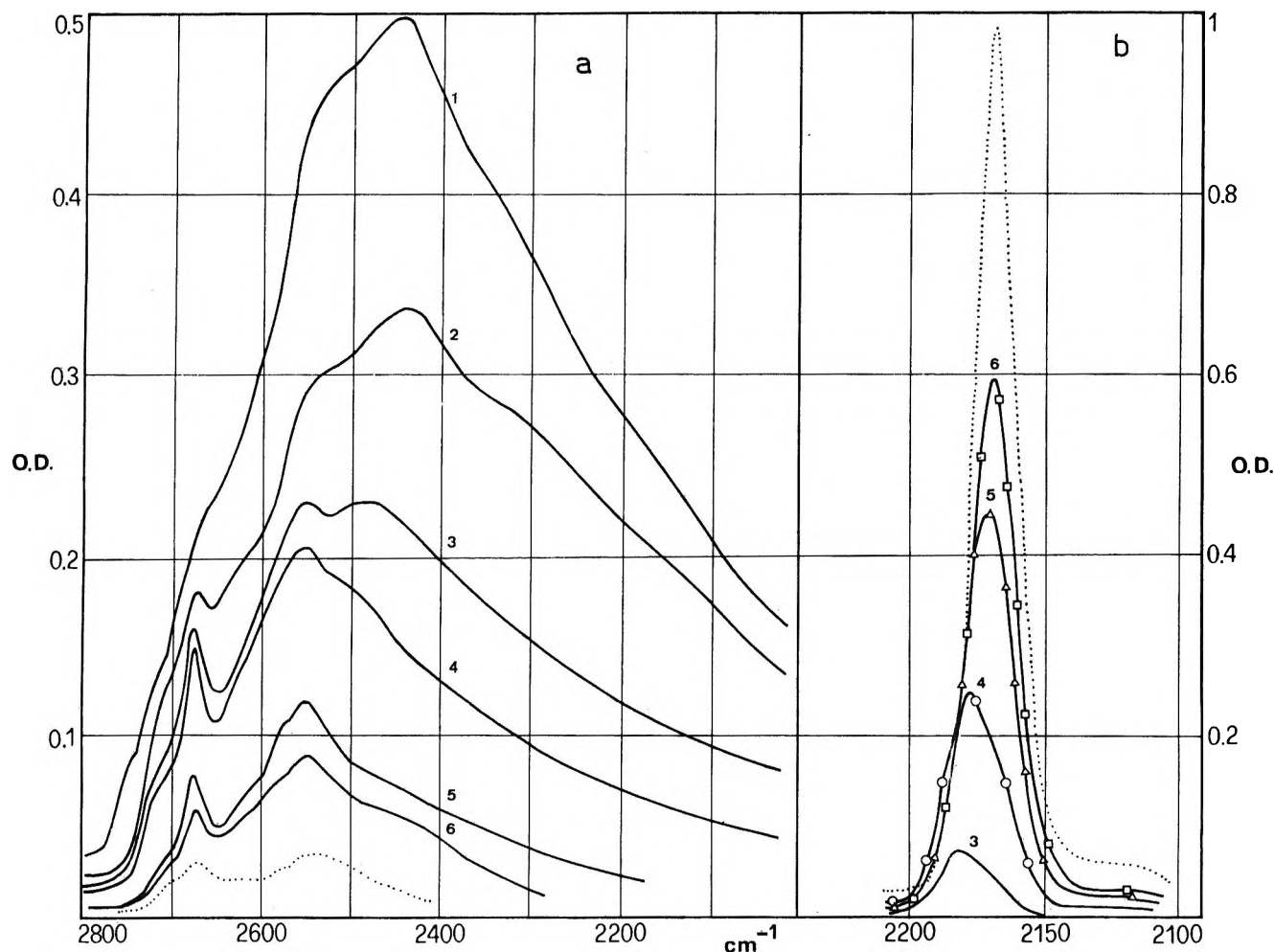


Figure 7. (a) Infrared spectra of α - Cr_2O_3 (optical density vs. wavelength in cm^{-1}): curve 1, after adsorption of D_2O (equilibrium pressure 4 Torr); curves 2-6, D_2O degassing, times and temperatures being 1 hr at 100° , 1 hr at 200° , 1 hr at 300° , 1 hr at 400° , and 13 hr at 400° ; dotted line, after phases II-III. (b) Infrared spectra of α - Cr_2O_3 (optical density vs. wavelength in cm^{-1}): curves 3-6, CO adsorption at room temperature (equilibrium pressure 40 Torr) on a sample at various hydration degrees. Degassing times are as reported in Figure 7a; dotted curve, CO adsorption at room temperature (equilibrium pressure 40 Torr) after phases II-III.

to nonstoichiometric oxygen in the bulk, they should be particularly intense in the case of amorphous samples and decline by hydrogen reduction at 800° , when bulk mobility is certainly excited.

Spectra of Figure 4 clearly demonstrate that none of the above hypotheses is true. In particular a D_2O exchange causes a gain of transparency in the 1000 – 800 - cm^{-1} region, but none of the bands under discussion is eliminated. The only possible explanation is that they are characteristic of crystalline chromia and that any contribution of OH bending modes is unimportant. This seems to be confirmed by the weakness of OH stretching absorptions in the 3800 – 3000 - cm^{-1} region, after the whole series of thermal treatments. Our assignment is also supported by the comparison of our spectra with those obtained by Marshall, *et al.*,¹⁷ on chromia monocrystals (Table I). Few of our bands below 950 cm^{-1} are not reported by Marshall, *et al.* We believe that they are still characteristic of the crystalline form and that their observation is particu-

larly difficult in the case of monocrystals, due to the very strong band intensity at 600 – 700 cm^{-1} , brought about by the sample thickness. These bands can be easily explained according to Marshall's hypothesis (Table I), and their assignment to crystal modes seems to be confirmed. The above comparison between amorphous and crystalline phases emphasizes the importance of ir spectroscopy in examining the crystalline status of transparent materials. Similar considerations have been reported by Burwell, *et al.*,¹⁰ that used the low frequency range.

Spectra of Figure 4 are also characterized by big differences in the 750 – 800 - cm^{-1} interval that cannot be explained with certainty. It is known that particle size strongly influences ir spectra of solids; therefore, we think that the observed differences might be mainly determined by the surface area of examined samples.

(17) R. Marshall, S. S. Mitra, P. J. Gielisse, J. N. Plende, and L. C. Mansur, *J. Chem. Phys.*, **43**, 2893 (1965).

Table I. Frequencies and Assignment of α -Chromia

Marshall, <i>et al.</i> ^a	This work
	810 ($2E_1'$)
	845 ($E_1' + E_2'$)
880	888
	940 ($E_1' + E_3'$)
975	974
1010	1013
1040	1043
1066	1075
1097	1095
1137	1142
1167	1168
1225	1225
1247	1243
1283	1285
1332	1330

^a Reference 17.

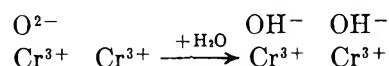
Finally, the spectrum of α -chromia exhibits a couple of bands at approximately 1380 cm^{-1} of changeable intensity and peculiar behavior. Since we think that no crystal modes are involved, they will be discussed in more detail in part III.

The weakness of bands due to surface hydroxyl modes supports the hypothesis that, after phases II and III, the (001) face is highly dehydrated. More arguments in favor of the above viewpoint are brought by the adsorbing capacity towards CO and will be discussed later. Figures 8a and b show two models for a fully dehydrated (ideal) (001) face. On it, half the amount of oxygen ions present in a close-packed structure is left as to maintain the electric neutrality. Models a and b are not the only models that can be drawn, but they are just two of the most likely; besides an overall neutrality they also maintain the local neutrality as much as possible. Chromium ions with coordination number 4 and 5 are present in equal concentration. We cannot exclude that ions with coordination 3 could be present, but they are quite unlikely. Our model of a (001) face is rather similar to that suggested by Stone¹⁸ for faces perpendicular to the (001). Real samples are not completely dehydrated (residual hydroxyls would prove it) and Cr ions of coordination 6 can thus be present. Two such possibilities are presented in Figures 8c and d and have been obtained from a and b assuming the dissociative chemisorption of few water molecules.

Water Adsorption at Room Temperature. The first doses of water (or heavy water) are quickly chemisorbed on α -Cr₂O₃ (Figures 5a and c, curves 2-4). The absence of any appreciable absorption at $\sim 1600\text{ cm}^{-1}$ clearly indicates that in this phase the chemisorption is entirely dissociative. On the other hand, the spectral modifications in the 2700-2000- (in the case of D₂O)

and in the 1000-750-cm⁻¹ regions (in the case of H₂O) suggest that few different types of surface hydroxyls are formed. In the former region (OD stretching) two bands are observed that are quite narrow, isolated, and centered at 2700 and 2675 cm⁻¹, respectively, also a broad absorption with apparent maximum at 2430 cm⁻¹, that is probably complex, for at higher coverages two shoulders are visible at ~ 2600 and 2535 cm⁻¹. Also, at higher coverages, this band grows much more than the couple at 2700 and 2675 cm⁻¹.

The beginning of a nondissociative adsorption (water pressure ~ 0.5 Torr) is indicated by the appearance of a band at 1590 cm⁻¹ and at water pressures of few Torr a second undissociated species is revealed by another peak at 1630 cm⁻¹ that becomes predominant for even higher amounts of H₂O sorbed. This behavior and the frequency coincident with the bending mode of liquid water suggest that water molecules adsorbed at high coverages are hydrogen bonded to surface hydroxyls. Molecular water, whose bending mode falls at 1590 cm⁻¹, is strongly held and cannot be removed at room temperature but only upon degassing at 150-200°. We think that these water molecules are adsorbed onto c.u.s. chromic sites through a coordinative bonding. In fact the H₂O bending mode in aquo complexes of transition metals normally falls at lower frequencies than in the vapor phase,¹⁹ and Costa, *et al.*,²⁰ observe the bending mode of the complex (CH₃COO)₄Cr·2H₂O in the 1610-1580-cm⁻¹ range. The adsorption of H₂O at room temperature can be summarized as follows. (a) Dissociative chemisorption probably occurs through the mechanism



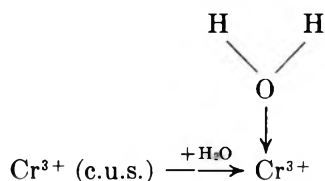
It presumably occurs on more unsaturated ions first. Hydroxyls so formed would be "bridged" between two metal ions and should have a spectroscopic behavior similar to "bridged" hydroxyls in polynuclear complexes.²¹ Figures 8a and b show that, in principle, there are no limitations to dissociative chemisorption of water, which should lead to a close-packed layer of OH⁻ groups. In practice H₂O chemisorption, both at room temperature and at 400°, always leaves some Cr³⁺ c.u.s. ions able to coordinate undissociated molecules, proving that the dissociative mechanism is limited, possibly by collective electronic properties. (b) Coordinative chemisorption occurs through the mechanism

(18) F. S. Stone, *Chimia*, **23**, 490 (1969).

(19) I. R. Beattie, T. R. Gilson, and G. A. Ozin, *J. Chem. Soc. A*, **4**, 534 (1969).

(20) G. Costa, E. Pauluzzi, and A. Puxeddu, *Gazz. Chim. Ital.*, **87**, 885 (1957).

(21) K. Nakamoto, "Infrared Spectra of Inorganic and Coordination Compounds," Wiley, New York, N. Y., 1963.



active sites being chromium ions that have not been coordinatively saturated according to mechanism a. (c) Physical adsorption occurs through the formation of hydrogen bondings on a monolayer saturated by mechanisms a and b.

CO Chemisorption at Room Temperature. Several authors^{10,14,22-24} have studied the adsorption of CO onto α -chromia and chromia gel. It has been found that the differential heat of adsorption of CO on α -chromia strongly varies with coverage.²² All the authors observed that CO is reversibly sorbed by samples that are oxygen free. Spectra in Figures 6a and b relative to the chemisorption of CO at different coverages on crystalline and amorphous chromia lead to the following observations.

(a) The stronger of the two bands is at higher frequency than gaseous CO and is quite similar to the band observed on chromia-silica.^{2a} Such raised frequency can be ascribed to the formation of a σ bond between CO and surface sites with none or very small π contribution, as discussed in a previous paper.^{2a} Active sites would be Cr^{3+} c.u.s. ions. In fact CO adsorption is completely inhibited by pyridine that is a hard base and forms a stable adduct with the hard Cr^{3+} ion (unpublished results).

(b) The lower the coverage, the harder the desorption (Figure 6a), in agreement with the differential heats situation.²² Also the frequency is influenced by coverage. In particular, on passing from spectrum 1 to spectrum 2 there is a sudden rise (2170 to 2178 cm^{-1}), and at lower coverages any further frequency raise is gradual. This behavior and the fact that there is an intersection of the two curves seem to suggest that the band at 2178 cm^{-1} is due to a new species, which is absent at higher coverages. When carefully inspected, the spectra relating to lower coverages (curves 2-5) are still complex, for they change in shape and half-bandwidth (this phenomenon is particularly evident on passing from curve 2 to 3). The residual absorption, that is centered at 2184 cm^{-1} , is clearly "tailed" on the low frequency side. This band cannot be completely eliminated on room temperature degassing, as observed by other authors.¹⁰

Frequency changes with changing coverage can be due either to lateral interactions or to site heterogeneity, and any distinction between the two causes is rather difficult. The former effect, particularly at high coverages, can only partially explain the abrupt peak shift from spectrum 1 to 2, for any coverage effect should be more gradual and would never originate distinct species. In a following paper the presence of Cr^{3+} c.u.s. ions

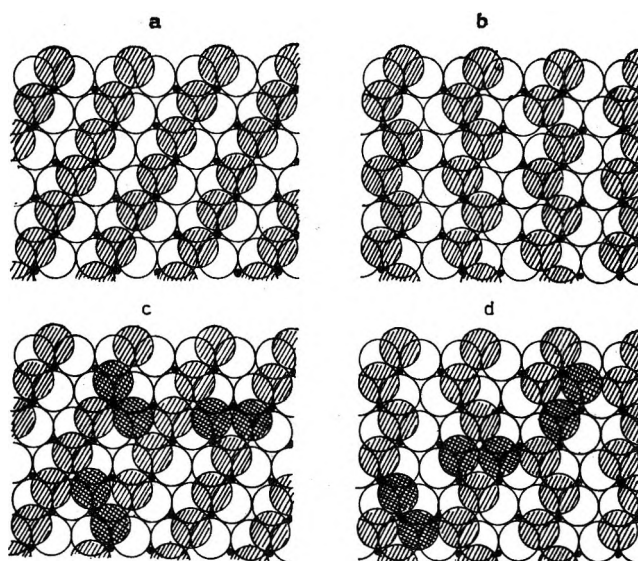
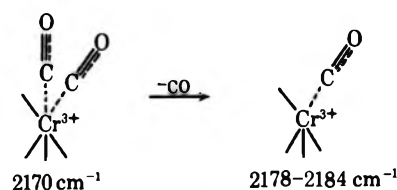


Figure 8. Two possible models (a and b) for a completely dehydrated (001) face: \circ , O^{2-} ions of the underlying layer; \bullet , Cr^{3+} ions; \odot , O^{2-} ions of the upper layer. Two possible models (c and d) of a partially hydrated (001) face: \bullet , surface hydroxyls.

with two coordinative vacancies will be considered. Therefore we might postulate that at high θ values, two CO molecules could be coordinated, leading to spectroscopically different species. Due to the weakness of the metal-carbon bond, the asymmetric and symmetric CO stretching modes are not expected to be resolvable.



This hypothesis would require combined gravimetric and spectroscopic measurements to be proved. Frequency variations, as well as band-width and shape changes at lower coverages (curves 2-5), can be mainly attributed to surface heterogeneity, in that any perturbing effect due to dipole interactions should be negligible.

We have already indicated that in our adsorbent the (001) face is definitely predominant, so that we think the observed heterogeneity not to be due to the presence of other crystallographic faces, but to the existence of different Cr^{3+} c.u.s. ions, yielding σ bonds of different intensity. On the other hand, such a heterogeneity, though undoubted, when revealed by CO adsorption only originates a frequency shift range of few wave numbers and will not be discussed here any longer, for

(22) D. A. Dowden and W. E. Garner, *J. Chem. Soc.*, 893 (1939).

(23) R. A. Beebe and D. A. Dowden, *J. Amer. Chem. Soc.*, **60**, 2912 (1938).

(24) D. S. MacIver and H. H. Tobin, *J. Phys. Chem.*, **64**, 451 (1960).

any tedious and lengthy reasoning would miss experimental evidence. The argument will be discussed in more detail in part II, where the spectrum of chemisorbed oxygen can only be understood in terms of several local configurations.

(c) Bands due to chemisorbed CO are broader in the case of amorphous nonstoichiometric Cr_2O_3 than in the case of $\alpha\text{-Cr}_2\text{O}_3$, as expected for a more heterogeneous, random material. Also this aspect will be further shown up by O_2 chemisorption (part II). The frequency of σ -bonded CO is always higher in amorphous Cr_2O_3 samples and we think that this is accounted for by the presence of nonstoichiometric oxygen rather than by a more pronounced heterogeneity. In fact, this oxygen excess might produce surface chromium ions in a higher oxidative status than three and thus capable of stronger σ bondings.

(d) CO adsorbed on both amorphous and crystalline samples produces a broad, weak band at $\sim 2130\text{ cm}^{-1}$ that is very stable to desorption. An analogous absorption has been observed on silica-supported chromia,^{2a} and the assignment is the same: few CO molecules are adsorbed onto surface chromium ions, through a bond with some π contribution. These sites are thought not to be Cr^{2+} ions produced during reduction (phase III), because they should not appear on merely activated, amorphous, and nonstoichiometric samples. Crystalline samples that chemisorbed O_2 and were degassed at 400° exhibit an even stronger intensity at 2130 cm^{-1} upon adsorption (unpublished results). Part II will show how a 400° outgassing does not completely eliminate adsorbed oxygen thus excluding the presence of Cr^{2+} ions on the surface. In this way we get another proof that no Cr^{2+} ions are responsible for the band at 2130 cm^{-1} .

CO Adsorbing Sites and Surface Dehydration. After a prolonged contact with H_2O at room temperature, no activity towards CO is exhibited by α -chromia. This fact is explainable in terms of the discussed rehydration reactions that eliminate Cr^{3+} c.u.s. ions. Adsorptive capacity of CO should be gradually restored upon degassing at high temperatures, as already pointed out with different techniques in the case of Cr_2O_3 gel.¹⁰ Figures 7a and b, showing that CO adsorption begins after a 200° degassing and increases thereafter for higher activation temperatures, clearly demonstrate the close similarity between $\alpha\text{-Cr}_2\text{O}_3$ and Cr_2O_3 gel. We have already indicated that coordinated water is desorbed at $\sim 200^\circ$ and therefore we think that Cr^{3+} c.u.s. sites, capable of chemisorbing CO, are first formed at such temperature. Also a reaction opposite to the mechanism of the dissociative chemisorption would begin at 200° . It becomes predominant at higher temperatures, and new Cr^{3+} c.u.s. ions should be formed causing a constant increase in the ability to adsorb CO. Our results tend to confirm that this is the case and that adsorbed CO gives a direct estimate of Cr^{3+}

c.u.s. surface concentration. This hypothesis has also been proposed by Burwell for the gel.¹⁰ The dehydration probably generates Cr^{3+} c.u.s. ions with different local configurations; they could differ either in the number or in the nature of ligands, relative concentrations of the various types being a complex function of dehydration degree. Heterogeneous sites can originate σ bonds of different strength and a CO spectrum varying with surface dehydration is expected. Figure 7b confirms our viewpoint, in that the band maximum clearly varies with activation temperature. On the other hand, this frequency shift range is very narrow ($2184\text{--}2170\text{ cm}^{-1}$), and no information on the real nature of such surface sites heterogeneity can be deduced.

As previously indicated, a 13-hr dehydration at 400° of a rehydrated sample does not restore the whole CO activity as it was after phases II and III. This fact seems to suggest that samples after phases II and III are in a more dehydrated surface condition. In fact the whole CO activity is only restored if the degassing at 400° is followed by a treatment corresponding to phases II and III (Figure 7b, dotted line). Meanwhile, the concentration of surface hydroxyls is further decreased (see OD stretching region in Figure 7a, dotted line). Of the two operations, only the oxidation of phase II can bring about a hydroxyl decrease and a hydrated sample that underwent the treatment at phase III only did not exhibit any ability to adsorb CO. This idea has been already postulated by Burwell, *et al.*,¹⁰ when accounting for the difference between their results and those of MacIver, *et al.*,²⁴ suggesting that the latter authors, by using a several redox cycle technique, finally got a highly dehydrated surface situation. A guide in the assignment of surface hydroxyl bands can come from Figure 7a, where spectra of the OD stretching region for different dehydration temperatures are reported.

The rehydration experiment (Figure 5a) seemed to suggest that only bands at 2700 and 2675 cm^{-1} could be assigned to free or nonstrongly interacting surface OD groups. A broader absorption at $\sim 2430\text{ cm}^{-1}$, already present at the lowest coverages, might be due to hydrogen-bonded hydroxyls. Desorption spectra of Figure 7a partly confirm the above conclusions in that upon high temperature degassing the absorption at $\sim 2430\text{ cm}^{-1}$ quickly declines. But another complex absorption, roughly centered at 2550 cm^{-1} (with shoulders at 2600 and 2575 cm^{-1}) still remains and does not decline any faster than bands at 2700 and 2675 cm^{-1} . It must therefore be due to nonstrongly interacting hydroxyls, though hydrogen-bonded species responsible for a broad tail between 2500 and 2200 cm^{-1} are still on the surface (Figures 5 and 6). A similar complex situation has also been observed by Peri²⁵ on γ -alumina,

(25) J. B. Peri, *J. Phys. Chem.*, **69**, 211 (1965).

where five bands due to "free" hydroxyls in different local configuration were present in the 3800–3700-cm⁻¹ range. On the (001) face of α -Cr₂O₃ the number of possible species, higher than in the case of γ -Al₂O₃, would lead to an almost continuous variation of energy situation and could account for the complex spectrum, whose components are only partially resolved.

Conclusion

From the above discussion, we conclude the following. (1) H₂O is chemisorbed on α -Cr₂O₃ both through a dissociative mechanism and by forming a coordinative bonding. (2) There are several types of weakly

interacting surface hydroxyls, and they can be accounted for assuming that (001) face is predominant. (3) On a dehydrated surface many Cr³⁺ ions are present with different coordinative situations. (4) CO is mainly chemisorbed through the formation of weak σ bonds to Cr³⁺ c.u.s. ions. (5) Active sites can be generated on α -Cr₂O₃ by dehydration at high temperatures as well as on Cr₂O₃ gel. (6) Burwell's theory is quite useful in explaining the observed phenomena and can also be used for crystalline phases.

Acknowledgments. This research has been supported by the Consiglio Nazionale delle Ricerche.

An Infrared Study of Surface Properties of α -Chromia.

II. Oxygen Chemisorption

by A. Zecchina, S. Coluccia, L. Cerruti, and E. Borello*

Istituto di Chimica Fisica dell'Università di Torino, Turin, Italy (Received October 19, 1970)

Publication costs assisted by the Consiglio Italiano delle Ricerche (C.N.R.)

Oxygen interaction with α -Cr₂O₃ has been studied by ir spectroscopy. The chemisorption is dissociative, leading to different Cr=O surface groups. The Cr=O stretching frequency depends both on the coordination number of the adsorbing chromium ions (coordinative heterogeneity) and on the environment of the new formed groups (ligand heterogeneity). At high temperatures surface migration phenomena are observed and islands of high valence oxides are formed, as already suggested by other authors.

Introduction

The O₂-Cr₂O₃ system has been studied by several authors, and few coherent conclusions have been reached. In particular there is a good agreement on the room temperature chemisorption to be dissociative, as indicated by the high adsorption heat. On the other hand, no agreement exists on the nature of surface oxygen adsorbed at various temperatures. Dowden and Garner¹ assume that O₂ is chemisorbed at room temperature to form Cr=O groups. Weller and Voltz² think that, at room temperature, oxygen is in the form of O²⁻ ions and that at higher temperature an oxide layer is formed at the surface with Cr valency up to 6. McIver and Tobin³ postulate the formation of O²⁻ or O⁻ ions in the dissociative chemisorption at low temperatures but do not justify the big difference that other authors¹ observed in the adsorption heat between 0 and -196°. Finally Burwell, *et al.*,⁴ think that O₂ chemisorption at -78° leads to O₂²⁻ groups. For more details on oxygen chemisorption see also a review

by Winter.⁵ The only infrared study of surface oxygen was carried out by Shopov and Palazov⁶ on Cr₂O₃ gel but, due to the high temperatures employed, we think that their spectra refer to bulky layers of chromium oxides (like CrO₃) more than to real surface complexes.

Our purpose is to contribute to the understanding of the Cr₂O₃-O₂ interactions in view of the powerful aid usually given by ir spectroscopy to band characterization problems and heterogeneity identifications.

Experimental Section

α -Cr₂O₃ samples were prepared as described in part I. Also ir spectra have been run as described in the previous paper.

- (1) D. A. Dowden and W. E. Garner, *J. Chem. Soc.*, 893 (1939).
- (2) W. Weller and S. E. Voltz, *J. Amer. Chem. Soc.*, **76**, 4695 (1954).
- (3) D. S. McIver and H. H. Tobin, *J. Phys. Chem.*, **64**, 451 (1960).
- (4) R. L. Burwell, Jr., L. Haller, K. C. Taylor, and J. F. Read, *Advan. Catal.*, **19**, 62 (1969).
- (5) E. R. S. Winter, *ibid.*, **10**, 196 (1958).
- (6) D. M. Shopov and A. N. Palazov, *Kinet. Katal.*, **6**, 864 (1965).

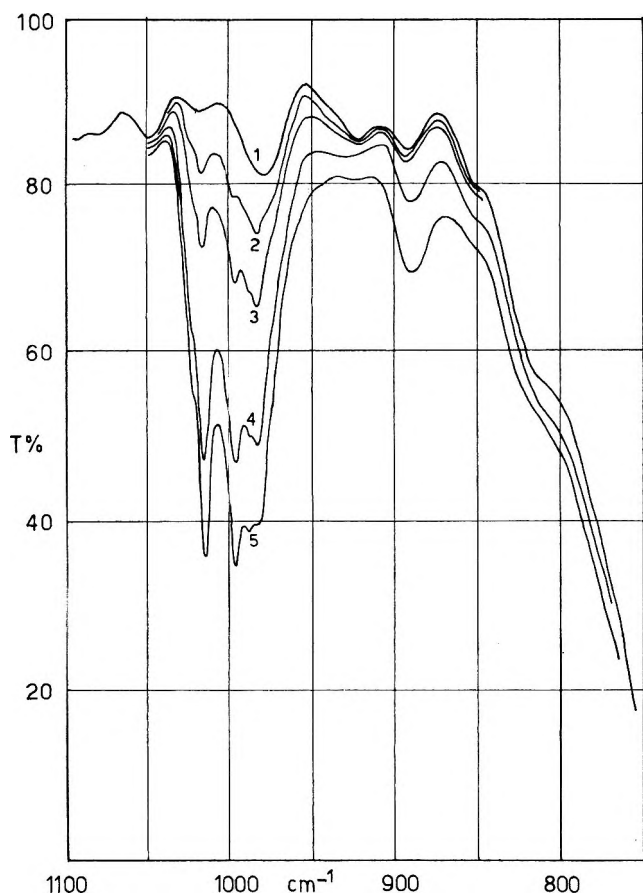


Figure 1. Infrared spectra of α - Cr_2O_3 (% transmission vs. wavelength in cm^{-1}): curve 1, background after phases I-III; curves 2-4, at increasing oxygen coverages at room temperature; curve 5, saturated with oxygen.

O_2 Adsorption at Room Temperature. Figure 1 shows ir spectra of various amounts of O_2 adsorbed on a α - Cr_2O_3 sample that underwent the whole series of pre-treatments described in part I. (These samples will be hereafter referred to as samples A.) Increasing oxygen coverages were obtained allowing small amounts of gas (approximately 2×10^{18} molecules each) into the cell and assuming the chemisorption to be complete when a residual pressure of 5×10^{-4} Torr was read on the Pirani gauge. A few minutes was required for the first doses to be consumed, suggesting that a fast reaction was taking place. Higher oxygen pressures (5×10^{-4} to 40 Torr) did not cause any rapid change of band intensity, but a slow chemisorption was revealed by a slight time-dependent increase of the bands in the 1040 - 750 - cm^{-1} range. The reproducibility of O_2 chemisorption at room temperature is evident if Figure 1 (curve 5), Figure 5 (solid line), Figure 6 (broken line), and Figure 7 (solid line) are compared. They refer to different A samples and only minor differences are visible except for a peak at 1016 cm^{-1} , whose intensity depends on the dehydration of the surface (see Discussion). The spectrum of chemisorbed oxygen is thus expected to be sensitive to water contamination.

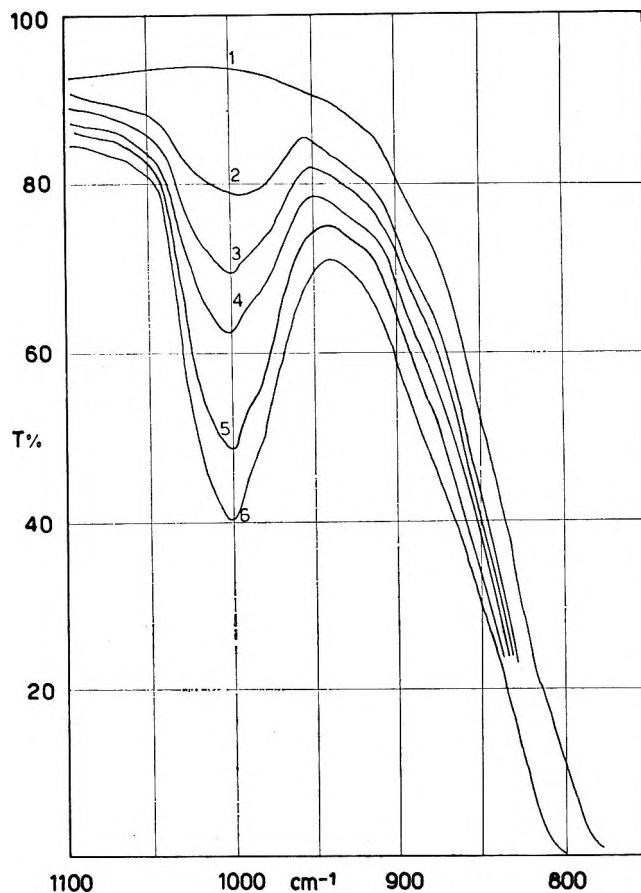


Figure 2. Infrared spectra of amorphous Cr_2O_3 (% transmission vs. wavelength in cm^{-1}): curve 1, background; curves 2-5, at increasing oxygen coverages at room temperature; curve 6, saturated with O_2 .

Oxygen chemisorption produces three groups of ir absorptions at 1040 - 970 , 900 - 880 , and 850 - 750 cm^{-1} , the first one being definitely the most intense at room temperature. It is complex and five components are visible at 1024 , 1016 , 995 , 986 , and 980 cm^{-1} . Owing to band sharpness and good sample transparency, peak positions have been observed with high accuracy (± 1 cm^{-1}). Also, it has been possible to observe that most of the bands change their position from one experiment to another in a narrow range (± 3 cm^{-1}) probably due to minor causes that we cannot identify yet. Only crystalline samples exhibit the above band complexity.

Figure 2 shows ir spectra relative to O_2 chemisorbed at room temperature onto amorphous Cr_2O_3 , coverages and all experimental conditions being as for Figure 1. A broad absorption is visible at ~ 1000 cm^{-1} that does not exhibit any definite structure.

Oxygen chemisorption has also been studied on crystalline samples of various surface hydration. An A sample was allowed to react with D_2O for 1 hr at 400° and pumped off at room temperature to a final pressure of 10^{-5} Torr. Heavy water was used for rehydration purposes to avoid absorption bands due to OH groups from 1100 to 700 cm^{-1} (part I). At this point the surface

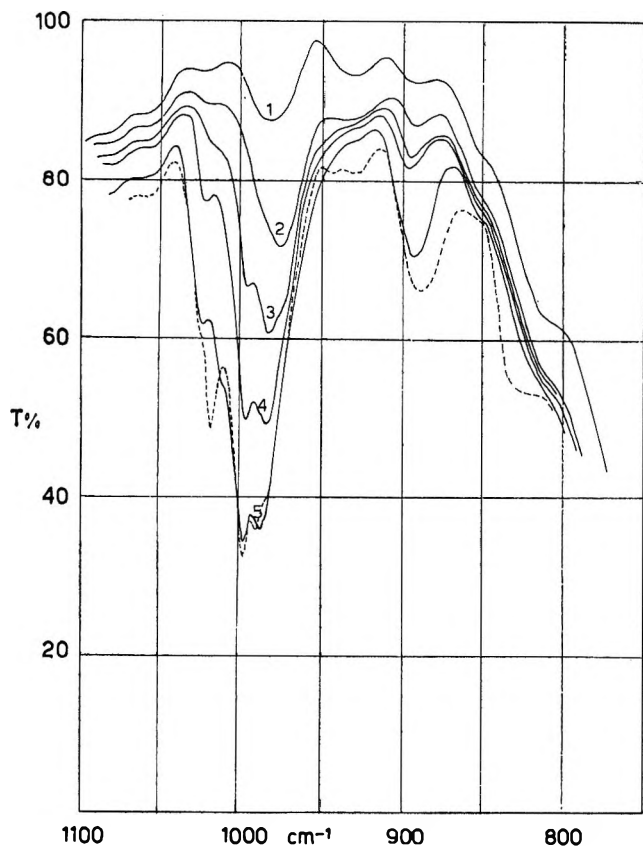


Figure 3. Infrared spectra of α - Cr_2O_3 (% transmission vs. wavelength in cm^{-1}): oxygen (40 Torr) on samples at various dehydration degrees. Dehydration times and temperatures are: curve 1, 1 hr at room temperature; curve 2, 1 hr at 200° ; curve 3, 1 hr at 300° ; curve 4, 1 hr at 400° ; curve 5, 13 hr at 400° ; dotted curve, 1 hr at 800° .

was completely hydrated, as reported in part I. Oxygen was allowed into the cell, and the ir spectrum was recorded. This first rehydration-oxidation operation was followed by a reduction with CO at 400° to remove chemisorbed oxygen, if any, and then degassing at 400° to eliminate the reduction products. The whole series of operations (exhaustive rehydration, evacuation, oxygen exposure, reduction with CO, degassing at 400°) was then repeated several times just varying the evacuation temperature of the rehydrated sample. In this way, different dehydration conditions were obtained in turn and oxygen chemisorption at room temperature was checked with the usual spectroscopic technique. Notice that this set of operations did not produce appreciable variations of surface area and a drastic dehydration at 800° caused a loss of surface area of only 20%. Figure 3, showing the ir spectra of chemisorbed oxygen in various conditions, indicates (a) rehydrated samples that have been dehydrated at temperatures up to 100° do not chemisorb oxygen; (b) O_2 -active sites start being produced by dehydration at temperatures higher than 100° ; (c) dehydration at 100 – 300° originates O_2 -active sites leading to absorptions in the 1000 – 970-cm^{-1} range (curves 2

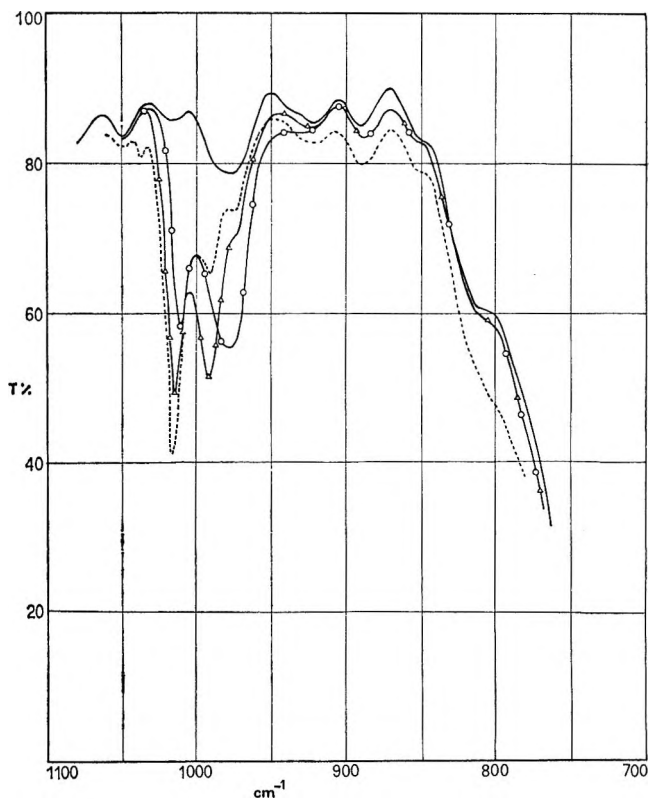


Figure 4. Infrared spectra of α - Cr_2O_3 (% transmission vs. wavelength in cm^{-1}): —, background after phases I–III; —○—, contacted with N_2O (40 Torr) at room temperature; —△—, after pumping off the gaseous phase at room temperature (residual pressure $\sim 10^{-5}$ Torr); ·····, after degassing at 400° , 1 hr (residual pressure $\sim 10^{-5}$ Torr).

and 3); (d) at 400° sites are formed that produce bands in the 1000 – 1040-cm^{-1} range (curves 4 and 5) (the band at 995 cm^{-1} is intensified becoming the strongest of the whole spectrum); (e) an 800° dehydration mainly forms O_2 -active sites leading to the band at 1016 cm^{-1} . Its intensity is still lower than on samples A or on samples whose activity towards oxygen has been completely restored by means of treatments of phases II and III, which bring them back to the conditions of samples A.

Infrared spectra of O_2 chemisorbed on samples that have been reduced with H_2 instead of CO are not reported, for they are all similar to the spectra of oxygen on samples rehydrated and dehydrated at 400° (Figure 3, curve 5). The latter are hereafter termed samples B; their surface hydration is higher than for samples A.

Nitrous oxide has also been used as an oxidizing agent on samples A. Figure 4 clearly shows that N_2O decomposes at room temperature, giving ir absorption bands that are typical of chemisorbed oxygen, though coverages are lower than those obtainable with molecular oxygen. As previously observed by Winter⁵ N_2O is also reversibly absorbed in a nondissociative fashion. Active sites for N_2O molecules are Cr^{3+} c.u.s.

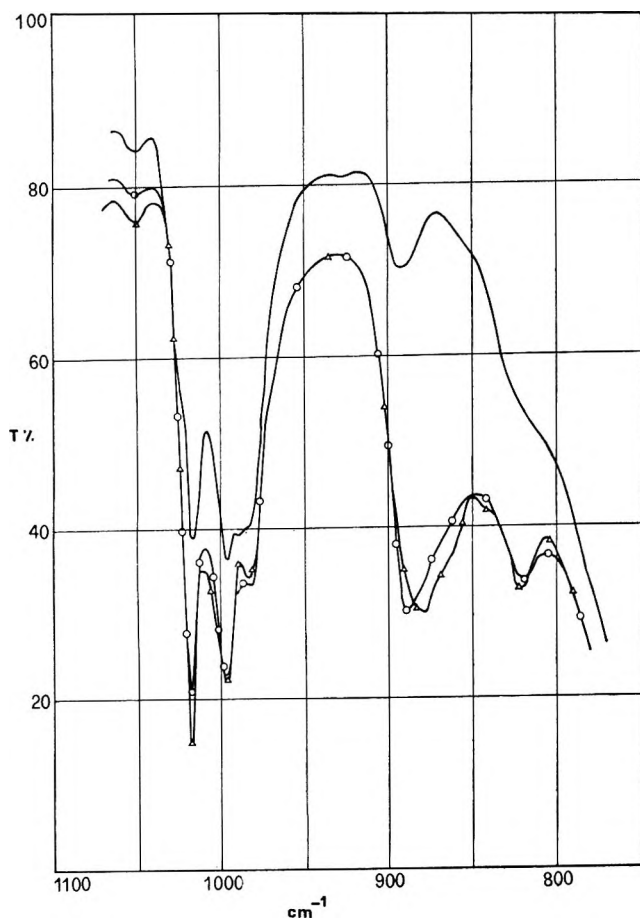


Figure 5. Infrared spectra of $\alpha\text{-Cr}_2\text{O}_3$ (% transmission vs. wavelength in cm^{-1}): —, full oxygen coverage at room temperature (p 40 Torr); $-\circ-\circ-$, after heating in O_2 at 200° ; $-\Delta-\Delta-$, after heating in O_2 at 400° .

atoms (as defined in part I) that have not been saturated by oxygen atoms coming from the initial, fast decomposition. This matter will be discussed in more detail elsewhere. The spectrum of chemisorbed oxygen coming from decomposed N_2O depends on whether undecomposed N_2O is still present on the surface or whether it has been pumped off. When the N_2O molecules are present, a band of medium intensity at 1016 cm^{-1} and a stronger and broader one at $975 \pm 3\text{ cm}^{-1}$ are observed. Upon degassing at room temperature, the former absorption is strongly intensified, a new band appears at 993 cm^{-1} , and the broad one at 975 cm^{-1} disappears. The phenomenon can be indefinitely reproduced through N_2O exposure and evacuation cycles. In particular the final spectrum after evacuation is simpler than that coming from molecular oxygen.

O_2 Adsorption at Higher Temperatures. The continuous curve of Figure 5 refers to the maximum oxygen coverage obtainable at room temperature on a sample A. When temperature is gradually raised, the following spectral modifications are observed (other curves of Figure 5): (a) the 995-cm^{-1} band slightly grows; (b)

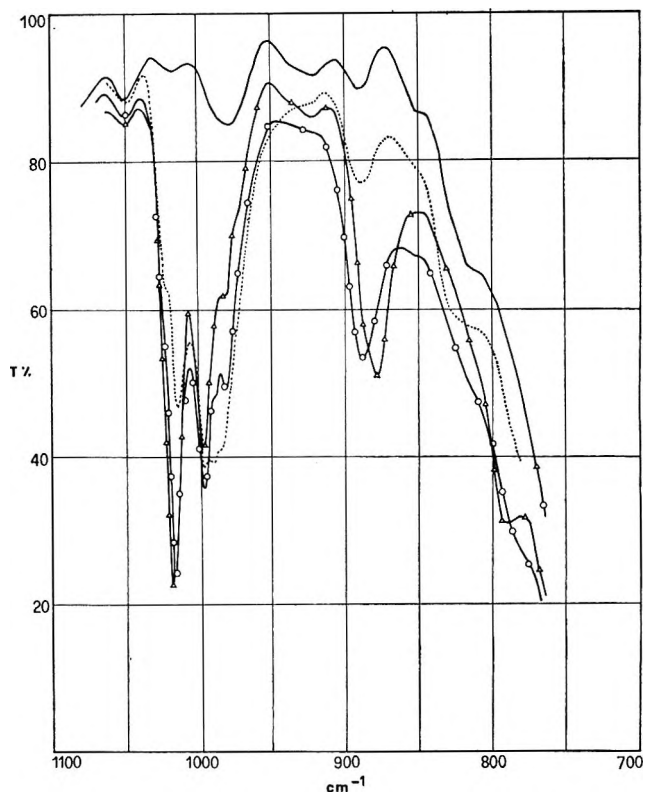


Figure 6. Infrared spectra of $\alpha\text{-Cr}_2\text{O}_3$ (% transmission vs. wavelength in cm^{-1}): —, background after phases I-III; - - -, full oxygen coverage at room temperature (p 40 Torr); $-\circ-\circ-$, after degassing at 200° , 1 hr; $-\Delta-\Delta-$, after degassing at 400° , 1 hr.

the absorption at $1016\text{--}1024\text{ cm}^{-1}$ strongly increases; (c) the band between 900 and 880 cm^{-1} also strongly increases; (d) a new absorption is formed between 820 and 850 cm^{-1} .

Stability of Surface Oxygen to Desorption. The various surface species originated by O_2 chemisorption at room temperature are very stable and are not eliminated by prolonged outgassing at 400° (Figure 6). Bands at 980 and 986 cm^{-1} only are severely weakened, when the outgassing temperature is increased, suggesting that the corresponding surface species could be reversible. On the other hand, an increased intensity at 1016 , at $900\text{--}880$, and at $850\text{--}750\text{ cm}^{-1}$ might mean that a surface rearrangement is involved, causing some species to be transformed into others of higher stability. In other words, at 400° surface oxygen would migrate on the surface rather than being desorbed. The spectrum after degassing at 400° (Figure 6) is very similar to that reported in part I, Figure 3, relative to oxygen chemisorption at 400° (equilibrium pressure 5×10^{-2} Torr).

A Preliminary Investigation of Surface Oxygen Mobility. The above observations made necessary an investigation of surface oxygen mobility. Two experiments have been performed, and the results are reported in Figures 7 and 4, respectively. The first one

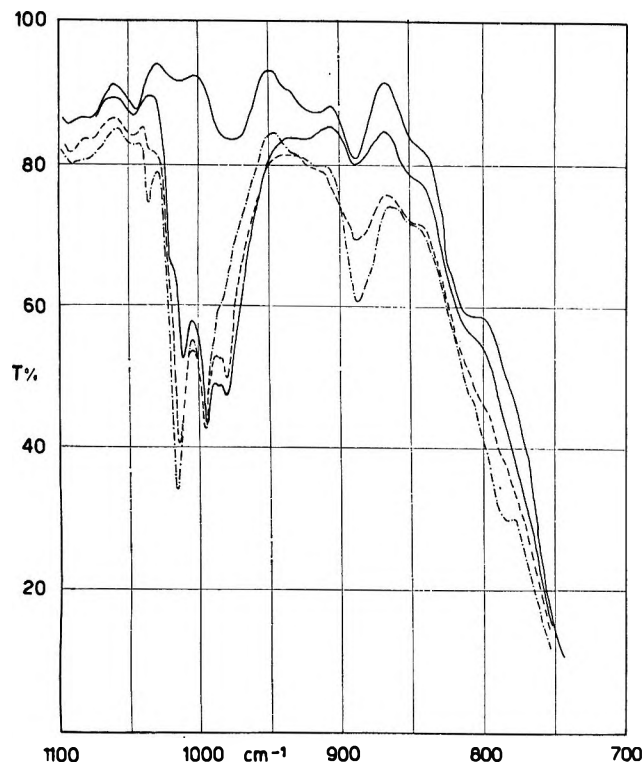


Figure 7. Infrared spectra of α - Cr_2O_3 (% transmission vs. wavelength in cm^{-1}): —, background after phases I-III and full oxygen coverage; ---, after heating at 200° , 1 hr in a static vacuum; - · - ·, after heating at 400° , 1 hr in a static vacuum.

was run as follows. Oxygen was chemisorbed, and the excess was pumped off at room temperature to a final pressure of 10^{-5} Torr. The cell was then closed, the sample was warmed up at various temperatures up to 400° , and the ir spectra were recorded after every thermal treatment. No pressure was developed in the cell at any stage meaning that the amount of chemisorbed oxygen remained constant. The second experiment was as follows. N_2O was allowed onto an A sample, and the excess was pumped off at room temperature to complete the elimination of reversibly bonded N_2O . The spectrum was recorded, and a series of thermal treatments were performed in a static vacuum as for the previous experiment. Also in this case no pressure was developed in the cell, and the amount of chemisorbed oxygen remained unchanged. The band at 1016 cm^{-1} was intensified to the detriment of bands at 986 and 980 cm^{-1} in the first case and a band at 993 cm^{-1} in the second. In both cases a new absorption was formed at 1035 cm^{-1} , and few bands at lower frequencies were intensified. It is concluded that no oxygen is desorbed whatsoever and that there is a complex surface equilibrium which depends on temperature and coverage.

Discussion

Surface Groups Originated by Oxygen Chemisorption. All of the reported spectra clearly indicate that oxygen

is chemisorbed onto α -chromia to form surface species with characteristic ir absorptions. By comparison with several compounds and complexes of chromium and other transition metals⁷⁻¹⁴ the conclusion might be drawn that such species involve oxygen atoms bonded to Cr ions with bonding indexes close to two. A first question arises on whether all of the observed bands are due to different Cr=O groupings or whether a few of them have to be attributed to surface complexes with more than one ir-active normal mode in the frequency range under consideration (e.g., CrO_2 , CrO_3 , CrO_4 , Cr_2O_7 , etc.). We believe that at least for absorptions at 1040 – 970 cm^{-1} the former hypothesis is true. In fact: (a) Bands at 1035 , 1016 , 995 , 986 , and 980 cm^{-1} are all independent of one another and of absorptions at lower frequencies, as suggested by the fact that their relative intensities are changeable with sample treatments (Figures 1 and 3), thermal conditions (Figures 4–7), and oxidizing agent (Figure 4). (b) They exhibit different reaction rates with CO, H_2 , and D_2 . (The interaction of various gases on α - Cr_2O_3 will be discussed in a following paper.) Absorptions located at lower wave numbers are independent of the above but might be connected with one another and could be due to different normal modes of one surface complex only. In fact they grow together with increasing adsorption temperature (Figure 5) and upon surface oxygen diffusion (Figures 4, 6, 7). Nevertheless the intensity ratio is rather changeable.

The major difference between absorptions in the 1040 – 970 - and those in the 900 – 750-cm^{-1} range is that the latter are quite intense only when adsorption temperatures higher than room temperature are employed. The 1035-cm^{-1} band is different from all of the others in that it only forms at high temperatures in very special cases (Figures 4 and 7). Absorptions due to MO groups at such high frequencies have only been observed for VOCl_3 ¹⁵ and VOBr_3 ¹⁶ while no ir spectrum is reported for CrOCl_3 although this compound has been isolated. From the above considerations we must conclude that oxygen is chemisorbed at room temperature with dissociation to form several Cr=O species. Our result only disagrees with some other authors^{2,3} conclusions in that we exclude that surface oxygen is in the form of O^- or O^{2-} groups, but it is linked to metal ions

(7) C. G. Barraclough, J. Lewis, and R. S. Nyholm, *J. Chem. Soc.*, 3552 (1959).

(8) H. Stammreich, D. Sala, and K. Kawai, *Spectrochim. Acta*, **17**, 226 (1961).

(9) H. Kon, *J. Inorg. Nucl. Chem.*, **25**, 933 (1963).

(10) D. Brown, *J. Chem. Soc.*, 4944 (1964).

(11) W. P. Griffith, *ibid.*, 245 (1954); *ibid.*, A, 211 (1969); *ibid.*, 2270 (1969).

(12) I. R. Beattie and T. R. Gilson, *ibid.*, 2322 (1969).

(13) J. A. Campbell, *Spectrochim. Acta*, **21**, 1333 (1965).

(14) J. A. Campbell, *ibid.*, **21**, 851 (1965).

(15) K. Ueno and A. E. Martell, *J. Phys. Chem.*, **60**, 934 (1956).

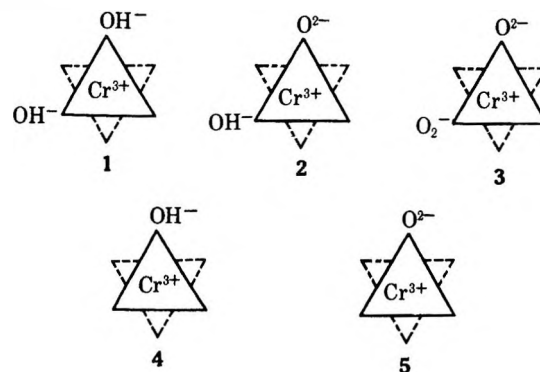
(16) F. A. Miller and W. K. Baer, *Spectrochim. Acta*, **17**, 112 (1961).

through *essentially* covalent double bonds, as already suggested by Dowden and Garner.¹ No direct information can derive from the spectra on surface oxygen coverage. Nevertheless other authors' results⁴ suggest that the adsorbed amount is much less than required for exhaustive saturation of all Cr^{3+} ions on a (001) face (9.8 ions for 100 \AA^2). Spectroscopic evidence of Cr^{3+} ions still present on $\alpha\text{-Cr}_2\text{O}_3$ containing preadsorbed oxygen has been obtained by adsorbing pyridine, H_2O , and CO_2 (results submitted for publication). As far as oxygen chemisorbed at high temperature is concerned (bands at $900\text{--}750 \text{ cm}^{-1}$), the assignment is rather involved. From a merely spectroscopic point of view, absorptions in that region could be due to complexes of the CrO_4^{x-} type, or to their polymers, where x is 2, 3, 4.¹²⁻¹⁴ It is quite likely that at least one of the observed bands is due to a normal mode of M—O—M groups that are present in all $[\text{CrO}_4]^{2-}$ polymeric structures. In this regard, even chromium trioxide can be thought of as a polymer of the tetrahedral $[\text{CrO}_4]$ unit.⁷ Bands in the $900\text{--}750\text{-cm}^{-1}$ range are missing when room temperature chemisorption has taken place, and only form at higher temperatures. This fact supports the above assignment in that monomeric and polymeric CrO_4^{2-} complexes would require a surface rearrangement to be formed that only could be brought about by temperature enhanced surface mobility. Other authors² previously suggested that oxygen at high temperature produces surface islands of high valence oxides of poorly definable structure.

The Nature of Active Sites. Oxygen chemisorption at room temperature on samples A leads to five bands in the $1040\text{--}970\text{-cm}^{-1}$ range, which is typical of Cr=O stretching modes. There is thus evidenced a heterogeneity of $\alpha\text{-Cr}_2\text{O}_3$ surface toward oxygen that ought to be clarified. On our α -chromia preparation, face (001) is by far the most abundant (see part I) and, as Davis¹⁷ and McIver, *et al.*,³ did, we shall limit our discussion to sites that can be generated on it. In other words we exclude that the observed heterogeneity is due to the presence of more than one crystallographic face. The experiment of Figure 3 clearly indicated that adsorptive capacity of face (001) towards O_2 increased with dehydration. Therefore the nature of active centers that are created upon dehydration has to be investigated.

Every surface chromium ion in the hydrated oxide is surrounded by six ligands (see part I), three of which are lattice oxygen ions and three are surface groupings (either OH^- or coordinated water). Upon outgassing, H_2O is eliminated that was coordinated or has been formed by condensation of two hydroxyls. In the first steps of such a dehydration process Cr^{3+} c.u.s. ions would be produced with one coordinative vacancy only, but later, ions with two vacancies could be formed. The latter sites are not favored by ligand field theory, but such possibility cannot be excluded in that surface strains force such a nonfavored situation. The exis-

Scheme I



tence on the (001) face of Cr^{3+} c.u.s. ions with three coordinative unsaturations can be ruled out because their formation is unlikely also in severe dehydration conditions. Moreover, the mobility of surface oxygen, which is quite appreciable above 400° ,^{5,18,19} certainly would further reduce their probability, for the surface oxygen is expected to move in order to maintain a local as well as an overall stoichiometry. Therefore let us conclude that a dehydrated (001) face contains Cr^{3+} c.u.s. ions with one or two coordinative unsaturations (see also Figure 8 of part I). This situation represents an important surface heterogeneity that could be indicated as a "coordinative heterogeneity." Ions with one vacancy only (coordination 5, strained square pyramids) will be predominant for medium dehydration temperatures, and ions with two vacancies (coordination 4, strained tetrahedra) will be appreciably formed at higher temperatures. Obviously the determination of concentration ratios as a function of dehydration temperature is at present almost impossible.

A second type of heterogeneity must be considered that would be termed "ligand heterogeneity." It comes from the fact that there are several ways to make Cr^{3+} c.u.s. ions, with either one or two vacancies, that are represented in the Scheme I. This type of heterogeneity is evidenced in Figures 8c and d of part I. In the above pictures dotted lines represent the layer of lattice O^{2-} ions immediately below the surface. For sake of simplicity, it is supposed to be unstrained with respect to the bulk situation.

On studying carbon monoxide chemisorption on variously hydrated $\alpha\text{-Cr}_2\text{O}_3$ samples (part I), we saw how CO can be thought as a test molecule for coordinative unsaturation. Chemisorbed oxygen probably gives information on both coordinative and ligand heterogeneity because in this case the stretching frequency of the metal-adsorbate bond can be directly observed. Oxygen chemisorption at room temperature leads to the formation of Cr=O groups. Therefore five different chromium-oxygen stretching frequencies are

(17) R. J. Davis, "Chemisorption," W. E. Garner, Ed., Academic Press, New York, N. Y., 1957.

(18) F. S. Stone, *Advan. Catal.*, **13**, 1 (1962).

(19) K. Hauße, *ibid.*, **6**, 213 (1955).

expected, corresponding to the five situations of Scheme I. Spectra of Figure 1 clearly show that five bands are present in the 1024–980-cm⁻¹ region, and, in particular, a doublet is at 1024–1016 and a triplet at 995–980 cm⁻¹. This correspondence does not seem to be fortuitous, because it is accompanied by several minor observations that are reported below. There is a clear separation of 20 wave numbers between the two groups of bands, while the doublet lies within 8 cm⁻¹ and the triplet within 15 cm⁻¹. A great deal of spectroscopic literature leads to the conclusion that M=O stretching frequency increases with decreasing coordination number. This is particularly true in the case of VOCl₃¹⁵ (coordination number 4), V₂O₅ (coordination 5),¹² and VO complexes in which V has an octahedral coordination.²⁰ Therefore the doublet should be assigned to structures 4 and 5 of Scheme I and the triplet to structures 1–3. This tentative assignment seems to be necessary if other facts are taken into consideration: water and pyridine adsorption at room temperature onto preadsorbed oxygen (part IV) quickly eliminates the doublet. In fact structures 4 and 5 of Scheme I after oxygen chemisorption still have the possibility of adsorbing water and pyridine because they are still c.u.s. This possibility is obviously missing in the case of structures 1–3, when saturated by chemisorbed O₂. Also spectra of Figure 3 are in agreement with the above assignment, for we observe that only one absorption at 980–986 cm⁻¹ is formed when oxygen is chemisorbed onto poorly dehydrated samples. When higher dehydration temperatures are employed and sites with two coordinative vacancies are probably formed, the higher frequency doublet is formed upon oxygen chemisorption.

Finally our assignment is consistent with the results obtained in the experiments on surface oxygen mobility that are reported above. From all we have seen so far it might be concluded that what we termed "coordinative heterogeneity" plays a major role in the energetic differentiation of active sites and that the "ligand heterogeneity" causes a further minor differentiation. In this discussion we only took into consideration the local situation of adsorbing chromium ions, every influence of neighboring groups being disregarded. This simplification is fair to more than a first approximation in that the spectroscopic behavior of our surface groupings is well defined and very similar to the behavior of mononuclear chromium complexes and compounds. On the other hand, it must be kept in mind that surface ligands (OH⁻ and O²⁻ c.u.s. ions) are also ligands of neighboring metals ions, and that newly introduced ligands, by gas adsorption, can partially saturate coordinative vacancies of nearby ions. These considerations recall the collective character of surface and would account for several slightly different situations that might be produced around a given surface group on considering at least the six surrounding positions.

The collective character of surface also suggests that the adsorption of a ligand onto a metallic site can modify the electron situation of neighbors. In particular, if adsorption takes place through electron transfer from adsorbate to adsorbent, the affinity of free sites is expected to decrease with increasing coverage. This fact is revealed in the ir spectra by a lowering of force constants that is particularly evident when pyridine is adsorbed onto chemisorbed oxygen. Besides the differentiations given by the first two types of heterogeneity, several minor effects can contribute to the overall complexity of the spectra and can also account for small frequency shifts that are observed in the oxygen bands owing to pretreatment conditions and coverage. Such minor effects can also explain the sensitivity of chemisorbed oxygen bands to the presence of N₂O weakly bonded onto neighboring sites (see Figure 4).

So far the discussion only dealt with oxygen bands in the 1024–980-cm⁻¹ range which are by far the most important in the case of room temperature chemisorption. Weak bands are also formed at 900–880 and 850–750 cm⁻¹ (Figure 1), which become much stronger when oxygen is chemisorbed at higher temperature. Our assignment was to complex CrO₄^{z-} groupings, either monomeric or polymeric. They likely come from the rearrangement of species at higher frequency. The required amount of energy for this rearrangement could be supplied at room temperature by the chemisorption process itself, which is highly exothermic.

Surface Layer Mobility and the Anomalous Band at 1035 Cm⁻¹. The ir spectrum of chemisorbed oxygen remaining on the surface after a prolonged degassing at 400° (Figure 6) is practically the same (except for a band at 1035 cm⁻¹) as the spectrum that is obtained when a sample that chemisorbed oxygen at room temperature is warmed up to 400° under a static vacuum (Figure 7). As already observed in the Experimental Section, this demonstrates that on raising the temperature all the observed modifications have to be attributed to enhanced surface mobility, oxygen desorption only playing a minor role.² Experiments that are reported in Figures 4, 6, and 7 allow the following considerations: (a) Groups responsible for absorption at 1000–970 cm⁻¹ decrease in concentration with temperature. In particular, the bands at 980 and 986 cm⁻¹ are the most sensitive, and when they are completely eliminated the band at 995 cm⁻¹ also starts declining. (b) The destruction of the above species gives rise to bands at 1040–1000, 900–880, and 850–750 cm⁻¹. When the operation is performed under a static vacuum (Figures 4 and 7) a weak absorption is also formed at 1035 cm⁻¹, which has been previously assigned to a Cr=O stretching, where Cr is in a tetrahedral coordination.

(20) J. Selbin, L. H. Holmes, Jr., and S. P. McGlynn, *J. Inorg. Nucl. Chem.*, **25**, 1359 (1963).

What is observed above demonstrates that low absorbing species are produced by destruction of the higher absorbing ones. Surface rearrangement leading to those transformations is favored by surface mobility which becomes important between 200 and 400°. The destruction of CrO groups with Cr in an octahedral coordination also generates higher absorbing species, where Cr has a coordination number lower than 6. This suggests that at high temperatures ligands of octahedral species are removed from the central ion, leading to species of lower coordination. Removed ligands would migrate to form complex oxide islands of high valence. The formation of a band at 1035 cm^{-1} is probably accounted for because a tetrahedrally coordinated Cr can be generated by migration of two ligands from an octahedral structure or of one ligand only from a square-pyramidal one. The absence of the 1035- cm^{-1} species, when dynamic vacuum conditions are employed, might be ascribed to a lower stability.

Conclusion

Ir spectroscopy has been used to characterize chemisorbed oxygen onto a metallic oxide. The following information has been obtained. (1) O_2 chemisorption at room temperature is dissociative. (2) Oxygen atoms

are linked to the surface through covalent double bonds. (3) Active sites are generated by surface dehydration. (4) α -Chromia surface (001) is highly heterogeneous, site differences being mainly brought about by initial coordination number of Cr ions and by the type of ligands. (5) At high temperature complex "chromate-like" groupings are formed. (6) At high temperature, surface mobility promotes an equilibrium among adsorbed species.

The above conclusions still do not give a complete picture of the O_2 - Cr_2O_3 system, more experiments being required mainly concerning the "high temperature species" and the interaction at lower temperature (from room temperature to 78°K). Different experimental techniques are at present under study, to approach the problem from different points of view.²¹

Acknowledgment. This work has been supported by the Consiglio Nazionale delle Ricerche.

(21) NOTE ADDED IN PROOF. Since submission of this paper we have become acquainted with two papers by A. A. Davidov, *et al.* [*Kinet. Katal.*, 10, 919, 1103 (1969)], in which they found some bands due to oxygen adsorbed on polycrystalline Cr_2O_3 in the spectral region 820–1020 cm^{-1} . They assign them to stretching modes of groups M–O on different crystal faces having a band order between 1 and 2.

An Infrared Study of Surface Properties of α -Chromia.

III. Adsorption of Carbon Dioxide¹

by A. Zecchina, S. Coluccia, E. Guglielminotti, and G. Ghiotti

Istituto di Chimica Fisica dell'Università di Torino, Turin, Italy (Received October 19, 1970)

Publication costs assisted by the Consiglio Italiano delle Ricerche (C.N.R.)

An ir investigation has been done of CO_2 adsorbed onto an α - Cr_2O_3 sample in which the (001) face is predominant. Two different types of interaction are observed: a strong chemisorption leading to bidentate carbonates and bicarbonates and a weak chemisorption whose products are "organic" carbonates. CO_2 adsorption confirms a great heterogeneity even in a one-face system. Surface hydroxyls and Cr^{3+} c.u.s.- O^{2-} c.u.s. couples are mainly revealed.

Introduction

Parts I and II dealt with H_2O , D_2O , CO , and O_2 adsorption on α - Cr_2O_3 . In this paper the chemisorption of carbon dioxide onto the same catalyst is discussed and a few mechanisms are proposed.

Ir spectroscopy has been widely used to study CO_2 adsorption onto various oxides^{2–9} and onto chromium oxide supported by alumina¹⁰ and silica.¹¹ No spectro-

scopic data are available relative to CO_2 adsorption onto nonsupported chromia, but other techniques have

(1) Correspondence should be sent to E. Borello, Istituto di Chimica Fisica dell'Università di Torino, Turin, Italy.

(2) (a) J. H. Taylor and C. H. Amberg, *Can. J. Chem.*, **39**, 535 (1961); (b) M. Courtois and S. J. Teichner, *J. Chim. Phys.*, **59**, 272 (1962).

(3) S. Matsushita and T. Nakata, *J. Chem. Phys.*, **36**, 665 (1962).

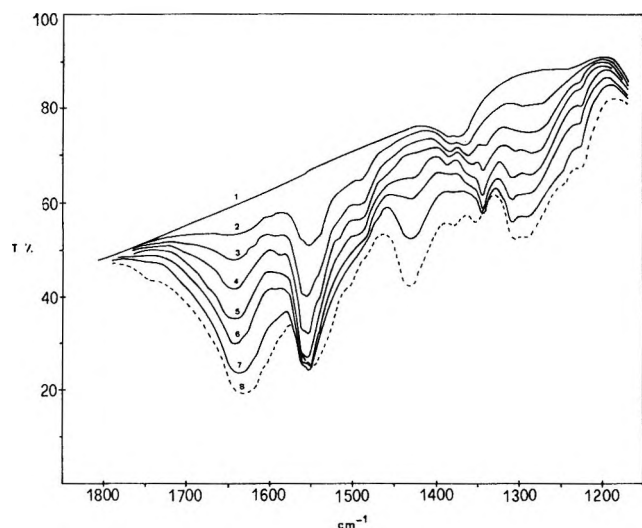


Figure 1. Ir spectra of α - Cr_2O_3 at increasing CO_2 coverages at room temperature: curve 1, background; curves 2-6, equilibrium pressures of CO_2 are in the 10^{-4} to 10^{-1} Torr range; curve 7, equilibrium pressure 1 Torr; curve 8, equilibrium pressure 40 Torr (% transmission vs. wavelength in cm^{-1}).

been employed so far.¹²⁻¹⁴ Previous experiments (parts I and II) showed that α -chromia surface contains coordinatively unsaturated chromium ions (Cr^{3+} c.u.s.), coordinatively unsaturated oxygen ions (O^{2-} c.u.s.), and hydroxyl groups (OH^-). Oxygen and carbon monoxide interact only with Cr^{3+} c.u.s. ions. Water molecules are mainly dissociated on Cr^{3+} c.u.s. and O^{2-} c.u.s. ions. Carbon dioxide is nondissociatively chemisorbed on all sites, and its importance as a test molecule of surface heterogeneity is complementary to the use of the above gases.

Experimental Section

Several α -chromia samples have been prepared as described in part I, and CO_2 chemisorption has been investigated in the same spectroscopic conditions there reported. We would point out again that in our α - Cr_2O_3 preparation no micropores are present and (001) face is definitely predominant.

Results

The ir spectrum of α -chromia is reported in Figure 1, curve 1, and has been discussed previously (part I). It is well reproduced in all of the samples employed except for the complex bands at 1375 cm^{-1} , whose intensity varies from one sample to another and is never strong.¹ Curves 2-6 of Figure 1 are the spectra of chemisorbed CO_2 recorded at increasing coverages in equilibrium conditions. It is quite evident that even small doses of CO_2 produce ir spectra of surprising complexity. Curves 2-6 correspond to the adsorption up to the equilibrium pressure of 0.1 Torr. The 1800 - 1150-cm^{-1} range contains four complex bands: one is

at 1780 - 1580 cm^{-1} with maximum at $\sim 1640\text{ cm}^{-1}$, another is at 1580 - 1450 cm^{-1} with maximum at $\sim 1560\text{ cm}^{-1}$, a third one is at $\sim 1430\text{ cm}^{-1}$, and the last one is at 1400 - 1150 cm^{-1} , exhibiting a broad absorption and two peaks at 1340 and 1225 cm^{-1} . Curves 7-8 correspond to equilibrium pressures of 1 and 40 Torr; an increased intensity is observed in the whole range except for the absorption at 1560 cm^{-1} that is shifted to lower frequencies (1550 cm^{-1}) and the band at 1340 cm^{-1} that is shifted to higher frequencies (1350 cm^{-1}). A strong band is developed at 2360 cm^{-1} that is not reported in the figure. Pressures above 40 Torr do not produce any further change in the spectrum. Absorptions in the 1100 - 750-cm^{-1} region are not reported in the figure, their identification being almost impossible due to their weakness and to the presence of background bands and bending modes of residual surface hydroxyls perturbed by adsorbed CO_2 . Figure 2 shows the ir spectra relative to the room temperature desorption of adsorbed CO_2 from an initial equilibrium pressure of 40 Torr. All of the previously mentioned absorptions are severely weakened except for the 1550-cm^{-1} band which is shifted back to 1560 cm^{-1} and the 1350-cm^{-1} band which is shifted to 1340 cm^{-1} . Moreover, the peaks at 1225 and 1340 cm^{-1} are better resolved owing to decreased broad absorption between them. The 2360-cm^{-1} band is eliminated in less than 1 min. Total elimination of chemisorbed CO_2 cannot be obtained at room temperature, a few hours degassing at 400° being required for it. Spectra relating to degassing at temperatures higher than 25° are not reported because spectral modifications are caused by enhanced temperature, suggesting that other surface species are involved. Figure 3 shows the spectra obtained when CO_2 was adsorbed (with the procedure described above) onto a sample that was prepared in the usual way and then contacted with 10 Torr of O_2 at 400° for 30 min, reduced with CO at 400° , and degassed at the same temperature. Curves 2-5 (pressures lower than 0.1 Torr) mainly differ from the corresponding ones of Figure 1 in that two bands at 1590 and 1305 cm^{-1} are more evident and the bands at 1430 and 1225 cm^{-1} are definitely

(4) W. I. Stuart and T. L. Whateley, *Trans. Faraday Soc.*, **61**, 2763 (1965).

(5) P. Pichat, J. Véron, B. Claudet, and M. V. Mathieu, *J. Chim. Phys.*, **63**, 1026 (1966).

(6) J. V. Evans and T. L. Whateley, *Trans. Faraday Soc.*, **63**, 2769 (1967).

(7) S. J. Gregg and J. D. F. Ramsay, *J. Phys. Chem.*, **73**, 1243 (1969).

(8) N. D. Parkyns, *J. Chem. Soc.*, 410 (1969).

(9) M. Primet, Thesis, Lyon, 1970.

(10) L. H. Little and C. H. Amberg, *Can. J. Chem.*, **40**, 1997 (1962).

(11) A. Zecchina, C. Morterra, G. Ghiotti, and E. Borello, *J. Phys. Chem.*, **73**, 1292 (1969).

(12) D. A. Dowden and W. E. Garner, *J. Chem. Soc.*, 893 (1939).

(13) M. S. McIver and H. H. Tobin, *J. Phys. Chem.*, **64**, 451 (1960).

(14) R. L. Burwell, Jr., G. L. Haller, K. C. Taylor, and J. F. Read, *Advan. Catal.*, **20**, 1 (1969).

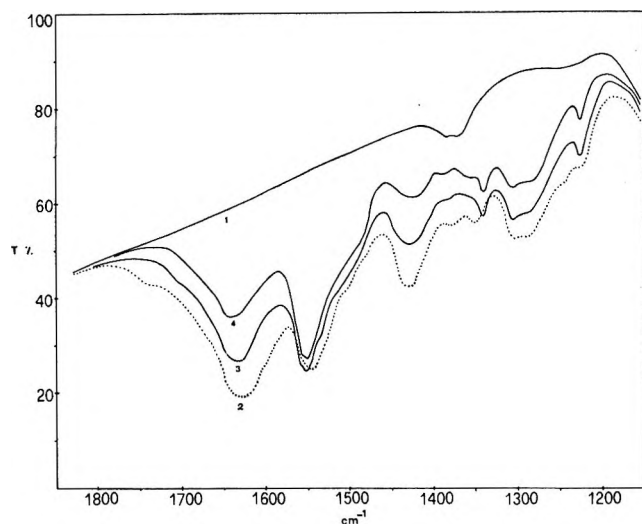


Figure 2. Ir spectra of α -Cr₂O₃ at different CO₂ desorption stages: curve 1, background; curve 2, curve 8 of Figure 1; curve 3, after 1-min degassing at room temperature; curve 4, after 1-hr degassing at room temperature (% transmission vs. wavelength in cm⁻¹).

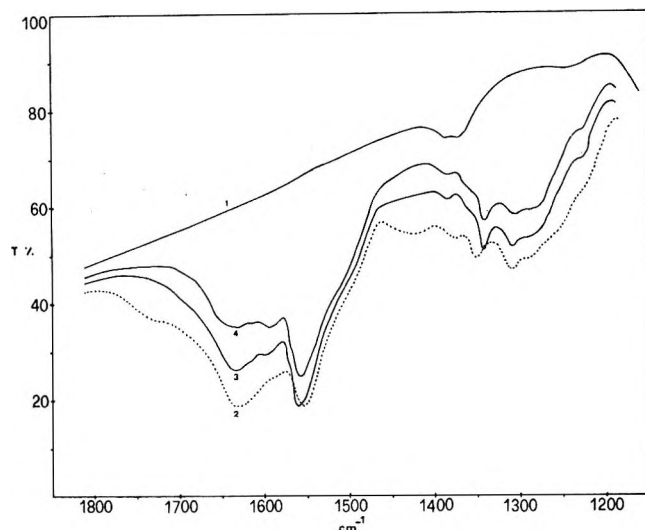


Figure 4. Ir spectra of a severely dehydrated α -Cr₂O₃ sample at different CO₂ desorption stages: curve 1, background; curve 2, curve 6 of Figure 3; curve 3, after 1-min degassing at room temperature; curve 4, after 1-hr degassing at room temperature (% transmission vs. wavelength in cm⁻¹).

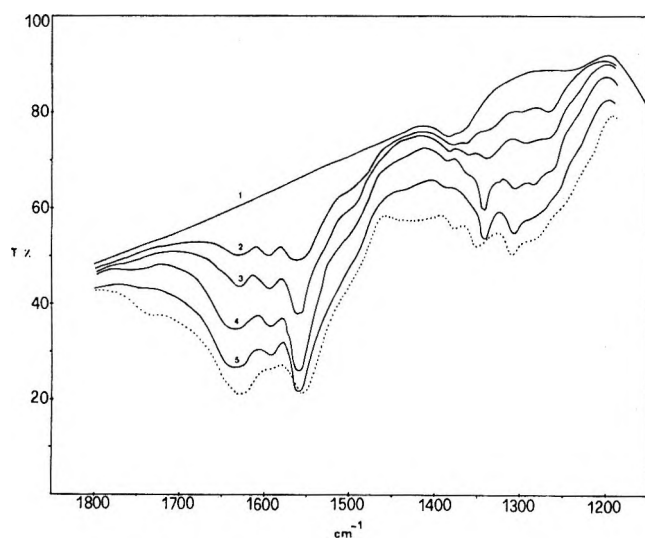


Figure 3. Ir spectra of a severely dehydrated α -Cr₂O₃ sample at increasing CO₂ coverages at room temperature: curve 1, background; curves 2-5, equilibrium pressures of CO₂ are in the 10⁻⁴ to 10⁻¹ Torr range; curve 6, equilibrium pressure 40 Torr (% transmission vs. wavelength in cm⁻¹).

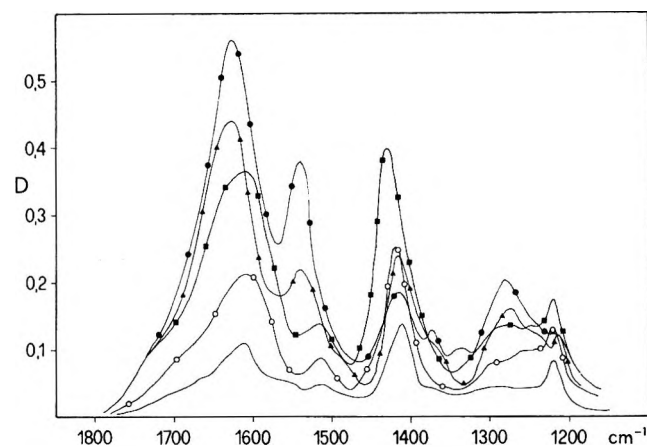


Figure 5. Ir spectra of CO₂ (40 Torr) on a α -Cr₂O₃ sample at various dehydration degrees. Dehydration times and temperatures are: —, 1 hr at 100°; —○—○—, 1 hr at 200°; —■—■—, 1 hr at 300°; —▲—▲—, 1 hr at 400°; —●—●—, 13 hr at 400° (optical density vs. wavelength in cm⁻¹).

weaker. The spectrum at the top pressure (40 Torr) differs from the corresponding one of Figure 1 because the bands at ~ 1560 and 1640 cm⁻¹ almost have equal intensity and the band at 1430 cm⁻¹ is quite weaker. Also in this case a strong band is observed at 2360 cm⁻¹. Figure 4 shows the spectra during a room temperature degassing of the sample of Figure 3, curve 6.

To confirm that active sites on chromium oxide are produced upon surface dehydration the experiment reported in Figure 5 has been run. Notice that this ex-

periment and its goal are very similar to others previously described relative to CO and O₂ chemisorption. An α -Cr₂O₃ sample was heated with water vapor at 400° as to have a fully hydrated surface. After a room temperature evacuation, such a sample did not exhibit any activity towards CO₂. A 30-min degassing was done at 100° , and the ir spectrum was recorded before and after CO₂ reaction. All of the chemisorbed CO₂ was then removed by degassing at 400° , and the sample was rehydrated with H₂O at 400° . A dehydration at 200° was performed and the CO₂ activity was checked. Such a cycle was repeated several times only

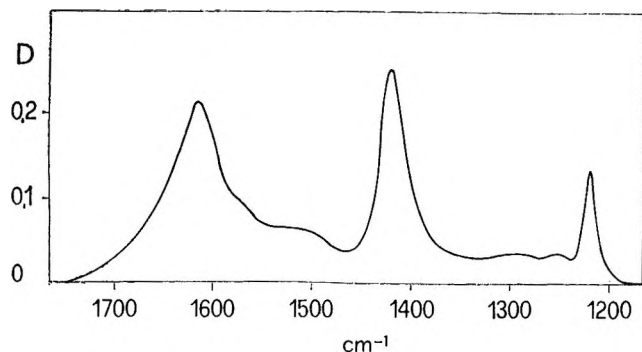


Figure 6. Ir spectra of CO_2 (40 Torr) on a $\alpha\text{-Cr}_2\text{O}_3$ sample oxidized at room temperature and reduced in hydrogen at 150° (optical density vs. wavelength in cm^{-1}).

changing the dehydration temperature, the evolution of the ir spectra with varying dehydration temperature being clearly shown in Figure 5. We point out that for dehydration temperatures up to 200° undissociated water is still present on the surface. In part I we indicated that a sample which preadsorbed oxygen and has been reduced in H_2 at 150° only contains surface hydroxyls. The interaction of CO_2 with such a surface is illustrated in Figure 6. Few bands of very weak intensity are observed along with three strong absorptions at 1620, 1425, and 1225 cm^{-1} . When the reduction was made with deuterium, the CO_2 spectrum was very much the same except for the band at 1225 cm^{-1} that was shifted to 975 cm^{-1} . Carbon dioxide is supposed¹⁴ to interact both with Cr^{3+} ions and surface oxygen ions. Some experiments have been run to investigate the CO_2 behavior on a surface that does not contain either of the two types of sites. We saw in part II that Cr^{3+} ions irreversibly chemisorb O_2 . Curve 3 of Figure 7 is the spectrum of 40 Torr of CO_2 equilibrated with a sample that preadsorbed O_2 , and curve 4 of Figure 7 shows that only three weak bands remain at 1610, 1430, and 1225 cm^{-1} after a 1-min evacuation. This behavior is well reproduced on a sample which preadsorbed pyridine. (Pyridine chemisorption onto chromium sites will be discussed elsewhere.)

The ir spectrum of carbon dioxide chemisorbed at high temperature is rather different from that at room temperature and is reported in Figure 8. A decreased intensity is observed of the bands at higher frequencies (above 1575 cm^{-1}) and a higher intensity of the bands at ~ 1500 and at $1350\text{--}1400\text{ cm}^{-1}$.

Reproducibility of the CO_2 - $\alpha\text{-Cr}_2\text{O}_3$ Interaction. The ir spectrum of chemisorbed CO_2 does not depend on the background band at 1375 cm^{-1} and slightly varies with oxygen pretreatments. This is evident from the experiments of Figures 1 and 3, in which oxygen pretreatments were run at pressures of 0.05 and 10 Torr, respectively. Also, the observed differences are mainly due to different dehydration conditions and small amounts of water vapor on samples prepared as the one of Figure

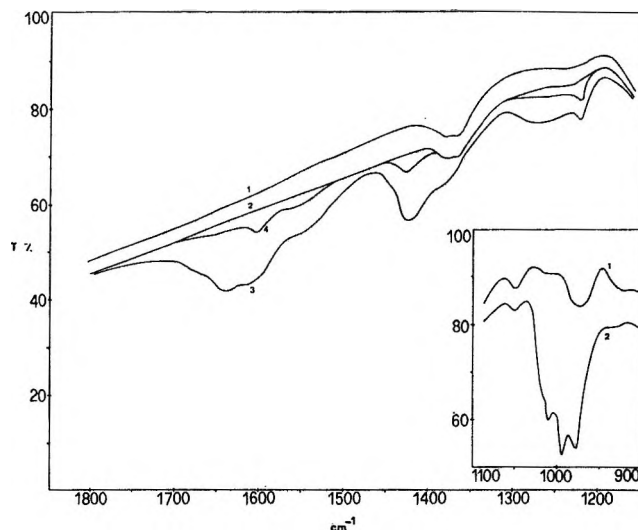


Figure 7. Ir spectra of CO_2 (40 Torr) on a $\alpha\text{-Cr}_2\text{O}_3$ sample oxidized at room temperature: curve 1, background; curve 2, after contact with O_2 and evacuation at room temperature; curve 3, after contact with CO_2 (40 Torr); curve 4, after 1-min degassing at room temperature ($\%$ transmission vs. wavelength in cm^{-1}).

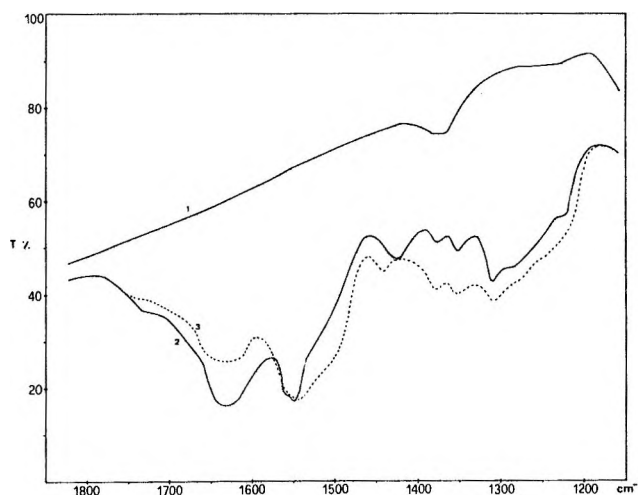


Figure 8. Temperature effect on CO_2 chemisorption: curve 1, background; curve 2, ir spectrum of CO_2 (40 Torr) chemisorbed at room temperature; curve 3, after 1-hr heating at 400° ($\%$ transmission vs. wavelength in cm^{-1}).

3 lead to CO_2 spectra as that of Figure 1. Curve 6 of Figure 5 shows how a sample that has been treated with H_2O cannot be dehydrated upon degassing at 400° to the extent of oxygen-treated samples. Spectra of chemisorbed CO_2 as the ones of Figure 1 or 3 can only be obtained upon further oxygen treatments that definitely promote surface dehydration as mentioned in parts I and II.

Discussion

Assignment of the Background Band at 1375 cm^{-1} . The band centered at 1375 cm^{-1} (curve 1, Figure 1) has

been also observed in other oxides.^{8,10} It is produced during the reduction with CO which follows the chromia crystallization in oxygen (see part I). Its spectral position is fairly constant, but its intensity varies from one sample to another and, on the same sample, through different redox cycles. It is not affected by degassing temperatures as high as 400–450° and is fully eliminated with oxygen at 400° to form weak bands at 1550 and 1350 cm⁻¹, which can be pumped off at 400°. Finally it is not affected by the adsorption of other gases nor is the adsorption of other gases affected by it. Parkyns⁸ found in the background spectra of γ -Al₂O₃ a strong band at 1380 cm⁻¹ which he partially ascribed to the cell employed. Little and Amberg¹⁰ observed both on chromia and chromia/alumina a band at 1370 cm⁻¹ that could be intensified by heating with CO (but not with CO₂) and which they assigned to carbonate ions. We do agree with this interpretation and think that our peak could be ascribed to carbonate ions formed through an activated process in a highly symmetric arrangement. In fact, simple carbonate ions have a mode in the 1470–1420-cm⁻¹ range.¹⁵ Oxygen treatment would destroy the complexes to produce CO₂, which likely generates different carbonates absorbing at 1550 and 1350 cm⁻¹ (see below).

Assignment of the Spectrum of Adsorbed CO₂. Burwell, *et al.*,¹⁴ suggested that both on chromia gel and α -chromia adsorbing sites can be thought as produced upon surface dehydration. Our former results (parts I and II) fully agree with this viewpoint. No adsorptive capacity towards CO₂ is exhibited by a fully hydrated sample, an activity only being developed upon degassing in the 100–200° range. The overall amount of adsorbed CO₂ is directly related to the outgassing temperature. With increasing dehydration the shape of the spectrum of adsorbed CO₂ gradually varies, suggesting that active sites change both in number and in nature with outgassing temperature. The hypothesis (already proposed in parts I and II) that surface ions become active sites as a consequence of coordinative unsaturation allows a closer comparison between surface complexes and coordination compounds for assignment purposes. On the basis of this method alone it is yet impossible to distinguish among all of the carbonate-like species that are likely formed on the surface. In fact results obtained by many authors, which have been summarized by Little,¹⁶ show that very rarely a strict correspondence is observed between inorganic and surface complexes. This is not surprising, for inorganic complexes are individual molecules and surface groups belong to a much more complex network. For example, an oxygen ion coordinatively unsaturated that might enter into a surface carbonate group is bridged between two octahedra. Also, an oxygen atom of adsorbed CO₂ saturates a coordinative vacancy that belongs to two neighboring octahedra (see Figure 8 of part I). It is therefore quite important to check the spectral varia-

tions of the adsorbed phase with varying number, nature, and distribution of active sites in order to understand where and how the surface complexes are formed. As previously described, CO₂ has been put into contact with highly dehydrated surfaces (Figures 1 and 3), with variously hydrated samples (Figures 5 and 6), and with surfaces saturated with O₂ (Figure 7) and pyridine. The structures that will be proposed can still contain some uncertainties, mainly due to the tremendous spectral complexity. In fact the ir spectrum of α -Cr₂O₃ saturated with CO₂ (Figure 1, curve 8) is much more crowded than in the case of chromia/silica¹¹ or chromia/alumina¹⁰ so that it is difficult to correlate the bands and to decide which species are actually present on the surface. Unfortunately no information can be derived from the 1100–750-cm⁻¹ region, as previously mentioned. Nevertheless, some assignments can be made, by considering first the chemisorption of CO₂ at equilibrium pressures up to 0.1 Torr only. We think that every single assignment is mainly justified, more than in itself, by the reasonable consistency of the overall picture.

Adsorption of CO₂ at p ≤ 0.1 Torr. Bands at 1620, 1430, and 1225 Cm⁻¹. Although the band at 1430 cm⁻¹ (Figure 1, curves 2–6) is not the most intense one, we think that it is related to particularly important sites and will be considered first. Bands in this frequency range (1450–1400 cm⁻¹) have been previously observed on oxides and metals^{2a,3,10,17,18} and have been assigned either to the only normal mode of carbonate ions of D_{3h} symmetry^{2a,3,10,17} or to the low frequency mode of carboxylate groups.¹⁸ Neither of the above assignments applies to our band, for we believe that it is connected with two other bands at 1620–1610 and 1225 cm⁻¹, respectively. This is not particularly evident from Figure 1 but can be deduced from the experiments of Figures 5 and 6. Figure 6 shows three strong bands in the above positions, and spectra of Figure 5 indicate how, on increasing the dehydration temperature, three bands similar to those of Figure 6 grow first and then decrease, other absorptions becoming predominant. This definitely proves that surface hydroxyls are involved in the mechanism; Figure 6 refers to the interaction of CO₂ with a highly hydrated surface and Figure 5 to a sample on which free hydroxyls are first formed (upon desorption of hydrogen-bonded H₂O) and then eliminated through the reaction 2OH⁻ → H₂O + O²⁻. The comparison of Figures 1 and 3 reveals that on a more dehydrated surface the bands at 1225 and 1430 cm⁻¹ are weaker and the absorption above 1580 cm⁻¹ is

(15) B. M. Gatehouse, S. E. Livingstone, and R. S. Nyholm, *J. Chem. Soc.*, 3137 (1958).

(16) L. H. Little, "Infrared Spectra of Adsorbed Species," Academic Press, New York, N. Y., 1966.

(17) C. E. O'Neill and D. J. C. Yates, *Spectrochim. Acta*, **17**, 953 (1961).

(18) R. P. Eishens and W. A. Pliskin, *Advan. Catal.*, **9**, 662 (1957).

simpler. We think that the bands are due to a bicarbonate group; the antisymmetric mode being at 1620 cm^{-1} , the symmetric one at 1430 cm^{-1} . The 1225-cm^{-1} peak would be the OH bending mode as proved by the shift to 975 cm^{-1} upon deuteration. Due to heavy light scattering in the high frequency region, it has been impossible to observe the OH stretching mode that is expected⁸ to absorb around 3600 cm^{-1} . The existence of surface bicarbonates has already been proposed,^{6,8,9} and our results are in good agreement with Parkyns⁸ ones on $\gamma\text{-Al}_2\text{O}_3$. The highest difference is in the symmetric mode, but this mode is known to vary in a wide range.¹⁹ Figure 2 shows that the surface bicarbonate is stable to room temperature degassing and is removed at 200° .

Bands at 1560 and 1340 Cm^{-1} . The band at 1560 cm^{-1} is the most intense one at low equilibrium pressures (Figure 1, curves 2-6) and is associated with the band at $\sim 1340\text{ cm}^{-1}$. They are both shifted at high CO_2 pressure (Figure 1, curve 8) and are the only bands (besides those due to bicarbonates) that are not affected by room temperature evacuation. They cannot be ascribed to carboxylate ions for they do not correspond to the frequencies reported by Spinner²⁰ for many R-CO_2^- compounds. They are also associated with absorptions in the $1100\text{-}800\text{-cm}^{-1}$ range which are not present in the case of carboxylate but are typical of carbonates and therefore our assignment is to carbonate ions. On a merely spectroscopic basis it cannot be decided whether our carbonates are mono- or bidentate, since our frequencies are right in the middle of the two characteristic regions.¹⁶ The experiments of Figure 7 clearly show that the two bands are missing when the surface is saturated with oxygen (a similar result is obtained with pyridine), and this turns the assignment in favor of the bidentate structure. In these complexes an oxygen atom of the carbon dioxide would saturate a coordination vacancy of the chromium ion, and the carbon atom interacts with a nonsaturated surface oxygen. The formation of this species should be favored by the dehydration that produces Cr^{3+} c.u.s.- O^{2-} c.u.s. couples (see part I), and the experiment of Figure 5 indicates that this is the case. Blyholder²¹ obtained a couple of bands at 1560 and 1330 cm^{-1} on oxidizing the CO-Ni system and his assignment was also to bidentate carbonates. Also on MgO ⁶ the lower absorbing mode of a bidentate carbonate has been observed at 1325 cm^{-1} , well above the expected range ($1270\text{-}1260\text{ cm}^{-1}$).

Bands above 1580 and at 1325-1250 Cm^{-1} . The broad absorption above 1580 cm^{-1} is rather complex (Figure 1, curves 2-6), has a maximum at $\sim 1640\text{ cm}^{-1}$, and includes the high frequency mode of bicarbonate groups. It is quite simpler in the spectra of Figure 3 (curves 2-5) for the mode of bicarbonates is missing and a band is reasonably well resolved at $\sim 1590\text{ cm}^{-1}$ that could only be guessed in Figure 1. It can be assumed that in this region two absorptions are mainly

present at 1590 and 1635 cm^{-1} . We think that also these are the antisymmetric stretch of bidentate carbonates in other surface arrangements than those previously discussed. The low frequency modes of these species are likely in the broad absorption at $1325\text{-}1250\text{ cm}^{-1}$ and cannot be resolved with certainty (from the spectra of Figures 3 and 4 they could be tentatively localized at 1305 and 1285 cm^{-1} , respectively). Evacuation experiments at room temperature (Figures 2 and 4) conclusively correlate the absorption above 1580 cm^{-1} with those at $1325\text{-}1250\text{ cm}^{-1}$, and these ranges fit better than those previously reported.¹⁶ CO_2 adsorbed on ThO_2 ⁵ gives rise to two bands at 1610 and 1290 cm^{-1} , which have been assigned to bidentate carbonates.

Bands at 1490 and 1365 Cm^{-1} . Only minor quantities of monodentate carbonates are formed on $\alpha\text{-Cr}_2\text{O}_3$ surface which are responsible for two weak bands at ~ 1490 and 1365 cm^{-1} (Figure 1, curves 2-6). The spectral splitting agrees well with that of similar inorganic complexes,^{15,22} and the positions are fairly close to those assigned to monodentate carbonates on MgO .⁶ These surface complexes are very stable and can only be removed on degassing at about 400° .

CO_2 Adsorption at Higher Pressures (1-40 Torr). Equilibrium pressures above 0.1 Torr induce strong modification in the spectrum, as observed in Figure 1, curves 7 and 8. In detail, the overall intensity above 1575 cm^{-1} is enhanced with a pronounced shoulder at $\sim 1740\text{ cm}^{-1}$; bands at 1430 and at $1325\text{-}1200\text{ cm}^{-1}$ are intensified; bands at 1560 and 1340 cm^{-1} are slightly shifted. A strong band is formed at $\sim 2360\text{ cm}^{-1}$, which is not reported in the figure. At pressures higher than 40 Torr no further modifications are produced. All of the new formed species are weakly held, and a 1-min degassing at room temperature gets rid of them entirely.

Band at 2360 Cm^{-1} . Bands so close to the gaseous CO_2 frequency have been already observed on $\text{Cr}_2\text{O}_3/\text{SiO}_2$ ¹¹ and on $\gamma\text{-Al}_2\text{O}_3$.⁸ They can be assigned to CO_2 weakly adsorbed onto cationic sites, which still preserves its linear structure.

Band at 1740 Cm^{-1} . It is quite probably due to structures of the "organic" carbonate type which alone exhibit such a high CO stretching frequency.¹⁵ The other mode should be below 1280 cm^{-1} and could partially account for the increased intensity in that region (Figure 1, curve 8). The presence of this kind of carbonate has been previously observed on other materials.^{8,11}

Bands at 1575-1700 and $\sim 1440\text{ Cm}^{-1}$. Several

(19) F. A. Miller and C. H. Wilkins, *Anal. Chem.*, **24**, 1254 (1952).

(20) E. Spinner, *J. Chem. Soc.*, 4217 (1964).

(21) G. Blyholder, "Proceedings of the 3rd International Congress on Catalysis," North-Holland Publishing Co., Amsterdam, 1964.

(22) J. Fujita, A. E. Martell, and K. Nakamoto, *J. Chem. Phys.*, **36**, 339 (1961).

bands contribute to the increased intensity in the 1575–1700-cm⁻¹ region, and the assignment is therefore quite difficult. The presence of newly formed bidentate carbonates, whose lower mode would still be at 1325–1200 cm⁻¹, cannot be excluded, but we think that the major feature of this region is a band centered at ~1630 cm⁻¹. It seems to be connected with a new band at ~1440 cm⁻¹, and both frequencies are close to those previously assigned to bicarbonate groups. Even so we exclude the same assignment for the 1630–1440-cm⁻¹ couple for two reasons. There is no increase of the band at 1225 cm⁻¹ nor the appearance of a new band in that area. All of the surface bicarbonates so far observed exhibit a much higher stability. The only possible assignment is to carboxylate-type groups, also because no bands in the 1100–800-cm⁻¹ region seem to be connected to the above, and our frequencies fit fairly well with those reported by Spinner.²⁰

CO₂ Adsorption on O₂-Treated Catalyst. Carboxylate groups seem to be the most abundant component in the spectrum of CO₂ adsorbed onto preadsorbed oxygen, for Figure 7 shows two intense bands at 1640 and 1435 cm⁻¹. The same spectrum also contains weaker bands above 1700 and at 1275 cm⁻¹ probably due to small amounts of organic carbonates. A 1-min degassing at room temperature (curve 4) leaves three weak peaks at 1610, 1430, and 1225 cm⁻¹ assigned to bicarbonates indicating that adsorbed O₂ does not interact with surface hydroxyls. In this experiment it is fairly evident that no bands below 1100 cm⁻¹ are associated with the two bands at 1640 and 1435 cm⁻¹ (there is no spectral change in that region when CO₂ contacts the catalyst) and the assignment to carboxylate groups seems to be confirmed. A similar behavior is observed when CO₂ reacts with a catalyst that adsorbed pyridine, though in this case several bands due to pyridine make the spectral identification rather involved. All of the surface species and suggested assignments are summarized in Table I.

Table I: Assignments of Carbonate-Like Surface Species

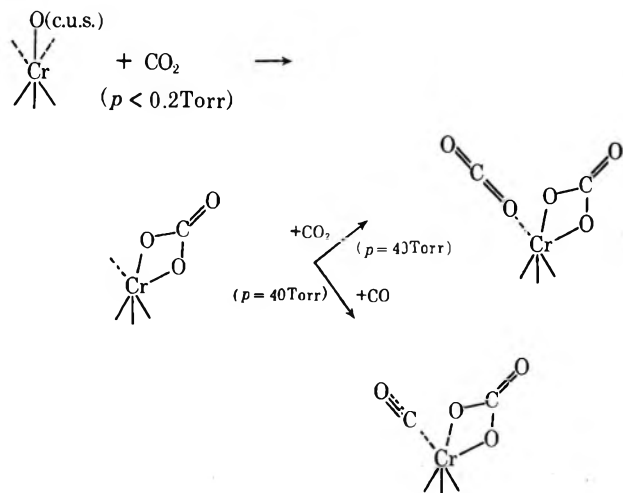
	Frequencies, cm ⁻¹	Assignments
Strong chemisorption	1620–1430–1225	Bicarbonates
	1560–1340	Bidentate carbonates
	1590–1305	Bidentate carbonates
	1635–1285	Bidentate carbonates
	1490–1365	Monodentate carbonates
Weak chemisorption	1740–below 1280	Organic carbonates
	1630–1440	Carboxylates
	2360	Linear CO ₂

The Structure of Surface Complexes and the Nature of Surface Sites. The results reported here indicate that CO₂ is chemisorbed through several mechanisms leading

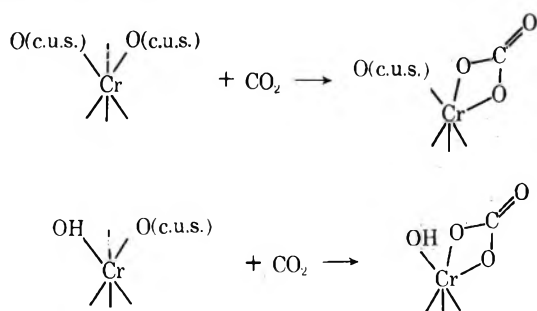
to different carbonate-like species. Moreover, two types of chemisorption are distinguishable: a strong chemisorption giving rise to surface species that need long times or high temperatures to be desorbed and a weak chemisorption leading to surface species that are quickly removed at room temperature. Surface sites are formed either by dehydration (see parts I and II) and are Cr³⁺ c.u.s. ions and O²⁻ c.u.s. ions, or are surface hydroxyls, the dehydration process never being complete. Active chromium ions can have one or two coordinative vacancies, as discussed previously (see Figure 8 of part I). Active centers for O₂ and CO adsorption are the cationic sites only, but CO₂ can interact with cations, anions, cation–anion couples, and hydroxyls.

Strong Chemisorption. On the basis of the above assignments, strong chemisorption would occur on surface hydroxyls, on Cr³⁺ c.u.s.–O²⁻ c.u.s. couples, and on O²⁻ c.u.s. ions. The first interaction, leading to bicarbonates, only begins when molecular water is desorbed, suggesting that cationic vacancies are needed. The mechanism is probably similar to Parkyns³ one on γ -Al₂O₃. The second interaction has been already discussed: an oxygen atom of CO₂ saturates a vacancy on a chromium ion and the carbon is coordinated by O²⁻ c.u.s. ion, the product being a bidentate carbonate. Two types of bidentate carbonates have been identified revealing that Cr³⁺ c.u.s.–O²⁻ c.u.s. couples of different nature are present on the surface. Different properties previously reported for the two carbonate groups confirm the heterogeneity and lead to some considerations. Let us consider the 1560–1340-cm⁻¹ bands first. The small spectral shift caused by high CO₂ pressures could be ascribed to lateral interaction between these groups and other groups formed at high coverages or to an overall variation of the electronic situation with coverage. However another interpretation seems to be more convincing, that which takes into consideration chromium unsaturation properties. Let us assume that bidentate carbonates at 1560–1340 cm⁻¹ are formed on a pair of sites whose chromium ion has two coordinative unsaturations. Either of the two vacancies would be saturated, the other one still being available for a further interaction. If CO is now allowed onto the sample, the 1560–1340-cm⁻¹ couple is shifted (more than it would be with 40 Torr of CO₂) and a band is formed at ~2200 cm⁻¹, due to chemisorbed CO (see part I). If the second coordinative vacancy is saturated by another CO₂ molecule, this might be thought to retain its linear structure and to contribute to the band at 2360 cm⁻¹. This weakly polarized species is quickly removed by evacuation at room temperature (less than 1 min) while the CO adsorbing at 2200 cm⁻¹ would need a longer evacuation. Such higher adsorption energy accounts for the higher shift induced in the 1560–1340-cm⁻¹ couple. Also, as no other bands in the spectrum are affected by high CO₂ (or CO) coverages,

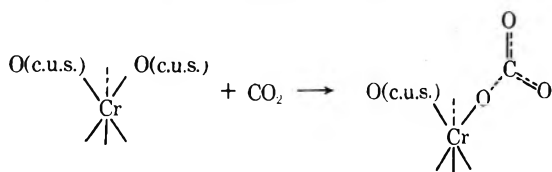
it seems quite likely that the interaction occurs on the same site, as summarized in the scheme below. The other



bidentate carbonates (bands above 1580 and at 1200–1325 cm^{-1}) are presumably formed on pairs of sites whose chromium ion has one coordinative unsaturation only. The lower stability of this second type of bidentate species is consistent with its assignment. In fact the crystal field stabilization is much higher on passing from coordination number 4 to 5 than from 5 to 6.¹⁴ Chromium ions with coordination number 5 (one coordinative unsaturation only) on highly dehydrated surfaces can be present in two structures, whose reaction with CO_2 would be



It is significant that in the frequency ranges now under consideration we actually observe two pairs of bands. We cannot try any more detailed assignment of the two species, but this correspondence between the number of possible structures and spectroscopic data is rather remarkable. The activity of the isolated O^{2-} c.u.s. ions is quite low, as the weak bands due to monodentate carbonates (couple at 1490–1365 cm^{-1}) indicate. Figure 8 shows that monodentate formation is more abundant if CO_2 is adsorbed at high temperature, suggesting that an activated process is involved. Similar observations have been reported on ThO_2 .⁵ From the fore-



going discussion, we might conclude that strong chemisorption is mainly due to Cr^{3+} c.u.s.– O^{2-} c.u.s. couples, isolated cations, and isolated anions exhibiting a feeble activity.

Weak Chemisorption. It is mainly responsible for organic carbonates, carboxylates, and linearly bonded CO_2 . Regardless of the correctness of this assignment, which is tentative especially in the case of carboxylates, the existence of a weak adsorption is by itself remarkable. In fact our spectroscopic evidence shows that all the quantitative determinations by Burwell¹⁴ and by McIver and Tobin¹³ refer to the strongly chemisorbed CO_2 only, and not to the exhaustive adsorption. We saw that a surface saturated with O_2 (or pyridine) weakly chemisorbs CO_2 and that the species so formed are the same obtained at high CO_2 coverages. This means that both CO_2 and O_2 (or pyridine) leave on the surface a certain amount of sites capable of weak interaction with CO_2 , though Figure 8 of part I indicated that all the Cr^{3+} c.u.s.– O^{2-} c.u.s. couples were in theory available to form bidentate carbonates. On a merely spectroscopic basis we cannot identify the limiting factors of CO_2 strong chemisorption and of O_2 or pyridine adsorption. These might be simple steric effects or, more likely, electronic factors or other properties of the surface as a whole. It is important anyway that infrared spectroscopy reveals weak interactions that are hardly detectable with other techniques.

The 2360- cm^{-1} band has been already discussed as due to linear CO_2 weakly interacting with chromium ions. Organic carbonates are originated from CO_2 molecules adsorbed onto Cr^{3+} c.u.s.– O^{2-} c.u.s. couples whose ions belong to different octahedra. We think that also carboxylate groups are originated from CO_2 molecules interacting with Cr^{3+} c.u.s.– O^{2-} c.u.s. couples rather than with one ion only. If the interaction of a Cr ion with one of the CO_2 oxygens and of the carbon with an O^{2-} ion varies the $\text{O}=\text{C}=\text{O}$ angle, both stretching modes become active.²³

CO_2 weak chemisorption as well as strong chemisorption seems therefore to reveal coordinatively unsaturated anion–cation couples.

Conclusions

(1) The overall spectral complexity suggests a surprising surface heterogeneity despite the presence of one crystallographic face only. (2) There are few types of heterogeneity (already suggested in parts I and II) that are confirmed. In fact the distinction between two types of bidentate carbonates reveals a coordinative heterogeneity (initial coordination number 4 or 5). The existence of two types of bidentates on chromium ions with coordination number 5 reveals a ligand heterogeneity. (3) Our spectroscopic data are

(23) N. B. Colthup, L. H. Daly, and S. E. Wiberley, "Introduction to Infrared and Raman Spectroscopy," Academic Press, New York, N. Y., 1964.

in excellent agreement with some results by Burwell, *et al.*¹⁴ In particular, (a) the nature of surface species depends on the degree of dehydration, (b) the total amount of strongly chemisorbed CO₂ slightly increases with activation temperature, for surface hydroxyls are active sites as well, (c) the amount of CO₂ that is not removed at 200° increases with increasing activation times and temperatures, because bidentate carbonates formed on highly dehydrated surfaces are more strongly held than bicarbonates that are predominant at low

dehydration degrees. (4) Strong chemisorption of CO₂ does not saturate surface activity as a further weak chemisorption clearly indicates. (5) CO₂ chemisorption reveals Cr³⁺ c.u.s.-O²⁻ c.u.s. couples as main active sites. (6) Relative concentrations and distribution of surface species vary with adsorption temperature.

Acknowledgment. This research has been supported by the Consiglio Nazionale delle Ricerche.

The Absorption Spectrum of e_{aq}⁻ in the Temperature Range -4 to 390°

by B. D. Michael, Edwin J. Hart,* and Klaus H. Schmidt

Chemistry Division, Argonne National Laboratory, Argonne, Illinois 60439 (Received February 12, 1971)

Publication costs assisted by the Argonne National Laboratory

The effect of temperature on the absorption spectrum of e_{aq}⁻ has been determined from -4 to 390°. Measurements below 100° were made using conventional pulse radiolysis techniques. Above 100° solutions were sealed into thick-walled high purity silica capillaries and irradiation took place within a thermostatically controlled oven. Absorptions were detected to 1.7 μ using a germanium infrared diode and a pulsed xenon arc light source. In the range -4 to 90° the shift of peak absorption energy is -0.003 eV/°C, in good agreement with earlier work.¹ The half-intensity width of the absorption is 0.885 ± 0.03 eV and no significant temperature dependence exists. The product $G\epsilon_{\max}$ is 5.23 ± 0.09 × 10⁴ (molecules/100 eV) × (M⁻¹ cm⁻¹) at 25°, with a linear temperature dependence of 19 ± 11 per °C. Above 100° the e_{aq}⁻ (D₂O) absorption maximum shifts continuously to lower energies with increasing temperature to and above the critical temperature (371°), the rate being -0.0015 eV/°C at 350°. The half-width of the absorption shows little change between 200 and °390 (average value 0.82 eV); however, the absorption becomes markedly less symmetrical with increasing temperature, favoring high-energy transitions. Over this broad temperature range where the structure of water changes drastically, our spectrum indicates that the electron interacts strongly with the surrounding water molecules and produces a stable entity. The trapping of electrons at supercritical temperatures where water is >95% monomeric indicates that preformed traps are not required for this process.

Introduction

With the hope of more clearly delineating the nature of the cavity and the mechanism of electron trapping in water, we have studied the absorption spectrum of e_{aq}⁻ in liquid water in the temperature range -4 to 390°. Earlier work¹ employing a γ-ray method for e_{aq}⁻ generation established that the band maximum, λ_{max}, shifts to longer wavelengths with increasing temperature. The reported energy shift of the absorption maximum, $E_{\lambda_{\max}}$, was 2.9 × 10⁻³ eV/deg in the 10-96° range of temperature. Our present studies by pulse radiolysis confirm this temperature coefficient. In addition we establish that the absorption spectrum is unaffected by pH and that the product of the e_{aq}⁻ yield, $g(e_{aq}^-)$, and the molar extinction coefficient at λ_{max}, ε_{λ_{max}}, [$g(e_{aq}^-) \times \epsilon_{\lambda_{\max}}$], is substantially constant from -4 to 90°. Thus, even though the struc-

ture of water changes appreciably over this temperature range, the needed trapping sites are either available or created by the electron.

Electrons hydrate at temperatures up to 390° and λ_{max} continues to shift to longer λ but with a constantly decreasing temperature coefficient. Because of the rapid reaction of e_{aq}⁻ with the products of radiolysis (e_{aq}⁻, H, OH, H⁺, H₂O) at temperatures above 100°, the maximum absorbance was measured during a 3-μsec electron pulse instead of after a much shorter electron pulse. We compare our results with those obtained in metal-NH₃ solutions and in F centers, and conclude that there is strong interaction between e_{aq}⁻ and the surrounding water molecules in the cavity.

(1) W. C. Gottschall and E. J. Hart, *J. Phys. Chem.*, **71**, 2102 (1967).

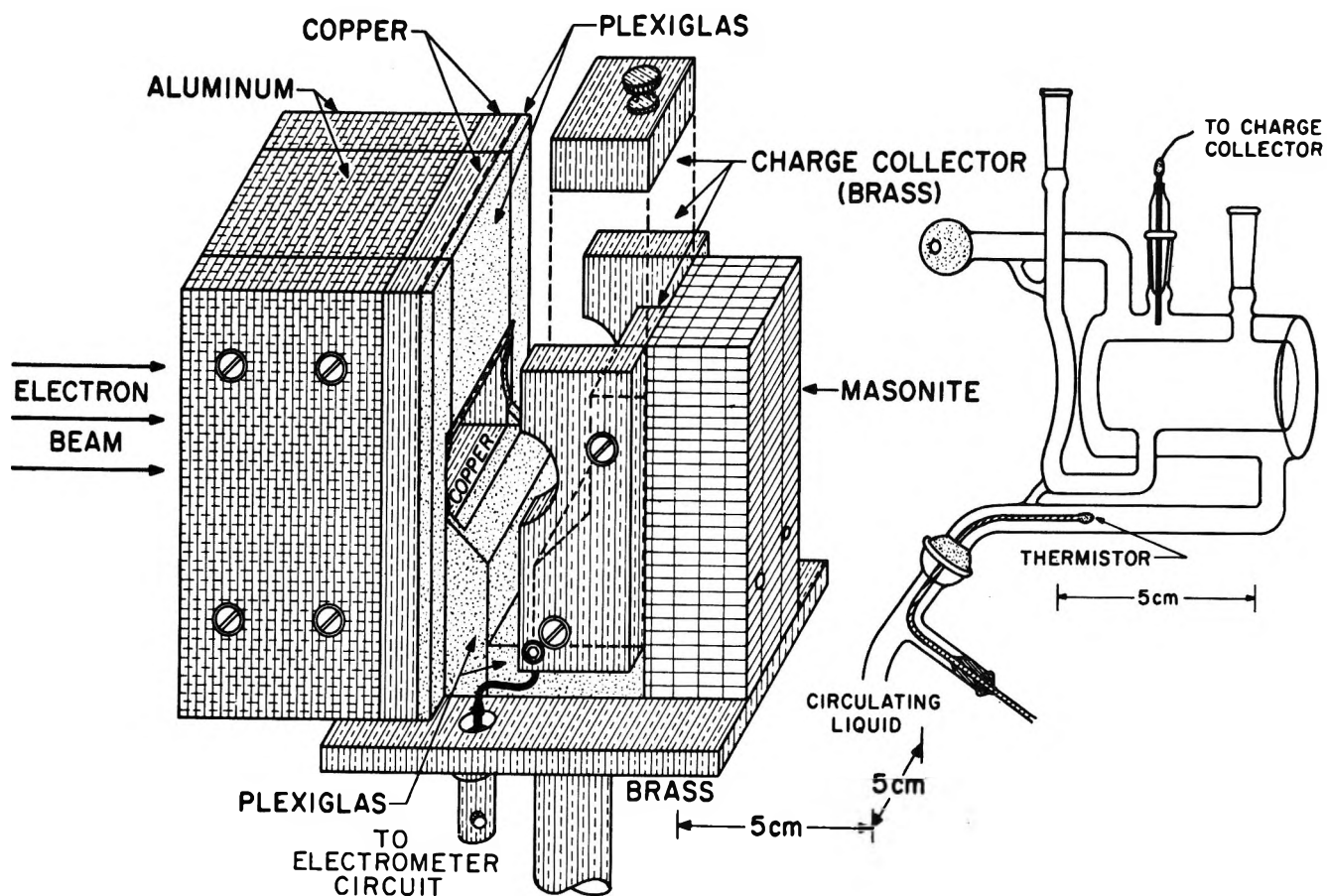


Figure 1. Details of jacketed cell and holder showing electron beam collimator and charge collector. (The 5-cm indicators refer to the dimensions in the x and y planes.)

Some conclusions are also drawn regarding e_{aq}^- rate constants in superheated water.

Experimental Section

Temperature Range -4 to 90° . *Preparation of Solutions.* Previously described methods that ensured minimum contamination with CO_2 were used.² For the determination of the effect of temperature on the e_{aq}^- spectrum the solutions used were flushed and saturated with prepurified hydrogen (Matheson) and the pH was adjusted in the range 9.5–10.0 by the addition of small quantities of a 1 M NaOH stock solution. The solution used to obtain the spectrum at pH 13 was prepared in a similar manner, but also contained 20 mM ethanol to minimize reaction between OH radicals and the small amount of carbonate ion introduced with the alkali.

Single or repetitive 15-MeV electron pulses from an Applied Radiation Company linear accelerator were used. The pulse duration was adjusted in the range 0.4–4.0 μ sec as required. The pulsed beam current was approximately 80 mA. To improve dose uniformity in the cell the beam was broadened with quadrupole magnet focusing and scattered with a $1/16$ -in. aluminum plate so that the pulsed current entering the cell was approximately 25 mA.

The jacketed cell and its holder, consisting of a collimator and Faraday cup, are shown in Figure 1. The bodies and connecting capillaries of the inner and outer vessels were made of fused silica and optical end windows of "Suprasil." The temperature in the inner cell was regulated by flowing water from a thermostatically regulated bath (Haake, Berlin) through the jacket. The temperature of the water entering the jacket was measured by a thermistor probe (Yellow Springs Instrument Co., Model 42 SC) and was controlled within $\pm 0.5^\circ$. The half-time for thermal equilibration of the inner cell was found to be 0.5 min, therefore several minutes was allowed for stabilization following changes in the temperature settings or changes of solutions.

The electron beam was collimated by an aluminum-copper shield with a rectangular opening the size of the irradiation cell. In this way the radiation field just covered the cell and its jacket. The range of the 15-MeV electrons was considerably greater than the outer diameter of the jacket and thus the majority of these electrons were stopped in the insulated brass charge collector behind the cell. The resulting charge was stored on a 10- μ F low leakage capacitor and measured with an electrometer (Keithley, Model 610 BR). The

(2) K. Schmidt and E. J. Hart, *Advan. Chem. Ser.*, **81**, 267 (1968).

unwanted loss of charges due to ionization currents in the irradiated air was found to be greatly reduced by the insulating layer of Plexiglas on the face of the collimator adjacent to the charge collector. The electrode entering the cell jacket (Figure 1) was used to convey the charge deposited in the cell to ground or the charge measuring circuit as required. The dose deposited in the cell was determined by correlating the charge collected with the oxidation of Fe^{2+} in the Fricke dosimeter. Under our conditions of irradiation $G(\text{Fe}^{3+}) = 15.6$.³ These charge-dose calibrations held indefinitely at constant electron beam energy. Under these conditions the dose is directly proportional to the charge collected.

For low temperature work sufficient ethanol was mixed with the circulating water to prevent freezing. To avoid condensation, the entire cell holder was covered with an enclosure which was flushed with dry nitrogen. To prevent any e_{aq}^- absorption produced in the few millimeters light path in the jacket from interfering, approximately 1% of acetone was added to the circulating water.

The schematic arrangement of the photomultiplier and the associated measuring devices is shown in Figure 2. The absorption signals were viewed and photographed using an oscilloscope (Fairchild 767 H), and were also amplified further (Tektronix 132-H) and passed to a boxcar integrator (P.A.R. CW-1) and passed to a digital voltmeter.

A 450-W xenon lamp, a Bausch and Lomb high intensity monochromator, and a 7102 photomultiplier (RCA) were used in the detection system. The long wavelength cutoff was at 1125 nm and filters were used to reduce the levels of scattered and higher order diffracted light from the monochromator.

The boxcar integrator was used to integrate a portion of absorption signal during a certain interval (or "gate") after the electron pulse. The width of the gate was 1 μsec and its start was delayed to about 1 μsec after the electron pulse. The absorption signal decayed approximately 10% during the gate interval. The output of the boxcar integrator was read as a steady dc potential, using a digital voltmeter.

By repeated pulsing, usually in a 1-sec burst of 30 pulses, absorption signals could be accumulated in the boxcar integrator, giving a considerable improvement in the overall signal to noise ratio by statistical averaging. This was particularly important near the long wavelength cutoff of the photomultiplier.

Temperature Range 203–390°. At these elevated temperatures it was necessary to contain the solutions in a cell that would withstand pressures up to 250 atm. Also, to minimize the light loss due to the infrared absorption of water, it was desirable to limit the optical path length in the solution to several millimeters, and to use heavy water. We sealed the solutions into thick-walled Suprasil capillaries of 9 mm outside diameter and 3 mm inside diameter (Figure 3). The capillary tubes

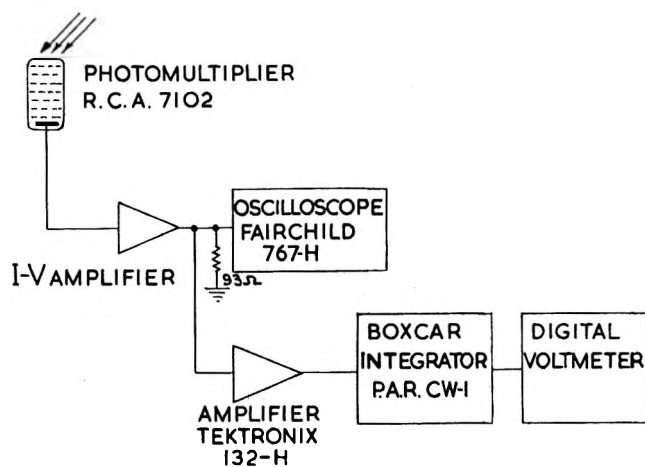


Figure 2. Photomultiplier circuit showing boxcar integrator arrangement.

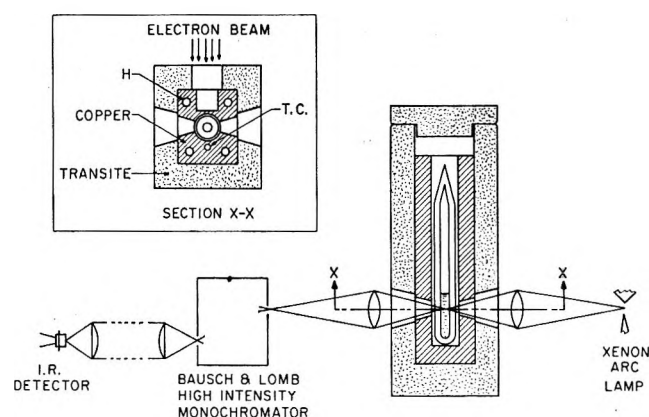


Figure 3. High temperature cell, holder, and schematic diagram of optical system (not to scale).

were evacuated and thoroughly baked out before addition of the triply distilled D_2O . Then the water sample was degassed and finally sealed off under an atmosphere of D_2 . After addition of the water all cells were heated at 400° in order to test their suitability for these experiments. The ratio of liquid to cell volumes was arranged such that the critical density was not exceeded.

The cell holder (Figure 3) consisted of a copper block, gold-plated to prevent oxidation and thermally insulated with Transite. The holder was bored out to allow the electron and analyzing light beams to pass through the liquid well below the meniscus. The copper block, H (Figure 3, inset), was heated electrically. The block temperature was measured and controlled, using a thermocouple, T.C., connected to a galvanometer-operated thermostat, which regulated the power to the heaters. By using a mercury in glass thermometer in place of the cell it was found that the temperature could be controlled within $\pm 1^\circ$.

The cell holder was electrically insulated from ground

(3) K. Sehested, E. Bjergbakke, O. L. Rasmussen, and H. Fricke, *J. Chem. Phys.*, **51**, 3159 (1969).

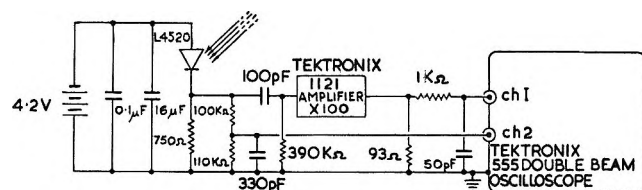


Figure 4. Germanium infrared photodetector circuit.

and the electron-beam charge that was stopped by it was measured, as in the lower temperature studies, to monitor the dose delivered in each pulse. The doses were approximately 10 krad per pulse.

A pulsed 450-W xenon arc lamp was used. A light shutter was placed between the lamp and the cell. The arc was imaged on the entrance slit of a Bausch and Lomb high intensity monochromator. Filters were used to attenuate scattered and higher order diffracted light and the combined effective proportion of these was less than 1%. The exit beam from the monochromator passed outside the accelerator radiation shield and was focused on the photodetector.

A germanium photodiode (L4520, Philco-Ford) was used as the photodetector. This diode had a circular sensitive area of 0.8 mm². It was operated with a reverse bias of 4.2 V (Figure 4). The overall response time was 0.1 μsec. The circuit was arranged so that simultaneous oscillograms could be taken of the absorption transient and the lamp pulse intensity on microsecond and millisecond time scales, respectively (Figure 5). The 8-msec lamp pulse established I_0 . The lamp shutter was opened shortly before the absorption signal was recorded. A second electron pulse was then given with the shutter closed and this was used to determine the Čerenkov signal and the dark current level of the photodetector. See the traces in the 390° recordings in Figure 5. The differences measured between the two pairs of traces so obtained gave the absorption and the I_0 .

The linearity of the detector was checked, using millisecond light pulses at 910 nm with neutral density filters calibrated at the same wavelength on a Cary 14 spectrophotometer. No significant departure from linearity could be found over the range of photocurrents covered, which was 17 to 500 μA. Tests made on a similar diode (L4520, 0.03 mm² sensitive area), using nanosecond light pulses, showed two stages of response, the first occurring within less than 1 nsec, the second following over several nanoseconds. Further tests on this smaller detector, using pulse radiolysis absorption signals in the nanosecond time range, showed an even slower component of the response extending to about 100 nsec. To prevent these anomalies from affecting our results we used the detector only to make relative absorption measurements in the microsecond time range. Also, the photocurrent during the lamp pulse was maintained near the constant value of

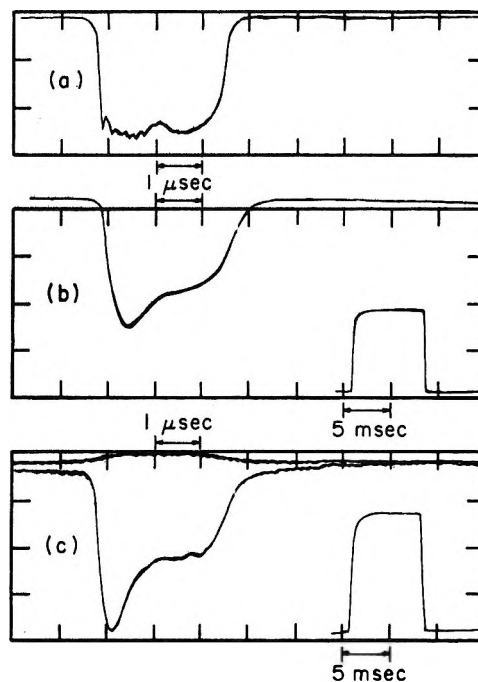


Figure 5. Tracings of electron pulse and the associated absorption, Čerenkov, and the xenon lamp signals: (a) electron pulse profile; (b) left, e_{aq}^- absorption signal at 203°, right, associated xenon light flash; (c) left, top curve, Čerenkov signal; bottom curve, e_{aq}^- absorption signal at 390°; right, associated xenon light flash.

about 100 μA at all wavelength settings by placing suitable neutral density filters in the light path.

Results and Discussion

Effect of pH on the Absorption Spectrum. Well established is the fact that the spectrum of e_{aq}^- is independent of pH and its mode of formation.^{4,5} However, the criterion used was the position of the maximum and not the overall form of the curve. Besides, the reports⁶⁻⁸ of an infrared absorption band in irradiated alkaline glasses, assigned to dielectron, $(e_2^-)_{aq}$, indicated that some distortion of the e_{aq}^- band might be expected at long λ if this species was present. Therefore, we investigated the spectrum of e_{aq}^- under conditions favorable and unfavorable to $(e_2^-)_{aq}$ formation.

The spectrum of e_{aq}^- is identical in acid, slightly basic, and strongly alkaline solutions. Figure 6 supports this conclusion. In this figure the solid line is drawn through the average of the experimental points

(4) E. J. Hart in "Radiation Chemistry of Aqueous Systems," G. Stein, Ed., Weizmann Science Press of Israel, Jerusalem, 1968, p 73.

(5) E. J. Hart and M. Anbar, "The Hydrated Electron," Wiley-Interscience, New York, N. Y., 1970, p 174.

(6) L. Kevan, D. R. Renneke, and R. J. Friauf, *Solid State Commun.*, **6**, 469 (1968).

(7) O. F. Khodzhaev, B. G., Ershov, and A. K. Pikaev, *Izv. Akad. Nauk SSSR, Ser. Khim.*, 246 (1968).

(8) N. Basco, G. A. Kenney, and D. C. Walker, *Chem. Commun.*, 917 (1969).

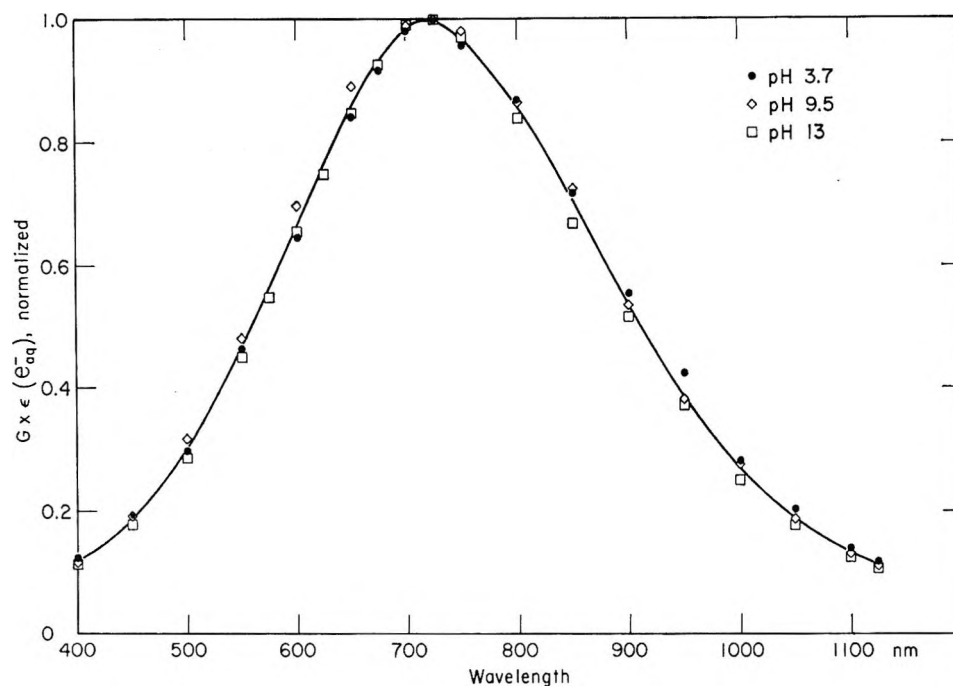


Figure 6. Effect of pH on the absorption spectrum of e_{aq}^- : \circ , pH 3.7, \diamond , pH 9.5; \square , pH 13.

obtained in solutions at pH values of 3.7, 9.5, and 13. The spectral range covered is from 400 to 1100 nm. Since dielectron formation is unfavorable in the acid solution and more favorable in the strongly alkaline solution, the lack of a difference at long λ indicates no contribution of $(e_2^{2-})_{aq}$ to our spectrum in the alkaline solutions.

Dielectron formation from e_{aq}^- is favored at high dose rates and after long decay periods in alkaline- H_2 saturated solutions, because of the reaction



However, identical spectra were obtained in pH 13 H_2 -saturated solutions at dose rates varying from 0.01 to 1.0 krad/pulse. Furthermore the relative absorption is independent of the time of measurement after the electron pulse. Delays of 30 and 92 μ sec after creation of e_{aq}^- produced relative absorbances identical with those obtained immediately after the pulse. Therefore, under our conditions of measurement there is no indication of an $(e_2^{2-})_{aq}$ component in our spectrum shown in Figure 6.

Effect of Temperature in the -4 to 90° Range at pH 9.5. With increasing temperature the e_{aq}^- spectrum shifts toward longer wavelengths. Over the range of temperatures from -4 to 90° in liquid water containing 30 μ M NaOH there is no discontinuity or alteration in the spectra shown in Figure 7. We also measured spectra at 4, 10, and 15° . In Figure 7 the normalized product of the yield, $G(e_{aq}^-)$, and the molar extinction coefficient of e_{aq}^- , $\epsilon(e_{aq}^-)$ (abbreviated to $G \times \epsilon$), is given as a function of λ over the range from 400 to 1100 nm for temperatures of -4 , 10, 25, 50, 70, and 90° . $G \times \epsilon$ is re-

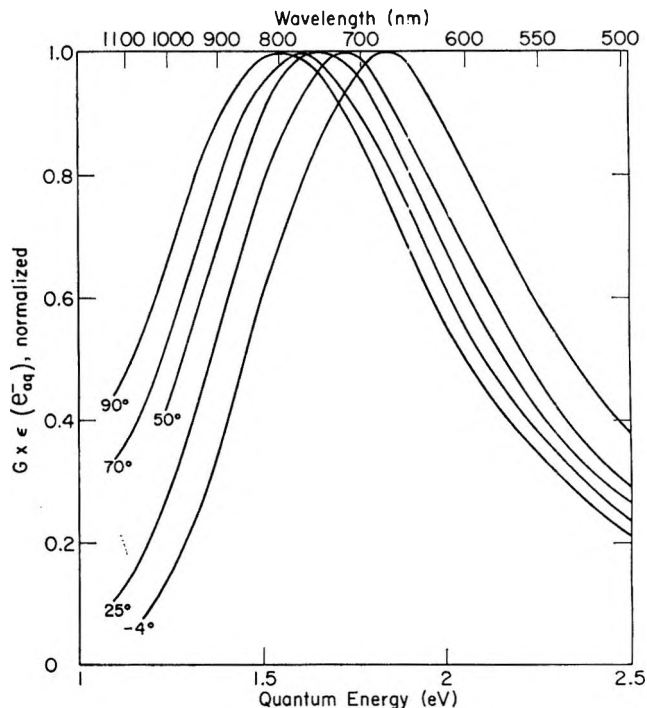


Figure 7. Effect of temperature on the absorption spectrum of e_{aq}^- in range from -4 to 90° .

lated to the optical density OD, dose in eV/l., and cell depth, d , by the relation

$$G \times \epsilon = \frac{(OD)6.02 \times 10^{25}}{\text{Dose}(d)}$$

Molar extinction coefficients $\epsilon_{\lambda_{max}}$ were calculated from Figure 7 by assuming the established 25° value of

10,600 $M^{-1} \text{ cm}^{-1}$ at 578 nm.^{9,10} Then from the ratio absorbance (λ_{max})/absorbance (578 nm) of 1.74 we obtain $\epsilon_{\lambda_{\text{max}}} = 1.84 \times 10^4 M^{-1} \text{ cm}^{-1}$. This gives us a yield $G(e_{aq}^-)$ of 2.83 at pH 9.5, since $G \times \epsilon = 52,290$. Our yield is between that of 2.65 for neutral water and 3.04 for pH 13.¹⁰

The product, $G \times \epsilon$, while nearly constant, increases slightly with rising temperature. The results given in Table I may be represented by

$$\frac{\Delta(G \times \epsilon)}{\Delta T} = (19.1 \pm 6)/^\circ\text{C}$$

The shift in λ_{max} amounts to $-0.0030 \text{ eV}/^\circ\text{C}$, and is closely linear over this temperature range (see Figure 8). Within the limits of experimental error, this value is

Table I: Effect of Temperature on the Product, $G(e_{aq}^-) \times \epsilon$

Temp, °C	$G(e_{aq}^-) \times \epsilon$ [$e_{aq}^- (100\text{-eV})^{-1}$] $M^{-1} \text{ cm}^{-1}$]
-4	51,425
+4	51,865
25	52,290
50	52,935
70	53,955
90	52,760

identical with $-0.0029 \text{ eV}/^\circ\text{C}$ reported from steady-state γ -ray irradiations.¹ The band half-width has a mean value of $0.855 \pm 0.03 \text{ eV}$, indicating little or no temperature dependence.

Effect of Temperature in the 200 to 390° Range. The shift of $E_{\lambda_{\text{max}}}$ toward lower energies observed in the -4 to 90° range continues at elevated temperatures. The relative absorbance is given in Figure 9 as a function of quantum energy for temperatures of -4 , 90 , 203 , 300 , 361 , and 390° . Heavy water was used at temperatures above 200° where the measurements were made on the liquid at the saturation vapor pressure of water. The absorption curves change from a nearly symmetrical shape for temperatures up to 203° to an unsymmetrical shape that broadens toward higher energies at the higher temperatures. However, the general shape and half-widths are maintained and it is clear that the electron hydrates at these elevated temperatures. Over this broad temperature range the structure of water changes drastically. Even so the electron is able to organize a hydration sphere around itself indicating a strong interaction with the neighboring four water molecules.

Quantitative Analysis of the e_{aq}^- Absorption Signals in D_2O at 203 and 330°. At all temperatures from 203 to 390° , the e_{aq}^- absorption signals have a characteristic shape with a peak shortly after the beginning of the pulse and a shoulder during the second half. Relative to the

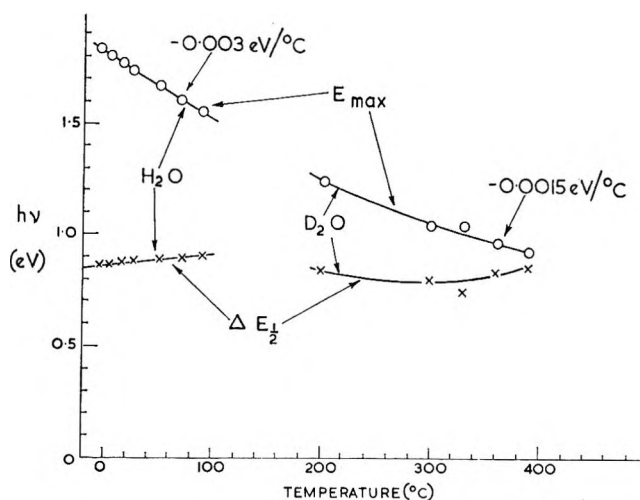


Figure 8. Effect of temperature on the energy of the maximum of the e_{aq}^- absorption band ($E_{\lambda_{\text{max}}}$) and its half-width $\Delta E_{1/2}$.

maximum the height of the shoulder diminishes with increasing temperature. See the e_{aq}^- absorption contours of Figures 5 and 10. The flat pulse profile of the 15-MeV electron pulse is also given in these figures.

The shape of these e_{aq}^- absorption signals provides useful information regarding rate constants, possible information regarding radiolysis yields, and the relative importance of e_{aq}^- reactions at high temperatures. The curve shape may be exactly simulated by the use of a computer program¹¹ in which all essential chemical reactions and their known rate constants with values extrapolated to the respective temperatures by the Arrhenius equation are considered. As activation energies, we used available published values or 3.6 kcal/mol, the activation value for water diffusion. A 7% correction to this value¹² was added because of the effect of viscosity.¹³ Table II shows the reactions, rate constants, activation energies, and yields used for our calculations at 203° and 330° . Some calculations were also carried out for 300 , 351 , and 390° . The variations of pD ¹⁴ and absorbed dose (because of density changes) with temperature were taken into account. The results of these calculations are illustrated in Figure 10.

Curves 2 and 3 of Figure 10 show fair agreement between experiment and calculation for 203° , when the extrapolated rate constants and standard yields are used. Consequently, up to this temperature, we con-

(9) J. Rabani, W. A. Mulac, and M. S. Matheson, *J. Phys. Chem.*, **69**, 53 (1965).

(10) E. M. Fielden and E. J. Hart, *Radiat. Res.*, **32**, 564 (1967).

(11) K. H. Schmidt, Argonne National Laboratory Report, ANL-7693, March 1970.

(12) M. Anbar and E. J. Hart, *J. Phys. Chem.*, **71**, 3700 (1967).

(13) I. Kirshenbaum, "Physical Properties and Analysis of Heavy Water," McGraw-Hill, New York, N. Y., 1951, p 33.

(14) E. U. Frank, *Angew. Chem.*, **73**, 309 (1961).

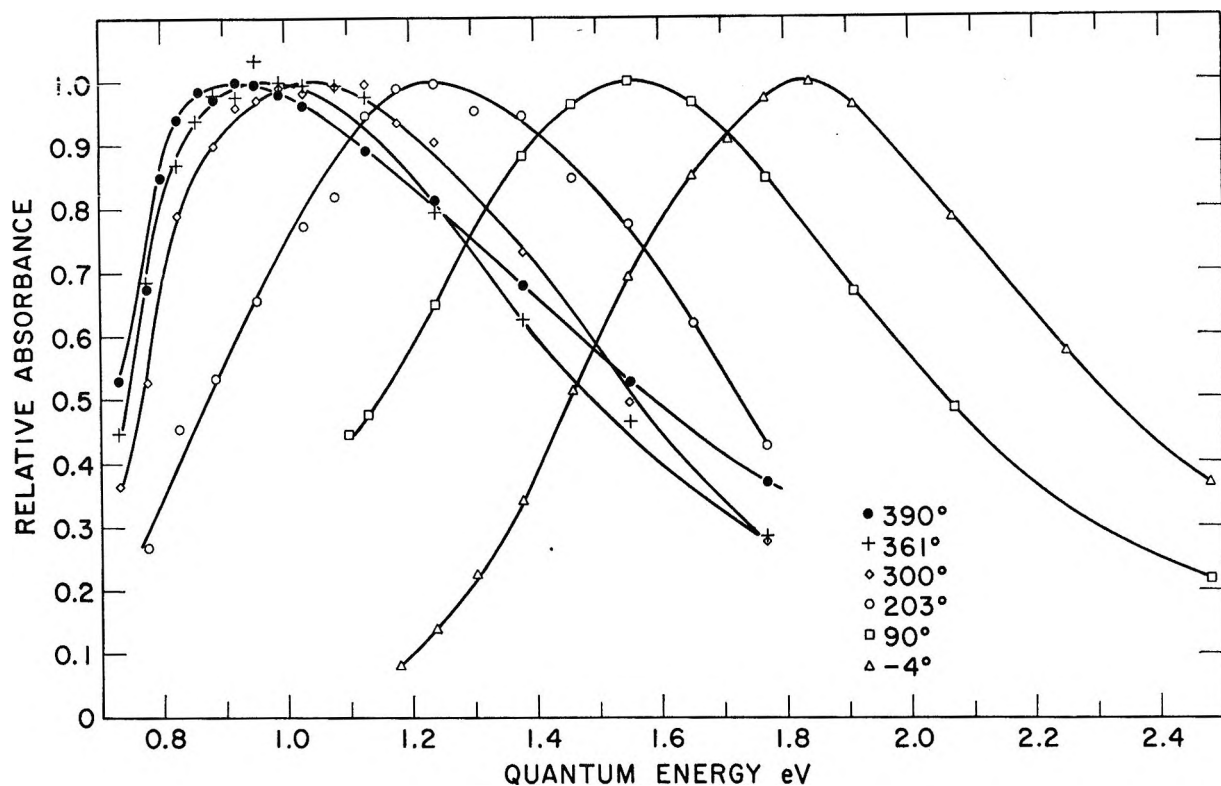


Figure 9. Effect of temperature in the range from -4 to 390° on the relative absorbance of e_{aq}^- as a function of quantum energy. D_2O replaced H_2O at temperatures above 90° .

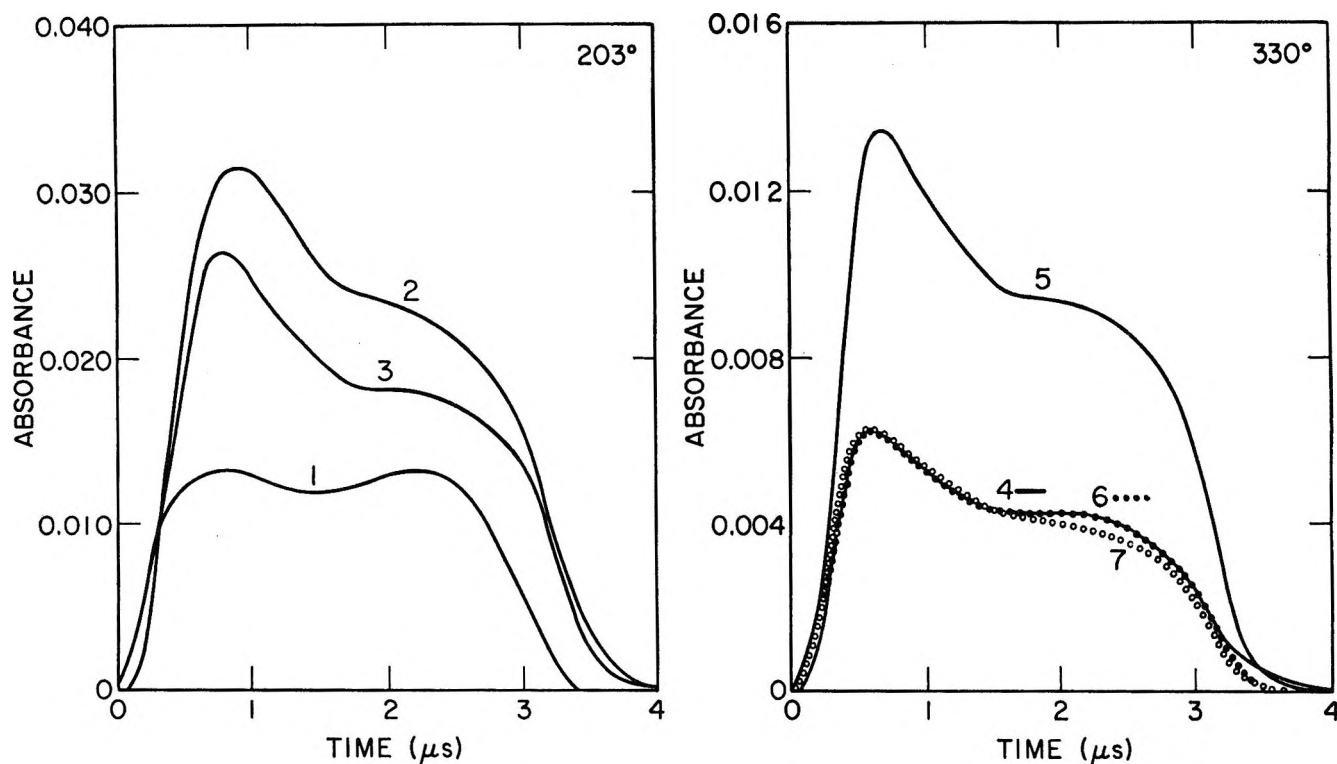


Figure 10. Kinetic analysis of e_{aq}^- signals measured at high temperatures: (1) profile of electron beam pulse (ordinate in relative units); (2) experimental curve for 203° ; (3) curve calculated using published rate constants extrapolated to 203° (4th column in Table II); (4) experimental curve for 330° (lower solid line); (5) curve calculated using published rate constants extrapolated to 330° (5th column in Table II); (6) curve calculated using increased rate constants (6th column in Table II closely matches curve 4); (7) curve calculated using rate constants from 5th column in Table II and increased radical yields, $G_D = 10$ and $G_{OD} = 12.5$.

Table II: Reactions, Rate Constants, and Activation Energies Used for the Computer Calculations^{a-c}

Reaction	E_a , kcal/mol	Rate constants, $M^{-1} \text{ sec}^{-1}$			
		25° (exptl)	203° ^d	330° ^d	330° (best fit)
$e_D^- + OD$	3.75	$2.8 \times 10^{10} e$	3.0×10^{11}	6.9×10^{11}	1.7×10^{12}
$e_D^- + D^+$	3.75 ^f	$1.7 \times 10^{10} e$	1.8×10^{11}	4.2×10^{11}	1.0×10^{12}
$e_D^- + e_D^-$	5.2 ^g	$6.0 \times 10^9 e$	1.6×10^{11}	5.1×10^{11}	2.5×10^{12}
$e_D^- + D$	3.75	$2.8 \times 10^{10} e$	3.0×10^{11}	6.9×10^{11}	1.7×10^{12}
$e_D^- + D_2O$	4.5 ^h	1.25 ^e	21	58	170
$e_D^- + D_2O_2$	3.75	$1.2 \times 10^{10} e$	1.3×10^{11}	3.0×10^{11}	5.0×10^{11}
$D^+ + OD^-$	2.35 ⁱ	$8.4 \times 10^{11} j$	3.6×10^{11}	6.0×10^{11}	6.0×10^{11}
$OD + D$	3.75	$8.0 \times 10^9 k, l$	8.5×10^{10}	2.0×10^{11}	2.0×10^{11}
$D + D$	3.75	6.3×10^9	6.7×10^{10}	1.6×10^{11}	1.6×10^{11}
$OD + D_2$	3.75	$1.6 \times 10^7 e$	1.7×10^8	4.0×10^8	4.0×10^8
$OD + OD$	3.75	$4.2 \times 10^9 k$	4.5×10^{10}	1.1×10^{11}	1.1×10^{11}

^a $g(e_D^-) = 3.1$; $g(D^+) = 3.2$; $g(OD^-) = 0.1$; $g(D) = 0.4$; $g(OD) = 2.9$; $g(D_2O_2) = 0.7$; $g(D_2) = 0.4$;^{b,c} $g(OD^-) = g(OH^-)$ was assumed.^c ^b E. M. Fielden and E. J. Hart, *Radiat. Res.*, **33**, 426 (1968). ^c K. H. Schmidt and S. M. Ander, *J. Phys. Chem.*, **73**, 2846 (1969). ^d Extrapolated. ^e E. J. Hart and M. Fielden, *J. Phys. Chem.*, **72**, 577 (1968). ^f See ref 5, p 174. ^g See ref 1. ^h E. M. Fielden and E. J. Hart, *Trans. Faraday Soc.*, **64**, 3158 (1968). ⁱ Calculated from A. Iverson, *J. Phys. Chem.*, **68**, 515 (1964). ^j G. Ertl and H. Gerischer, *Z. Elektrochem.*, **66**, 520 (1962). ^k P. Pagsberg, H. Christiansen, J. Rabani, G. Nilsson, J. Fenger, and S. O. Nielson, *J. Phys. Chem.*, **73**, 1029 (1969). ^l M. Anbar and P. Neta, *Int. J. Appl. Radiat. Isotopes*, **18**, 493 (1967).

clude that the 203° rate constants and radical and molecular product yields of Table II are reasonably reliable. However, they cannot be used at temperatures above 300°.

At temperatures in the 300 to 390° range, the calculated signals are considerably larger than the experimental ones, the disparity increasing regularly with increasing temperature. Curve 5 in Figure 10 demonstrates the magnitude of this deviation for 330°. In an attempt to obtain a better fit we considered three modifications. (a) All e_{aq}^- rate constants were increased by a factor of 2.5 to 5 (column 6 of Table II). The resulting curve is number 6 in Figure 10. (b) The yield of water dissociation was increased to $G(D) = 10$ and $G(OD) = 12.5$. See curve 7 of Figure 10. (c) By lowering the yield, $G(e_D^-)$, to 1.1, a good fit is also obtained. With these limited experimental data it is clear that we cannot distinguish between an increase in e_D^- rate constants and an increase in the water dissociation yields.

In any of these cases, no reliable statements can be made about individual e_D^- rate constants.

Increased radiation-induced dissociation above 300° may be the most likely explanation of our results. Although the radical yields $G(H)$ and $G(OH)$ of liquid water heated to 250° do not increase,¹⁵ these yields for water vapor are about 11.^{16,17} Since yields in this range explain the contours of our e_{aq}^- absorption curves, it is possible that the radiolysis of liquid water above 300° approaches that of the vapor. These enhanced radical yields provide an additional stabilization factor in preventing water decomposition in water-moderated reactors operating at elevated temperatures.

Acknowledgment. This work was performed under the auspices of the U. S. Atomic Energy Commission.

(15) C. J. Hochanadel, *Proc. Int. Conf. Peaceful Uses At. Energy*, 1955, **7**, 521 (1956).

(16) R. F. Firestone, *J. Amer. Chem. Soc.*, **79**, 5593 (1957).

(17) J. H. Baxendale and G. P. Gilbert, *ibid.*, **86**, 516 (1964).

Vibrational Spectra of *tert*-Butyl Cyanide

by G. A. Crowder

Department of Chemistry and Killgore Research Center, West Texas State University, Canyon, Texas 79015
(Received February 4, 1971)

Publication costs assisted by the Robert A. Welch Foundation

Infrared and Raman spectra have been obtained for *tert*-butyl cyanide, and a vibrational assignment has been made. The assignment is supported by normal coordinate calculations made with valence force constants transferred from force fields for saturated hydrocarbons and nitriles.

Introduction

Vibrational spectra have been studied for several compounds whose molecules are symmetrical tops that contain the *tert*-butyl group, including isobutane,^{1,2} 2,2-dimethyl-2-butyne,³ and the *tert*-butyl halides.^{4,5} A tentative frequency assignment for *tert*-butyl cyanide has been given by Westrum and Ribner,⁶ who used the assignment to calculate the vibrational contribution to the entropy. However, they used several frequencies in their assignment that they transferred from *tert*-butyl acetylide or isobutane. In addition, there seem to be inconsistencies when their assignment is compared with that of other *tert*-butyl compounds. Therefore, infrared and Raman spectra were determined for *tert*-butyl cyanide, and normal coordinate calculations were made in order to make a vibrational assignment.

Experimental Section

Infrared spectra were obtained for the liquid and vapor in the region 200–4000 cm^{-1} with a Beckman IR-12 spectrophotometer. The Raman spectrum of the liquid was obtained with a Jarrell-Ash 25-100 dual monochromator, photon counting spectrometer, by Dr. J. Paul Devlin. The sample of *tert*-butyl cyanide was obtained from K & K Laboratories and was distilled under reduced pressure before use. No impurities were detected by gas chromatography.

Results and Discussion

A molecule of *tert*-butyl cyanide is a symmetric top belonging to the C_{3v} point group and therefore has its fundamental vibrations distributed as $9 a_1 + 4 a_2 + 13 e$, including the methyl torsions ($a_2 + e$). The a_1 and e vibrations are both infrared and Raman active, but the a_2 vibrations are inactive in both. The Raman bands due to the a_1 vibrations should be polarized and the e bands should be depolarized.

The infrared and Raman spectra are shown in Figure 1 and the wave numbers for the bands observed are listed in Table I.

Vibrational Assignment. Methyl Stretching Modes. Westrum and Ribner⁶ list only two bands observed in the CH_3 stretching region for *tert*-butyl cyanide, at

2875 and 2934 cm^{-1} , and they list three other values transferred from *tert*-butyl acetylide. There were four infrared bands and six Raman bands observed in the region 2880–3000 cm^{-1} in the present investigation. The 2990- cm^{-1} infrared vapor state band is the strongest band in the spectrum, and the corresponding Raman band at 2995 cm^{-1} is depolarized, so this band is due to an e species vibration and is assigned to both e asymmetric CH_3 stretches. This leaves the other three infrared bands to be assigned to the remaining three CH_3 stretching modes. Assignment of these bands cannot be made with certainty.

Methyl Deformation and Rocking Modes. Four infrared bands were observed in the methyl deformation region, 1350–1500 cm^{-1} , but only two Raman bands were observed. The four bands are to be assigned to three asymmetric methyl deformations ($a_1 + 2e$) and two symmetric deformations ($a_1 + e$). The 1486- cm^{-1} band is assumed to be due to two accidentally degenerate vibrations ($a_1 + e$). The 1468- cm^{-1} band is assigned to the other e deformation, and the symmetric deformations are assigned as 1377 (a_1) and 1406 (e) cm^{-1} .

There are several infrared bands in the region where the methyl rocking bands should be observed. The rocks are distributed as $a_1 + a_2 + 2 e$, so only three observed bands can be assigned to methyl rocking modes ($a_1 + 2 e$). Westrum and Ribner used the frequencies 765, 869, 935, and 1145 cm^{-1} for the four rocks in their entropy calculation. However, all four of these bands were observed in the infrared spectrum so the band assigned to the a_2 rock must be incorrect. In addition, only two of these bands are consistent with the assignment of *tert*-butyl acetylide,³ for which the frequencies should not differ very much from the cyanide. For the

(1) J. H. Schachtschneider and R. G. Snyder, *Spectrochim. Acta*, **19**, 117 (1963).

(2) R. G. Snyder and J. H. Schachtschneider, *ibid.*, **21**, 169 (1965).

(3) N. Sheppard, *J. Chem. Phys.*, **17**, 455 (1949).

(4) D. E. Mann, N. Acquista, and D. R. Lide, *J. Mol. Spectry.*, **2**, 575 (1958).

(5) W. Huttner and W. Zeil, *Spectrochim. Acta*, **22**, 1007 (1966).

(6) E. F. Westrum and A. Ribner, *J. Phys. Chem.*, **71**, 1216 (1967).

Table I: Infrared and Raman Wave Numbers of *tert*-Butyl Cyanide

Ir (vap)	Ir (liq)	Raman (liq)	Assignment ^a
3560 vvw	3555 vw		$\nu_{14} + \nu_{23}$
3503 vvw	3480 vw		$\nu_1 + \nu_{23}$
3360 vw	3350 vw		$\nu_9 + \nu_{14}$
3250 vw			$\nu_2 + \nu_9$
3205 vw			$\nu_3 + \nu_{22}$
3130 vw	3108 w		$\nu_1 + \nu_{26}$
2990 vs	2981 vs	2995 (d) m	ν_{14}, ν_{15}
		2971 (p) w	?
2951 m	2941 s	2943 (p) ms	ν_1
2939 m	2913 ms	2923 (p) m	ν_{16}
		2902 (p) w	$2\nu_{18}$
2890 m	2880 ms	2885 (p) w	ν_2
2840 vw		2806 vw	$\nu_5 + \nu_{18}$
2620 vw	2608 vw		$\nu_5 + \nu_6$
2510 vw	2485 vw		$2\nu_6$
2430 vw	2422 vw		$2\nu_{20}$
2320 vw	2308 w		$\nu_5 + \nu_{22}$
2251 m	2238 s	2245 (p) ms	ν_3
2070 vw	2060 vw		$\nu_7 + \nu_{20}$
1670 mw	1670 vw		$\nu_4 + \nu_{26}$
1608 w	1630 vw		$\nu_8 + \nu_{22}$
1495			
1486 s	1481 s	1473 (d?) m	ν_4, ν_{17}
1479			
1477			
1468 s	1464 s	1461 (d?) m	ν_{18}
1456			
1415			
1406 mw	1403 mw		ν_{19}
1387			
1377 s	1374 s		ν_5
1368			
1325 vw			$\nu_9 + \nu_{22}$
1257			
1250 s	1244 s	1247 vw	ν_6
Ca. 1245			
1217 s	1212 s	1209 (d) m	ν_{20}
1140 w	1150 w		$\nu_{22} + \nu_{26}$
1033 w	1039 w	1045 w	ν_{21}
947			
939 m	939 mw	945 m	ν_{22}
Ca. 930			
880 w	874 w	878 (p) m	ν_7
843 vw	850 vvw		$\nu_8 + \nu_{26}$
820 vw			
805 vw	800-820 vvw		
755 w	770 w	773 vw	$2\nu_9$
727 w	741 vw		$\nu_9 + \nu_{24}$
695			
687 m	687 m	693 (p) vs	ν_8
680			
	578 vw	585 vw	ν_{23}
375 w	380 mw	384 w	ν_9
360 w	Ca. 365 w	369 (d) w	ν_{24}
		198 (d) vs	ν_{26}

^a The assignment is given in terms of Herzberg's nomenclature. The unobserved methyl torsions are expected around 250 cm^{-1} (a_2) and 300 cm^{-1} (e), and would be designated ν_{13} and ν_{25} , respectively.

acetylide, the methyl rocks were assigned as $885(a_1)$, $931(e)$, and $1029(e)\text{ cm}^{-1}$. Three bands with frequencies very near these values were observed for the cyanide in both infrared and Raman spectra with the 880-cm^{-1} Raman band being highly polarized. Actually, the C-C stretching vibrations are expected to mix strongly with the methyl rocking modes of the same species.

Skeletal Stretching Modes. The stretching vibrations involving the carbon and nitrogen atoms are distributed as $3a_1 + e$. The C≡N stretch (a_1) can easily be assigned to the band observed at 2251 cm^{-1} in the vapor state infrared spectrum. The Raman band at 2245 cm^{-1} is highly polarized. The symmetric CC_3 stretch (a_1) can be assigned to the strong polarized Raman band at 695 cm^{-1} , which agrees well with the value of 690 cm^{-1} for *tert*-butyl acetylide. Westrum and Ribner assign the other two C-C stretching bands at 1209 and 1247 cm^{-1} , with the 1247-cm^{-1} value being transferred from *tert*-butyl acetylide. A misprint in their paper lists both bands as singly degenerate, so it must be assumed that the 1207-cm^{-1} band is the one they assign to the e stretch, analogous to the assignment for the acetylide. Both these bands have been observed in the infrared and Raman spectra with the 1209-cm^{-1} band being depolarized and, therefore, assigned to the e species. The strong infrared bands observed at 1250

Table II: Observed and Calculated Wave Numbers for *tert*-Butyl Cyanide

	Obsd	Calcd	Assignment
			a_1
	2951	2963	$\nu(\text{CH}_3)$, asym
	2890	2884	$\nu(\text{CH}_3)$, sym
	2251	2236	$\nu(\text{CN})$
	1486	1485	$\delta(\text{CH}_3)$, asym
	1377	1406	$\delta(\text{CH}_3)$, sym
	1250	1312	$\rho(\text{CH}_3) + \nu(\text{C-C})$
	880	890	$\rho(\text{CH}_3) + \nu(\text{C-C})$
	687	671	$\nu(\text{CC}_3)$, sym
	375	375	$\delta(\text{CC}_3)$, sym
			a_2
	...	2960	$\nu(\text{CH}_3)$, asym
	...	1470	$\delta(\text{CH}_3)$, asym
	...	1017	$\rho(\text{CH}_3)$
			e
	2990	2963	$\nu(\text{CH}_3)$, asym
	2990	2961	$\nu(\text{CH}_3)$, asym
	2939	2884	$\nu(\text{CH}_3)$, sym
	1486	1486	$\delta(\text{CH}_3)$, asym
	1468	1470	$\delta(\text{CH}_3)$, asym
	1406	1436	$\delta(\text{CH}_3)$, sym
	1217	1237	$\nu(\text{CC}_3) + \rho(\text{CH}_3) + \delta(\text{CH}_3)$
	1033	1040	$\rho(\text{CH}_3)$
	939	941	$\rho(\text{CH}_3) + \nu(\text{CC}_3)$
	578 (liq)	537	$\rho(\text{CC}_3)$
	360	377	$\delta(\text{CC}_3)$, asym
	198 (liq)	203	$\delta(\text{CCN})$

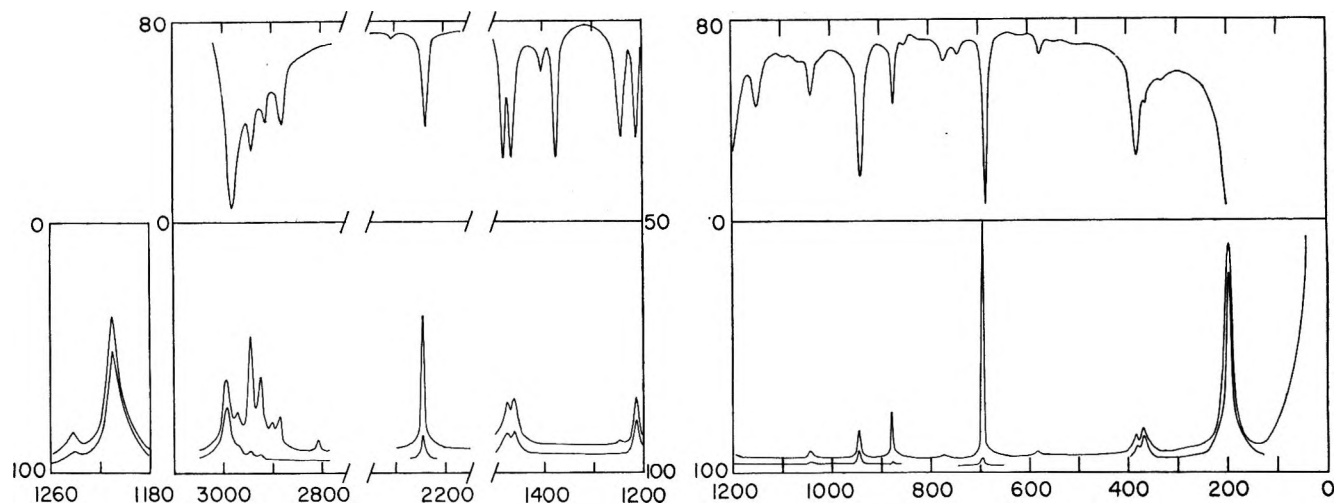


Figure 1. Upper curve, infrared spectrum of neat liquid, 0.007 mm above 1200 cm^{-1} and 0.10 mm below 1200 cm^{-1} . Lower curves, Raman spectra of neat liquid showing polarization of bands. Ordinate in per cent transmittance, abscissa in cm^{-1} .

and 1217 cm^{-1} have approximately the same intensity, but the 1209- cm^{-1} band in the Raman spectrum is much more intense than the 1247- cm^{-1} band, and it might be expected that the more intense band would be due to the a_1 vibration. This region of the Raman spectrum was run again with increased sensitivity, as shown in Figure 1, and the 1209- cm^{-1} band definitely appears depolarized and must be assigned to the e vibration. The 1247- cm^{-1} band, although weak, does seem to be somewhat polarized and was assigned to the a_1 band, in spite of the fact that the theoretical P-R separation for the a_1 bands is about 20 cm^{-1} . The P branch was observed as a shoulder, and the P-R separation of the vapor state infrared band may actually be greater than the 12 cm^{-1} indicated in Table I.

It is not correct to assign these two bands to C-C stretching vibrations because they involve a mixture of normal modes. For that reason, it is perhaps surprising that these frequencies are as constant as they are in different compounds. For example, the values of these two frequencies for 2,2-dimethylbutane, 2,2-dimethyl-3-butene, and 2,2-dimethyl-3-butyne are 1258 and 1217, 1271 and 1209, and 1247 and 1205 cm^{-1} , respectively.³

Skeletal Bending Modes. The bending vibrations that are associated with the skeletal chain may be described as a CC_3 symmetric deformation (a_1), doubly degenerate CC_3 asymmetric deformations (e), doubly degenerate C-C \equiv N bending (e), and doubly degenerate CC_3 rock (e). The assignment given here for the four bands essentially agrees with that given by Westrum and Ribner, with there being a slight difference in the wave numbers involved. The C-C \equiv N bending band was observed only in the Raman spectrum as a very strong depolarized band at 198 cm^{-1} because the

band peak was below the range of the infrared instrument used.

The CC_3 rock, asymmetric deformation, and symmetric deformation are assigned to the infrared bands observed at 578 (liquid), 375, and 360 cm^{-1} , respectively.

Normal Coordinate Calculations. Calculations were made for *tert*-butyl cyanide from force constants transferred from a force field for saturated hydrocarbons² and one for nitriles.⁷ The 18 force constants used were not refined because the calculation was made simply to support the proposed vibrational assignment. Therefore, presentation of the details of the calculation is not justified, but the frequencies calculated from the transferred force constants are given in Table II.

Entropy of *tert*-Butyl Cyanide at 298.15°K. Westrum and Ribner calculated with their vibrational assignment a vibrational contribution to the entropy at 298.15°K of 10.26 cal/deg mol, for a total S° of 79.86 cal/deg mol, as compared with an experimental value of 79.63 cal/deg mol. The present vibrational assignment gives a vibrational contribution of 10.02 cal/deg mol, for a total calculated entropy of 79.62 cal/deg mol.

Acknowledgments. This work was supported by The Robert A. Welch Foundation, Houston, Texas, and by West Texas State University. The author is grateful to Dr. J. Paul Devlin for obtaining the Raman spectrum, and to Dr. R. G. Snyder for supplying symmetry coordinates for the *tert*-butyl group.

(7) R. Yamadera and S. Krimm, *Spectrochim. Acta*, **24A**, 1677 (1968).

Ionic Radii from Scaled Particle Theory of the Salt Effect

by W. L. Masterton,* David Bolocofsky, and Tei Pei Lee

Department of Chemistry, University of Connecticut, Storrs, Connecticut 06268 (Received January 13, 1971)

Publication costs assisted by the University of Connecticut Research Foundation

Equations derived from the scaled particle theory of the salt effect are used to obtain hard-sphere radii of ions in aqueous solution. For the alkali halide ions, Waddington crystal radii give the best fit to experimentally determined salting coefficients; the radii of Goldschmidt and Pauling are somewhat less satisfactory, while those of Gourary and Adrian give poor agreement. Using Waddington radii for the alkali halide ions, the following values are obtained for the effective radii of polyatomic ions: $\text{OH}^- = 1.52 \text{ \AA}$, $\text{NO}_3^- = 1.96 \text{ \AA}$, $\text{NH}_4^+ = 1.43 \text{ \AA}$, $(\text{CH}_3)_4\text{N}^+ = 2.51 \text{ \AA}$, $(\text{C}_2\text{H}_5)_4\text{N}^+ = 3.08 \text{ \AA}$, $(n\text{-C}_3\text{H}_7)_4\text{N}^+ = 3.49 \text{ \AA}$, $(n\text{-C}_4\text{H}_9)_4\text{N}^+ = 3.81 \text{ \AA}$.

Introduction

The radii of ions are important parameters in correlating thermodynamic data for solutions of electrolytes. Two recent reviews^{1,2} emphasize the role of precise values of ionic radii in any attempt to give a structural interpretation to the free energy and entropy of hydration of electrolytes or to their molal volumes in aqueous solution. In equations used to correlate and interpret these properties, crystal radii are commonly used. Earlier workers employed the crystal radii of Pauling³ or Goldschmidt,⁴ which are very similar to one another (Table I). More recently, the radii of Gourary and Adrian⁵ have been used. They differ significantly from previous sets; the cationic radii are considerably larger than those of Pauling or Goldschmidt while those of anions are smaller. Another set of crystal radii suggested by Waddington⁶ appears to have received less attention.

Theoretical considerations suggest that radii of ions in aqueous solution should be nearly the same as in the solid state. Benson and Copeland⁷ point out that the electrostatic field around an ion in solution should be nearly as great as in the crystal lattice; they estimate that solution radii should exceed crystal radii by at most 0.02 Å. Batsanov⁸ uses a method similar to that of Pauling to estimate ionic radii in solution; he concludes that solution radii of cations should be about 0.02 Å greater than crystal radii while those of anions should be smaller by about 0.04 Å.

In principle, ionic radii in aqueous solution could be determined by fitting data for the thermodynamic properties of electrolytes to equations derived from structural considerations. In practice, such equations have proven to be inadequate for this purpose. To illustrate, consider the equation commonly used for partial molal volume

$$V^\circ = \frac{4}{3}\pi N r^3 + V^\circ(\text{elect}) + V^\circ(\text{disorder}) \quad (1)$$

where V° is the partial molal volume of an ion at infinite dilution, N is Avogadro's number, r is the hard-

sphere radius of the ion, $V^\circ(\text{elect})$ is the volume change due to electrostriction, and $V^\circ(\text{disorder})$ corrects for "dead space" in the vicinity of the ion. In order to use this equation to obtain r , the other terms would have to be known accurately. Unfortunately, this is not the case. In the first place, there is some question as to how the partial molal volume of an electrolyte should be split up into its ionic components; for example, V° of the Cl^- ion has been assigned values ranging from 18 to 24 cc/mol. Moreover, there is considerable uncertainty as to the magnitude of the electrostriction term, particularly for small ions.

Blandamer and Symons⁹ attempted to choose between different sets of ionic radii by fitting data for the free energy and entropy of hydration of ions. They showed that when either of these quantities is plotted against $1/r^2$, all of the alkali halide ions fall on a smooth curve if Gourary and Adrian radii are used. Other sets of radii lead to two separate curves, one for cations and another for anions. It is difficult to say how much significance should be attached to this observation, which is semiquantitative at best.

Methods of estimating ionic radii from nonthermodynamic properties of electrolyte solutions have proven to be equally unsatisfactory. In general, the calculated

(1) J. E. Desnoyers and C. Jolicoeur in "Modern Aspects of Electrochemistry," Vol. 5, J. O'M. Bockris and B. E. Conway, Ed., Plenum Press, New York, N. Y., 1969, Chapter 1.

(2) F. J. Millero in "Structure and Transport Processes in Water and Aqueous Solutions," R. A. Horne, Ed., Wiley-Interscience, New York, N. Y., 1970, Chapter 15.

(3) L. Pauling, "The Nature of the Chemical Bond," 3rd ed, Cornell University Press, Ithaca, N. Y., 1960.

(4) V. M. Goldschmidt, *Skrifter Norske Videnskaps-Akad. Oslo, I, Math. Naturv. Kl.*, 1, 21 (1926).

(5) B. S. Gourary and J. F. Adrian, *Solid State Phys.*, 10, 127 (1960).

(6) T. C. Waddington, *Trans. Faraday Soc.*, 62, 1482 (1966).

(7) S. W. Benson and C. S. Copeland, *J. Phys. Chem.*, 67, 1194 (1963).

(8) S. S. Batsanov, *J. Struct. Chem. (USSR)*, 4, 158 (1963).

(9) M. J. Blandamer and M. C. R. Symons, *J. Phys. Chem.*, 67, 1304 (1963).

Table I: Crystal Radii in Ångströms

Ion	Pauling	Gold- schmidt	Gourary and Adrian	Wad- dington
Li ⁺	0.60	0.68	0.94	0.74
Na ⁺	0.95	0.98	1.17	1.01
K ⁺	1.33	1.33	1.49	1.32
Cl ⁻	1.81	1.81	1.64	1.82
Br ⁻	1.95	1.96	1.80	1.98
I ⁻	2.16	2.20	2.05	2.24

radii appear to depend upon the property studied and the particular equation used to represent that property. Stern and Amis¹⁰ point out that "Stokes law" radii of ions, obtained from the simple equation

$$r = \frac{0.814|Z|}{\eta\lambda_0} \quad (2)$$

(Z = charge of ion, η = viscosity of water, λ_0 = limiting equivalent conductivity of ion), are generally smaller than crystal radii (e.g. K⁺ = 1.20 Å, Cl⁻ = 1.18 Å). However, Eucken,¹¹ by introducing a correction factor into eq 2, arrived at radii somewhat larger than those in the solid state (e.g., K⁺ = 2.32 Å, Cl⁻ = 2.14 Å).

A promising approach to the estimation of radii of ions and molecules in solution is offered by the scaled particle theory developed by Reiss, *et al.*^{12,13} This theory has been applied successfully to predict thermodynamic properties of pure liquids, including molten salts,¹⁴ and mixtures of nonelectrolytes.^{15,16} Pierotti¹⁷ used scaled particle theory to obtain expressions for various thermodynamic properties of aqueous solutions of nonelectrolytes, including their solubilities, enthalpies and entropies of solution, and partial molal volumes of the solutes. In each case, good agreement was obtained with experiment.

Mayer¹⁴ and Pierotti¹⁷ have pointed out that when the hard-sphere radius of an ion or molecule, which plays an important role in equations derived from scaled particle theory, is treated as a variable to fit thermodynamic data, the value obtained is in excellent agreement with that derived by other reliable methods. In particular, hard-sphere radii of ions which give the best fit to equations for the compressibility or surface tension of molten alkali halides agree closely with internuclear distances in the gaseous molecules. For example, the Na-Cl distance in the NaCl molecule, as determined spectroscopically, is 2.36 Å; the mean value found by fitting compressibility and surface tension data is 2.39 Å.

Recently, scaled particle theory has been extended¹⁸⁻²⁰ to calculate an important thermodynamic property of aqueous electrolyte solutions: their effect on the solubility of nonelectrolytes. Briefly, what is done is to derive expressions for the free energy of

cavity formation and the energy of interaction of a molecule in the cavity with surrounding solvent species. In an electrolyte solution, the solvent is taken to be a mixture of water molecules and ions. By comparing the free energy terms in the presence and absence of ions, it is possible to predict the direction and magnitude of the "salt effect," the effect of the salt on the solubility of the nonelectrolyte.

Equations derived from scaled particle theory have been remarkably successful in reproducing salt effect data. Shoor and Gubbins¹⁸ find excellent agreement with theory for solubility data in the Ar-KOH system, even at high electrolyte concentrations. In contrast, classical electrostatic theories of the salt effect are at variance with experiment for this system. The theory of Debye and McAulay²¹ predicts argon solubilities up to ten times as great as those observed; that of Conway, *et al.*,²² actually predicts negative solubilities at high KOH concentrations.

Masterton and Lee²⁰ used scaled particle theory to derive an expression for the salting coefficient, k_s

$$k_s = \frac{1}{C_s} \log \frac{S_0}{S} \quad (3)$$

(S_0 = solubility of nonelectrolyte in pure water, S = solubility in electrolyte solution of molarity C_s). Calculated values of k_s are in considerably better agreement with experiment with a wide variety of alkali halide systems than those obtained from earlier theories of the salt effect, such as that of McDevit and Long.²³ To cite an extreme case, for the SF₆-NaCl system, where k_s is known to be 0.215, scaled particle theory predicts a value of 0.202 as opposed to 0.358 for the McDevit-Long theory. Only for systems in which the nonelectrolyte is an aromatic hydrocarbon does scaled particle theory give relatively inaccurate values of k_s . The difficulty here is presumably related to uncertainties in the interaction energy term, which makes a par-

(10) K. H. Stern and E. S. Amis, *Chem. Rev.*, **59**, 1 (1959).

(11) A. Eucken, "Lehrbuch der Chemischen Physik," Vol. II, Akademische Verlagsgesellschaft, Geest und Partig, K. G., Leipzig, 1949, pp 1080-1083.

(12) H. Reiss, H. L. Frisch, and J. L. Lebowitz, *J. Chem. Phys.*, **31**, 369 (1959).

(13) H. Reiss, H. L. Frisch, E. Helfand, and J. L. Lebowitz, *ibid.*, **32**, 119 (1960).

(14) S. W. Mayer, *J. Phys. Chem.*, **67**, 2160 (1963).

(15) J. L. Lebowitz, E. Helfand, and E. Praestgaard, *J. Chem. Phys.*, **43**, 774 (1965).

(16) R. A. Pierotti, *J. Phys. Chem.*, **67**, 1840 (1963).

(17) R. A. Pierotti, *ibid.*, **69**, 281 (1965).

(18) S. K. Shoor and K. E. Gubbins, *ibid.*, **73**, 498 (1969).

(19) M. Lucas, *Bull. Soc. Chim. Fr.*, 2994 (1969).

(20) W. L. Masterton and T. P. Lee, *J. Phys. Chem.*, **74**, 1776 (1970).

(21) P. Debye and J. McAulay, *Phys. Z.*, **26**, 22 (1925).

(22) B. E. Conway, J. E. Desnoyers, and A. C. Smith, *Phil. Trans. Roy. Soc., London, Ser. A*, **256**, 389 (1964).

(23) W. F. McDevit and F. A. Long, *J. Amer. Chem. Soc.*, **74**, 1773 (1952).

ticularly large contribution to k_s for aromatic molecules.

The expression derived for k_s from scaled particle theory (ref 20) is extremely sensitive to the values chosen for ionic radii. To illustrate, consider the H_2 -NaCl system, for which k_s has been determined experimentally to be 0.111. The value of k_s calculated from scaled particle theory, using Pauling radii to obtain the hard-sphere diameters of Na^+ and Cl^- , is also 0.111. If one increases these radii by only 5%, the calculated k_s is 0.138, an increase of about 25%. The sensitivity of k_s to ionic radius increases with the size of the nonelectrolyte molecule. In the SF_6 -NaCl system, an increase of 5% in the values assumed for ionic radii changes the calculated k_s from 0.202 to 0.302.

From the examples cited it appears that the interpretation of salt effect data by equations derived from scaled particle theory offers a potentially valuable approach to choosing appropriate ionic radii to describe the thermodynamic properties of aqueous electrolyte solutions. By comparing measured values of k_s for alkali halide systems to those calculated using different sets of crystal radii (Pauling, Goldschmidt, Gourary and Adrian, Waddington) it should be possible to determine which set best reproduces salt effect data. It should also be possible to use this approach to obtain rather precise values for the thermodynamic radii of such polyatomic ions as OH^- , NO_3^- , NH_4^+ , and tetraalkylammonium ions, R_4N^+ , which are difficult to estimate from crystal lattice measurements.

Calculation of Ionic Radii from k_s

The detailed expression for k_s derived from scaled particle theory for slightly soluble nonelectrolytes in a solution of a 1:1 salt at 25° is given in ref 20 (eq 5, 11, 19, and 32 of that paper). For a given salt–nonelectrolyte pair, k_s is a function of the parameters: $\sigma_1, \sigma_2, \sigma_3, \sigma_4$ = hard-sphere diameters of nonelectrolyte molecule, water molecule, cation, and anion, respectively; ϕ_0 = apparent molal volume at infinite dilution of the electrolyte; $\epsilon_1/k, \epsilon_2/k$ = energy parameters of nonelectrolyte and water, respectively; $\alpha_1, \alpha_3, \alpha_4$ = polarizabilities of nonelectrolyte, cation, and anion, respectively.

Values of these parameters, except for σ_3 and σ_4 , were taken from the literature. Apparent molal volumes were those given by Millero.² The parameters for water ($\sigma_2, \epsilon_2/k$) and the nonelectrolytes ($\sigma_1, \epsilon_1/k, \alpha_1$) are from Pierotti^{16,17} or Hirschfelder, *et al.*²⁴ Ion polarizabilities were taken from Conway²⁵ for the alkali halide ions, Shoor and Gubbins¹⁸ (OH^-), Landolt–Bernstein²⁶ (NH_4^+, NO_3^-), and Gilkerson and Stewart²⁷ (R_4N^+). The systems included are ones for which reliable values of k_s are available and for which scaled particle theory has been shown to be in good agreement with experiment. Specifically, systems involving aromatic hydrocarbons are excluded.

Our objective is to find values of σ_3 and σ_4 which, when substituted into the expression for k_s given in ref

20, give the best fit to experimental salting coefficients. Before making this comparison, it is necessary to examine closely the relationship between calculated and observed values of k_s . If one goes through the derivation for the salting coefficient given in ref 20, it is clear that the exact expression for k_s is

$$k_s(\text{calcd}) = \lim_{C_s \rightarrow 0} \frac{1}{C_s} \log \frac{X_0}{X} \quad (4)$$

where X_0 and X are the mole fraction solubilities of nonelectrolyte in pure water and in an electrolyte solution of molarity C_s . Values of k_s reported in the literature may deviate from calculated salting coefficients for two reasons.

(1) Measured salting coefficients are obtained from solubility data at finite electrolyte concentrations. In some systems reported in the literature, only a single concentration was involved; in others, data at a series of salt concentrations were treated graphically or analytically to obtain an average value of k_s . Seldom if ever have investigators carried out the extrapolation required by eq 4.

(2) In reporting experimental values for k_s , authors have seldom expressed the solubility of nonelectrolyte in terms of its mole fraction. More frequently, molarity has been used. In some systems, molality was used as a concentration unit for both nonelectrolyte and electrolyte.

The first factor seems unlikely to lead to serious discrepancies between calculated and experimental values of k_s . Examination of salt effect data for alkali halide systems²⁸ suggests that the ratio $(1/C_s) \log X_0/X$ is virtually independent of C_s , at least up to electrolyte concentrations as high as 1–2 mol/l. For systems involving tetraalkylammonium salts, there is evidence for greater variation; fortunately, for most of these systems, data are available at low concentrations (0.1 mol/l.) where the effect is expected to be small. Tentatively at least, it appears valid to compare values of k_s calculated from scaled particle theory to experimental salting coefficients which conform to the equation

$$k_s(\text{exptl}) = \frac{1}{C_s} \log \frac{X_0}{X} \quad (5)$$

On the other hand, the type of concentration unit used to express nonelectrolyte solubility can affect the value reported for k_s . At any value of C_s , $k_s(\text{exptl})$ obtained from eq 5 can vary significantly from that ob-

(24) J. O. Hirschfelder, C. F. Curtiss, and R. B. Bird, "Molecular Theory of Gases and Liquids." Wiley, New York, N. Y., 1954.

(25) B. E. Conway, "Electrochemical Data," American Elsevier, New York, N. Y., 1952.

(26) Landolt–Bernstein, "Zahlenwerke und Functionen aus Physik, Chemie, Astronomie, Geophysik, Technik," Vol. 1, Berlin, Germany, Part 1, 1950, p 404.

(27) W. R. Gilkerson and J. L. Stewart, *J. Phys. Chem.*, **65**, 1465 (1961).

(28) F. A. Long and W. F. McDevitt, *Chem. Rev.*, **51**, 119 (1952).

Table II

	$k_d(\text{exptl})$													
	He	Ne	Ar	Kr	Xe	H ₂	O ₂	N ₂	N ₂ O	SF ₆	CH ₄	C ₂ H ₂	C ₂ H ₄	C ₂ H ₆
LiCl	0.067 ^a	0.076 ^a	0.114 ^a 0.103 ^b	0.135 ^a	0.083 ^d	0.144 ^e	0.122 ^d	0.099 ^f	0.164 ^a	0.125 ^d	0.111 ^d	0.152 ^d	0.152 ^d	0.152 ^d
NaCl	0.099 ^a 0.075 ^c	0.115 ^a	0.152 ^a 0.149 ^b 0.140 ^c	0.165 ^a	0.111 ^d	0.151 ^e 0.151 ^f	0.150 ^d	0.122 ^h	0.215 ^a	0.154 ^d 0.167 ^e	0.112 ^h	0.150 ^d	0.189 ^d 0.182 ^e	
NaBr	0.106 ^a	0.137 ^c	0.134 ^b	0.144 ^a	0.097 ⁱ	0.120 ⁱ 0.145 ^e	0.102 ^h 0.101 ^f 0.089 ^g	0.186 ^a	0.090 ^h 0.083 ^h	0.102 ^h 0.101 ^f 0.089 ^g	0.090 ^h 0.083 ^h	0.069 ^h		
KCl	0.086 ^a	0.133 ^c	0.130 ^b	0.141 ^a	0.104 ^d	0.124 ⁱ	0.080 ^h	0.183 ^a	0.088 ^f 0.080 ^h	0.169 ^a	0.129 ^d	0.084 ^d	0.130 ^d	
KBr	0.080 ^c	0.130 ^b	0.127 ^b	0.143 ^a	0.104 ^d	0.086 ⁱ	0.078 ^f	0.146 ^f	0.326 ^k	0.197 ^k	0.069 ^h			
KI	0.104 ^c	0.101 ^a	0.179 ^k	0.113 ^a	0.073 ^j	0.189 ^f 0.129 ^k 0.157 ^f 0.103 ^j	0.180 ^e 0.199 ^f	0.096 ^h 0.099 ^f 0.065 ^h 0.070 ^j 0.051 ^f 0.044 ^h 0.040 ^h	0.141 ^a	0.110 ^a	0.071 ^l	0.030 ^h	0.082 ^l	
KOH	0.150 ^k		0.084 ^b	0.084 ^a										
NaOH														
NaNO ₂	0.080 ^c	0.088 ^g	0.023 ^m	0.000 ^a -0.019 ^a	-0.036 ^a				0.026 ^a 0.031 ^a					
KNO ₃														
NH ₄ Cl	0.045 ^a													
NH ₄ Br														
Me ₄ NCl														
Me ₄ NBr														
Me ₄ NI	0.016 ^a													
Et ₄ NBr	-0.010 ^a													
Et ₄ NI														
<i>n</i> -Pr ₄ NBr														
<i>n</i> -Pr ₄ NI														
<i>n</i> -Bu ₄ NBr														

^a T. J. Morrison and N. B. B. Johnstone, *J. Chem. Soc.*, 3655 (1955). ^b A. Ben Naim and M. Egel-Thal, *J. Phys. Chem.*, **69**, 3250 (1965). ^c H. L. Clever and C. J. Holland, *J. Chem. Eng. Data*, **13**, 411 (1968). ^d T. J. Morrison and F. Billett, *J. Chem. Soc.*, 3819 (1952). ^e A. Fackel and G. Hertzberg, *Z. Phys. Chem.*, **195**, 1 (1950). ^f G. Geffcken, *ibid.*, **49**, 257 (1904). ^g G. Akerlof, *J. Amer. Chem. Soc.*, **57**, 1196 (1935). ^h W. Manchot, M. Jahrstorfer, and H. Zepfer, *Z. Anorg. Allgem. Chem.*, **141**, 45 (1924). ⁱ C. G. MacArthur, *J. Phys. Chem.*, **20**, 495 (1916). ^j W. Knopp, *Z. Phys. Chem.*, **48**, 97 (1904). ^k S. K. Shoor, R. D. Walker, Jr., and K. E. Gubbins, *J. Phys. Chem.*, **73**, 312 (1969). ^l W. Y. Wen and J. H. Hung, *ibid.*, **74**, 170 (1970). ^m A. Ben Naim, *ibid.*, **71**, 1137 (1967).

tained using the expressions more commonly found in the literature, where concentrations are given in mol/l. of solution

$$k_s' = \frac{1}{C_s} \log \frac{C_0}{C} \quad (6)$$

(C_0 , C = molar solubilities of nonelectrolyte in pure water and electrolyte solution of molarity C_s , respectively) or in mol/1000 g of water

$$k_s'' = \frac{1}{m_s} \log \frac{m_0}{m} \quad (7)$$

(m_0 , m = molal solubilities of nonelectrolyte in pure water and electrolyte solution of molality m_s , respectively).

The equations relating $k_s(\text{exptl})$ to k_s' and k_s'' are readily shown to be

$$k_s(\text{exptl}) = k_s' + \frac{0.0360 - \phi/1000}{2.30} \quad (8)$$

where ϕ is the apparent molal volume of the electrolyte, and

$$k_s(\text{exptl}) = \frac{m_s}{C_s} (k_s'' + 0.0360/2.30) \quad (9)$$

where m_s and C_s are the molality and molarity, respectively, of the electrolyte solution in which the solubility of the nonelectrolyte is measured.

The difference between $k_s(\text{exptl})$ and k_s' can be either positive or negative depending upon the nature of the electrolyte. Using eq 8, one can show that in a 1 *M* solution of NaCl, $k_s(\text{exptl})$ exceeds k_s' by 0.008; in 1 *M* KI, $k_s(\text{exptl})$ is 0.005 less than k_s' . In general, $k_s(\text{exptl})$ always exceeds k_s'' . For the NaCl-CH₄ system, where k_s'' is reported to be 0.135 in a 1 *M* solution, $k_s(\text{exptl})$, obtained from eq 9, is 0.154. For the KI-CH₄ system at the same concentration, k_s'' is 0.107 while $k_s(\text{exptl})$ is 0.129.

In Table II are listed values of $k_s(\text{exptl})$ obtained from literature data with the aid of eq 8 and 9. These are to be compared with salting coefficients calculated from scaled particle theory (ref 20). By choosing different values for the hard-sphere ionic diameters σ_3 and σ_4 , it becomes possible to decide which ionic radii ($\sigma_3/2$, $\sigma_4/2$) give the best fit to the values of $k_s(\text{exptl})$ for the various systems.

Results and Discussion

Alkali Halide Ions. The four sets of crystal radii for the alkali halide ions (Table I) were used to calculate salting coefficients which were then compared with the values of $k_s(\text{exptl})$ for the alkali halide systems listed in Table II. The results are summarized in Table III, where the average value of the quantity

$$\Delta k_s = k_s(\text{calcd}) - k_s(\text{exptl})$$

Table III: Average Values of $\Delta k_s = k_s(\text{calcd}) - k_s(\text{exptl})$

Ion	No. of systems	Pauling	Goldschmidt	Gourary and Adrian	Waddington
Li ⁺	14	-0.025	-0.011	-0.040	+0.002
Na ⁺	26	-0.020	-0.013	-0.043	-0.002
K ⁺	32	-0.031	-0.020	-0.049	-0.010
Cl ⁻	46	-0.020	-0.014	-0.041	-0.005
Br ⁻	12	-0.023	-0.016	-0.047	-0.006
I ⁻	14	-0.047	-0.024	-0.058	-0.006

is listed for all of the systems involving a particular ion.

It is clear from Table III that the best fit is obtained when Waddington crystal radii are used. Indeed, the agreement with these radii is remarkably good considering the uncertainties in many of the molecular parameters and in $k_s(\text{exptl})$.

Goldschmidt radii give a slightly poorer fit; the average error is somewhat larger using Pauling radii. In both cases, $k_s(\text{calcd})$ is, on the average, too small. Since the derivatives $dk_s/d\sigma_3$ and $dk_s/d\sigma_4$ are both positive (ref 20), this suggests that Goldschmidt and Pauling radii are slightly too small to accurately reproduce salting coefficients.

The radii of Gourary and Adrian give the poorest agreement of the four sets. To take a typical case, for the CH₄-LiCl system, where $k_s(\text{exptl})$ is 0.125, the calculated k_s using Gourary and Adrian radii is only 0.079; Pauling, Goldschmidt, and Waddington radii give successively better fits (0.095, 0.109, 0.123).

The results obtained here argue against the contention of Blandamer and Symons⁹ that Gourary and Adrian radii are to be preferred above others in describing the thermodynamic properties of electrolyte solutions. Clearly, these radii are unsatisfactory so far as interpreting salt effect data is concerned. By the same token, it appears that Waddington radii merit more attention than they have received up to this point.

Polyatomic Ions. Using Waddington radii for the counterions (*i.e.*, alkali halide ions), it is possible to find the radius of a polyatomic ion which, when substituted into the expression for k_s derived from scaled particle theory, gives the best fit to $k_s(\text{exptl})$ for a particular system. Choosing the NaNO₃-He system as an example, if one uses the Waddington radius of Na⁺, 1.01 Å, then $\sigma_3 = 2(1.01 \text{ Å}) = 2.02 \text{ Å}$; use of this number and the other appropriate parameters with $k_s = 0.080$ gives an expression with only one unknown, σ_4 . By trial and error or with the aid of a computer, one finds that the best fit is obtained when $\sigma_4 = 3.85 \text{ Å}$, *i.e.*, with a NO₃⁻ ion radius of $(3.85 \text{ Å})/2 = 1.93 \text{ Å}$.

This type of calculation was carried out for each system involving a polyatomic ion for which $k_s(\text{exptl})$ was available. Table IV lists the mean radius obtained for each ion with the average deviation from the

mean. The latter is quite small, of the order of ± 0.05 Å. This narrow range is partially explained by the high sensitivity of $k_s(\text{calcd})$ to small variations in σ_3 or σ_4 . Nevertheless, it lends considerable support to this method of obtaining effective hard sphere radii of ions in aqueous solution. It will be noted that for the ions $(n\text{-C}_3\text{H}_7)_4\text{N}^+$ and $(n\text{-C}_4\text{H}_9)_4\text{N}^+$ relatively few values of $k_s(\text{exptl})$ are available (3 and 2 systems, respectively). Accordingly, one can expect the radii assigned to these ions to be somewhat less reliable than those of other polyatomic ions.

Table IV: Radii of Polyatomic Ions

Ion	No. of systems	Radius, Å	Av dev
OH ⁻	11	1.52	± 0.06
NO ₃ ⁻	13	1.96	± 0.03
NH ₄ ⁺	11	1.43	± 0.05
(CH ₃) ₄ N ⁺	5	2.51	± 0.04
(C ₂ H ₅) ₄ N ⁺	7	3.08	± 0.04
(<i>n</i> -C ₃ H ₇) ₄ N ⁺	3	3.49	± 0.05
(<i>n</i> -C ₄ H ₉) ₄ N ⁺	2	3.81	± 0.05

It is interesting to compare radii of polyatomic ions calculated from the scaled particle theory of the salt effect with those estimated using other methods. In some cases the agreement is excellent. For the NH₄⁺ ion, Pauling³ calculates an empirical crystal radius of 1.48 Å in good agreement with the value found here, 1.43 Å. For the NO₃⁻ ion, two estimates are available. Couture and Laidler²⁹ proposed a semiempirical equation for the effective radius of an oxyanion MO_{*n*}⁻

$$r = 0.25n(d + 1.40 \text{ \AA}) \quad (10)$$

where d is the M-O bond distance. Applying this equation to the nitrate ion, with $n = 3$ and $d = 1.24$ Å, r is calculated to be 1.98 Å. Stern and Amis¹⁰ used a somewhat different approach to arrive at a value of 1.89 Å. The nitrate ion radius listed in Table IV, 1.96 Å, falls between these two values.

Previous estimates of the radius of the OH⁻ ion range from 1.40 Å, the van der Waals radius of oxygen, to 1.76 Å, calculated by Pauling³ for the univalent radius of the oxide ion. The value found here, 1.52 Å, falls between these extremes. It is interesting that the radius of the OH⁻ ion found from scaled particle theory is somewhat larger than that of the H₂O molecule, 1.38 Å, as calculated by Pierotti¹⁷ from solubility data. The same effect is found if one compares internuclear distances in crystals. One half of the O-H-O distance in the alkali metal hydroxides, NaOH and KOH, is about 1.5 Å;³⁰ a similar calculation for the H₂O molecule, based on the O-H-O distance in ice, gives an effective radius of 1.38 Å.

The radii of tetraalkylammonium ions obtained here

are considerably smaller than those of Robinson and Stokes,³¹ who estimated values of 3.47, 4.00, 4.52, and 4.94 Å for (CH₃)₄N⁺, (C₂H₅)₄N⁺, (*n*-C₃H₇)₄N⁺, and (*n*-C₄H₉)₄N⁺, respectively. The Robinson and Stokes radii for (CH₃)₄N⁺ and (C₂H₅)₄N⁺ were obtained from measurements on atomic models and, in effect, represent a maximum radius from the center of the nitrogen atom to the most distant hydrogen atom in the alkyl group. It seems reasonable to suppose that the effective radii in solution would be smaller. This is also suggested by calculations carried out by Hepler *et al.*,³² who, from a detailed analysis of internuclear distances in the compounds (CH₃)₄NCl and (CH₃)₄NBr, arrived at an effective radius of 2.67 Å for (CH₃)₄N⁺, reasonably close to the scaled particle radius. The Robinson and Stokes values for (*n*-C₃H₇)₄N⁺ and (*n*-C₄H₉)₄N⁺ were obtained by using an empirical equation to relate the radius of R₄N⁺ to the molecular volume of a hydrocarbon of similar structure. Since the proportionality constant in this equation is based on the values assumed for (CH₃)₄N⁺ and (C₂H₅)₄N⁺, it is hardly surprising that radii calculated for the higher homologs are also too large.

Another method of estimating effective radii for tetraalkylammonium ions involves the use of a semiempirical equation relating molal volume in solution to ionic radius. For an ion of the type R₄N⁺, the uncertainties discussed earlier in connection with eq 1 should be of relatively minor importance. The molal volumes of these ions are so large (80 cc/mol or greater) that an error of ± 6 cc/mol in V° has little effect on the calculated radius. Moreover, since the radii themselves are large, the electrostriction term, which is inversely related to radius, is relatively small (of the order of a few cc/mol). Of the many equations relating V° to r which have been proposed, we choose two of the simpler, those of Mukerjee³³ and Glueckauf.³⁴

$$\text{Mukerjee } V^\circ = 4.48r^3 - 8.0/r \quad (r \text{ in \AA}) \quad (11)$$

$$\text{Glueckauf } V^\circ = 2.52(r + 0.55)^3 - \frac{33}{r + 1.38} \quad (12)$$

(To compare these equations to eq 1, note that V° (disorder), which is a positive quantity, has been incorporated into the first term on the right; the second term represents $V^\circ(\text{elect})$).

Table V lists radii of the tetraalkylammonium ions calculated from eq 11 and 12. The V° values were obtained from partial molal volumes of the halide salts in

(29) A. M. Couture and K. J. Laidler, *Can. J. Chem.*, **35**, 207 (1957).

(30) A. F. Wells, "Structural Inorganic Chemistry," Oxford University Press, London, 1962.

(31) R. A. Robinson and R. H. Stokes, "Electrolyte Solutions," 2nd ed, Butterworths, London, 1959, pp 124-125.

(32) L. G. Hepler, J. M. Stokes, and R. H. Stokes, *Trans. Faraday Soc.*, **61**, 20 (1965).

(33) P. Mukerjee, *J. Phys. Chem.*, **65**, 740 (1961).

(34) E. Glueckauf, *Trans. Faraday Soc.*, **61**, 914 (1965).

Table V: Radii of Tetraalkylammonium Ions from Molal Volumes

Ion	V° , cc/mol	Eq 11, Å	Eq 12, Å
$(\text{CH}_3)_4\text{N}^+$	85	2.70	2.78
$(\text{C}_2\text{H}_5)_4\text{N}^+$	145	3.20	3.37
$(n\text{-C}_3\text{H}_7)_4\text{N}^+$	210	3.62	3.86
$(n\text{-C}_4\text{H}_9)_4\text{N}^+$	272	3.94	4.24

water solution (ref 2), taking V° for Cl^- , Br^- , and I^- to be 22, 29, and 41 cc/mol, respectively.

The radii calculated from molal volumes are considerably smaller than those of Robinson and Stokes, by about 0.7–1.0 Å. In contrast, they are somewhat larger (0.2–0.4 Å) than those calculated from the scaled particle theory of the salt effect. This discrepancy may result from the effect these ions have on the structure of water. It is generally believed that the tetraalkylammonium ions in solution surround themselves with a

clathrate-like cage of water molecules,³⁵ which would presumably lead to an increase in volume. Millero² takes this factor into account by including an extra positive term, $V^\circ(\text{caged})$, on the right-hand side of eq 1. Failure to include such a term in eq 11 and 12 would, in effect, cause the volume increase to be incorporated into the term involving r . In this way, one would arrive at radii somewhat larger than those corresponding to a hard sphere model.

Acknowledgment. This work was supported by the National Science Foundation under Grant GP-6163 and by funds provided by the United States Department of the Interior as authorized under the Water Resources Act of 1964, Public Law 88-379. Computer time was donated by the University of Connecticut Computer Center under funds provided by the National Science Foundation.

(35) H. S. Frank and W. Y. Wen, *Discuss. Faraday Soc.*, **24**, 133 (1957).

Investigations on the Ion-Exchange and Ionic Transport Properties of Glass Membranes in Molten Salts by an Electrolytic Transport Technique

by T. J. van Reenen, Marie van Niekerk, and W. J. de Wet*

Chemistry Division, National Nuclear Research Centre, Private Bag 266, Pretoria, South Africa (Received August 10, 1970)

Publication costs borne completely by The Journal of Physical Chemistry

The ion-exchange and ionic transport properties of Pyrex, soda lime glass, and fused silica were investigated for pairs of light alkali cations at elevated temperatures. The results obtained for the ion-exchange constants by using an electrolytic transport technique are in good agreement with those obtained by an equilibrium sorption method. Besides this, it was also found that the mobility ratios of cation pairs are strongly dependent on the ionic composition of glass. This fact implies that a correlation of experimental and theoretical membrane potentials for glass membranes in molten salts is presumably not straightforward. Results obtained along these lines are presented.

Introduction

The ion-exchange and ionic transport properties of glasses are of interest from both a fundamental and practical point of view, as were discussed by several previous authors.^{1–10} In both respects ion selective glass electrodes justify special emphasis because of the considerable interest in recent years^{6,8,10} in the use and further development of ion selective electrodes in general for the direct and specific measurement of activities of ions in aqueous solutions. In molten systems, glass membranes have been applied very successfully as ionic

conductive barriers for reference electrodes¹¹ and only recently have the possibilities of the cation specific

- (1) S. S. Kistler, *J. Amer. Ceram. Soc.*, **45**, 59 (1962).
- (2) M. E. Nordberg, E. L. Mochel, H. M. Garfinkel, and J. S. Olcott, *ibid.*, **47**, 215 (1964).
- (3) A. J. Burggraaf and J. Cornelissen, *Phys. Chem. Glasses*, **5**, 123 (1964).
- (4) H. M. Garfinkel, *Appl. Opt.*, **7**, 789 (1968).
- (5) Y. K. Delimarskii and R. F. Markov, "Electrochemistry of Fused Salts," English translation by Sigma Press, Washington, D. C., 1961.
- (6) K. H. Stern, *Chem. Rev.*, **6**, 355 (1966).

properties of glasses been emphasized¹²⁻²⁰ for developing ion selective electrodes for use under these conditions.

For development work and eventual full utilization of ion selective glass electrodes for use at elevated temperatures, it is essential that methods be found to assess quantitatively the characteristics of glass membranes pertaining to membrane potentials. On the phenomenological theory of membrane potentials of ion selective electrodes further corroborative studies would in addition be required to derive full benefits from such possible future developments. Although the ion-exchange theory of membrane potentials, as originally suggested by Teorell²¹ and developed by Conti and Eisenman,²² can presumably be accepted with a great measure of confidence, it must be remembered that most published work reported on establishing the validity of the above theory was done in aqueous systems with glass membranes, using mostly tracer diffusion techniques.^{7,8} It is well known that glass surfaces under these conditions are covered with hydrated layers^{8,18} with different properties than those of the dry glass, and observed time variations of membrane potentials are attributed to this phenomenon. The ultimate influence of this on steady membrane potentials eventually measured has not as yet been quantitatively assessed. For this and other reasons attempts under aqueous conditions are still being made by several investigators to verify the above theory, some of which are using rather indirect methods, such as frequency dependence studies of impedances of membranes²³ and surface charge characterization of membranes.²⁴

It is felt that for a stringent test of the above theory and for characterization of glass in general as membranes for ion selective electrodes in molten systems, reliable data on ion-exchange and ionic transport properties of glasses should be obtainable by electrolytic transport techniques, provided that sufficiently large electrolysis currents can be attained for total displacement of mobile ions in membranes. From these properties values for the controlling parameters of the above theory are supposedly directly obtainable. This procedure was originally suggested by Conti and Eisenman,²² who derived expressions for studying the above properties of membranes under nonzero current conditions. Such a procedure is indeed feasible for glasses as it has been known for a long time^{25,26} that the light alkali metal cations are responsible for the electrolytic conduction properties of ordinary glasses which become quite appreciable toward the softening temperatures of the glasses. A few investigators^{18,27,28} have in fact used electrolytic transport techniques on glass membranes in molten salts, but to our mind have unfortunately not pursued this sufficiently far to have taken full advantage of what the procedure has to offer. It was consequently decided to investigate the above approach using pairs of light alkali cations as mobile ions and Pyrex,

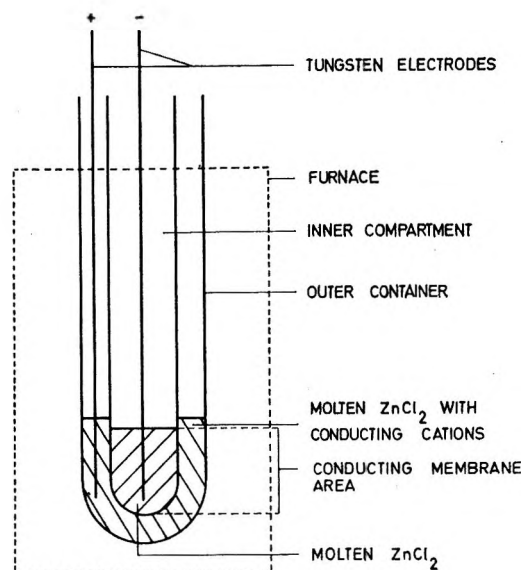


Figure 1. Fused salt electrolytic cell used for the determination of K_{ij} , n , and u_j/u_i .

soda lime glass, and fused silica tubes as membranes. Our investigations along these lines are reported below.

Basis of the Experimental Investigations. Conti and Eisenman²² derived general flux equations for examining the properties of membranes under nonzero electric current conditions for a binary mobile ion system. Their final equations (eq 80 and 81 of ref 22) predict that for applied voltages across membranes

- (7) G. Eisenman, *Advan. Anal. Chem. Instrum.*, **4**, 213 (1965).
- (8) G. Eisenman, "Glass Electrodes for Hydrogen and Other Cations," Marcel Dekker, New York, N. Y., 1967.
- (9) W. J. de Wet, *J. S. Afr. Chem. Inst.*, **22**, 168 (1969).
- (10) A. K. Covington, *Chem. Brit.*, **9**, 388 (1969).
- (11) R. W. Laity in "Reference Electrodes," D. G. Ives and G. J. Janz, Ed., Academic Press, New York, N. Y., 1961.
- (12) K. H. Stern, *J. Phys. Chem.*, **72**, 1963 (1968).
- (13) J. Hladik, M. Saunier, and G. Morand, *C. R. Acad. Sci., Ser. C*, **263**, 357 (1966).
- (14) T. Forland and L. U. Thulin, *Acta Chem. Scand.*, **21**, 1211 (1967).
- (15) K. Notz and A. G. Keenan, *J. Phys. Chem.*, **70**, 662 (1966).
- (16) A. G. Keenan, K. Notz, and F. L. Wilcox, *ibid.*, **72**, 1085 (1968).
- (17) R. H. Doremus, *J. Electrochem. Soc.*, **115**, 924 (1968).
- (18) R. H. Doremus, *J. Phys. Chem.*, **72**, 2877 (1968).
- (19) H. M. Garfinkel, *ibid.*, **72**, 4175 (1968).
- (20) H. M. Garfinkel, *ibid.*, **73**, 1766 (1969).
- (21) H. Teorell, *Proc. Soc. Exptl. Biol. Med.*, **33**, 282 (1935).
- (22) P. Conti and G. Eisenman, *Biophys. J.*, **5**, 511 (1965).
- (23) M. J. D. Brand and G. A. Rechnitz, *Anal. Chem.*, **40**, 1185 (1969).
- (24) Th. F. Tadros and J. Lyklema, *J. Electroanal. Chem.*, **22**, 9 (1969).
- (25) G. Schultze, *Ann. Phys. (Leipzig)*, **40**, 335 (1913).
- (26) C. A. Kraus and E. H. Darby, *J. Amer. Chem. Soc.*, **44**, 2783 (1922).
- (27) A. G. Keenan and W. H. Duewer, *J. Phys. Chem.*, **73**, 212 (1969).
- (28) H. M. Garfinkel, *ibid.*, **74**, 1764 (1970).

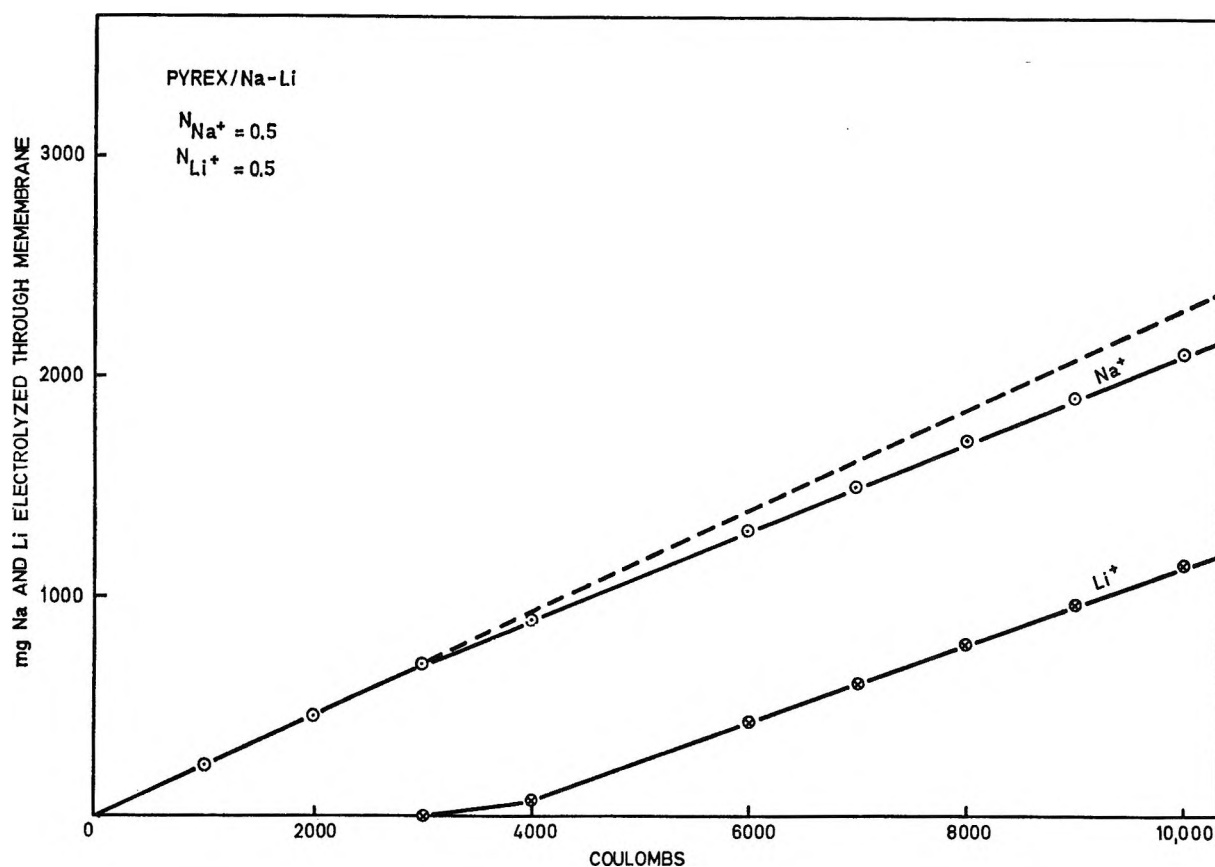


Figure 2. Variation of alkali cation contents of the inner compartment with coulombs electrolyzed for the system Pyrex—Na—Li. The broken line indicates the continuation of the sodium line were lithium absent.

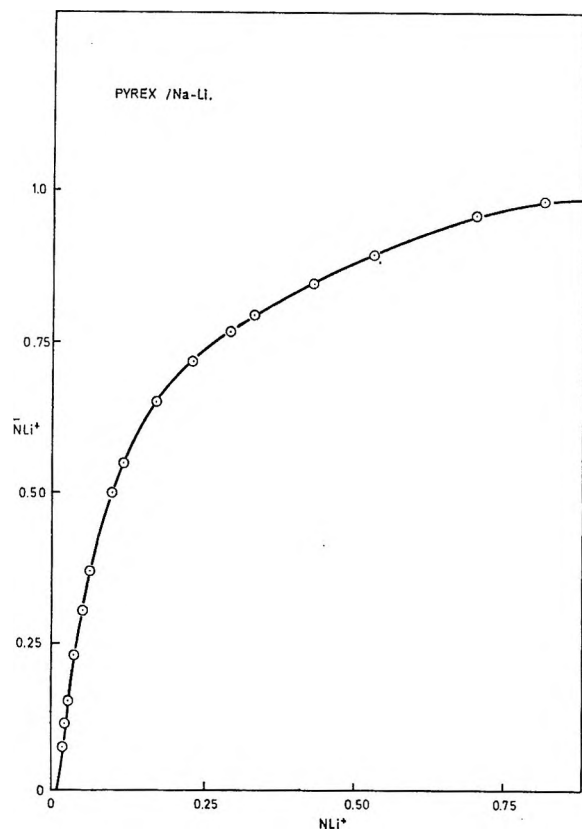


Figure 3. Ion-exchange isotherm for the system Pyrex—Na—Li.

which are large in comparison with membrane potentials, only the cationic composition of the mobile ions in the anodic solution would determine the respective cation currents through a glass membrane. At steady-state conditions this implies that apart from the fact that the fluxes through the membrane for a constant composition of the solution from which the ions migrate into the membrane remain constant, the ion fractions of sites occupied by the particular ions are constant throughout the membrane and the total current passing through the membrane becomes proportional to the applied voltage. The important point to note in their equations is that the relative flux of the two ions through the membrane is determined by the mobility ratio of the ions in the membrane as well as by the thermodynamic equilibrium constant of ion exchange of the ions with the membrane and obviously by the ionic composition of the anodic solution.

Experimental Section

Using the experimental arrangement shown in Figure 1 the applicability of the two equations referred to above was investigated for Pyrex, soda lime glass, and fused silica membranes in Na—Li or K—Na chloride mixtures using anhydrous zinc chloride as solvent. The fused silica tubes were obtained from Heraeus-Scott Quarzschmelze in Germany while Glasstubes and Components of England supplied the soda lime glass tubes. An-

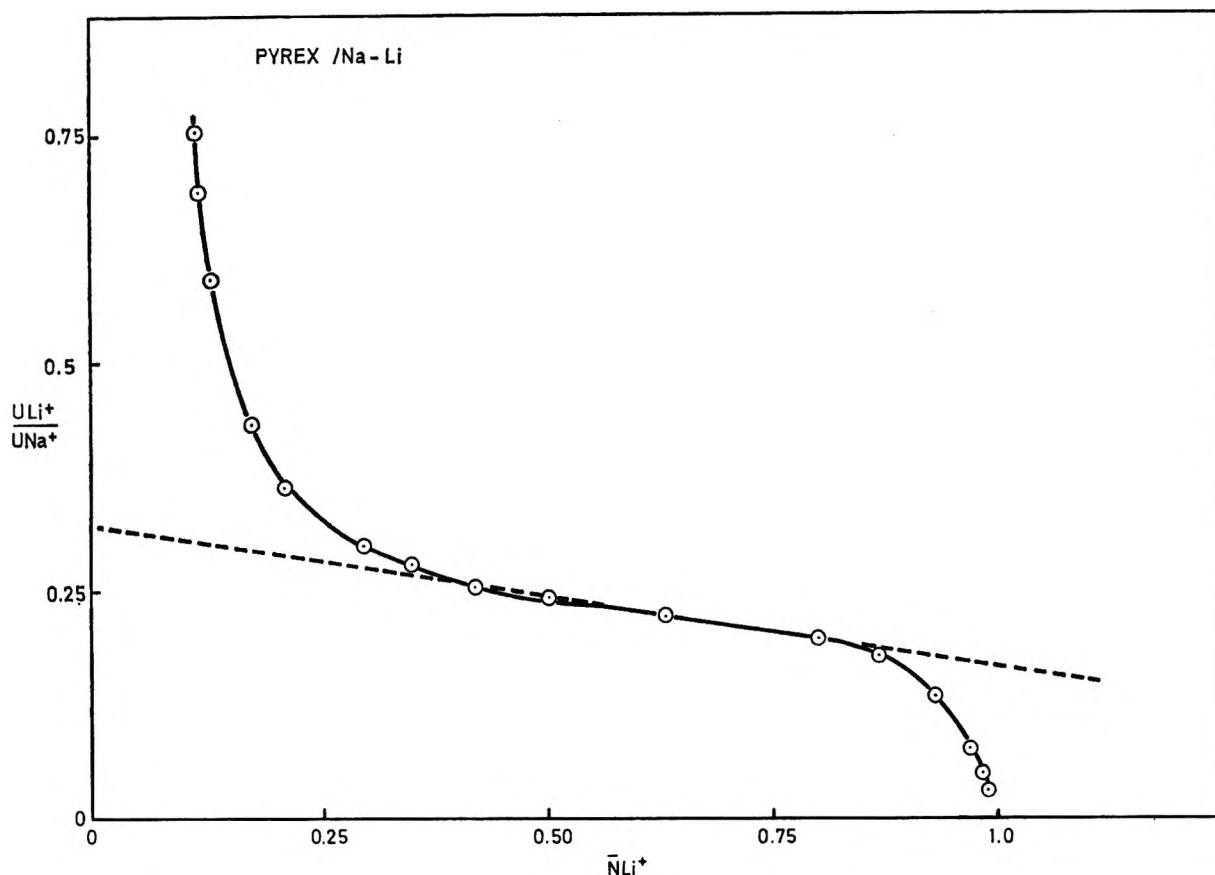


Figure 4. Mobility ratio curve as a function of the ionic composition of the glass membrane for the system Pyrex—Na—Li.

hydrous zinc chloride was prepared by bubbling dry chlorine gas through purified molten zinc contained in a glass pot. Zinc chloride could be transferred directly from this container to the compartments of electrolytic cells without the possibility of moisture contamination. During the experimental runs the molten salts were kept moisture-free below dried oxygen-free blanket gas. Dried sodium and potassium chlorides were used as such but due to the hygroscopic nature of lithium chloride the latter was prepared *in situ* by electrolysis through Pyrex tubes using the experimental technique of this paper. The sodium of the Pyrex tubes was initially displaced by lithium before being used for this purpose. In most of the experiments of this paper the combined mole fractions of the alkali chloride mixtures in the zinc chloride solvent were between 0.3 and 0.5. Temperatures used were 550° for Pyrex, 600° for the fused silica membranes, and 450° for the soda lime glass membranes. The applied voltages used depended to a large extent on the alkali contents of the glasses and varied from about 20 V for soda lime glass and Pyrex membranes to about 300 V for fused silica membranes. The selectivities of the glasses were found not to be dependent on applied voltage as would be expected from the Conti and Eisenman equations. Current densities used were between 1 and 20 mA/cm². It was confirmed that for these systems the displacement of the alkali

ions was completely reversible, *i.e.*, that the glass membranes can be restored to their original alkali ion compositions by reversing the electrolysis current. The electrolytic currents are further solely carried by the alkali cations. Structural changes of the glass membranes also appeared negligible. Silver, gold, and copper ions are analogously transported in glass, but structural changes in the glass appear to take place. Upon displacing sodium in glass by any of these ions, intense coloring results and on reversal of electrolysis these ions are deposited as finely divided metal in the glass. For these reasons our experiments were done only with Li, Na, and K as mobile cations.

Initially, in a series of electrolysis experiments for the system Pyrex—Na—Li, the qualitative validity of the Conti and Eisenman equations was confirmed by electrolyzing a number of Pyrex membranes to various coulomb values (up to the point of lithium breakthrough, *i.e.*, when lithium first appears in the inner compartment) followed by subsequent chemical analysis on etched fractions of the glass. It was found that ion-exchange equilibrium is established as electrolysis proceeds, and at the lithium breakthrough point the whole membrane is in ion-exchange equilibrium with the solution from which uptake of the cations had taken place.

Using the above procedure and extending the elec-

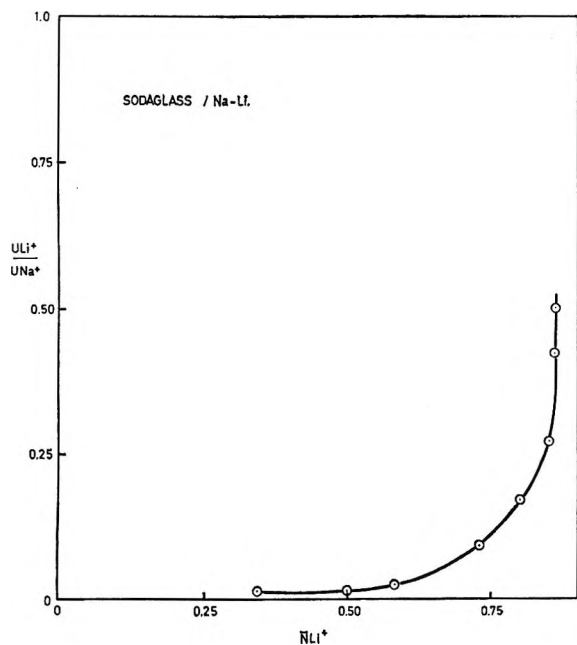


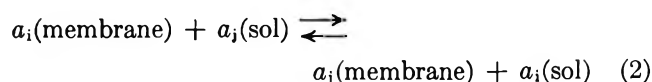
Figure 5. Mobility ratio curve as a function of the ionic composition of the glass membrane for the system soda lime glass—Na—Li.

trollysis to coulomb values far in excess of the point of complete ion-exchange equilibrium throughout the membrane, it is possible to determine the relative fluxes of the migrating ions through the glass membrane by taking dip samples from the inner compartment (see Figure 1) at regular intervals during electrolysis and by subsequent chemical analysis on the anodic melt solution and the equilibrated glass membrane. A typical graphical representation of the composition variation of the inner compartment with coulombs electrolyzed is shown in Figure 2 for the Pyrex—Na—Li system. From the slopes of the lines in these figures the mobility ratios can be directly obtained by knowing the ionic compositions of the equilibrated glass membranes. The above experiments have been repeated using various melt compositions and glass membranes. From the results obtained the ion-exchange isotherms were plotted (see Figure 3 for the Pyrex—Na—Li system) as well as the mobility ratio curve (see Figure 4) for the Pyrex—Na—Li system. In Figures 5 and 6 the mobility ratio curves are given for the soda lime glass—Na—Li and fused silica—Na—Li systems.

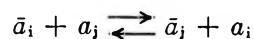
To obtain values for the thermodynamic ion-exchange equilibrium constants, K_{ij} , for the above systems the following expressions were used

$$K_{ij} = \frac{[\bar{N}_j]^n [a_i]}{[\bar{N}_i]^n [a_j]} \quad (1)$$

for the ion-exchange reaction



or



where a_i and a_j are the activities of the cationic species ($i = \text{Na}$ and $j = \text{Li}$ or K), \bar{a} and \bar{N} refer to activities and ion fractions of the cationic species in the membrane, and n is the nonideality factor depending on cations i and j and the properties of the membrane. This factor was originally introduced to account for activities of ions in solid ion exchangers such as zeolites. More recently studies^{19,20} of ion exchange on glasses confirmed that the introduction of n is required for glasses.

Equation 1 can be rewritten as follows^{19,20}

$$\log \frac{N_j}{N_i} - \frac{A}{2.303RT} (1 - 2N_i) = n \log \frac{\bar{N}_j}{\bar{N}_i} - \log K_{ij} \quad (3)$$

in which N and \bar{N} represent the particular ionic fractions of mobile ions in the melt and ion exchanger, respectively. The parameter A is equal to -1120 cal/mol and -522 cal/mol for the Na—Li and Na—K chloride composition systems, respectively.²⁹ This rational form of the thermodynamic equilibrium constant could be used since it was observed that the ion-exchange distributions for our systems did not change noticeably with solvent dilution.

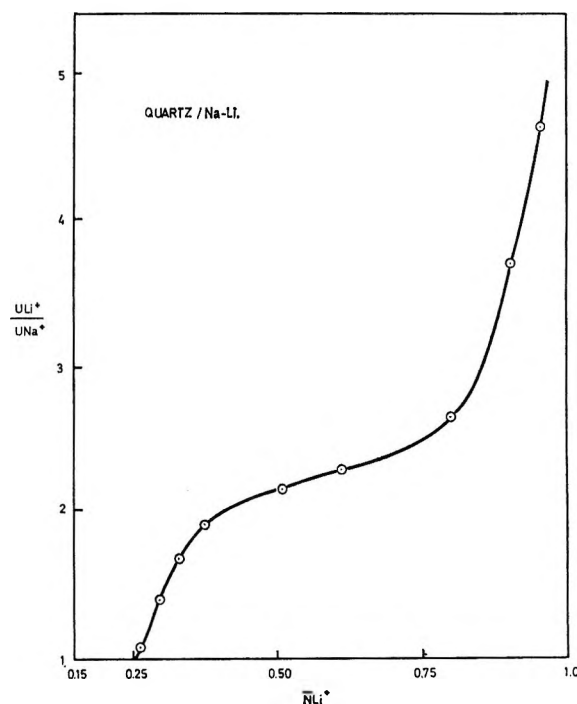


Figure 6. Mobility ratio curve as a function of the ionic composition of the glass membrane for the system fused silica—Na—Li.

(29) L. S. Hersh and O. J. Kleppa, *J. Chem. Phys.*, **42**, 1309 (1965)

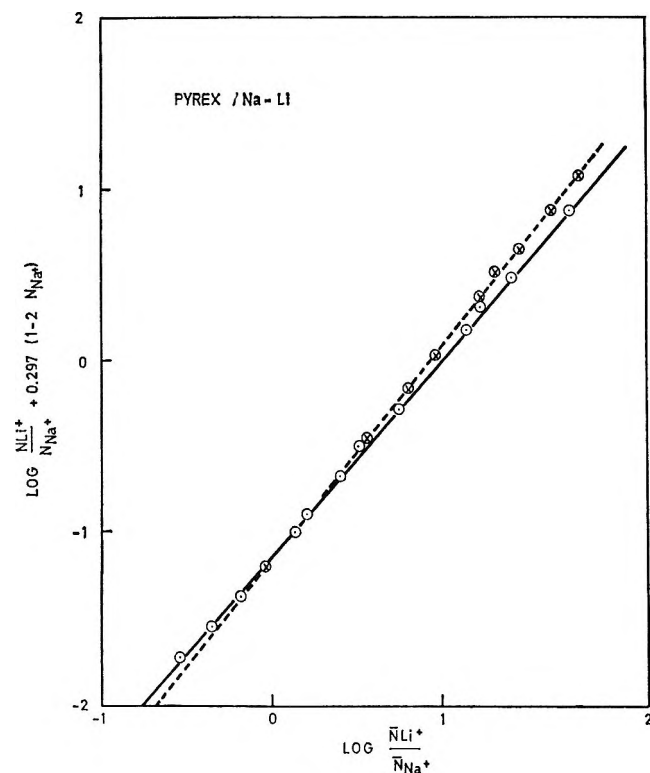


Figure 7. Plot of eq 3 for the system Pyrex—Na—Li: O, electrolytic method; X, equilibrium sorption method.

A graphical presentation of the results in Figure 3 according to eq 3 is given in Figure 7. If eq 3 is correct as far as the basic assumption regarding the activity coefficients of the ionic species in the solutions as well as in the glass membrane are concerned, then a plot of the left-hand side of eq 3 vs. $\log \bar{N}_j / \bar{N}_i$ should give a straight line with slope equal to n and intercept equal to $\log 1/K_{ij}$. For all the systems investigated straight lines were obtained. K_{ij} and n values obtained, using a least-squares fit, are given in Table I. These results indicate that the value of n is independent of the ionic composition of the membrane for each system and that eq 3 is a satisfactory expression for obtaining K_{ij} values. For all the systems the values of K_{ij} and n were also determined by equilibrium sorption experiments following Garfinkel's procedure.^{19,20} In separately sealed inert containers (Supremax glass tubes), glass powder (–200 mesh) was equilibrated with a molten salt mixture for times of up to 500 hr. Subsequent chemical analyses on the melts and glass powders enabled the determination of the ion-exchange isotherms. These results were also inserted in eq 3 and plotted as depicted in Figure 7 for the Pyrex—Na—Li system.

Using the above results membrane potential studies were done on the system Pyrex—Na—Li with the experimental arrangement shown in Figure 8. The cell allowed a direct measurement of the membrane potential. It was realized that judicious choices for the

Table I: Experimental Values Obtained for n , K_{ij} , and u_j/u_i ^a

Ion pair	Glass	n	K_{ij}	$\frac{u_j/u_i}{\bar{N}_j} = 0.5$
Electrolytic				
Na—Li	Pyrex	1.15	13.80	0.224
Na—K	Pyrex	1.24	0.60	0.15
Na—Li	Soda lime glass	3.11	80.5	0.014
Na—Li	Fused silica	1.80	1.7	2.30
Static				
Na—Li	Pyrex	1.25	14.13	
Na—K	Pyrex	1.26	0.57	
La—Li	Soda lime glass	2.07	81.3	
Na—K	Soda lime glass	1.67	5.5	

^a $i = \text{Na}$ and $j = \text{Li}$ or K .

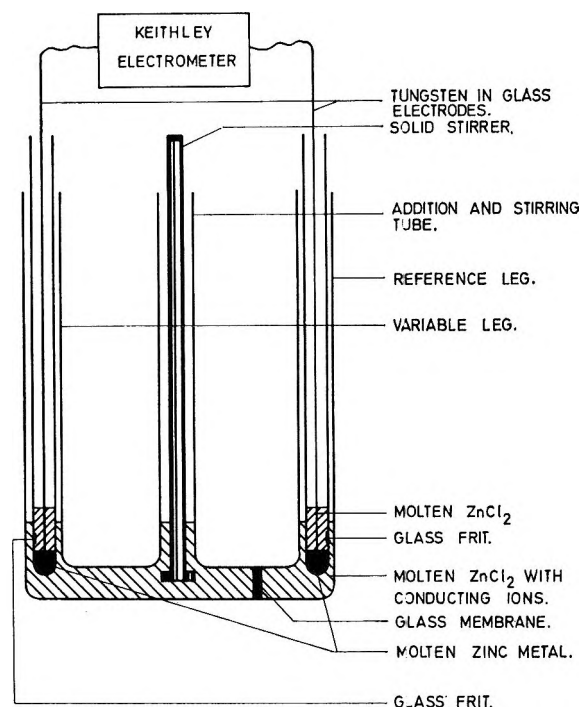


Figure 8. Experimental arrangement used for emf measurements.

melt compositions were essential if an attempt was to be made to correlate experimentally measured and theoretically calculated values of membrane potentials. The reason for this is that the mobility ratio is not independent of the ionic composition of the membrane for our systems and experimental conditions as can be seen in Figures 4–6. We feel that this important aspect has been overlooked by most previous investigators in their assumption of a constant mobility ratio. This assumption has also been made by Eisenman and his coworkers in the derivation of the ion-exchange theory equations. In this theory the expression obtained by Eisenman, *et al.*, for the difference in electrical potential (V_0) between two solutions of the same solvent (see Figure 9) separated by a cation-exchange membrane such as

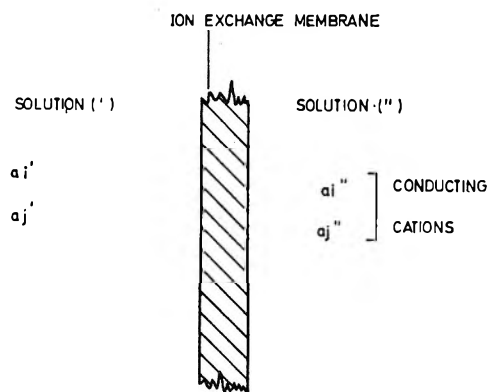


Figure 9. Ion-exchange membrane arrangement in ion selective electrodes.

glass, at zero electrical current for two monovalent conducting cations, is²²

$$V_0 = \frac{nRT}{F} \ln \frac{(a_i')^{1/n} + \frac{u_j}{u_i} (K_{ij} a_j')^{1/n}}{(a_i'')^{1/n} + \frac{u_j}{u_i} (K_{ij} a_j'')^{1/n}} \quad (4)$$

where R , T , and F are the gas constant, the absolute temperature, and the Faraday constant, respectively, and u_j/u_i is the mobility ratio of the ionic species in the membrane.

The total potential in eq 4 can be written as the sum of the diffusion potential in the interior of the membrane and boundary potentials at the two interfaces between the membrane and solutions

$$\begin{array}{ccccccc} V_0 & + & V_B' & + & & & \\ \text{total} & & \text{Donnan boundary} & & & & \\ \text{potential} & & \text{potential with} & & & & \\ & & \text{solution (')} & & & & \\ & & & & V_D & + & V_B'' \\ & & & & \text{diffusion} & & \text{Donnan boundary} \\ & & & & \text{potential} & & \text{potential with} \\ & & & & & & \text{solution (')} \end{array}$$

Only the expression for the diffusion potential, V_D , is altered if a correction is introduced to allow for a variable mobility ratio. The following equation has been derived.^{18,30}

$$V_D = \frac{nRT}{F} \int_{\bar{N}_i'}^{\bar{N}_i''} \frac{(u_j/u_i - 1)}{\bar{N}_j u_j/u_i + \bar{N}_i} d\bar{N}_i \quad (5)$$

For the Pyrex—Na—Li system the dependence of u_{Li}/u_{Na} can be approximated by a straight line for $0.2 \leq \bar{N}_{Na} \leq 0.6$.

$$u_{Li}/u_{Na} = 0.156\bar{N}_{Na} + 0.162 \quad (6)$$

Substituting eq 6 in eq 5 and integrating the following expression is found for the diffusion potential

$$V_D = \frac{nRT}{F} \left[-0.5 \ln (0.162 + 0.994\bar{N}_{Na} - 0.156\bar{N}_{Na}^2) - 0.325 \ln \left(\frac{0.055 + 0.302\bar{N}_{Na}}{2.043 - 0.302\bar{N}_{Na}} \right) \right]_{\bar{N}_{Na}'}^{\bar{N}_{Na}''} \quad (7)$$

For the experimental study N_{Na} was taken as 0.935 (equivalent to $\bar{N}_{Na} = 0.6$) for the reference side of the cell. The initial composition of the melt for the "variable" side of the cell was chosen identical with that of the reference side and by additions of LiCl to this side, taking potential readings each time, the experimental curve in Figure 10 was obtained for the range $0.2 \leq \bar{N}_{Na} \leq 0.6$. Using eq 7 for the diffusion potential in conjunction with the boundary potential equations a theoretical analysis of the experiment was performed using the values for K_{NaLi} and n given in Table I. Assuming an average value for u_j/u_i , the Eisenman, *et al.*, equation (eq 4) could also be compared. The calculated values for the potentials have also been plotted in Figure 10.

Discussion

The results obtained in this investigation are in agreement with the equations of Conti and Eisenman mentioned above for describing electrolytic transport of cations across glass membranes. The electrolytic transport technique used first lent itself very satisfactorily to the determination of ion-exchange isotherms of glass (under the conditions of this study). K_{ij} and n values derived from these isotherms are in good agreement with the values obtained for these entities by the equilibrium sorption method on powdered samples of the same glass. This has been quite encouraging for placing considerable confidence in the determined values of K_{ij} and n . In fact, the greatest discrepancy found between the two methods is that shown in Figure 7. In the ion-exchange isotherms obtained for the Pyrex systems no deviations were observed due to the two-phase structure of Pyrex glass²⁰ for the ion-fraction ranges covered in this investigation. The second, and we feel the most significant, contribution of the electrolytic transport method to glass studies is that the mobility ratio of cations, under electrical potential gradients, can be determined at constant ionic composition throughout the glass membrane for various ionic compositions. The latter aspect is also important for various other purposes since membranes of various ionic compositions can be prepared from the same glass, structurally speaking.

The values obtained for K_{ij} , n , and average u_j/u_i given in Table I indicate considerable variations in magnitude from one type of glass to the next and also with different combinations of cation pairs. These values are functions of a number of factors, the most important being cationic sizes, site affinities, and glass structure.

(30) R. H. Doremus, *J. Phys. Chem.*, **68**, 2212 (1964).

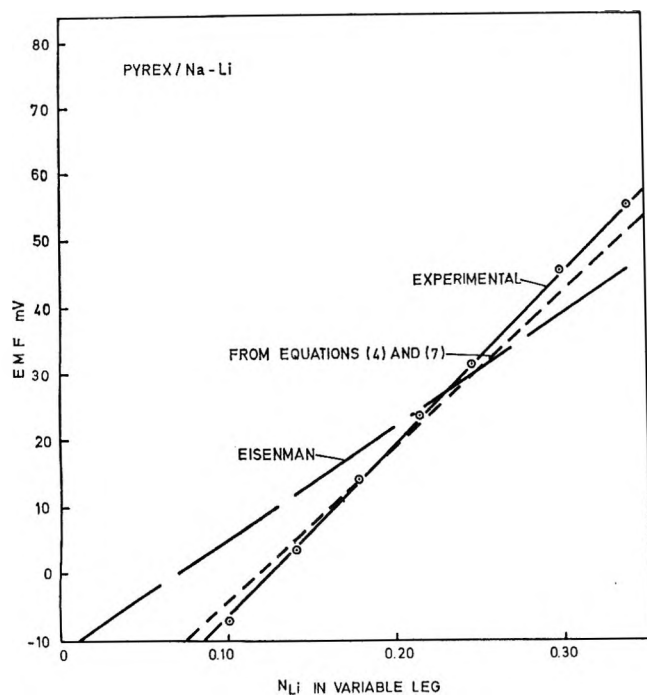


Figure 10. Comparison of experimental and theoretical emf results.

These aspects have been discussed to a limited extent in the literature¹²⁻²⁰ and will not be elaborated on in this report except to point out a feature not previously pertinently mentioned, namely, that although K_{ij} and u_j/u_i are independently or separately determinable, these two entities are related as can be seen clearly from the results in Table I for the Pyrex systems since high values for K_{ij} result in low u_j/u_i values. The shapes of the mobility ratio curves in Figures 4-6, however, also require further comment. The form of the curves in Figures 5 and 6 can be explained from the observations made on transference numbers of mixed glasses. For these glasses it was found that the conductance of the cation present in low abundance is relatively depressed. Explanations were offered for this behavior (see ref 6). The curve in Figure 4 is, however, just the opposite to what is expected and we have not as yet succeeded in explaining this result. We think that this anomalous behavior of Pyrex also cannot be attributed to the fact that Pyrex is a two-phase glass.

Although only a single experiment on membrane potentials which has been analyzed theoretically has been conducted so far, it may be said that indications

are that the ion-exchange theory of membrane potentials appears to give good agreement with experimental results for glass membranes in molten salts, and even more so, if corrections are introduced in the final equations of the diffusion potential for variations of mobility ratios with ionic compositions of the glass. This latter supposition is apparently in some contradiction to the results of recent studies^{28,31,32} on the characteristics of the controlling parameters of membrane potentials in molten salt systems. Based on deductions from measured membrane potentials as well as from electrolytic methods it was found in these investigations that the mobility ratio is apparently independent of the ionic composition of the membrane for experimental conditions quite different from those of this investigation. Investigations are presently being conducted to study the temperature dependence of K_{ij} and u_j/u_i over the temperature range of 300° to about 600° over the whole ionic composition range for the systems given above. Preliminary results already obtained indicate relatively significant deviations of both parameters at low temperatures (below about 450°) as compared with their higher temperature behavior which is possibly due to ion sieve effects becoming pronounced at the lower temperatures. Most of the previous investigations referred to above were in fact done at low temperatures and it is felt that a comparison of reported results and conclusive assessment of the real state of affairs can only be done once more extensive data are available. Another aspect to be established now is to ascertain whether the mobility ratio for a cation pair is identical under chemical and electrical potential gradients in glass. If this is not so, the basic Nernst-Planck flux equations used by Eisenman, *et al.*, will require modification to obtain final equations which should then account for experimental observations. A program is also presently underway to investigate the possibility of correlating diffusion data in the absence of electrical potential gradients with values of u_j/u_i determined by the described electrolytic method on membranes of the same glass. Progress along these lines will be reported in future.

Acknowledgment. The authors are indebted to the South African Atomic Energy Board for permission to publish this paper.

(31) K. H. Stern, *J. Phys. Chem.*, **74**, 1323 (1970).

(32) K. H. Stern, *ibid.*, **74**, 1309 (1970).

Ellipsometric Investigations of Anodic Film Growth on Iron in Neutral Solution. The Prepassive Film

by H. Wroblowa, V. Brusica, and J. O'M. Bockris*

The Electrochemistry Laboratory, The University of Pennsylvania, Philadelphia, Pennsylvania 19104
(Received December 31, 1970)

Publication costs assisted by the Office of Saline Water, Department of the Interior

Transient ellipsometry has been applied to examine the mechanism of the electrolytic growth of the prepassive film on iron (borate buffer, neutral solution) prior to its passivation. The metal was clamped at a series of potentials in the so-called active region and the film growth observed at constant potential. Correspondingly, a series of constant currents has been suddenly applied to the electrode and the film growth observed under these conditions. In a region in which no change of film constitution was indicated, the ellipsometric parameter Δ is proportional to the thickness of the film. Thickness at constant potential is linearly proportional to time of growth up to about 0.3 of a monolayer; thereafter it is proportional to $\log t$. Film growth commences less than 0.01 sec after switching on the current. Stirring does not affect the rate of growth. At constant time the growth rate is independent of the potential. Comparison of the form of the galvanostatic transients in the prepassive region with that in the passive range indicates that the prepassive film is ferrous; it is not an adsorbed ionic layer; it is $\text{Fe}(\text{OH})_2$. At the passivation peak, it is 1–2 monolayers in thickness. The suggested mechanism is: discrete centers grow two-dimensionally (rotation of screw dislocation) up to 30% coverage. Coverage ("thickness") increases proportionally with time at constant potential. At higher coverages, the growth involves a rapid place exchange step with a rate-determining Temkin discharge of OH^- onto sites in which the Fe is already attached to an OH, displaced into the first layer beneath the surface. These mechanisms are unique in yielding the observed growth laws. Quantitative consistency is fair.

I. Introduction

Examination of the mechanism of passive-layer formation has been radically changed by the introduction of the transient ellipsometry, applied in the region above the current peak. However, such information, even when supplemented by electrochemical and other means (*e.g.*, Mössbauer spectra) would lead to little appreciation of the film growing *before* the peak of the current. Is it a two-dimensional phase oxide, or does it consist of an increasing adsorption of O^{2-} or OH^- ions or other anions? By what growth laws does the coverage of the electrode increase? What mechanism is consistent with such laws? Answers to these questions are almost the answer to the question: What is the mechanism of passivation?

Earlier, the information was difficult to obtain for the submonolayer quantities involved. Sensitive (and transient) ellipsometry allows a reasonably sure analysis.

II. Experimental Section

Experimental technique has been discussed elsewhere,^{1–6} and also is described in the proceedings of two symposiums on ellipsometry.^{7,8}

Ellipsometer and Ellipsometry. The instrument (Rudolph-Sons Inst.) was modified: Δ , the phase retardation, and ψ , the amplitude diminution, could be determined (a) by manual rotation of polarizer and analyzer (steady state) and (b) by a continuous re-

coding of the intensity transients for ≥ 0.01 sec, as described elsewhere³ (transients). The experimental Δ and ψ values were compared with Δ and ψ calculated for the known λ (5461 Å), n_{sol} (1.338), angle of incidence (68.05), n_{Fe} and k_{Fe} and different values of the film thickness, L , n_{F} , and k_{F} ; these last three were *assumed* to vary within reasonable limits in a way similar to the manner described in ref 5.

Such a comparison leads to (a) evaluation of the minimal possible thickness at each potential, (b) regions of possible values for n_{F} , k_{F} , and L_{F} , and (c) if one of the unknown parameters, *e.g.*, thickness, was determined separately (*i.e.*, by coulometry, see below), values of n_{F} and k_{F} could be evaluated.

Electrochemical Cell and Electrodes. The three-elec-

- (1) V. Brusica, Thesis, University of Pennsylvania, 1971.
- (2) J. O'M. Bockris, M. A. Genshaw, V. Brusica, and H. Wroblowa, Symposium on Passivation, Cambridge, England, 1970.
- (3) V. Brusica, M. A. Genshaw, and B. D. Cahan, *J. Appl. Opt.*, **9**, 1634 (1970).
- (4) A. K. N. Reddy, M. A. Genshaw, and J. O'M. Bockris, *J. Chem. Phys.*, **48**, 671 (1968).
- (5) J. O'M. Bockris, A. K. N. Reddy, and B. Rao, *J. Electrochem. Soc.*, **113**, 1133 (1966).
- (6) W. Paik, M. A. Genshaw, and J. O'M. Bockris, *J. Phys. Chem.*, **74**, 4266 (1970).
- (7) E. Passaglia, R. Stromberg, and J. Kruger, *Nat. Bur. Std. (U. S.) Spec. Publ.*, No. 256 (1964).
- (8) "Proceedings of the Symposium on Recent Developments in Ellipsometry," N. M. Bashara, A. B. Buckman, and A. C. Hall, Ed., North-Holland Publishing Co., Amsterdam, 1969.

trode cell was air-tight, with Teflon and Kel-F body, quartz windows, and removable top and bottom.

A Pd bead saturated with hydrogen in the same solution, and Pt or Pd foil, separated by a frit, were used as the reference and counter electrode, respectively (all of the potentials are referred to nh scale). The working electrode, a polycrystalline iron rod, 99.998%, was embedded into the bottom of the cell, mechanically polished, washed, assembled into the rest of the cell, and positioned at the ellipsometric table.

Solution. Boric acid and borax were used to prepare solutions of pH 8.5 and 7.6, respectively; the solution was prepared in a closed system, under nitrogen atmosphere, preelectrolyzed for 17–20 hr prior to experiment, and introduced into the cell *via* air-tight connections.

Optical Reference State. This was obtained by potentiostatic reduction at -740 mV, where $\bar{\Delta}$ and $\bar{\psi}$ were determined.

Potentiostatic Oxidation and/or Reduction. This was carried out by a fast, single-step application of a preset desired potential; Δ (or ψ) and Q (mC/cm^2) were continuously recorded. After a "steady state" was reached, Δ , ψ , and the current were determined and the electrode was reduced.

Galvanostatic Oxidation and/or Reduction. By means of a mercury relay switch, the potentiostat was disconnected and a preset current applied. The oxidation current was varied from $8 \mu\text{A}$ to $4 \text{mA}/\text{cm}^2$. The reduction current was $30 \mu\text{A}/\text{cm}^2$. The Δ (or ψ) values and potential were continuously recorded.

The Number of Millicoulombs Spent in Oxidation and Reduction. Q was continuously recorded in potentiostatic work. It was calculated from the Δ -time or potential-time curves in the case of galvanostatic oxidation and reduction.

III. Results

Initial reduction of the iron electrode leads to $n_{\text{Fe}} = 3.24$ and $k_{\text{Fe}} = 3.98$, close to the values obtained on hydrogen reduced iron.^{9,10}

Potentiostatic Oxidation (Steady State). Δ and ψ measured as a function of the potential are given in Figure 1. The electrode was reduced (potentiostatically or galvanostatically) and only if $d(\Delta, \psi)_{\text{ox}} \approx d(\Delta, \psi)_{\text{red}}$ was it assumed that the change of optical parameters is a function of the formation and removal of a film. (Roughening is discussed elsewhere.¹¹) The millicoulombs obtained in the reduction are given in Figure 2.

It was found that Δ (and, also the quantity, Q) increases linearly with change of the potential in the active region and at constant current density. It begins to change from the value for the reference state at -580 mV. The ψ value does not start to change until the potential of the peak of the current has been reached (see Figure 1). Correspondingly, a plot of the param-

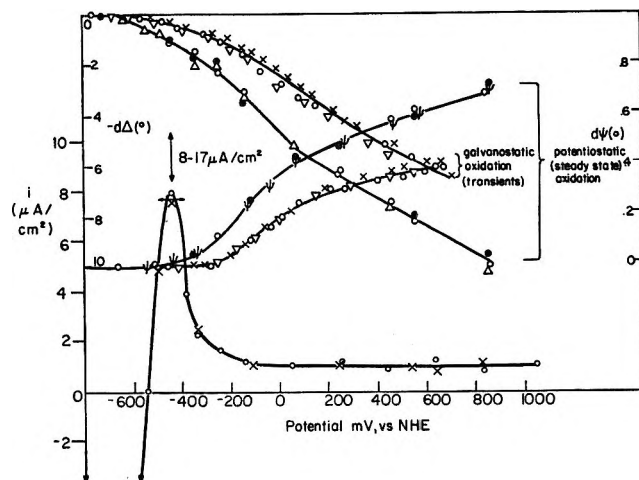


Figure 1. Variation of Δ and ψ with potential in steady-state (three experiments marked Δ , ψ ; \circ ; and \bullet) and transient (\times , 0.8; \circ , 0.32; and ∇ , 0.08 mA/cm^2) oxidation; i - V relationship is obtained in steady-state oxidation.

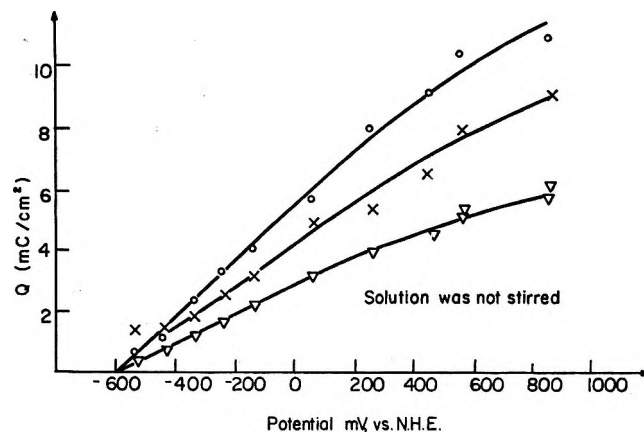


Figure 2. Q (mC/cm^2) as a function of oxidation potential, obtained during oxidation (\circ), reduction (\times , ∇), and corrected for H_2 (∇).¹

ter Δ , against the corresponding ψ for a series of potentials (Figure 3), shows three regions, with respect to slope. It is reasonable to assume that constancy of slope and the linear increase of Q mean constancy of n and k , *i.e.*, the presence, during the potential interval in which the slope is constant, of a single species. Then, in such a region, the change of Δ will be proportional only to the change of film thickness. On this basis, the continuously recorded plots of Δ values as a function of time are equivalent to thickness-time relations, and it is on this basis that the present approach to film growth is based. (See Figures 4–6.)

Figures 5 and 6 give the following important relations

(9) A. B. Winterbottom, "Optical Studies of Metal Surfaces," *Kgl. Nor. Vidensk. Selsk. Skr.*, 1 (1955).

(10) H. T. Yolken and J. Kruger, *J. Opt. Soc. Amer.*, 55, 842 (1965).

(11) V. Brusica, M. A. Genshaw, and J. O'M. Bockris, unpublished work.

$$L_t = At \quad (0.01 < t < 0.1 \text{ sec})$$

with $A = 8$

$$L_t = B + C \log t \quad (0.05 < t < 1200 \text{ sec})$$

for the potential of -540 and -490 mV with $C = 1.35 \text{ \AA}$, independent of potential.

Galvanostatic Oxidation Transients. Continuous recording of Δ (or ψ) and potential at constant current density for a variety of values of this parameter results in a typical curve as given in Figure 7 or 8. Several important features should be noted: (a) the influence of stirring is negligible (Figure 7); (b) the change of Δ starts immediately, *i.e.*, within 0.01 sec, after the current has been switched on; (c) when the Δ and ψ relations as a function of time at constant current density are replotted as Δ and ψ vs. potential (Figure 1), one obtains similar relations as those observed in potentiostatic steady state. There is, however, a noticeable tendency, particularly clearly indicated in the

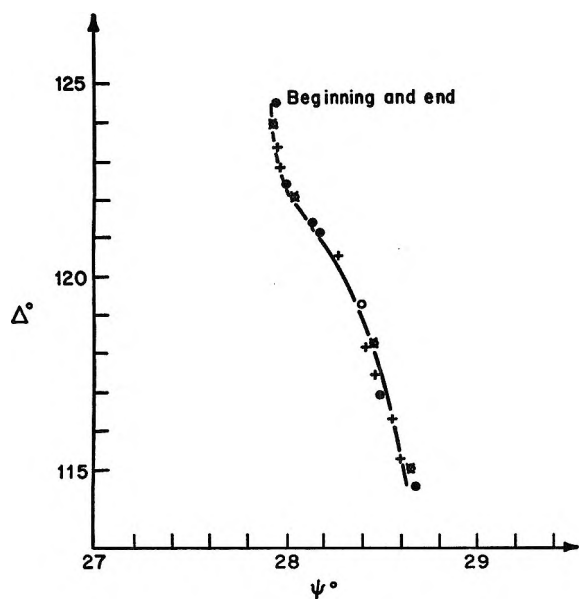


Figure 3. Δ - ψ relationship with increasing potential (three different experiments).

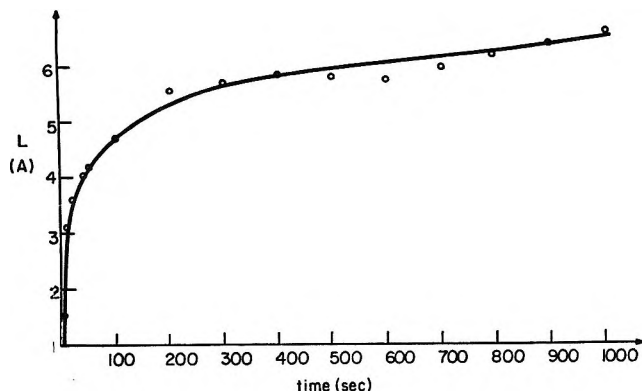


Figure 4. Increase of film thickness with time of potentiostatic oxidation at -490 mV, nhe.

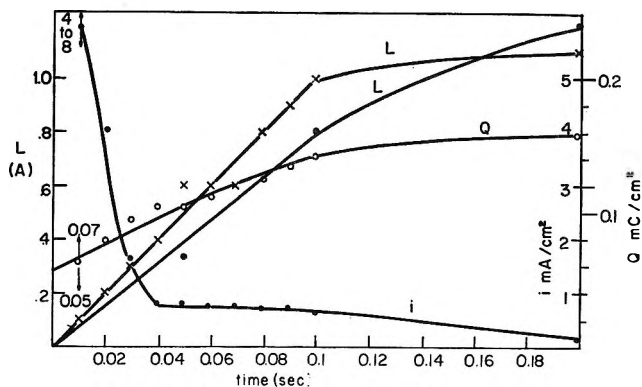


Figure 5. Variation of L (\times), i (mA/cm^2 , \bullet), and Q (mC/cm^2 , \circ) during the initial stages of film growth at -490 mV and variation of L (\bullet) at -540 mV, nhe in unstirred solution.

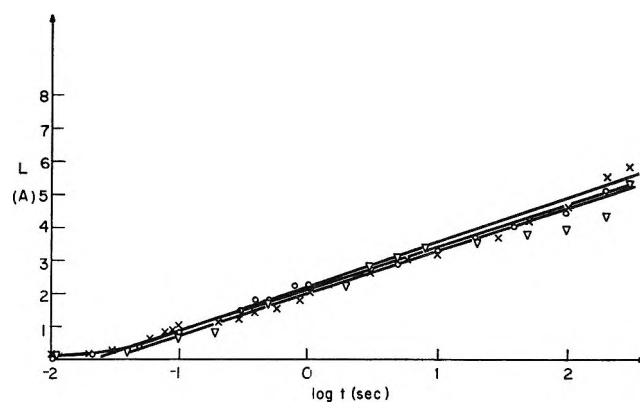


Figure 6. L - $\log t$ variation during potentiostatic oxidation at (\circ) -540 and (\times) -490 mV in unstirred solution and at -540 mV in stirred solution (∇).

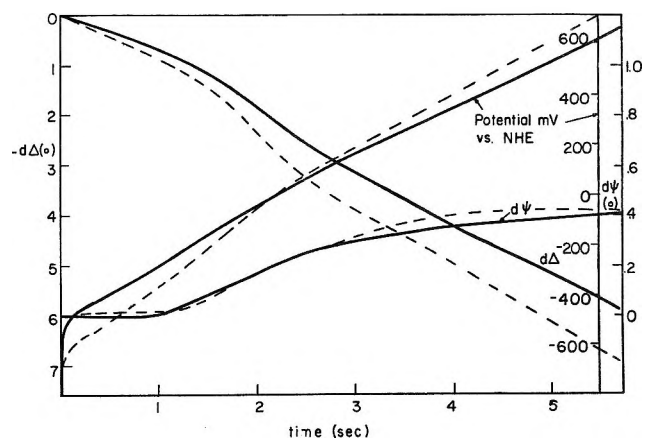


Figure 7. Variation of Δ , ψ , and potential with time of galvanostatic oxidation in unstirred (solid lines) and stirred (dashed lines) solutions; $i = 0.8 \text{ mA}/\text{cm}^2$.

third region, of shifting the Δ line towards higher Δ (without change in slope) as the i decreases, *i.e.*, the time of oxidation increases. The latter observation will be discussed separately.¹²

(12) H. Wroblowa, V. Brusica, and J. O'M. Bockris, unpublished work.

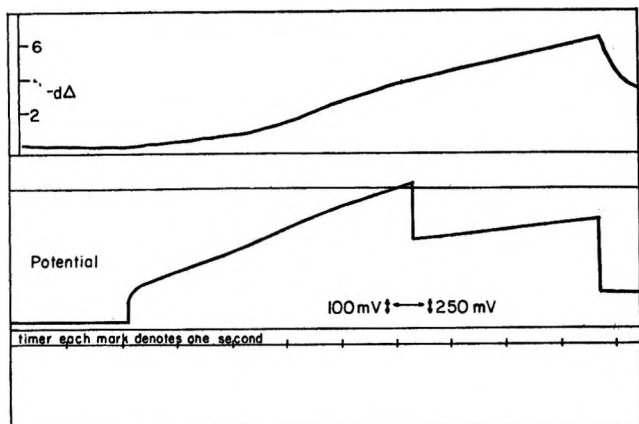


Figure 8. Example of intensity (Δ) and potential change during the anodic oxidation with 0.16 mA/cm^2 in the solution of pH 7.6.

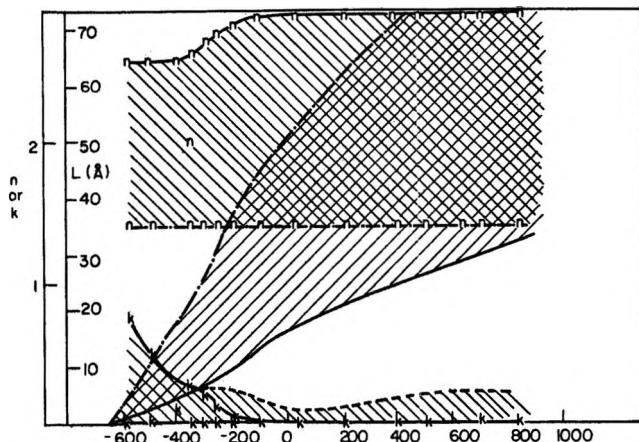


Figure 10. Variation of the possible film thickness, n , and k of the film with potential (steady state, no stirring). The thick line refers to the minimum possible thickness and corresponding n and k .

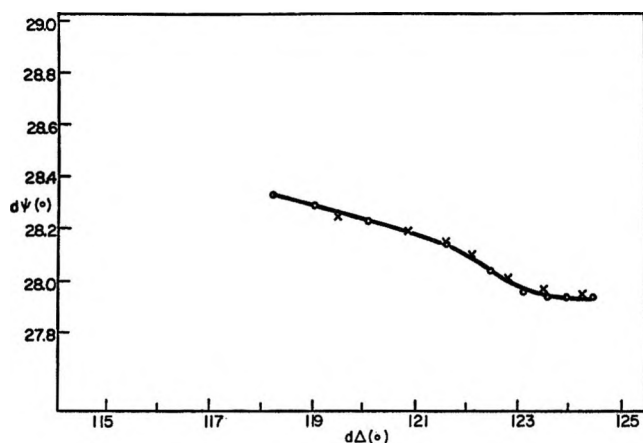


Figure 9. Variation of Δ with ψ during the galvanostatic oxidation (O) and subsequent potentiostatic reduction (X).

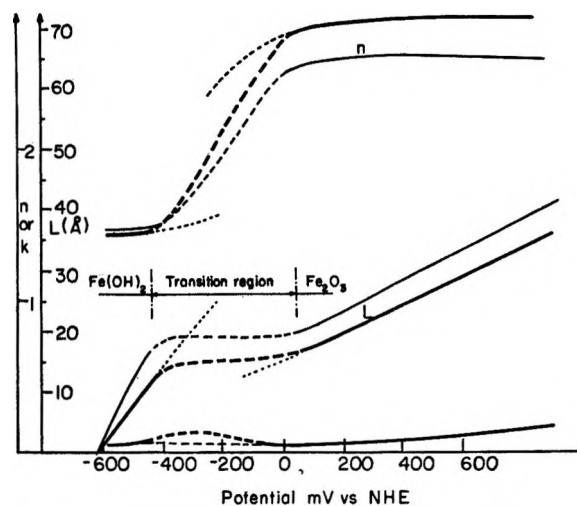


Figure 11. Variation of L , n , and k during the passivation of iron (steady state, no stirring): thick line, L (n and k) obtained with Q_{cath} , corrected for H_2^+ ; thin line, L (n and k) were obtained with Q_{cath} , average of $Q_{\text{cath total}}$, and Q_{cath} , corrected for H_2 .

Also, if the galvanostatic oxidation is followed by potentiostatic reduction, basically the same Δ - ψ curve is retraced (Figure 9).

IV. Discussion

1. *Film Composition.* Ellipsometrically, a minimum possible film thickness was determined, as well as the regions of possible values for L , n , and k of the film (Figure 10). Using the coulometric results (Figure 2) n , k , and L of the film were determined (Figure 11) as a function of potential. Figure 11 gives the probable composition of the film which was deduced as follows.

(a) The slope of the Δ - ψ (varying potential) and Δ -time curves (constant current) (Figures 1, 3, and 7) indicate that for film formation in the *passive* region, there are two characteristic regions of the ellipsometric plots [Δ - ψ at a series of potentials and current densities (Figures 1 and 3), and Δ - t at constant current (Figure 7)]. Hence in the passive region, film formation from the metal passes through more than one phase, e.g., through a ferrous on the way to a ferric state.

(b) In Δ - t and Q - t relations, obtained during reduction at constant current density of the passive film, there are always two regions.^{1,2} When one calculates the coulombs in these regions, it is found that the ratio of Q_1/Q_2 is close to 1:2. This is regarded as evidence which supports that the *passive* film is a ferric film, and its reduction passes through the stages: $\text{Fe}^{3+} \rightarrow \text{Fe}^{2+} \rightarrow \text{Fe}$.

(c) In the prepassive region (below the peak) the galvanostatic transients do not show the two regions, but only one. Calculation of the relation of Q_1 to Q_2 in the transition region around and above the peak shows Q_1/Q_2 is 1: x where $x > 2$ indicating that the film here is compared with both ferric and ferrous compounds.

(d) The film cannot be an *adsorbed layer*, for the Δ values obtained during its formation (in the region be-

low the peak) are substantially greater than those found by Genshaw and Chiu,¹³ or by Paik, *et al.*,⁸ in their study of adsorbed ionic layers. The passivating film is hence a ferrous phase oxide.

(e) A ferrous phase oxide suggests Fe(OH)₂ or FeO. If FeO is assumed, the expected film thickness from coulometry is below the minimal film thickness from ellipsometry. (Assuming that a reasonable range in values of n and k were utilized to interpret the ellipsometric data independently of coulometry.)

Hence, before the current peak in the passivation of Fe, a phase oxide, Fe(OH)₂, is formed.

2. *The Thickness of the Phase Oxide at the Current Peak.* (a) *From Ellipsometry.* Analysis of purely ellipsometric results indicates the region of possible values of L of 4 to 16 Å (Figure 10).

(b) *From Cathodic Coulometry.* About 0.7 mC/cm² after correction for the corresponding deposition of hydrogen.¹

The film thickness was calculated with the assumptions shown in Table I. The variation of film thickness

Table I: Evaluation of the Film Thickness at $E = E_p$

Roughness factor	Experimentally determined 0.7–1.2 mC/cm ²			
	Moles Fe ²⁺ /cm ² (calcd from experimental Q)	Layers of Fe(OH) ₂ formed ($\rho = 3.41$)	N° layers of HOFeOH formed (ionic radii)	N° layers of HOFeOH formed, if each Fe in metal reacts
1	3.63–6.2	2.1–3.6	1.6–2.8	1.3–2.25
1.2	3.25–5.1	1.7–2.9	1.2–1.9	1–1.6
1.4	2.6–4.5	1.5–2.5	0.9–1.5	0.7–1.2

with potential is linear if it is assumed that the Fe(OH)₂ has a bulk density. One finds, for RF (roughness factor) = 1 and using a lower limit for Q (Figure 6, 11)

$$dL/dV = 48 \text{ \AA}/V; \quad dL/d \log t = 1.35 \text{ \AA}$$

3. *The Growth Mechanism.* The Δ and potential-time relationships obtained during the galvanostatic transients do not indicate an induction time or an influence of stirring. Hence, direct formation by discharge, not dissolution-precipitation, is indicated.

The linear increase of the thickness in the region of 0–1 Å may be a result of (i) increasing electrode coverage by OH⁻, *i.e.*, increasing adsorption; or (ii) formation of discrete centers (nuclei).

Initial Stages. Increasing Coverage with OH⁻. Assuming that buildup of coverage proceeds according to



the current can be divided into the part spent in dissolution (i_1) and the part spent in film formation (i_2). The total current (i_a) will depend on the fraction, θ , covered *i.e.*

$$i_a = (i_1 + i_2)(1 - \theta) \quad (2)$$

Then

$$\frac{d\theta}{dt} = i_2(1 - \theta) \quad (3)$$

A thickness of 0.5 to 1 Å corresponds to an OH⁻ coverage of 17 to 35.8% ($L_{\text{monolayer}} = 2r_{(\text{O}^{2-} \approx \text{OH}^-)} = 2 \times 1.4 \text{ \AA}$). According to eq 3, the reaction rate ($d\theta/dt \approx dL/dt$) should decrease as coverage increases, which is contrary to observation (Figure 5).

Growth of Discrete Centers. Experimental results show a linearity between the thickness and time, *i.e.*, dL/dt (proportional to i_2) is constant, independent of time. Qualitative similarity between experiment and theory can thus be obtained only if the increase of thickness is due to one-dimensional growth of the centers formed by simultaneous nucleation as expected from

$$i_2 = zFkS_tN_0 \quad (4)$$

where N_0 is the number of the growth sites at $t = \infty$, k is the rate constant for the growth of the nuclei, and S_t is the area of growing nucleus.

(a) *One-Dimensional Growth, Outward from the Electrode.* The increase of the average thickness with time can be due to instantaneous formation of a small number of nuclei ($L_{t=0.01} \approx 0$) and their growth outward from the electrode. Such nuclei would have to grow to a relatively large height to account for the observed variation of thickness. Physically the model would have to break down because it cannot give a consistent answer to the questions: (i) What is the origin of the Fe²⁺ for the outer layers of the nuclei? (ii) Why does the mechanism of film formation change when a certain (average) thickness is reached?

(b) *One-Dimensional Growth on the Electrode Surface.* Suppose that a number of small crystallites one monolayer thick have been formed on the electrode surface, along steps or screw dislocations. Then, one-dimensional growth of the nucleus could be followed by the moving of the edge of the step along the surface and/or around the point where screw dislocation emerges. The observed increase of thickness would be proportional to the size of the original screw dislocation and the total number of these active sites.

After the Burgers vector has rotated once around the dislocation, the surface on which a further rotation could give rise to a second layer is in fact now an oxide and thus cannot give a supply of Fe²⁺ for further surface diffusion to the growth sites on the crystal edge. Hence, no further growth *by this mechanism* can occur.

The expected concentration of dislocations on a mechanically polished surface is 10¹¹ to 10¹² sites cm⁻².

(13) Y. Ch. Chiu and M. A. Genshaw, *J. Phys. Chem.*, **73**, 3571 (1969).

Let a small portion,¹⁴ say 1%, of these be active. At the end of the linear growth law the average thickness is 1 Å, and the radius of a screw dislocation is assumed to be 10^{-5} cm. Thus, the area per patch is $\pi(10^{-5})^2$ and the total volume $10^9 h \pi (10^{-5})^2 = 10^{-8}$ cm³, with $h = 3.3$ Å, a reasonable magnitude based on the unit cell of Fe(OH)₂.

The surface area covered with film will be $(Nr^2\pi)$, 30%. (If nucleation starts on, say 10^8 active sites and if the height of the nucleus is, say, 4.47 Å (*c* axis in Fe(OH)₂), *r* becomes 2.6×10^{-5} cm, and the electrode is 22% covered.) Thus, 22–30% is the maximal coverage of the model, which gives the average thickness of 1 Å, and a minimal height of a nucleus as 3.3–4.47 Å.

This mechanism gives a reaction rate independent of time, as it is based on one-dimensional growth of the nuclei, and also allows for the change in the film growth mechanism at longer times, after a further rotation could give rise to a second layer which would be in fact now an oxide.

Later State of Prepassive Film Growth, $0.05 (0.1) < t < 700 (1200)$ Sec. Starting at film thicknesses below monomolecular, *L*-*t* becomes a logarithmic (Figure 6), *i.e.*

$$L_t = B \ln t + c \quad (5)$$

Is the further increase of thickness due to two-dimensional or three-dimensional growth?

The steady-state *i*-*V* curve for iron dissolution was calculated and the current compared with the observed one: *i*₀ for iron dissolution was estimated from the work of Bockris, Drazic, and Despic¹⁵ to be 1.65×10^{-7} at a pH of 8.5 and taking $C_{\text{Fe}^{2+}}$ as 10^{-6} mol/l. It was assumed that α_{anodic} equals $3/2$, *i.e.*, that the same dissolution mechanism applies as observed in pH range 1–5¹⁵ and similar to that postulated for alkaline solutions by Kabanov, Burstein, and Frumkin.¹⁶ Thus, comparison of the current for iron dissolution and that experimentally observed indicated a decrease of the free surface area to a small percentage of the value from $\theta = 0.3$ during film growth, which is, therefore, two-dimensional. Similarly, the coulombs recorded in the first 100 sec is 0.7 mC/cm², equivalent to 5.1 Å of the initial film (or about a monolayer).

The mechanism for film formation must give the observed relationship between *L*, *t*, and potential, *i.e.*

$$L_V = F(V) + k \ln t \quad (6)$$

and

$$L_t = AV + f(t) \quad (7)$$

Thus, we are looking for the mechanism which will give the reaction rate $dL/dt_{i,v}$ constant, *i.e.*, the steady-state current of film formation will not depend on potential. [From $(dL/dt)_{t=700 \text{ sec}} = 0.001$ Å/sec (Figure 4) if steady state equals 10^{-8} A/cm²; showing that the

i-*V* curve as given in Figure 1 is preferentially determined by $i_{\text{dissolution}}$.]

Several mechanisms are consistent with an *L*-log *t* relation.

(a) *A Rate-Determining Chemisorption Step.* In Temkin kinetics this gives an expression for the reaction rate in agreement with experiment. However, the ellipsometry indicates a phase oxide.

(b) *Place Exchange Mechanism.* Lanyon and Trapnell¹⁷ suggested that the initial oxidation of a metal may be determined by interchange of adsorbed oxygen with underlying metal atoms. Bare metal atoms are exposed to the surface, made available for adsorption.

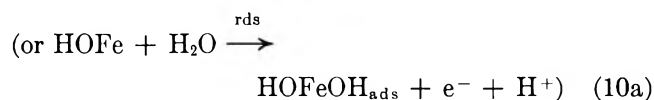
In the beginning, ($\theta \simeq 0$) interchange will take place readily; toward the end ($\theta \rightarrow 1$) interchange involves the parallel alignment of dipoles and will take place with difficulty, *i.e.*, the activation energy increases with the amount of material reacted. It is this feature which gives rise to a logarithmic growth law.

However, the growth of the film is lateral, hence may occur via a vacancy migration along the surface. If so, the increase of the energy of activation with increasing coverage, expected in the place exchange theory, cannot be understood.

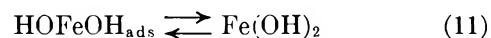
(c) *A Consistent Mechanism for the Prepassive Film Growth, at $t > 0.1$ Sec.* The following mechanism is suggested



with the fast place exchange



followed by



Assuming that the heat of adsorption of OH on iron decreases linearly with coverage, the rate equation for the rate-determining step (rds) under Temkin conditions is

$$\frac{d\theta_F}{dt} = k_3 C_{\text{OH}} - \theta_{\text{HOFe}} e^{-\beta f(\theta_T)} e^{\beta FV/RT} \quad (12)$$

(14) H. Kita, M. Enyo, and J. O'M. Bockris, *Can. J. Chem.*, **39**, 1670 (1961).

(15) J. O'M. Bockris, D. Drazic, and A. R. Despic, *Electrochim. Acta*, **4**, 325 (1961).

(16) B. N. Kabanov, R. Burstein, and A. Frumkin, *Discuss. Faraday Soc.*, **1**, 259 (1947).

(17) A. H. Lanyon and B. M. W. Trapnell, *Proc. Roy. Soc., Ser. A*, **227**, 387 (1955).

From (9)

$$\theta_{\text{HOFe}} \rightleftharpoons k_2 \theta_{\text{FeCH}} \quad (13)$$

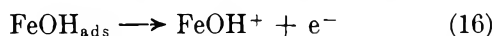
and from (8)

$$\theta_{\text{FeOH}} = k_1 c_{\text{OH}^-} (1 - \theta_{\text{T}}) e^{-f(\theta_{\text{T}})/RT} e^{\beta FV/RT} \quad (14)$$

It was assumed that the first electron transfer is not a rate-determining step. The latter is in agreement with kinetics of iron dissolution observed in acid¹⁵ and suggested for alkali,¹⁶ which may have similar first reaction steps as the initial film formation.^{16,18,19} Once the first step has occurred, and being exothermic, it liberates energy, utilized in affecting place exchange; the latter step may be easy as incorporation may be helped by existing defects at the surface. Fast place exchange would offer a new reaction site, *i.e.*, new iron ions available for further slow adsorption with a second electron transfer being assumed to be a rate-determining step. Combining (12-14) gives

$$\frac{d\theta_{\text{F}}}{dt} = k_1 k_2 k_3 c_{\text{OH}^-}^2 (1 - \theta_{\text{T}}) e^{-3\beta f(\theta_{\text{T}})/RT} e^{3\beta FV/RT} \quad (15)$$

If $0.2 < \theta_{\text{T}} < 0.8$, one can neglect the preexponential $(1 - \theta_{\text{T}})$ term. Also, $\theta_{\text{T}} = \theta_{\text{Fe(OH)}_2} + \theta_{\text{FeOH}}$. Since FeOH is consumed not only in the film formation, but also in a parallel reaction of iron dissolution



and Fe(OH)₂ is accumulating at the surface, it is assumed that $\theta_{\text{FeOH}} \ll \theta_{\text{F}}$ and $\theta_{\text{T}} \approx \theta_{\text{F}}$. Assuming also $\beta = 0.5$ and with c_{OH^-} being constant at constant pH, the reaction rate for film formation can be rewritten as

$$\frac{d\theta_{\text{T}}}{dt} = k_4 e^{3/2 FV/RT} e^{-3/2 f(\theta_{\text{T}})/RT} \quad (17)$$

Integrating, with $f(\theta_{\text{T}}) = r\theta$

$$\theta_{\text{T}} = \frac{2RT}{3r} (k_4 + 3/2 FV/RT + 2.3 \log t) \quad (18)$$

and one expects

$$\left(\frac{d\theta}{d \log t} \right)_v = \frac{(2.3)(2)RT}{3r} \quad (19)$$

and

$$\left(\frac{d\theta}{dV} \right)_t = \frac{F}{r} \quad (20)$$

in agreement with experiment. In order to compare these predictions of the model with experiment, the variations of $\theta_{\text{Fe(OH)}_2} \approx \theta_{\text{T}}$ are expressed as a function of film thickness, which are experimentally known.

If $\text{RF} = 1$, $\theta_{\text{Fe(OH)}_2} = 1$ when $L = 4.5 \text{ \AA}$. Hence

$$\left(\frac{d\theta}{d \log t} \right)_v = \frac{dL}{4.5 d \log t} \quad (21)$$

$$\left(\frac{dL}{d \log t} \right)_v = \frac{(4.5)(2.3)(2)RT}{3r} \quad (22)$$

$$\left(\frac{dL}{dV} \right)_t = \frac{4.5F}{r} \quad (23)$$

From (22) and the experimental value of $dL/(d \log t) = 1.4 \text{ \AA}$, r is 3.3 kcal, giving dL/dV of $32 \text{ \AA}/V$, reasonably in accord with the experimentally observed $48 \text{ \AA}/V$.

Relatively easy place exchange may be expected to occur only in the first one or two layers; with thicker films, place exchange would be expected to be rate determining.

Acknowledgments. The authors wish to express their thanks to Drs. Damjanovic and Drazic for the helpful discussions and to the Office of Saline Water (Grant No. 14-01-0001-1320) and the American Institute for Iron and Steel for the support of this work.

(18) U. Ebersbach, K. Schwabe, and K. Ritter, *Electrochim. Acta*, 12, 927 (1967).

(19) K. Schwabe, private communication.

The Effect of Magnetic Fields on the pH of Water

by T. I. Quickenden,*¹ D. M. Betts, B. Cole, and M. Noble

Department of Chemistry, University of Queensland, St. Lucia, 4067, Brisbane, Australia (Received February 16, 1971)

Publication costs borne completely by The Journal of Physical Chemistry

No changes in pH were observed after doubly distilled water was passed through magnetic fields in the range 0 to 24,000 G. The pH was recorded continuously using a glass electrode inserted in a flow system which led the water through the field at flow rates between 1.08 and 200 ml min⁻¹. The glass electrode was sufficiently distant from the magnet for it, and the water sample, to be in a region of zero field. No evidence was obtained to support the claims of Joshi and Kamat,² who reported apparently permanent pH changes of up to +0.62 unit in water which had been passed through a magnetic field. It was shown that changes of this magnitude would be energetically improbable.

According to Joshi and Kamat,² magnetic fields in the range 1900–5700 G (1 G = 10⁻⁴ Wb m⁻²) permanently change the pH of distilled water by up to +0.62 pH unit. Similar observations have been reported³ for naturally occurring waters. Measurements^{4–6} of magnetic effects on the physical properties of water have usually been part of an investigation of the reduction of boiler scale which results when the water supplied to a boiler is passed through a magnetic field. A variety of explanations have been proposed for this phenomenon and one such explanation² involves a magnetically induced change in the pH of water. This present publication records an unsuccessful attempt to reproduce the pH changes reported by Joshi and Kamat.²

Experimental Section

The pH of the water was measured on a Townson and Mercer recording pH meter equipped with a Titron glass electrode (Type A) and an automatic temperature compensator. The magnetic field was provided by a 4700-G Rola permanent magnet Type PM45 with a pole gap of 1.9 cm and a pole diameter of 6.4 cm.

Doubly distilled water, which had been stored in a 5-l. Pyrex glass flask, was passed through the magnetic field *via* an all-glass Pyrex siphon of internal diameter 0.4 cm. Following Joshi and Kamat,² the water was equilibrated with atmospheric carbon dioxide. The glass electrode, a thermometer, and the temperature compensating probe were all incorporated in a 17-ml glass bulb which was an integral part of the glass siphon. The magnetic field was applied to the water in the siphon at a point 30 cm before the glass bulb. Movement of the magnet to or from this position caused only a transient deflection on the pH meter of less than 0.005 pH unit, irrespective of whether the water was present or not.

Room temperature varied slowly during the experiments from 299.6 to 302.9°K. The measured pH

showed a temperature dependence of 0.02 pH unit °K⁻¹. This figure includes the effect of temperature on the pK_w of water and the effect of any inadequacy in the automatic temperature compensator. During any one run with the permanent magnet the temperature changed by less than 0.3°K.

The surface of the glassware is a potential source or recipient of protons and hydroxyl ions. To minimize pH changes due to surface desorption, all the glassware was soaked for 15 hr in an alkaline cleaning mixture containing detergent and sodium hexametaphosphate. After rinsing in once distilled water, the glassware was soaked for several days in two successive batches of doubly distilled water. After this treatment, the same glassware was used without further cleaning throughout the whole series of measurements which were carried out over a period of several months. This cleaning procedure would be expected to maintain contamination from the glass at a low or steadily decreasing level. No systematic trend in the pH was observed over the period of measurement.

The pH meter and chart recorder were earthed at a common point in order to minimize electrical interference. The normal operations and movements in the vicinity of the pH meter had no detectable effect on the recorded pH.

In order to carry out a measurement, water was passed through the glass siphon at a constant, measured rate, which was controlled by restricting the air flow to the reservoir with capillary tubes of various sizes.

(1) To whom all correspondence should be sent at the Department of Physical and Inorganic Chemistry, University of Western Australia, Nedlands, 6009, Western Australia.

(2) K. M. Joshi and P. V. Kamat, *J. Indian Chem. Soc.*, **43**, 620 (1966).

(3) T. Kohout, *Vod. Hospod.*, **12**, 458 (1962).

(4) D. M. Umanskii, *Sov. Phys.-Tech. Phys.*, **10**, 1720 (1966).

(5) S. A. Bruns, V. I. Klassen, and A. K. Kon'shina, *Kolloid. Zh.*, **28**, 153 (1966).

(6) R. Delhez, *Cent. Belge Etude Corros., Rapp. Tech.*, **No. 747** (1961).

The pH of the flowing water was recorded for approximately 10 min. The magnet was then placed in position and the pH recorded for twice the time it took for the water to pass from the magnet to the glass electrode. The magnet was then removed and the pH recorded again for at least 10 min. Although the recorded pH was displaced slightly to a new value whenever the flow rate was changed, it nevertheless fluctuated by less than ± 0.04 pH unit during any series of measurements at constant flow rate. Magnetically induced changes as small as 0.04 pH unit would have been detectable by this method.

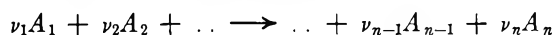
Results and Discussion

Flow rates of 1.08, 8.2, 8.7, 9.8, 11.6, and 12.7 ml min^{-1} were examined as described above, but in no case was any systematic change in pH observed. The flow rates examined were in the range investigated by Joshi and Kamat² and the flux density used was close to the figure of 4800 G used by these workers in one of their measurements.

In order to test the possibility that pH changes are produced only by fields of certain critical intensity, the permanent magnet was replaced by an electromagnet which was varied continuously from 0 to 24,000 G over a period of 20 min. pH changes as small as 0.1 pH unit could be measured by this method. No such changes were observed at flow rates between 3.2 and 200 ml min^{-1} .

The results presented here provide no evidence for the pH changes reported by Joshi and Kamat. These workers attributed the pH changes to magnetically induced changes in the ionization constant of water. This explanation is not tenable thermodynamically.

It can be shown⁷ that when a magnetic field is applied to an equilibrium reaction



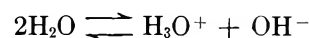
between nonferromagnetic substances, that the equilibrium constant changes from K to K_H where

$$K_H = K \exp \frac{\sum_i \nu_i \chi_i H^2}{2RT} \quad (1)$$

In this equation, which is expressed in unrationalized cgs-emu units, H is the magnetic intensity, χ_i is the molar magnetic susceptibility of species i , and T is the absolute temperature.

At room temperature (300°K) and at the maximum field of 5700 G ($H \approx 5700$ Oe) used by Joshi and Kamat, eq 1 predicts that K_H differs from K by only 2 parts in 10^7 , even in the optimal case where a paramagnetic substance with $\chi_i = 2 \times 10^{-4}$ $\text{cm}^3 \text{mol}^{-1}$ is in equilibrium with a diamagnetic substance for which $\chi_i = -1 \times 10^{-6}$ $\text{cm}^3 \text{mol}^{-1}$.

The derivation of eq 1 assumes that the change of volume on magnetization is negligible and that the magnetic susceptibility of the material is independent of the magnetic intensity. The former approximation is generally true and the second holds except for ferromagnetic materials and a few other unusual cases.⁸ In the present situation both assumptions should hold for the three species involved in the equilibrium



In view of the above calculations and in view of the measurements presented here, it is doubtful whether the observations of Joshi and Kamat² represent a property of water. It may further be concluded that magnetically induced changes in the pH of water are not a feasible explanation for any inhibition of boiler scale which results⁶ when the water supplied to a boiler is passed through a magnetic field.

(7) R. Delhez, *Bull. Soc. Roy. Sci. Liege*, **26**, 161 (1957).

(8) E. A. Guggenheim, "Thermodynamics," 3rd ed, North Holland Publishing Co., Amsterdam, 1957, p 430.

Solubility of Helium and Argon in Liquid Sodium

by Ewald Veleckis,* Sanat K. Dhar, Fred A. Cafasso, and Harold M. Feder

Argonne National Laboratory, Argonne, Illinois 60439 (Received March 25, 1971)

Publication costs assisted by the Argonne National Laboratory

The solubilities of helium and argon in liquid sodium were determined as functions of pressure and temperature. The data obeyed Henry's law to at least 9 atm. In the temperature range 330–550°, the solubilities may be represented by the following linear equations: helium, $\log \lambda = 0.516 - 3078T^{-1}$; argon, $\log \lambda = 1.08 - 4462T^{-1}$; where λ is the Ostwald coefficient. The 95% confidence limits of the mean value of λ predicted by these equations are $\pm 4\%$ for helium and $\pm 16\%$ for argon. For the standard state defined as 1 mol of ideal gas confined to a volume equal to the molar volume of sodium, the heats of solution are 14.1 ± 0.6 kcal/mol for helium and 20.4 ± 2.1 kcal/mol for argon. The results are compared with experimental data of others and with calculations based on existing theoretical models.

Introduction

The thermodynamics of alloy formation is sufficiently complex that especially simple binary systems are desirable objects of theoretical and experimental study. The noble gases presumably dissolve in liquid metals as neutral atoms; if so, the polarization of the dissolved atoms by the fluctuating fields of the solvent should be the only source of attractive interactions. The electronic structures of the alkali metals are better understood than those of other metals; hence the use of the alkali metals as solvents for the noble gases should simplify the evaluation of these polarization forces. The alkali metal-noble gas solutions, therefore, constitute a class of especially simple binary alloys worthy of study. Measurement of the solubilities of noble gases in liquid alkali metals affords a convenient method of evaluating the thermodynamics of alloy formation.

Measurements of the solubility of noble gases in liquid metals, or theoretical discussions thereof, are sparse. Epstein¹ calculated the solubility of helium in sodium using Hildebrand's solubility parameters. McMillan² predicted the solubility of xenon in liquid bismuth, which was subsequently measured by Eshaya and Kenney,³ Mitra,⁴ and Hewitt, Lacey and Lyall.⁵ Johnson and Shuttleworth⁶ and Johnson⁷ measured the solubility of krypton in liquid Pb, Sn, Ag, Cd, and In and attempted to rationalize their results. The only data reported on the solubility of noble gases in liquid alkali metals are those by Mitra,⁴ who measured the solubility of xenon in sodium; by Slotnick, Kapelner, and Cleary,⁸ who measured the solubility of helium in liquid lithium and potassium; and by Thormeier,⁹ who measured the solubility of helium and argon in liquid sodium concurrently with the present study. Except for an inconclusive test in the Li-He system,⁸ the validity of Henry's law had not been examined for noble gas-metal systems prior to this work. Departures from Henry's law at moderate pressures were not expected; however, to support the presumption of a

solution as single, neutral atoms, a conclusive test of Henry's law was deemed necessary.

In the present work attention was focussed on the temperature and pressure variations of the solubility of helium and argon in liquid sodium. These systems were of interest for the reasons already given; in addition, helium and argon are generally used as cover gases in liquid sodium-cooled nuclear reactors, and information on their solubilities in sodium is needed by reactor designers.

Experimental Section

The equilibration and separation technique used was adapted from Grimes, Smith, and Watson¹⁰ who had applied it to the determination of the solubility of noble gases in fused salts. In the present work liquid sodium was saturated with the gas whose solubility was to be measured at a preselected temperature and pressure. The saturated sodium was transferred to another container, where the solution was stripped of the dissolved species by sparging. The desired component of the resulting gas mixture was concentrated by selective adsorption and quantitatively assayed. This procedure incorporates special features which assure adequate

(1) L. F. Epstein, KAPL-Memo-LFE-10, Knolls Atomic Power Laboratory, Schenectady, N. Y., Jan 9, 1952.

(2) W. G. McMillan, LMFR-12, Brookhaven National Laboratory, Upton, N. Y., June 1955.

(3) A. M. Eshaya and W. F. Kenney, BNL-617 (T-186), Brookhaven National Laboratory, Upton, N. Y., Jan 1959.

(4) C. Mitra, Eng.Sc.D. Dissertation, Columbia University, 1959.

(5) G. F. Hewitt, J. A. Lacey, and E. Lyall, *J. Nucl. Energy*, **1**, 167 (1960).

(6) G. W. Johnson and R. Shuttleworth, *Phil. Mag.*, **4**, 957 (1959).

(7) G. W. Johnson, *ibid.*, **6**, 943 (1961).

(8) H. Slotnick, S. M. Kapelner, and R. E. Cleary, PWAC-380, Pratt and Whitney Aircraft Division of United Aircraft Corp., Middletown, Conn., Feb 24, 1965.

(9) (a) K. Thormeier, *Atomkernenergie*, **14**, 449 (1969); (b) K. Thormeier, *Nucl. Eng. Des.*, **14**, 69 (1970).

(10) W. R. Grimes, N. V. Smith, and G. M. Watson, *J. Phys. Chem.*, **62**, 862 (1958).

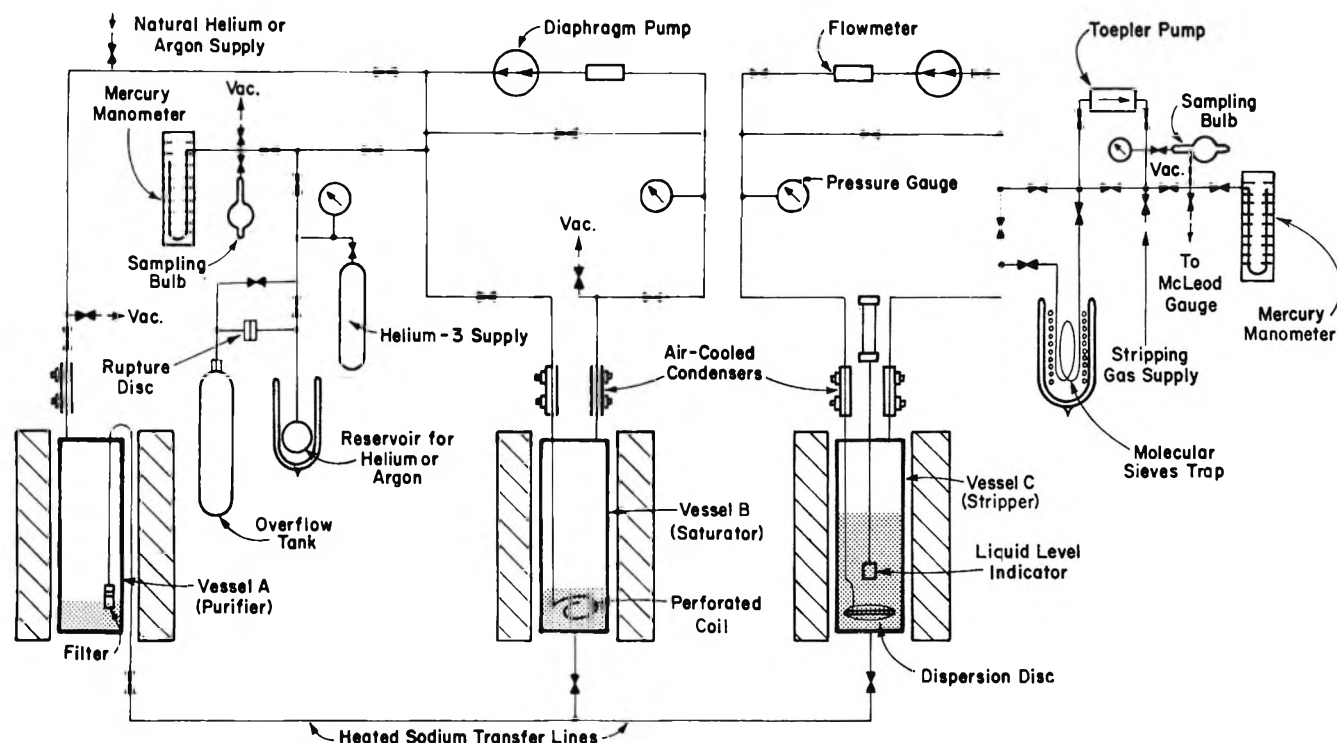


Figure 1. Schematic diagram of gas solubility apparatus.

equilibration, complete separation, and quantitative analysis, even though the expected gas solubilities are very small. These features include (1) means for removing suspended solid particles (which may capture small bubbles) from the liquid to be saturated, (2) prolonged bubbling of the saturating gas through the liquid, (3) a prolonged quiescent period to promote the coalescence and escape of gas bubbles, (4) very slow transfer of a portion of the saturated liquid *via* a bottom outlet to avoid the inclusion of liquid from the vicinity of certain surfaces,¹¹ (5) a prolonged sparging period to promote the stripping of the dissolved species, and (6) a procedure for distinguishing the stripped gas from extraneous sources of the same material. A similar approach was used by Slotnick, *et al.*, for the measurement of the solubility of helium in liquid lithium and potassium. A description of their apparatus is not readily available, so details of the apparatus used in the present work are given below.

Apparatus. Figure 1 is a schematic diagram of the apparatus. Three cylindrical vessels (4.5 in. diam, 16 in. high) fabricated from stainless steel (SS 316) were interconnected by heated $\frac{1}{4}$ -in. sodium transfer lines equipped with needle valves. In vessel A ("purifier") filtration was carried out periodically as a precaution against the accumulation of solid sodium oxide particles from air leakage. Saturating gas was bubbled through the liquid contained in vessel B ("saturator") *via* a coiled tube with sixty $\frac{3}{16}$ -in. perforations directed toward the bottom of the vessel. In vessel C ("stripper") the stripping gas was introduced through a Micro

Metallic Corp. 10-cm stainless steel dispersion disk with a $5\text{-}\mu$ mean pore size. The volume of sodium in this vessel was calculated from its geometry and the sodium level. The level was measured to the nearest 0.5 cm with a Mine Safety Appliances Corp. liquid-level probe.

The three vessels were heated with 20 in. high Marshall Products Co. split-type electric furnaces. Temperature was measured in each vessel with a Chromel-Alumel thermocouple in a thermowell.

Separate gas circulation loops made of $\frac{1}{4}$ -in. stainless steel (SS 304) tubing were connected to the saturator and to the stripper. Each loop contained a diaphragm pump (Lapp Pulsafeeder, Model CP-1) designed for pressures up to 15 atm, a flow meter (Hastings Mass Flowmeter, Model LF), and a Bourdon pressure gauge. Air-cooled condensers located just above each vessel prevented sodium vapor from entering the gas circulation systems. The condensers were periodically heated to free them of sodium. In these loops all valves exposed to sodium were equipped with Stellite seats, while those in less critical positions had Teflon seats.

Materials. ^3He (99.5%) was purchased from the Mound Laboratory, Miamisburg, Ohio and ultrahigh purity (99.999%) natural helium from the Matheson Company; an isotopic mixture of these ($\sim 30\%$ ^3He) was prepared by condensing appropriate amounts of

(11) The sodium-gas interfaces may be enriched in the saturating gas by adsorption. *Cf.*, ref 3, 6, and 7.

each on activated charcoal (Barnebey-Cheney Type 513) cooled to 4°K. Ultrahigh purity (99.999%) argon was purchased from the Matheson Co.; it contained no detectable helium. Reactor grade sodium was purified *in situ* by periodic transfers of sodium (heated to 500°) to the purifier, where it was cooled to 150° and passed through a porous metal filter to remove insolubles. At 150° the solubility of oxygen (the main impurity) is ~ 2 ppm.¹²

Procedure for Helium. Approximately 2.5 l. of liquid sodium in the saturator was heated to and maintained at the desired temperature, and the isotopic helium mixture was pumped through it at a rate of 1 l./min for 2 hr. Pumping was then stopped and the sodium was left undisturbed overnight. Throughout this period the saturator temperature was maintained constant and the pressure (predetermined by the quantity of gas in the saturator loop) was measured. The needle valves in the sodium transfer line between the saturator and stripper were then slightly opened until ~ 2 l. of sodium was transferred into the closed, evacuated stripper. During this period of ~ 5 min the helium pressure in the saturator was maintained at its initial value by the admission of additional isotopic helium mixture. The sodium in the stripper was cooled \sim to 130° and stripped of the dissolved helium by continuously pumping 1 l. of argon at atmospheric pressure through the dispersion disk at 750 cm³/min for 2 hr. When the stripping was complete the volume of sodium which had been transferred was measured.

The gas mixture in the stripper loop generally contained from 0.01 to 0.15% helium. To enhance the accuracy of analysis it was desirable to concentrate the helium. This was done by Toepler-pumping the mixture through liquid nitrogen-cooled Molecular Sieves (Linde Company Type 5A) into a sampling bulb of known volume. In this process the argon was nearly quantitatively and selectively retained on the sieves, and the final helium concentration was at least 95%. Tests of the recovery procedure with known quantities of helium indicated that recovery of 0.4 cm³-atm or more was nearly quantitative. With smaller quantities, recoveries decreased, *e.g.*, with 0.04 cm³-atm the recovery was 65%. A calibration curve of per cent recovery *vs.* quantity of helium was obtained and applied to the analytical data.

The concentration of the helium isotopes was determined by mass spectrometry. The function of the added ³He was to distinguish between the helium obtained on exsolution from sodium and any tramp (⁴He) helium. Any decrease in the ³He relative concentration would have been attributed to dilution by natural helium, and an appropriate correction would have been made; no such correction was ever necessary.

Procedure for Argon. Natural argon was the solute gas and helium was used for sparging. The resulting helium-argon mixture contained from 5×10^{-4} to $2 \times$

10^{-2} % argon. The argon concentration was increased by pumping the mixture through a controlled leak into a liquid nitrogen-cooled Molecular Sieves 5A trap. The trap was heated to 300° and a measured portion of the desorbed gas was assayed for argon. The assayed samples contained from 4×10^{-2} to 3% argon, ~ 0.1 % nitrogen, the balance being helium. Tests of this procedure with argon-helium mixtures of known compositions showed that within experimental uncertainties a quantitative recovery of argon was achieved.

The gas analyses were made with a gas chromatograph designed for an adequate separation of argon and nitrogen. The column was made of 8 ft long, $\frac{1}{4}$ in. diam stainless steel tubing packed with Molecular Sieves 5A, operated at 0°; its output was measured with a thermal-conductivity detector. The nitrogen was assumed to have originated from air inleakage, and a correction was made for the corresponding amount of argon in air. This correction never exceeded 1%.

Results

The procedures described above were followed in most experiments. To establish that these procedures led to valid results, variations were made in the preliminary experiments; *e.g.*, the time of bubbling was varied from 0.5 to 3 hr, the rate of bubbling was varied from 0.5 to 1 l./min, the quiescent period was extended from overnight to several days, and multiple stripping was attempted. From the results of these preliminary runs we concluded that with respect to the time element the procedures used led to the required degree of saturation and stripping.

The experimental isothermal pressure dependence of solubility was determined from 14 measurements at $\sim 500^\circ$ for helium and from 8 measurements at $\sim 480^\circ$ for argon. The results are shown in Figures 2 and 3 where the solubilities of helium (corrected to exactly 500°) and of argon (corrected to exactly 480°) are plotted against the gas pressure. The corrections were based on the isobaric temperature coefficients of solubility determined in this work. The experimental points were fitted by the method of least squares to unconstrained linear equations. On the basis of statistical F tests, the displacements of the lines from the origins and their deviations from linearity were found to be insignificant. This can be seen in Figures 2 and 3 by the position of the 95% confidence limits. The solubility data, therefore, obey Henry's law to at least 9 atm pressure.

The solubilities of helium and argon were measured at approximately 50° intervals between 330 and 550° with at least quadruplicate determinations at each temperature.¹³ The temperatures are believed to be accurate to within 1°.

(12) V. J. Rutkauskas, LA-3879, Los Alamos Scientific Laboratory, Los Alamos, N. M., July 15, 1968.

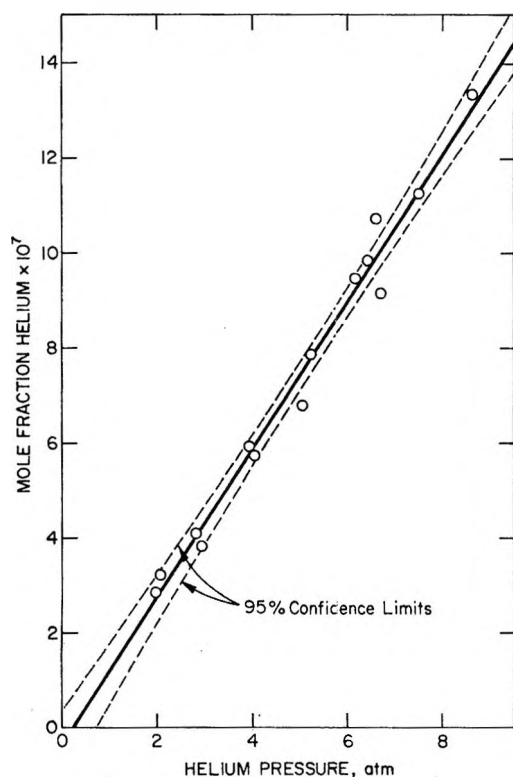


Figure 2. Pressure dependence of the solubility of helium in sodium at 500°.

Gas solubilities are conventionally expressed in terms of two different units:¹⁴ (1) Henry's law constant, K_H , atom fraction of solute in solution per atmosphere of gas pressure; and (2) Ostwald coefficient, $\lambda = C_{sol}/C_g$, the ratio of the concentration of the solute in the solution to the concentration of the solute in the gaseous phase in equilibrium with it. Thus, the Ostwald coefficient may be regarded as the partition coefficient of a solute between a gaseous and a liquid phase. When the gaseous phase is pure and ideal, the units K_H and λ are related to each other by the equation $\lambda = R'TdK_H/M$, where $R' = 82.06 \text{ cm}^3\text{-atm/deg-mol}$ is the gas constant, T is the Kelvin temperature, d is the density of the solvent, and M is its molecular weight. (For liquid sodium¹⁵ $d(\text{g/cm}^3) = 0.950 - (2.30 \times 10^{-4})t - (1.46 \times 10^{-8})t^2 + (5.64 \times 10^{-12})t^3$, where t is the temperature in degrees centigrade, and $M = 22.99 \text{ g/mol}$.) Heats of solution may be calculated from the temperature coefficients of solubility by the relations

$$\bar{H}_2(\text{soln}, T, P) - H_2^0(g, T, P = 1 \text{ atm}) = -R[\partial \ln K_H / \partial (1/T)] \quad (1)$$

and

$$\bar{H}_2(\text{soln}, T, P) - H_2^0(g, T, P = R'T d/M) = -R[\partial \ln \lambda / \partial (1/T)] \quad (2)$$

The heats of solution defined in eq 1 and 2 differ from one another with respect to the choice of the standard

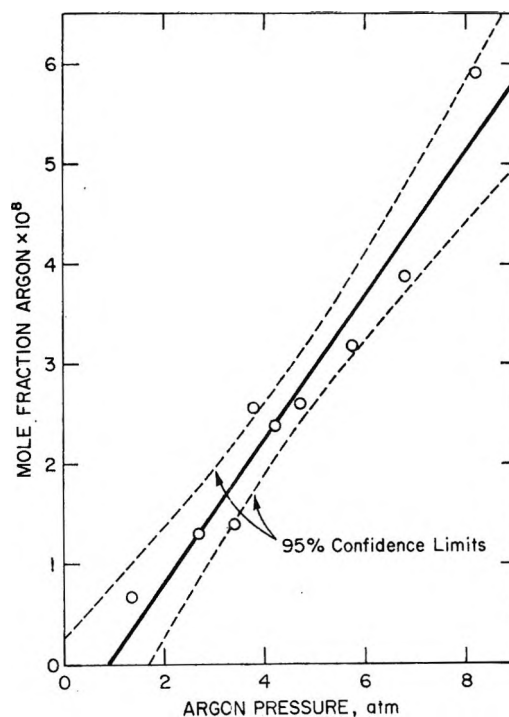


Figure 3. Pressure dependence of the solubility of argon in sodium at 480°.

state of the solute. The standard state used in eq 1 is 1 mol of ideal gas at temperature T and a pressure of one atmosphere; that used in eq 2 is 1 mol of ideal gas at temperature T in a volume equal to the molar volume of solvent.

Helium. The results of 30 determinations for the solubility of helium in sodium are shown in Figure 4. Over the range 350–550° the data were well fitted to linear equations¹⁶ by the method of least squares

$$\log K_H = -3.161 - 2833T^{-1} \quad (3a)$$

or

$$\log \lambda = 0.516 - 3078T^{-1} \quad (3b)$$

A statistical analysis showed that a mean result of a prolonged series of measurements would be predicted by eq 3 with an uncertainty (95% confidence level) of less than 4%. For the standard state defined as 1 mol of ideal gas at 1 atm, the heat of solution is $13.0 \pm 0.4 \text{ kcal/mol}$; for the standard state defined as 1 mol of ideal gas in a volume equal to the molar

(13) Complete tabulation appears in Report ANL-7802 available from National Technical Information Service, U. S. Department of Commerce, Springfield, Va. 22151.

(14) A general review of these units is presented by R. Battino and H. L. Clever, *Chem. Rev.*, **66**, 395 (1966).

(15) J. P. Stone, *et al.*, NRL-6241, Naval Research Laboratory, Washington, D. C., Sept 24, 1965; G. H. Golden and J. V. Tokar, ANL-7323, Argonne National Laboratory, Argonne, Ill., August 1967.

(16) For technical purposes the solubility of natural helium expressed in weight units is given by $\log (\text{ppb/atm He}) = 5.090 - 5.099T^{-1}$, where T is in degrees Rankine.

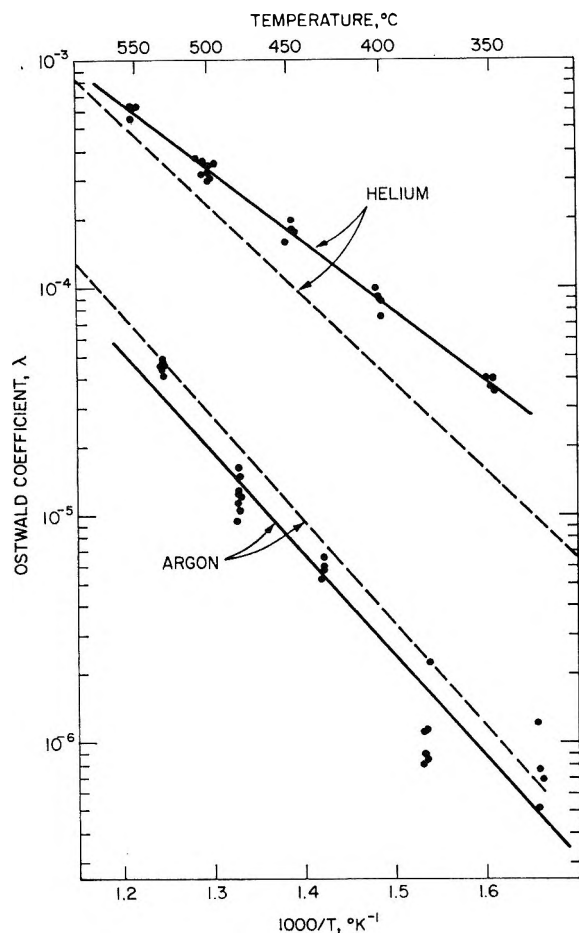


Figure 4. Temperature dependence of the solubility of helium and argon in sodium: —●—, this work; ---, Thormeier.

volume of sodium, the heat of solution is 14.1 ± 0.6 kcal/mol.

The helium solubility line reported by Thormeier^{9,17} is also shown in Figure 4. At higher temperatures the two studies agree within experimental error. At lower temperatures, however, the results diverge. The disagreement is reflected in the heats of solution—16.4 kcal/mol, reported by Thormeier, is well outside the error limits assigned to the presently reported heat, 13.0 ± 0.4 kcal/mol. The main differences between our procedure and Thormeier's appear to be in the manner of equilibrating the saturating gas with the liquid and the manner of stripping and analyzing the dissolved gas. Thormeier pumped liquid sodium into a tank containing the saturating gas, instead of bubbling the saturating gas through the sodium. For stripping, Thormeier used evacuation rather than sparging, and the quantity of recovered gas was determined in a volumeter without compositional analysis. In the light of these differences and in the absence of an error or reproducibility analysis by Thormeier, it is difficult to comment further on the source of discrepancy.

Argon. The results for argon are shown in Figure 4. Over the range 330–530° the solubility data (30 points)

were well fitted to linear equations¹⁸ by the method of least squares

$$\log K_H = -2.59 - 4221T^{-1} \quad (4a)$$

or

$$\log \lambda = 1.08 - 4462T^{-1} \quad (4b)$$

The 95% confidence limits of the predicted mean values of K_H or λ calculated from eq 4 are $\pm 16\%$. Owing to the difficulty of assaying gas mixtures containing less than 5 mol % argon, the reproducibility of the argon results was noticeably inferior to that of the helium results.

The heat of solution of argon in sodium is 19.3 ± 2.1 kcal/mol when the standard state of argon is taken as 1 mol of ideal gas at 1 atm, or 20.4 ± 2.1 kcal/mol when the standard state corresponds to 1 mol of ideal gas in a volume equal to the molar volume of sodium.

Thormeier's results for the solubility of argon in sodium^{9,17} are also shown in Figure 4. The 16% relative uncertainty we have assigned to our results overlaps Thormeier's solubility line at all temperatures, and his reported heat of solution, 20.0 kcal/mol, agrees well with the value 19.3 ± 2.1 kcal/mol from this work.

Discussion

The solubility of noble gases in liquid metals have been examined on the basis of theoretical models. Epstein¹ proposed the following thermodynamic model. Consider a binary system composed of two phases: a dilute solution of a noble element (2) in a solvent (1) and a gaseous phase containing only the noble element. At equilibrium, the chemical potential of the noble element will be the same in both phases.

$$\mu_2(\text{sol}, T, P) = \mu_2(\text{g}, T, P) \quad (5)$$

For the chemical potential of the noble element in the solution, one may write

$$\mu_2(\text{sol}, T, P) = R'T \ln x_2 \gamma_2 + \mu_2^0(l, T, P) \quad (6)$$

where x_2 is the mole fraction, γ_2 the activity coefficient of the solute, and the superscript ⁰ refers to a standard state consisting of the pure, liquid noble element at temperature T and pressure P . (Above the critical temperature this standard state is a hypothetical one.) For the gas phase at the same temperature and pressure

$$\mu_2(\text{g}, T, P) = R'T \ln P + \beta P + \mu_2^0(\text{g}, T, 1 \text{ atm}) \quad (7)$$

In eq 7 the virial series has been terminated at β , the

(17) Solubility results reported in ref 9 are expressed in units of a technical atmosphere, ata. This unit is equal to a pressure of 1 kg/cm². The appropriate conversion factor is 1 atm = 1.0333 ata.

(18) For technical purposes the solubility of argon expressed in weight units is given by $\log (\text{ppb}/\text{atm Ar}) = 6.65 - 7598T^{-1}$, where T is in degrees Rankine.

second virial coefficient of the gas. The chemical potential of the pure, liquid noble element under its own vapor pressure, P_2^0 , may be written as

$$\mu_2^0(l, T, P_2^0) = R'T \ln P_2^0 + \beta P_2^0 + \mu_2^0(g, T, 1 \text{ atm}) \quad (8)$$

Combination and rearrangement of eq 5-8 yields

$$\ln K_H \equiv \ln (x_2/P) =$$

$$-\ln P_2^0 + (P - P_2^0)(\beta - V_2^0)/R'T - \ln \gamma_2 \quad (9a)$$

or

$$\ln \lambda = \ln (R'T/P_2^0 V_1) +$$

$$(P - P_2^0)(\beta - V_2^0)/R'T - \ln \gamma_2 \quad (9b)$$

In eq 9 $\mu_2^0(l, T, P_2^0) - \mu_2^0(l, T, P)$ was taken to be equal to $V_2^0(P_2^0 - P)$, where V_2^0 is the molar volume of the pure, liquid noble element. The activity coefficient of the solute was estimated through the use of Hildebrand's solubility parameters.¹⁹

$$\ln \gamma_2 = \ln (V_2^0/V_1) +$$

$$(1 - V_2^0/V_1) + V_2^0(\delta_2 - \delta_1)^2/RT \quad (10)$$

With this estimate

$$\ln \lambda = \ln (R'T/P_2^0 V_2^0) - V_2^0(\delta_2 - \delta_1)^2/RT +$$

$$(P - P_2^0)(\beta - V_2^0)/R'T - (1 - V_2^0/V_1) \quad (11)$$

The problem may also be examined in atomistic terms by considering the interaction between the solvent and the solute, the latter being treated as a quasi-gas moving freely in the volume occupied by the solution. Under these conditions, the molar chemical potential of the solute may be expressed by the equation²⁰

$$\mu_2(\text{sol}, T, P) = -N_0\chi_2 + P\bar{V}_2 -$$

$$RT \ln \phi_2(T) + RT \ln C_{\text{sol}} \quad (12)$$

where χ_2 is the molecular potential energy of a solute, relative to the state of infinite separation, \bar{V}_2 is the partial molar volume of the solute, $\phi_2(T)$ is the partition function of the solute, including both translational and internal degrees of freedom, and C_{sol} is the concentration of solute in solution.

Similarly, for the gaseous phase, the molar chemical potential may be written as

$$\mu_2(g, T, P) = -RT \ln \phi_2(T) + RT \ln C_g \quad (13)$$

where C_g is the concentration of solute in the gas and it is assumed that the translational and internal degrees of freedom of the solute are unaffected by the solution process.

Equations 5, 12, and 13 may be combined to yield

$$RT \ln \lambda \equiv RT \ln (C_{\text{sol}}/C_g) = N_0\chi_2 - P\bar{V}_2 \quad (14)$$

The quantity $(-N_0\chi_2 + P\bar{V}_2)$ represents the reversible work of adding 1 mol of solute to the pure solvent to form an infinitely dilute solution. For solution of

gases in liquids, Uhlig²¹ proposed the replacement of the quantity $(-N_0\chi_2 + P\bar{V}_2)$ by the sum of two terms: μ_c , the reversible work required to make a mole of internal cavities, of a size corresponding to the molar volume of the solute, in the body of the solvent; and μ_i , the reversible work corresponding to the interaction of the solute with the surrounding solvent. Several methods have been proposed for the evaluation of these terms. Uhlig considered μ_c to be equal to the work done to make internal surfaces against the solvent's macroscopic surface tension; he did not attempt to evaluate the interaction term independently. McMillan² estimated the energy of cavity formation to be the product of the surface area of the cavity and a microscopic surface energy. The latter was estimated as $1/4$ of the energy of vaporization per unit area occupied by solvent atoms in the normal surface. The energy of interaction was calculated with the London equation for the dispersion forces between the solute and only the nearest-neighbor solvent molecules. Johnson and Shuttleworth⁶ proposed a model similar to Uhlig's except that the translational modes of the solute molecules are supplemented by vibrational ones; *i.e.*, $(-N_0\chi_2 + P\bar{V}_2) = \mu_c + \mu_i + \mu_{\text{vib}}$. They considered μ_c to be given by the surface area of a solute atom multiplied by the surface energy of the solvent, approximated μ_i (by a comparison with surface adsorption potentials) to be constant at -5 kcal/mol, and estimated the vibrational contribution, $\mu_{\text{vib}} = H_{\text{vib}} - TS_{\text{vib}}$, of the solute by taking H_{vib} and S_{vib} to be equal to the enthalpy and entropy of the solvent. In addition, Johnson and Shuttleworth did not assign equal values to the partition function of component 2 in the gaseous and in the solution phases (see eq 12 and 13). Instead, for the gas, the partition function was represented by its translational component, $(2\pi mkT)^{3/2}/h^3$, and, for the solution phase, by the number density of the solvent. Using the Johnson and Shuttleworth approach, Slotnick, *et al.*,⁸ found the predicted solubilities of helium in liquid lithium and potassium to be about 600 times as large as the experimental results. Pierotti,²² in a more sophisticated treatment, evaluated μ_c as the free energy of cavity formation in a hard-sphere fluid, using methods developed by Reiss, *et al.*²³ The interaction term, μ_i , was evaluated in terms of an integrated form of the Lennard-Jones (12-6) potential with the Kirkwood-Muller equation for the dispersion forces.

All of the models capable of quantitative evaluation were tested against the solubilities of helium and argon in liquid sodium. The results are shown in Table I.

(19) J. H. Hildebrand and R. L. Scott, "The Solubility of Nonelectrolytes," 3rd ed, Reinhold, New York, N. Y., 1950, p 131.

(20) R. Fowler and E. A. Guggenheim, "Statistical Thermodynamics," The University Press, Cambridge, 1956, p 373.

(21) H. H. Uhlig, *J. Phys. Chem.*, **41**, 1215 (1937).

(22) R. A. Pierotti, *ibid.*, **67**, 1840 (1963).

(23) H. Reiss, H. L. Frisch, E. Helfand, and J. L. Lebowitz, *J. Chem. Phys.*, **32**, 119 (1960).

Table I: Ostwald Coefficients for Solution of Helium and Argon in Liquid Sodium at 300 and 500°

Model	Na-He		Na-Ar	
	300°	500°	300°	500°
Epstein ¹	6.65×10^{-10}	1.54×10^{-6}	7.14×10^{-6}	2.60×10^{-4}
McMillan ²	0.86	0.89	>1	>1
Johnson and Shuttleworth ⁶	6.47×10^{-2}	1.79×10^{-1}	3.72×10^{-5}	2.90×10^{-4}
Pierotti ²²	1.26×10^{-2}	2.78×10^{-2}	5.24×10^{-3}	1.25×10^{-2}
Observed (this work)	1.36×10^{-6}	3.24×10^{-4}	1.98×10^{-7}	2.04×10^{-6}

In the Epstein model the predicted solubility depends markedly on the value assigned to the hypothetical quantity P_2^0 . Values of P_2^0 were obtained by extrapolation of the vapor pressure equations from the accessible regions to the supercritical regions. These equations were

$$\begin{aligned} \text{helium}^{24} \quad \log P_2^0(\text{atm}) &= 1.848 - \\ &7.948T^{-1} - 0.1363T^{-2} + 4.363T^{-3} \\ \text{argon}^{25} \quad \log P_2^0(\text{atm}) &= 3.964 - 346T^{-1} \end{aligned}$$

For this model conventional values²⁶ were used: $V_{\text{He}}^0 = 32 \text{ cm}^3$; $V_{\text{Ar}}^0 = 28 \text{ cm}^3$; $\delta_{\text{He}} = 0.5 \text{ cal}^{1/2} \text{ cm}^{-3/2}$; $\delta_{\text{Ar}} = 7.5 \text{ cal}^{1/2} \text{ cm}^{-3/2}$; $\delta_{\text{Na}} = 30$ (300°) and 29 (500°) $\text{cal}^{1/2} \text{ cm}^{-3/2}$. The second virial coefficients were taken to be $10.76 \text{ cm}^3/\text{mol}$ (300°) and $10.14 \text{ cm}^3/\text{mol}$ (500°) for helium²⁷ and $10.77 \text{ cm}^3/\text{mol}$ (300°) and $17.76 \text{ cm}^3/\text{mol}$ (500°) for argon.²⁸

In McMillan's model the interaction term was calculated from $\mu_i = -Z^{(3/2)}(\alpha_1\alpha_2/a_{12}^6)[I_1I_2/(I_1 + I_2)]$, where α is the atomic polarizability ($\alpha_{\text{He}}^{29} = 0.204 \times 10^{-24} \text{ cm}^3$, $\alpha_{\text{Ar}}^{29} = 1.63 \times 10^{-24} \text{ cm}^3$, $\alpha_{\text{Na}}^{29} = 29.7 \times 10^{-24} \text{ cm}^3$), I is the ionization potential ($I_{\text{He}}^{30} = 24.581 \text{ eV}$, $I_{\text{Ar}}^{30} = 15.756 \text{ eV}$, $I_{\text{Na}}^{30} = 5.138 \text{ eV}$), a_{12} is the distance between the centers of the solute and solvent atoms ($a_{\text{Na-He}} \cong 3.21 \times 10^{-8} \text{ cm}$, $a_{\text{Na-Ar}} \cong 3.60 \times 10^{-8} \text{ cm}$), and Z is the number of nearest sodium neighbors, estimated to be 9.4 and 11.8 for helium and argon, respectively. The cavity term, μ_c , was calculated from $\mu_c = \pi a_{12}^2 \Delta H_1^v / 4N_0\sigma$, where ΔH_1^v is the heat of vaporization of sodium (23.7 kcal/mol) and σ is the area occupied by a solvent atom on the surface ($\sigma_{\text{Na}} \cong 24.8 \times 10^{-16} \text{ cm}^2$).

In Johnson and Shuttleworth's model the cavity term was calculated from $\mu_c = 4\pi a_2^2 \gamma_1^0$, where a_2 is the radius of the solute atom ($a_{\text{He}} \cong 1.32 \times 10^{-8} \text{ cm}$, $a_{\text{Ar}} \cong 1.70 \times 10^{-8} \text{ cm}$) and γ_1^0 is the hypothetical surface energy of liquid sodium at 0°K (220 erg/cm²).³¹ For the calculation of the vibrational term the enthalpy and entropy of sodium³² were taken to be 4.16 kcal/mol and 18.7 cal/deg-mol at 300° and 5.57 kcal/mol and 20.8 cal/deg-mol at 500°, respectively.

The reader is referred to Pierotti's paper²² for details of his model. Here, the calculated solubility is a sensitive function of the value selected for the hard-sphere diameter of the solvent. We have selected 3.19 Å at 300° and 3.12 Å at 500° as the hard-sphere diameter of

sodium, as discussed by Ascarelli.³³ The values for the atomic magnetic susceptibilities²⁹ required for the calculation of the Kirkwood-Muller interaction term were taken to be $\chi_{\text{He}} = -2.90 \times 10^{-30} \text{ cm}^3$, $\chi_{\text{Ar}} = -3.24 \times 10^{-29} \text{ cm}^3$, and $\chi_{\text{Na}} = -9.00 \times 10^{-29} \text{ cm}^3$.

Examination of Table I shows that Epstein's model predicts solubilities both much larger and much smaller than those observed. A major weakness of this model is the need for extrapolation of the vapor pressure of the solute to unphysical regions. For helium, in particular, the quantum effects which dominate the vapor pressure of the liquid at low temperatures would be poorly taken into account by simple extrapolation to higher temperatures. The models proposed by McMillan, by Johnson and Shuttleworth, and by Pierotti yield solubilities generally higher than those observed. It is suggested that the inadequacies of these models stem primarily from their estimates of the cavity-formation term. These estimates, which may be adequate for insulating solvents, seem to fail for metallic solvents. A theoretical model which specifically deals with the electronic work of cavity formation in a metallic solvent seems required. Such a model has been developed in this laboratory and will be described elsewhere.³⁴

Acknowledgments. We wish to thank Dr. Irving Johnson for helpful discussions, R. M. Yonco, G. W. Redding, R. A. Blomquist, and M. T. Perin for technical assistance, and Dr. M. H. Barsky and A. F. Panek for gas chromatographic analyses. This work was performed under the auspices of U. S. Atomic Energy Commission.

- (24) W. H. Keesom, "Helium," Elsevier, Amsterdam, 1942, p 191.
 (25) A. M. Clark, F. Din, and J. Robb, *Ned. Tijdschr. Natuurk.*, **17**, 876 (1951).
 (26) Reference 19, pp 324, 435.
 (27) W. G. Schneider and J. A. H. Duffie, *J. Chem. Phys.*, **17**, 751 (1949); J. L. Yntema and W. G. Schneider, *ibid.*, **18**, 641 (1950).
 (28) E. Whalley, Y. Lupien, and W. G. Schneider, *Can. J. Chem.*, **31**, 722 (1953).
 (29) H. Margenau, *Rev. Mod. Phys.*, **11**, 1 (1939).
 (30) G. Herzberg, "Atomic Spectra and Atomic Structure," Dover Publications, New York, N. Y., 1944, p 200.
 (31) J. Bohdanský and H. E. J. Schins, *J. Inorg. Nucl. Chem.*, **29**, 2173 (1967).
 (32) "JANAF Thermochemical Tables," Dow Chemical Co., Midland, Mich., June 30, 1962.
 (33) P. Ascarelli, *Phys. Rev.*, **173**, 271 (1968).
 (34) H. C. Schnyders and H. M. Feder, unpublished work.

Transitions in Mesophase Forming Systems. I. Transformation

Kinetics and Pretransition Effects in Cholesteryl Myristate¹

by Fraser P. Price* and Joachim H. Wendorff

Polymer Science and Engineering, University of Massachusetts, Amherst, Massachusetts 01002 (Received January 13, 1971)

Publication costs assisted by the National Institutes of Health

The volume-temperature behavior of highly purified cholesteryl myristate has been studied between 25 and 85° using sensitive dilatometers. Equilibrium pretransitional effects were present on the low-temperature and absent on the high-temperature side of all three transitions. The cholesteric state shows unusual behavior in two ways—first its expansion coefficient exceeds that of the liquid and second a thermally reversible transition in texture but not in structure occurs within it. The transformation kinetics fit the Avrami equation yielding values of n of 4, 2, and 2 for the smectic-solid, the cholesteric-smectic, and the isotropic liquid-cholesteric transformations, respectively. The liquid-cholesteric and the cholesteric-smectic transformations take place by the formation of disklike nuclei (50–500 Å in radius) which subsequently grow into rods. The calculated interfacial energies are extremely small (ca. 0.1 erg/cm²). The consequences of this are discussed.

Usually the melting of a crystalline molecular solid to an isotropic liquid takes place in a single step at the melting temperature. However, there are a significant number of crystalline substances which make the transition from the three dimensionally ordered crystalline state to the random disorder of the isotropic liquid in more than one step. There are some in which the molecules become rotationally disordered while maintaining their positional order, subsequently to lose this order in a first-order transition to the isotropic liquid. Among these, *inter alia*, are a number of linear paraffinic hydrocarbons,^{2–4} which become disordered about their long axis, and camphor and other substances with essentially spherical molecules,⁵ which become disordered about all three axes of rotation simultaneously. There are other compounds which become positionally but not rotationally disordered in a series of transitions. These are the mesophase forming or liquid crystal forming substances.^{6,7} These substances, generally, have molecules that are rigid and either rodlike or disklike in shape. The thermodynamically stable mesophases are mobile compared to the crystalline solid and flow readily. The various liquid crystal phases lying between the solid and the isotropic liquid are designated as smectic and nematic. A special subgroup of the nematic phase is the cholesteric. This phase is similar to the nematic except that here there is an imposed helical rotation, which in certain textures results in extremely large optical rotatory power. The esters of cholesterol as a group are capable of forming cholesteric and smectic mesophases.

Relatively little is known about the energetic factors that control mesophase structure. It is known that in these phases the intermolecular forces are very small

compared to those in normal crystalline solids. This is evidenced by heats of transitions between mesophases and between a mesophase and the isotropic liquid that are only a very small fraction (2–5%) of the heat of transition from the crystalline solid to the lowest lying mesophase.⁸ There exists no information about the energy barriers that make the mesophases thermodynamically stable and that retard transformations to lower lying states. It is through investigation of the kinetics of phase transformation between the mesophases themselves and between the mesophases and the isotropic liquid or the crystalline solid that such information can be developed. It is with such studies that the present paper, and those to follow, deal.

This first paper describes studies of the transitions of cholesteryl myristate. This substance, a central member of a series of cholesteryl esters of long-chain saturated fatty acids, has 13 carbons exclusive of the carboxyl. This substance was chosen as starting material, because neither its smectic nor its cholesteric phase is monotropic, because it is biologically based, and because much information is available concerning the properties of this substance. Further work will

(1) This work was supported by Grant No. HE 13188 from the National Institutes of Health.

(2) (a) A. R. Ubbelohde, "Melting and Crystal Structure," Oxford University Press, London, 1965; (b) H. L. Finke, M. E. Gross, G. Waddington, and H. M. Huffman, *J. Amer. Chem. Soc.*, **76**, 333 (1954).

(3) J. D. Hoffman and B. F. Decker, *J. Phys. Chem.*, **57**, 520 (1953).

(4) A. R. Ubbelohde, *Trans. Faraday Soc.*, **34**, 282 (1938).

(5) W. R. Green and D. R. Wheeler, *J. Mol. Cryst.*, **6**, 1 (1969).

(6) G. H. Brown and W. C. Shaw, *Chem. Rev.*, **57**, 1049 (1957).

(7) G. W. Gray, "Molecular Structure and the Properties of Liquid Crystals," Academic Press, New York, N. Y., 1962.

(8) R. S. Porter, E. M. Barrall, II, and J. F. Johnson, *Accounts Chem. Res.*, **2**, 53 (1969).

be carried out on other cholesteryl esters of this series and reported in subsequent papers.

The volume of the system was selected as the thermodynamic property to study and dilatometry the technique of choice. This method was chosen because it is convenient, inexpensive, and capable of high precision. The data which are obtained are volume-time sets with the temperature as a running parameter. The isothermal plots can be interpreted in the same way as has been done in the case of other melt-solid transitions (*viz.*, polymers), in terms of the Avrami equation⁹ which yields two constants n and K . The study of n and K provides information about the modes of nucleation and growth of the transforming regions. The temperature coefficient of the constant K can be used to calculate the energetic properties of the processes, that is, the barriers to diffusion and the interfacial energies. In the course of the present studies, information about the equilibrium volume-temperature behavior also was developed. This is used in conjunction with other information such as that derived from X-ray diffraction, calorimetric, and light scattering studies to elucidate more clearly the states of the mesophases themselves.

Experimental Section

Apparatus and Methods. The use of dilatometers is a very powerful and accurate method for studying phase transitions. In this method the volume-time change is measured at constant temperature after a sudden change of the temperature from above the transition temperature to below the transition temperature. The amount of the sample which is not transformed at the time t is given by means of the equation

$$F(t) = \frac{V_{\infty} - V_t}{V_{\infty} - V_0} \quad (1)$$

Here V_0 , V_t , and V_{∞} refer to the volume of the system, respectively, at zero time, time t , and at infinite time.

The dilatometers used in this study were of the sealed-off type described elsewhere.¹⁰ In this device the values of the volume differences ($V_{\infty} - V_t$), ($V_{\infty} - V_0$) are related to the height differences of the mercury level ($h_{\infty} - h_t$) and ($h_{\infty} - h_0$) in the capillary. Here h_{∞} , h_t , and h_0 are the heights of the mercury at infinite time, time t , and zero time, respectively. Depending on the measurement under consideration, dilatometers with different shapes and sizes were used. Dilatometers with disklike bulbs turned out to be the most suitable type for studies of the transformation to the solid state. These had a large mercury-sample interface which made it possible, as was proved by the reproducibility of the data, to avoid void formation in the solid. For studying the mesophase-mesophase transition and the isotropic liquid-mesophase transition, dilatometers of cylindrical shape were used.

In these transitions the fluidity of the phases is high enough so that there is no danger of void formation.

The amount of the samples, within the dilatometer, was normally about 3 g. The capillary was of precision bore tubing of diameter 1 or 0.5 mm. With this sample and capillary size the change in height of the mercury is between 20 and 80 cm for the solid-smectic transition and about 4% of this for both the smectic-cholesteric and the cholesteric-isotropic transitions. The height of the mercury in the capillary was read to ± 0.01 mm with a Gaertner cathetometer.

For the study of pretransition effects a thermostating arrangement was used which permitted control of the temperature to better than 0.01° . It consisted of a wide-mouthed Dewar-type flask which was immersed in the constant temperature bath. This flask was filled with the paraffin oil thermostating liquid used in the main thermostat. The space between the walls of the Dewar was not permanently evacuated but could be filled with air when large temperature changes had to be made quickly and could be evacuated when a constant temperature was desired.

The thermometer which was used to establish the temperature of the phase transitions was calibrated in distilled, degassed boiling water taking into account the ambient air pressure. The difference between the actual temperature and the temperature given by the thermometer was 0.1° . Three thermostatic baths were used: the first bath for annealing the samples at a constant temperature slightly above the transition temperature, the second bath for controlling the temperature during the transition, and the third bath for the long-time annealing of the samples at temperatures well above the isotropic melting temperature. The temperature control of each bath was better than 0.1° . It turned out that the best results as judged by the reproducibility of the data were obtained by quickly moving the dilatometer from bath one to bath two. The temperature adjustment of the sample took place within 1.5 to 3 min depending on the temperature difference between the baths and the shape and size of the dilatometer.

Corrections. As the transition between the mesophases and between the isotropic liquid and the mesophases happens in a period of time comparable to that needed to attain constant temperature, corrections have to be made to the measured mercury height. These corrections must take into account the facts that (a) the sudden change of the temperature causes a change of the volume of the dilatometer itself, the mercury, and the untransformed sample. (b) The time of immersion of the dilatometer is not the time during which the sample inside has been at the crystallization temperature. This is a zero time effect.

(9) M. Avrami, *J. Chem. Phys.*, **7**, 1103 (1939); **8**, 212 (1940).

(10) N. Bekkedahl, *J. Res. Nat. Bur. Stand.*, **42**, 145 (1949).

(c) Initially the sample temperature is not the same throughout. The surface may be at the crystallization temperature when the interior is warmer. This is a nonisothermal effect.

Corrections for these effects were carried out as follows.

1. *Nontransition Correction.* The volume-time dependence after a sudden change of the temperature (0.3 to 5.0°) was established in temperature regions, in which no transformation took place. Curves of time *vs.* the mercury height in the capillary were constructed for various temperature differences totally within either the isotropic or the cholesteric state. These curves were used to correct the crystallization curves for the effects mentioned in (a) above.

2. *Zero-Time Correction.* If the dilatometer is transferred from the annealing bath to the crystallization bath, for some time the surface temperature differs from the bath temperature because of the limited heat conductivity of the glass wall of the dilatometer, the limited rate of heat transfer from the bath oil to the surface of the dilatometer, and the heat transfer into the sample. To measure the time, t_i , between the transfer and the time at which the surface of the sample is first at the crystallization temperature, cholesteryl acetate was put into a dilatometer of the same shape and size. Cholesteryl acetate has, in contrast to cholesteryl myristate, the advantages that the isotropic liquid-cholesteric state transformation can easily be detected by its intense blue color even in a very thin layer, and the transition occurs without any induction period. To determine t_i the sample was abruptly cooled down from different temperatures above the transition temperature to a constant temperature below the transition temperature and the moment of appearance of the blue color at the sample surface noted. It turned out that t_i was within the sensitivity of the time measurement constant for the studied temperature differences (0.3 to 5°).

In both the cholesteryl myristate and the cholesteryl acetate filled dilatometers, the isothermal height-time curves after abrupt temperature changes could be expressed by $(h_\infty' - h_t')/(h_\infty' - h_0') = \exp(-at)$, where h_∞' , h_t' , and h_0' are the mercury heights at infinite time, time t , and zero time, respectively. This relation was followed so long as the time did not exceed a critical value, t_{crit} , and so long as there was no change of state. It was found for the cholesteryl acetate filled dilatometer that t_i was equal to $1/a$. This indicates that both the acetate- and the myristate-filled dilatometers can be characterized by the same value of a . This is gratifying for it vindicates our assumptions about the identical heat transfer behavior of the two instruments.

3. *Nonisothermal Corrections.* The volume V_c within which crystallization can occur increases with time up to the moment when all regions of the sample

are at the same temperature, the crystallization temperature. To derive correct kinetic values from the overall shape of the transition curve, corrections for the actual volume at the crystallization temperature must be made. We assume that the temperature change within the sample takes place at a boundary which moves through the sample. The volume V_c can then be derived from the isothermal height-time curve in the same initial phase state after the abrupt change of the temperature by means of the expression

$$V_i'(t') = (h_0' - h_t')/(h_0' - h_\infty')$$

Thus the values of $(V_\infty - V_t)/(V_\infty - V_0)$ corrected as in (1) above must be further corrected to yield

$$F(t) = \frac{V_t - V_\infty}{V_0 - V_\infty} \frac{1}{V_i'(t')} \quad (2)$$

Here the expression $F(t)$ is the weight fraction of material untransformed at the time t , if all regions of the sample had been at the crystallization temperature during all the time. With increasing time this correction becomes less important. We estimate the error in the specific volume by this technique and after these corrections to be between 0.01 and 0.001%. The error in the volume coefficient of thermal expansion is $\pm 1\%$. The specific volume change is about 0.2% for the isotropic-cholesteric and the cholesteric-smectic transitions and about 5% for the smectic-solid transition. It is thus possible to detect extents of transition of 0.5 to 5% for the two former transitions and 0.02 to 0.2% in the latter. These errors lead to estimated errors in the Avrami constants (see eq 4) of 10% in K and 0.15 in n . While it is realized that eq 2 applies strictly to the volume fraction and not the weight fraction, we believe that the other errors in the system are sufficiently large to make conversion of weight into volume fraction superfluous.¹¹

The above-mentioned corrections were applied to the kinetic runs. In the determination of equilibrium specific volume curves all time-dependent effects can be made negligible. In these determinations corrections were made for the change in volume of the glass dilatometer and for the change of volume of that portion of the mercury which moved from a warm zone beneath the thermostating liquid surface to the cooler capillary above or *vice versa*.

X-Ray Measurements. X-Ray diffraction patterns were obtained using a flat plate transmission camera. The radiation was unresolved Cu $K\alpha$ (1.5418 Å). Pinhole collimation was used. The sample-plate distance was 7.3 cm.

Optical Microscopy. Microscopic observations of the isotropic-cholesteric and cholesteric-smectic transitions were made with a Zeiss Type WL research mi-

(11) F. P. Price, *J. Appl. Phys.*, **36**, 10 (1965).

croscope. Usually, crossed polars were employed. The sample was located in a glass cell 1 cm in diameter. The thickness of the sample was about 1 mm. A thin glass cover slip was separated from the surface of the sample by a 0.3-mm spacer. In this way it was possible to study the transition behavior of cholesteryl myristate without the influence of the glass-sample interface.

Temperature manipulation of the sample was carried out on a hot stage, the temperature of which was controlled by circulating liquid from a thermostatic bath or by a second heating system, consisting of a heating tape and a transformer. The temperature control was better than $\pm 0.1^\circ$. The magnification was $320\times$. The distance between scale markers in the pictures is 0.05 mm.

Materials. Samples of cholesteryl myristate were obtained from Eastman Kodak Co., Rochester, N. Y. The ACS reagent grade mercury which was used within the dilatometer and for the calibration of the capillary and the pycnometer was obtained from Sargent-Welch Co.

Purification. The cholesteryl myristate samples were recrystallized from *n*-pentyl alcohol, washed several times in a water-ethanol mixture, and dried at 50° under vacuum conditions (rotating pump) until no further change in the weight could be observed. In each recrystallization about 75% of the material is lost. Two samples were prepared: one recrystallized once (designated sample A), the other recrystallized three times (designated sample B).

The purities of the samples were estimated from the equation of van't Hoff

$$T_s = T_0 - [RT_0^2N/\Delta H](1/F) \quad (3)$$

where T_s = melting temperature, T_0 = melting temperature of the pure compound, ΔH = heat of fusion of the pure compound,¹² F = fraction of material liquid, N = mole fraction of impurities, and R = gas constant.

This equation expresses the initial dependence of T_s upon $1/F$ under the assumptions that (a) the melting is not sharp because of impurities rather than because of other effects such as premelting, and (b) the impurities are more soluble in the melt than in the solid. The usual assumption is that they are not soluble in the solid state but are soluble in the liquid state.

In the present instance it is not known how well the assumptions are obeyed, for it is conceivable that impurities such as cholesteryl laurate and palmitate could cocrystallize with the myristate.

The results for the two samples of equilibrium melting experiments in the solid-smectic transition are duplicated in Table I.

It is clear that the extra recrystallizations did not significantly decrease the measured impurity content of sample B over sample A. The melting points,

Table I: Determination of Purity of Samples^a

	Sample A	Sample B
Times recrystallized	1	3
Melting range, $^\circ\text{C}$	1.5	1.6
T_0 , $^\circ\text{C}$	70.5	70.6
Range of F of linear portion of eq 3	1.0-0.2	1.0-0.7
Initial slope, $^\circ\text{C}$	0.13	0.15
Mol % impurity	0.6	0.7

^a $\Delta H = 18.7$ cal/g for cholesteryl myristate.¹²

melting ranges, and calculated impurities are all essentially identical. However the range of transformation over which the plots of T_s vs. $1/F$ was linear is much shorter in the case of sample B. Here it was found that a plot of $\ln F$ vs. $1/T$ ($^\circ\text{K}^{-1}$) was linear over the entire melting range. The slope of this line is $-2.63 \times 10^{+5}$ ($^\circ\text{K}$) which leads to an "energy" of 524 kcal/mol. The curvature observed here and the "energy" would seem to indicate some sort of activated premelting phenomenon. In fact, we have made X-ray diffraction studies of the crystalline myristate which indicate considerable disordering as the solid-smectic transition is approached. In spite of the differences between the two samples noted in Table I, the equilibrium volume-temperature curves for the two samples were identical for the solid smectic, cholesteric, and isotropic phases.

Results and Discussion

Equilibrium Relations. The equilibrium volume-temperature relations were established by waiting at each temperature long enough so that no further change in the mercury level occurred. The results of those studies are displayed in Figures 1 and 2. The figures indicate that for each transition there is some pre-transition effect on the low-temperature side. There is never any observable indication of a pretransition on the high-temperature side. This indicates that these transitions in reality are first order. We have made detailed examinations of results presented by other investigators purporting to demonstrate pretransition effects on the high-temperature side of mesophase transitions.¹²⁻¹⁹ In our opinion this evidence is, at

(12) G. J. Davis, R. S. Porter, and E. M. Barrall, II, *Mol. Cryst. Liq. Cryst.*, **10**, 1 (1970).

(13) A. Ferguson and S. J. Kennedy, *Phil. Mag.*, **26**, 41 (1938).

(14) E. M. Barrall, II, R. S. Porter, and J. F. Johnson, *J. Chromatog.*, **21**, 392 (1962).

(15) W. A. Hoyer and A. W. Nolle, *J. Chem. Phys.*, **24**, 803 (1956).

(16) H. Arnold, *Z. Phys. Chem.*, **226**, 146 (1964).

(17) E. M. Barrall, II, R. S. Porter, and J. F. Johnson, *J. Phys. Chem.*, **71**, 895 (1967).

(18) R. S. Porter and J. F. Johnson, *J. Appl. Phys.*, **34**, 51, 55 (1963).

(19) W. R. Runyan and A. W. Nolle, *J. Chem. Phys.*, **27**, 1081 (1957).

Table II: Summary of Equilibrium Volume-Temperature Relations for Cholesteryl Myristate

Temp, °C	State	Transition volume change, %	α , °C ⁻¹	A , kcal/mol	T_0	$\sqrt{\Sigma\delta^2/\eta}$
$T \leq 69.0$	Solid		3.29×10^{-4}			
$69.0 \leq T \leq 70.5$		4.94		524	70.5	0.006
$70.5 \leq T \leq 78.1$	Smec.		7.04×10^{-4}			
$78.1 \leq T \leq 78.6$		0.14		254	78.6	0.007
$78.6 \leq T \leq 83.4$	Chol.		11.2×10^{-4}			
$83.4 \leq T \leq 83.8$		0.17		548	83.8	0.007
$83.8 \leq T$	Iso. liq.		7.99×10^{-4}			

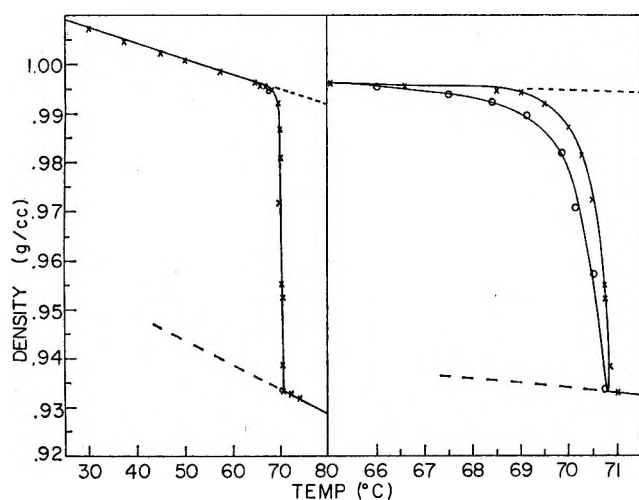


Figure 1. Density-temperature plots for the solid-smectic transition in cholesteryl myristate: O, sample A; X, sample B.

best, inconclusive. Since the dilatometric technique employed in this investigation is unambiguous and of very high precision, the conclusion is forced upon us that to within the precision of this technique there are no pretransitional effects on the high-temperature side and that the clustering of the type postulated by Frenkel²⁰ is not observable.

It has been postulated that the temperature sensitivity of the cholesteric phase immediately above the smectic-cholesteric transition is a kind of pretransitional effect.²¹ However, it is not certain that this phenomenon, which exhibits itself in the helical colored structures, occurs in anticipation of the transition or is independent of it. In any event, cholesteryl myristate shows no such phenomenon.

The quantitative aspects of the data are presented in Table II. Here are summarized the volume change at the transition temperature, the volume coefficient of expansion ($\alpha = (1/V_0)(dV/dT)$), and the constant A in the expression for the equilibrium volume fraction in the high-temperature phase $F = \exp[-(A/R)((1/T) - (1/T_0))]$, in the transition region. Here T_0 is the transition temperature. The last column of Table II

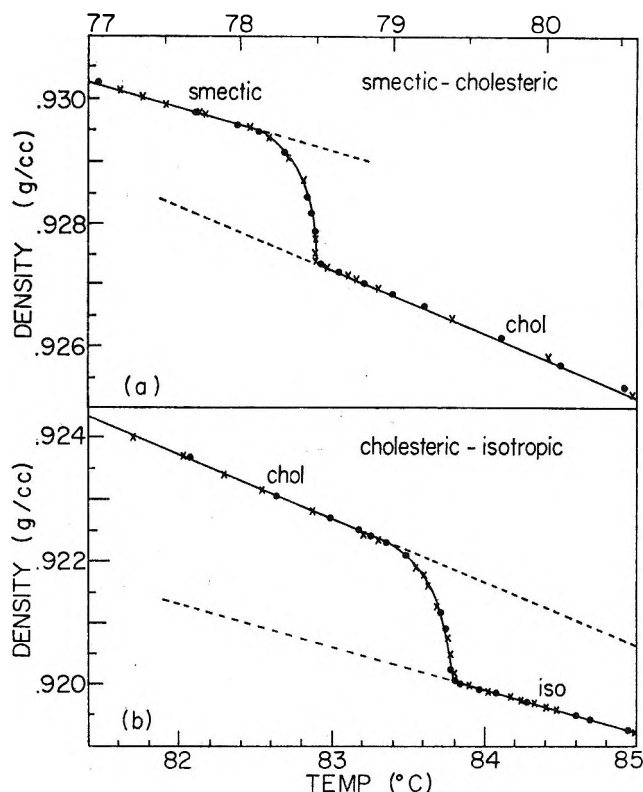


Figure 2. Density-temperature plots for the smectic-cholesteric and cholesteric-isotropic liquid transitions in cholesteryl myristate, sample B: ●, temperature decreasing; X, temperature increasing.

gives the variance of F , $\sqrt{\Sigma\delta^2/\eta}$, where $\delta = F_{\text{calcd}} - F_{\text{obsd}}$ and η is the number of experimental observations.

The transition temperatures are taken to be the upper end of the transition regions. They are 70.5, 78.6, and 83.8° for the solid-smectic, the smectic-cholesteric, and the cholesteric-isotropic liquid transitions, respectively. These values agree well with those of previous investigators.¹² Also in conformity with other studies the largest change in volume occurs at the solid-smectic transition being 30 to 40 times those

(20) J. Frenkel, "Kinetic Theory of Liquids," Dover Publications, New York, N. Y., 1965.

(21) P. H. Keating, *Mol. Cryst.*, **8**, 315 (1969).

of the other transitions.¹⁸ It is further noteworthy that the expansion coefficient of the cholesteric phase is nearly 50% greater than that of the isotropic liquid. This phenomenon has been observed in the other cholesteryl esters to be described in later papers in this series. It must mean that the ability of the cholesteric phase to increase in order with decreasing temperature is greater than that of the liquid.

Kinetic Studies. Many years ago it was shown that isothermal transformations with impingement could be described by the so-called Avrami equation⁹

$$F(t) = e^{-Kt^n} \quad (4)$$

where $F(t)$ = volume fraction not transformed, t = time, n = a constant dependent in the modes of nucleation and growth of the transforming regions, and K = a constant dependent on the mode of nucleus injection and the shape of the transforming regions.

The assumptions implicit in this equation and the consequent restrictions on its validity have been discussed elsewhere.¹¹ We are aware of these restrictions but in the current study we will correlate $F(t)$ with t by eq 4 assuming that $F(t) = (V_\infty - V_t)/(V_\infty - V_0)$ and introducing the corrections noted above in the Experimental Section. It should be noted that eq 4 is of such a form that any function of $F(t)$ when plotted against $\log t$ should have the same shape and should be superposable by transposition along the $\log t$ axis with a transposition factor of $K^{1/n}$.

In the present studies only the overall transformation kinetics are reported. Work to be reported in the future dealing with the morphology and the kinetics of growth of the transforming regions will permit detailed interpretation of the values of K presented here in terms of the energetics of nucleation and growth in these systems.

Smectic-Solid Kinetics. The transformation kinetics of only sample A and not sample B of the cholesteryl myristate was studied in the smectic-solid transition. This was done because it was felt that the small differences in impurity content between the two samples would not influence the kinetics of a transition in which the overall enthalpy change was as large as 18 cal/g.¹² In the other transformations the enthalpy changes are much smaller, and these were studied with both samples. The transformation into the solid state showed a strong dependence on the annealing conditions. After being briefly heated into the smectic, cholesteric, or isotropic states the crystallization to the solid on cooling took place very rapidly at temperatures, below 65°. However, the data were not reproducible, which indicates that there must have existed nuclei whose properties depended on the temperature and time of annealing. It was not until after an annealing at 95° for a period of some days that the data became reproducible. After this treatment it was normally sufficient to anneal the sample at

95° for 0.5 hr before the crystallization was induced. Even then at temperatures below 50° even after this treatment small deviations were observed. These were eliminated by annealing at 95° for 1 day between measurements. The crystallization behavior was now independent of the state from which the sample was quenched to the crystallization temperature regardless of the initial state, isotropic, cholesteric, or smectic. Crystallization into the solid state always took place from the smectic state. This occurred because the induction period for the transition into the solid state is very much longer than the times required for complete transition from either the cholesteric to the smectic state or from the isotropic liquid to the cholesteric to the smectic state. This phenomenon was verified experimentally for each solid crystallization by the observation that prior to the transformations the mercury level in the capillary was always consistent and was that characteristic of the smectic state.

A sample which had been in the solid state for more than 1 week without any heat treatment showed the same behavior as before the prolonged annealing at 95°. The data became reproducible again only after annealing the sample at 95° for several days. This shows that no irreversible change within the sample was induced by the annealing. The main differences in behavior before and after annealing are that after annealing (1) the period in which the total crystallization takes place increases, especially at low crystallization temperatures, and (2) the induction period increases, particularly at crystallization temperatures above 50°. At temperatures below about 50° the crystallization takes place after only a short induction period. Over the whole temperature range studied (25–70°) the rate of crystallization decreases with increasing temperature. As the crystallization temperature is raised, at about 50° there is a change in behavior: the induction period suddenly increases, but the rate of crystallization does not change significantly. At still higher temperatures the rate decreases and the induction period increases with increasing temperature. To determine relative nucleation rates at various temperatures, the sample was crystallized at various constant temperatures ranging from 45 to 55°. The crystallization was interrupted at different times (different amounts of the fraction transformed) by abruptly changing the temperature of the bath from the crystallization temperature to 65°. It had been established that at 65° no further nucleation took place during the time of the measurements. Thus the transformation rate at this temperature is a measure of the number of nuclei present in the sample at the time at which the temperature was changed. It turned out that at temperatures above 47° only very few nuclei were formed during the whole crystallization. Below this temperature the nucleation rate increased very rapidly. However, below 47°

the crystal growth rate is very large and is increasing rapidly with decreasing temperature. It was thus not possible to get reliable relative nucleation rates.

These results show unambiguously that nucleation processes control the behavior of cholesteryl myristate in the transition from the smectic to the solid state. The sudden change of this behavior around 50° is directly related to the change of rate and mode of nucleation. Very probably 50° lies at the upper limit of the temperature range where the nucleation is homogeneous. Above 50° crystallization starts on only a few nuclei which are heterogeneous in nature. Since these nuclei frequently reside on the wall of the dilatometer, the rate of transformation depends on the particular dilatometer (its shape and wall treatment).

When the transformation to the solid state was performed between 60 and 70.5° , the density of the material formed was about 0.4% lower than material formed at lower temperatures. The coefficients of thermal expansion of both materials were identical. X-Ray diffraction patterns were obtained of both the low- and high-density materials. The high-density (low-temperature) material showed rings indicative of large numbers of randomly oriented small crystals. The low-density (high-temperature) material showed spots and arcs indicative of strongly correlated orientation of a few large crystals. The various d spacings for the two materials were calculated. Of the 12 spacings calculated for the high-density material (some observed up to fourth order) only one was missing from low-density material. We conclude that the low density results not from another crystal form but from voids in the crystallized mass which is composed of a relatively few large crystals.

The results of the kinetic runs are summarized in Figure 3 and Table III. In Figure 3 the runs at 50.6° and below have been shifted to correspond to a crystallization temperature of 45.5° (25° supercooling). Here all the curves have the same shape and are superposable. The shift factors are given. This indicates that a single mechanism is operating in this temperature range. The runs above 50.6° have been shifted to correspond to a temperature of 65.5° (5° supercooling). Here superposition is no longer possible. The curves can no longer be fitted to eq 4. The differences in behavior above and below about 50° substantiates the concept that homogeneous nucleation sets in at about this temperature. Further evidence for homogeneous nucleation of the transforming region is supplied by the values of n of 4 shown in Table III.

An Avrami exponent of n of 4 means that the transforming regions are most probably spheres and that their number is increasing linearly with time. It is interesting to note that spherulitic structures have been shown to exist in solid cholesteryl myristate by both microscopic and light scattering studies.²²

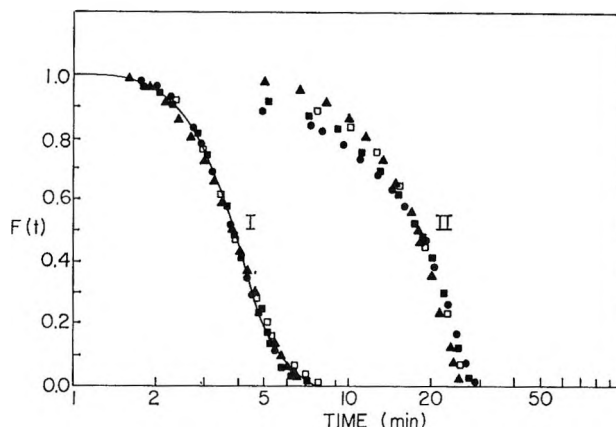


Figure 3. Plots of $F(t)$ vs. \log (time) for smectic-solid transition. Curve I data shifted to 25° supercooling, shift factor in brackets: \square , 40.3° [2.30]; \bullet , 45.5° [1.0]; \blacksquare , 47.6° [0.52]; \blacktriangle , 50.5° [0.27]. Curve II data shifted to 5° supercooling, shift factor in brackets: \square , 53.0° [2.57]; \bullet , 62.5° [1.58]; \blacksquare , 65.1° [1.0]; \blacktriangle , 67.6° [0.34].

Table III: Avrami Constants for the Smectic-Solid Transformation in Cholesteryl Myristate (Sample A)

$T, ^\circ\text{C}$	n	K, min^{-4}
40.3	3.9	1.7×10^{-2}
45.5	4.1	3.9×10^{-4}
47.6	4.0	4.5×10^{-6}
50.6	3.9	5.8×10^{-6}
	Av 4.0	

The temperature dependence of K is negative and very large, exceeding four orders of magnitude for a 10° interval. Such magnitudes are indicative of nucleation controlled processes. However, K is influenced by the nucleation and growth rates as well as by the growth mode of the transforming regions. In the absence of information about the magnitudes and temperature coefficients of the growth rates of the spherulites it is useless to speculate further about the meaning of the magnitude of K and its temperature coefficient. Work is currently in progress to measure the spherulitic growth rates as a function of temperature in this temperature region.

Cholesteric-Smectic Kinetics. This transformation is very mobile, taking place in a short time (*ca.* 5 min). Thus no large supercooling is possible. The largest supercooling which was feasible for this technique was about 3.5° . Figure 4 shows the corrected dependence of $F(t)$ on \log time at various constant crystallization temperatures.

In Figure 4 the results from the various runs for both samples A and B have been shifted to correspond to a run in which the temperature was 77.6° (a supercooling of 1°). For a given sample the curves are

(22) M. B. Rhodes, R. S. Porter, W. Chu, and R. S. Stein, *Mol. Cryst. Liq. Cryst.*, **10**, 731 (1970).

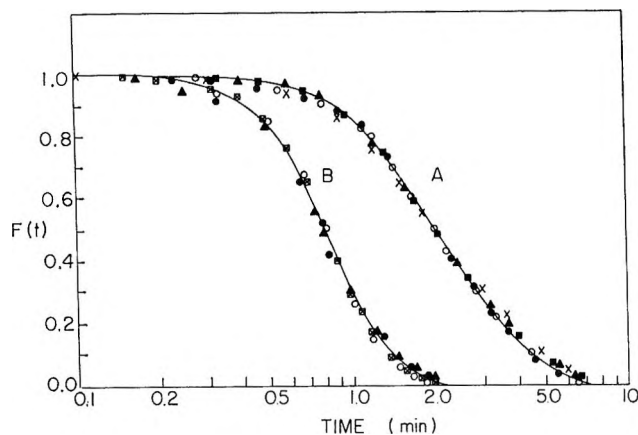


Figure 4. Plots of $F(t)$ vs. \log (time) for cholesteric-smectic transition. Data shifted to 1° supercooling, shift factor in brackets. Curve A, sample A: \times , 78.5° [0.45]; \bullet , 78.0° [0.65]; \circ , 76.9° [1.75]; \blacksquare , 76.0° [2.60]; \blacktriangle , 74.9° [3.70]. Curve B, sample B: \times , 78.2° [0.30]; \blacktriangle , 77.8° [0.70]; \circ , 77.5° [1.00]; \bullet , 76.9° [1.65].

essentially superposable. This indicates that in each sample a single transformation mechanism is operating over the temperature range studied. The set of normalized curves for sample B is steeper than and is not quite superposable upon the set for sample A. These observations indicate, first, that the values of K are larger for sample B than for sample A, and second, that the values of n differ slightly for the two samples. The figures in Table IV bear these contentions out. The results are summarized quantitatively in Table IV.

Table IV: Avrami Constants for the Cholesteric-Smectic Transition in Cholesteryl Myristate

$T, ^\circ\text{C}$	n	K, min^{-2}	
74.9	2.0	3.9×10^{-1}	sample A
76.0	1.9	2.7×10^{-1}	
76.9	2.0	2.0×10^{-1}	
78.0	2.0	1.4×10^{-1}	
78.1	2.0	6.4×10^{-2}	
	Av 2.0		
76.9	2.0	1.8	sample B
77.5	2.1	1.1	
77.8	2.1	5.5×10^{-1}	
78.2	2.1	9.1×10^{-2}	
	Av 2.1		

The quantity K in the Avrami equation contains a product of nucleation and growth rates. In the present transformation because both the cholesteric and the smectic states are quite mobile, it seems not unreasonable to assume that the growth rates are diffusion controlled and hence will not be very sensitive to temperature. In such an event the temperature dependence of K will be that of the nucleation rate and the magnitude and form of the temperature depen-

dence should permit some inferences to be drawn regarding interfacial energies and shapes of the developing nuclei. Classical nucleation theory²³ indicates that in this situation if the developing nuclei can enlarge in three dimensions, plots of $\ln K$ vs. $1/[T(\Delta T)^2]$ should be linear, while if the nuclei are disklike and can enlarge in radius but not in height, plots of $\ln K$ vs. $1/T(\Delta T)$ will be linear, provided the surface energy of the flat end surfaces is negligible compared to that of the cylindrical surfaces. The appropriate plots were made for the data in Table IV and whereas the plots of $1/T(\Delta T)^2$ showed appreciable curvature over their whole length, the plots of $1/T(\Delta T)$ were satisfactory straight lines so long as the transformation temperature was below 78.1° . When the transformation temperature was at or above this temperature, the observed values of K were much higher than those the extrapolation from the low-temperature values would indicate. Now, 78.1° is the lower end of the pretransition region for the smectic-cholesteric transition. Further, classical nucleation theory indicates that the slope of the $\ln K$ vs. $1/T\Delta T$ line should be $[\pi h \sigma^2 T_T]/[K \Delta H]$ where σ is the interfacial energy of the cylindrical surfaces of the disk, h is its height, T_T is the transition temperature (here 78.8°), and ΔH is the enthalpy per unit volume of this transition. Thus all other things being equal, the magnitude of K varies inversely in an exponential manner as $\sigma^2/\Delta H$. In the pretransition region as the temperature is raised, the value of ΔH must decrease (the two phases become more alike). Likewise σ must decrease. Now σ and ΔH arise from similar causes and so long as σ depends more strongly on those causes than does $(\Delta H)^{1/2}$, the value of $\sigma^2/\Delta H$ will decrease, thereby yielding an abnormally large K . Usually it is assumed that $\sigma \cong (1/3)\Delta H$ which would be ample to explain why the values of K at 78.1° and above are too large. Therefore, we feel justified in rejecting from consideration values of K obtained at temperatures of 78.1° and above and now turn to manipulation of the lower temperature data. By employing a value of the enthalpy of transition of 0.56 cal/g^{12} and assuming $h = 10 \text{ \AA}$ in the formulas indicated above, we calculate values of σ of 0.15 and 0.12 erg/cm² for samples A and B, respectively. It should be acknowledged that a value of $h = 10 \text{ \AA}$ is somewhat arbitrary. However, σ varies only as $(h)^{1/2}$ and, within wide limits, the choice of the size of h will not affect the calculated results sufficiently to vitiate the semiquantitative aspects of the conclusions. These values of interfacial energy are very small indeed. They reflect, first, the fact that only very small forces hold these systems together and, second, that even though the driving force for the transformation is very small, so

(23) F. P. Price, "Nucleation," A. C. Zettlemoyer, Ed., Marcel Dekker, New York, N. Y., 1970, Chapter 8.

also must the retarding forces be small for the transformation to progress at an appreciable rate. It is worth noting that the protrusions that form on the smectic phase structures called "batonets"⁷ also indicate similar small interfacial energies. Only with small interfacial energies will small fluctuations in shape be sufficiently unstable to grow to protrusions of observable size. Even though the slopes and hence the values of σ calculated therefrom are sensibly the same for both samples A and B, the absolute magnitudes of the K 's for sample B are 6 to 15 times those of sample A at the same supercoolings. Phenomenologically this means that the preexponential term in the expression for the nucleation rate is larger for sample B than for sample A. We have no satisfactory explanation why the additional recrystallization of sample B should produce this effect. The values of the radius of the critical sized nucleus obtained from $r = \sigma/\Delta H$ range from 60 to 250 Å depending on the sample and the supercooling. They depend on the choice of the magnitude of the disk height h only through σ and again so long as the value h is chosen in a reasonable range the conclusions will be at least semiquantitatively valid. Thus the picture that emerges is that the nuclei are disks. Since there is a nucleation rate, the value of $n \equiv 2$ must indicate rods increasing both in number and in length. Hence the disklike nuclei must elongate into rods as time progresses. Light scattering experiments are in progress to check this hypothesis.

Isotropic-Cholesteric Kinetics. This transformation is even more mobile than is the cholesteric-smectic one. It was therefore possible to obtain data only over a very limited temperature range. At 81.6° (2.2° supercooling), the half-time of the transformation was 1 min. Figure 5 shows, for both samples, the dependence of $F(t)$ upon log time. Here as in Figure 4 the data for the various runs have been shifted to a supercooling of 1° ($T = 82.8^\circ$). The curves for each sample are superposable and in addition the sets for the two samples are also superposable. Further, the shape of these curves is the same as that for sample A in Figure 4.

Table V: Avrami Constants for the Isotropic-Cholesteric Transition in Cholesteryl Myristate

$T, ^\circ\text{C}$	n	K, min^{-2}	
82.7	2.0	2.4×10^{-1}	sample A
82.1	2.0	3.7×10^{-1}	
81.6	2.0	4.9×10^{-1}	
	Av 2.0		
83.3	2.0	5.8×10^{-1}	sample B
82.9	1.9	2.5×10^{-1}	
82.4	1.9	1.4	
82.1	1.9	2.3	
	Av 1.9		

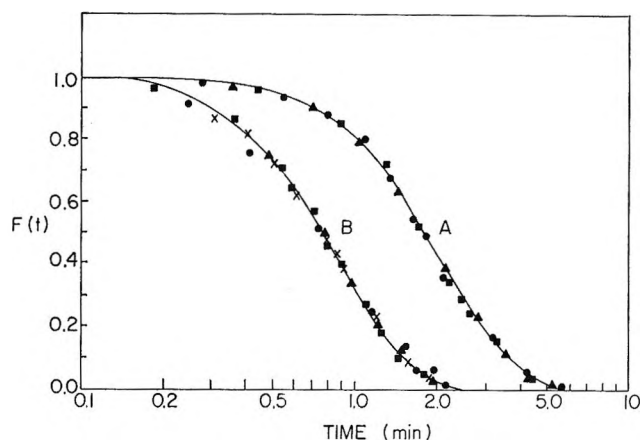


Figure 5. Plots of $F(t)$ vs. log (time) for the isotropic-cholesteric transition. Data shifted to 1° supercooling, shift factor in brackets. Curve A, sample A: ●, 82.7° [1.1]; ▲, 82.1° [1.7]; ■, 81.6° [2.2]. Curve B, sample B: ■, 83.3° [1.0]; ▲, 82.9° [0.9]; ×, 82.4° [1.4]; ●, 82.1° [1.7].

The quantitative aspects of these runs are summarized in Table V.

As in the case of the cholesteric-smectic transition, plots of $1/T(\Delta T)^2$ vs. $\ln K$ are not linear but plots of $1/T(\Delta T)$ are. Similarly, the values of K obtained at temperatures at the edge of the cholesteric-isotropic pretransition region are too large. The same rationalization arguments that were advanced in the smectic-cholesteric case are applicable here. Again it seems reasonable to assume the nuclei are disklike. Using a value of $\Delta H = 0.41 \text{ cal/g}^{12}$ and assuming $h = 10 \text{ \AA}$, values of σ , the cylindrical surface energy, were calculated from the slopes of the $\ln K$ vs. $1/T\Delta T$ plots. They were 0.09 and 0.16 erg/cm² for samples A and B, respectively. The radii of the critical size nuclei calculated from these energies range from 100 to 400 Å depending on the sample and the supercooling. It is worth noting that although in the cholesteric-smectic transition essentially identical values of σ were obtained for samples A and B, in the present case the value of σ for sample B is almost twice that for sample A. It is not clear why this should be the case.

Here in the case of the isotropic-cholesteric transformation as in the cholesteric-smectic transition, the nuclei appear to be disks. The number of disks increases with time and the disks grow into rods as the transformation proceeds.

Visual Observations of Cholesteric-Smectic Transition. This transition was observed using the microscope and the thermostated hot stage. Crossed polars were used. The sample was first brought into the cholesteric state, and the temperature was lowered as rapidly as possible to around 76° and to induce transition at the surface the cover slip was removed. The observed field became brighter; the low birefringence regional structure of the cholesteric state discussed below

changed to a spherulitelike pattern for a very short period. These patterns then changed very quickly to platelets, which grew very rapidly, perhaps because of the large supercooling. When the transition starts within the sample, no further observations can be made. It seems that this transition really involves nucleation and growth of ordered regions.

Visual Observations of the Isotropic-Cholesteric Transition. A number of investigators have noted that when this material is cooled from the isotropic into the cholesteric phase, a transparent blue fluid is formed.²⁴⁻²⁸ We have made, under well-defined time and temperature conditions, microscopical observations on this blue liquid. These studies were made using the thermostated hot stage described in the Experimental Section. At the beginning of each measurement the sample was heated to 95° for several minutes and then cooled within 2 min to a constant transformation temperature. This treatment always resulted, in the appearance, first of a blue color and then, after some time, in the appearance of whitish regions. In the initial stages of the process it was not very easy to detect these regions because they were of low birefringence and not very distinct. However, as time passed they became more and more distinct. Even so, their birefringence was not very high. Their shape and size did not appear to change with time. The regions seemed to appear nearly all at the same time. The diameter of these regions is about 0.003-0.005 mm. Figure 6 is a photomicrograph of a field of these regions. This photomicrograph shows the distribution in the whiteness and size of the regions. At somewhat lower temperatures white areas developed within the dark isotropic matrix and the whiteness of all regions increased. Even though these observations indicate significant birefringence, we believe this structure of low birefringence to lie within the blue range of other observers. Direct visual observations, discussed below, of samples in dilatometers undergoing the isotropic-cholesteric transition bear this out. At even lower temperatures near the cholesteric-smectic transition within the cholesteric state, strongly birefringent focal conic structures appear.

To determine whether the low birefringence structure arises from fixed points (predetermined nuclei), a sample was several times heated up to just above the melting point and then cooled down to a constant temperature within the cholesteric region. A comparison of the pictures taken after each run shows that there are differences in the structures which cannot be explained merely by a displacement caused by the volume changes during the melt followed by subsequent crystallization. This means that there is no significant number of pre-existing nuclei in the melt, even at temperatures just about the cholesteric-isotropic transition. Sometimes a different pattern was obtained which showed platelets of different shapes and sizes, which with time became

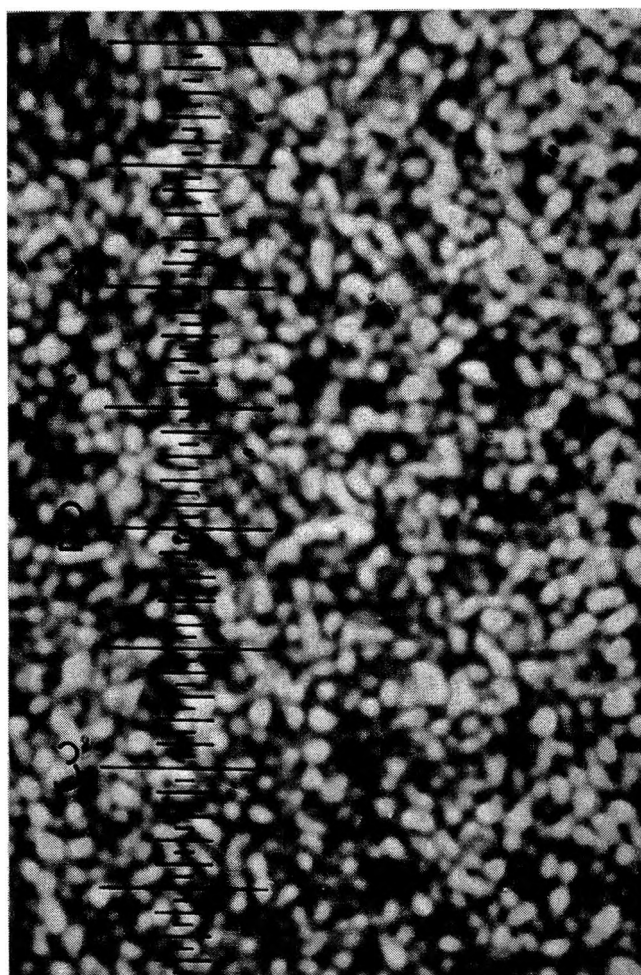


Figure 6. Photomicrograph of blue cholesteric phase; crossed nicols. Distance between numbered scale lines is 100 μ .

more and more distinct in the same way as the low birefringence pattern. These platelet patterns were obtained: (1) if the sample was heated up just to the formation temperature of the isotropic melt and then slowly cooled down to a temperature just below the transition temperature; (2) if the sample was cooled down from 95° to a temperature slightly above the melting point and then after some minutes to a temperature just below the transition temperature. After this treatment the platelet structure developed more easily in a thin layer and around added impurities, whereas in thick layers only very small and very few platelets could be observed with most of the sample showing the low birefringence structure. These results indicate significant influences of interfaces on the properties of cholesteryl myristate in the cholesteric state.

(24) Reference 7, pp 189, 190.

(25) A. Saupe, *Mol. Cryst.*, **7**, 59 (1969).

(26) J. L. Ferguson, N. N. Goldberg, and R. J. Nadalin, "Liquid Crystals," Gordon and Breach, New York, N. Y., 1966, pp 89, 105.

(27) G. Friedel, *Ann. Phys.*, **18**, 273 (1922).

(28) O. Lehmann, *Z. Phys. Chem.*, **56**, 750 (1906).

We have also made direct visual observations of the transformation taking place in a dilatometer. Here, if the sample is heated up from the smectic into the cholesteric phase, the sample is turbid and white. In heating to higher temperatures within the cholesteric state the white turbid modification vanishes at 83.0°, giving rise to the blue transparent modification. The change of modifications is not accompanied, as is shown by Figure 2, by detectable change in the volume nor of the expansion coefficient. On cooling the sample at a constant rate of about 1°/hr within the cholesteric state the transition from the blue to the turbid state takes place between 79.5 and 79.0°. If, however, the sample is cooled stepwise with sufficient time being allowed at each temperature, the transition appears to be reversible and to have a transition temperature of 83.0°. Stirring and shaking at temperatures between 83 and 80° facilitates the transformation to the turbid state; above 83° the transition cannot be thus induced. The first of these effects has been known for

many years;²⁸ the second effect has never been reported. The transition temperature of 83° was observed for both samples A and B and thus appears to be independent of both purification processes and dilatometers. It then appears that the 83° is actually a transition temperature (although without detectable changes in volume or expansion coefficient) for a reversible change in texture but not a change in structure. To our knowledge this is the first observation of a texture transition that is reversible with temperature. Texture changes are usually irreversible and undoubtedly the reversibility here observed is the result of the very small forces holding the molecules in the arrangement characteristic of the cholesteric state.

Acknowledgment. The authors wish to express their gratitude to Professor R. S. Stein and Professor R. S. Porter for much helpful discussion during the course of this study. Thanks are also due to Mr. R. Ulrich for assistance with the microscopy.

Transitions in Mesophase Forming Systems. II. Transformation

Kinetics and Properties of Cholesteryl Acetate¹

by Fraser P. Price* and Joachim H. Wendorff

Polymer Research Institute, University of Massachusetts, Amherst, Massachusetts 01062 (Received January 13, 1971)

Publication costs assisted by the National Institutes of Health

The equilibrium density-temperature relationships of several crystalline phases of cholesteryl acetate have been studied with precision dilatometry. The solid SI formed from the isotropic liquid between 94 and 107° shows a broad (20°) premelting range. Another solid SII is formed from the cholesteric state between 41 and 91°. This solid is less dense than SI to which it transforms upon heating above 90°. Also solid II reversibly transforms to another solid SIII at about 40° with a volume change of 0.5%. Solid III can be formed directly by transformation from the cholesteric state below 40°. The cholesteric state has a transient existence which permitted a rough delineation of its volume-temperature behavior between only 80 and 92°. It has, in common with the other cholesteric states, an expansion coefficient exceeding that of the isotropic liquid of the same compound. The kinetics of the isotropic-cholesteric transformation were too rapid to be measured, but those of the cholesteric-solid SII were studied. Analysis of the cholesteric-SII transformation in terms of the Avrami equation gave an n of 4 and values of K ranging from 10^{-1} to 10^{-3} between 80 and 90°. This indicates sporadic nucleation of spheres.

Introduction

The esters of cholesterol are a class of compounds which exhibit mesophase behavior. That is, they can exist in a number of stable phases whose order is intermediate between that of the crystalline solid and the isotropic liquid. We are concerned with delineating by means of a precise technique, dilatometry, the density

differences and the kinetics of transformation among these phases. The first paper in this series dealt with cholesteryl myristate.² Myristic acid, a long saturated fatty acid, lies in length near the middle of the available

(1) Supported by Grant No. HE13188 from the National Institutes of Health.

(2) F. P. Price and J. H. Wendorff, *J. Phys. Chem.*, **75**, 2839 (1971).

acid moieties of the cholesteryl esters. Since we are interested in studying the effect of structure upon the behavior of liquid crystals, cholesteryl acetate is a rational choice for the next investigation, and it is with this ester that the present paper is concerned. In cholesteryl myristate, both the mesophases, smectic and cholesteric, are enantiotropic. In cholesteryl acetate, there is no smectic phase and the cholesteric phase is monotropic. In addition, this ester has been shown to have several solid crystalline states.³

This paper presents the results of studies of equilibrium density-temperature relationships among the several phases. The results of kinetic studies of the transformation into the solid state are also given. The rate of transition into the cholesteric state is too rapid to be amenable to study by the techniques employed.

Experimental Section

Samples of cholesteryl acetate were obtained from the Eastman Kodak Co., Rochester, N. Y. They were purified by a single recrystallization from *n*-pentyl alcohol, as described in the first paper of this series.²

The experimental and computational techniques used in the present study were the same as those described in the previous paper.² Calorimetry was the only new technique employed here. Measurements were made in a differential scanning calorimeter, DSC-1, Perkin-Elmer Corp., Norwalk, Conn. The heating rates and cooling rates were varied between 0.625 and 80°/min. The calorimeter was calibrated using the heat of transition of cholesteryl acetate as determined by Barrall, *et al.*⁴ Before each measurement, the sample was annealed at 120° for 4 hr. The precision of measurements made with this instrument has been described elsewhere.⁴

Results and Discussion

We will first consider the equilibrium volume-temperature relationships in the various crystalline solid states. These states are attained by crystallization from the liquid in appropriate temperature regions.

In the first experiment, prior to measurement, the sample was heated to 120° for 25 hr in an attempt to assure reproducibility. This was done because studies on cholesteryl myristate² have shown a strong dependence of the properties of the resulting crystalline solid on the temperature and time of annealing. It eventually turned out that with cholesteryl acetate an annealing time of 4 hr at 120° was sufficient to obtain reproducible results.

Solid (SI). If the sample was cooled down from 120° to a constant crystallization temperature between 94 and 107°, crystallization took place after an induction period. This period decreased with decreasing crystallization temperature. The crystals were nucleated, and their growth took place from the isotropic liquid rather than the cholesteric state. This was

proved by the water-white clarity of the sample and by the mercury level before transformation. This level was that obtained by linear extrapolation of the isotropic state to the crystallization temperature. The crystals formed after long times at various temperatures in this region (94–107°) had identical density-temperature behavior regardless of the temperature of preparation. This indicates that only one solid phase (SI) is attained from the isotropic liquid in this temperature regime. If this solid was cooled to room temperature, no change of the density or of the thermal expansion coefficient was observed after 4 days. A like treatment at 60° also showed no change of these properties. The equilibrium density-temperature behavior of this phase is plotted in Figure 1. This phase shows a broad

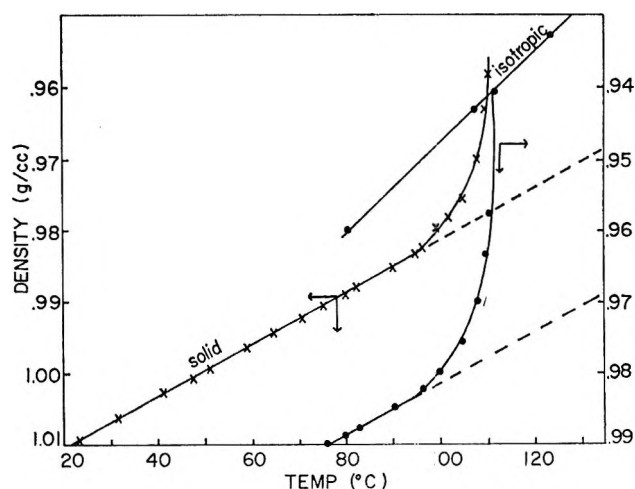


Figure 1. Equilibrium density-temperature curves for cholesteryl acetate solid SI.

melting region of about 20°, the high temperature limit of which is 112°. If this broad melting region arises from impurities, the van't Hoff equation can be used to determine the amount of these impurities.

The results presented in Figure 1 do not conform to the van't Hoff equation. Other investigators have found that it is not possible to interpret the dependence of molten fraction on temperature by means of the van't Hoff equation.⁵ In fact, we have pointed out in a previous paper² that this melting region can be a property of the pure sample itself. If it is assumed that previous to the transition to the isotropic state an intracrystalline decrease in order takes place, for instance by the transfer of molecules from lattice points to places between lattice points, the change of density

(3) (a) E. M. Barrall II, R. S. Porter, and J. F. Johnson, *J. Phys. Chem.*, **70**, 385 (1966); (b) G. E. H. Hellwig and A. W. Neumann, *Kolloid Z.*, **229**, 40 (1969).

(4) E. M. Barrall, II, R. S. Porter, and J. F. Johnson, *J. Phys. Chem.*, **71**, 895 (1967).

(5) B. J. Bulkin and D. Grunbaum in "Liquid Crystals and Ordered Fluids," R. S. Porter and J. F. Johnson, Ed., Plenum Press, New York, N. Y., 1970, p 303.

or relative volume can be interpreted by means of the equation⁵

$$F = \exp[-(A/R)((1/T) - (1/T_0))] \quad (1)$$

Here F is the fraction of the sample transformed, T is the temperature ($^{\circ}\text{K}$), T_0 is the transition temperature ($^{\circ}\text{K}$), and A is an energy.

The results displayed in Figure 1 do conform to eq 1 with significant deviations only at the high-temperature end of the transformation. Such deviations have been found by others.^{6,7} The slope of the $\ln F$ vs. $1/T$ plot yields an energy of 64.7 kcal/mol.

It is, as noted in the previous paper,² of course possible that impurities, too, have an influence on the melting properties of the sample. The major effect, however, seems to be due to a disordering process of the type outlined above.

Solid (SII). If a cholesteryl acetate sample is cooled from above 112° down to a temperature between 41 and about 91° , a second solid phase (SII) is formed. This solid has a lower density and a slightly smaller thermal expansion coefficient than the solid phase SI. That over all this temperature region only one solid is formed is indicated by the identical density and thermal expansion behavior of samples crystallized at various temperatures. The equilibrium dependence of density upon temperature for SII is shown in Figure 2 and Table I. Prior to the growth of crystals of SII, a transition from the isotropic state to the cholesteric state takes place. This is proved by a change of the sample from water-white to colored (green to red, depending on the temperature), and by a halt in the contraction of the sample. This halt is at a volume that is smaller than that obtained by extrapolation of the volume of the isotropic liquid to the crystallization temperature. The temperature dependence of the density of the cholesteric state as determined by these halts is shown in Figure 3 and in Tables I and II. Apparently the cholesteric state is not very stable, for between 80 and 90° , the system remains in this state for only a short time before transforming to the crystalline solid, SII. The length of time of dwell in the cholesteric state decreases with decreasing temperature, and at temperatures below 80° , there is no halt in the contraction of the sample. Crystallization still takes place from those regions which have become cholesteric as evidenced by the transient colors appearing prior to the formation of the turbid crystalline phase. It is worth noting that here, as in the case of cholesteryl myristate, the coefficient of thermal expansion of the cholesteric state exceeds that of the isotropic liquid. This indicates that the ordering of the cholesteric state increases more rapidly with decreasing temperature than does the ordering of the isotropic liquid.

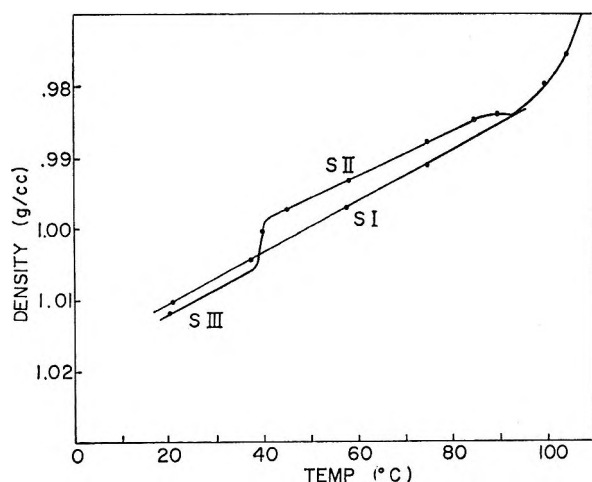


Figure 2. Equilibrium density-temperature curves for cholesteryl acetate solids SI, SII, and SIII.

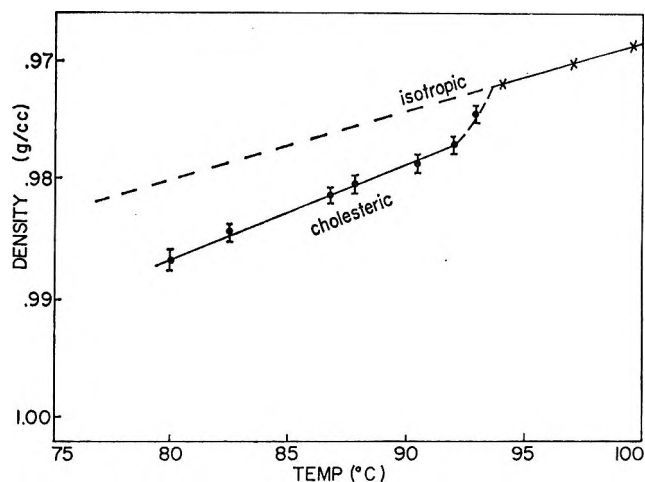


Figure 3. Density-temperature behavior of the cholesteric phase of cholesteryl acetate.

parently the cholesteric state is not very stable, for between 80 and 90° , the system remains in this state for only a short time before transforming to the crystalline solid, SII. The length of time of dwell in the cholesteric state decreases with decreasing temperature, and at temperatures below 80° , there is no halt in the contraction of the sample. Crystallization still takes place from those regions which have become cholesteric as evidenced by the transient colors appearing prior to the formation of the turbid crystalline phase. It is worth noting that here, as in the case of cholesteryl myristate, the coefficient of thermal expansion of the cholesteric state exceeds that of the isotropic liquid. This indicates that the ordering of the cholesteric state increases more rapidly with decreasing temperature than does the ordering of the isotropic liquid.

Table I: Volume Expansion Coefficients of the Phases of Cholesteryl Acetate

Temperature range, $^{\circ}\text{C}$	Phase	$\alpha \times 10^4$, $^{\circ}\text{C}^{-1}$
25-90	SI	3.7
25-40	SIII	3.7
40-90	SII	3.1
80-92	Cholesteric	9.4
95-120	Isotropic	6.8

If solid phase SII is heated up to temperatures above 90° , there is observed, over a range of several degrees, a transition to the solid phase SI. When crystallization from the isotropic liquid is carried out in the range of 90 - 94° , the final densities attained are identical with those obtained by heating the solid SII to the same

(6) A. Kofler, *Arch. Pharm.*, **8**, 281 (1943).

(7) I. G. Chistyakov, *Sov. Phys. Cryst.*, **5**, 917 (1961); **8**, 57 (1963).

Table II: Transition Volume Changes among the Phases of Cholesteryl Acetate

Transition	Temp, °C	Volume change, %
SI-isotropic	95	4.1
Cholesteric-isotropic	92	0.6
SI-SII	90	0.08
SII-SIII	40	0.5

temperature. It is not possible to decide whether the crystallization from the isotropic state proceeds by crystallization to solid phase SII with a subsequent partial transition to SI or whether the transitions to SI and SII proceed simultaneously.

If after heating a sample in phase SII to above 95° the sample is cooled, the behavior characteristics of SI are found. Here again, no further change in specific volume was found in 4 days at room temperature. It thus appears that SII is metastable with respect to SI and, if heated to temperatures of 90 to 95°, will spontaneously transform to the more stable SI.

Solid (SIII). If the crystallization was done at temperatures between room temperature and about 40°, a third solid phase, SIII, was observed with a density slightly higher than that of the solid phase SI and with about the same thermal expansion as the solid SI. This behavior is summarized in Tables I and II. The crystallization again takes place from the cholesteric state. If this solid phase is heated to 40°, a transition to the solid SII is observed. This transition is reversible. In like manner, the solid SII which has been obtained by a crystallization between 40 and 90° shows a reversible transition to the solid SIII. No transition was observed between the solid SIII and either of the other solid phases after 4 days at room temperature. After heating the sample to temperatures above 90°, only the solid SI was observed at all temperatures.

There are some indications that at crystallization temperatures below room temperature or even at room temperature the solid SIII is no longer formed. At these low temperatures, the value of the density is between that of solid III and solid I. On heating to temperatures above 40° the density is slightly higher than the density of the solid SII. Since the crystallization takes place at these low temperatures within a very short time, a change in mechanism could perhaps not be observed, because the crystallization takes place during the process of cooling to the crystallization temperature.

The quantitative aspects of the equilibrium density-temperature behavior are summarized in Tables I and II.

X-Ray Studies. Diffraction patterns were obtained from solids SI to SIII at room temperature. The "d"

Table III: Room Temperature "d" Spacings of Solids I and III of Cholesteryl Acetate

Distance, Å	Solid I	Solid III
35.3	vs	vs
18.4	vs	vs
12.0	w	w
6.55	w	w
5.84	vs	vs
5.43	s diffuse	s sharp
4.93	s	s
4.72	} one broad ring	s } triplet, sharp
4.63		
4.33	Not observed	vw
4.02	vw	vw
3.82	w	w
2.97	w	w

spacings calculated from these patterns are shown in Table III.

The diffraction patterns were complete rings which indicates that there was no preferred orientation of the crystals. One sample was cooled down from 120 to about 70° in a thin layer to allow for a rapid change of the sample temperature. The X-ray pattern at 28° (room temperature) of this sample showed the same spacings as did the X-ray pattern of the solid SI shown in Table III. The diffuse rings of the solid I show a certain amount of disorder in two spatial orientations. This is consistent with the interpretation of the broad melting region being due to pretransition effects. More refined X-ray diffraction studies are now in progress to more fully explore the pretransition effects on the solid SI-isotropic transition.

DSC Studies. As the cholesteric state persists only for a very short time before crystallization starts, it is not very easy to measure the heat of transition for the isotropic-cholesteric transition. However, by cooling at rates between 80 and 40°/min, it was possible to obtain a rough estimate of the heat of transition. At lower cooling rates a superposition of the isotropic-cholesteric transition peak and the cholesteric-solid transition peak occurred. The average value of the heat of transition, determined from six measurements at various cooling rates, is 0.59 ± 0.01 cal/g. This value is in good agreement with those obtained for the isotropic-cholesteric transitions in other cholesteryl esters.⁸ No heat was observed for the transition, solid II-solid I and solid III-solid II. This could mean that the heats of transition are very small. It could also mean that these transitions are not first order.

Kinetic Studies (Range 107-94°). In this temperature range the crystallization takes place after an induction period which decreases with decreasing temperature.

(8) G. J. Davis, R. S. Porter, and E. M. Barrall, II, *Mol. Cryst. Liq. Cryst.*, **10**, 1 (1970).

The crystallization times after the induction period were 14, 8, and 3 min at supercoolings of 7.0, 13.5, and 17°, respectively, while the crystallization times for the myristate were 35, 20, and 15 min at supercoolings of 5.5, 11.0, and 15.5°, respectively. Thus at comparable supercoolings in this temperature range the acetate crystallizes more rapidly than does the myristate. In addition, the induction times of the acetate are shorter than those of the myristate. The crystallization starts from a few points near the dilatometer wall. The number of crystalline regions depends on the crystallization temperature and the dilatometer. The crystallization rate measured under these conditions is also influenced by the geometry of the dilatometer. We have already discussed this problem in the paper which dealt with cholesteryl myristate.² In both the myristate and the acetate transformations, it is clear that the nucleation is heterogeneous, starting at the walls. This, in addition to the large size and small number of transforming regions, precludes rational use of the Avrami⁹ equation in describing the crystallization of cholesteryl acetate in this temperature region.

Kinetic Studies below 90°. In this temperature range the transformation to the crystalline solid state always takes place from the cholesteric state even though the system was initially in the isotropic liquid state. The isotropic-cholesteric transformation is so rapid that no useful kinetic measurements could be made. The presence of the cholesteric state was always indicated by the appearance of color. Between 80 and 90°, the isotropic-cholesteric transformation was sufficiently slow that the rate of volume decrease showed a halt. It was this halt which permitted establishment of the curves in Figure 3. As the temperature decreased, the rate of the isotropic-cholesteric transformation increased as did the rate of the cholesteric-solid transformation. At temperatures below 80°, there was no halt in the rate of volume decrease to indicate the cholesteric state, but its presence was shown by transient colors. It is clear that the cholesteric state is always quite metastable, but the barrier to transformation to the crystalline solid decreases sufficiently rapidly with temperature so that below 80° the cholesteric state has only a very evanescent existence. Figure 4 shows plots of $F(t)$, the fraction untransformed, vs. log (time) for the cholesteric-solid transformation at various temperatures. In these plots, at the three higher temperatures it was possible to correct for the initial formation of the cholesteric state, and in these the curves all have the same shape. In the run at 67.5° the correction was not possible, and the curve shows a much smaller slope. In Table IV are displayed for the three highest temperatures the constants n and K from the Avrami equation.^{2,9} At temperatures below 79°, Avrami kinetics are unapplicable.

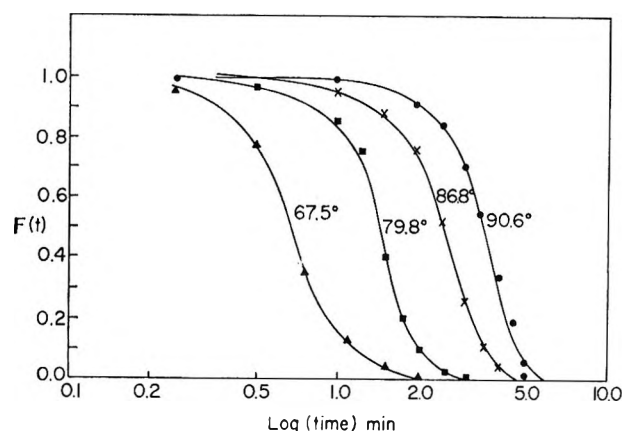


Figure 4. Plots of $F(t)$ vs. log (time) for the transformation to crystalline (SII) cholesteryl acetate at several temperatures.

Table IV: Avrami Constants for the Cholesteric-Solid Transformation in Cholesteryl Acetate

T , °C	Super-cooling	n	K , min^{-4}
79.8	32.2	4.0	1.4×10^{-1}
86.8	26.2	4.0	1.4×10^{-2}
90.6	21.4	4.0	3.7×10^{-3}

Here, as in the case of the myristate, the value of n is 4, which indicates random nucleation of spheres. However, in the absence of morphological data, it is not profitable to explore this area further at the present time.

The Avrami K 's for the comparable transformation in cholesteryl myristate² are 5.3×10^{-6} , 4.5×10^{-5} , 3.9×10^{-4} , and 1.2×10^{-2} at supercoolings of 20, 23, 25, and 30°, respectively. Comparison of these figures with those of Table IV shows that the transformation at the same degree of supercooling is faster in the case of cholesteryl acetate than in the case of cholesteryl myristate. However, the temperature dependence of K is greater for the myristate. Again in the absence of morphological information or data on the rates of nucleation or growth of the transforming regions, it does not appear profitable to speculate upon the underlying reasons for the difference between the acetate and the myristate. Suffice it to state that microscopical studies are underway to delineate both the morphology and growth rates of the transforming regions.

Acknowledgments. The authors wish to express their gratitude to Professors R. S. Porter and R. S. Stein for much helpful discussion during the course of this study. Thanks are also due to C. W. Griffen for help with the DSC measurements.

(9) M. Avrami, *J. Chem. Phys.*, **7**, 1103 (1939); **8**, 212 (1940).

The Radiolysis of Liquid *n*-Butane

by Noboru Fujisaki, Shoji Shida,* Yoshihiko Hatano, and Kuniyasu Tanno¹

Laboratory of Physical Chemistry, Tokyo Institute of Technology, Meguro-ku, Tokyo, Japan (Received March 8, 1971)

Publication costs borne completely by The Journal of Physical Chemistry

The effects of radical scavenger (O_2) and electron scavenger (SF_6) on the yields of C_1 - C_4 products formed in the radiolysis of liquid *n*-butane at 0° have been examined. Furthermore, the isotopic analysis of hydrocarbon products, methane, ethane, ethylene, and propane, formed in the radiolysis of equimolar mixtures of n - C_4H_{10} - n - C_4D_{10} have been made in the presence and absence of the scavengers. It is shown that some 60% of methane formed from *n*-butane containing $0.02 M O_2$ is produced by bimolecular processes, the formation of which is interpreted in terms of the hydrogen abstraction of hot methyl radicals. By assuming that the isotopically mixed ethanes and propanes from n - C_4H_{10} - n - C_4D_{10} - $0.02 M O_2$ systems represent products formed by ion-molecule reactions, the yields of fragment ions, $C_2H_4^+$, $C_2H_5^+$, n - $C_3H_7^+$, *sec*- $C_3H_7^+$, and $C_3H_6^+$, have been estimated. These yields are generally small ($G \leq 0.2$) and suggest that the fragmentation of the parent ions does not occur extensively in the liquid-phase radiolysis of *n*-butane. The fact that the G value of nitrogen formed from n - C_4H_{10} -($0.08 M$) N_2O decreased from 3.5 to 2.5 upon the addition of $0.22 M O_2$ suggests that oxygen of high concentrations scavenges electrons as well as free radicals in irradiated liquid alkanes.

I. Introduction

Recently, great advances have been made in our understanding of the radiolysis of hydrocarbons. However, concerning the radiolysis of hydrocarbons in the liquid phase some important problems still remain obscure.² On the fragmentation of the parent ions in the liquid phase Scala and Ausloos^{3a} and Koob and Kevan^{3b} studied, respectively, the radiolyses of 2-methylbutane and propane using perdeuterated compounds, and Tanno, Miyazaki, and Shida the radiolyses of propane,⁴ isobutane,⁵ isopentane,⁵ 2,3-dimethylbutane,⁵ neopentane,⁶ and 2,2,4-trimethylpentane⁶ by using charge scavengers. From these studies it is now clear that the fragmentation of parent ions is much smaller in the liquid phase than in the gas phase. The determination of the yields of fragment ions in the liquid phase, however, cannot be said to be satisfactorily quantitative. The reasons are, for example: (i) the possibility that the neutralization of fragment ions with electrons occurs simultaneously with the hydride-ion transfer reaction with parent alkane molecules,⁵ and (ii) the possibility that the hydrogen abstraction of hot radicals or the recombination and disproportionation reaction of free radicals in spurs can be alternative to the hydride-ion transfer reaction as nonscavengeable and bimolecular processes. Although the present study has never resolved these problems unequivocally, it was carried out with the hope that cumulation of such small advances as this could reveal the factors governing the fragmentation of parent ions in the liquid phase.

n-Butane was judged to be a suitable compound for the present purpose, since information is available concerning the fragmentation of parent ions from radiolytic^{7,8} and mass spectrometric studies⁹⁻¹² carried out in the gas phase. In connection with the previous work

on the hydrogen formation from liquid *n*-butane,¹³ an attempt was also made to explore the mechanism of formation of butenes as the counterpart of hydrogen.

II. Experimental Section

n-Butane used in this study was obtained from Taka-chiho Trading Co., and used after the usual degassing and trap-to-trap distillations. Gas chromatographic analysis of the *n*-butane showed only 0.001% isopentane as major impurity so that it could be used without any further purification. Perdeuterated *n*-butane was prepared by exhaustive reduction of perdeuterated 1,3-butadiene, supplied from Merck of Canada, with D_2 .¹³ The perdeuterated butane was first purified by introducing small quantities of the material on a homemade gas chromatograph with a benzyl ether column. The material trapped from the helium stream was subse-

- (1) Deceased.
- (2) For a review see: R. A. Holroyd in "Fundamental Processes in Radiation Chemistry," P. Ausloos, Ed., Interscience, New York, N. Y., 1968, Chapter 7.
- (3) (a) A. A. Scala and P. Ausloos, *J. Chem. Phys.*, **47**, 5129 (1967); (b) R. D. Koob and L. Kevan, *Trans. Faraday Soc.*, **64**, 706 (1968).
- (4) K. Tanno and S. Shida, *Bull. Chem. Soc. Jap.*, **42**, 2128 (1969).
- (5) K. Tanno, S. Shida, and T. Miyazaki, *J. Phys. Chem.*, **72**, 3496 (1968).
- (6) K. Tanno, T. Miyazaki, K. Shinsaka, and S. Shida, *ibid.*, **71**, 4290 (1967).
- (7) R. P. Borkowski and P. Ausloos, *J. Chem. Phys.*, **39**, 818 (1963).
- (8) T. Miyazaki, S. Arai, S. Shida, and S. Sunohara, *Bull. Chem. Soc. Jap.*, **37**, 1352 (1964).
- (9) B. Steiner, C. F. Giese, and M. G. Inghram, *J. Chem. Phys.*, **34**, 189 (1961).
- (10) W. A. Chupka and J. Berkowitz, *ibid.*, **47**, 2921 (1967).
- (11) V. Čermák and Z. Herman, *Collect. Czech. Chem. Commun.*, **30**, 169 (1965).
- (12) D. Beck and A. Niehaus, *J. Chem. Phys.*, **37**, 2705 (1962).
- (13) S. Shida, N. Fujisaki, and Y. Hatano, *ibid.*, **49**, 4571 (1968).

quently reintroduced on a 3-m activated alumina column in order to remove the last traces of hydrocarbon impurities. After the gas chromatographic purification, the butane was further purified by low-temperature trap-to-trap distillations. Gas chromatographic analysis of the butane showed that it had sufficient purity and was useable without any further purification. Mass spectrometric analysis indicated that the *n*-butane-*d*₁₀ contained 5.5% *n*-butane-*d*₉. Sulfur hexafluoride (>98.0%), nitrous oxide (>99.9%), and oxygen (>99.9%) were used as received.

The irradiation of the butane was carried out in Pyrex sample tubes (6 cm long, 0.3 cm i.d.) fitted with break-off tips. The tubes, which were attached to a vacuum line, were filled with about 0.25 ml of *n*-butane. The volume of the vapor phase above the liquid level in these sample tubes is estimated to be about 0.20 ml. The *n*-butane-O₂ mixtures were prepared by condensing *n*-C₄H₁₀ into the sample tube at -196°, and subsequently introducing a certain amount of oxygen, which has vapor pressure of 165 mm at -196°. The solubilities of additives at 0° in *n*-butane were calculated by using the Ostwald absorption coefficients of sulfur hexafluoride (1.3),¹⁴ nitrous oxide (3.5),¹⁴ and oxygen (0.34)¹⁵ in cyclohexane. The samples were irradiated by ⁶⁰Co γ rays at a dose rate of 4.76×10^{19} eV/g hr. The dose rate was determined by Fricke dosimetry using $G(\text{Fe}^{3+}) = 15.6$. For the thin sample tubes used here the $G(\text{Fe}^{3+})$ may be somewhat smaller than the usual value on account of the wall effect, but the correction for it was not made. Unless otherwise specified, samples were irradiated to a total dose of 1.67×10^{20} eV/g.

The hydrocarbon products were analyzed with a Shimadzu GC-1C gas chromatograph with a flame ionization detector. A 3-m activated alumina column was used at 60° for the separation of C₁-C₄ hydrocarbons except 1-butene, whose peak overlapped with that of *trans*-2-butene. When necessary, products, ethane, ethylene, and propane, were separately trapped at -196° for isotopic analysis after emerging from an activated alumina column. The separation of ethane from sulfur hexafluoride was performed by a 3-m Chromosorb 104 column in place of an activated alumina column by which the two peaks were not separated. After removing the helium, the products were introduced into a Hitachi RMU-5 mass spectrometer. Methane was collected at -196° for the isotopic analysis with a Toepler pump, together with hydrogen and oxygen which were oxidized or reduced completely in a copper oxide-copper furnace kept at 250°. The same technique as described above was applied to measure the yield of nitrogen from the C₄H₁₀-N₂O-O₂ system.

The isotopic analyses of methane, ethane, ethylene, and propane were based on the reference mass spectra obtained as follows: methane, CD₄ and CH₄ from pure samples, CD₃H, CD₂H₂, and CH₃D from the literature;¹⁶ ethane, C₂D₆ and C₂H₆ from pure samples,

C₂D₅H, C₂D₄H₂, C₂D₃H₃, C₂H₅D₂, and C₂H₅D from mass spectra obtained by Amenomiya and Pottier;¹⁷ ethylene, C₂D₄ and C₂H₄ from pure samples, C₂D₃H and C₂H₃D from the literature.¹⁸ Propane, C₃D₈ from pure sample, CD₃CDHCD₃, CD₃CD₂CD₂H, and CD₃-CDHCD₂H from mass spectra obtained by Ausloos, *et al.*¹⁹ The relative yield of propane lighter than C₃D₆H₂ could not be determined, since the structure of the propane-*d*₆ cannot be specified, and the cracking patterns of some of the isomeric propane containing five, four, or three D atoms are not available. However, it can be said that the structure of C₃D₆H₂ consisted mainly of CD₃CDHCD₂H.

III. Results

The 100-eV yields of products from pure *n*-C₄H₁₀ are independent of dose between 5×10^{19} and 3.3×10^{20} eV/g, as shown in Figure 1, except those of olefinic products, which begin to exhibit a slight dose dependence within this dose range. The effect of oxygen on the product yields at dose of 1.67×10^{20} eV/g is shown in Figure 2. It is seen that a sharp decrease in yield of each product at low oxygen concentration (~ 0.005 M)

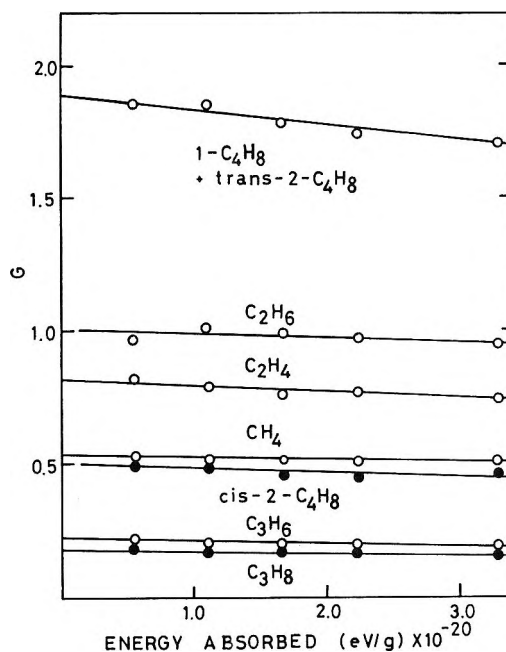


Figure 1. Product yields as a function of dose for irradiated liquid *n*-butane at 0°.

(14) T. Saito, K. Takahasi, and S. Sato, *Bull. Chem. Soc. Jap.*, **41**, 2603 (1968).

(15) S. Sato, private communication.

(16) F. L. Mohler, V. H. Dibeler, and E. Quinn, *J. Res. Nat. Bur. Stand.*, **61**, 171 (1958).

(17) Y. Amenomiya and R. F. Pottier, *Can. J. Chem.*, **46**, 1735 (1968).

(18) V. H. Dibeler, F. L. Mehler, and M. de Hemptinne, *J. Res. Nat. Bur. Stand.*, **53**, 107 (1954).

(19) A. A. Scala, S. G. Lias, and P. Ausloos, *J. Amer. Chem. Soc.*, **88**, 5701 (1966).

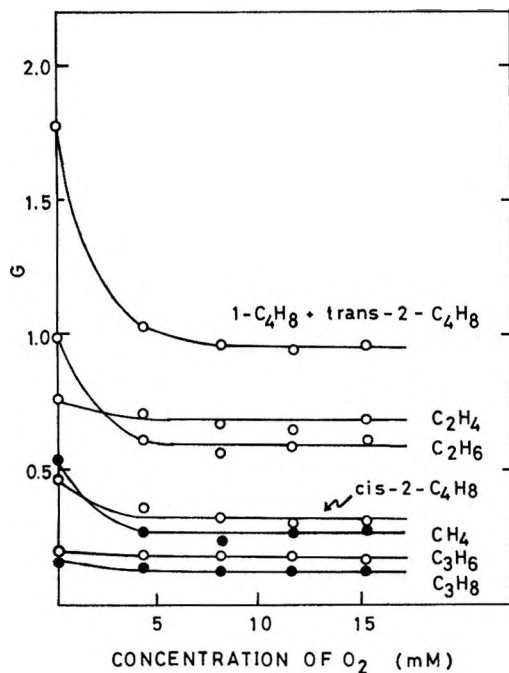


Figure 2. Effect of oxygen on the product yields from liquid *n*-butane at 0°.

is followed by gradual decrease with increasing concentration of oxygen. It should be noted here that the typical radical recombination products such as 3-methylpentane were reduced below the limit of detection, when 0.02 *M* O₂ is added. The effect of sulfur hexafluoride on the product yields is shown in Figure 3, in which the *G* values of products do not attain plateau values even at the highest concentration of SF₆ employed (~0.5 *M*). It is worth noting that in Figure 3 the yield of propane increases upon the addition of SF₆ by about 25%. This increase is attributed to the enhanced hydride-ion transfer reaction of C₃H₇⁺ which otherwise undergoes neutralization with electron to give propylene. Figure 4 shows the variation of product yields from *n*-butane containing 0.4 *M* SF₆ as a function of oxygen concentration. The experimental results on the product yields in the presence and absence of the

Table I: The *G* Values of Products Formed in the Radiolysis of Liquid *n*-C₄H₁₀^{a,b}

Additive	None	O ₂ ^c	SF ₆ ^d	O ₂ ^c + SF ₆ ^d
Methane	0.52	0.27	0.41	0.21
Ethane	0.99	0.58	0.48	0.35
Ethylene	0.78	0.67	0.22	0.24
Propane	0.16	0.12	0.20	0.17
Propylene	0.20	0.18	0.05	0.04
<i>trans</i> -2-Butene + 1-butene	1.80	0.95	0.75	0.10
<i>cis</i> -2-Butene	0.46	0.32	0.28	0.18

^a Dose, 1.67 × 10²⁰ eV/g. ^b Irradiation temperature, 0°. ^c Concentration of O₂, 0.02 *M*. ^d Concentration of SF₆, 0.4 *M*.

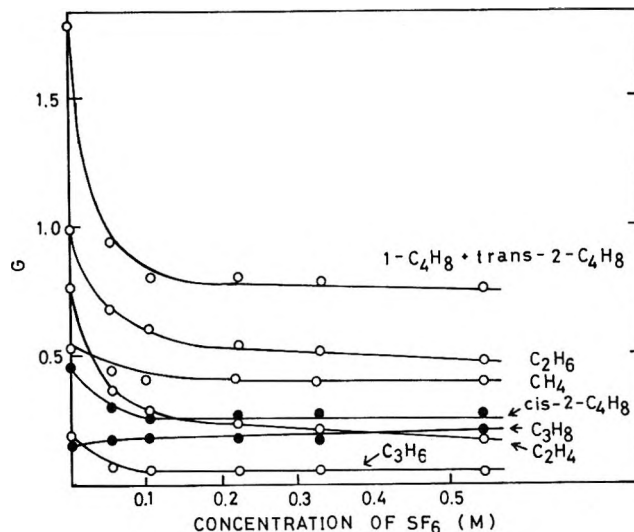


Figure 3. Effect of sulfur hexafluoride on the product yields from liquid *n*-butane at 0°.

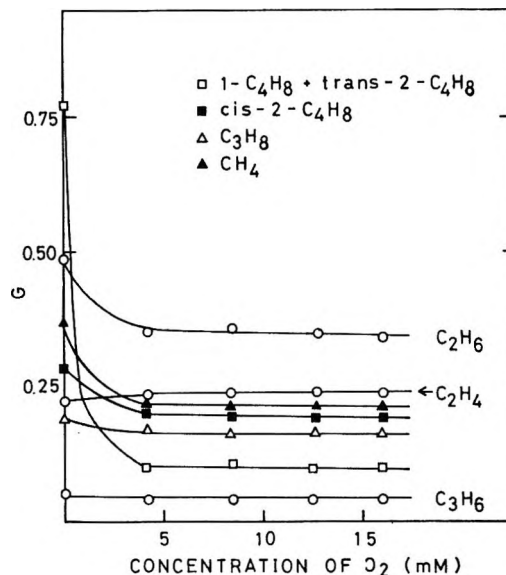


Figure 4. Effect of oxygen on the product yields from liquid *n*-butane containing 0.4 *M* SF₆.

Table II: The Effect of Oxygen on the Yields of Nitrogen from Solutions of Nitrous Oxide in *n*-Butane

N ₂ O, <i>M</i>	O ₂ , <i>M</i>	<i>G</i> (N ₂)
0.08	0	3.5
0.08	0.02	3.5
0.08	0.22	2.5
0.08	0.27	2.4

scavengers are tabulated in Table I. Table II shows that the nitrogen yield from the *n*-C₄H₁₀-(0.08 *M*)N₂O solution decreases from 3.5 to 2.5 upon the addition of 0.22 *M* O₂.

Table III: Isotopic Distribution of Methane^{a-c}

System	<i>G</i> (methane) ^d	Methane, %			
		CD ₄	CD ₃ H	CDH ₃	CH ₄
C ₄ D ₁₀	N.d. ^f	95.6	4.4		
C ₄ H ₁₀ -C ₄ D ₁₀	0.52	12.3	26.7	8.4	52.6
C ₄ H ₁₀ -C ₄ D ₁₀ -(0.02 <i>M</i>)O ₂ ^e	0.27	24.2	16.8	12.5	46.5
C ₄ H ₁₀ -C ₄ D ₁₀ -(0.06 <i>M</i>)O ₂		23.6	17.7	12.0	46.7
C ₄ H ₁₀ -C ₄ D ₁₀ -(0.2 <i>M</i>)O ₂		19.4	14.5	10.1	56.0
C ₄ H ₁₀ -C ₄ D ₁₀ -(0.4 <i>M</i>)SF ₆	0.41	13.9	27.0	8.4	50.7
C ₄ H ₁₀ -C ₄ D ₁₀ -(0.1 <i>M</i>)O ₂ -(0.4 <i>M</i>)SF ₆	0.21	22.6	17.6	12.6	47.2

^a Dose, 2.96×10^{20} eV/g. ^b Irradiation temperature, 0°. ^c The ratio C₄H₁₀/C₄D₁₀ is 1.0. ^d The *G* values of methane produced from pure *n*-C₄H₁₀. ^e The *G* values of methane remain constant above 0.02 *M* O₂. ^f N.d. = not determined.

Table IV: Isotopic Distribution of Ethane^{a-c}

System	<i>G</i> (ethane) ^d	Ethane, %					
		C ₂ D ₆	C ₂ D ₅ H	C ₂ D ₄ H ₂	C ₂ D ₂ H ₄	C ₂ H ₆ D	C ₂ H ₆
C ₄ D ₁₀	N.d. ^f	95.3	4.7				
C ₄ H ₁₀ -C ₄ D ₁₀	0.99	19.1	18.6	1.9	1.4	16.9	42.1
C ₄ H ₁₀ -C ₄ D ₁₀ -(0.02 <i>M</i>)O ₂ ^e	0.58	27.4	10.4	4.0	4.0	7.8	46.4
C ₄ H ₁₀ -C ₄ D ₁₀ -(0.06 <i>M</i>)O ₂		27.2	10.2	3.4	3.4	11.5	44.3
C ₄ H ₁₀ -C ₄ D ₁₀ -(0.2 <i>M</i>)O ₂		27.8	11.1	2.0	2.3	11.0	45.8
C ₄ H ₁₀ -C ₄ D ₁₀ -(0.4 <i>M</i>)SF ₆	0.48	20.4	17.6	2.6	3.3	14.3	41.8
C ₄ H ₁₀ -C ₄ D ₁₀ -(0.1 <i>M</i>)O ₂ -(0.4 <i>M</i>)SF ₆	0.35	24.9	14.2	2.5	4.0	12.2	42.2

^a Dose: 2.96×10^{20} eV/g. ^b Irradiation temperature, 0°. ^c The ratio C₄H₁₀/C₄D₁₀ is 1.0. In the absence of O₂ the ethane fraction contains about 2-3% C₂H₃D₃. ^d The *G* values of ethane produced from pure *n*-C₄H₁₀. ^e The *G* values of ethane remain constant above 0.02 *M* O₂. ^f N.d. = not determined.

Table V: Isotopic Distribution of Ethylene^{a-c}

System	<i>G</i> (ethylene) ^d	Ethylene, %			
		C ₂ D ₄	C ₂ D ₃ H	C ₂ H ₃ D	C ₂ H ₄
C ₄ D ₁₀	N.d. ^f	95.9	4.1		
C ₄ H ₁₀ -C ₄ D ₁₀	0.78	34.7	3.8	2.5	59.0
C ₄ H ₁₀ -C ₄ D ₁₀ -(0.02 <i>M</i>)O ₂ ^e	0.67	40.4	2.2	3.1	54.3
C ₄ H ₁₀ -C ₄ D ₁₀ -(0.06 <i>M</i>)O ₂		40.3	1.9	1.9	55.9
C ₄ H ₁₀ -C ₄ D ₁₀ -(0.2 <i>M</i>)O ₂		38.2	2.8	3.2	55.8
C ₄ H ₁₀ -C ₄ D ₁₀ -(0.4 <i>M</i>)SF ₆	0.22	33.3	2.5	2.8	61.4
C ₄ H ₁₀ -C ₄ D ₁₀ -(0.1 <i>M</i>)O ₂ -(0.4 <i>M</i>)SF ₆	0.24	35.4	2.8	4.3	57.5

^a Dose, 2.96×10^{20} eV/g. ^b Irradiation temperature, 0°. ^c The ratio C₄H₁₀/C₄D₁₀ is 1.0. ^d The *G* values of ethylene produced from pure *n*-C₄H₁₀. ^e The *G* values of ethylene remain constant above 0.02 *M* O₂. ^f N.d. = not determined.

Table VI: Isotopic Distribution of Propane^{a-c}

System	<i>G</i> (propane) ^d	Propane (relative intensity)			
		C ₃ D ₈	CD ₃ CDHCD ₃	CD ₂ CD ₂ CD ₂ H	C ₃ D ₆ H ₂
C ₄ D ₁₀	N.d. ^g	100		(5.4) ^f	
C ₄ H ₁₀ -C ₄ D ₁₀	0.16	100		(123) ^f	N.d.
C ₄ H ₁₀ -C ₄ D ₁₀ -(0.02 <i>M</i>)O ₂ ^e	0.12	100	30	53	20
C ₄ H ₁₀ -C ₄ D ₁₀ -(0.2 <i>M</i>)O ₂		100	27	54	20
C ₄ H ₁₀ -C ₄ D ₁₀ -(0.4 <i>M</i>)SF ₆	0.20	100		(118) ^f	N.d.
C ₄ H ₁₀ -C ₄ D ₁₀ -(0.1 <i>M</i>)O ₂ -(0.4 <i>M</i>)SF ₆	0.17	100	69	31	10

^a Dose, 2.96×10^{20} eV/g. ^b Irradiation temperature, 0°. ^c The ratio C₄H₁₀/C₄D₁₀ is 1.0. ^d The *G* values of propane produced from *n*-C₄H₁₀. ^e The *G* values of propane remain constant above 0.02 *M* O₂. ^f Relative intensity of (CD₃CDHCD₃ + CD₂CD₂CD₂H). ^g N.d. = not determined.

The isotopic distributions of methane, ethane, ethylene, and propane formed from the equimolar mixtures of $n\text{-C}_4\text{H}_{10}\text{-}n\text{-C}_4\text{D}_{10}$ with and without O_2 or SF_6 are, respectively, given in Table III-VI, in which the corrections for the presence of $\text{C}_4\text{D}_9\text{H}$ in the $n\text{-butane-}d_{10}$ material are minor and have not been made. The isotopic distribution of the heavier (d_6 , d_5 , and d_4) and the lighter (d_2 , d_1 , and d_0) ethanes could be determined within ± 2 and $\pm 10\%$, respectively. Since it is difficult to interpret thoroughly the mass spectrometric cracking pattern of isotopically mixed propanes formed in the absence of oxygen, only relative intensities of C_3D_8 and $\text{C}_3\text{D}_7\text{H}$ are given in Table VI. The relative intensities of propanes formed in the presence of oxygen are calculated with an assumption that oxygen completely inhibited the formation of $\text{CD}_3\text{CD}_2\text{CH}_3$, resulting from recombination reaction of radicals.

IV. Discussion

Effects of Added Oxygen. The radiation chemistry of several liquid-phase hydrocarbon systems containing oxygen has been interpreted on the basis that the only important reaction is the scavenging of thermal free radicals,^{3,20,21} and the experimental results reported here are interpreted in the same way to the first approximation. However, the electron affinity of the oxygen molecule is reported to be positive, being 0.43 eV,²² and scavenging of electrons by oxygen is known to occur in polar media.^{23,24} Oxygen may, in fact, scavenge electrons in irradiated liquid alkane systems because the yield of nitrogen from $\text{C}_4\text{H}_{10}\text{-(}0.08\text{ M)}\text{N}_2\text{O}$ system was decreased definitely by the addition of 0.2 M O_2 (Table II). The decreases in nitrogen yields are explicable by postulating that competition for electrons and/or negative species originating from electrons occurs between N_2O and O_2 . Nevertheless, we assume that the most important function of oxygen is to scavenge thermal free radicals in the range of concentration used ($<0.02\text{ M}$). There are two reasons for this assumption. (i) The effect of oxygen saturates at relatively low concentration ($\sim 0.005\text{ M}$) as shown in Figure 2. On the other hand, the effect of sulfur hexafluoride, an electron scavenger, does not saturate even at 0.5 M, as shown in Figure 3. Thus, because of the large difference between the concentrations at which the effects of both scavengers saturate approximately, the scavenging of electrons by oxygen should be slight at low concentration. (ii) If electrons and thermal free radicals were almost all scavenged by 0.005 M O_2 , the yields of each product from $\text{C}_4\text{H}_{10}\text{-(}0.005\text{ M)}\text{O}_2$ system should be less than that from $\text{C}_4\text{H}_{10}\text{-(}0.5\text{ M)}\text{SF}_6$ system. This is not the case.

Since the G value and isotopic distribution of a product, e.g., methane formed from $\text{C}_4\text{H}_{10}\text{-C}_4\text{D}_{10}$ mixtures with and without O_2 is measurable, the extent to which the yield of methane formed by unimolecular processes is affected upon the addition of O_2 is, in principle, calcu-

lable if the isotopic effects appearing in reaction kinetics were known. If an appreciable decrease in yield of unimolecular methane was observed upon the addition of O_2 , it follows that oxygen interacts with precursors of unimolecular methane such as electrons and excited molecules. Lack of the knowledge of isotopic effects appearing in reaction kinetics, however, does not permit us to determine accurately the extent to which oxygen quenches precursors of unimolecular products.

Formation of Methane. The fact that the G value of methane is decreased from 0.52 to 0.27 by the addition of 0.02 M O_2 indicates that about half of methane produced is formed *via* reactions involving thermal methyl radicals. The decrement of methane yield caused by the addition of oxygen is in good agreement with the G value (0.28) of methyl radicals measured by the radioiodine method,²⁵ if it is considered that in the radiolysis of pure liquid $n\text{-butane}$ a small fraction of methyl radicals combine with other radicals.

It is worth noting that a fairly large fraction of methane formed from the $\text{C}_4\text{H}_{10}\text{-C}_4\text{D}_{10}\text{-O}_2$ and $\text{C}_4\text{H}_{10}\text{-C}_4\text{D}_{10}\text{-SF}_6\text{-O}_2$ systems consists of CD_3H and CH_3D (Table III). We will consider processes by which the bimolecular methane nonscavengeable by oxygen is formed. There are three possible explanations: (i) ion-molecule reactions, (ii) disproportionation reaction of radicals in spurs, and (iii) hydrogen-atom abstraction reaction of hot methyl radicals.^{3b} First, the possibility of (i) must be examined. Although comparison of results obtained from the mass spectrometer and from the irradiation of liquid system cannot be simple, it is to be noted that the most abundant ion in the mass spectrum of $n\text{-butane}$ is C_3H_7^+ and that the ratio $\text{C}_3\text{H}_7^+/\text{CH}_3^+$ is about 17. On the other hand, the G value of propyl ion in irradiated liquid $n\text{-butane}$ is estimated to be about 0.1, as will be discussed later on. Thus, if the same ratio $\text{C}_3\text{H}_7^+/\text{CH}_3^+$ is assumed to be applied to the irradiated liquid $n\text{-butane}$, although this statement is not necessarily quantitatively correct,⁷ it follows that the yield of bimolecular methane formed by hydride-ion transfer reaction of methyl ion is negligible. Since typical radical recombination products ($\text{C}_5\text{-C}_8$) were reduced below the limit of detection when 0.02 M O_2 is added, disproportionation reaction of radicals in spurs may be unimportant for the production of methane in question. Moreover, since the formation of bimolecular methane nonscavengeable by radical scavenger has also been observed in the gas-phase radiolysis

(20) S. K. Ho and G. R. Freeman, *J. Phys. Chem.*, **68**, 2189 (1964).

(21) R. O. Koch, J. P. W. Houtman, and W. A. Cramer, *J. Amer. Chem. Soc.*, **90**, 3326 (1968).

(22) J. L. Pack and A. V. Phelps, *J. Chem. Phys.*, **44**, 1870 (1966).

(23) S. Gordon, E. J. Hart, M. S. Matheson, J. Rabani, and J. K. Thomas, *Discuss. Faraday Soc.*, **36**, 193 (1963).

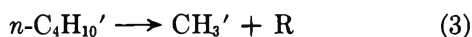
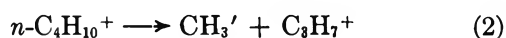
(24) S. Arai and L. Dorfman, *J. Chem. Phys.*, **41**, 2190 (1964).

(25) R. H. Schuler and R. R. Kuntz, *J. Phys. Chem.*, **67**, 1004 (1963).

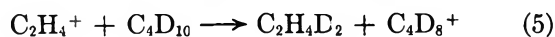
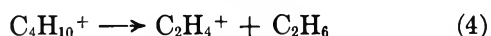
of *n*-butane,⁷ the bimolecular methane is considered not to be characteristic of in-spur reactions. Thus it is reasonable to conclude that hydrogen-atom abstraction reaction of hot methyl radicals is responsible for the production of methane in question



where CH_3' denotes the hot methyl radical. Since the yield of bimolecular methane from the C_4H_{10} - C_4D_{10} - O_2 system is not reduced appreciably even when 0.5 *M* SF_6 is added, it is unlikely that the hot methyl radicals are produced *via* decomposition of excited molecule formed by neutralization. The hot methyl radicals may be produced *via* the decomposition of the parent ions or of the excited molecules formed by direct excitation

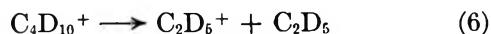


Formation of Ethane and Ethylene. We will be concerned here with ethane and ethylene formed by non-thermal radical reactions. The results on the isotopic distribution of ethanes show that $\text{C}_2\text{D}_4\text{H}_2$ and $\text{C}_2\text{H}_4\text{D}_2$ constitute a minor fraction of ethanes formed from C_4H_{10} - C_4D_{10} mixture, but they constitute a rather large fraction of ethanes formed from the C_4H_{10} - C_4D_{10} - O_2 and C_4H_{10} - C_4D_{10} - O_2 - SF_6 systems (Table IV). The formation of $\text{C}_2\text{D}_4\text{H}_2$ and $\text{C}_2\text{H}_4\text{D}_2$ indicates, thus, occurrence of the fragmentation of the parent ion followed by H_2^- (D_2^-) transfer reaction of the type



The *G* value of ethylene ion can be given by $2[G(\text{C}_2\text{-D}_4\text{H}_2) + G(\text{C}_2\text{H}_4\text{D}_2)]$, which is equal to ~ 0.05 ; all yields here refer to the oxygen-scavenged system. The estimated *G* value is regarded as ϵ lower limit, since ethylene ion is known to undergo H^- transfer reaction besides H_2^- transfer reaction.²⁶ Furthermore, ethylene ion may undergo in part the neutralization reaction of the type, $\text{C}_2\text{H}_4^+ + \text{e}^- \rightarrow \text{C}_2\text{H}_4$.

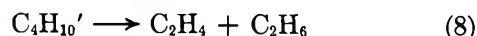
The formation of $\text{C}_2\text{D}_5\text{H}$ and $\text{C}_2\text{H}_5\text{D}$, the total *G* value of which is ~ 0.2 , may indicate the occurrence of hydride-ion transfer reaction of the type



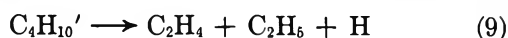
The following two facts make it difficult to estimate exactly the *G* value of the ethyl ions. (i) The hydride-ion transfer reaction cannot be distinguished from hot ethyl radical reaction. (ii) The ethyl ion formed may undergo in part the neutralization reaction of the type; $\text{C}_2\text{H}_5^+ + \text{e}^- \rightarrow \text{C}_2\text{H}_5$ or $\text{C}_2\text{H}_4 + \text{H}$.

The results on the isotopic distribution of ethylenes show that ethylenes formed from the C_4H_{10} - C_4D_{10}

systems are almost all C_2H_4 and C_2D_4 . According to the decomposition mode (8)

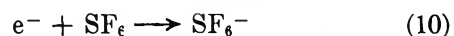


The *G* values should be equal for unimolecular ethylene and ethane formed from the C_4H_{10} - O_2 system. However, the *G* values of unimolecular ethylene and ethane are not equal, being 0.57 and 0.3,²⁷ respectively. Consequently, reaction 9 or its analogs which lead to $G(\text{C}_2\text{H}_4)_{\text{unimolecular}} > G(\text{C}_2\text{H}_6)_{\text{unimolecular}}$ are also responsible for the production of unimolecular ethylene.

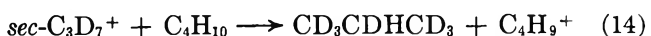
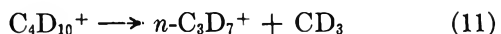


Evidence has been given for the occurrence of reaction 9 in the gas-phase photolysis of *n*-butane at 1067-1048 Å.²⁸ The occurrence of reaction 9 suggests the formation of a highly excited molecule (radical), the decomposition of which is not inhibited by collisional deactivation even in the liquid.

Formation of Propane. The yield of propane is scarcely affected by the addition of oxygen as shown in Figure 2, indicating that propane is almost all produced *via* nonthermal radical reaction. It is characteristic that the *G* value of propane from C_4H_{10} - O_2 mixture is increased by 40% upon the addition of sulfur hexafluoride (Table I). The increase in yield of propane is due to scavenging of the electron by sulfur hexafluoride



Electron scavengers are known to delay neutralization processes and thus would be expected to enhance the possibility that a fragment ion, propyl ion, reacts with *n*-butane. Similar phenomena have been observed in the liquid-phase radiolysis of 2-methylbutane^{3a} and isobutane.⁵ Although the yields of $\text{CD}_3\text{CDHCD}_3$, $\text{CD}_3\text{-CD}_2\text{CD}_2\text{H}$, and $\text{CD}_3\text{CDHCD}_2\text{H}$ from the C_4H_{10} - C_4D_{10} - O_2 system are small as shown in Table VI, their formation indicates the occurrence of the fragmentation of parent ion followed by ion-molecule reactions of the types



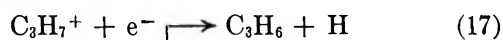
The fragmentation process of a parent ion such as (11) was suggested to occur in the liquid-phase radiolysis of

(26) L. W. Sieck and S. K. Searles, *J. Amer. Chem. Soc.*, **92**, 2937 (1970).

(27) The *G* value obtained by subtracting the yield of bimolecular ethane from the total ethane yield from the C_4H_{10} - C_4D_{10} - O_2 system.

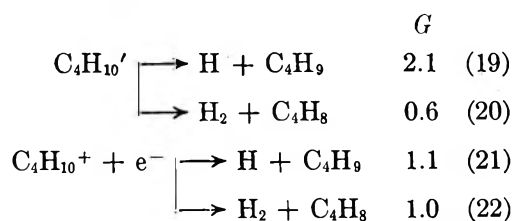
(28) P. Ausloos and S. G. Lias, "Preprints of International Conference on Photochemistry, Munich 1967," Part I, p 211.

n-butane by the fact that the yield of methyl radical exceeds that of propyl radical.²⁹ When the production of propane from oxygen-scavenged system originates mainly from reactions 12, 14, and 16, the *G* values of propyl and propylene ion are estimated to be ~ 0.1 and ~ 0.02 , respectively, from the results given in Table VI. The estimated *G* value for propyl ion, however, should be a lower limit, because the propyl ion may undergo in part a neutralization reaction to give propylene or propyl radical prior to the hydride-ion transfer reaction in the liquid phase.³⁰



A recent study demonstrates that $\text{C}_3\text{D}_7\text{H}$ product formed in the gas-phase radiolysis of the $n\text{-C}_4\text{H}_{10}\text{-}n\text{-C}_4\text{D}_{10}\text{-O}_2$ mixture is about 80% $\text{CD}_3\text{CDHCD}_3$ and 20% $\text{CD}_3\text{CD}_2\text{CD}_2\text{H}$ and that the percentage of $\text{CD}_3\text{-CD}_2\text{CD}_2\text{H}$ increases with increase of total pressure of the mixture.³¹ As shown in Table VI, $\text{C}_3\text{D}_7\text{H}$ formed in the liquid-phase radiolysis of the $\text{C}_4\text{H}_{10}\text{-C}_4\text{D}_{10}\text{-O}_2$ system is about 40% $\text{CD}_3\text{CDHCD}_3$ and 60% $\text{CD}_3\text{CD}_2\text{-CD}_2\text{H}$. Thus the ratio $\text{CD}_3\text{CDHCD}_3/\text{CD}_3\text{CD}_2\text{CD}_2\text{H}$ is smaller for the propanes formed in the liquid-phase radiolysis than for the propanes formed in the gas-phase radiolysis. This change in the ratio is ascribed to that the rearrangement of *n*-propyl ion to *sec*-propyl structure, which increases in importance with increasing internal energy of *n*-propyl ion,³¹ is inhibited to a certain extent in solution by collisional deactivation of *n*-propyl ion. It is of interest to note that the ratio $\text{CD}_3\text{CDHCD}_3/\text{CD}_3\text{CD}_2\text{CD}_2\text{H}$ is larger for propanes formed from the $\text{C}_4\text{H}_{10}\text{-C}_4\text{D}_{10}\text{-O}_2\text{-SF}_6$ than from the $\text{C}_4\text{H}_{10}\text{-C}_4\text{D}_{10}\text{-O}_2$ system (Table VI). This trend may be reasonably explained by the fact that the increased lifetime against neutralization of *n*-propyl ion upon the addition of sulfur hexafluoride enhances the possibility of rearrangement of *n*-propyl ion to *sec*-propyl structure.

Formation of Butenes. In a previous paper,¹³ we have proposed primary processes by which hydrogen is formed in the liquid-phase radiolysis of *n*-butane. The primary processes are



where $\text{C}_4\text{H}_{10}'$ represents an excited *n*-butane molecule formed by direct excitation and H represents both thermal and hot hydrogen atoms.^{13,32} The *G* values for each process were inferred from the effects of radical scavenger and electron scavenger on the hydrogen yield.¹³ In the present investigation, we have tried to

correlate the *G* value of total butene deduced from the primary processes of hydrogen formation with that of total butene measured and have found that the correlation is moderately satisfactory as shown in the following. From the *G* value of hydrogen atoms given above, the *G* value is estimated for butyl radicals formed in the absence of additive to be 6.4, which is equal to $2G(\text{H})$ plus the *G* value of butyl radicals resulting from hydrogen-atom abstraction reaction of $\text{C}_1\text{-C}_3$ radicals, the latter being negligible compared with $2G(\text{H})$.³³ On the other hand, the *G* value of C_8 dimers is estimated to be 1.8 by the interpolation of the yield of dimers in the radiolysis of liquid *n*-pentane²¹ and propane,³⁴ and the *G* value of $\text{C}_5\text{-C}_7$ products resulting from recombination reaction of the butyl radicals with $\text{C}_1\text{-C}_3$ radicals was reported to be 0.6.⁸ Thus, the *G* value of butene resulting from the disproportionation reaction between butyl radicals is estimated to be $[(6.4 - (1.8 \times 2) - 0.6)]/2 = 1.1$. Neglecting the *G* value of butene resulting from disproportionation reaction between butyl radical and $\text{C}_1\text{-C}_3$ radicals, the *G* value of total butene is estimated to be 2.7, which is the sum of the *G* values of butene resulting from the disproportionation reaction between butyl radicals and that of butene resulting from the unimolecular decomposition reactions 20 and 22. Agreement between the measured *G* value, 2.3, and the estimated *G* value, 2.7, for total butene is moderate. The *G* value for butene formed in the presence of oxygen may be estimated to be 1.6, which is the *G* value of unimolecular hydrogen produced *via* reactions 20 and 22. The estimated *G* value of butene is somewhat larger than the measured *G* value of butene, 1.3. Finally, *G* values may be estimated for butene formed in the presence of both oxygen and sulfur hexafluoride to be 0.6, which is the *G* value of unimolecular hydrogen produced *via* reaction 20. The estimated *G* value of butene, 0.6, is again somewhat larger than the measured *G* value of butene, 0.3. A mode of decomposition of excited molecules such as (9), which leads to the formation of a certain radical other than butyl radical as the counterpart of hydrogen atom, may account for the disagreement between the estimated and measured *G* values for butene.

Acknowledgments. The authors wish to thank Dr. S. Sato for valuable suggestions. They are also indebted to Mr. H. Sakurai for mass spectrometric analyses.

(29) C. E. McCauley and R. H. Schuler, *J. Amer. Chem. Soc.*, **79**, 4008 (1957).

(30) The decrease (0.13 *G* unit) of propylene by the addition of SF_6 is due to the inhibition of the neutralization of the parent ion and of C_3H_7^+ ions with electrons. If the decrease is taken as the *G* value of reaction 17 alone because of our ignorance of the fractions of these effects, then the upper limit of C_3H_7^+ yield will be ~ 0.23 .

(31) S. G. Lias, R. E. Rebert, and P. Ausloos, *J. Amer. Chem. Soc.*, **92**, 6430 (1970).

(32) Y. Hatano and S. Shida, *J. Chem. Phys.*, **46**, 4784 (1967).

(33) W. P. Bishop and R. F. Firestone, *J. Phys. Chem.*, **74**, 2274 (1970).

(34) R. D. Koob and L. Kevan, *Trans. Faraday Soc.*, **64**, 422 (1968).

The Radical Anions of Vitamin A Aldehyde and Related Schiff Bases^{1a}

by C. M. Lang,^{1b} J. Harbour, and A. V. Guzzo*

Chemistry Department, University of Wyoming, Laramie, Wyoming 82070 (Received March 8, 1971)

Publication costs assisted by the U. S. Atomic Energy Commission

Radical anions of *all-trans*-retinal and a number of *N*-retinylidene Schiff bases were prepared. Their esr spectra were recorded and a hyperfine coupling constant assignment is given for the radical anion of the *N*-retinylidene-*n*-butylamine Schiff base. The possibility of a charge-transfer process in the initial events of vision is discussed.

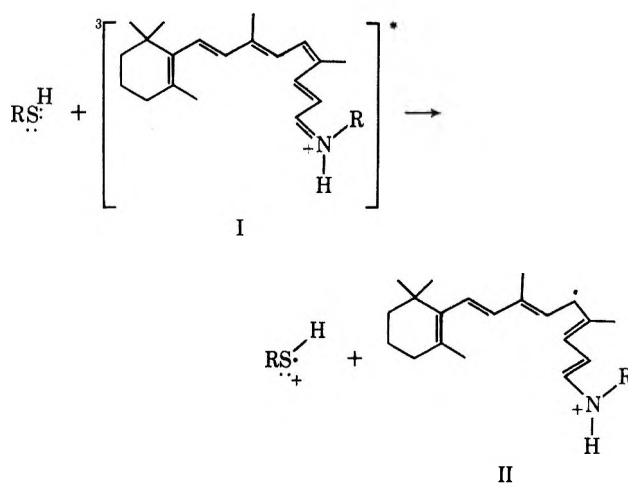
Introduction

For some time the observation of photoinduced electron spin resonance (esr) signals associated with retinal material^{2,3} has intrigued workers interested in the mechanism of visual excitation.⁴ If such a signal indeed exists and could be attributed to some stage in the bleaching of rhodopsin, then an electron-transfer process might be operative in the initial events of vision. However, confirmation of these reports is lacking and there is evidence that no *obvious* esr signal can be elicited from retinal material by light.^{1,5,6}

Nevertheless the concept of charge transfer is worth pursuing for several reasons. For instance it has been assumed that the photoisomerization of the 11-*cis*-*N*-retinylidene chromophore which exists in rhodopsin proceeds through a triplet state.^{7,8} This of course is very reasonable except that recent work⁹ has shown that the quantum yield for photoisomerization of 11-*cis*-retinal to the *all-trans* form in solution is 0.2. The same study also reports that the quantum yield for the isomerization of the oxime of retinal, a close analog of the *N*-retinylidene Schiff base, is less than 0.2. Since the quantum yield of the same process taking place in the visual cell has a quantum yield of between 0.6 and 0.7, it would seem that the *in vivo* process takes a different, more efficient route.

With regard to this point we expect free radicals to catalyze the isomerization of these polyenes and, of course, this is part of the stimulus behind proposing radical participation. For instance if the electron donor were a nearby sulfhydryl group the mechanism shown in the next column may be proposed. Structure I represents the 11-*cis*-chromophore, protonated as it is supposed to exist in rhodopsin.¹⁰ Structure II is the proposed product of the electron-transfer reaction and we have depicted only that valence bond structure which illustrates the resultant single bond character produced about the 11-12 bond.

Finally, Grady and Borg¹¹ have shown that irradiation of retinal and retinol at low temperatures produces radicals observable *via* esr. They postulate the participation of a charge-transfer phenomenon although bond cleavage cannot be ruled out.



At this point, before proceeding further, the lack of an esr signal in rhodopsin preparations must be rationalized. If we assume a charge-transfer process as depicted above, several reasonable explanations immediately present themselves.

(1) The esr signal due to the *N*-retinylidene anion, considered here in the doublet state, may be so broad as to be unobservable. The broadening might be due to rapid interconversion between conformers which would modulate the magnetic environment of the odd electron producing a form of lifetime broadening.¹²

(2) The remaining unpaired electron on the donor

(1) (a) This work has been supported by the Atomic Energy Commission through Contract No. AT(11-1)-1627; (b) N.D.E.A. Predoctoral Fellow.

(2) M. Ostrovskii and L. Kayashin, *Dokl. Akad. Nauk*, **151**, 1050 (1964).

(3) W. Johnson, *Fed. Proc., Fed. Amer. Soc. Exp. Biol.*, **23**, 384 (1963).

(4) G. Wald, P. K. Brown, and I. R. Gibbons, *J. Opt. Soc. Amer.*, **53**, 20 (1963).

(5) E. W. Abrahamson and S. E. Ostroy, *Progr. Biophys. Mol. Biol.*, **17**, 194 (1967).

(6) A. Guzzo, unpublished results.

(7) K. Inuzuka and R. Becker, *Nature*, **219**, 383 (1968).

(8) J. R. Weisenfeld and E. W. Abrahamson, *Photochem. Photobiol.*, **8**, 487 (1968).

(9) A. Kropf and R. Hubbard, *ibid.*, **12**, 249 (1970).

(10) R. A. Morton and G. A. Pitt, *Biochem. J.*, **59**, 128 (1955).

(11) F. Grady and D. Borg, *Biochemistry*, **7**, 675 (1968).

and the odd electron on the anion may remain coupled and produce a singlet or triplet system.¹³ No paramagnetism is, of course, expected if the system remains as a singlet. In the triplet state only a weak half-field esr signal might be observed. If the triplet had only a transient lifetime and could be viewed as a true charge-transfer state,¹⁴ the possibility of observing an esr signal would depend on the lifetime.

(3) If a doublet state is formed its lifetime may be so short as to prevent any sizable concentration of radical building up. This would be the case if the transferred electron were to revert to its original donor after the isomerization process.

In the present study we have examined point 1 above to see if radical anions of retinal and Schiff bases of retinal can indeed be observed *via* esr after electrolytic reduction.

Experimental Section

Several electrolytic cell designs have been suggested for use in producing radical anions. The recent design by Glass¹⁵ has an advantage in that it is simply constructed and because of its small size may be used for both esr and optical spectral measurements. This cell, modified slightly, is shown in Figure 1. Approximately 5 ml of solvent is required to half-fill the mixing bulb and the lower tube.

In a typical sample preparation, sufficient quantity of compound was weighed into the mixing bulb so that the resulting solution was 0.001 *M* in starting material. In addition, approximately 75 mg (0.05 *M*) of tetra-*n*-butylammonium perchlorate (Matheson Coleman and Bell, polarographic grade) was added as supporting electrolyte. The cell was attached to a vacuum line and evacuated to less than 10^{-5} mm; solvent was then vapor transferred into the mixing bulb. The glass wool frit serves to separate the two electrolysis chambers and prevent convection. The cell was operated at a constant current using a voltage divided, dc power supply, and a microammeter. The electrolysis potential was obtained by trial, electrolyzing first at very low current and progressively increasing the current. In a typical experiment, $I_{\text{cell}} = 2 \mu\text{A}$, $V_{\text{cell}} = 10 \text{ V}$, $V_{\text{supply}} = 300 \text{ V}$. The electron spin resonance detection system used in this study was a Varian E-3, X-band (~ 9250 MHz) epr spectrometer employing 100-kHz field modulation. The sample holder was a multipurpose TE₁₀₂ reflection cavity designed to handle the Varian E-4557-9 temperature controller accessories and E-4550 temperature controller. While no attempts were made to calibrate the resolution of the instrument, it appeared that the specifications stated were being realized and that the field homogeneity was great enough to resolve 50-MG lines.

Optical spectra were obtained from the samples in electrolysis cells described above. They were inserted into a dewar provided with quartz optical windows.

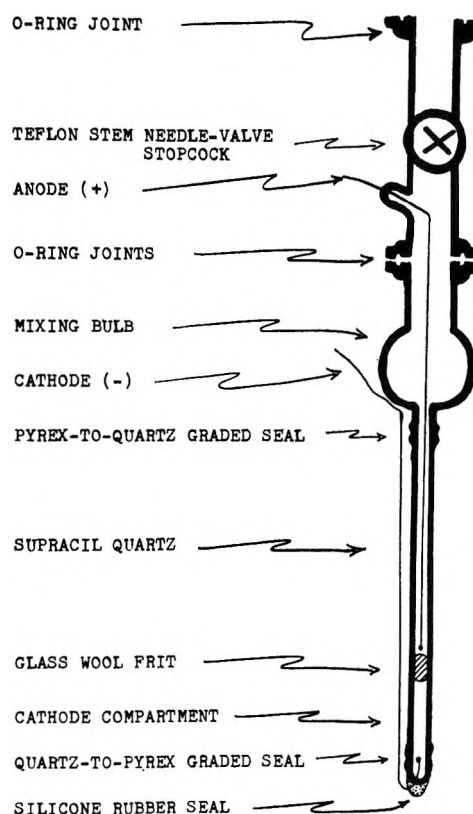


Figure 1. Uv-esr electrolysis cell.

After appropriate masking of the sample, uv-visible spectra were obtained with the Cary Model 14 spectrophotometer. The temperature of the sample was adjusted with a small heater element wrapped around the sample holder. Thus any temperature higher than the coolant temperature could be obtained.

all-trans-Retinal was obtained from the Eastman Distillation Products Industries, and used without further purification. The Schiff bases were obtained from Dr. Paul Blatz of this department. Solvents used in this investigation were 1,2-dimethoxyethane (DME) and tetrahydrofuran (THF). The former was obtained "Puris Grade" from the Aldrich Chemical Co., while the latter as "Chromotoquality Reagent Grade" from Matheson Coleman and Bell. Each solvent was refluxed 5 hr over lithium aluminum hydride (LiAlH₄) followed by distillation onto fresh LiAlH₄. The solvents were stored in glass containers with approximately 0.1 g of anthracene and small amounts of potassium

(12) We refer here to interconversions between different molecular geometries by twisting about the essential single bonds. If the rate of interconversion is comparable to the hyperfine interaction frequency for a given proton, broadening may occur. See A. Carrington and A. D. McLachlan, "Introduction to Magnetic Resonance," Harper and Row, New York, N. Y., 1967, p 213.

(13) H. M. McConnell, *J. Chem. Phys.*, **25**, 709 (1956).

(14) J. N. Murrell, *Quart. Rev. Chem. Sec.*, **15**, 191 (1961).

(15) G. Glass and R. West, Abstracts, 157th National Meeting of the American Chemical Society, Minneapolis, Minn., 1969, No. INOR 123.

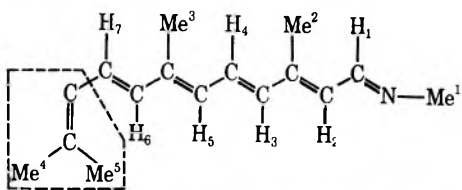
metal. Connection to the vacuum line was through all-metal valves.

All molecular orbital computations were carried out using the University of Wyoming Philco Model 211 computer. At the Hückel level of approximation a Fortran IV program, authored by T. Janiszewski and obtained from the Quantum Chemistry Program Exchange (Bloomington, Ind.) as QCP376, was used.

Molecular Orbital Calculations. Short of isotopic substitution which would require extensive and difficult synthetic procedures, it is possible to gain some insight into the hyperfine coupling constant assignment by a calculational approach. Clearly the assignment will not be unambiguous but some features of interest should emerge.

Hückel molecular orbital (HMO) computations¹⁶ were performed¹⁷ on two models taken to approximate the π framework of the *N*-retinylidene-*n*-butylamine (RBA) radical anion. Model A assumed complete removal of the last double bond from conjugation with the major part of the polyene chain. This would arise if the plane of the atoms in the box indicated in Table I were perpendicular to the plane including the remaining centers. Model B assumes an entirely planar system.

Table I: Calculated and Observed Hyperfine Coupling Constants for the π -Framework of *N*-Retinylidene-*n*-butylamine Radical Anion



Atom	Coupling constants, G		
	Model A ^a	Model B ^a	Observed
N	3.4	2.8	7.2
H ₁	1.9	1.4	2.4
H ₂	1.1	1.0	1.2
H ₃	0.8	0.9	0
H ₄	3.5	2.6	3.6
H ₅	0.0	0.2	0
H ₆	0.0	0.2	0
H ₇	4.1	3.4	3.6
Me ¹	2.3 (CH ₂)	1.9 (CH ₂)	2.4
Me ²	2.4	2.6	1.2
Me ³	3.4	3.8	4.8
Me ⁴		3.0 (CH ₂)	
Me ⁶		3.0	

^a In model A we have assumed the five double bonded π system exclusive of the dotted box above. Model B has included the entire π system.

The numerical values of the parameters required in the calculation—Coulomb and resonance parameters—are given in Table II. The parameters given for the atoms C', C'', and N' (the notation adopted is that

Table II: Parameter Values Used in HMO Calculations

Atom	Coulomb parameter, h_r	Resonance parameter, k_{rs}
C	0.0 ^a	$k_{CC} = 1.00^a$
N	0.50 ^a	$k_{NC} = 0.80^a$
N'	0.39 ^b	$k_{NC} = 0.80^b$
C'	-0.13 ^c	$k_{CC} = 1.00^c$
C''	-0.05 ^c	$k_{CC} = 0.86^c$
X (= H ₃)	-0.50 ^c	$k_{XC} = 2.50^c$

^a H. Susuki, "Electronic Absorption Spectra and Geometry of Organic Molecules," Academic Press, New York, N. Y., 1967.

^b The Coulomb parameter was set equal to 0.39 for HMO calculations on *N*-methyl-substituted Schiff bases (*cf.* text) while the NC bond is treated as a pyridine bond. ^c R. E. Moss, N. A. Ashford, R. G. Lawler, and G. K. Fraenkel, *J. Chem. Phys.*, **51**, 1765 (1969).

C-CH₃ is represented by C'-C''-X and N-CH₃ is represented by N'-C''-X) were used in treating methyl substituents on unsaturated systems. This is essentially a hyperconjugative model with H₃ = X.

For the *N*-methyl-substituted Schiff base new values of $h_{N'}$ and $k_{N'C''}$ were required. With methyl substitution to a carbon π center $h_{C'}$ = -0.13 while h_C = 0 for unsubstituted π centers. For methyl substitution to a nitrogen π center the value of h_N must also be altered. It was assumed that the correction to h_N is inversely proportional to the electronegativity of nitrogen,¹⁹ that is

$$h_N(\text{cor}) = \frac{X_C}{X_N} h_C(\text{cor})$$

where X_C and X_N are the Pauling electronegativity values for carbon and nitrogen; and $h_C(\text{cor})$ is the correction to h_C for methyl substitution on a π center. Thus

$$h_N(\text{cor}) = \frac{2.5}{3} (-0.13) = -0.11$$

and $h_{N'} = h_N - h_N(\text{cor}) = 0.50 - 0.11 = 0.39$. Using these values the coupling constants a_N were found using the unpaired electron density obtained from the Hückel coefficients and the McConnell²⁰ relationship $a_N =$

(16) E. Hückel, *Z. Phys.*, **70**, 204 (1931).

(17) We investigated several molecular orbital calculational methods. The most intriguing was the INDO approach developed by Pople¹⁸ which can treat both σ - and π -type radicals. After a close examination of Pople's major effort¹⁸ at predicting spin densities on a large variety of radicals, and some preliminary calculations of our own, we concluded that this technique, at least using the parameters given by Pople, would not be any more useful for our purposes than the simple Hückel method.

(18) J. A. Pople, D. L. Beveridge, and P. A. Dobosh, *J. Amer. Chem. Soc.*, **90**, 4201 (1968).

(19) A. Streitwieser, Jr., "Molecular Orbital Theory for Organic Chemists," Wiley, New York, N. Y., 1967.

(20) H. M. McConnell, *J. Chem. Phys.*, **24**, 632 (1956).

Q_{PN} . The proportionality constant Q was taken to be -22.5 G for hydrogens attached to π centers and 25 G for nitrogen π centers.

The coupling constants found are given in Table I along with our tentative assignment of the experimental values.²¹ Clearly the lack of symmetry in the molecules and the poor resolution lead to uncertainties; however, this appears to be a reasonable assignment.

Results

It was found that alkali-metal reduction of retinal and of Schiff bases derived from retinal could be effected, but in all cases no hyperfine structure could be observed in the esr patterns recorded. With a number of other Schiff bases²² it was found that bond rupture occurred quite easily followed by recombination of the various fragments. We thus had difficulty determining whether the esr signal observed was due to the radical of interest or other species. Consequently we turned to milder, controlled reduction techniques and employed electrolytic reduction at a platinum electrode.

In general we found that radical anions prepared from the compounds of interest were only moderately stable. Radical anions derived from ketones appeared to be most stable and those derived from Schiff bases and aldehydes quite unstable (radicals of aldehydes appeared most unstable).

It is quite possible that the esr signals recorded are broadened as a result of the short lifetimes of the radicals.

Esr Studies. Retinal. For *all-trans*-retinal in either DME or THF as solvent and with tetra-*n*-butylammonium perchlorate as supporting electrolyte, a free radical was generated with the esr spectrum given in Figure 2. It did not appear possible to improve upon the resolution of this signal either by changes in temperature or concentration. The conditions given for obtaining the spectrum of Figure 2 were apparently optimal for this species. On the basis of this spectrum it was not possible to make any assignment of hyperfine coupling constants.

N-Retinylidene-n-butylamine Schiff Base. This compound appeared to be the most stable of the Schiff bases prepared from retinal. Electrolytic reductions, again using either DME or THF as solvent, produced a radical which gave the esr spectrum reproduced in Figure 3.

The spectrum appeared to be temperature dependent. In a typical esr experiment, a solution containing approximately 10^{-3} M Schiff base and 0.05 M supporting electrolyte was electrolyzed at -90° . During the electrolysis the magnetic field was repetitively swept through the free electron region, that is $+50$ G through $H_0 = 3270$ G for the bridge system used. At this temperature no signal was ever observed; however, visual examination of the sample cell revealed that a reaction was taking place on the cathode surface. A red material was observed to form instantly upon the onset of

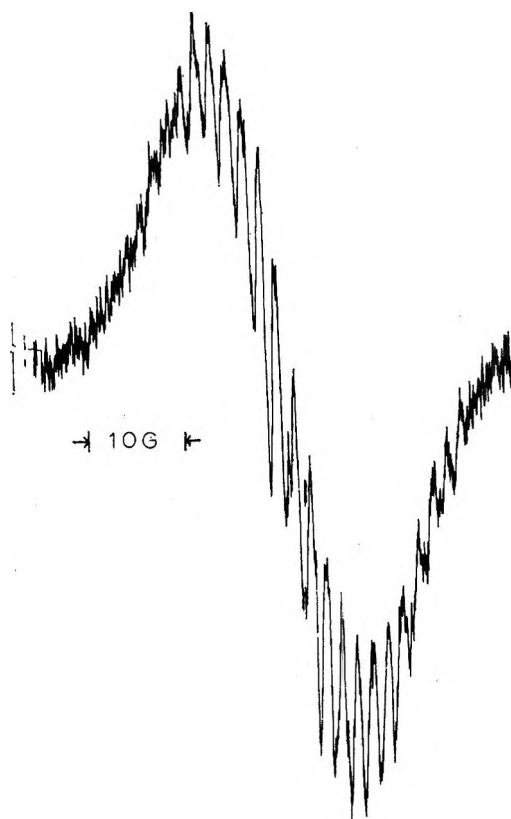


Figure 2. ESR spectrum of the electrolytically produced radical anion of *all-trans*-retinal; recorded at -70° in THF.

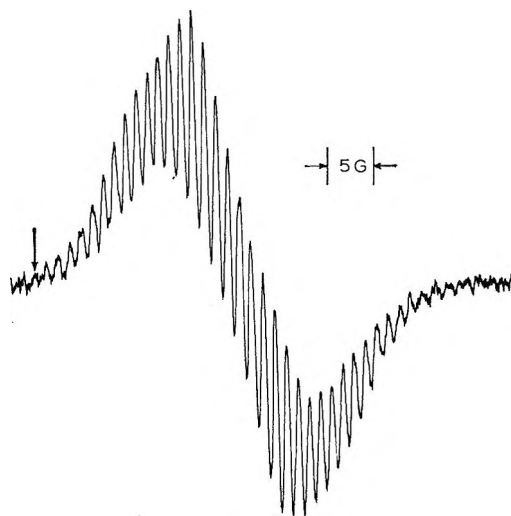


Figure 3. ESR spectrum of the *N*-retinylidene-*n*-butylamine radical anion; recorded at -20° in THF.

(21) It is by no means obvious why model A should be preferred over model B. An examination of other related systems indicates that the cyclohexene ring may have to be considered. For instance, studies on neutral retinoic acid,²³ β -ionone,²⁴ and the β -ionone radical anion²⁵ indicate that in each of these species the ring is twisted ~ 40 - 50° out of coplanarity with the polyene chain, and thus is not entirely removed from conjugation.

(22) C. M. Lang and A. Guzzo, unpublished observations.

(23) C. H. Stan and C. H. McGillavry, *Acta Crystallogr.*, **16**, 62 (1963).

(24) C. Y. Chan and R. J. W. LeFevre, *J. Chem. Soc. B*, 180 (1963).

(25) J. Harbour and A. Guzzo, manuscript in preparation.

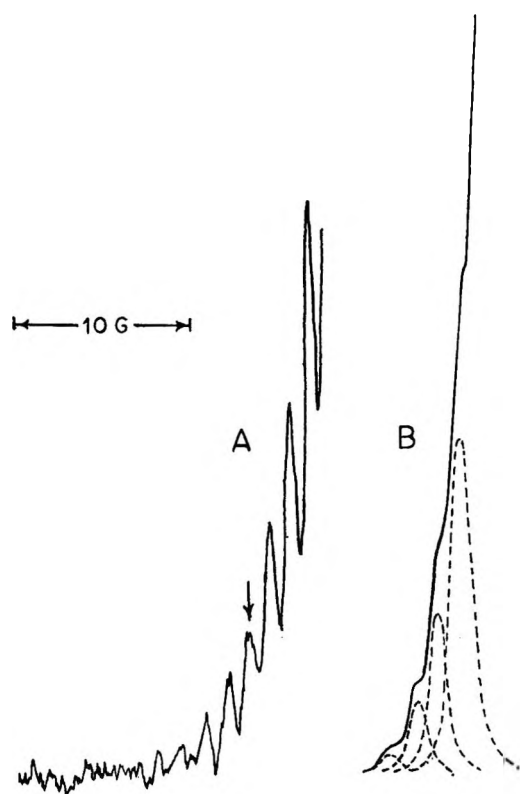


Figure 4. ESR spectrum of *N*-retinylidene-*n*-butylamine radical anion in THF; recorded at -20° at high gain: (A) winglines of the spectrum as recorded where the arrow indicates the outermost line evident in Figure 3; (B) integrated winglines illustrating the 1:4:9:18 intensity ratio of the outermost lines.

electrolysis and this material diffused slowly through the cathode compartment.

If, after 5–10 min of continuous electrolysis at -90° , the electrolysis is terminated and the temperature increased to above -70° , a broad signal begins to develop. At -20° the maximum intensity of the signal is realized and hyperfine structure develops. Further increases in temperature result in rapid decay of the signal.

If one generates the radical at -20° and continues to electrolyze at this temperature, the signal grows in intensity with no change in resolution. If the temperature is lower (-40°) the total intensity decreases even if electrolysis is continued. At a still lower temperature the hyperfine structure is again lost. (These experiments, including the synthesis of the Schiff base from retinal, were also carried out only in dim red light. No differences were noted in the resulting ESR spectra.)

N-Retinylidene-*tert*-butylamine Schiff Base. Using procedures identical to those described above, radicals of the *N*-retinylidene-*tert*-butylamine Schiff base were prepared. We were unable to obtain good data for this radical; however, the ESR spectrum resembled that obtained from the *n*-butylamine Schiff base but was much weaker.

Spectral Assignment. We attempted an analysis of the ESR spectrum obtained from the anion radical of the

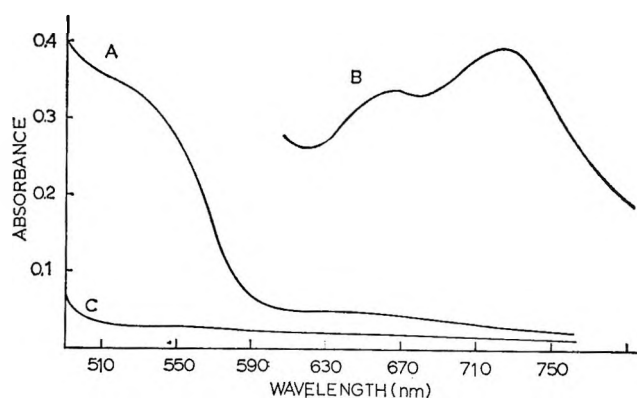


Figure 5. Optical absorption spectrum of the *all-trans*-retinal radical anion recorded at -79° in THF: (A) immediately after the onset of electrolysis; (B) after approximately 5 min of electrolysis; (C) before electrolysis.

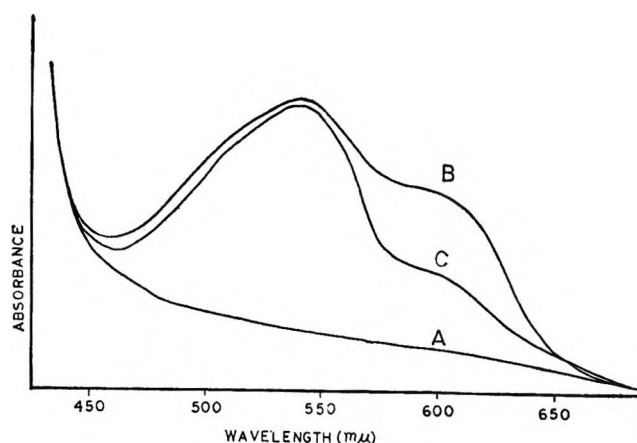


Figure 6. Electronic spectra of electrolyzed *N*-retinylidene-*n*-butylamine in THF at -20° : (A) prior to electrolysis; (B) after 10 min of continuous electrolysis; (C) immediately after termination of electrolysis.

N-retinylidene-*n*-butylamine Schiff base only. Clearly with the poor resolution encountered this was difficult; however, of numerous assignments tried we found only one which gave satisfactory agreement. In Figure 4 the ESR spectrum of a particularly high concentration of radical is given. Integration of the spectrum (point by point) and subsequent resolution into individual absorptions of an approximately gaussian shape indicated that the first lines of the spectrum should be in an approximate 1:4:9:18 ratio. In addition it was necessary to account for the very large intensity ratio between the first line and the center line. With this information we arrived at the coupling constants given in Table I. One nitrogen interaction was required (7.2 g) as were twelve proton interactions of various magnitudes. Clearly not all the possible interacting nuclei were required. A tentative assignment of the hyperfine constants to specific nuclei was made on the basis of calculated coupling constants. This is discussed below.

Optical Spectra. Optical absorption spectra of the anion radicals of *all-trans*-retinal and the *N*-retinylidene-

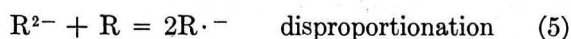
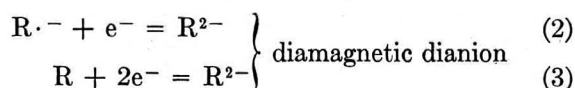
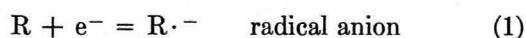
dene-*n*-butylamine Schiff base were recorded. The curves obtained are given in Figures 5 and 6, respectively.

Discussion

From these studies it is clear that moderately stable radical anions can be generated from *all-trans*-retinal and several *N*-retinylidene Schiff bases. The most stable species encountered was the *N*-retinylidene-*n*-butylamine radical anion and more detailed studies were carried out on it. In the context of our experiments we found that at low temperatures we were able to generate predominantly diamagnetic species (it is clear from the color changes in the cathode compartment of the electrolytic cell that some reduced species was being formed). Only at temperatures above -80° do we observe the production of the free radical in sizable quantities.

Optical absorption spectra suggest the formation of at least two species. In Figure 6 it can be seen that at -20° and after termination of electrolysis the rate of decrease of the two peaks found was quite different. At this same temperature we also observed a decrease in the esr signal upon termination of electrolysis. At very low temperatures wherein only a very weak esr signal could be observed, -80 to -90° , it was found that the 610-nm peak in the optical absorption spectrum also appeared quite weak. This behavior suggests that the long wavelength peak observed at 610 nm is due to the radical.

The reactions taking place in the sample cell may involve the following



We have observed with retinal at least that *exhaustive* electrolysis even at room temperature produces a deep red color in the cathode compartment yet no esr signal can be observed. This would be consistent with reactions 1, 2, and 3 in that all species exist as the doubly reduced dianion. When this solution is mixed with unreduced retinal from the upper part of the cell a green paramagnetic solution is obtained (see Figure 5). This observation is consistent with reaction 5.

Further verification of these electrolysis results may be obtained from a study of the relevant polarographic

work carried out on these and related polyenes. Hoijtink and Van Schooten^{26,27} have shown that in nonprotic or nonaqueous solvents reactions 1 and 2 proceed exclusively and that 3 is their sum. Blout and Fields²⁸ argue that the first reduction wave they see using 2,4,6,8,10-dodecapentaenal is due to reaction 1 and that this is followed by dimerization of the radicals into a *gem*-dihydroxy compound. This seems inconsistent with the mixing experiment described above which is consistent with the disproportionation reaction 5.

The production of diamagnetic dimers, reaction 4, has been observed in other systems²⁹ when radicals are prepared by alkali metal reduction. In these cases it is postulated that the metal counterion acts as a bridge between two radical anions. It is not known however if dimer formation can occur with electrolytic reduction as carried out in our experiments.

The assignment of the hyperfine coupling constants in the *N*-retinylidene-*n*-butylamine Schiff base radical anion, while somewhat uncertain, does show that the unpaired electron is distributed over the entire polyene chain. The coupling constants we obtain indicate that the largest unpaired spin density is at the nitrogen of the Schiff base link. This is an interesting finding since it has been postulated that the visual chromophore in rhodopsin is protonated at this position (or is at least complexed to some Lewis acid) and carries a positive charge. The possibility of electron transfer would appear to be enhanced.

It does not appear that there are broadening processes inherent to the polyene structure which prevent observation of the esr signal. We have rapidly frozen samples of these radical anions to -196° and still observed signals—albeit with the absence of any hyperfine. Thus we are forced to conclude that the *N*-retinylidene radical anion, if it existed in any of the intermediates of rhodopsin bleaching, should be observed with esr. Since our studies and those of others have been negative, participation of the radical must be ruled out.

Charge transfer, however, remains as a possibility to be considered if we now restrict ourselves to the case of (1) coupled electrons producing a singlet or triplet state, or (2) a rapid return of the transferred electron upon isomerization.

(26) G. J. Hoijtink and J. Van Schooten, *Recl. Trav. Chim. Pays-Bas*, **72**, 691 (1953).

(27) G. J. Hoijtink, J. Van Schooten, E. de Boer, and W. Aalhersberg, *ibid.*, **73**, 355 (1954).

(28) M. Fields and E. R. Blout, *J. Amer. Chem. Soc.*, **70**, 930 (1948).

(29) N. Hirota and S. I. Weissman, *ibid.*, **86**, 2538 (1964).

^{129}I Mössbauer Studies of the Chemical Effects of Nuclear Transformations in Compounds of Tellurium

by J. L. Warren, C. H. W. Jones,* and P. Vasudev

The Chemistry Department, Simon Fraser University, British Columbia, Canada (Received February 10, 1971)

Publication costs assisted by the National Research Council of Canada

The chemical effects of the $^{129\text{m}}\text{Te} \rightarrow ^{129}\text{Te}$ isomeric transition and the $^{128}\text{Te}(n,\gamma)^{129}\text{Te}$ nuclear reaction have been studied in telluric acid and several related tellurium-oxygen compounds, using the ^{129}I 27.8-keV 15-nsec Mössbauer transition as a probe. The ^{129}I Mössbauer emission spectra of the following compounds, labeled in separate experiments with ^{129}Te and $^{129\text{m}}\text{Te}$, have been recorded against a standard Na^{129}I absorber: H_6TeO_6 , $(\text{H}_2\text{TeO}_4)_n$, $\alpha\text{-TeO}_3$, tetragonal TeO_2 , H_2TeO_3 , and Te metal. The neutron irradiation of H_6TeO_6 , TeO_2 , and Te metal with the production of ^{129}Te -labeled sources was also studied. Chemical effects of the isomeric transition and (n,γ) reaction were clearly observed in H_6TeO_6 and $(\text{H}_2\text{TeO}_4)_n$ but not in TeO_2 , H_2TeO_3 , or Te metal. Where molecular decomposition was observed, a single decomposition product, apparently the TeO_3^{2-} ion, was identified. On heating telluric acid containing the $^{129}\text{TeO}_3^{2-}$ recoil product, a single-step annealing reaction was observed in which $^{129}\text{TeO}_3^{2-} \rightarrow ^{129}\text{Te(VI)}$. The results of these Mössbauer studies are compared with those of previous radiochemical studies of similar transformation schemes. An analysis of the data for the ^{129}Te -labeled sources provides further estimates of the parameter $[(q_{\text{at}}(\text{Te})Q^{125})/(q_{\text{at}}(\text{I})Q^{129})](1 + \eta^2/3)$ and $\rho^{125}\text{Te}/\rho^{129}\text{I}$, the radius ratio for ^{125}Te and ^{129}I , and also allows a comparison of the bonding in tetragonal and orthorhombic TeO_2 . The study of tellurium compounds using double labeling with ^{125}Te and ^{129}Te is illustrated.

Introduction

Studies of the chemical effects of nuclear transformations in solids have generally been carried out in the past by means of standard radiochemical analytical techniques.^{1,2} Following the nuclear transformation, the solid is dissolved in a suitable solvent and the form of the radioactively labeled daughter molecules identified by chemical analysis. The results obtained from such investigations, however, are open to many interpretations since chemical reactions may occur, involving the labeled recoil products, both during and following dissolution. It is therefore of some interest to attempt to identify the chemical products formed directly in the solid, and to compare the results of such experiments with radiochemical studies on the same (or at least comparable) systems. Mössbauer spectroscopy allows the direct study of the molecular fragments formed in a solid following a nuclear reaction or radioactive decay for several specific nuclei, and this tool has been applied by several groups in the past.³⁻⁶ In the present work we have employed the 27.8-keV, 15-nsec Mössbauer transition of ^{129}I , populated in the decay of ^{129}Te , as a probe to investigate in detail the chemical effects associated with several nuclear transformations in solid telluric acid and related tellurium-oxygen compounds. The results of these experiments are compared with those of previous radiochemical studies.⁷

The system chosen for the present investigation has several distinct advantages for this type of study. Thus a comparison of the effects of several different

transformation sequences may be carried out in the same compound, as illustrated in Figure 1.⁸ In compounds labeled with the 69-min ^{129}Te isotope, the ^{129}I Mössbauer transition will reflect the chemical effects, if any, of the preceding β^- decay. For the $^{129\text{m}}\text{Te}$ labeled compounds the molecular fragmentation produced by the Auger charging accompanying the internal conversion in the isomeric transition to the ground state ^{129}Te may be observed. Finally, in compounds prepared with enriched ^{128}Te the effects accompanying the $^{128}\text{Te}(n,\gamma)^{129}\text{Te}$ reaction may be studied. In each instance, radiochemical studies have been made of the same or comparable transformations.

One aspect of radiochemical studies of recoil atoms in solids which has attracted wide attention in the past is the so-called thermal annealing process.^{1,2} When the solid is heated following the nuclear transformation,

(1) A. G. Maddock and R. Wolfgang in "Nuclear Chemistry," Vol. II, L. Yaaffe, Ed., Academic Press, New York, N. Y., 1968, p 186.

(2) G. Harbottle, *Annu. Rev. Nucl. Sci.*, **15**, 89 (1965).

(3) See H. H. Wickman and G. K. Wertheim in "Chemical Applications of Mössbauer Spectroscopy," V. I. Goldanskii and R. H. Herber, Ed., Academic Press, New York, N. Y., 1968, p 548.

(4) C. E. Violet and R. Booth, *Phys. Rev.*, **144**, 225 (1966).

(5) P. Jung and W. Trifthäuser, *ibid.*, **175**, 512 (1968).

(6) J. F. Ullrich and D. H. Vincent, *J. Phys. Chem. Solids*, **1189** (1969).

(7) C. H. W. Jones and J. L. Warren, *J. Inorg. Nucl. Chem.*, **30**, 2289 (1968).

(8) C. M. Lederer, J. M. Hollander, and I. Perlman, Ed., "Table of Isotopes," Wiley, New York, N. Y., 1968, p 273.

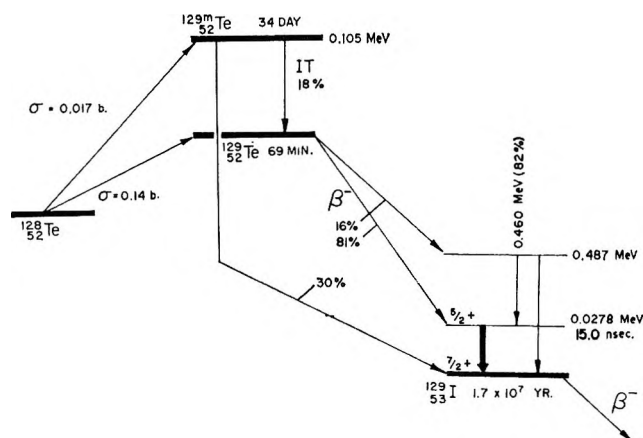


Figure 1. The production and decay of ^{129m}Te and ^{129}Te showing the 27.8-keV Mössbauer transition in ^{129}I .

chemical reactions occur in which the radioactively labeled molecular fragments formed in the preceding transformation take part. These reactions generally lead to the re-formation of the parent molecule, as observed on subsequent radiochemical analysis. The system chosen for the present study allows the investigation, by Mössbauer spectroscopy and radiochemical analysis, of the thermal annealing reactions following both (n,γ) activation and the $^{129m}\text{Te} \rightarrow ^{129}\text{Te}$ isomeric transition. In the latter case the radioactive equilibrium achieved between the long-lived, 34-day ^{129m}Te and the 69-min ^{129}Te daughter allows the study of the annealing process at a variety of temperatures in the same sample, as will be discussed below.

Several Mössbauer studies have been made by other workers of the chemical effects accompanying nuclear reactions in tellurium compounds,⁶ and radioactive decay^{4,5} in tellurium, iodine, and antimony compounds, employing the 35.5-keV 1.6-nsec transition in ^{125}Te . The broad natural line width and the small isomer shifts and quadrupole splittings observed for the ^{129}Te transition lead to very poorly resolved spectra when more than one tellurium species is present. This in turn has led to difficulty in the identification of tellurium fragments formed in the nuclear transformations.⁵ Pasternak⁹ has pointed out the marked advantages of utilizing the ^{129}I transition as a probe for studying the chemistry of tellurium compounds (following the decay of ^{129}Te), in that this transition has a relatively narrower line width and exhibits large isomer shifts and quadrupole splittings.

Prior to the present investigation, Perlow¹⁰ had investigated the $^{127m}\text{Te} \xrightarrow{\beta^-} ^{127}\text{I}$ decay in ^{127}Te -labeled telluric acid, measuring the 57-keV 1.9-nsec ^{127}I Mössbauer spectrum. Pasternak had studied the ^{129}I Mössbauer spectra for chemically prepared $\text{H}_6^{129}\text{TeO}_6$, and for samples of tellurium metal and TeO_2 (orthorhombic) which had been neutron irradiated.^{9b}

Experimental Section

A. Isotope Labeling. For the decay studies, samples were prepared labeled with both the 34-day ^{129m}Te and 69-min ^{129}Te isomers. In the (n,γ) studies, the samples to be irradiated were prepared with $>99\%$ enriched ^{128}Te . Double-labeling experiments were also performed using enriched ^{125}Te to allow characterization of the compounds prepared using ^{125}Te Mössbauer absorption spectroscopy.

^{129m}Te was obtained by irradiating ^{128}Te in the N.R.U. reactor at Chalk River at $\text{ca. } 10^{14} \text{ n cm}^{-2} \text{ sec}^{-1}$ for 2 weeks. The irradiated metal was dissolved in nitric acid. Contaminating ^{131}I activity was removed by extraction into chloroform, and the solution evaporated to dryness. The residue was used in the preparations to be described below.

^{129}Te used in the labeling studies was obtained by employing a radiochemical isomer separation.¹¹ Telluric acid was prepared labeled with ^{129m}Te . In a 6 N HCl solution, the $\text{H}_6^{129m}\text{TeO}_6 \rightarrow ^{129}\text{Te}$ isomeric transition produces bond rupture and stabilization of the ^{129}Te daughter in the IV oxidation state in $>90\%$ of events. On bubbling SO_2 through the solution in the presence of tellurite carrier, the ^{129}Te is selectively reduced to Te metal, the ^{129m}Te remaining in solution as telluric acid. The separated ^{129}Te -labeled metal was then immediately used in a series of very rapid preparations.

The (n,γ) investigations were carried out by irradiating ^{128}Te -enriched compounds in the core of the University of Washington, Seattle, reactor at a flux of $2 \times 10^{12} \text{ n cm}^{-2} \text{ sec}^{-1}$, at an ambient temperature of about 70° . The irradiations lasted 30–60 min. In some instances samples were irradiated in an insulated capsule packed with solid CO_2 to minimize annealing of recoil induced defects. In the irradiations only the 69-min ^{129}Te isotope is produced in significant quantities and the Mössbauer experiments were immediately carried out at the reactor site.

B. Chemical Preparations. The tellurium metal irradiated at N.R.U. was a fine amorphous powder, as obtained from Oak Ridge. Other samples of tellurium metal were prepared by precipitation from acid solution using SO_2 , and by melting the metal in an evacuated quartz tube at 600° and allowing it to cool slowly.

Telluric acid was prepared from TeO_2 dissolved in HNO_3 by permanganate oxidation and precipitated by the addition of nitric acid.¹² Samples of telluric acid thus prepared were used as the starting reagent to prepare the other compounds. The polymer $(\text{H}_2\text{TeO}_4)_n$ and $\alpha\text{-TeO}_3$ were made by heating telluric acid.¹³

(9) (a) M. Pasternak and S. Bukshpan, *Phys. Rev.*, **163**, 297 (1967); (b) M. Pasternak, *Symp. Faraday Soc.*, **1**, 119 (1967).

(10) (a) G. J. Perlow in ref 3, p 377; (b) G. J. Perlow and M. R. Perlow, *J. Chem. Phys.*, **45**, 2193 (1966).

(11) C. H. W. Jones and J. L. Warren, *ibid.*, **53**, 1740 (1970).

(12) F. C. Mathers, C. M. Rice, H. Broderick, and R. Forney, *Inorg. Syn.*, **3**, 145 (1950).

Table I

Compd	¹²⁵ Te		¹²⁹ I		η
	δ^a mm/sec	$e^2qQ(1 + \eta^2/3)^{1/2}$ MHz/sec	δ^b mm/sec	e^2qQ MHz/sec	
Te metal	+0.50 ± 0.15	-446 ± 6	+0.52 ± 0.13	-349 ± 11	0.69 ± 3.2
H ₆ TeO ₆ mono- clinic	-1.23 ± 0.09		-3.59 ± 0.11	+192 ± 5	3
(H ₂ TeO ₄) _n	-1.20 ± 0.05		-3.44 ± 0.03		
α -TeO ₃	-1.01 ± 0.07		-3.05 ± 0.4		
TeO ₂	+0.74 ± 0.11	+388 ± 5	+2.74 ± 0.14	+812 ± 21	0.52 ± 0.07
H ₂ TeO ₃	+0.63 ± 3.34	+385 ± 16	+1.74 ± 0.17	+839 ± 21	0.40 ± 0.6

^a δ quoted with respect to Cu¹²⁵I source. ^b δ quoted as isomer shifts for absorption spectra relative to a Zn¹²⁹Te source. This means subtracting 0.46 mm/sec from the emission spectrum δ and then reversing the sign. $e^2qQ(1 + \eta^2/3)^{1/2}$ for ¹²⁵Te was obtained in MHz/sec by multiplying Δ , the quadrupole splitting in mm/sec, by the conversion factor $2E\gamma/hc = 57.44$ MHz/mm.

Further decomposition at 550° produced TeO₂.¹³ A solution of TeO₂ in nitric acid was neutralized with NaOH solution and at neutrality a white precipitate of H₂TeO₃ separated out.¹⁴

The compounds as prepared above were characterized by thermogravimetric analysis, ir spectroscopy, powder X-ray diffraction studies, and ¹²⁵Te Mössbauer absorption spectroscopy. The measured ¹²⁵Te Mössbauer parameters are given in Table I, and are in good agreement with previously reported values.^{15,16} The telluric acid was found by ir and X-ray diffraction studies to be the monoclinic form¹⁷ and no cubic form could be detected. The polymer gave the reported ir spectrum,¹⁸ and thermogravimetry indicated the theoretical weight loss. The α -TeO₃ gave the reported ir spectrum.¹⁶ However, on the suggestion of Maddock¹⁶ we examined the ¹²⁵Te Mössbauer absorption spectra of α -TeO₃ which showed the presence of between 10 and 40% TeO₂ impurity in different samples. The TeO₂ prepared at 550° was found to be the pure tetragonal form. Tellurous acid, H₂TeO₃, is an unstable compound which readily loses water to give TeO₂. Samples of H₂TeO₃ were characterized by showing that they yielded pure TeO₂ on dehydration at 120°.

C. Mössbauer Experimental. In the early work, spectra were recorded using a T.M.C. 301 constant acceleration spectrometer synchronized with a T.M.C. 306 400-channel analyzer operating in the multiscale mode. A simple styrofoam-insulated cryostat was used in maintaining the source and absorber at $\approx 80^\circ\text{K}$. Much of the work was subsequently performed with an NSec. AM-1 constant acceleration spectrometer and cryoflask coupled to an N.D. 2000 series 512 channel analyzer. The velocity scale of both spectrometers was routinely calibrated using Na₂[Fe(CN)₅NO]·2H₂O and α -Fe₂O₃ for which the standard parameters were assumed.¹⁹

In all ¹²⁹I experiments a 15-mg cm⁻² NaI (anhydrous) absorber was used and this was confirmed as a single-line absorber against a Zn^{129m}Te source. The source and absorber were routinely held at liquid nitrogen tem-

perature, although some experiments using the NSec. system were performed at $\approx 10^\circ\text{K}$ using liquid helium. The 27.8-keV ¹²⁹I γ -ray was measured using a thin NaI(Tl) scintillation detector. Sources prepared in this work ranged in thickness from 10 to 50 mg cm⁻² and in activity from 0.1 to 2 mCi.

For the ¹²⁵Te absorption experiments, a 25-mCi ¹²⁵I in Cu source (New England Nuclear) was used and the 35.5-keV γ -ray monitored using a Xe(CO₂) proportional detector and gating on the 6-keV escape peak.

D. Data Treatment. Spectra were computer fitted, using a program which allowed the constraining of line positions, intensities, and line widths. In many of the unresolved ¹²⁹I quadrupole split spectra, the constraints could not be totally removed, even in the latter part of the fitting. However, the confidence which can be placed in the computer fits obtained may be judged by the internal consistency of the results obtained.

Quadrupole split spectra were fitted according to the general expression^{9,20}

$$\delta_{ij} = \frac{Ce^2qQ}{4E_\gamma} \frac{(C_0^* + C_2^*\eta^2)}{2I^*(I^* - 1)} - \frac{Ce^2qQ}{4E_\gamma} \frac{(C_0 - C_2\eta^2)}{2I(I - 1)} + \delta'$$

from which values for δ' , the isomer shift, e^2qQ , the quadrupole coupling constant, and η , the asymmetry

(13) J. Rosicky, J. Laub, and J. Pavel, *Z. Anorg. Allgem. Chem.*, **334**, 312 (1965).

(14) F. Féher, "Handbook of Preparatory Inorganic Chemistry," Vol. I, G. Brauer, Ed., Academic Press, New York, N. Y., 1963, p 447.

(15) T. C. Gibb, R. Greatrex, N. N. Greenwood, and A. C. Sarma, *J. Chem. Soc. A*, 212 (1970).

(16) N. E. Erickson and A. G. Maddock, *ibid.*, **A**, 1665 (1970).

(17) O. N. Breusov, O. I. Vorob'eva, N. A. Druz', T. B. Revzina, and B. P. Sobolev, *Izv. Akad. Nauk SSSR, Neorg. Mater.*, **2**, 264 (1966).

(18) H. Siebert, *Z. Anorg. Allgem. Chem.*, **301**, 161 (1959).

(19) A. H. Muir, K. J. Ande, and H. M. Coogan, "Mössbauer Effect Data Index 1958-1965," Interscience, New York, N. Y., 1966, p 26.

(20) The theory of the quadrupole splitting for ¹²⁹I Mössbauer spectra has been discussed in detail previously in the literature. In particular ref 9b gives a full discussion of the factors influencing the line positions in the spectra.

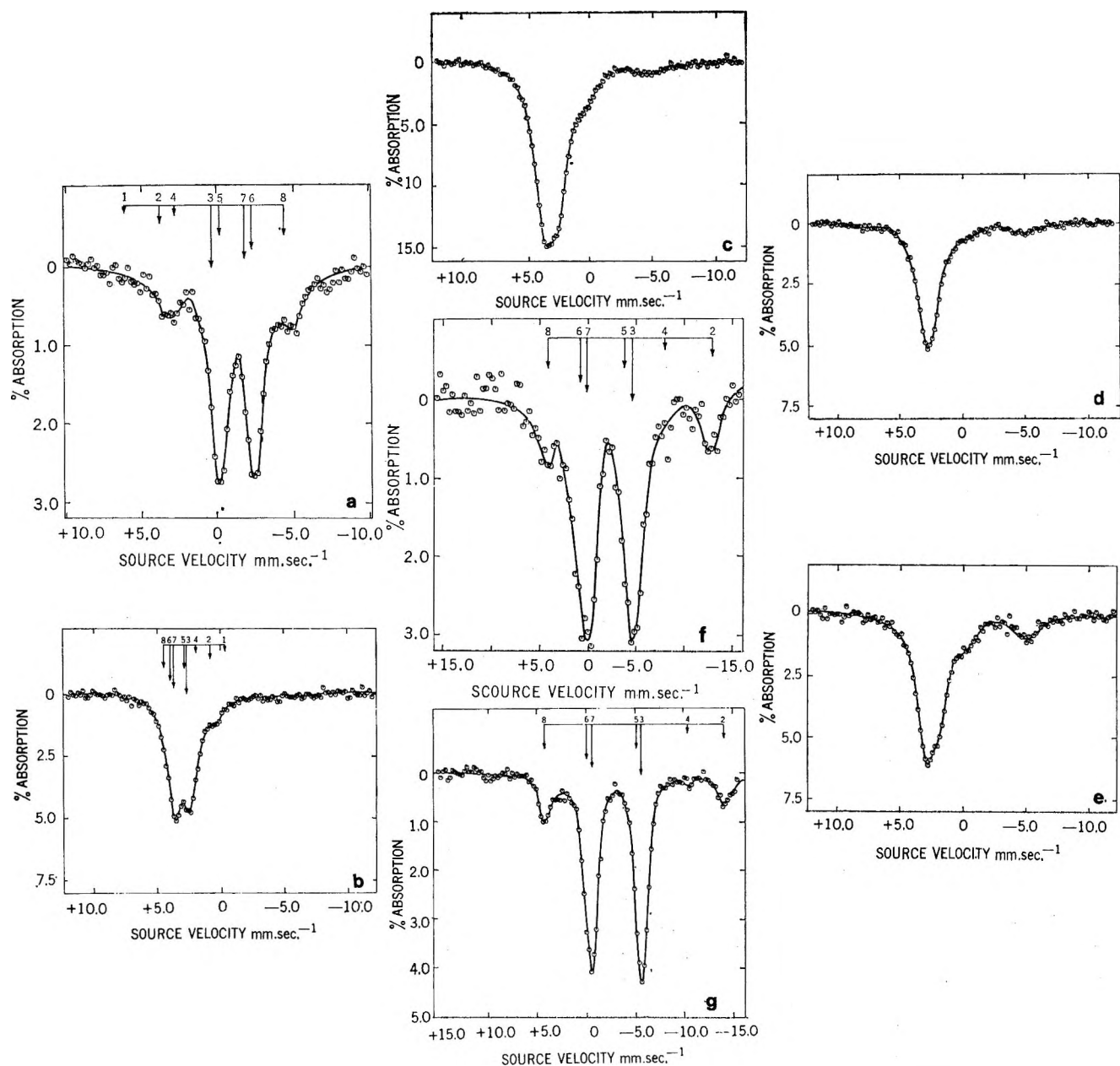


Figure 2. The experimentally measured emission spectra of ^{129}Te -labeled sources measured against a Na^{129}I absorber. All spectra were recorded at 80°K except where noted: (a) elemental tellurium; (b) monoclinic $\text{H}_6^{129}\text{TeO}_6$; (c) monoclinic $\text{H}_6^{129}\text{TeO}_6$, liquid He temperature; (d) $(\text{H}_2^{129}\text{TeO}_4)_n$; (e) $\alpha\text{-}^{129}\text{TeO}_3$ contaminated with TeO_2 ; (f) $\text{H}_2^{129}\text{TeO}_3$; (g) tetragonal $^{129}\text{TeO}_2$. There was significant line broadening in the liquid He experiment attributable to vibrations produced by the boil off of He.

parameter, were obtained, the other symbols in this expression taking their normal meaning.⁹

Results and Discussion

^{129}Te -Labeled Sources. The ^{129}I Mössbauer emission spectra observed for the different ^{129}Te -labeled sources are shown in Figure 2 and the spectrum parameters are shown in Table I.

The tellurium metal ^{129}I spectrum reported here is identical with that previously reported by Pasternak for neutron-irradiated tellurium metal.^{9a} Similarly the telluric acid spectrum is in good agreement with Pasternak's work.^{9b} The liquid helium spectrum for

$\text{H}_6^{129}\text{TeO}_6$ showed a greatly increased σ_0 effect, although the spectrum was less well resolved than that at 80°K . However, the two spectra computed to give the same parameters within the error of the fit.

The ^{129}I emission spectrum of monoclinic $\text{H}_6^{129}\text{TeO}_6$ may be interpreted as exhibiting a small quadrupole splitting. This interpretation was proposed by Pasternak^{9b} and also by Perlow,¹⁰ who observed that the ^{127}I emission spectrum of $\text{H}_6^{127}\text{TeO}_6$, in which the β^- decay of ^{127m}Te directly populates the Mössbauer level, was a broad unresolved line. Both investigators proposed that distortion from regular octahedral geometry about the tellurium atom in monoclinic telluric acid, $\text{Te}(\text{OH})_6$,

was reflected in the iodine Mössbauer spectrum, the daughter iodine remaining bonded to the -OH groups. The X-ray crystal structures of both cubic and monoclinic telluric acid have been discussed by Dutton and Cooper,²¹ who noted several inconsistencies in the reported data. The ir spectra of both cubic and monoclinic telluric acid have been studied in detail¹⁶⁻¹⁸ and provide evidence that the symmetry about the tellurium atom in the cubic form is octahedral, while it is distorted in the monoclinic form, probably by intermolecular hydrogen bonding between adjacent -OH groups.¹⁶ Thus the bands in the ir spectrum of the monoclinic form near 660 cm^{-1} corresponding to the Te-OH stretch¹⁶ are indicative of nonoctahedral geometry about the tellurium. The ir spectra of many samples of telluric acid prepared in the present work were all identical and were in excellent agreement with the data of Erickson and Maddock¹⁶ for the monoclinic form. Powder X-ray photographs were also in agreement with the reported pattern for the monoclinic form.¹⁷

If in the decay of $\text{H}_6^{129}\text{TeO}_6$ the iodine atom remained bonded to the -OH groups of the parent molecule, not only would a small quadrupole splitting be observed, but the Mössbauer isomer shift of the daughter iodine should be comparable to that observed in the absorption spectra of compounds containing IO_6^{5-} or its related ions. The isomer shift for ^{129}I observed in the present work (Table I) is -3.59 mm sec^{-1} which is in reasonable agreement with -3.35 mm sec^{-1} reported for $\text{Na}_3\text{H}_2\text{IO}_6$ by Rama Reddy, *et al.*,²² the latter giving a single line indicative of octahedral geometry in this molecule about the iodine.

Thus the interpretation that in the decay of monoclinic $\text{H}_6^{129}\text{TeO}_6$ the ^{129}I remains bonded to the six hydroxyl groups is consistent with the ir spectral data relating to the distortion in octahedral geometry about the tellurium, and with the expected Mössbauer isomer shift.

For the polymer $(\text{H}_2\text{TeO}_4)_n$ a much smaller quadrupole splitting was observed, the spectrum being essentially a broadened single line with an isomer shift close to that of $\text{Na}_3\text{H}_2\text{IO}_6$. This is again consistent with the ir data, which show lines arising from the inequivalent Te-OH stretch modes in monoclinic telluric acid, and only a broad line with essentially no fine structure for the polymer. It is apparent that in the polymer the geometry around the tellurium must be very close to octahedral.

A small amount of contaminant was observed in the spectra of the H_6TeO_6 (Figure 2c) and $(\text{H}_2\text{TeO}_4)_n$ (Figure 2d,e) sources, which may have been TeO_2 . Thus a small absorption was observed at *ca.* 4 mm/sec which may correspond to part of the quadrupole split spectrum of TeO_2 .

In $\alpha\text{-TeO}_3$ the presence of TeO_2 impurity is clearly discernible, the assignment of lines being made on the basis of the pure TeO_2 ^{129}I spectrum. The ^{129}I emission

and ^{125}Te absorption spectra on the same samples of $\alpha\text{-TeO}_3$ gave very close agreement for the per cent of TeO_2 impurity present in the samples. The $\alpha\text{-TeO}_3$ molecules themselves yield, on β^- decay, a single ^{129}I line with about the same isomer shift as observed in $\text{H}_6^{129}\text{TeO}_6$ and $(\text{H}_2^{129}\text{TeO}_4)_n$. The large positive values of the isomer shift in the emission spectra show that in all three Te(VI) compounds, the tellurium employs (spd) hybrid orbitals in bonding to the ligand -OH and -O leading to a low s electron density at the nucleus. In monoclinic H_6TeO_6 the ligands are arranged in a distorted octahedron, while in the polymeric compounds $(\text{H}_2\text{TeO}_4)_n$ and TeO_3 the geometry approaches much more closely to octahedral. In each instance, following the β^- decay, the iodine remains bonded to the ligands of the precursor molecule.

In H_2TeO_3 the ^{129}I emission spectrum had an isomer shift characteristic of an iodate ion, and with an asymmetry parameter, η , and a quadrupole coupling constant similar to those observed by nqr for the HIO_3 molecule.²³ Again, following β^- decay, the parent molecular configuration is retained. In TeO_2 the ^{129}I spectrum is again quadrupole split. Only one iodine lattice site is observed following the decay and the iodine presumably finds itself in the same lattice environment as the parent tellurium.

For the purpose of the present study, the results of Figure 2 and Table I provide the very basic information of the Mössbauer spectrum for an ^{129}I nucleus present at a lattice site identical with that of the parent tellurium in each of these compounds. However, several other pieces of general information can be abstracted from these spectra.

Thus, while the ^{129}I emission spectrum in monoclinic telluric acid exhibited a measurable quadrupole splitting, the ^{125}Te absorption spectrum did not. This is a consequence of the small quadrupole moment of the ^{125}Te excited nucleus and the large natural line width of the ^{125}Te transition. Pasternak^{9a} has determined a value for the ratio of the quadrupole coupling constants for ^{125}Te and ^{129}I nuclei in equivalent lattice sites in orthorhombic TeO_2 and $\text{Te}(\text{NO}_3)_4$. He found

$$\frac{q_{\text{at}}(\text{Te})Q^{125}}{q_{\text{at}}(\text{I})Q^{127}}(1 + \frac{1}{3}\eta^2)^{1/2} = 0.28$$

where q is the electrostatic field gradient at the nucleus, Q is the quadrupole moment, and η the asymmetry parameter.

From the values of the present work for H_2TeO_3 and tetragonal TeO_2 , and those of Pasternak, it is found that

(21) W. A. Dutton and W. C. Cooper, *Chem. Rev.*, **66**, 657 (1966).

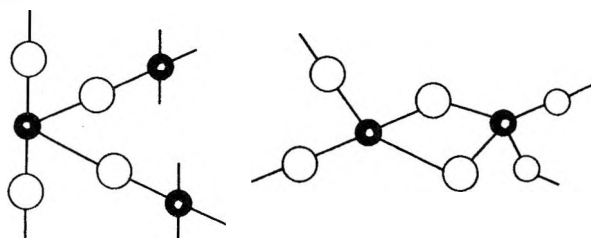
(22) K. Rama Reddy, F. De Sousa Barros, and S. De Benedetti, *Phys. Lett.*, **20**, 297 (1966).

(23) R. Livingstone and H. Zeldes, *J. Chem. Phys.*, **26**, 351 (1959).

$$\frac{q_{\text{at}}(\text{Te})Q^{125}}{q_{\text{at}}(\text{I})Q^{129}}(1 + \frac{1}{3}\eta^2)^{1/2} = 0.45$$

Note that this is the ratio for the isotopes ^{125}Te and ^{129}I and that the ^{127}I values have been transposed into ^{129}I values. On this basis, given the measured quadrupole coupling for ^{129}I in monoclinic telluric acid, it is apparent that Δ , the quadrupole splitting for ^{125}Te , should be 1.7 mm/sec. Since the natural line width for the ^{125}Te transition is 5.32 mm/sec such a small quadrupole splitting is not resolved.

It is also of interest to examine the ^{129}I data for tetragonal TeO_2 , which shows a different isomer shift from that of the orthorhombic modification, but the same quadrupole coupling constant and asymmetry parameter. Zemann²⁴ had discussed the structure for these two polymeric crystal modifications. In both instances the tellurium is four-coordinate and the oxygens are disposed in a distorted trigonal bipyramidal arrangement with an equatorial position unoccupied. However, in the tetragonal form each oxygen is bonded to different telluriums (corner bridging) while in the orthorhombic modification two of the four bridging oxygens are shared by two adjacent telluriums (edge bridging)



tetragonal TeO_2	orthorhombic TeO_2
$\delta = +2.74 \pm 0.14$	$\delta = +1.52 \pm 0.01$ mm/sec
$e^2qQ = +812 \pm 21$	$e^2qQ = +786 \pm 7$ MHz/sec
$\eta = 0.52 \pm 0.07$	$\eta = 0.55 \pm 0.05$
(This work)	(ref 9a)

The similarity in the disposition of bonds about the tellurium is reflected in the similar quadrupole couplings and asymmetry parameters. The difference in isomer shifts presumably derives from differences in s character of the parent Te-O bonds in the two forms. Thus the more negative isomer shift in the emission spectrum of the tetragonal form is evidence of a higher s-electron density at the ^{129}I nucleus, corresponding to a lower s character in Te-O bonds than in orthorhombic TeO_2 . If we assume, on the basis of this large negative isomer shift, that in tetragonal TeO_2 the bonding is pure p, involving no s character, then we can calculate the number of holes in the p shell of the iodine from the standard isomer shift expression^{25,26}

$$\delta = 1.5h_p - 0.54$$

where δ is the isomer shift in millimeters second⁻¹ and h_p is the number of holes in the 5p shell of the iodine.

This leads to a value of $h_p = 2.1$. The same value for the quadrupole coupling in the two forms indicates the same value for U_p , the p electron deficit where U_p is defined as $U_p = -U_z + (U_x + U_y)/2$. If we make the assumption that this, together with the known similarity in coordination and geometry, implies similar values for h_p in the two modifications, then we can calculate the amount of s character in the Te-O bonds for the orthorhombic TeO_2 , using the general expression²⁵

$$\delta = -8.2h_s + 1.5h_p - 0.54$$

where δ , the isomer shift, is in millimeters sec⁻¹ and h_s is the number of holes in the 5s shell of the iodine. We then find that the participation of 0.16 s electron in the bonding in the orthorhombic form is sufficient to lead to the observed difference in isomer shift from that of the tetragonal form.

Lastly, the ^{125}Te and ^{129}I data presented here allow a redetermination of the isomer shift ratio, $\delta^{125}\text{Te}/\delta^{129}\text{I}$, and thus the ratio of the changes in nuclear radii, $\rho^{125}\text{Te}/\rho^{129}\text{I}$, occurring in the Mössbauer transitions for these two nuclei. Ruby and Shenoy²⁷ determined this ratio to be +0.31. However, Gibb, *et al.*,¹⁵ were critical of their analysis, since it relied on the measurement of δ for tellurium and iodine compounds which in some instances were not isoelectronic or isostructural. In the present case we are able to compare the ^{125}Te and ^{129}I data for nuclei in precisely the same lattices. The analysis is shown in Figure 3. From a least-squares fit to the data of Figure 3, we find

$$\frac{\delta^{125}\text{Te}}{\delta^{129}\text{I}} = +0.29; \quad \frac{\rho^{125}\text{Te}}{\rho^{129}\text{I}} = 0.28$$

It is apparent from Figure 3 that the data for tellurium metal lie a long way off the least-squares fit. This implies that following the decay of ^{129}Te in tellurium metal the ^{129}I finds itself in a lattice environment quite different from that of the parent tellurium. This point was previously raised by Pasternak,^{9a} who noted that the quadrupole coupling data for ^{129}I and ^{125}Te in tellurium metal yielded an anomalous value for

$$\frac{q_{\text{at}}(\text{Te})Q^{125}}{q_{\text{at}}(\text{I})Q^{129}} \left(1 + \frac{\eta^2}{3}\right)^{1/2}$$

^{129m}Te-Labeled Sources and Neutron Irradiated Samples. In discussing the results for the ^{129m}Te-labeled sources it must be noted that the high X-ray back-

(24) J. Zemann, *Z. Kristallogr., Kristallgeometrie, Kristallphys., Kristallchem.*, **127**, 319 (1968).

(25) S. Bukshpan, C. Goldstein, and J. Soriano, *J. Chem. Phys.*, **51**, 3976 (1969).

(26) The proposal that the bonding in the iodate ion and in the iodine interhalogen compounds may be described in terms of pure p bonds has been extensively discussed in the literature, *e.g.*, see ref 10. The equation given here is taken from the recent ref 22.

(27) S. L. Ruby and G. K. Shenoy, *Phys. Rev.*, **186**, 326 (1969).

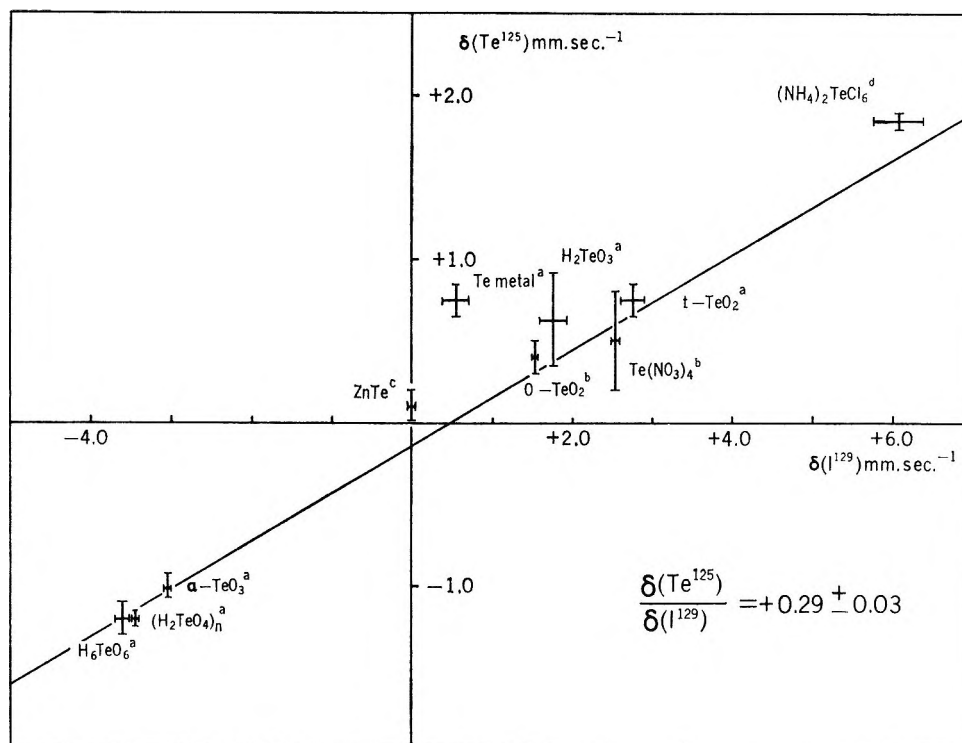


Figure 3. The isomer-shift plot for ^{125}Te and ^{129}I measured in the same parent tellurium compound. The ^{129}I isomer shifts are again quoted for an absorption experiment. The least-squares fit is shown: (a) this work; (b) reference 9a; (c) reference 4; (d) reference 11.

ground from the internal conversion of the isomeric transition leads to very small $\%$ effects. The Te X-rays overlap the 27.8-keV Mössbauer transition and cannot be resolved with a NaI(Tl) detector.

For experiments with elemental tellurium it was found that $^{129\text{m}}\text{Te}$ and ^{129}Te -labeled sources prepared by precipitation from solution gave identical spectra. Moreover, samples of tellurium metal, as obtained from Oak Ridge, which were neutron irradiated to give $^{129\text{m}}\text{Te}$ or ^{129}Te sources also gave the same spectrum. Furthermore, melting $^{129\text{m}}\text{Te}$ sources and allowing the molten metal to crystallize gave samples which again yielded the same ^{129}I spectrum. It is concluded that in elemental tellurium, in the several different forms in which samples were prepared, no physical effects of either the isomeric transition or (n, γ) reaction were observed. Moreover, the ^{129}I nuclei were found to be in identical lattice environments in each of these samples and thus no phase effects were observed.

Of the tellurium oxycompounds, telluric acid showed the most clear effects of molecular disruption accompanying both the isomeric transition and thermal neutron capture. In Figure 4 are shown sample spectra for several telluric acid sources. In these experiments, $\text{H}_6^{129\text{m}}\text{TeO}_6$ sources were allowed to reach radioactive equilibrium with the daughter ^{129}Te at either liquid helium or liquid N_2 temperature, and the Mössbauer spectrum was then recorded at that temperature. In one experiment an aqueous solution of $\text{H}_6^{129\text{m}}\text{TeO}_6$

was frozen at 80°K and the spectrum for the ice matrix recorded at that temperature. For the (n, γ) experiment the irradiation was performed at ambient temperature in the Seattle reactor. These experiments were repeated on many samples of H_6TeO_6 , all of which were shown by ir and ^{125}Te absorption spectroscopy to be free of contaminating TeO_2 .

A comparison of the data of Figure 4 with those of Figure 2 clearly shows that following isomeric transition or neutron capture in telluric acid, the ^{129}Te atoms are stabilized in the solid not only in the parent H_6TeO_6 form, but also apparently as a Te(IV) fragment. The spectra of Figure 4 could be accurately computer fitted, assuming the presence of a Te(VI) component identical with monoclinic telluric acid and a tellurite ion with the

Table II

Source	—Distribution ^a of products in %—	
	$^{129}\text{Te(VI)}$	$^{129}\text{Te(IV)}$
$\text{H}_6^{129\text{m}}\text{TeO}_6$ liquid N_2	53 ± 3	47 ± 3
$\text{H}_6^{129\text{m}}\text{TeO}_6$ liquid He	56 ± 3	44 ± 3
$\text{H}_6^{129\text{m}}\text{TeO}_6$ (ice)	50 ± 3	50 ± 3
$\text{H}_6^{129\text{m}}\text{TeO}_6$ (n, γ), 343°K	59 ± 3	41 ± 3
$(\text{H}_2^{129\text{m}}\text{TeO}_4)_n$ liquid N_2	63 ± 3	37 ± 3
$(\text{H}_2^{129\text{m}}\text{TeO}_4)_n$ liquid Ne	62 ± 3	38 ± 3

^a Computed from the relative areas under the absorption peaks, assuming that the recoil free fractions for the two parent Te species are the same.

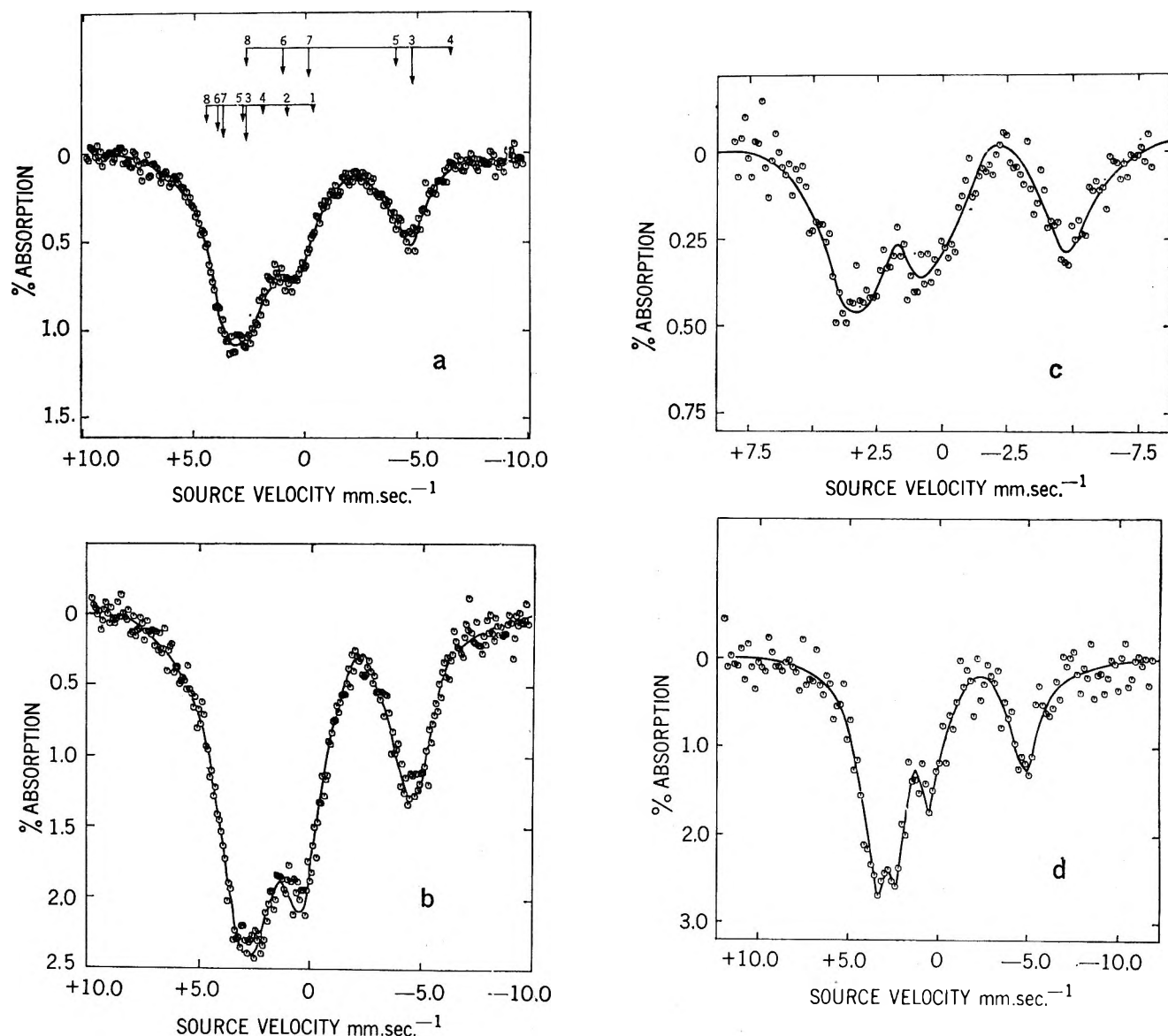


Figure 4. The experimentally measured emission spectra for ^{129m}Te -labeled sources: (a) $\text{H}_6^{129m}\text{TeO}_6$ at 80°K ; (b) $\text{H}_6^{129m}\text{TeO}_6$ at liquid He temperature; (c) $\text{H}_6^{129m}\text{TeO}_6$ in H_2O ice at 80°K ; (d) H_6TeO_6 neutron-irradiated (at 70°) to produce ^{129}Te recoil atoms in the source.

same δ and e^2qQ as for H_2TeO_3 but with $\eta = 0$. The results of these analyses are shown in Table II. It is implicit in these analyses that there are no effects of the β^- decay in these compounds and that the ^{129}I spectra accurately reflect the chemical forms of the ^{129}Te atoms following the transformation.

Independently prepared sources yielded reproducible spectra, although the analyses of the relative areas in the absorption spectra deriving from the Te(VI) and Te(IV) fractions yielded differences of $\pm 3\%$. In all the telluric acid sources the lower valence fraction could be fitted assuming the same values for δ and e^2qQ , and these values correspond to those of a parent TeO_3^{2-} ion. If H_2TeO_3 itself were formed as a product of the decomposition, then the lower valence fraction would have an asymmetry parameter, η . Since η is

only reflected in the positions of lines 4 and 8 in a quadrupole split spectrum, it is very difficult in the present case to totally exclude the possibility that H_2TeO_3 is formed. However, it was found that if it was assumed that $\eta = 0$, then a statistically more acceptable fit was obtained for all of the spectra of Figure 2. On this basis we conclude that the product of decomposition was probably the tellurite ion.

It is interesting that in the molecular decomposition accompanying the nuclear transformation the bonding to the tellurium changes very markedly in character. In the parent H_6TeO_6 molecule the tellurium is employing $5s^2$ electrons in forming bonds with the $-\text{OH}$ groups leading to a low s -electron density at the nucleus, as reflected in the isomer shift. Following molecular fragmentation, the tellurium is now employing almost pure

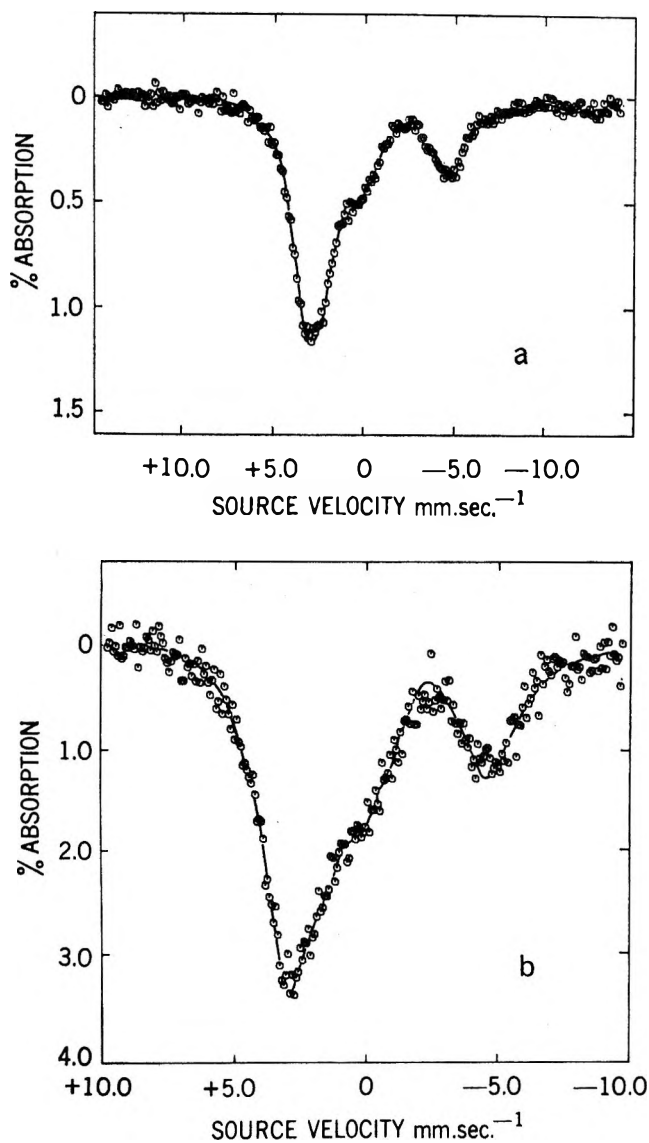


Figure 5. Spectra for $(\text{H}_2^{129\text{m}}\text{TeO}_4)_n$: (a) 80°K ; (b) liquid He temperature.

p-orbital bonding, again as reflected in the isomer shift, which now indicates a high s-electron density at the parent tellurium nucleus. Thus the molecular disruption which occurs does not lead simply to a change in the coordination number of the tellurium, but leads to a very fundamental change in the nature of the bonding.

In the polymer, molecular fragmentation was observed following the isomeric transition as shown in Figure 5 and Table II. The yield of the Te(IV) fragment was now significantly decreased in comparison with that for telluric acid. Again the samples used in these experiments were found to be totally free of TeO_2 or any other tellurium impurity.

For TeO_3 the known presence of TeO_2 impurity from the preparation considerably complicated the interpretation of the spectra obtained, since the unresolved split spectrum of TeO_2 overlapped that of any decom-

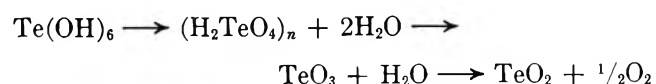
position products formed in the nuclear transformation. For this reason results for TeO_3 are not presented here.

In tetragonal TeO_2 the spectra obtained for sources labeled with $^{129\text{m}}\text{Te}$, or which had been neutron irradiated, were identical with those obtained for ^{129}Te sources, showing the total absence of any chemical effects of the transformations. Similarly H_2TeO_3 sources labeled with $^{129\text{m}}\text{Te}$ again gave spectra identical with those of ^{129}Te -labeled sources. Neutron irradiation studies were not carried out on H_2TeO_3 .

From the above results several conclusions can be drawn. Chemical effects accompanying the isomeric transition and (n, γ) reaction were positively identified in H_6TeO_6 and following the isomeric transition in $(\text{H}_2\text{-TeO}_4)_n$. No such effects were observed in the Te metal, TeO_2 , or H_2TeO_3 . In the Te(VI) compounds only one decomposition product was formed, tentatively identified as a TeO_3^{2-} ion, and this same product was formed in both the isomeric transition and (n, γ) reaction. In TeO_2 and H_2TeO_3 there was no evidence for the stabilization of higher oxidation states. Thus the chemical effects of the nuclear transformation in this system are quite simple, leading to molecular decomposition where this can occur, and the presence of the ^{129}Te recoil atom in a simple, stable chemical form in the solid.

Both the isomeric transition and (n, γ) reaction lead to the deposition of energy at the recoil site in the crystal, and in a certain fraction of events the energy made available is great enough to lead to fragmentation of the parent molecule. The isomeric transition is internally converted in $\approx 100\%$ of events and this leads to an Auger cascade, with ensuing electronic excitation and multiple ionization of the daughter atom. In the (n, γ) reaction the daughter atom acquires kinetic energy of recoil as a consequence of momentum conservation. Electronic excitation and ionization may also occur if low energy states in the γ cascade have high internal conversion coefficients. The results of the present work show that in telluric acid these two different transformations have the same net effect, leading to fragmentation of the parent molecule in a certain fraction of events, and the formation of TeO_3^{2-} .

The mode of decomposition observed following the nuclear transformation shows several differences from normal thermal decomposition. In the latter, as shown in Figure 2, telluric acid first polymerizes, then eliminates H_2O with the formation of polymeric TeO_3 and finally loses O to give TeO_2 .



In the nuclear transformation in H_6TeO_6 there was no evidence for the formation of polymer $(\text{H}_2^{129}\text{TeO}_4)_n$ or TeO_3 , which would give a single line in the Mössbauer spectrum overlapping the quadrupole split spectrum of

monoclinic H_6TeO_6 . Also the observed decomposition product appeared to be TeO_3^{2-} rather than TeO_3 .

The above results show some similar trends to those obtained by Jung and Trifthäuser⁵ in studying the chemical form of ^{125}Te observed following electron capture of $Na^{125}IO_4$. In that instance Na_2TeO_4 and TeO_3 were proposed as the only products of the decay. In $Na^{125}IO_3$, the tellurium daughter was observed in the form Na_2TeO_3 and TeO_3 . In the present work there was no evidence for the stabilization of higher oxidation states in H_2TeO_3 and TeO_2 .

Lebedev²⁸ is reported to have studied the effects of the $^{125m}Te \rightarrow ^{125}Te$ isomeric transition in H_6TeO_6 and observed a broad unsymmetrical absorption peak, which was ascribed to the presence of unresolved lines due to decomposition products, formed in the decay, overlapping the H_6TeO_6 absorption. The $^{125m}Te \rightarrow ^{125}Te$ isomeric transition is also reported²⁹ to produce several stable tellurium charge states in glasses, although details of these experiments have not been published. These reports are certainly consistent with the findings of the present work.

Investigations⁶ of thermal neutron capture in tellurium metal and tetragonal TeO_2 , using the ^{125}Te transition as the probe, showed the absence of any effects in those lattices, again consistent with the present work.

Annealing Effects. The study of annealing effects in telluric acid provided further concrete evidence of the occurrence of molecular decomposition accompanying both the I.T. and (n, γ) reaction. In describing these experiments it must be emphasized that in the $^{129m}Te \rightarrow ^{129}Te$ isomeric transition, the daughter ^{129}Te atoms exist in radioactive equilibrium with the parent ^{129m}Te atoms and that equilibrium is reached in about 8 hr. This radioactive equilibrium permits the study of the effect of temperature on the chemical products formed in the isomeric transition.

Thus on allowing a sample of $H_6^{129m}TeO_6$ to reach radioactive equilibrium at 100° , then cooling the sample to liquid N_2 temperature, and immediately recording the Mössbauer spectrum for a short counting period (≈ 40 min), the chemical effects of the isomeric transition at 100° were observed. Of the ^{129}Te atoms decaying to populate the Mössbauer level in ^{129}I during the 40-min counting period, $\approx 80\%$ were born in the isomeric transition at the elevated temperature before the spectrum was recorded. Obviously, in such an experiment the counting period had to be kept very short, and as a consequence the spectra obtained had poor statistics. Nevertheless, as can be seen from Figure 6, annealing reactions were clearly observed at $373^\circ K$, leading to a decrease in all of the lines of the quadrupole split Te(IV) fraction and an increase in the Te(VI) fraction.

For a sample allowed to reach transient equilibrium at room temperature, the spectrum accumulated over 40 min was very similar to that for a sample which

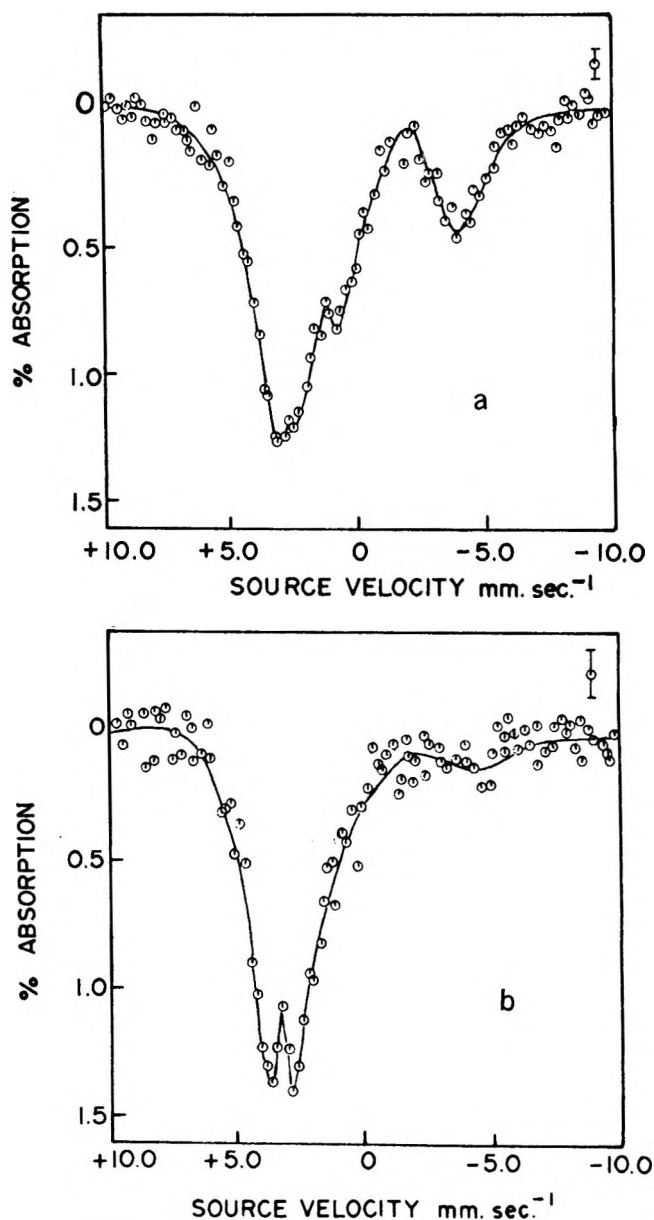


Figure 6. A comparison of spectra for $H_6^{129m}TeO_6$ allowed to reach equilibrium at: (a) $80^\circ K$; (b) $373^\circ K$.

reached equilibrium at $80^\circ K$. Thus no annealing was observed between 80 and $298^\circ K$.

It was found that if a sample was heated several times at 100° and its spectrum recorded after each heat treatment, cycles of annealing carried out in this way gave quite reproducible results, and the sample gave no evidence of macroscopic decomposition during these experiments. Moreover, in one experiment, following heating at 100° and immediately recording the Mössbauer spectrum for 40 min, the sample was maintained at liquid N_2 temperature and spectra were recorded for 1-hr

(28) V. A. Lebedev, R. A. Lebedev, A. M. Babeshkin, and A. N. Nesmeyanov in ref 3, p 621.

(29) L. Grodzins in "Perturbed Angular Correlations," E. Karlsson, E. Mathias, and K. Seigbahn, Ed., North-Holland Publishing Co., Amsterdam, 1964, p 335.

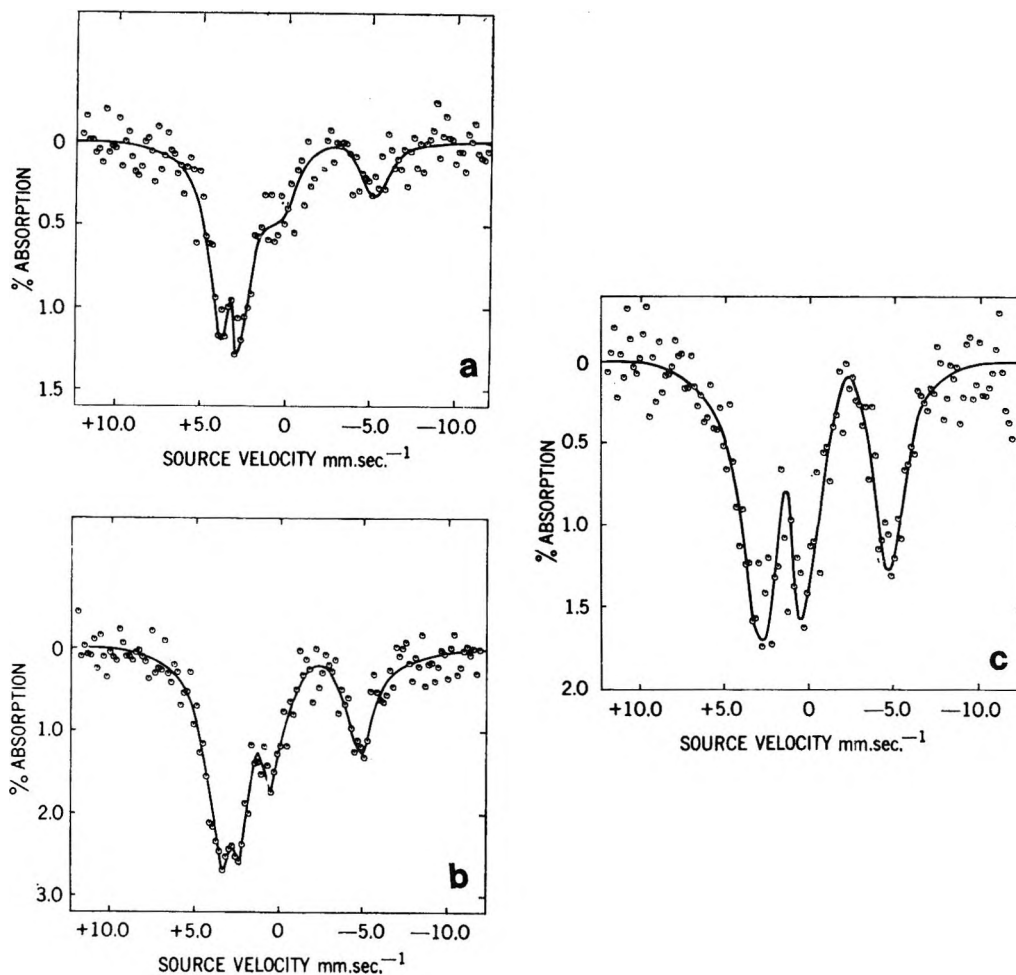


Figure 7. Spectra for H_6TeO_6 samples irradiated in the Seattle reactor: (a) irradiated at 70° and heated for 10 min at 100° following the irradiation; (b) irradiated at 70° ; (c) irradiated in solid CO_2 . The differences in per cent absorption in the different spectra reflect in part differences in the time following the irradiation before these short-lived sources were placed in the spectrometer.

counting periods every hour. It was observed that the Te(IV) fraction reappeared in the spectrum and this "regrowth" was characterized by the 69-min half-life of the ^{129}Te daughter. This provided irrefutable evidence that the Te(IV) reaction was a product of molecular decomposition accompanying the isomeric transition.

It was important to establish whether the spectra of Figure 6 were evidence of a temperature dependence of the isomeric transition process itself, or whether they represented an annealing reaction in which stable Te(IV) fragments formed in the crystal in the decay event were subsequently annealing to yield Te(VI) molecules. An experiment was therefore carried out in which the sample was allowed to reach transient equilibrium at room temperature over an 8-hr period and was then heated at 100° for 15 min. The spectrum was then immediately recorded at liquid N_2 temperature. The spectrum obtained was very similar to that for a sample allowed to reach transient equilibrium at 100° . This is interpreted as evidence that the process occurring was a chemical reaction involving stabilized Te(IV) fragments

in the crystal and that there was no temperature dependence of the isomeric transition process itself.

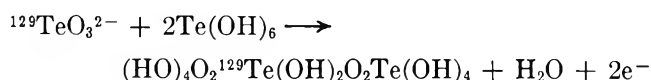
Similar experiments to the above were carried out on neutron-irradiated samples of telluric acid. In Figure 7 are shown spectra for samples which were neutron irradiated at room temperature, solid CO_2 temperature, and for a sample heated to 100° for 10 min immediately following the irradiation prior to recording the spectrum. These experiments clearly show that irradiation at room temperature and annealing at 100° both resulted in a lower Te(IV) fraction than irradiation at solid CO_2 temperature. A chemical reaction occurred at elevated temperatures leading to a decrease in the Te(IV) fraction and an increase in the Te(VI) fraction.

All of these annealing reactions were characterized by the same properties; they led to the conversion of the Te(IV) fraction into a Te(VI) form, in a single-step reaction in which no intermediate products were observed. One is left to conjecture as to the mechanism of the annealing reaction which occurs. Certainly the annealing reaction leads to a fundamental change in the

Table III

Transformation	Temperature of decay or irradiation, °K	Mössbauer study		Radiochemical study	
		Observed recoil products	Distribution in %	Observed recoil products	Distribution in %
$H_6^{129m}TeO_6 \xrightarrow{I.T.} {}^{129}Te$	298	H_6TeO_6	53	Te(VI)	64
		TeO_3^{2-}	47	Te(IV)	36
$H_6^{128}TeO_6 \xrightarrow{n,\gamma} {}^{129}Te$	343	H_6TeO_6	59	Te(VI)	56.3
		TeO_3^{2-}	41	Te(IV)	42.7
$H_6^{129}TeO_6 \xrightarrow{\beta^-} {}^{129}I$	80	IO_6^{5-}	100		
$H_6^{131m}TeO_6 \xrightarrow{\beta^-} {}^{131}I$	80			IO_4^-	20
	(dissolved at room temperature)			IO_3^-	69
				I^-	11

nature of the bonding to the tellurium, the pure p bonding in TeO_3^{2-} changing to that of spd hybrids in the Te(VI) form. One can invoke a simple oxidation of the TeO_3^{2-} to $TeO_3 + 2e^-$; however it is difficult to see how, in the telluric acid matrix, this could lead to a six- or four-coordinate tellurium, yielding an essentially single-line ${}^{129}I$ spectrum. On the basis of the known propensity of telluric acid to polymerize on heating, a quite plausible reaction path might be



Such a reaction may occur within the unusual environment of the recoil site at temperatures considerably below that at which polymerization normally occurs in telluric acid.

Comparison with Radiochemical Results. In Table III the main features of the results of the Mössbauer study are briefly compared with those for the previously reported radiochemical study.⁷

Considering the ${}^{129}Te$ recoil atoms, the radiochemical investigations provided only a simple description of the labeled products, observed following dissolution, in terms of the Te(VI) and Te(IV) oxidation states. The Mössbauer study, in contrast, allowed a more positive identification of the chemical forms of the ${}^{129}Te$ recoil atoms present in the solid. However it is apparent that, since the recoil product distribution in the solid was in fact extremely simple in this case, the radiochemical study gave a fairly accurate description of the processes which occurred. In examining the results of annealing experiments, the Mössbauer work clearly showed that the annealing reaction was a single-step process in which the TeO_3^{2-} fragment was converted into a Te(VI) molecule. The radiochemical study did not provide such detailed information about the nature of the annealing reaction.

A quantitative comparison of the data obtained by the two techniques is not very meaningful, because the recoil-free fractions for the different tellurium products observed in the Mössbauer spectra may be different.

However, it can be concluded that the results appear to be in reasonable agreement.

Turning to the results on the effects of β^- decay, it is clear that the two studies provided different information. The Mössbauer experiments show that following β^- decay at liquid N_2 temperature in ${}^{129}Te$ -labeled telluric acid, the daughter ${}^{129}I$ remains bonded to the ligand $-OH$ groups over a time long by comparison with the 15-nsec half-life of the Mössbauer transition. In comparison in ${}^{131m}Te$ -labeled telluric acid allowed to undergo β^- decay at $80^\circ K$, warmed to room temperature, and dissolved for radiochemical analysis, a spectrum of ${}^{131}I$ -labeled chemical products was observed. The internal conversion accompanying the decay of ${}^{131m}Te$ in some 18% of events cannot be the sole explanation for the observed product distribution. There are two possible explanations for the radiochemical results, one being that the IO_6^{5-} ion decomposes in the H_6TeO_6 lattice at room temperature, and the other that chemical reactions occur following dissolution which yield the observed product distribution.

There is evidence from the radiochemical work to support the proposal that the ${}^{131}IO_6^{5-}$ ion must decompose in the $H_6{}^{131m}TeO_6$ lattice following the β^- decay. Thus, if following the decay of the ${}^{131m}Te$ the solid is heated before dissolution, the distribution of ${}^{131}I$ activity between the forms I^- , IO_3^- , and IO_4^- observed in solution is found to change markedly.⁷ This shows that the ${}^{131}I$ -labeled fragment present in the solid following the decay undergoes a chemical or physical change in the solid on heating.

In this instance it would be advantageous to be able to study the ${}^{129}Te \xrightarrow{\beta^-} {}^{129}I$ decay at, or near, room temperature using the Mössbauer technique to see if in fact the IO_6^{5-} ion does fragment following the decay. Experiments were attempted in which the spectrum of $H_6{}^{129m}TeO_6$ was recorded at 142 and $113^\circ K$, using slurries of *n*-pentane and isopentane with liquid nitrogen to maintain the source and absorber at these temperatures. Unfortunately however no measurable resonance absorption was observed.

Acknowledgments. The authors wish to thank Dr. F. Brown, Head of the Solid State Research Branch at Atomic Energy of Canada Ltd., Chalk River, and Professor A. L. Babb and the staff at the reactor at the University of Washington, Seattle, for their kind assistance in performing the many reactor irradiations involved in this work. We also thank Dr. A. J. Stone

and Dr. A. G. Maddock of the University of Cambridge, England, the former for kindly providing us with a copy of his Mössbauer computer program and the latter for making available a preprint of his work on ^{125}Te Mössbauer absorption spectroscopy. A grant from the National Research Council of Canada is gratefully acknowledged.

NOTES

Freezing Point Depression Measurements in *N*-Methylacetamide As a Solvent

by O. D. Bonner* and G. B. Woolsey

*Department of Chemistry, University of South Carolina,
Columbia, South Carolina 29208 (Received December 11, 1970)*

*Publication costs borne completely by The Journal of
Physical Chemistry*

Persons interested in the chemistry of aqueous solutions frequently find it instructive to study solutions in other solvents of high dielectric constant such as *N*-methylacetamide (NMA), acetonitrile, dimethyl sulfoxide, ethylene carbonate, etc. Studies involving NMA were begun in this laboratory in 1961 and because of the experimental difficulties with this solvent the first results were published¹ only in 1964. A summary of these experimental findings should precede the new data to be presented.

Physical Properties of NMA

Most of the earlier work in this solvent was due to Dawson and coworkers. He reported² in 1957 a melting point "above 29.5°" and a dielectric constant of 165.5 at 40°. Several fractional freezings were reported³ in 1961 to yield a material having a freezing point of 30.2°. We have noted that these purification techniques indeed give material of this quality but that when solid NMA is stored in a *dry* atmosphere near its melting point a layer of liquid material is soon evident. We therefore resorted to zone-refining and obtained a material melting at $30.55 \pm 0.01^\circ$ which is the highest melting point reported to this time. This figure is substantiated by the recent data of Kreis and Wood.⁴ The dielectric constant of this material at 40° is 184.3 ± 0.5 for fresh solvent samples extrapolated to zero time. The value falls rather rapidly with time, however, and approaches the value reported earlier. This

was the first indication to us of the instability of pure NMA when maintained in the liquid form at 40°. There was no possibility of the involvement of water in this closed system. Liquid NMA was found to be more stable at 32°, and a dielectric constant for the pure material was found to be 191.3 ± 0.5 compared to the interpolated⁵ literature value of 173.6. It was further observed that the melting point of zone-refined NMA decreased with time if it were maintained in the liquid state. It was also noted, but not reported, that NMA "decomposition" was slowest for the pure material in glass containers. The rate was accelerated when solutes were added and was much faster when the liquid was in contact with a metal surface.

Freezing Point Depression Measurements

A cryoscopic constant of 6.65 ± 0.05 was reported¹ for NMA by an extrapolation of $\Delta T/m$ for solutions of carbon tetrachloride, *o*-dichlorobenzene, and bromobenzene to infinite dilution. This value was confirmed⁶ for solutions of *meso*-erythritol, ethyl oxalate, phthalonitrile, phenanthrene, and 1,1,2,2-tetrachloro-1,2-difluoroethane. It was found, however, that there was considerable curvature in the $\Delta T/m$ vs. m plots in very dilute solutions (below 0.05 m). The values of $\Delta T/m$ remained much more constant between 0.05 and 0.2 m and an extrapolation using data for concentrations greater than about 0.06 m would yield a cryoscopic constant of about 6.0 ± 0.2 . This observation is in-

(1) O. D. Bonner, C. F. Jordan, and K. W. Bunzl, *J. Phys. Chem.*, **68**, 2450 (1964).

(2) L. R. Dawson, E. D. Wilhoit, R. R. Holmes, and P. G. Sears, *J. Amer. Chem. Soc.*, **79**, 3004 (1957).

(3) L. R. Dawson, R. C. Sheridan, and H. C. Eckstrom, *J. Phys. Chem.*, **65**, 1829 (1961).

(4) R. W. Kreis and R. H. Wood, *J. Chem. Thermodyn.*, **1**, 523 (1969).

(5) G. R. Leader and J. F. Gormley, *J. Amer. Chem. Soc.*, **73**, 5731 (1951).

(6) O. D. Bonner, K. W. Bunzl, and G. W. Woolsey, *J. Phys. Chem.*, **70**, 788 (1966).

teresting in the light of some unpublished data by Wicker.⁷ Cryoscopic measurements on 15 solutions of alkali metal salts between concentrations $\nu m = 0.2$ and 2.6 (or the limit of solubility) yielded values of the freezing point constant varying between 5.45 and 6.81 with a reported average value of 5.98 ± 0.24 . Since it has been observed¹ that the behavior of electrolytes and nonelectrolytes is very similar in NMA, these two sets of results probably represent the range of "non-ideality" of the various solutes in concentrations above 0.1 *m* in both instances.^{1,7} It may be noted that there is a considerable uncertainty in the extrapolated value of K_f when the most dilute solutions are 0.1 *m*. By way of contrast the value¹ of 6.65 ± 0.05 obtained from the shorter extrapolations (more dilute solutions) although 10% higher in value, has an uncertainty of less than 1%.

Decomposition of NMA

Additional studies have been undertaken in an effort to rationalize the unusual behavior reported for solutions of NMA and also to explain, if possible, the different values^{1,4} of 27.4 and 31.8 cal/g for the heat of fusion of NMA when measured by different methods. The latter discrepancy is partially explained by the data of Bradbury and Elliot,⁸ who report very careful spectral studies of solid NMA and NMA-*d* which confirm that liquid regions persist in the crystal down to 20° even when the vapor is crystallized under vacuum onto AgCl.

Freezing point measurements which depend on the final melting of microcrystals must also be affected by any impurities present. Since we had observed that the melting point of zone-refined NMA decreased by about 0.2° when maintained in the liquid state for longer than 2 hr, it was decided to attempt to increase the concentration of any decomposition products and identify them. Methylamine is one of the most probable decomposition products, and it was detected in the following manner. A sample of zone-refined NMA was placed in a vacuum fractional distillation apparatus and a liquid trap containing phenyl isothiocyanate at -5° was inserted between the receiver and the vacuum pump. Crystals were formed, which when recrystallized from ethanol melted at 111°. A possible decomposition reaction giving this product is



The other decomposition product, *N,N*-diacetylmethylamine, is difficult to detect by infrared or nmr techniques when it is present in small amounts in NMA because of their similarity of structure. The difficulty in the removal of this decomposition product by distillation is understood when its bp of 198° is compared with that of NMA at 206°. Zone refining is effective because of the amine's melting point of -43° compared to the 30.5° melting point of NMA.

Summary

It appears from the above information that NMA is not suitable as a solvent in which exact measurements of colligative properties are to be made.

1. Dry, liquid NMA decomposes in a short time (~2 hr at 32°) to give a solution containing about 0.03 *m* of impurities as measured by the lowering of the freezing point.

2. This decomposition appears to be accelerated by a metal container or by any solutes which are present.

3. Freezing point depression measurements¹ in dilute solutions of zone-refined material appear to be in error by about 0.2° each, corresponding to this degree of solvent decomposition.

4. Extrapolations from more concentrated solutions⁷ where this error is a smaller portion of the total depression are not accurate.

5. Emf studies³ in which stock solutions of HCl in NMA are maintained in the liquid state for a considerable period of time must, of necessity, be suspect. The reaction of HCl with CH_3NH_2 should increase the equilibrium decomposition of NMA. The use of acidic nonelectrolytes⁷ such as benzoic acid as cryoscopic standards would be expected to have a similar effect.

(7) R. K. Wicker, Ph.D. Dissertation, University of Delaware, 1966.

(8) E. M. Bradbury and A. Elliot, *Spectrochim. Acta*, **19**, 995 (1963).

Reactions of Iodine with Olefins. II. Radiative Neutron Capture Induced Reactions of Iodine-128 with Various C₅ Isomers: Evidence for a Mechanism Other Than Autoradiolysis in the Condensed State

by R. L. Ayres, O. C. Gadeken, and E. P. Rack*

Department of Chemistry, University of Nebraska, Lincoln, Nebraska 68508 (Received September 21, 1970)

Publication costs assisted by the Division of Research, U. S. Atomic Energy Commission

As pointed out in several recent reviews^{1,2} the relative contributions of the various physical processes such as charge, electronic excitation, recoil, and electromagnetic radiation accompanying the (n,γ) activation process in heavy halogens are not well understood. Present mechanistic theories have been derived from studies of the n,γ and I.T. induced organic yields and corresponding product distributions of various halogens in a

(1) J. E. Willard, *Proc. Conf. Chem. Effects Nucl. Transformations*, **1**, 221 (1965).

(2) A. G. Maddock and R. Wolfgang in "Nuclear Chemistry," Vol. 2, L. Yaffe, Ed., Academic Press, New York, N. Y., 1968, pp 185-248.

Table I: Comparison of the Radiolysis Produced ^{131}I Organic Products^a from the Reactor Irradiation of I_2 (^{131}I) Solutions of the Various C_5 Hydrocarbon Isomers with the Corresponding ^{128}I Products^a Produced by the Nuclear Activation of ^{127}I ^{b-d}

System	CH_3I	$\text{C}_2\text{H}_5\text{I}$	$\text{C}_3\text{H}_7\text{I}$	$\text{C}_4\text{H}_9\text{I}$	$\text{C}_5\text{H}_{11}\text{I}$	$\text{C}_6\text{H}_{13}\text{I}$	2- and 3- $\text{C}_5\text{H}_9\text{I}$	1- $\text{C}_5\text{H}_9\text{I}$	CH_2I_2	Total organic yield
Pentane- ^{131}I ^e	6.1	...	14.1	...	10.9	1.0	51.0	17.0	...	
- ^{128}I ^o	6.4	2.0	13.7	1.8	12.3	3.1	35.6	25.0	...	
1-Pentene- ^{131}I ^h	3.0	2.7	7.8	0.5	5.6	3.2	49.8	25.5	1.7	30.6
- ^{128}I ^o	7.4	6.3	8.8	3.8	6.3	5.5	29.1	31.6	4.4	
<i>cis</i> -2-Pentene- ^{131}I ^h	9.3	0.6	5.2	...	4.0	0.8	58.3	15.6	6.3	
- ^{128}I ^o	25.9	4.7	10.3	1.1	7.4	5.2	31.1	4.3	6.6	32.3
<i>trans</i> -2-Pentene- ^{131}I ^h	10.1	...	4.9	...	4.3	1.3	60.8	15.8	1.4	
- ^{128}I ^o	21.6	4.2	11.1	4.2	4.7	5.3	34.5	6.3	7.2	39.9

^a Expressed as per cent of total activity detected. ^b All ^{128}I organic yields determined with 1×10^{-2} mole fraction of I_2 present and 30-sec irradiation time to minimize any radiolytic contributions. All the samples were irradiated in the Omaha, Nebraska V.A. Hospital TRIGA reactor at a flux of 1.1×10^{11} neutrons $\text{cm}^{-2} \text{sec}^{-1}$ and an accompanying γ -irradiation flux of 3×10^{11} eV $\text{g}^{-1} \text{min}^{-1}$. ^c All separations performed on a 10-ft column of 5% by wt di(2-ethylhexyl) sebacate on 50-60 mesh firebrick, temperature programmed from 25 to 125° at 10°/min, with a He flow rate of 100 ml/min. ^d C_4 and C_3 saturated and unsaturated iodides were not separated. ^e Obtained from ref 5. ^f No peak reported. ^o 1×10^{-2} mf I_2 . ^h 1×10^{-3} mf I_2 (^{131}I). ⁱ No peaks detected.

variety of aliphatic, aromatic, and alkyl halide solvents. In most instances such solvent media (target molecules) would be expected to exhibit little or no internal chemical selectivity with respect to product formation *via* an ion-molecule or free-radical mechanism. Therefore, we have investigated the $^{127}\text{I}(n,\gamma)^{128}\text{I}$ and radiolytically induced product distributions of ^{131}I in various pentene isomers which might be expected to exhibit an internal chemical selectivity to the various possible modes of product formation by virtue of the electron-rich double bond.

Studies of the "thermal" addition of iodine to the various pentene isomers employed in this study have shown^{3,4} that iodine adds to the double bond by a light-induced free radical catalyzed process. Therefore, special precautions were taken to shield the samples from light during preparation, irradiation, and extraction. As was previously reported,^{3,4} no detectable "thermal" addition of iodine occurred under these conditions.

The respective organic yields and product distributions resulting from the (n,γ) activation of ^{127}I in *n*-pentane, 1-pentene, *cis*-2-pentene, and *trans*-2-pentene were determined and are presented in Table I for comparison with the corresponding ^{131}I product distributions obtained by radiolytic processes in similar binary I_2 -olefin systems.

Comparison of the ^{131}I radiolytically induced product distributions (by reactor irradiation) with the corresponding ^{128}I product distributions in Table I shows two major differences between the relative quantities of the various products produced by these dissimilar processes. (1) A significant increase in the relative yields of the individual fragmentation products, in most instances $\geq 50\%$ produced by the (n,γ) -activation process in comparison to the radiolytically produced fragmentation products, and (2) the C_5 iodides produced by the radiol-

ysis process exhibit less sensitivity to the isomeric composition of the C_5 hydrocarbon, whereas the yields of the C_5 iodides obtained from the (n,γ) activation show a definite preference for addition of the activated iodine at the position of the double bond.

These differences between the product distributions of the organic iodides resulting in the two processes clearly suggest that the widely accepted "autoradiation hypothesis"⁵ does not adequately explain the total product distributions observed for the (n,γ) activation of iodine in these systems. Therefore, other mechanisms must account, either in part or completely, for the formation of the observed products in these systems.

Several alternate processes, not considered by the "autoradiation hypothesis," are displacement reactions whereby the iodine atom or ion replaces a hydrogen atom or radical from a solvent molecule in a biomolecular process by virtue of its excess kinetic energy and/or the formation of products through ion-molecule reactions with ions produced by the vacancy cascade associated with the internal conversion of the activated iodine and/or the subsequent neutralization of this highly charged species by charge exchange with the surrounding media.

Shaw and coworkers^{6,7} suggested that for an activation process resulting in a subsequent Auger cascade (such as the internal conversion accompanying the radiative neutron capture process of iodine in our sys-

(3) P. S. Skell and R. R. Parlis, *J. Amer. Chem. Soc.*, **86**, 2956 (1964).

(4) (a) R. L. Ayres, C. J. Michejda, and E. P. Rack, *ibid.*, **93**, 1389 (1971); (b) R. L. Ayres, Ph.D. Thesis, The University of Nebraska, 1970.

(5) P. R. Geissler and J. E. Willard, *J. Phys. Chem.*, **67**, 1675 (1963).

(6) M. D. Mia and P. F. D. Shaw, *Radiochim. Acta*, **6**, 172 (1966).

(7) A. J. R. deFonseca, K. Fuller, A. Latham, and P. F. D. Shaw, *Radiochem. Radioanal. Lett.*, **2**, 69 (1969).

tem) the highly charged daughter atom shares its charge among neighboring molecules, causing some to dissociate. Therefore, the activated species will react with the more diffuse radicals, such as those produced by autoradiolysis, only if it escapes chemical combination with the more localized ions and radicals produced by the neutralization of the activated atom. This type of mechanism could be expected to produce both ionic and radical iodine and/or hydrocarbon precursors leading to the eventual stabilization of the (n,γ) -activated ^{128}I in organic combination.

In a recent study of the ion-molecule reactions of various simple olefins, Henis⁸ was able to account for the observed products formed in all of the reactions studied by assuming seven selection factors.⁹ Assuming these qualitative rules also apply to ion-molecule reactions between iodine atoms or ions with olefin ions or molecules, respectively, the observed product distributions found for the (n,γ) -induced reactions of ^{128}I in the C_5 pentene isomers could be accounted for. In particular rules 3 and 4 (see ref 9) would account for the preferential addition at the double bond site and rule 5 for the extremely small quantities of diiodo products observed. Although rule 7 conflicts with the large quantities of methyl iodide found in our systems, particularly for the 2-pentene systems, the potentially higher energy nature of the ion-molecule reactions in our systems could account for this violation. In fact the apparent violation of rule 7 supports the inference that the highly charged and excited iodine specie produced by the (n,γ) activation and subsequent internal conversion processes is responsible for the formation of a portion of the observed products (*i.e.*, a highly energetic species such as this would be expected to furnish sufficient excitation energy to the hydrocarbon molecules forming the solvent cage, during charge neutralization, to overcome the energy barrier for loss of CH_3 radicals by the subsequently ionized pentenes). This is supported by the marked increase in yield for the CH_3I product formed by the (n,γ) activation over that for the radiolytic process, in that the production of ions by radiolytic processes would be expected to more closely resemble the low

energy electron impact ionization employed by Henis⁸ than the charge transfer process envisioned for the (n,γ) activation.

Gas phase studies have shown¹⁰⁻¹² the bimolecular replacement reactions of species attacked by ^{128}I to result in total organic yields of only a few per cent, except in CH_4 systems. Thus this type of process would not be expected to contribute appreciably to the total yields observed in condensed systems unless the probability for this type of reaction is greatly altered by the change in phase.

It is well known, however, that the change of phase could greatly alter the probability of product formation *via* a bimolecular replacement reaction by caging of the ^{128}I in the vicinity of radicals and excited molecules produced by deposition of the kinetic energy of the recoil iodine in or near the solvent cage. Also, the greatly increased collision density in the condensed phase would be expected to significantly increase the stabilization of the ^{128}I -containing products formed by kinetic energy dependent processes (*i.e.*, bimolecular displacement reactions) could also account for the observed differences in the relative product distribution observed in this work.

Acknowledgment. The support of the U. S. Atomic Energy Commission, Contract No. At(11-1)-1617, is gratefully acknowledged. This is AEC document COO-1617-25.

(8) J. M. S. Henis, *J. Chem. Phys.*, **52**, 282 (1970).

(9) Selection rules reported by Henis: (1) no significant rearrangement of parent ions; (2) positive charge located at a secondary carbon in the parent ion; (3) site of the unpaired electron may be considered the active or attacking site on the ion; (4) addition occurs at either double-bond site (steric factors may favor primary sites when they are available); (5) fragmentation involving more than one bond is not probable; (6) fragmentation occurs most favorably at the tertiary carbon in the intermediate; (7) loss of CH_3 radicals generally will not occur (possibly due to unfavorable thermochemistry).

(10) E. P. Rack and A. A. Gordus, *J. Chem. Phys.*, **34**, 1855 (1961); *ibid.*, **36**, 287 (1962).

(11) G. Levey and J. E. Willard, *ibid.*, **25**, 904 (1956).

(12) A. A. Gordus and J. E. Willard, *J. Amer. Chem. Soc.*, **79**, 4609 (1957).

RADIATION CHEMISTRY

ADVANCES IN CHEMISTRY SERIES NOS. 81 AND 82

Seventy-seven papers and 34 abstracts from the International Conference on Radiation Chemistry at Argonne National Laboratories, chaired by Edwin J. Hart. Includes review and research papers from 12 countries besides U.S., Canada, and England, including 8 from U.S.S.R. and two other East European countries.

Volume I groups papers on radiation in aqueous media, radiation of biological systems, dosimetry, and one plenary lecture.

Volume II has papers on radiation of gases, of solids, and of organic liquids, plus three plenary lectures.

No. 81 Radiation Chemistry—I
No. 82 Radiation Chemistry—II

616 pages with index

558 pages with index

Each \$16.00

Ordered together \$30.00

Cloth (1968)

Set of L.C. cards free with library orders.

Other books in the ADVANCES IN CHEMISTRY SERIES in physical and colloid chemistry include:

No. 68 Mössbauer Effect and its Application in Chemistry. Ten papers that will familiarize chemists with Mössbauer spectroscopy as an analytical tool, for studying chemical bonding, crystal structure, electron density, magnetism, and other properties. 178 pages

Cloth (1967) \$8.00

No. 67 Equilibrium Concepts in Natural Water Systems. Sixteen papers represent the collaboration of aquatic chemists, analytical chemists, geologists, oceanographers, limnologists, and sanitary engineers, working with simplified models to produce fruitful generalizations and valuable insights into the factors that control the chemistry of natural systems. 344 pages

Cloth (1967) \$11.00

No. 64 Regenerative EMF Cells. Seventeen papers survey current progress and research on regenerative systems for converting and storing electrical energy. Principal emphasis is on thermally regenerative systems, but chemical and photochemical systems are considered. 309 pages

Cloth (1967) \$11.00

No. 63 Ordered Fluids and Liquid Crystals. Twenty-two studies on characterization, properties, and occurrence of these phenomena in many substances such as tristearin, p-azoxyanisole, mono- and di-hydric alcohols, phospholipids and polypeptides. 332 pages

Cloth (1967) \$11.50

No. 58 Ion-Molecule Reactions in the Gas Phase. Eighteen papers survey spectrometric and other methods for producing and studying ion-molecule reactions, such as pulsed sources for studying thermal ions, reactions in flames and electrical discharges. 336 pages

Cloth (1966) \$10.50

No. 54 Advanced Propellant Chemistry. Primarily directed to the search for new oxidizers; 26 papers survey oxygen-containing oxidizers, fuels and binders, fluorine systems including oxygen difluoride and difluoramines and liquid systems. 290 pages

Cloth (1966) \$10.50

No. 47 Fuel Cell Systems. Developments in theory, performance, construction, and new systems for the energy converter that is proving itself in military and space uses. 360 pages

Cloth (1965) \$10.50

No. 43 Contact Angle, Wettability, and Adhesion. Twenty-six papers on theoretical and practical approaches to wettability and adhesion; with summary of the surface chemical studies of W. A. Zisman, the 1963 Kendall Award winner. 389 pages

Cloth (1964) \$10.50

No. 40 Mass Spectral Correlations. By Fred W. McLafferty. Over 4000 spectral listed by mass/charge ratios of fragment ions with the most probable original structures for each. 117 pages

Paper (1963) \$6.00

No. 33 Solid Surfaces and the Gas-Solid Interface. Thirty-seven papers from the Kendall Award Symposium honoring Stephen Brunauer. Theory and techniques for studying surface phenomena. 491 pages

Cloth (1961) \$12.00

No. 31 Critical Solution Temperatures. By Alfred W. Francis. CST answers the question, "Do two liquids mix?" and is widely used for screening solvents. Over 6000 systems are included, 70% with a hydrocarbon as one component; nearly 1100 non-hydrocarbon solvents are listed. 246 pages

Cloth (1961) \$8.00

No. 29 Physical Properties of Chemical Compounds—III. By Robert R. Dreisbach. Supplements earlier volumes with properties of 434 aliphatic compounds and 22 miscellaneous compounds and elements. Index to volumes I, II, and III. 489 pages

Cloth (1961) \$10.00

No. 25 Physical Functions of Hydrocolloids. Papers on natural gums, gelatin pectins and related polysaccharides, and theoretical and functional aspects of hydrocolloids, emulsions, foams, and dispersions. Strong food industry emphasis. 103 pages

Paper (1960) \$5.00

No. 22 Physical Properties of Chemical Compounds—II. By Robert R. Dreisbach. Properties of 476 alkanes, haloalkanes, alkenes, haloalkenes, diolefins, and alkynes. 491 pages

Cloth (1959) \$10.00

No. 18 Thermodynamic Properties of the Elements. By D. R. Stull and G. C. Sinke. Tabulated values of heat capacity, heat content, entropy, and free energy function of solid, liquid, and gas states of first 92 elements in range of 298° to 3000°K. Some auxiliary data frequently included. 491 pages

Cloth (1956) \$8.00

No. 15 Physical Properties of Chemical Compounds. By Robert R. Dreisbach. Tables of parameters for calculating physical properties of 511 organic cyclic compounds. 536 pages

Cloth (1955) \$10.00

All books postpaid in U.S. and Canada; plus 30 cents in PUAS and elsewhere.

Order from: SPECIAL ISSUES SALES,
AMERICAN CHEMICAL SOCIETY
1155 SIXTEENTH ST., N.W.
WASHINGTON, D.C. 20036

CHEMICAL REACTIONS IN ELECTRICAL DISCHARGES

ADVANCES IN CHEMISTRY SERIES NO. 80

Thirty-seven papers from a symposium sponsored by the Division of Fuel Chemistry and the Division of Physical Chemistry of the American Chemical Society, chaired by Bernard D. Blaustein.

A wide range of topics are covered in these papers by chemists, physicists, and engineers including treatments of decomposition and dissociation reactions, ion-molecule reactions, chemical syntheses, and chemical engineering aspects and physics of reactions in electrical discharges.

514 pages with index

Clothbound (1969)

\$15.00

Set of L.C. cards free with library orders upon request

Other books in ADVANCES IN CHEMISTRY SERIES on topics of industrial interest include:

- | | |
|---|--|
| <p>No. 85 Stabilization of Polymers and Stabilizer Processes. Twenty-two papers survey progress and report recent work on a variety of stabilization problems—thermal stabilization, antioxidants and antiozonants for polyolefins, rubbers, and rubbers containing polymers. Other topics include microbial stabilization, ultraviolet light absorbers, and fire retardants. 332 pages
Cloth (1968) \$12.00</p> <p>No. 78 Literature of Chemical Technology. Forty articles discuss the literature of many aspects of chemical technology, including chlor-alkali and electrochemistry, ceramics, rocket propulsion, photography, medicinal chemistry, leather and glue, waxes, textile, paper, soap, plastics, coatings, explosives, petroleum, dyes, aerosols, pesticides, and foods. Special attention is given to rubber with eight articles and one on carbon black. Included for each article is discussion of special literature sources and services, books, periodicals, patent classes, and bibliographies. 732 pages
Cloth (1968) \$17.50</p> <p>No. 76 Oxidation of Organic Compounds—II. Thirty-one papers on gas phase oxidations, homogeneous catalysis, applied oxidation, and synthetic processes. 438 pages
Cloth (1968) \$13.50</p> <p>No. 70 Homogeneous Catalysis. Industrial Applications and Implications. Concentrates on reactions in solution. Reviews the kinds of substances that can be used as homogeneous catalysts and how they function, contrasts homogeneous with heterogeneous catalysis, reviews industrial applications of homogeneous catalysis, and treats in detail many special topics. 283 pages
Cloth (1968) \$10.50</p> <p>No. 69 Fuel Gasification. Waning natural gas supplies and the threat of nuclear fuels are renewing interest in converting solid fuels to high B.t.u. gas. Sixteen studies survey current research in the U.S. and elsewhere from which commercial processes seem imminent. 276 pages
Cloth (1967) \$10.50</p> <p>No. 64 Regenerative EMF Cells. Seventeen papers survey current progress and research on regenerative systems for converting and storing electrical energy. Principal emphasis is on thermally regenerative systems, but chemical and photochemical systems are considered. 309 pages
Cloth (1967) \$11.00</p> <p>No. 51 Selective Oxidation Processes. Surveys methods for selectively oxidizing petroleum fractions by vapor phase and liquid phase processes, such as hydroxylation of aromatics and olefins; covers use of SO₂, NO₂, and O₃ and surveys carbanion oxidation. 177 pages
Cloth (1965) \$8.00</p> | <p>No. 48 Plasticization and Plasticizer Processes. Seventeen papers survey recent studies on plasticizer action, properties, and production. Includes chapters on glass transition, plasticizer mobility, processes for phthalates and other plasticizers, and antiplasticizers. 200 pages
Cloth (1965) \$8.00</p> <p>No. 46 Patents for Chemical Inventions. What to do about your patentable idea before you call the attorney. 117 pages
Cloth (1964) \$5.50</p> <p>No. 38 Saline Water Conversion—II. Fourteen papers from two symposia; includes recovery of minerals from sea water, minimizing scale formation, wiped thin-film distillation, diffusion still, solar flash evaporation, osmosis, electro dialysis (3 papers), research in Israel, hydrate process. 199 pages
Paper (1963) \$8.00</p> <p>No. 34 Polymerization and Polycondensation Processes. An I&EC Division symposium with emphasis on unit processes. Twenty-one papers on addition polymerization, polycondensation reactions, commercial polymerization processes, and equipment design. 260 pages
Paper (1962) \$10.00</p> <p>No. 27 Saline Water Conversion. A Water and Waste Chemistry Division symposium; includes thermodynamics of desalting, solvent extraction, freezing, centrifugal phase barrier recompression distillation, multistage flash evaporation, ion exchange, osmosis, and electrochemical demineralization. 246 pages
Paper (1960) \$9.00</p> <p>No. 21 Ozone Chemistry and Technology. Sixty papers from the International Ozone Conference; includes ozone chemistry, high concentration ozone, ozone analysis and technology, formation in electrical discharge, toxicity, sterilization, and water purification. 465 pages
Cloth (1959) \$10.00</p> <p>No. 19 Handling and Uses of Alkali Metals. Nineteen articles on the chemistry, manufacture, and use of the alkali metals; five are devoted solely or partly to lithium, two to potassium, the remainder to sodium. 177 pages
Paper (1957) \$7.00</p> <p>No. 5 Progress in Petroleum Technology. Survey of 25 years of progress at the ACS Diamond Jubilee. Thirty-two papers on all aspects of petroleum processing and products. 392 pages
Cloth (1951) \$8.00</p> |
|---|--|

All books postpaid in U.S. and Canada; plus 20 cents foreign and PUAS.

Order from SPECIAL ISSUES SALES
AMERICAN CHEMICAL SOCIETY
1155 SIXTEENTH ST., N.W.
WASHINGTON, D.C. 20036